Mario Barbatti
Antonio Carlos Borin
Susanne Ullrich   *Editors*

# Photoinduced Phenomena in Nucleic Acids I

## Nucleobases in the Gas Phase and in Solvents

Springer

**355**
# Topics in Current Chemistry

## Aims and Scope

The series Topics in Current Chemistry presents critical reviews of the present and future trends in modern chemical research. The scope of coverage includes all areas of chemical science including the interfaces with related disciplines such as biology, medicine and materials science.

The goal of each thematic volume is to give the non-specialist reader, whether at the university or in industry, a comprehensive overview of an area where new insights are emerging that are of interest to larger scientific audience.

Thus each review within the volume critically surveys one aspect of that topic and places it within the context of the volume as a whole. The most significant developments of the last 5 to 10 years should be presented. A description of the laboratory procedures involved is often useful to the reader. The coverage should not be exhaustive in data, but should rather be conceptual, concentrating on the methodological thinking that will allow the non-specialist reader to understand the information presented.

Discussion of possible future research directions in the area is welcome.

Review articles for the individual volumes are invited by the volume editors.

**Readership: research chemists at universities or in industry, graduate students**.

More information about this series at
http://www.springer.com/series/128

Mario Barbatti • Antonio Carlos Borin •
Susanne Ullrich

Editors

# Photoinduced Phenomena in Nucleic Acids I

Nucleobases in the Gas Phase and in Solvents

With contributions by

M. Barbatti · V. Barone · A.C. Borin ·
C.E. Crespo-Hernández · M.S. de Vries · A. Giussani ·
L. González · M. Hochlaf · R. Improta · S. Mai ·
P. Marquetand · L. Martínez-Fernández · S. Matsika ·
M. Merchán · M. Pollum · M. Richter · D. Roca-Sanjuán ·
M. Schwell · J. Segarra-Martí · S. Ullrich

∅ Springer

*Editors*
Mario Barbatti
Max-Planck-Institut für Kohlenforschung
Mülheim an der Ruhr
Germany

Susanne Ullrich
Department of Physics and Astronomy
The University of Georgia
Athens
Georgia, USA

Antonio Carlos Borin
Institute of Chemistry
University of São Paulo
São Paulo
Brazil

Printed on acid-free paper

# Preface

Photoinduced processes in nucleic acids are phenomena of fundamental importance for our biosphere. Ultraviolet solar radiation has been a continuous factor of evolutionary pressure since early biotic ages by triggering mutations, cell death, and carcinogenesis. The study of how UV radiation impacts nucleic acids has a long history, which parallels the evolution of our understanding of genetics from the beginning of the twentieth century. It has, however, been mainly in the last decade that major knowledge gaps have been filled in the field. This has been achieved thanks to the development of advanced spectroscopic techniques and computational models, which have allowed real-time observation and simulation of the evolution of electronic excitations caused by radiation.

This book embraces a broad range of topics in nucleic-acid research. It brings together leading specialists from different subfields, providing a deep overview of the current state of knowledge, including recent achievements, open problems, and comprehensive lists of references. While each chapter was developed as a thematic and self-contained text, a certain degree of overlap was maintained to interrelate individual contributions. Consequently, the chapters can be read in any order and the reader can profit from the diverse perspectives on the same subjects originating from different authors.

In the two volumes, theoretical, computational, experimental, and instrumental aspects are discussed. It is hoped, therefore, that they are of value to a wide spectrum of readers – students, scientists, and technologists. The first volume focuses (but not exclusively) on the spectroscopy and dynamics of photoexcited nucleobases and their analogues in different environments. The emphasis of the second volume is on larger fragments, from base pairs to duplexes, and on phenomenological aspects, including physiological effects, prebiotic chemistry, and charge-transport phenomena.

Editing a book of such a broad scope, involving so many different topics, sometimes felt an overwhelming experience. It began with the difficult task of selecting, among a large community composed of highly-active and successful researchers, those who would be invited to contribute a chapter. Although we had

to make some hard choices, we think that we have achieved a balanced result, with an approximately equal share of experimentalists and theorists from more than ten countries in Europe, North and South America, and Asia. Considering that the invited contributors are leaders in their fields, they were free to organize their chapters, taking only into account the broad subject area provided by us.

We are glad that, exactly as planned, the book turned out to be a very well integrated collection of independent chapters, where the focus is on reviews of particular topics rather than on the research of individual groups or the presentation of new data. Naturally, we must acknowledge all the authors for their efforts and insightful contributions. We are also grateful to all the reviewers of individual chapters, whose constructive critique was invaluable to the success of this text.

We thank Massimo Olivucci, who invited us to edit these volumes for Topics in Current Chemistry. We also express our gratitude to Arun Manoj Jayaraman from Springer, who patiently coordinated the publishing project.

For us, editing this book was a challenging task, constantly bringing us face-to-face with phenomena outside our area of expertise. We can only hope that the readers enjoy the same informative and enlightening experience.

Mario Barbatti
Antonio Carlos Borin
Susanne Ullrich

# Contents

# Photoinduced Processes in Nucleic Acids

**Mario Barbatti, Antonio Carlos Borin, and Susanne Ullrich**

**Abstract** Photoinduced processes in nucleic acids are phenomena of fundamental interest in diverse fields, from prebiotic studies, through medical research on carcinogenesis, to the development of bioorganic photodevices. In this contribution we survey many aspects of the research across the boundaries. Starting from a historical background, where the main milestones are identified, we review the main findings of the physical-chemical research of photoinduced processes on several types of nucleic-acid fragments, from monomers to duplexes. We also discuss a number of different issues which are still under debate.

**Keywords** DNA fragments · Excited states · Excitons · Nucleobases · UV radiation

## Contents

M. Barbatti (✉)
Max-Planck-Institut für Kohlenforschung, Kaiser-Wilhelm-Platz 1, 45470 Mülheim an der Ruhr, Germany
e-mail: barbatti@kofo.mpg.de

A.C. Borin (✉)
Institute of Chemistry, NAP-PhotoTech, The USP Consortium for Photochemical Technology, University of São Paulo, Av. Prof. Lineu Prestes, 748 05508-000 São Paulo, SP, Brazil
e-mail: ancborin@iq.usp.br

S. Ullrich (✉)
Department of Physics and Astronomy, University of Georgia, Athens, GA 30602, USA
e-mail: ullrich@physast.uga.edu

# Abbreviations

| | |
|---|---|
| (6–4)PD | (6–4) Pyrimidine-pyrimidone dimer |
| 1Me-Cyt | 1-Methyl-cytosine |
| 5F-Cyt | 5-Fluoro-cytosine |
| 9Me-Ade | 9-Methyl-adenine |
| ADC(2) | Algebraic diagrammatic construction to second order |
| Ade | Adenine |
| Ado | Adenosine |
| AMD | Adiabatic molecular dynamics |
| AMP | Adenosine monophosphate |
| AT | Adenine–thymine pair |
| CASSCF | Complete active space self-consistent field |
| CC2 | Coupled-cluster to approximated second order |
| CI | Configuration interaction |
| CPD | Cyclobutane pyrimidine dimer |
| Cyt | Cytosine |
| d(ApG) | Adenine–guanine dinucleotide |
| dA | Deoxyadenosine |
| dAMP | Deoxy-AMP |
| DFT | Density functional theory |
| dT | Thymidine |
| FU | Fluorescence up-conversion |
| GC | Guanine–cytosine pair |
| GP | Gas phase |
| Gua | Guanine |
| IC | Internal conversion |
| MRCI | Multireference configuration interaction |
| R2PI | Resonant two-photon ionization |
| T:T | Stacked thymines |
| T<>C | Thymine–cytosine CPD |
| T<>T | Thymine–thymine CPD |
| TA | Transient absorption |
| TDDFT | Time-dependent density functional theory |

| TD-DFTB | Time-dependent density functional tight binding |
| Thy | Thymine |
| TR-IY | Time-resolved ion yield |
| TR-PES | Time-resolved photoelectron spectroscopy |
| TR-TAS | Time-resolved transient absorption spectroscopy |
| TSH | Trajectory surface hopping |
| Ura | Uracil |
| W | Water |

# 1 Introduction

Interest in photoinduced effects in nucleic acids is deeply linked to the history of DNA itself. In fact, less than one decade after Miescher isolated the "nuclein" in 1869 [1], the bactericidal effect of UV radiation was discovered and became a fertile field of investigation [2]. When it was finally determined in 1928 that this lethal effect of UV radiation was caused by its absorption by nucleic acids, it raised the first speculations that DNA could be related to growth and reproduction [3], a fact only finally confirmed in 1944 [4]. Since then, immense effort has been dedicated to understanding exactly how radiation and nucleic acids interact. One major motivation for this interest rests, naturally, on health aspects: UV radiation is the main environmental agent triggering skin carcinogenesis [5]. Furthermore, mutagenic effects of radiation have also helped to shape life on Earth. In fact, it might be that even the evolutionary selection of nucleic acids as hereditary agents was partially induced by their physical-chemical response to the very high levels of UV radiation in the early-biotic world. From these initial motivations, the research on photoinduced effects in nucleic acids also points to a future where optical devices will take advantage of the unique charge-transport properties of these biological polymers.

In this chapter, we quickly survey many of these themes while pointing to specific literature. Most of these topics will also be examined in depth in the remaining chapters of this book. Given the overwhelming breath of the field, spreading over different disciplines, from basic physical chemistry to medical and applied engineering, even a quick survey needs to be limited to restricted boundaries. We will focus on experimental and theoretical research on physical-chemical aspects of how nucleic-acid fragments respond to photoactivation.

This chapter is organized as follows. In Sect. 2 the main historical milestones of the field are summarized; a survey of the basic properties of the absorption and emission spectra of nucleic acids is presented in Sect. 3. In Sect. 4 the current state of knowledge concerning the photodynamics of several nucleic-acid fragments, from monomers to duplexes, is presented, based mainly on results from time-resolved experiments and computational modeling. Finally, in Sect. 5, several different topics currently under debate are discussed. Needless to say, the selection of these topics was a very personal choice, reflecting our specialties.

## 2   Historical Background

In this section we survey the main milestones in research on photoinduced effects in nucleic acids (Table 1), bringing us to the current state of this field.

The knowledge that UV radiation may have a deleterious effect on organisms dates back to long before the discovery of how nucleic acids encode genetic information. In 1877, Downes and Blunt discovered that sunlight has a bactericidal effect [2] and later, in 1893, Ward demonstrated that this effect was caused by the "blue-violet half of the spectrum" [20]. At the dawn of the twentieth century, Finsen showed that the bactericidal action of UV radiation could be used to cure cutaneous tuberculosis [7]. For this discovery he was awarded the Nobel Prize in Physiology or Medicine in 1903.

In the late 1920s, Altenburg demonstrated that UV radiation could induce mutations in fruit flies [3] and Gates found that the bactericidal action spectrum peaked at 260–270 nm and correlated with "some single essential substance in the cell" [21]. Gates also seems to have been the first to recognize that this substance could be nucleic acids. In fact, he noted that the association between nucleic-acid absorption and lethal action would have "wider significance in pointing to these substances as essential elements in growth and reproduction" [9], an exceptional insight which would be confirmed only years later when the role of DNA in heredity was finally determined [4]. Meanwhile, one can find, for instance, claims that nucleic acids "act as a protecting sheath to the encased proteins, thus preventing their dissociation by the action of ultraviolet" [22].

**Table 1**   Milestones in the investigations of UV effects on nucleic acids

| Year | Milestones |
| --- | --- |
| 1865 | Maxwell theory of electromagnetism |
| 1869 | Miescher discovers DNA [1] |
| 1877 | Bactericidal effect of sunlight is discovered [2] |
| 1896 | Unna proposes that UV radiation could cause skin cancer [6] |
| 1903 | Finsen is awarded the Nobel Prize for using UV to treat cutaneous tuberculosis [7] |
| 1928 | Mutagenic effect of UV in fruit flies is observed [3] |
| 1928 | Relation between UV and skin cancer in animals is shown experimentally [8] |
| 1928 | Gates associates bactericidal action to nucleic acid absorption [9] |
| 1944 | Heredity function of DNA is discovered [4] |
| 1953 | Watson and Crick double-helix model is published [10] |
| 1962 | Photoinduced pyrimidine dimers as cause of DNA damage is proposed [11] |
| 1982 | UV-induced mutation hotspots in DNA are identified [12] |
| 1995 | Crystal structure of DNA photolyase from *E. coli* is determined [13] |
| 2001 | Time-resolved spectroscopy of nucleosides is published [14, 15] |
| 2002 | Conical intersections in nucleobases are computationally determined [16–18] |
| 2007 | Ab initio nonadiabatic dynamics simulations of cytosine–guanine pair are published [19] |

In 1896, Unna associated excessive exposure to solar radiation, especially UV, to skin cancer [6]. In the 1930s, through animal research, it was established that UV radiation could cause skin cancer [8, 23, 24]. Consequently, a large amount of effort was dedicated to the characterization of UV-induced carcinogenesis (see [25] for a review) and also photoinduced repair [26]. The determination of the molecular structure of DNA [10] paved the way for the discovery that photochemically-formed pyrimidine dimers cause biological damage [11].

The spectroscopy of nucleic acids has been investigated since the 1930s [27–30]. The very low luminescence of these compounds under physiological conditions – an important indicator of the occurrence of internal conversion – has also been known for a long time [29, 31, 32]. Nevertheless, time-resolved spectroscopy of nucleic acids has been a much more recent development [14, 15].

Computational investigations into the electronic excitation of nucleic-acid fragments date back to the 1970s, when a number of simulations based mainly on semiempirical approaches helped with the assignment of measured absorption spectra. These early works are reviewed in [33]. In the 1990s, with the advance of computational capabilities and theoretical methods, the first high-level simulations of the absorption and emission spectra of the nucleobases were reported [34–36]. In the early 2000s, the importance of conical intersections for explaining the photophysics of nucleobases [16–18] emerged from a series of studies performed by a number of groups. A few years later, the first ab initio nonadiabatic dynamics simulations of nucleobases and base pairs were published [19, 37].

## 3   Absorption and Emission

The five nucleobases composing DNA and RNA – adenine, guanine, cytosine, thymine, and uracil (Scheme 1) – are good UV chromophores, with absorption peaks at about 260 and 200 nm (Fig. 1 and Table 2) and maximum extinction coefficients between 8,000 and 15,000 $M^{-1}$ $cm^{-1}$ [28–30, 39, 42]. For a discussion of high resolution spectroscopy of nucleic acids, see de Vries [43]; for photoelectron spectroscopy, see DOI: 10.1007/128_2014_550.

In comparison, the DNA spectrum peaks at 260 nm and has an extinction coefficient of about 6,800 $M^{-1}$ $cm^{-1}$ [38]. It presents strong hyperchromism and the absorbance of denatured DNA is about 30% higher than that of native DNA [44]. Together with urocanic acid (peaking at 280 nm) [45], proteins (peaking at 280 nm because of aromatic residues), and melanin (broad absorption below 300 nm) [46], DNA is one of the main UV chromophores in mammalian skin [47]. In fact, common analytical methods for determining the DNA concentration and protein contamination in DNA samples are based on the measurement of the 260-nm absorption and of the 280/260-nm absorption ratio [48].

Thanks to the UV absorption by the ozone layer in the atmosphere, the solar irradiance in this range of wavelengths is very much reduced at the Earth's surface (Fig. 1) [40, 41]. Although this greatly decreases the probability of photoexcitation of DNA, it still occurs, being the main cause of skin cancer [49].
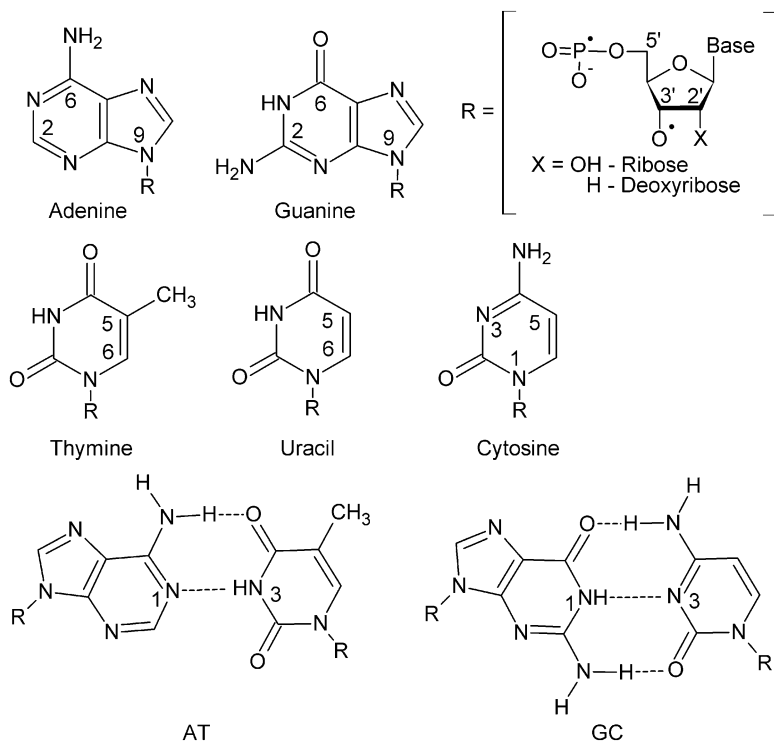
**Scheme 1** Natural nucleobases and base pairs
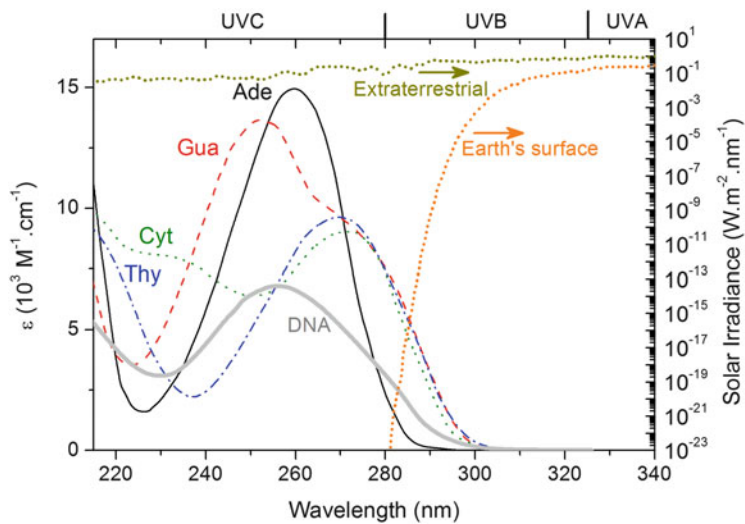


**Fig. 1** Absorption spectra of native human DNA [38] and of DNA nucleobases in water [39]. Terrestrial [40] and extraterrestrial [41] solar UV irradiance

**Table 2** Band maximum ($\lambda_{max}$), extinction coefficient ($\varepsilon$), and quantum yield ($\phi$) for absorption and fluorescence of the nucleobases in water (W, pH 7) and in the gas phase (GP). sh - shoulder

| Base | Phase | Absorption | | | Fluorescence | | |
|------|-------|------------|---|------|--------------|---|------|
| | | $\lambda_{max}$ (nm) | $\varepsilon$ ($10^3$ M$^{-1}$ cm$^{-1}$) | Refs. | $\lambda_{max}$ (nm) | $\phi$ ($10^{-4}$) | Refs. |
| Ade | W | 260, 207 | 15, – | [28, 39] | 321 | 2.6 | [32] |
| | GP | 252, 207 | 12, – | [28] | | | |
| Gua | W | 252, 271 (sh) | 14, 10 | [39] | 328 | 3.0 | [32] |
| | GP | 293, 284 | | [29] | | | |
| Cyt | W | 269, 230 | 10, 8 | [39] | 314 | 0.8 | [32] |
| | GP | 290 (sh),~260 | | [28] | | | |
| Thy | W | 207, 269 | 10, 8 | [30, 39] | 338 | 1.0 | [33] |
| Ura | W | 258, 202 | 8, 9 | [42] | 309 | 0.5 | [32] |
| | GP | 244, 205 (sh) | | [28] | | | |

DNA luminescence is very low, similar to its building blocks, whose quantum yields are on the order of $10^{-4}$ (Table 2) [32, 33]. This implies that dissipation of the UV radiation energy happens through internal conversion mechanisms, which time-resolved spectroscopy and computational simulations have determined to occur on picosecond timescales for individual nucleobases and paired bases, but which can take much longer in single and double strands [39].

## 4  Photodynamics

Motivated by the need to understand the mutagenic and carcinogenic effects of UV radiation, photodynamic properties of the individual nucleobases, nucleosides, nucleotides, base pairs, and single and double strands have been intensively studied, as can be appreciated throughout this book. Collectively, the literature has demonstrated the validity of a bottom-up approach, in which the understanding acquired at the molecular level is transitioned, in a stepwise fashion, from minimal models to a realistic system. The individual steps contributing to this endeavor are reviewed below and a short survey of experimental results is given in Table 3.

From monomers in the gas phase to DNA in vivo, different processes act to stabilize the excited nucleic-acid system (Fig. 2). At the monomer level (Fig. 2a), deactivation after UV excitation is ultrafast (subpicosecond to picosecond time scales) and involves conical intersections induced either by ring deformation or by hydrogen dissociation [85]. In the case of base pairs (Fig. 2b), the internal conversion pathways followed by the monomers are complemented by intermolecular ultrafast proton-transfer processes [86]. When dealing with stacked bases (Fig. 2c), single strands, and double strands, the situation is blurred, as the relaxation processes become very much dependent on the specific sequence of nucleobases. The overall picture is that monomer and base-pair pathways are replaced by – or may co-exist with – excimer processes [65]. In vivo, the situation is even more complex

**Table 3** Survey of experimental time constants for deactivation of nucleobases, derivatives, and other DNA fragments. When numbers are given for method, they indicate the probe wavelength (nm) for ionization in TRPES experiments

| | | $\tau_1$ (fs) | $\tau_2$ (ps) | $\tau_3$ (ps) | $\tau_4$ (ns) | $\lambda_{pump}$ (nm) | Method | Refs. | Other Refs. |
|---|---|---|---|---|---|---|---|---|---|
| Ade | GP | 100 | 1.1 | – | – | 267 | 2 × 400 | [50] | [51–64] |
| | W | - | 0.64 | 8.5 | – | 266 | 238 | [53] | |
| 9Me-Ade | GP | 110 | 1.3 | – | – | 267 | 2 × 400 | [50] | |
| Ado | W | – | 0.21 | – | – | 266 | 238 | [53] | |
| AMP | W | – | 0.33 | – | – | 266 | TA | [65] | |
| Gua | GP | 148 | 0.36 | – | – | 267 | 2 × 400 | [50] | [59, 62, 66] |
| | GP | 140 | 2.3 | – | – | 267 | 2 × 400 | [67] | |
| Cyt | GP | 160 | – | 1.86 | – | 267 | 2 × 400 | [50] | [51, 56, 59, 62, 68–72] |
| | W | – | – | 1.0 | – | 265 | TA | [73] | |
| 5F-Cyt | GP | – | 0.3 | 17 | – | 266 | 3 × 800 | [74] | |
| | W | – | – | 88 | – | 265 | TA | [73] | |
| 1Me-Cyt | GP | – | 0.5 | – | – | 270 | 3 × 800 | [74] | |
| Thy | GP | 105 | – | 5.12 | – | 267 | 2 × 400 | [50] | [51, 59, 62, 65, 70, 75–77] |
| | GP | – | – | 6.4 | 0.1 | 267 | 3 × 800 | [59] | |
| Ura | GP | 130 | – | 1.05 | – | 267 | 2 × 400 | [50] | [51, 56, 59, 70, 75–78] |
| | GP | – | – | 2.4 | – | 267 | 3 × 800 | [59] | |
| AT | GP | 120 | 1.3 | 6.1 | – | 267 | 3 × 800 | [79] | |
| $A_2$ | GP | 180 | 1.5 | >10 | – | 267 | 3 × 800 | [79] | |
| $T_2$ | GP | 100 | 2.3 | >100 | – | 267 | 3 × 800 | [79] | |
| d(ApG) | W | <100 | 0.2–2.5 ($IC_{monomer}$) | 6–10 (AG*) | 0.124 (AG*/$S_0$) | 260 | TA/FU | [80] | |
| $(dA)_{18}$ | W | <400 (FC/AA*) | – | – | 0.126 (AA*/$S_0$) | 266 | TA | [65] | [81, 82] |
| $(dT)_{18}$ | $D_2O$ | – | ~0.54 ($\pi\pi$*/$S_0$) | ~1 (CPD) | 0.1 ($n\pi$*/$S_0$) | 272 | IR TA | [83] | [65] |

|  | W |  |  |  |  |  |  |
|---|---|---|---|---|---|---|---|
| (dA)$_{18}$·(dT)$_{18}$ | W | <400 (FC/AA*) | – | | 0.150 (AA*/S$_0$) | 266 | TA | [65] |
| d(AT)$_9$·d(AT)$_9$ | W | <400 (FC/AT*) | – | | 0.051 (AT*/S$_0$) | 266 | TA | [65] |
| T<>T → T:T | | – | <10 (C5-split) | 90 (C6-split) | 0.25, 0.7 (CT) | 400 | TA | [84] |
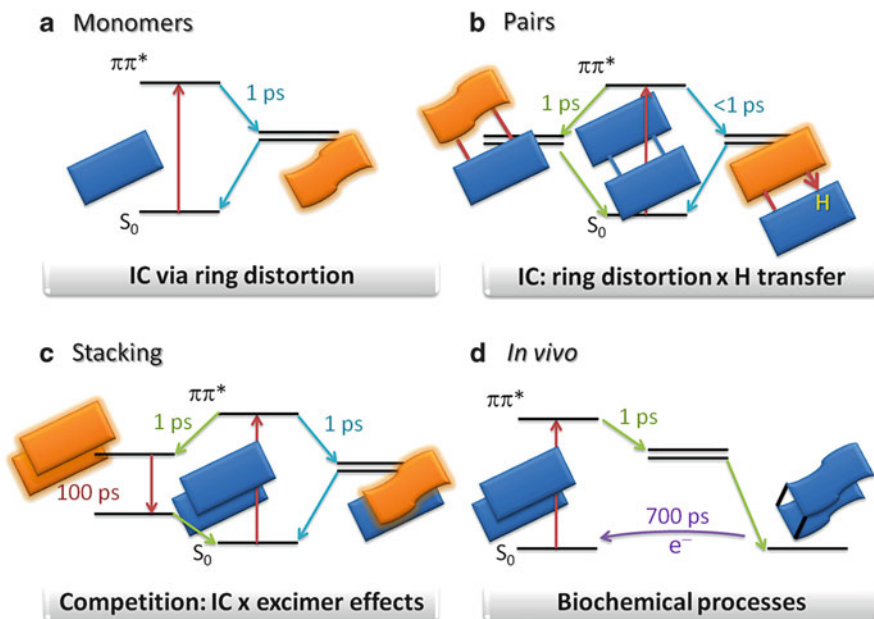
**Fig. 2** Schematic excitation and relaxation processes in monomers, base pairs, strands, and in vivo. (**a**) For monomers, ultrafast internal conversion (IC) takes place via ring distortion and dissociation processes [85]. (**b**) For base pairs, in addition to monomer processes (*left*), ultrafast IC may also occur via proton transfer along the hydrogen bonds (*right*) [86]. (**c**) For stacked bases, ultrafast formation of long-living excimers (*left*) competes with ultrafast IC in the monomers (*right*) [65]. (**d**) In cellular medium, ultrafast IC causes pyrimidine dimerization, while diverse enzymatic processes may be activated for repair in longer time scales [54]

(Fig. 2d) and, besides all these processes, diverse biochemical mechanisms are in action, including enzymatic excision and photorepair of pyrimidine dimers [84].

## 4.1 Monomers

The photophysical characteristics of all nucleobases will be discussed individually in this section. Despite their structural differences, all nucleobases share some common photophysical features and general trends [51]. (1) Ultrafast internal conversion is completed within a few picoseconds. (2) Lifetimes of the purine bases are generally shorter and described by a single time constant. (3) Pyrimidine bases show more complex deactivation dynamics with multiple and slightly longer time constants. (4) All time constants generally decrease with higher initial excitation energy. (5) The excited-state lifetimes of the nucleosides in polar solvents are generally shorter than those of the gas-phase species. (6) Structural modification of nucleobases may change the lifetimes by orders of magnitude. These experimental

observations are largely based on time-resolved pump-probe measurements in a molecular beam (gas-phase), including time-resolved ion yield (TR-IY) and photoelectron (TR-PES) spectroscopies, and condensed-phase transient absorption techniques (TR-TAS) with additional contributions from fluorescence lifetime measurements. Specific discussions on reaction pathways and the dynamics of nucleobases can be found in Giussani et al. [87] and Mai et al. [88], respectively, while solvation effects are discussed in Pollum et al. [89] and Improta [90]. A comprehensive discussion of modified nucleobases can be found in Pollum et al. [89] and Matsika [91].

### 4.1.1    Purine Bases

For the purine nucleobases, TR-IY and TR-PES showed bi-exponential decays with time constants of <100 fs and ~1.2 ps for adenine and <100 fs and ~360 fs for guanine following photoexcitation at 267 nm (Table 3) [50, 51]. TR-PES studies on adenine, extended to a larger wavelength range, displayed a clear trend in the second time constant, which decreased from 1,035 to 700 fs between the excitation wavelengths of 265–200 nm [92]. For both purine bases, the experimentally observed bi-exponential decay was interpreted as initial population of the $\pi\pi^*$ state, followed by relaxation on the $n\pi^*$ surface to a conical intersection that leads back to the electronic ground state. This picture has been revised by more recent theoretical studies and the longer time constant is now assigned primarily to a C2-atom puckering pathway on the $\pi\pi^*$ state (see atom numbering in Scheme 1) and, to a lesser extent, an additional C6-atom puckering pathway [85, 93]. At high excitation energies, experiment and theory have shown that dissociative $\pi\sigma^*$ states play a significant role in the deactivation of adenine [16, 92, 94]. This competition among the different reaction pathways is discussed in more detail in Sect. 5.1.

In water, the time-resolved spectrum of adenine under 263-nm irradiation shows two time constants – a major component of 0.18 ps and another component of 8.8 ps. Based on their relative contributions to the signal, they have been associated with deactivation of different tautomers. The short time constant has been attributed to 9H-adenine, while the long time constant has been assigned to the deactivation of 7H-adenine [52, 53, 95, 96]. Recent simulations have shown, however, that the 7H tautomer should contribute to the short time constant as well, through water–adenine electron transfer [97].

The adenosine and guanosine nucleosides in water, as measured by TR-TAS at 263-nm photoexcitation, show single-exponential decay times of 290 and 460 fs, respectively [14], which are in close agreement with fluorescent lifetime measurements on the nucleotides, and interpreted in analogy to the mechanisms in isolated nucleobases. Recently, it has been proposed that deactivation of adenosine follows a different pathway in comparison to adenine, with occurrence of intramolecular proton transfer along an OH···N3 hydrogen bond [98].

### 4.1.2 Pyrimidine Bases

The photophysics of the pyrimidine bases is far richer, with various time constants which may be associated with competing relaxation pathways, intersystem crossings, and the existence of multiple tautomers [17, 99, 100]. This complexity is reflected in inconsistencies throughout experimental studies, where fitting procedures based on multiple exponentials have yielded femtosecond to nanosecond time constants which have then been interpreted with various photochemical models. For 267-nm photoexcitation, time constants extracted from TR-IY and TR-PES data with a bi-exponential fit yield ~0.1 and 5 ps and 0.1 and 1 ps for thymine and uracil, respectively (Table 3) [50]. The presence of a nanosecond component is inconclusive [101, 102] as is an additional, intermediary time constant of ~500 fs obtained from TR-PES data for 250-nm photoexcitation [51].

For thymine and uracil, ab initio dynamics simulations [85, 103] relate the time constants to a competition between two major reaction pathways. Part of the population relaxes quickly to the ground state through a $\pi\pi^*$ state, similar to the purine bases. The remaining population is trapped in the second excited state (also with $\pi\pi^*$ character) and relaxes to the $n\pi^*$ minimum (first excited state) before completing the internal conversion to the ground state after a few picoseconds.

In the case of cytosine, the presence of three tautomeric forms (1:1:0.25 for keto: enol:keto-imino) in the molecular beam adds experimental challenges. TR-IY experiments have distinguished between the photodynamics of the keto and enol tautomeric forms based on their characteristic absorption spectra (keto origin at 314 nm; enol origin at 278 nm) [68] and via chemical substitution [74]. With 280- and 290-nm photoexcitation, the observed dynamics are described by three exponential decay components of <0.1 ps, ~1 ps, and a long picosecond-nanosecond contribution, which can unambiguously be assigned to the biologically relevant keto tautomer [68]. The first two time constants have been assigned to motion out of the Franck–Condon region of the initially excited $\pi\pi^*$ state, followed by internal conversion to the ground state either from the $\pi\pi^*$ state or via the $n\pi^*$ state.

Computational simulations regarding the latter internal-conversion step are still contradictory [85, 104–107]. Although the computational models tend to show similar pathways and conical intersection structures, differences in the energetic balances of the several potential energy surfaces which depend on the computational method have a major impact on the output distribution. However, one striking feature observed in different simulations is deactivation of a significant fraction of excited cytosine in a region with a three-state crossing (see also Sect. 5.2).

The presence of a long time constant is again controversial [74]. It has tentatively been associated with intersystem crossing, but excited-state tautomerization into the low-energy $n\pi^*$ state of the keto-imino tautomer has also been proposed [68]. Time-resolved experiments performed with photoexcitation wavelengths shorter than 278 nm may include a mixture of contributions from the keto and enol tautomers. Comparison with methylated cytosine, where the enol form has been eliminated, allows separation of the individual contributions [74]. It was found

that enol cytosine decays an order of magnitude slower than the keto tautomer, with time constants decreasing from 45 to 3 ps for excitation wavelengths ranging down to 260 nm. The internal conversion mechanism is presumed to be similar to the keto tautomer, but requires surpassing a slightly higher barrier along the pathway to the conical intersection with the ground state [104]. Experimentally, time-resolved studies to date have not differentiated the photodynamics of the keto-imino tautomer, but they are expected to resemble those of the keto tautomer.

In aqueous solution, TR-TAS revealed single-exponential decays of 540, 210, and 720 fs for thymidine, uridine, and cytidine, respectively, which have been associated with internal conversion to the ground state [14].

### 4.1.3 Modified Bases

Even minor structural modifications, such as tautomerization [108, 109] or chemical substitution of the ring moiety [110–113], have been shown to alter profoundly the photochemistry of the natural DNA bases discussed above. Adenine and 2-aminopurine, with strikingly different emission quantum yields, are a classic example [108]. On a molecular level, these dissimilarities can be understood in terms of restrictions on the access to efficient nonradiative deactivation pathways available to the natural nucleobases. Fluorescent analogues are of fundamental and practical interest. For example, they may serve as fluorescent markers in biological imaging applications with minimal perturbations to the biomolecules because of their structural similarity to the natural counterpart [114, 115]. Substitution of one or more molecular ring atoms with sulfur or nitrogen produces thio- and aza-nucleobases, respectively, some of which show significant triplet quantum yields. They are good candidates for use as photosensitizers in photodynamic drug therapy because of their potential for singlet oxygen generation [116–118]. These possible applications, and also fundamental scientific interest in substitution effects on the excited-state dynamics of the natural nucleobases, have triggered experimental and theoretical studies of their thio- and aza-derivatives.

Thio-analogues

Absorption spectra of the thiobases are red-shifted compared to their natural analogues, placing their absorption maximum into the UVA spectral region [119–122]. Photoexcited thiobases primarily relax from the $S_2(\pi\pi^*)$ state via nonradiative pathways but instead of internal conversion back to the neutral ground state ($S_0$), excited-state flux is channeled into the triplet manifold [122–124]. Pathways for $T_1(\pi\pi^*)$ population, either via singlet or triplet $n\pi^*$ states, have been predicted theoretically [123–125]. Intersystem crossing occurs remarkably fast (hundreds of femtoseconds), with quantum yields close to unity [122, 126, 127]. The triplet state population eventually decays back to the ground state on nano- to microsecond timescales, predominantly nonradiatively [122, 128]. Although a small fraction

deactivates via phosphorescence, self-quenching by other molecules in the ground state has been reported [129].

Aza-analogues

The photophysical properties of the azabases are less well characterized. Although some general patterns emerge, certain aspects regarding the intersystem crossing pathways remain inconclusive. Generally, the absorption spectrum of the azabases exhibits a slight red shift compared to the natural counterparts [130–132]. They can be classified into two opposing groups with either near unity or insignificant triplet quantum yields, with the energetic location of the $n\pi^*$ states playing a key role in accessibility [111, 130, 131]. 6-Azauracil and 8-azaadenine fall into the former group, while 8-azaguanine and 5-azacytosine are part of the latter [132]. For 6-azauracil and 8-azaadenine photoexcited to the $S_2(\pi\pi^*)$ state, the two mechanisms proposed for population of the triplet manifold are $S_2(\pi\pi^*) \rightarrow S_1(n\pi^*) \rightarrow T_1(\pi\pi^*)$ and $S_2(\pi\pi^*) \rightarrow T_2 (n\pi^*) \rightarrow T_1(\pi\pi^*)$ [133, 134]. These pathways are inaccessible in 8-azaguanine and 5-azacytosine, where the lowest singlet $n\pi^*$ state is higher in energy than the first two singlet $\pi\pi^*$ states [132].

## 4.2   Base Pairs

Molecular clusters with non-covalent interactions provide the next stepping stone in our endeavor to transition to more biologically relevant scenarios, where base stacking and pairing offer stability and recognition characteristics to DNA.

The photodynamics of adenine-thymine (AT) [79, 101, 102, 135] pairs have been investigated in a molecular beam with TR-IY and, in one instance, also coupled to photoelectron spectroscopy. Following 267-nm photoexcitation, the AT base pair relaxes with a triple-exponential decay of 0.12, 1.3, and 6.1 ps (Table 3). A primarily intramolecular relaxation mechanism has been proposed, in agreement with semiempirical dynamics simulations [136], noting the resemblance of the time constants to those of the adenine and thymine monomers. A similar conclusion was reached for the adenine-adenine ($A_2$) homodimer, but surprisingly this was not the case for thymine-thymine ($T_2$), which showed a significant discrepancy in the second time constant. A follow-up study [79] with thorough analysis of time-traces observed in fragmentation mass channels revealed time constants similar to the thymine monomer in the $TH^+$ trace and the authors proposed the presence of hydrogen bonded and stacked dimers in the molecular beam as a possible explanation.

Ab initio calculations predict hydrogen-bonded dimers to be the lowest energy structures [137]. On the other hand, experimentally, stacked thymine dimers have also been observed in a supersonic expansion, but without any evidence for stacked AT and $A_2$ structures [137]. It is therefore plausible that the $A_2^+$, $AT^+$, and $TH^+$

mass channels display the photodynamics of the hydrogen bonded cluster, which are similar to the monomers (intramolecular relaxation), whereas the $T_2^+$ channel represents the stacked configuration.

To date, accurate time constants from time-resolved gas-phase measurements are not available. IR-UV spectra of gas-phase GC base pairs in diverse conformations shows that the Watson–Crick arrangement has a distinctive broad UV spectrum, indicative of subpicosecond lifetimes [139]. Reaction pathway [140] and dynamics simulations [19, 136, 141] point to an intermolecular relaxation mechanism, where a conical intersection between the ground and the excited states is reached along a proton-transfer path between nucleobases.

## 4.3  Stacking, DNA Fragments

The investigation of fragments with stacked bases is a quickly growing area of experimental and computational research [65, 66, 80, 81, 83, 136, 142–148]. Besides their intrinsic interest, all this attention is also motivated by the connection of this area to photoinduced dimerization, related to health issues [5], and to the development of unusual plasmonic structures, which are of direct technological interest in organic electronics [149]. In-depth discussions of several aspects of excitation of large nucleic-acid fragments can be found in Plasser et al. [150], Chen et al. [151], and Lu et al. [152]. Physiological aspects of excitation of nucleobases are discussed in Häder et al. [153] and Cadet et al. [154]. For reviews of charge and energy transport in nucleic acids, see Changenet-Barret et al. [155] and Kawai and Majima [156].

While the gas-phase studies on individual nucleobases and base pairs summarized above have provided unprecedented spectroscopic details on the photochemical mechanisms, condensed-phase techniques have added exciting capabilities to investigate the effects of spatial organization in DNA fragments. For example, investigation of single stranded oligo- and polynucleotides provides insights into the effects of base stacking, sequences, and helical conformation in the absence of pairing. The latter can subsequently be introduced through the addition of a complementary strand in specifically designed duplexes.

Most strikingly and counterintuitive to the idea of inherent photoprotection, TR-TAS experiments on single polymer strands revealed decay times that are orders of magnitude longer than those of the isolated building blocks [39, 157]. In a simplified general picture their photophysics may be summarized as follows.

Single stranded homopolymers, e.g., $(dA)_{18}$, show both short (~1 ps) and long-lived components, which have been attributed to different degrees of base stacking [65, 158–160]. Specifically, poorly stacked regions decay similarly to monomers, while stacked sections, subject to electronic coupling between adjacent bases, decay more slowly. In stacked regions, photoexcitation populates Frenkel-exciton states, which are thought to be delocalized over two [161] neighboring bases and

decay in less than 1 ps to a long-lived intrastrand excimer/exciplex state. The latter relaxes to the electronic ground state on 10- to 200-ps timescales via charge recombination or, under certain circumstances, may result in mutagenic photochemical products. In unstacked and poorly stacked regions, UV excitation populates monomeric $\pi\pi^*$ states, which decay to the ground state in less than 1 ps.

Although this simplified picture brings some general elements to explain the excited-state relaxation in strands, the contributions of monomeric relaxation and excimer formation seem to be deeply dependent on the nucleobase sequences. For instance, the $(dT)_{18}$ homopolymer does not form excimers and follows the picosecond pathways of thymine monomers [65].

This line of experimental research has been systematically advancing towards more realistic scenarios as found in DNA, where base stacking and pairing typically go hand in hand. Overall, studies on duplex strands of complementary homopolymers or alternating base sequences, joined through hydrogen bonding, revealed, somewhat surprisingly, that intrastrand photodynamics are mostly preserved. For example, long-lived states in duplex $(dA)_{18} \cdot (dT)_{18}$ and $(dAdT)_9 \cdot (dAdT)_9$ resemble those of the $(dA)_{18}$ homopolymer [65]. Similar strand-localized excitation and relaxation dynamics have been observed in duplexes comprising GC base pairs [162, 163].

A large amount of computational and theoretical work addressing stacking is available as well: the characterization of the electronic states in terms of charge-transfer character and delocalization properties for different DNA fragments [164, 165], the time evolution of the populations through these states [81, 144], and the characterization of photoinduced dimerization [166, 167] have been the major goals. To accomplish them, excitonic models [146, 168, 169] and electronic-structure calculations [142, 170] have been employed over the last decade, helping to explain several aspects of the interaction of DNA with UV radiation, such as the origin of the hyperchromism already mentioned in Sect. 3 [44, 171].

Even though notable advances in our understanding of electron-transfer processes in DNA have been achieved [172] to the point that it has even been possible to model DNA-based molecular switches [173], other facets, such as the degree of exciton delocalization, are still under debate [174]. Taking the collective literature of experimental and theoretical studies into account, significant discrepancies regarding specific photochemical details emerge. Investigations of stacked fragments, for example, have resulted in a number of different scenarios, with a variety of electronic structures involving different degrees of energy and charge delocalization and a hierarchy of relaxation timescales, from subpicoseconds to nanoseconds [65, 80, 81]. Sometimes, even apparently contradictory pictures have emerged. For instance, while computational investigations of duplexes of Watson–Crick pairs in water predicted that charge-transfer states should be energetically higher than the bright states [142], investigations of polyadenine indicated that charge-transfer states are preferentially populated by low-energy UVA excitation [81]. Additionally, based on reaction-path simulations for $(dA)_{10} \cdot (dT)_{10}$, it has been shown that intramonomer relaxation processes could, in principle, account not only for the short time constants observed in duplexes, but also for the long ones, without

formation of excimers [143]. At the time of writing, no clear general picture of the relaxation processes following the excitation of fragments containing stacked bases has emerged.

### 4.3.1 Photoinduced Pyrimidine Dimers

Pyrimidine dimers are among the most important photoproducts of DNA excitation because of their close connection to cell lethality, mutagenesis, and carcinogenesis [5, 175, 176]. For this reason, they have been extensively investigated for decades [26, 177, 178] to characterize their formation [83], enzymatic recognition [179, 180], and repair [84, 181].

The formation of pyrimidine dimers (Scheme 2) can occur via direct UV excitation of DNA, or via photosensitization [175, 182, 183]. It has been shown that one of the most important dimers, T<>T, is formed within 1 ps after 272-nm excitation [83]. The formation of T<>T occurs through fast relaxation of the thymine–thymine complex in the $S_1$ state, followed by internal conversion to the ground state [147, 167, 184]. Triplet pathways for pyrimidine-dimer formation have also been reported [147, 184, 185]. At least for T<>T, the triplet pathways seem to be of minor importance [186] in the case of direct excitation of the nucleobases, although they may still play a major role in cases of photosensitization [182].

Repair of pyrimidine dimers is carried out by different enzymes [187–190] or other molecules [191–193], following a number of different mechanisms [183, 194]. The repair is triggered by an electron injection into the dimers [84, 166, 188, 195] and its efficiency is dependent on the specific sequence of bases neighboring the dimer [196, 197], among other factors [198]. It has been shown that CPD repair by photolyase [84] occurs through two sequential bond breakings within approximately 90 ps for T<>T. In addition, several hundreds of picoseconds are needed to transfer the electron back to the enzyme.
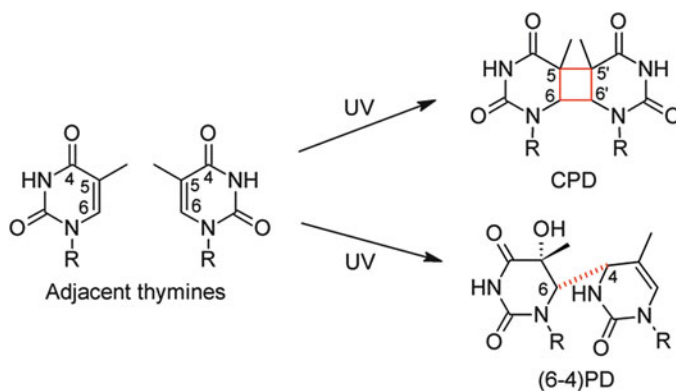


**Scheme 2** Cyclobutane and (6-4) pyrimidine–pyrimidone dimers formed from adjacent thymines

Several computational investigations are available, focusing either on spectro-scopic characterization [199, 200] or on particular mechanisms of formation [147, 167, 183, 184, 198, 201, 202] and repair [166, 183, 188, 203–208] of pyrimidine dimers. Many of these models are based on very realistic environments, which include solvent effects, DNA neighborhood, and binding interactions to enzymes [188, 203, 206, 209].

The repair of T<>T has been an especially puzzling issue for theorists. Simu-lations carried out by diverse methods [203, 204, 208] have predicted barriers which are too low to account for the experimental results. Metadynamics simula-tions employing a quantum mechanics/molecular mechanics model with an active site including the backbone and several amino acids with dispersion-corrected DFT, for instance, established an upper limit of 2.5 kcal/mol for this barrier [206], while the experimental activation energy for the repair has been estimated to be 4.02 kcal/mol [195]. Although this difference looks numerically small, it corresponds to a factor of ten in the reaction time.

# 5   Open Problems and Debates in the Field

## 5.1   Deactivation of Adenine: Multiple Pictures

It has been determined by several gas-phase time-resolved experiments that UV-excited adenine returns to the ground state within about 1 ps [50, 54–56]. How-ever, there are a few points of divergence among researchers in the field.

One first discrepancy is the role of NH dissociation. According to Stolow et al., after low-energy excitation (267 nm), deactivation of adenine in the gas phase takes place through NH dissociation ($\pi\sigma^*$ state) or ring-distortion pathways involving the $\pi\pi^*$ and $n\pi^*$ states, while only the latter are active at higher energies (250 nm) [55, 210]. This interpretation has been disputed by theoretical and experimental works, which show that ring-distortion pathways dominate at low energies, while NH dissociation happens above a certain onset between 247 and 200 nm [92–94, 211] (Fig. 3).

Although simulation results mostly favor ring-distortion pathways after excita-tion of adenine in the gas phase, there is an ongoing debate about which kind of distortion takes place. We will return to this issue in Sect. 5.4. More recent experimental data employing 267-nm excitation and strong field ionization have shown that the fragments of adenine, produced through dissociative ionization, group into two time windows, 750 fs and 1.25 ps [56]. Although not definitive, this piece of information suggests that two different ring-puckering reaction paths are activated, which the authors speculate may be associated with relaxation via the $L_b$ and the $n\pi^*$ minima.

Another point which is unclear about adenine deactivation is the short time constant revealed by the experiments. This time constant of about 100 fs has been
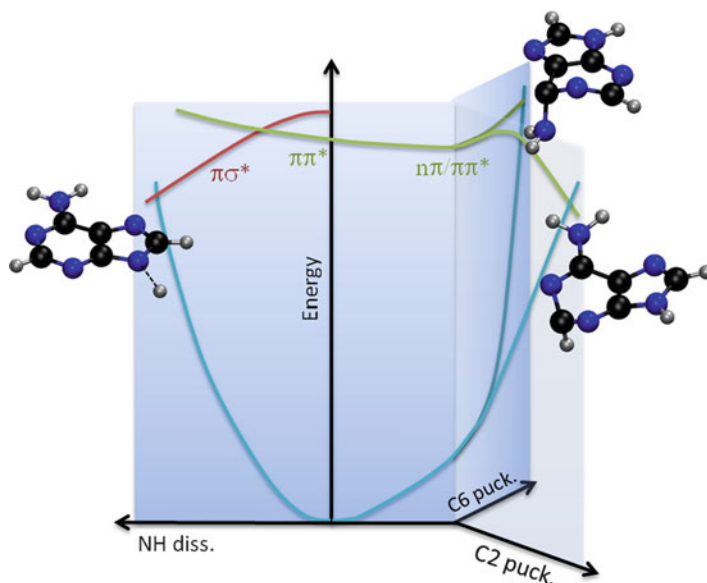
**Fig. 3** Schematic representation of the deactivation pathways in adenine. From the Franck–Condon region, adenine relaxes to a mixed $n\pi^*/\pi\pi^*$ $S_1$ minimum. From this minimum, puckering at C2 or C6 atoms can bring the molecule to conical intersections in the picosecond scale. For higher excitation energies, conical intersections formed by NH dissociation may also be reached

interpreted as an indication of deactivation to the ground state [212], but also as evidence of relaxation into the $S_1$ state [55, 213]. The scenario is even more complicated when it is taken into account that the ionization potential along the main reaction pathways changes significantly in relation to the ionization potential in the Franck–Condon region [214]. Experimentally, this potentially leads to loss of the ionization window before the conical intersection is reached and the measured time constant consequently underestimates the true relaxation time.

## 5.2 Cytosine: Tautomers, Triple Intersections, and Triplet States

Cytosine poses a challenge to time-resolved experiments because of the existence of multiple tautomers under molecular beam conditions. The broadband nature of femtosecond pulses and hence lack of spectral selectivity prohibits tautomer-specific measurements, except for the case of distinctly different absorption spectra. More typically, one has to resort to other means, such as chemical substitution, to correlate decay time constants with specific tautomeric forms. After 267-nm excitation in the gas phase, cytosine decays with two time constants, 160 fs and 1.86 ps

[50] (see Table 3; these values are 210 fs and 2.2 ps according to [68] and 500 fs and 4.5 ps according to [74]). It has recently been pointed out that the shorter time constant may split into two, 50 and 240 fs (262-nm excitation) [56] and there is also the possibility of a third time constant with much longer values for excitation near the band origin ($>$150 ps at 290 nm) [68]. While the short time constant increases linearly with the pump wavelength (from 200 fs at 260 nm to 900 fs at 290 nm), the second time constant – which is on the order of a few picoseconds – increases exponentially (from 2.7 ps at 260 nm to 45 ps at 285 nm) [74]. Moreover, the lifetime of cytosine seems to be very sensitive to substitutions at C5 (see numbering in Scheme 1). For instance, the second time constant for 5F-Cyt increases to 17 ps [74]. Additionally, this time constant disappears upon methylation at position 1 [74]. This complex decay pattern has led to multiple interpretations of cytosine deactivation. In particular, there are ongoing debates about the nature of the conical intersections [215], the role of tautomers [74], and the importance of triplet states [216].

The original model for cytosine deactivation proposed that the short time constant corresponds to the motion away from the Franck–Condon region, while the second, few-picosecond time constant corresponds to the internal conversion to $S_0$ [68]. This interpretation is not supported by dynamics simulations, which have shown that internal conversion should occur on a subpicosecond scale [105–107, 136, 215, 216]. There is no agreement, however, about which reaction path should be the most important. Dynamics based on CASSCF surfaces may predict dominance of a semi-planar conical intersection (large active space) [85, 107, 215], or of an intersection with out-of-plane $NH_2$ distortion (small active space) [106]. Dynamics based on semiempirical methods point to a major role of an intersection puckered at the C6 atom [105, 136].

The nature of the second time constant (a few picoseconds) is also unclear. It may, on the one hand, correspond to delayed internal conversion through a pathway escaping from the $S_1$ minimum [85]. On the other hand, the disappearance of the second time constant upon N1 methylation [74] may indicate that tautomeric effects are in place. In molecular beams, cytosine should be present as keto and enol tautomers [217]. Because N1 methylation should strongly reduce the enol population, the long time constant has been assigned to the internal conversion of the enol tautomer [74].

Returning to the short timescale, computational simulations have revealed an odd feature in cytosine potential energy surfaces: an energetically available three-state conical intersection involving $S_0$, $S_1$, and $S_2$ [218]. Dynamics simulations of cytosine in the gas phase based on CASSCF and CC2 surfaces using surface hopping and multiple spawning have shown that this three-state crossing region – corresponding to a quasi-planar geometry – may play an important role [106, 107, 215]. Even more astonishing, about 15% of cytosine deactivation took place through this kind of crossing in less than 100 fs, making it one of the fastest deactivation processes proposed so far.

When dealing with nonadiabatic transitions, transfers between states of the same multiplicity happen with much greater probability than transfers between states

with different multiplicities. For this reason, the picosecond deactivation of nucleobases have always been regarded as an internal conversion problem, with intersystem crossing appearing as residual elements on much longer timescales [219]. Recent surface-hopping dynamics with CASSCF for cytosine, including internal conversion and intersystem crossing, have shown that a notable amount of up to 20% of the keto population (but not enol) could be transferred to the lowest triplet state within 1 ps of the excitation [216, 220]. This picture, if confirmed by higher level simulations, has the potential to change deeply our understanding of the deactivation mechanisms in organic molecules.

## *5.3 Why Does Thymine Have the Longest Lifetime?*

Thymine has the longest excited-state lifetime among the five canonical nucleobases in the gas phase. According to [50], after 267-nm excitation, thymine shows a double-exponential deactivation with 105-fs and 5.12-ps time constants (Table 3). The long time constant, which has been assigned to the excited-state lifetime of thymine, was attributed at first to a trapping of the population in the $S_1$ ($n\pi^*$) state after a quick relaxation from the initially excited $S_2$ ($\pi\pi^*$) state [221]. As a second possibility, an independent study proposed that the deactivation occurred solely on the $\pi\pi^*$ state, without any major influence of the $n\pi^*$ state. In this case, the trapping site is located at another region of the $S_1$ surface at a minimum with $\pi\pi^*$ character [100]. Either way, from one of those $S_1$ minima, thymine would take a few picoseconds to find the seam of conical intersections to the ground state, explaining its longer lifetime. This interpretation has been disputed, since two sets of dynamics simulations predicted that the $S_2$ ($\pi\pi^*$) $\rightarrow$ $S_1$ ($n\pi^*$) relaxation time itself occurs on a few picoseconds [103, 222]. Hence both elongated $S_2$ ($\pi\pi^*$) $\rightarrow$ $S_1$ ($n\pi^*$) relaxation and then $S_1$ ($n\pi^*$) trapping, would contribute to the long time constant.

While $S_1$ ($n\pi^*$) trapping is easy to explain, a long $S_2$ ($\pi\pi^*$) lifetime is counter-intuitive. The barrier to deactivation from $S_2$ ($\pi\pi^*$) to $S_1$ ($n\pi^*$) is in principle too small to justify it [221, 223, 224]. It has been pointed out that it is difficult to rationalize the differences in lifetimes of thymine and uracil based only on the analysis of the potential energy curves computed with fully correlated methods [224]. Kinetic reasons may be behind the anomalous behavior of excited thymine, which, in spite of the small energy barriers, could spend substantial time spanning the flat $S_2$ ($\pi\pi^*$) surface until finding an intersection to $S_1$ ($n\pi^*$) [222]. However, it is still possible that the $S_2$ ($\pi\pi^*$) trapping is just an artifact of dynamics simulations limited to CASSCF surfaces. In fact, recent experiments based on ultrafast X-ray Auger probing indicate that thymine excitation at 266 nm should populate the $S_1$ ($n\pi^*$) state within only 200 fs [225].

## 5.4 Dynamics Simulation Cacophony

In the last few years, nonadiabatic dynamics of excited states has become an important method for determining the ultrafast behavior of excited molecules. These simulations have helped to explain how the molecules relax through the manifold of excited states. In particular, trajectory-based methods, such as multiple spawning and surface hopping, consider all nuclear degrees of freedom, without the need for a pre-selection of a reaction coordinate. On the contrary, the reaction coordinate emerges as the result of the simulation. Dynamics simulations of monomers, base pairs, and stacked fragments have been reported with different methods and at diverse electronic structure levels and, in spite of all information that they have provided, a less discussed aspect of these works is that simulations performed at different levels often lead to disparate results.

Divergences can be found in the simulations for all nucleobases. Take, for instance, adenine (Table 4). Dynamics simulated with ab initio MRCI predicts ultrafast deactivation through a C2-puckered conical intersection within 0.53 ps [37, 211], somewhat faster than the experimental lifetime, 1.1 ps. Dynamics simulated with semiempirical MRCI, however, predict that the deactivation should take place at a C6-puckered conical intersection within 0.9 ps [211]. Similar results are obtained for adenosine with another semiempirical CI procedure [136]. If dynamics is simulated with TDDFT with a number of different functionals, the lifetime is at least three times longer than the experimental value [211]. The same is true for dynamics with TD-DFTB [228], whose lifetime is a factor of ten longer than the experimental value. With ADC(2), deactivation takes place within 1.3 ps through C2- and C6-puckered intersections [226].

From a general standpoint, the problems with dynamics simulations are mainly related to the compromise between quality and computational costs. To perform dynamics with on-the-fly computation of electronic quantities, the computational level has to be downgraded by the use of small basis sets of double-$\zeta$ quality, usually without diffuse functions, the use of single-reference methods, and missing dynamic electron correlation. In the case of adenine, with three energetically close deactivation pathways (Fig. 3), the inaccuracies introduced by these approximations have dramatic effects on the fate of the simulations. The most serious problems with dynamics simulations seem to be caused by the electronic structure method rather than by the dynamics method. For instance, dynamics of uracil and thymine with surface hopping and multiple spawning with CASSCF lead to very similar results [103, 222].

The failure of TDDFT to describe the dynamics of adenine is not only because of the time-dependent procedure, but also the DFT ground-state deficiencies. In [211] it is shown that in-plane deformations of the pyrimidine ring are overstabilized in the ground state compared to out-of-plane deformations. When the excitation energies are added to these wrong ground-state surfaces, it results in ill-shaped excited-state surfaces. Curiously, one of the best results at the TDDFT level was

obtained with BHLYP functional, where an overestimation of the excitation energies led to error compensation.

One common approximation in most dynamics simulations is not to consider the influence of the probe signal. The deactivation time is directly compared to the time constant of the time-resolved experiments without considering, for instance, the effect of the ionization or stimulated-emission probabilities on the time constant. Recently, a number of works have started to address this feature in a more complete way by simulating the probing process [103, 229]. Nevertheless, the errors made by neglecting a full description of the probe process are usually secondary in comparison to the errors caused by bad description of the potential surfaces. A notable exception may be in the measurements of adenine in water reported in Buchner et al. [53]. In that work, it was shown that the long time constant associated with 7H-adenine pumped at 266 nm increases from 2.8 to 8.5 ps for probe wavelengths varying between 248 and 238 nm.

## 5.5 UVA or UVB: Which Is Most Dangerous?

There is a critical balance between DNA absorbance and solar irradiance which is of most fundamental importance for health. Although UVA irradiation at the Earth's surface is several orders of magnitude higher than UVB, UVA absorption by DNA is much smaller than UVB absorption (see Fig. 1). For this reason, there is a long-standing debate about which range of irradiation is most harmful in terms of

**Table 4** Deactivation of adenine in the gas phase according to dynamics simulations at different levels. C2, C6, and NH give the fraction of the excited population following each of the three main reaction paths. $\tau$ is the excited state lifetime

| Method | Electronic structure | C2 (%) | C6 (%) | NH (%) | $\tau$ (ps) | Refs. |
|--------|---------------------|--------|--------|--------|-------------|-------|
| TSH | MRCIS | 79 | 21 | – | 0.53 | [211] |
| TSH | OM2/MRCI | 5 | 95 | – | 0.90 | [211] |
| TSH | ADC(2) | 54 | 43 | 3 | 1.3 | [226] |
| TSH | TD-PBE | – | – | 100 | ~20 | [211] |
| TSH | TD-B3LYP | 25 | 0 | 75 | ~4.5 | [211] |
| TSH | TD-PBE0 | 0 | 0 | 0 | $\infty$ | [211] |
| TSH | TD-BHLYP | 100 | 0 | 0 | ~3.5 | [211] |
| TSH | TD-ωB97XD | 100 | 0 | 0 | ~8 | [226] |
| AMD | TD-CAM-B3LYP | 100 | 0 | 0 | ~4.5 | [211] |
| AMD | TD-M06-HF | 0 | 0 | 100 | ~9.5 | [211] |
| TSH | TD-DFTB | NA | NA | NA | 11 | [227] |
| TSH | FOMO/AM1 | 0 | ~100 | 0 | ~1.6 | [136] |
| Expt. | | | | | 1.1 | [50] |

*TSH* trajectory surface hopping, *AMD* adiabatic molecular dynamics, *NA* not available

carcinogenic effects [230]. (For sunburn (erythema), it is well established that UVB is much more harmful than UVA [231].)

Up to a decade ago, the predominant view was that, whatever the relative importance of UVA and UVB for initiating carcinomas, completely different mechanisms were in play for each case: on the one hand, UVB radiation would induce formation of CPD and (6–4)PD (Scheme 2); on the other hand, UVA could induce the formation of reactive oxygen species and free radicals which could lead to mutations [25] (see also [153, 154]).

This view has, however, shifted since the work of Mouret and co-authors [49]. Their work showed that both UVA and UVB induce pyrimidine dimerization. While UVB induces formation of a number of dimers, especially T<>T, T<>C, and thymine–cytosine (6–4)PD, UVA induces almost exclusively formation of T<>T. This distribution of dimers has intriguing implications. CPDs and (6–4) PDs are both able to block DNA synthesis and gene transcription. However, (6–4) PDs are more efficient than CPDs in blocking these processes. For this reason, while (6–4)PDs tend to kill the cell, CPDs are more prone to mutagenesis. Still considering that UVA has a deeper penetration depth in the skin than UVB, it adds to the possibility that UVA may be as much or even more harmful than UVB. This opens a series of questions about the most effective composition of sunscreens and the epidemiological effects of a reduction of the ozone layer, which would increase the UVB content, relative to UVA, of the solar radiation spectrum at the Earth's surface.

## 5.6   Does Ultrafast Deactivation Matter for Photostability?

It is quite often stated that the ultrashort lifetimes of nucleobases imply an enhanced photostability [109]. Although reasonable, this claim has not been thoroughly justified, although it also fits well with the missing signal of the biological tautomer of guanine in R2PI spectra, often interpreted as an indication of ultrafast deactivation of this tautomer [232, 233].

Even though it is likely that the ultrafast processes offer an enhanced photostability, it is also doubtful that they still play any essential role for life. First, long-lived excimers seem to be more important than ultrafast monomers when dealing with excited DNA [65]. Second, UV-screening by melanin [234] and other biochemical protective mechanisms [235] should be the leading protectors against mutagenesis.

However, this does not mean that photostability was never important. It may have exerted considerable selective pressure in early biotic ages and even before. The primitive atmosphere lacked a protective ozone layer and the UV levels at the surface would have been much higher than those observed today [236]. Without any intrinsic photostability, it is improbable that complex organic substances would have accumulated under these conditions. An example of this photostability in prebiotic chemistry can be found in 4-amino-1H-imidazole-5-carbonitrile.

This molecule, one of the most promising prebiotic precursors of purine nucleotides [237, 238], has a 20-h lifetime under 254-nm irradiation [239], providing time for conversion into a purine base [240]. However, survival for a few hours may also be too short to allow the synthesis of more complex products. In this case, photostability would have to be enforced by other complementary means, such as, for instance, ice cavities [241]. (For an in-depth discussion of prebiotic aspects of nucleic-acid photoprocesses, see Sandford et al. [242].)

Another result indicating that photostability may have played an important role in shaping life on Earth is the exceptionally short excited-state lifetime of Watson–Crick GC-pair conformations, compared to other GC-pair conformations, as revealed by IR-UV spectroscopy [139] and ab initio reaction paths [140]. Once more, if this ultrafast deactivation can be taken as evidence of photostability, it would imply that Watson–Crick conformations may have been selected over other conformations to compose all genetic code on Earth because of their intrinsic capacity to dissipate the radiation energy without undergoing photochemical processes.

Even if the relation between ultrafast processes and photostability is confirmed, its role in evolution of life will still remain open. At the same time that DNA has native bases that deactivate much faster than analogue molecules, as in the case of 9H-adenine (0.18 ps at 263 nm in water [52]) and 7H-adenine (8.8 ps [52]), other alternative bases also show ultrafast deactivation (for instance, hypoxanthine at 266 nm in water, 0.13 ps [243]), but do not appear in the genetic code. Naturally, many different selection pressures were active to produce modern RNA and DNA [244]. At this point, the importance of photostability in the primordial stages of life remains obscure.

### Conclusions

Thanks to a synergetic effort of experimental, instrumental, and theoretical research over the last few decades, our understanding of the photoinduced processes in nucleic acids has advanced to the point that many of the dynamic processes have been determined. It is now clear that the photodynamics of nucleic acid fragments involve very different processes when dealing with monomers, base pairs, stacked bases, single strands, or duplexes. These processes are also strongly influenced by the environment, be it vacuum, solution, or the native cell nucleus.

The knowledge of how nucleic acids respond to irradiation has shed light on diverse problems, including the impact of UV radiation on prebiotic and early-biotic chemistry and on photoinduced carcinogenesis. Moreover, current research in the field points to the use of photoinduced processes in nucleic acids to explore charge and energy transport in DNA, aiming at applications in organic electronics.

# References

1. Dahm R (2005) Dev Biol 278:274
2. Downes A, Blunt TP (1877) Proc R Soc Lond 26:488
3. Altenburg E (1928) Am Nat 62:540
4. Avery OT, Macleod CM, McCarty M (1944) J Exp Med 79:137
5. Douki T (2013) Photochem Photobiol Sci 12:1286
6. Unna PG (1896) The histopathology of the diseases of the skin. W. F. Clay, Edinburgh
7. Finsen NR (1901) Phototherapy. Edward Arnold Publishers, London
8. Findlay G (1928) Lancet 212:1070
9. Gates FL (1928) Science 68:479
10. Watson JD, Crick FHC (1953) Nature 171:737
11. Setlow RB, Setlow JK (1962) Proc Natl Acad Sci 48:1250
12. Brash DE, Haseltine WA (1982) Nature 298:189
13. Park H, Kim S, Sancar A, Deisenhofer J (1995) Science 268:1866
14. Pecourt J-ML, Peon J, Kohler B (2001) J Am Chem Soc 123:10370
15. Crespo-Hernández CE, Cohen B, Hare PM, Kohler B (2004) Chem Rev 104:1977
16. Sobolewski AL, Domcke W (2002) Eur Phys J D 20:369
17. Ismail N, Blancafort L, Olivucci M, Kohler B, Robb MA (2002) J Am Chem Soc 124:6818
18. Merchán M, Serrano-Andrés L (2003) J Am Chem Soc 125:8108
19. Groenhof G, Schafer LV, Boggio-Pasqua M, Goette M, Grubmüller H, Robb MA (2007) J Am Chem Soc 129:6812
20. Ward HM (1893) Proc R Soc Lond 53:23
21. Gates FL (1930) J Gen Physiol 14:31
22. Swanson CP (1943) J Gen Physiol 26:485
23. Roffo A (1934) Bull Cancer (Paris) 23:590
24. Funding G, Henriques O, Rekling E (1936) Internationaler Kongress für Lichtforschung 166
25. Narayanan DL, Saladi RN, Fox JL (2010) Int J Dermatol 49:978
26. Kelner A (1949) Proc Natl Acad Sci U S A 35:73
27. Holiday ER (1930) Biochem J 24:619
28. Clark LB, Peschel GG, Tinoco I (1965) J Phys Chem 69:3615
29. Duggan DE, Bowman RL, Brodie BB, Udenfriend S (1957) Arch Biochem Biophys 68:1
30. Shugar D, Fox JJ (1952) Biochim Biophys Acta 9:199
31. Longworth JW, Rahn RO, Shulman RG (1966) J Chem Phys 45:2930
32. Daniels M, Hauswirth W (1971) Science 171:675
33. Callis PR (1983) Annu Rev Phys Chem 34:329
34. Fülscher MP, Roos BO (1995) J Am Chem Soc 117:2089
35. Lorentzon J, Fülscher MP, Roos BO (1995) J Am Chem Soc 117:9265
36. Fülscher MP, Serrano-Andrés L, Roos BO (1997) J Am Chem Soc 119:6168
37. Barbatti M, Lischka H (2008) J Am Chem Soc 130:6831
38. Abdi S, Ali A (1999) Cancer Lett 142:1
39. Middleton CT, de La Harpe K, Su C, Law YK, Crespo-Hernández CE, Kohler B (2009) Annu Rev Phys Chem 60:217

40. Gueymard CA, Myers D, Emery K (2002) Sol Energy 73:443
41. Thuillier G, Hersé M, Simon P, Labs D, Mandel H, Gillotay D (1997) Sol Phys 171:283
42. Dixon JM, Taniguchi M, Lindsey JS (2005) Photochem Photobiol 81:212
43. de Vries MS (2014) UV-excitation from an experimental perspective: frequency resolved. Top Curr Chem. doi:10.1007/128_2014_560
44. D'Abramo M, Castellazzi CL, Orozco M, Amadei A (2013) J Phys Chem B 117:8697
45. Barbatti M (2011) Phys Chem Chem Phys 13:4686
46. Bassukas I, Galaris D, Tsolakidis A, Zionios G, Dimou A, Kaxiras E (2008) J Biomed Opt 13:014017
47. Antony RY (1997) Phys Med Biol 42:789
48. Gallagher SR, Desjardins PR (2001) Current protocols in protein science. Wiley, Hoboken
49. Mouret S, Baudouin C, Charveron M, Favier A, Cadet J, Douki T (2006) Proc Natl Acad Sci U S A 103:13765
50. Canuel C, Mons M, Piuzzi F, Tardivel B, Dimicoli I, Elhanine M (2005) J Chem Phys 122:074316
51. Ullrich S, Schultz T, Zgierski MZ, Stolow A (2004) Phys Chem Chem Phys 6:2796
52. Cohen B, Hare PM, Kohler B (2003) J Am Chem Soc 125:13594
53. Buchner F, Ritze H-H, Lahl J, Lubcke A (2013) Phys Chem Chem Phys 15:11402
54. Kang H, Jung B, Kim SK (2003) J Chem Phys 118:6717
55. Satzger H, Townsend D, Zgierski MZ, Patchkovskii S, Ullrich S, Stolow A (2006) Proc Natl Acad Sci U S A 103:10196
56. Kotur M, Weinacht TC, Congyi Z, Matsika S (2012) IEEE J Sel Top Quant 18:187
57. Ullrich S, Schultz T, Zgierski MZ, Stolow A (2004) J Am Chem Soc 126:2262
58. Satzger H, Townsend D, Stolow A (2006) Chem Phys Lett 430:144
59. Kang H, Lee KT, Jung B, Ko YJ, Kim SK (2002) J Am Chem Soc 124:12958
60. Chin CH, Mebel AM, Kim GS, Baek KY, Hayashi M, Liang KK, Lin SH (2007) Chem Phys Lett 445:361
61. Luhrs DC, Viallon J, Fischer I (2001) Phys Chem Chem Phys 3:1827
62. Peon J, Zewail AH (2001) Chem Phys Lett 348:255
63. Canuel C, Elhanine M, Mons M, Piuzzi F, Tardivel B, Dimicoli I (2006) Phys Chem Chem Phys 8:3978
64. Gustavsson T, Sarkar N, Vaya I, Jimenez MC, Markovitsi D, Improta R (2013) Photochem Photobiol Sci 12:1375
65. Crespo-Hernández CE, Cohen B, Kohler B (2005) Nature 436:1141
66. Röttger K, Schwalb NK, Temps F (2013) J Phys Chem A 117:2469
67. Mons M, Dimicoli I, Piuzzi F (2008) In: Shukla MK, Leszczynski J (eds) Radiation induced molecular phenomena in nucleic acids. Springer, The Netherlands, p 343
68. Kosma K, Schröter C, Samoylova E, Hertel IV, Schultz T (2009) J Am Chem Soc 131:16939
69. Nir E, Müller M, Grace LI, de Vries MS (2002) Chem Phys Lett 355:59
70. Hare PM, Crespo-Hernández CE, Kohler B (2007) Proc Natl Acad Sci U S A 104:435
71. Blancafort L, Cohen B, Hare PM, Kohler B, Robb MA (2005) J Phys Chem A 109:4431
72. Sharonov A, Gustavsson T, Carré V, Renault E, Markovitsi D (2003) Chem Phys Lett 380:173
73. Malone RJ, Miller AM, Kohler B (2003) Photochem Photobiol 77:158
74. Ho J-W, Yen H-C, Chou W-K, Weng C-N, Cheng L-H, Shi H-Q, Lai S-H, Cheng P-Y (2011) J Phys Chem A 115:8406
75. He Y, Wu C, Kong W (2003) J Phys Chem A 107:5145
76. Gustavsson T, Banyasz A, Lazzarotto E, Markovitsi D, Scalmani G, Frisch MJ, Barone V, Improta R (2006) J Am Chem Soc 128:607
77. Gustavsson T, Sarkar N, Lazzarotto E, Markovitsi D, Improta R (2006) Chem Phys Lett 429:551
78. Nachtigallova D, Lischka H, Szymczak JJ, Barbatti M, Hobza P, Gengeliczki Z, Pino G, Callahan MP, de Vries MS (2010) Phys Chem Chem Phys 12:4924

79. Kim NJ, Chang J, Kim HM, Kang H, Ahn TK, Heo J, Kim SK (2011) ChemPhysChem 12:1935
80. Stuhldreier MC, Temps F (2013) Faraday Discuss 163:173
81. Banyasz A, Gustavsson T, Onidas D, Changenet-Barret P, Markovitsi D, Improta R (2013) Chem Eur J 19:3762
82. Buchvarov I, Wang Q, Raytchev M, Trifonov A, Fiebig T (2007) Proc Natl Acad Sci U S A 104:4794
83. Schreier WJ, Schrader TE, Koller FO, Gilch P, Crespo-Hernández CE, Swaminathan VN, Carell T, Zinth W, Kohler B (2007) Science 315:625
84. Liu Z, Tan C, Guo X, Kao Y-T, Li J, Wang L, Sancar A, Zhong D (2011) Proc Natl Acad Sci U S A 108:14831
85. Barbatti M, Aquino AJA, Szymczak JJ, Nachtigallová D, Hobza P, Lischka H (2010) Proc Natl Acad Sci U S A 107:21453
86. Schultz T, Samoylova E, Radloff W, Hertel IV, Sobolewski AL, Domcke W (2004) Science 306:1765
87. Giussani A, Segarra-Martí J, Roca-Sanjuán D, Merchán M (2013) Excitation of nucleobases from a computational perspective I: reaction paths. Top Curr Chem. doi:10.1007/128_2013_501
88. Mai S, Richter M, Marquetand P, González L (2014) Excitation of nucleobases from a computational perspective II: dynamics. Top Curr Chem. doi:10.1007/128_2014_549
89. Pollum M, Martínez-Fernández L, Crespo-Hernández CE (2014) Photochemistry of nucleic acid bases and their thio- and aza-analogues in solution. Top Curr Chem. doi:10.1007/128_2014_554
90. Improta R, Barone V (2014) Excited states behavior of nucleobases in solution: insights from computational studies. Top Curr Chem. doi:10.1007/128_2013_524
91. Matsika S (2014) Modified nucleobases. Top Curr Chem. doi:10.1007/128_2014_532
92. Evans NL, Ullrich S (2010) J Phys Chem A 114:11225
93. Serrano-Andrés L, Merchán M, Borin AC (2006) Chem-Eur J 12:6559
94. Wells KL, Hadden DJ, Nix MGD, Stavros VG (2010) J Phys Chem Lett 1:993
95. Pancur T, Schwalb NK, Renth F, Temps F (2005) Chem Phys 313:199
96. Gustavsson T, Sharonov A, Onidas D, Markovitsi D (2002) Chem Phys Lett 356:49
97. Barbatti M (2014) J Am Chem Soc 136:10246
98. Tuna D, Sobolewski AL, Domcke W (2013) J Phys Chem A 118:122
99. Kistler KA, Matsika S (2007) J Phys Chem A 111:8708
100. Merchán M, González-Luque R, Climent T, Serrano-Andrés L, Rodriuguez E, Reguero M, Pelaez D (2006) J Phys Chem B 110:26471
101. Samoylova E, Lippert H, Ullrich S, Hertel IV, Radloff W, Schultz T (2005) J Am Chem Soc 127:1782
102. Samoylova E, Schultz T, Hertel IV, Radloff W (2008) Chem Phys 347:376
103. Hudock HR, Levine BG, Thompson AL, Satzger H, Townsend D, Gador N, Ullrich S, Stolow A, Martínez TJ (2007) J Phys Chem A 111:8500
104. Nakayama A, Harabuchi Y, Yamazaki S, Taketsugu T (2013) Phys Chem Chem Phys 15:12322
105. Lan Z, Fabiano E, Thiel W (2009) J Phys Chem B 113:3548
106. Hudock HR, Martínez TJ (2008) ChemPhysChem 9:2486
107. González-Vázquez J, González L (2010) ChemPhysChem 11:3617
108. Serrano-Andrés L, Merchán M, Borin AC (2006) Proc Natl Acad Sci U S A 103:8691
109. Serrano-Andrés L, Merchán M (2009) J Photochem Photobiol C Photochem Rev 10:21
110. Harada Y, Suzuki T, Ichimura T, Xu Y-Z (2007) J Phys Chem B 111:5518
111. Kobayashi T, Kuramochi H, Harada Y, Suzuki T, Ichimura T (2009) J Phys Chem A 113:12088
112. Kuramochi H, Kobayashi T, Suzuki T, Ichimura T (2010) J Phys Chem B 114:8782
113. Etinski M, Marian CM (2010) Phys Chem Chem Phys 12:15665

114. Guest CR, Hochstrasser RA, Sowers LC, Millar DP (1991) Biochemistry 30:3271
115. O'Neil MA, Barton JK (2002) J Am Chem Soc 124:13053
116. O'Donovan P, Perrett CM, Zhang X, Montaner B, Xu Y-Z, Harwood CA, McGregor JM, Walker SL, Hanaoka F, Karran P (2005) Science 309:1871
117. Karran P, Attard N (2008) Nat Rev Cancer 8:24
118. Reelfs O, Karran P, Young AR (2012) Photochem Photobiol Sci 11:148
119. Favre A, Saintomé C, Fourrey J-L, Clivio P, Laugâa P (1998) J Photochem Photobiol B Biol 42:109
120. Igarashi-Yamamoto N, Tajiri A, Hatano M, Shibuya S, Ueda T (1981) Biochim Biophys Acta (BBA) Nucl Acids Protein Synthesis 656:1
121. Zhang Y, Zhu X, Smith J, Haygood MT, Gao R (2011) J Phys Chem B 115:1889
122. Taras-Goślińska K, Burdziński G, Wenska G (2014) J Photochem Photobiol A 275:89
123. Martínez-Fernández L, González L, Corral I (2012) Chem Commun 48:2134
124. Martínez-Fernández L, Corral I, Granucci G, Persico M (2014) Chem Sci 5:1336
125. Cui G, Fang W-H (2013) J Chem Phys 138
126. Pollum M, Crespo-Hernández CE (2014) J Chem Phys 140
127. Reichardt C, Crespo-Hernández CE (2010) J Phys Chem Lett 1:2239
128. Vendrell-Criado V, Saez JA, Lhiaubet-Vallet V, Cuquerella MC, Miranda MA (2013) Photochem Photobiol Sci 12:1460
129. Salet C, Bensasson RV, Favre A (1983) Photochem Photobiol 38:521
130. Wierzchowski J, Wielgus-Kutrowska B, Shugar D (1996) Biochim Biophys Acta Gen Subj 1290:9
131. Kobayashi T, Harada Y, Suzuki T, Ichimura T (2008) J Phys Chem A 112:13308
132. Kobayashi T, Kuramochi H, Suzuki T, Ichimura T (2010) Phys Chem Chem Phys 12:5140
133. Gobbo JP, Borin AC, Serrano-Andrés L (2011) J Phys Chem B 115:6243
134. Gobbo JP, Borin AC (2012) J Phys Chem B 116:14000
135. Gador N, Samoylova E, Smith VR, Stolow A, Rayner DM, Radloff W, Hertel IV, Schultz T (2007) J Phys Chem A 111:11743
136. Alexandrova AN, Tully JC, Granucci G (2010) J Phys Chem B 114:12116
137. Šponer J, Leszczyński J, Hobza P (1996) J Phys Chem 100:5590
138. Bravaya KB, Kostko O, Ahmed M, Krylov AI (2010) Phys Chem Chem Phys 12:2292
139. Abo-Riziq A, Grace L, Nir E, Kabelac M, Hobza P, de Vries MS (2005) Proc Natl Acad Sci U S A 102:20
140. Sobolewski AL, Domcke W, Hättig C (2005) Proc Natl Acad Sci U S A 102:17903
141. Xiao S, Wang L, Liu Y, Lin X, Liang H (2012) J Chem Phys 137:195101
142. Plasser F, Aquino AJA, Hase WL, Lischka H (2012) J Phys Chem A 116:11151
143. Conti I, Altoe P, Stenta M, Garavelli M, Orlandi G (2010) Phys Chem Chem Phys 12:5016
144. Improta R, Santoro F, Barone V, Lami A (2009) J Phys Chem A 113:15346
145. Fingerhut BP, Oesterling S, Haiser K, Heil K, Glas A, Schreier WJ, Zinth W, Carell T, de Vivie-Riedle R (2012) J Chem Phys 136:204307
146. Emanuele E, Markovitsi D, Millié P, Zakrzewska K (2005) ChemPhysChem 6:1387
147. Zhang RB, Eriksson LA (2006) J Phys Chem B 110:7556
148. Chatterley AS, West CW, Roberts GM, Stavros VG, Verlet JRR (2014) J Phys Chem Lett 843
149. Kuzyk A, Schreiber R, Fan Z, Pardatscher G, Roller E-M, Hogele A, Simmel FC, Govorov AO, Liedl T (2012) Nature 483:311
150. Plasser F, Aquino AJA, Lischka H, Nachtigallova D (2014) Electronic excitation processes in single-strand and double-strand DNA: a computational approach. Top Curr Chem. doi:10.1007/128_2013_517
151. Chen J, Zhang Y, Kohler B (2014) Excited states in DNA strands investigated by ultrafast laser spectroscopy. Top Curr Chem. doi:10.1007/128_2014_570
152. Lu Y, Lan Z, Thiel W (2014) Computational modeling of photoexcitation in DNA single and double strands. Top Curr Chem. doi:10.1007/128_2014_533

153. Häder D-P, Richa, Sinha RP (2014) Physiological aspects of UV-excitation of DNA. Top Curr Chem. doi:10.1007/128_2014_531
154. Cadet J, Grand A, Douki T (2014) Solar UV radiation-induced DNA bipyrimidine photoproducts: formation and mechanistic insights. Top Curr Chem. doi:10.1007/128_2014_553
155. Changenet-Barret P, Hua Y, Markovitsi D (2014) Electronic excitations in guanine quadruplexes. Top Curr Chem. doi:10.1007/128_2013_511
156. Kawai K, Majima T (2014) Photoinduced charge-separation in DNA. Top Curr Chem. doi:10.1007/128_2013_525
157. Kleinermanns K, Nachtigallová D, de Vries MS (2013) Int Rev Phys Chem 32:308
158. Crespo-Hernández CE, Kohler B (2004) J Phys Chem B 108:11182
159. Vaya I, Miannay F, Gustavsson T, Markovitsi D (2010) ChemPhysChem 11:987
160. Vaya I, Changenet-Barret P, Gustavsson T, Zikich D, Kotlyar AB, Markovitsi D (2010) Photochem Photobiol Sci 9:1193
161. Takaya T, Su C, de La Harpe K, Crespo-Hernández CE, Kohler B (2008) Proc Natl Acad Sci U S A 105:10285
162. Crespo-Hernández CE, de La Harpe K, Kohler B (2008) J Am Chem Soc 130:10844
163. de La Harpe K, Crespo-Hernández CE, Kohler B (2009) ChemPhysChem 10:1421
164. Blancafort L, Voityuk AA (2007) J Phys Chem A 111:4714
165. Aquino AJA, Nachtigallová D, Hobza P, Truhlar DG, Hättig C, Lischka H (2011) J Comput Chem 32:1217
166. Faraji S, Dreuw A (2014) Annu Rev Phys Chem 65:275
167. Boggio-Pasqua M, Groenhof G, Schäfer LV, Grubmüller H, Robb MA (2007) J Am Chem Soc 129:10996
168. Hu L, Zhao Y, Wang F, Chen G, Ma C, Kwok W-M, Phillips DL (2007) J Phys Chem B 111:11812
169. Bittner ER (2007) J Photochem Photobiol A 190:328
170. Santoro F, Barone V, Improta R (2007) Proc Natl Acad Sci U S A 104:9931
171. Varsano D, Di Felice R, Marques MAL, Rubio A (2006) J Phys Chem B 110:7129
172. Siriwong K, Voityuk AA (2012) WIREs Comp Mol Sci 2:780
173. Řeha D, Voityuk AA, Harris SA (2010) ACS Nano 4:5737
174. Nielsen LM, Hoffmann SV, Nielsen SB (2013) Photochem Photobiol Sci 12:1273
175. Bastien N, Therrien J-P, Drouin R (2013) Photochem Photobiol Sci 12:1544
176. Richa, Sinha RP, Häder D-P (2014) Top Curr Chem doi:10.1007/128_2014_531
177. Sancar A (1996) Annu Rev Biochem 65:43
178. Setlow RB (1966) Science 153:379
179. Wijaya IMM, Zhang Y, Iwata T, Yamamoto J, Hitomi K, Iwai S, Getzoff ED, Kandori H (2013) Biochemistry 52:1019
180. Wilson TJ, Crystal MA, Rohrbaugh MC, Sokolowsky KP, Gindt YM (2011) J Phys Chem B 115:13746
181. Thiagarajan V, Byrdin M, Eker APM, Müller P, Brettel K (2011) Proc Natl Acad Sci U S A 108:9402
182. Cuquerella MC, Lhiaubet-Vallet V, Bosca F, Miranda MA (2011) Chem Sci 2:1219
183. Barbatti M (2014) ChemPhysChem 15:3342
184. Roca-Sanjuán D, Olaso-González G, González-Ramírez I, Serrano-Andrés L, Merchán M (2008) J Am Chem Soc 130:10768
185. Kwok W-M, Ma C, Phillips DL (2008) J Am Chem Soc 130:5131
186. Banyasz A, Douki T, Improta R, Gustavsson T, Onidas D, Vayá I, Perron M, Markovitsi D (2012) J Am Chem Soc 134:14834
187. Bang J, Kang Y-M, Park C-J, Lee J-H, Choi B-S (2009) FEBS Lett 583:2037
188. Domratcheva T (2011) J Am Chem Soc 133:18172
189. Li J, Uchida T, Todo T, Kitagawa T (2006) J Biol Chem 281:25551
190. Torizawa T, Ueda T, Kuramitsu S, Hitomi K, Todo T, Iwai S, Morikawa K, Shimada I (2004) J Biol Chem 279:32950

191. Anusiewicz I, Świerszcz I, Skurski P, Simons J (2012) J Phys Chem A 117:1240
192. Nguyen KV, Burrows CJ (2012) J Phys Org Chem 25:574
193. Nguyen KV, Burrows CJ (2011) J Am Chem Soc 133:14586
194. Krapf S, Weber S, Koslowski T (2012) Phys Chem Chem Phys 14:11518
195. Liu Z, Guo X, Tan C, Li J, Kao Y-T, Wang L, Sancar A, Zhong D (2012) J Am Chem Soc 134:8104
196. Law YK, Forties RA, Liu X, Poirier MG, Kohler B (2013) Photochem Photobiol Sci 12:1431
197. McCullagh M, Hariharan M, Lewis FD, Markovitsi D, Douki T, Schatz GC (2010) J Phys Chem B 114:5215
198. Improta R (2012) J Phys Chem B 116:14261
199. Ritze H-H, Hobza P, Nachtigallová D (2007) Phys Chem Chem Phys 9:1672
200. Curutchet C, Voityuk AA (2011) Angew Chem Int Ed 50:1820
201. Labet V, Jorge N, Morell C, Douki T, Grand A, Cadet J, Eriksson LA (2013) Photochem Photobiol Sci 12:1509
202. Yuan S, Zhang W, Liu L, Dou Y, Fang W, Lo GV (2011) J Phys Chem A 115:13291
203. Harrison CB, O'Nei LL, Wiest O (2005) J Phys Chem A 109:7001
204. Hassanali AA, Zhong D, Singer SJ (2011) J Phys Chem B 115:3860
205. Dou Y, Xiong S, Wu W, Yuan S, Tang H (2010) J Photochem Photobiol B 101:31
206. Masson F, Laino T, Rothlisberger U, Hutter J (2009) ChemPhysChem 10:400
207. Masson F, Laino T, Tavernelli I, Rothlisberger U, Hutter J (2008) J Am Chem Soc 130:3443
208. Yuan S, Shen Z, Zhang W, Dou Y, Lo GV (2014) Int J Biol Macromol 66:267
209. Woiczikowski PB, Steinbrecher T, Kubař TS, Elstner M (2011) J Phys Chem B 115:9846
210. Bisgaard CZ, Satzger H, Ullrich S, Stolow A (2009) ChemPhysChem 10:101
211. Barbatti M, Lan Z, Crespo-Otero R, Szymczak JJ, Lischka H, Thiel W (2012) J Chem Phys 137:22A503
212. Fabiano E, Thiel W (2008) J Phys Chem A 112:6859
213. Picconi D, Avila Ferrer FJ, Improta R, Lami A, Santoro F (2013) Faraday Discuss 163:223
214. Barbatti M, Ullrich S (2011) Phys Chem Chem Phys 13:15492
215. Barbatti M, Aquino AJA, Szymczak JJ, Nachtigallová D, Lischka H (2011) Phys Chem Chem Phys 13:6145
216. Mai S, Marquetand P, Richter M, González-Vázquez J, González L (2013) ChemPhysChem 14:2920
217. Bazso G, Tarczay G, Fogarasi G, Szalay PG (2011) Phys Chem Chem Phys 13:6799
218. Kistler KA, Matsika S (2008) J Chem Phys 128:215102
219. González L, González-Vázquez J, Samoylova E, Schultz T (2008) AIP Conf Proc 1080:169
220. Richter M, Marquetand P, González-Vázquez J, Sola I, González L (2012) J Phys Chem Lett 3:3090
221. Perun S, Sobolewski AL, Domcke W (2006) J Phys Chem A 110:13238
222. Szymczak JJ, Barbatti M, Soo Hoo JT, Adkins JA, Windus TL, Nachtigallová D, Lischka H (2009) J Phys Chem A 113:12686
223. Zechmann G, Barbatti M (2008) J Phys Chem A 112:8273
224. Yamazaki S, Taketsugu T (2011) J Phys Chem A 116:491
225. McFarland BK, Farrell JP, Miyabe S, Tarantelli F, Aguilar A, Berrah N, Bostedt C, Bozek JD, Bucksbaum PH, Castagna JC, Coffee RN, Cryan JP, Fang L, Feifel R, Gaffney KJ, Glownia JM, Martinez TJ, Mucke M, Murphy B, Natan A, Osipov T, Petrović VS, Schorb S, Schultz T, Spector LS, Swiggers M, Tenney I, Wang S, White JL, White W, Gühr M (2014) Nat Commun 5:4235
226. Plasser F, Crespo-Otero R, Pederzoli M, Pittner J, Lischka H, Barbatti M (2014) J Chem Theory Comput 10:1395
227. Mitrić R, Werner U, Wohlgemuth M, Seifert G, Bonačić-Koutecký V (2009) J Phys Chem A 113:12700
228. Lei Y, Yuan S, Dou Y, Wang Y, Wen Z (2008) J Phys Chem A 112:8497
229. Fingerhut BP, Dorfman KE, Mukamel S (2013) J Phys Chem Lett 4:1933

230. Mitchell D (2006) Proc Natl Acad Sci U S A 103:13567
231. Anders A, Altheide H-J, Knälmann M, Tronnier H (1995) Photochem Photobiol 61:200
232. Marian CM (2007) J Phys Chem A 111:1545
233. Yamazaki S, Domcke W, Sobolewski AL (2008) J Phys Chem A 112:11965
234. Meredith P, Riesz J (2004) Photochem Photobiol 79:211
235. Sancar A (2003) Chem Rev 103:2203
236. Sagan C (1973) J Theor Biol 39:195
237. Powner MW, Sutherland JD, Szostak JW (2010) J Am Chem Soc 132:16677
238. Boulanger E, Anoop A, Nachtigallova D, Thiel W, Barbatti M (2013) Angew Chem Int Ed 52:8000
239. Becker RS, Kolc J, Rotham W (1973) J Am Chem Soc 95:1269
240. Roy D, Najafian K, von Ragué SP (2007) Proc Natl Acad Sci U S A 104:17272
241. Attwater J, Wochner A, Pinheiro VB, Coulson A, Holliger P (2010) Nat Commun 1:76
242. Sandford SA, Bera PP, Lee TJ, Materese CK, Nuevo M (2014) Photosynthesis and photostability of nucleic acids in prebiotic extraterrestrial environments. Top Curr Chem. doi:10.1007/128_2013_499
243. Cohen J, Kohler B (2012) Phys Chem Chem Phys 14:10677
244. Rios AC, Tor Y (2013) Isr J Chem 53:469

# UV-Excitation from an Experimental Perspective: Frequency Resolved

**Mattanjah S. de Vries**

**Abstract** Electronic spectroscopy of DNA bases in the gas phase provides detailed information about the electronic excitation, which places the molecule in the Franck–Condon region in the excited state and thus prepares the starting conditions for excited-state dynamics. Double resonance or hole-burning spectroscopy in the gas phase can provide such information with isomer specificity, probing the starting potential energy landscape as a function of tautomeric form, isomeric structure, or hydrogen bonded or stacked cluster structure. Action spectroscopy, such REMPI, can be affected by excited-state lifetimes.

**Keywords** Clusters · Conical intersections · DNA bases · Hole burning · Nucleotides · R2PI · REMPI?

## Contents

M.S. de Vries (✉)

Department of Chemistry and Biochemistry, University of California, Santa Barbara, CA 93106-9510, USA
e-mail: devries@chem.ucsb.edu

# 1  Introduction

Understanding the response of DNA bases to UV radiation is critical for both practical and fundamental reasons [1–5]. Nucleobase photochemistry following UV absorption constitutes a fundamental step in radiation-induced DNA damage. Short excited-state lifetimes are often described as nature's strategy to protect the building blocks of life against UV photodamage. Furthermore, UV photo-selection may have played a key role in prebiotic chemistry on an early Earth. This photo-chemistry schematically involves two steps: absorption of a photon prepares the nucleobase in an excited state, followed by the ensuing chemistry. The first step, the excitation, can be probed by various forms of electronic spectroscopy. The second step, the dynamics of the excited state once it is formed, can often be followed in the time domain, which is the topic of the next chapter. This current chapter focuses on the frequency domain, probing primarily the excitation step. However, some time domain information also follows from the frequency domain because both steps are connected by Heisenberg's uncertainty principle, $\Delta E \Delta \tau \geq h/2\pi$, such that a shorter excited-state lifetime, $\tau$, corresponds to a larger linewidth, $\Delta E$.

The fate of a molecule upon irradiation depends on the shape of the excited-state potential energy landscape [6]. Electronic excitation places the molecule in the Franck–Condon region of the excited state, the starting point for a number of competing possible processes, such as fluorescence, internal conversion, intersystem crossing, or exciplex formation [7, 8]. The availability of these pathways and their relative rates, or associated excited-state lifetimes, determines the outcome of this competition and thus the product of the photochemistry. One molecule can therefore be intrinsically more resistant to damage than another, even though they absorb UV light equally. Furthermore, the same molecule can have different UV responses, depending on the molecular environment. Of particular interest in the case of the nucleobases is the rate of internal conversion, compared to other possible processes. Internal conversion returns the molecule to the electronic ground state in a radiationless way, and thus converts electronic energy to heat in the form of ground state vibrational energy. Heat can subsequently be safely dissipated to the environment. When internal conversion is fast enough to prevent other photochemical reactions from taking place, the molecule has a very short excited-state lifetime, $\tau^*$, and is stable against UV photodamage [9–12].

Rapid internal conversion, when available to a molecule, diffuses electronic energy by converting it to internal energy in the ground state, and therefore minimizes access to other photochemical pathways. Generally, the biologically most relevant forms of the purines and pyrimidines exhibit the shortest excited-state lifetimes, thus selectively minimizing the chances for photochemical damage in the molecular building blocks of life. In stark contrast, many other nucleobase derivatives, even isomers, have orders of magnitude longer lifetimes (see Fig. 1). In fact, ultrafast internal conversion – the same property found in many UV sunscreens – is observed for all nucleobases implicated in replication today and, intriguingly, there are no examples of canonical nucleobases which are highly
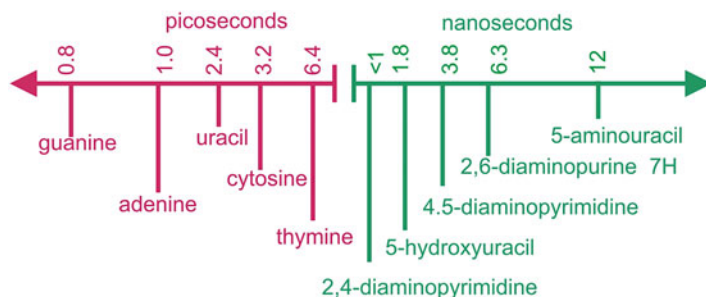
**Fig. 1** Compilation of gas-phase excited-state lifetimes of selected nucleobases and derivatives

fluorescent [1]. Strengthening the correlation between excited-state lifetime and the propensity for photoreaction is the observation that the minor DNA base 5-methylcytosine, with its tenfold longer lifetime than cytosine, is a hotspot for photodamage [13].

Evolution requires the existence of self-replicating molecules; the selection of the nucleobases as building blocks of those macromolecules would logically have taken place before any biological processes. Therefore, if the excited-state properties have played a role in a chemical selection of today's nucleobases, they are a relic of prebiotic chemistry on an early Earth.

The intramolecular mechanism governing the ultrafast internal conversion in single purines and pyrimidines is now emerging. The key is the occurrence of conical intersections which connect the excited-state potential energy surface, reached by photon absorption, to the ground state energy surface. The dramatic lifetime differences between derivatives of nucleobases appear to be caused by variations in the excited-state potential surfaces which restrict or slow access to these conical intersections [14].

The excited-state potential energy surface, and thus the corresponding electronic absorption and dynamics, is affected by molecular structure and by interactions, such as those with solvent molecules. To disentangle the different effects, it is desirable to study isolated molecules, which is possible in the gas phase under collision-free conditions. First, this makes it possible to observe intrinsic properties and explore the potential energy surfaces of the individual molecules. Second, by employing double resonance techniques, it is possible to perform isomer specific spectroscopy. Some details of how interactions affect excited states can be studied by cluster spectroscopy in the gas phase. Once intrinsic properties are mapped out, they may be extrapolated to bulk conditions, which are the subject of later chapters.

## 2 Vibronic Spectra

The nucleobases are heterocyclic aromatic compounds which absorb to their first excited electronic state in the 31,000–37,000 cm$^{-1}$ range. This range also forms the onset of absorption in the liquid phase. Figure 2 shows resonance enhanced
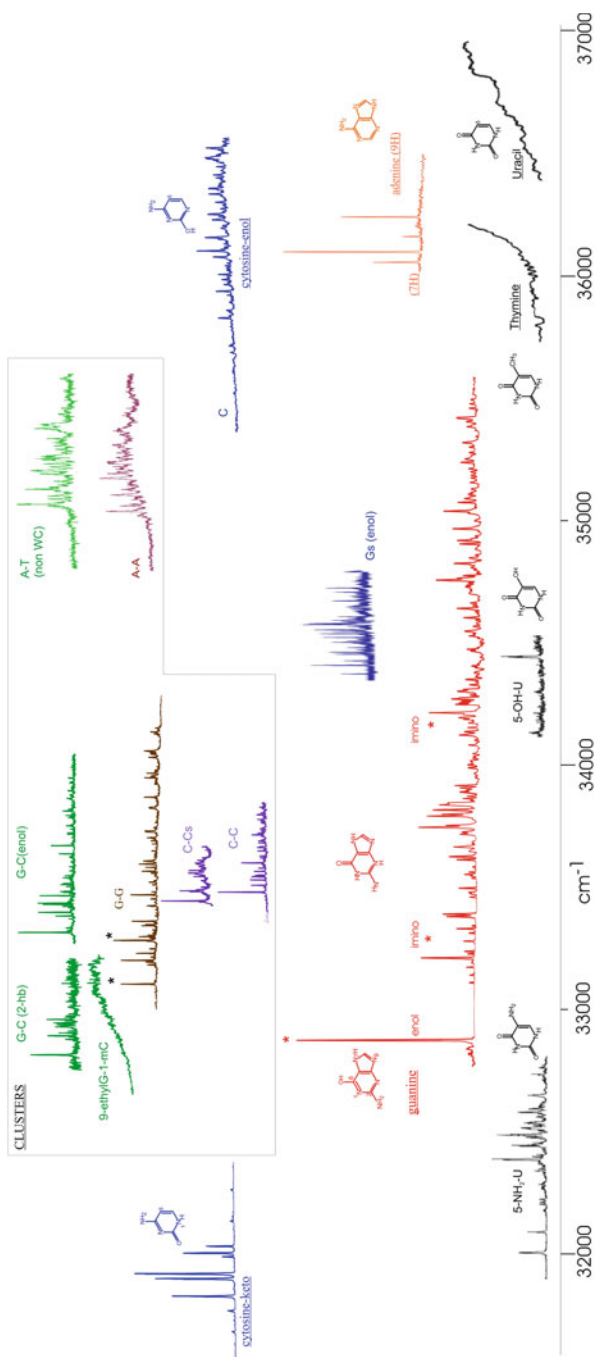
**Fig. 2** REMPI spectra of the canonical bases and their base pairs. *Asterisks* indicate origins of different tautomeric or structural isomers

**Table 1** Observed $S_1$ band origins of nucleobases, nucleosides, base-pairs, and assorted nucleobase derivatives

| | Compound | Origin cm$^{-1}$ | Remarks | References |
|---|---|---|---|---|
| Nucleobases | Guanine | 32,864 | 7H enol *syn* | [15] |
| | | 33,269 | Oxo-imino | [15] |
| | | 33,910 | Oxo-imino | [15] |
| | | 34,755 | N9H hydroxyl-amino | [15] |
| | Adenine | 36,105 | π–π* | [16, 17] |
| | | 36,062 | n–π* | [16, 17] |
| | Cytosine | 31,826 | Keto | [18] |
| | | ~36,000 | Enol | [18] |
| | Thymine | 36,000 | Broad onset | [19] |
| | Uracil | 36,700 | Broad onset | [19] |
| Nucleosides | Guanosine | 34,443 | Enol | [20] |
| | 2′-Deoxyguanosine | 34,436 | Enol | [20] |
| | 3′-Deoxyguanosine | 34,443 | Enol | [20] |
| Base-pairs | G–C | 33,314 | C in enol form | [21] |
| | | ~32,800 | Doubly H-bonded | [22] |
| | A–T | 35,064 | | [23] |
| | G–G | 33,103, 33,282 | | [24] |
| | A–A | 35,040 | | [16, 25] |
| | C–C | 33,483 | | [18] |
| Derivatives | 1-Methylcytosine | 31,908 | | [18] |
| | 5-Methylcytosine | 31,269 | | [18] |
| | 5-OH-uracil | 34,440 | | [26] |
| | 5-NH$_2$-uracil | 31,939 | | [26] |
| | 9-Methylguanine | 34,612 | | [24] |
| | 2,4-Diaminopyrimidine | 34,459 | Diamino | [27] |
| | 2,6-Diaminopurine | 34,881 32,215 | 9H diamino 7H diamino | [27] |
| Derivative pairs | 9-mG-1mC | 33,000 | Broad | [22] |
| | C-1mC | 33,419 | | [18] |
| | C-5mC | 32,500, 32,691, 32,916 | | [18] |
| | 5mC–5mC | 32,493, 32,691, 32,872 | | [18] |

M (as in 1mC) designates methyl

multiphoton ionization (REMPI) spectra of all of the canonical bases and some derivatives, as well as some of their clusters, representing base pair combinations. Asterisks indicate origins of different tautomers for the monomers and different hydrogen bonded structures for the clusters. Table 1 lists the respective $S_1 \leftarrow S_0$ origins.

Levy and coworkers reported the first REMPI spectra for uracil and thymine in 1988 [19]. The spectra were very broad, merely showing an onset of unstructured absorption around 36,000 cm$^{-1}$ for T and somewhat higher energy for U. These results suggested the absence of useful resolved spectroscopy for nucleobases. However, this picture changed with the first report of the resolved guanine REMPI spectrum [28], followed by those of adenine [29] and cytosine [30]. Observation of these spectra became possible with the employment of laser desorption jet cooling techniques, optimized for the study of these types of molecules [31–34].

The vapor pressure of the nucleobases at room temperature is too low for gas phase spectroscopy and heating to obtain sufficient vapor pressure causes thermal degradation. With some care, adenine can still be sufficiently heated in an oven to form a seeded supersonic beam, but this does not work satisfactorily for the other bases. Pulsed heating at a rate of the order of 1,000°K in 10 ns allows fragment-free vaporization of all bases and this heating rate can be achieved with pulsed laser desorption. Typical experiments use a Nd:YAG laser at 1,064 nm with 10 ns pulses of a fraction of a mJ/cm$^2$ to desorb from a graphite substrate, which is moved to expose fresh material in subsequent shots [32, 35, 36]. To permit spectroscopy, the desorbed molecules are entrained in a pulsed supersonic expansion, cooling them to internal temperatures corresponding to the order of 20 K [32]. Such temperatures are low enough for the vibronic spectroscopy described in this chapter, but it may be noted that ions in a cold trap can be cooled to lower temperatures by about an order of magnitude and entrainment in helium droplets leads to even lower temperatures [37, 38].

## 2.1 Spectroscopic Techniques

In molecular beams, direct absorption is generally not measurable because the optical density is too low. Intracavity techniques can sometimes be used, such as cavity ringdown [39] and microwave spectroscopy [40], but the common approach is a form of action spectroscopy, especially laser-induced fluorescence (LIF) and resonance-enhanced multiphoton ionization (REMPI). A consequence of this technical limitation is that the excited state becomes part of the detection method and thus the dynamics of the excited state can influence the outcome of the measurement. In particular, both LIF and REMPI are blind for transitions to an excited state with a lifetime significantly shorter than the laser pulse duration. The following sections will discuss some implications of this limitation for understanding excited-state behavior.

A major advantage of gas-phase spectroscopy is the ability to perform isomer-specific measurements by double resonance, or hole-burning techniques. Figure 3 schematically outlines this approach for the case of REMPI. Purple arrows indicate wavelengths which are scanned to obtain a wavelength-dependent spectrum. In Fig. 3a this produces a vibronic REMPI spectrum. In Fig. 3b the blue arrow represents the probe laser, set to a single resonant wavelength in the REMPI spectrum. Its ion signal comes from one specific isomer. The purple arrow represents the burn laser,
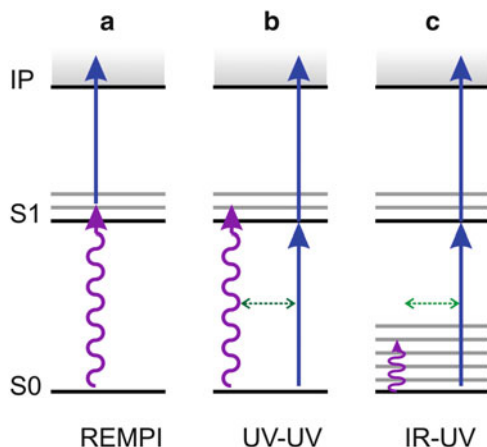
**Fig. 3** Schematic diagram of spectroscopic techniques. *Purple arrows* indicates wavelength that is being scanned to obtain a spectrum. *Blue arrows* indicate fixed wavelength. *Green arrows* indicate time delay between two laser pulses. (**a**) REMPI provides vibronic spectra. (**b**) UV–UV hole burning separates isomeric contributions to the UV spectrum. (**c**) IR–UV hole burning provides isomer selected ground state IR spectra

which precedes the probe laser by typically 100 ns. Whenever the burn laser is resonant with a transition it depletes the ground state and alters the Franck–Condon area, resulting in a dip in the ion signal from the probe laser, but only if both lasers interact with the same isomer population. Therefore, a scan with the probe laser produces an ion-dip spectrum which amounts to an isomer-selected rovibronic spectrum. In Fig. 3c, the same procedure is followed with an IR laser as probe laser to generate an isomer selected ground state IR spectrum. In Fig. 2, asterisks denote origins of different isomers, identified by double resonance spectroscopy.

Electronic spectra essentially contain information about the energy difference between the ground state and the excited state. By reducing the ground state vibrational population to $v = 0$ through cooling, vibronic spectral structure can provide additional information on the excited state. IR–UV hole burning, on the other hand, provides ground state vibrational frequencies which can be used to identify the starting structures of the excitation, especially tautomeric form and cluster structure. Further information can be derived from line contours for identifying excited-state symmetries and lifetimes.

The latter is demonstrated in Fig. 4, showing the comparison of a peak in the REMPI spectrum of 2,4-diaminopyrimidine with simulated lineshapes based on different Lorentzian linewidths [27]. The upper limit to the linewidth of 0.5 cm$^{-1}$ thus observed in this case corresponds to a lower limit in the excited-state lifetime of 10 ps.

Further information about the excited-state dynamics may be derived by comparing these electronic spectra, e.g., by comparing frequency shifts between various isomers and derivatives and by contrasting broad vs sharp spectra. Furthermore, since all these REMPI spectra were obtained with nanosecond pulses, the absence of signal from selected species may point to ultrafast internal conversion.
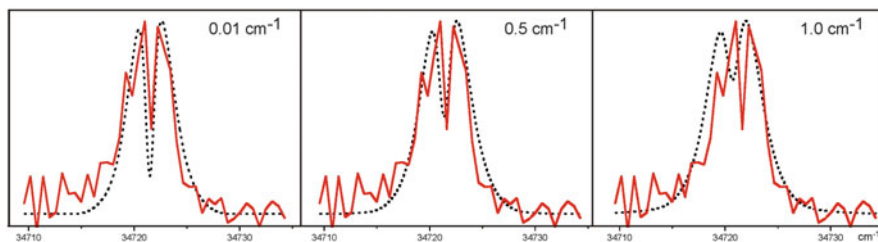
**Fig. 4** Detail of the 34,720 cm$^{-1}$ peak in the 2,4-DAPy REMPI spectrum, compared with simulations of the rotational envelope at three different Lorentzian linewidths [27]

## 3 Isomers

The origins on the UV spectra, obtained by REMPI, reflect the energies of the $S_1$ excited state relative to the $S_0$ ground state, which is difficult to obtain computationally with any reasonable accuracy. Figure 2 shows that both the purine and pyrimidine bases absorb in the same frequency range, but significant shifts exist between different related compounds. For example, adenine absorbs 3,000 cm$^{-1}$ to the blue of the lowest energy observed tautomer of guanine [27, 41]. Adenine, which is 6-aminopurine (6AP), also absorbs about 3,500 cm$^{-1}$ to the blue of its isomer 2-aminopurine (2AP). Comparing those two isomers, one notices not only the large difference in origin, but also the fact that the adenine spectrum features only a few lines while the 2-aminopurine spectrum is very extensive and covers a large frequency range [42]. These observations are consistent with a model that is summarized schematically in Fig. 5 [41]. This model assumes excitation to an $S_1$ state, which interacts with a second excited state through a curve crossing. This picture represents potential curves as a function of a single internuclear coordinate. In the more general case of multidimensional potential surfaces, to be discussed below, the curve crossing is replaced by a conical intersection. The second excited state may couple with the electronic ground state to quench fluorescence and phosphorescence. In the case of the purines, the $S_1$ state is likely to be of π–π* character and the second excited state is likely to be of n–π* character, to be discussed below. The absorption characteristics of the purines and their excited-state lifetimes then depend strongly on two parameters: (1) the relative energies of these two states and (2) the amount of electronic coupling between them.

Possible arrangements are shown schematically in Fig. 5. A curve crossing, as sketched schematically for 6AP, will typically lead to spectra which are diffuse or show a cutoff at absorption energies larger than that of the crossing. If, on the other hand, as sketched for 2AP, the interaction between the two excited states is weak, or if the $S_1$ state is significantly lower in energy, then we may expect a sharp and extended vibronic spectrum. A lower energy $S_1$ state is also consistent with the large observed red-shift. Finally, the other extreme is sketched in the inset. If the interaction is strong and the $S_1$ state is higher in energy, then it is possible to have a
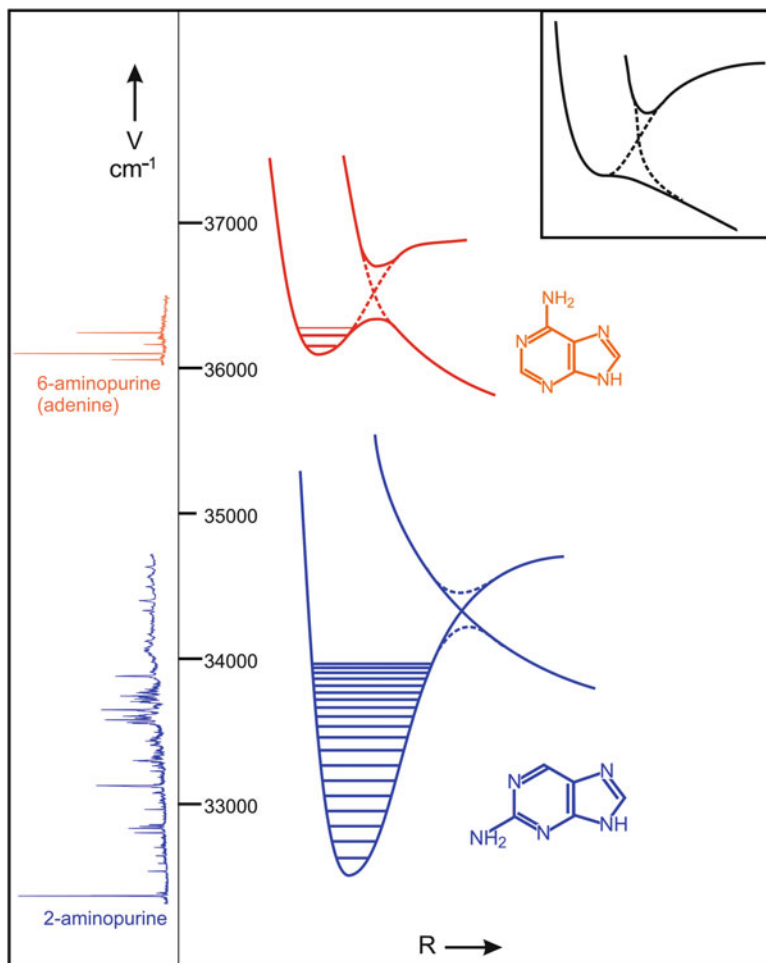
**Fig. 5** *Left* along vertical axis: REMPI spectra of 6-aminopurine (adenine) in *red* and 2-aminopurine in *blue*. *Right*: schematic potential energy diagrams of the excited state as a function one internuclear coordinate, representing a model with a curve crossing between $S_1$ and another excited state. The *inset* shows the case without a barrier, which would not produce a discrete spectrum; see text for details

barrierless curve crossing, resulting in a completely structureless vibronic spectrum and an extremely short excited-state lifetime.

Within this picture, the striking photochemical difference of purine and adenine as compared to 2-aminopurines is the result of the relative energies of the $\pi$–$\pi$* and the n–$\pi$* states. The fact that the origin for the 2AP spectrum is significantly to the red of the adenine spectrum implies that the $S_1$ state is lower in this case. Furthermore, the extent of the spectrum suggests that 2AP does *not* exhibit a curve crossing as sketched in Fig. 5, as opposed to adenine. Therefore the gas-phase spectra

suggest that the amino substitution in the 2-position of purine lowers the excited-state potential of the π–π* state, while substitution in the 6-position has little effect. This is fully consistent with solution results, as well as with circular dichroism measurements by Holmen et al. which identify a π–π* state about 4,000 cm$^{-1}$ below the n–π* state for 2AP [43].

# 4   Derivatives

When we consider more than one internuclear coordinate, we can describe the more general situation as illustrated schematically in Fig. 6. The crossings of multidimensional potential surfaces are conical intersections. These features can only occur in regions of the potential energy landscape which represent a deformation of the molecular frame from the ground state equilibrium geometry. The following case study of adenine derivatives serves as an example [29, 44–56]. For 4-aminopyrimidine (Fig. 7 top left), surface hopping calculations identified two conical intersections [57]: deformation at the C2-position (red circle) leads to deactivation of the excited state with a lifetime, $\tau^*$, of 1 ps, and deformation at the C5=C6 bond (blue rectangle) leads to deactivation with $\tau^*$ of 400 fs. Immobilizing the latter with a five-membered ring forms adenine with a single conical intersection due to the C2 deformation and $\tau^*$ of 1 ps. Figure 7 (bottom left) shows the geometry at this conical intersection as calculated by Marian et al. [58]. Substitution at the C2-position further modifies the excited-state potential and eliminates this conical intersection. Consequently, both 2,6-diaminopurine and 2-aminopurine have fluorescent excited states with lifetimes of the order of nanoseconds. In fact, the latter is used as a fluorescent tag in DNA research. In the same way, C5 substituents in pyrimidines alter excited-state lifetimes over a range of picoseconds to nanoseconds by modification of the topography of the potential energy surfaces around C5=C6 torsion and stretching coordinates [59–61]. Interestingly, the same coordinates are found to play a role in thymine photo-dimerization in



**Fig. 6** Schematic potential energy diagram (as function of two inter-nuclear coordinates) with two conical intersections connecting the $S_1$ excited state, via an intermediate state, with the $S_0$ ground state. *Arrows* indicate competing de-excitation pathways

UV absorption
fluorescence - ns
reaction < ns
internal conversion < ps
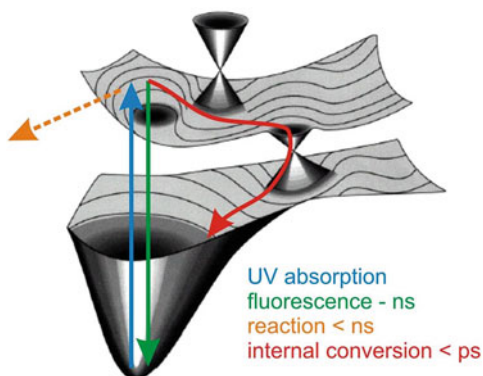
**Fig. 7** Ring deformations at C2 or C5=C6 lead to conical intersections which mediate internal conversion at different time scales depending on molecular structure: on the order of 1 ps for C2 pyramidalization (*bottom left*) and 400 fs for C5=C6 stretch and torsion. Details in text
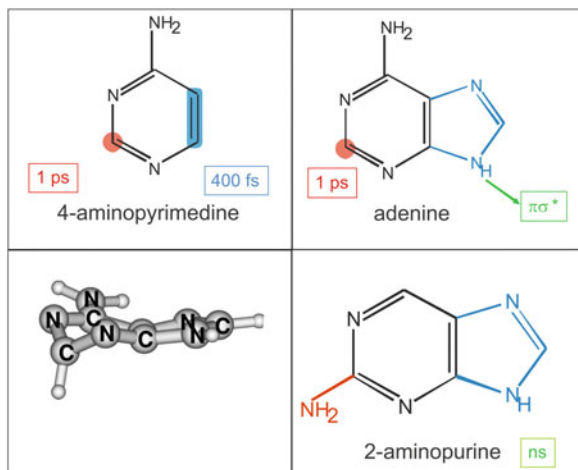
DNA [62]. Other excited states also need to be considered: N9–H motion forms an additional coordinate in adenine which can lead to a conical intersection with a πσ* state [16, 54]. A weakly absorbing nπ* state plays a role as well, in addition to the ππ* state, and can sometimes serve as a "dark state" with an extended lifetime [17, 63].

Furthermore, purine, the parent compound of adenine and guanine, forms triplet states in high yield [64]. Lifetimes also depend strongly on tautomeric forms, as discussed in Sect. 6 [15, 65–69]. Understanding these mechanisms helps explain how subtle structural differences between substituted nucleobases can produce excited-state lifetime differences of orders of magnitude.

A similar strong effect can be observed in uracil (U) derivatives upon substitution in the C5-position [26]. Two-photon ionization and IR/UV double resonance spectra of the uracil analogues, 5-OH–U and 5-NH$_2$–U, show that there is only a single tautomer present for each with an excited-state lifetime of 1.8 ns for 5-OH–Ura and 12.0 ns for 5-NH$_2$–Ura, as determined from pump-probe experiments. These lifetimes are 3 and 4 orders of magnitude longer, respectively, than that for unsubstituted uracil [70]. Nachtigallova et al. determined vertical excitation energies, excited-state minima, minima on the crossing seam, and reaction paths towards them by means of multi-reference ab initio methods [26]. They found sizeable barriers on these paths which provide an explanation for the lifetimes of several nanoseconds observed in the experiment.

Kistler and Matsika reported a similar effect for cytosine derivatives as well [60, 71]. For example, 5-methyl-2-pyrimidin-(1*H*)-one (5M2P, with a methyl substituent in the C5-position instead of the amino group in the C4-position) has a fluorescence lifetime which is orders of magnitude longer than the picosecond lifetime of cytosine [5, 63, 70, 72]. This excited-state lifetime difference correlates directly with a lower S$_1$ excitation energy for 5M2P, analogous to the energetic considerations for adenine vs 2-aminopurine.

## 5 Character of the Excited State

The character of the first excited states is not always entirely clear but generally the UV spectra contain contributions to two excited states, of $\pi\pi^*$ and $n\pi^*$ character, respectively [17, 46]. The $\pi$–$\pi^*$ transition carries most oscillator strength and the $n\pi^*$ state can function as a dark state for internal conversion, depending on whether the relative energies lead to the occurrence of conical intersections. In the case of adenine, Lee et al. characterized the excited states based on rotational band contour analyses [17]. They showed that the lowest $n\pi^*$ and $\pi\pi^*$ states can be labeled with their excited-state vibronic symmetry, and exhibit a strong $\pi\pi^*$–$n\pi^*$ vibronic coupling via an out-of-plane vibrational mode. They assigned the band at 36,062 cm$^{-1}$ as the n–$\pi^*$ transition and the 36,105 cm$^{-1}$ band as the $\pi$–$\pi^*$ transition by symmetry analysis. The band at 36,248 cm$^{-1}$ provides evidence of the strong $\pi\pi^*$–$n\pi^*$ vibronic coupling via an out-of-plane vibrational mode.

Sobolewski and Domcke showed that in the excited-state dynamics a $\pi\sigma^*$ can also play a role along an NH nuclear coordinate [73]. Motion along this coordinate can lead to hydrogen loss and Hunig et al. demonstrated this channel by detecting the dissociating hydrogen using Lyman-$\alpha$ excitation and analyzing the kinetic energy from the Doppler shift [54].
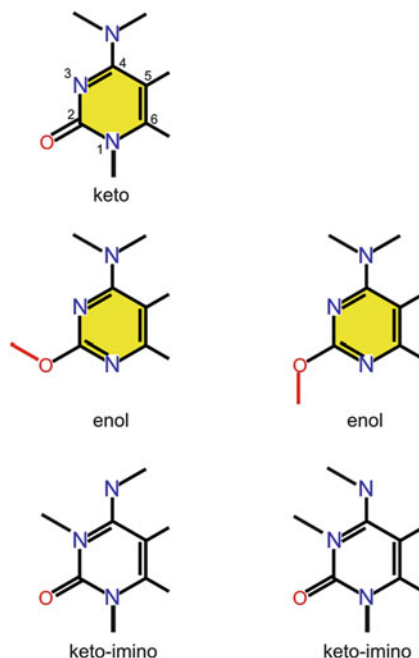
## 6 Tautomers

A complication in the study of nucleobase structure and dynamics is that these compounds exhibit multiple tautomeric forms. The electronic spectra, such as those in Fig. 2, may contain contributions of all the tautomers present in the beam.

As shown in Fig. 2, the $S_1 \leftarrow S_0$ transitions of the two most stable cytosine tautomers, keto and enol, are a remarkable 4,000 cm$^{-1}$ apart, while energetically they differ by only 0.03 eV [18, 30]. The third major tautomer, keto-imino, is significantly higher in energy [74–76] and not observed in these spectra (Fig. 8). The keto form is the biologically important one, with Watson–Crick base pairing in DNA, and predominant in solution. In matrix isolation, Szczesniak et al. observed both keto and enol forms with higher abundances for the latter and small contributions from the imino form [77]. Brown et al. have obtained rotational constants for all three tautomeric forms by microwave spectroscopy [78]. Schiedt et al. also identified the existence of keto and enol tautomers of neutral cytosine in the gas phase by anion spectroscopy [79].

Kosma et al. reported excited-state dynamics by probing with different excitation wavelengths in a range from 260 to 290 nm, which allowed them to distinguish between keto only vs mixed populations [80]. They conclude that the deactivation pathways are quite different for the different tautomers, with three time constants for keto-cytosine and two for the others. Theoretical treatments in the literature had focused on modeling the latter, while the new results point to the importance of

**Fig. 8** The major tautomers of cytosine. The IR–UV double resonance experiments observe the keto and enol forms (*yellow*) but do not distinguish between the two enol tautomers

tautomeric distinction in these analyses. For the keto form, the two faster channels, with femtosecond and picosecond lifetimes, are consistent with fast, but not barrierless, excited-state relaxation via conical intersections between the $^1\pi\pi^*$ and ground state [74]. The third channel with a lifetime of hundreds of picoseconds at 290 nm is proposed to involve excited-state tautomerization to a low-lying $^1n\pi^*$ state of the keto-imino tautomer [81]. The authors propose that, in the condensed phase, this channel would be quenched by rapid back hydrogen-transfer, catalyzed by hydrogen-bound water molecules [82, 83]. Consequently, this pathway would not alter the inherent photostability.

In most cases, electronic spectra of different tautomers do not exhibit significant shifts and thus vibronic spectra potentially consist of overlapping contributions from a number of tautomers. Such overlapping electronic spectra can be disentangled by IR–UV double resonance spectroscopy. However, an additional complication with this technique is that it is based on action spectroscopy in which the probe signal is multiphoton ionization. As a result this approach is blind for tautomers for which the excited-state lifetime is significantly shorter than the laser pulse. Such tautomers do not show up in the electronic spectrum to begin with.

A case in point is the so-called guanine puzzle [15, 68]. The REMPI vibronic spectrum consists of the overlapping spectra from four different tautomers, as determined by UV–UV hole burning [35, 84, 85]. However, the identification of the specific tautomers by IR–UV double resonance spectroscopy proved challenging. Two enol tautomers could easily be assigned based on the strong OH stretch
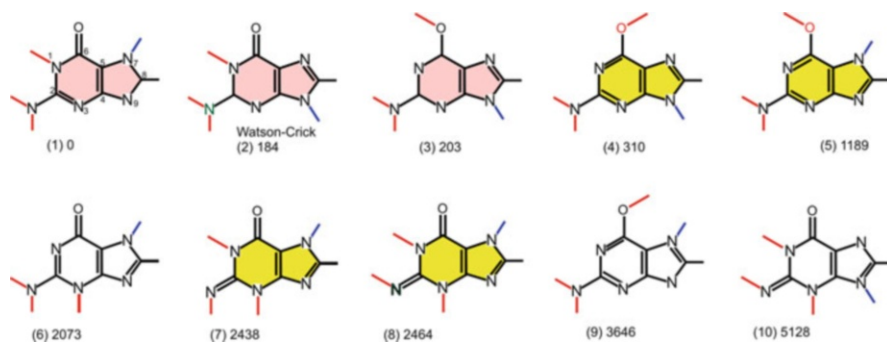
**Fig. 9** Ten of the lowest energy tautomers of guanine. Relative energies in wavenumbers from [66]. *Yellow* structures are observed in gas-phase nanosecond REMPI experiments. *Red* structures have sub-picosecond excited-state lifetimes. Structures *1–4* are observed in helium droplets. Keto–N9H is the Watson–Crick structure

around 3,600 cm$^{-1}$. However, the other two species were initially incorrectly assigned as keto tautomers. Figure 9 shows the ten lowest energy tautomers of guanine with relative energies in wavenumbers from [66]. Clearly the two keto tautomers (N7H and N9H) are the lowest energy forms and their IR spectra formed a quite reasonable match with calculated frequencies for these forms, making this a plausible assignment. However, subsequent data from a helium droplet experiment exhibited slightly different IR spectra which formed a better match with the keto forms [38]. This led to a re-analysis of the IR–UV data and a reassignment of the two tautomers from the keto to the imino form. This assignment was subsequently confirmed by IR–UV measurements in the imino stretch region below 2,000 cm$^{-1}$ [66]. Gas-phase microwave experiments also found the keto tautomers [40].

These observations are summarized in Fig. 9 in which the red tautomers were observed by the two techniques that involve direct absorption in the ground state (helium droplets and microwave), while the yellow tautomers were observed by the technique that involves action spectroscopy via the electronic excited state (REMPI). This difference suggests that the lowest energy forms are most abundant in the gas phase in all cases, but are not observed with REMPI because they have short-lived excited states. This explanation is confirmed by computations, showing a rapid internal conversion pathway through a conical intersection, which is not accessible for the higher energy enol and imino tautomers [68].

The tautomeric landscape of adenine is somewhat less varied than in the case of guanine because of the absence of the oxygen. Plützer and Kleinermanns reported IR–UV double resonance spectroscopy and observed two tautomers [51]. Both tautomers are of the amino form, with the 9H form most abundant and a small presence of the 7H form. This finding is consistent with microwave measurements by Brown et al. [86]. In conditions of jet cooling the imino form appears to be absent, although in the gas phase at elevated temperature the IR spectra seem to comprise multiple tautomers, including imino.

Microwave measurements of uracil in a heated cell suggest the diketo form as the most abundant. Brown et al. reported the first microwave measurements in a seeded molecular beam and also concluded that the diketo form was predominant [87, 88]. Viant et al. reported the first rotationally resolved gas-phase IR spectra of uracil [89]. This work employed a slit nozzle, an IR diode laser, and a multi-pass arrangement to obtain high-resolution IR absorption spectra of the out of phase $\nu_6$ stretching vibration. The rotational analysis unambiguously assigned this species to the diketo tautomer. Brown et al. also observed the diketo form of thymine in a seeded molecular beam, based on hyperfine structure [90].

## 7    Intermolecular Effects: Clusters

It is often assumed that the same internal conversion processes govern the subpicosecond de-excitation timescales of nucleobases in solution, albeit modified by solvent interactions. It is reasonable to postulate that the chromophore is affected primarily by the first solvent shell. Therefore many of the details of the dynamics in solution can be elucidated by studying clusters with small numbers of water molecules [35, 36, 91–96]. It appears that hydrogen bonding can play a role in two ways. First, the excited-state potential energy surfaces are modified, thus affecting possible trajectories through conical intersections. Second, the hydrogen bond itself provides another possible coordinate for coupling excited states and the ground state. This effect is not limited to hydrogen bonding with water, but may also play a role in base pairing and in intramolecular hydrogen bonds. This coordinate can be thought of as an analogue of the N–H stretch coordinate correlated with a $\pi\sigma^*$ state, and its associated conical intersections [73, 97–100]. In the latter case, if the $\pi\sigma^*$ potential surface fails to reconnect with $S_0$, the hydrogen can actually dissociate. In the hydrogen bonded case, the hydrogen is confined to the system and this coordinate can only mediate a single or double proton transfer.

An example is that the specific Watson–Crick (WC) structure in isolated GC nucleobase pairs has a short excited state lifetime which is explained by proton motion in the middle hydrogen bond [22, 101–103]. By contrast, in other GC base pair structures this coordinate does not lead to accessible conical intersections [22, 104]. Figure 10 shows the eight lowest energy structures of hydrogen bonded GC clusters, with the very lowest energy structure representing the WC structure. The two lowest energy structures, marked in red, were not directly observed in gas-phase experiments with nanosecond timescale REMPI detection, while the next two higher energy structures, marked in yellow, were observed and identified by IR–UV hole burning [21, 22, 104].

For AT base pairs, the Watson–Crick structure was also not identified; however in this case it is not the lowest energy structure so it is possible that it was insufficiently populated in the molecular beam [23]. In REMPI spectra of homo base pair combinations, the predicted lowest energy structure was not observed. This absence occurred for GG dimers [105], CC dimers [18], and AA dimers
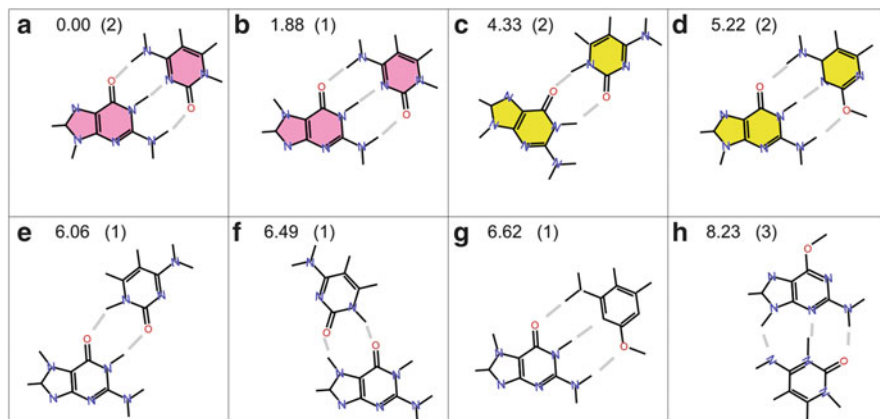
**Fig. 10** The lowest energy structures of hydrogen bonded GC clusters with energies in kcal/mol. *Yellow* structures were observed in REMPI experiments, while *red* structures were not

[25]. In these homodimers the missing structure is symmetric, so it is possible that an excimer state is formed with a considerable splitting, causing a shift in the UV band outside of the experimental range. However, it is also possible that the absence of those cluster structures in the REMPI spectra is because of short lived excited states which are dark in nanosecond timescale REMPI detection. For 9-methyladenine-adenine clusters, Plützer et al. identified a stacked structure, which they detected on the mass of protonated adenine. They interpreted their finding as involving hydrogen transfer from the 9H-position of the adenine. Schultz and coworkers reported indications of this process in time-resolved photoelectron spectroscopy studies of adenine and adenine-containing clusters [93, 106–108] and in nucleobase pair analogues [101, 109, 110].

Another structure in which hydrogen bonding occurs and possibly affects dynamics is in nucleosides in the *syn* configuration. Nir et al. found by double resonance spectroscopy that isolated guanosine indeed forms an internal hydrogen bond between 5′OH and 3N [111]. Nevertheless, they found a sharp REMPI spectrum, implying a relatively long-lived excited state. By contrast, an REMPI spectrum for adenosine has not been observed, suggesting a possibly short excited-state lifetime [112, 113]. It should be noted that, for guanosine in the gas phase only, the enol tautomer has been observed, so far, which suggests that the keto tautomer is selectively short-lived, analogously to the nucleobase. So whether and to what extent the shortened lifetime observed in solution is an intrinsic property of nucleosides remains an open question. Other aspects of the role of the sugar moiety in excited-state dynamics may also play a role. It has been proposed that the additional degrees of freedom provide a bath for quenching excited-state excitation. Furthermore, in solution the dynamics may be further complicated because the sugar also provides additional hydration sites.

Another intermolecular interaction is base stacking, which provides much of the stability in helices. In the π-stacked structural motif, exciplex formation appears to
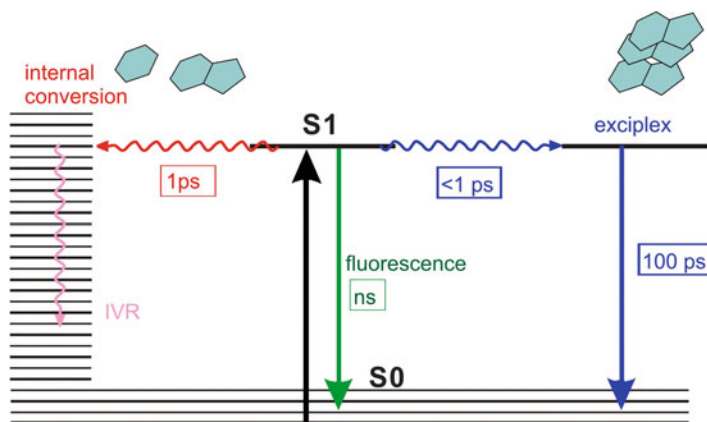
**Fig. 11** Simplified Jablonski diagram, showing major possible processes for deactivation of the excited state in nucleobases: Fluorescence is typically slow, in the nanosecond range. Internal conversion back to the ground state in the sub-picosecond time scale occurs for selected single bases and some hydrogen bonded base pairs. Exciton formation in stacked bases can lead to exciplex states in less than a picosecond for specific stacked structures. Those states subsequently decay to the ground state by charge recombination on the 100 ps time scale

play a major role in the photodynamics [113, 114]. The overlap of the π-clouds depends critically on the relative position of the molecules. For example, Schreier et al. have shown that thymine dimer formation in DNA is determined largely by conformational properties at the instant of excitation [115]. In solution phase experiments, Crespo-Hernández and Kohler and coworkers have shown that base stacking in single- and double-stranded DNA favors non-radiative decay via the formation of charge-transfer or exciplex states [116–118]. Such states decay much more slowly than the ππ* states in single bases (see Fig. 11). These considerations are the topic of the next chapter.

# 8   Summary

Electronic and vibrational spectroscopy of isolated nucleobases sheds light on excited-state dynamics indirectly in a number of ways. UV–VIS excitation spectroscopy probes the potential energy landscape in the Franck–Condon region, which establishes the starting conditions of any ensuing photochemistry. The combination with IR hole burning to obtain vibrational spectroscopy as well offers the important opportunity to obtain isomer selected data. This approach makes it possible to probe individual tautomers, structural conformers, isomers, and cluster structures. This isomer selectivity, as well as the fact that nucleobases can be studied free of interactions, provides unique insights into their intrinsic properties, unperturbed by any secondary effects of the biological environment. Therefore such

gas-phase experiments offer the best data for comparison with computational chemistry at the highest levels. The frequency domain is coupled with the time domain by the inverse relationship between energy and linewidth. Particularly in the 10–100 ps range, excited state lifetimes may be derived from spectra linewidths. Shorter lifetimes not only lead to extensive broadening but often render excited states unobservable by action spectroscopy, such as REMPI or LIF, with nanosecond timescale laser pulses. It is possible that future experiments in the frequency domain will provide additional insight into excited-state dynamics. Examples may include spectroscopy with shorter laser pulses, including a trade-off between time and frequency resolution, spectroscopic characterization of the hot ground state products of internal conversion, and more elaborate studies of clusters with water to detail the role of micro hydration.

**TOC Graphic**
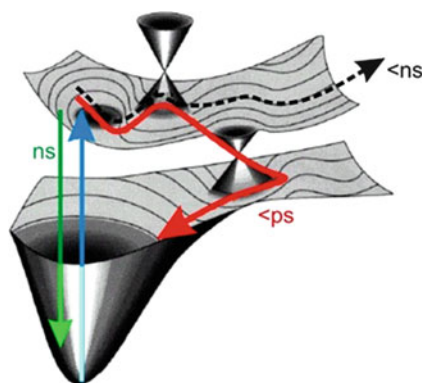


Following electronic excitation, probed in the frequency domain (blue), internal conversion (red) can compete with fluorescence (green) and other photochemical pathways (black).

# References

1. Middleton CT, de La Harpe K, Su C, Law YK, Crespo-Hernandez CE, Kohler B (2009) DNA excited-state dynamics: from single bases to the double helix. Annu Rev Phys Chem 60:217–239
2. Kleinermanns K, Nachtigallova D, de Vries MS (2013) Excited state dynamics of DNA bases. Int Rev Phys Chem 32(2):308–342

3. Gonzalez-Ramirez I, Roca-Sanjuan D, Climent T, Serrano-Perez JJ, Merchan M, Serrano-Andres L (2011) On the photoproduction of DNA/RNA cyclobutane pyrimidine dimers. Theor Chem Acc 128(4–6):705–711

4. Serrano-Andres L, Merchan M (2009) Are the five natural DNA/RNA base monomers a good choice from natural selection? A photochemical perspective. J Photoch Photobio C 10 (1):21–32

5. Crespo-Hernandez CE, Cohen B, Hare PM, Kohler B (2004) Ultrafast excited-state dynamics in nucleic acids. Chem Rev 104(4):1977–2019

6. Plasser F, Barbatti M, Aquino AJA, Lischka H (2012) Electronically excited states and photodynamics: a continuing challenge. Theor Chem Acc 131(1):1073

7. de Vries MS, Hobza P (2007) Gas-phase spectroscopy of biomolecular building blocks. Annu Rev Phys Chem 58:585–612

8. Matsika S (2004) Radiationless decay of excited states of uracil through conical intersections. J Phys Chem A 108(37):7584–7590

9. Otterstedt J-EA (1973) Photostability and molecular structure. J Chem Phys 58:5716–5725

10. Zgierski MZ, Fujiwara T, Lim EC (2008) Conical intersections and ultrafast intramolecular excited-state dynamics in nucleic acid bases and electron donor-acceptor molecules. Chem Phys Lett 463(4–6):289–299

11. Zgierski MZ, Fujiwara T, Kofron WG, Lim EC (2007) Highly effective quenching of the ultrafast radiationless decay of photoexcited pyrimidine bases by covalent modification: photophysics of 5,6-trimethylenecytosine and 5,6-trimethyleneuracil. Phys Chem Chem Phys 9(25):3206–3209

12. Zgierski MZ, Patchkovskii S, Fujiwara T, Lim EC (2005) On the origin of the ultrafast internal conversion of electronically excited pyrimidine bases. J Phys Chem A 109 (42):9384–9387

13. Tommasi S, Denissenko MF, Pfeifer GP (1997) Sunlight induces pyrimidine dimers preferentially at 5-methylcytosine bases. Cancer Res 57(21):4727–4730

14. Malone RJ, Miller AM, Kohler B (2003) Singlet excited-state lifetimes of cytosine derivatives measured by femtosecond transient absorption. Photochem Photobiol 77(2):158–164

15. Mons M, Piuzzi F, Dimicoli I, Gorb L, Leszczynski J (2006) Near-UV resonant two-photon ionization spectroscopy of gas phase guanine: evidence for the observation of three rare tautomers. J Phys Chem A 110(38):10921–10924

16. Kabelac M, Plützer C, Kleinermanns K, Hobza P (2004) Isomer selective IR experiments and correlated ab initio quantum chemical calculations support planar H-bonded structure of the 7-methyl adenine - adenine and stacked structure of the 9-methyl adenine–adenine base pairs. Phys Chem Chem Phys 6(10):2781–2785

17. Lee Y, Schmitt M, Kleinermanns K, Kim B (2006) Observation of ultraviolet rotational band contours of the DNA base adenine: determination of the transition moment. J Phys Chem A 110(42):11819–11823

18. Nir E, Hünig I, Kleinermanns K, de Vries MS (2003) The nucleobase cytosine and the cytosine dimer investigated by double resonance laser spectroscopy and ab initio calculations. Phys Chem Chem Phys 5(21):4780–4785

19. Brady BB, Peteanu LA, Levy DH (1988) The electronic spectra of the pyrimidine bases uracil and thymine in a supersonic molecular beam. Chem Phys Lett 147:538–543

20. Nir E, Imhof P, Kleinermanns K, de Vries MS (2000) REMPI spectroscopy of laser desorbed guanosines. J Am Chem Soc 122(33):8091–8092

21. Nir E, Janzen C, Imhof P, Kleinermanns K, de Vries MS (2002) Pairing of the nucleobases guanine and cytosine in the gas phase studied by IR-UV double-resonance spectroscopy and ab initio calculations. Phys Chem Chem Phys 4(5):732–739

22. Abo-Riziq A, Grace L, Nir E, Kabelac M, Hobza P, de Vries MS (2005) Photochemical selectivity in guanine-cytosine base-pair structures. Proc Natl Acad Sci USA 102(1):20–23

23. Plützer C, Hünig I, Kleinermanns K, Nir E, de Vries MS (2003) Pairing of isolated nucleobases: double resonance laser spectroscopy of adenine-thymine. Chem Phys Chem 4 (8):838–842
24. Nir E, Plützer C, Kleinermanns K, de Vries M (2002) Properties of isolated DNA bases, base pairs and nucleosides examined by laser spectroscopy. Eur Phys J D 20(3):317–329
25. Plützer C, Hünig I, Kleinermanns K (2003) Pairing of the nucleobase adenine studied by IR-UV double-resonance spectroscopy and ab initio calculations. Phys Chem Chem Phys 5 (6):1158–1163
26. Nachtigallova D, Lischka H, Szymczak JJ, Barbatti M, Hobza P, Gengeliczki Z, Pino G, Callahan MP, de Vries MS (2010) The effect of C5 substitution on the photochemistry of uracil. Phys Chem Chem Phys 12(19):4924–4933
27. Gengeliczki Z, Callahan MP, Svadlenak N, Pongor CI, Sztaray B, Meerts L, Nachtigallova D, Hobza P, Barbatti M, Lischka H, de Vries MS (2010) Effect of substituents on the excited-state dynamics of the modified DNA bases 2,4-diaminopyrimidine and 2,6-diaminopurine. Phys Chem Chem Phys 12(20):5375–5388
28. Nir E, Grace L, Brauer B, de Vries MS (1999) REMPI spectroscopy of jet-cooled guanine. J Am Chem Soc 121(20):4896–4897
29. Plützer C, Nir E, de Vries MS, Kleinermanns K (2001) IR-UV double-resonance spectroscopy of the nucleobase adenine. Phys Chem Chem Phys 3(24):5466–5469
30. Nir E, Muller M, Grace LI, de Vries MS (2002) REMPI spectroscopy of cytosine. Chem Phys Lett 355(1–2):59–64
31. Arrowsmith P, de Vries MS, Hunziker HE, Wendt HR (1988) Pulsed laser desorption near a jet orifice: concentration profiles of entrained perylene vapor. Appl Phys B 46:165–173
32. Meijer G, de Vries MS, Hunziker HE, Wendt HR (1990) Laser desorption jet-cooling of organic molecules. Cooling characteristics and detection sensitivity. Appl Phys B 51:395–403
33. Tembreull R, Lubman DM (1987) Resonant two-photon ionization in biomolecules using laser desorption in supersonic beam-mass spectrometry. Appl Spectrosc 41:431–436
34. Boesl U, Grotemeyer J, Walter K, Schlag EW (1986) Resonance ionization and time-of-flight mass spectrometry, high resolution, involatile molecules. Resonance Ionization Spectrosc 369:223–228
35. Piuzzi F, Mons M, Dimicoli I, Tardivel B, Zhao Q (2001) Ultraviolet spectroscopy and tautomerism of the DNA base guanine and its hydrate formed in a supersonic jet. Chem Phys 270(1):205–214
36. Saigusa H, Urashima S, Asami H (2009) IR-UV double resonance spectroscopy of the hydrated clusters of guanosine and 9-methylguanine: evidence for hydration structures involving the sugar group. J Phys Chem A 113(15):3455–3462
37. Boyarkin OV, Mercier SR, Kamariotis A, Rizzo TR (2006) Electronic spectroscopy of cold, protonated tryptophan and tyrosine. J Am Chem Soc 128(9):2816–2817
38. Choi MY, Miller RE (2006) Four tautomers of isolated guanine from infrared laser spectroscopy in helium nanodroplets. J Am Chem Soc 128(22):7320–7328
39. Chapo CJ, Paul JB, Provencal RA, Roth K, Saykally RJ (1998) Is arginine zwitterionic or neutral in the gas phase? Results from IR cavity ringdown spectroscopy. J Am Chem Soc 120 (49):12956–12957
40. Alonso JL, Pena I, Lopez JC, Vaquero V (2009) Rotational spectral signatures of four tautomers of guanine. Angew Chem Int Ed 48(33):6141–6143
41. Nir E, Kleinermanns K, Grace L, de Vries MS (2001) On the photochemistry of purine nucleobases. J Phys Chem A 105(21):5106–5110
42. Seefeld KA, Plützer C, Löwenich D, Häber T, Linder R, Kleinermanns K, Tatchen J, Marian CM (2005) Tautomers and electronic states of jet-cooled 2-aminopurine investigated by double resonance spectroscopy and theory. Phys Chem Chem Phys 7(16):3021–3026

43. Holmen A, Broo A, Albinsson B, Norden B (1997) Assignment of electronic transition moment directions of adenine from linear dichroism measurements. J Am Chem Soc 119:12240–12250
44. Broo A (1998) A theoretical investigation of the physical reason for the very different luminescence properties of the two isomers adenine and 2-aminopurine. J Phys Chem A 102:526–531
45. Andreasson J, Holmén A, Albinsson B (1999) The photophysical properties of the adenine chromophore. J Phys Chem B 103(44):9782–9789
46. Kim NJ, Jeong G, Kim YS, Sung J, Kim SK, Park YD (2000) Resonant two-photon ionization and laser induced fluorescence spectroscopy of jet-cooled adenine. J Chem Phys 113 (22):10051–10055
47. Mishra SK, Shukla MK, Mishra PC (2000) Electronic spectra of adenine and 2-aminopurine: an ab initio study of energy level diagrams of different tautomers in gas phase and aqueous solution. Spectrochim Acta pt A 56(7):1355–1384
48. Lührs DC, Viallon J, Fischer I (2001) Excited state spectroscopy and dynamics of isolated adenine and 9-methyladenine. Phys Chem Chem Phys 3(10):1827–1831
49. Kang H, Jung B, Kim SK (2003) Mechanism for ultrafast internal conversion of adenine. J Chem Phys 118(15):6717–6719
50. Sobolewski AL, Domcke W (2002) On the mechanism of nonradiative decay of DNA bases: ab initio and TDDFT results for the excited states of 9H-adenine. Eur Phys J D 20:369–374
51. Plützer C, Kleinermanns K (2002) Tautomers and electronic states of jet-cooled adenine investigated by double resonance spectroscopy. Phys Chem Chem Phys 4(20):4877–4882
52. Barbatti M, Lischka H (2007) Can the nonadiabatic photodynamics of aminopyrimidine be a model for the ultrafast deactivation of adenine? J Phys Chem A 111(15):2852–2858
53. Marian CM (2005) A new pathway for the rapid decay of electronically excited adenine. J Chem Phys 122:104314
54. Hünig I, Plützer C, Seefeld KA, Löwenich D, Nispel M, Kleinermanns K (2004) Photostability of isolated and paired nucleobases: N–H dissociation of adenine and hydrogen transfer in its base pairs examined by laser spectroscopy. ChemPhysChem 5(9):1427–1431
55. Crespo-Hernández CE, Cohen B, Hare PM, Kohler B (2004) Ultrafast excited-state dynamics in nucleic acids. Chem Rev 104:1977–2019
56. Zierhut M, Roth W, Fischer I (2004) Dynamics of H-atom loss in adenine. Phys Chem Chem Phys 6(22):5178–5183
57. Zechmann G, Barbatti M (2008) Ab initio study of the photochemistry of aminopyrimidine. Int J Quantum Chem 108(7):1266–1276
58. Marian CM (2005) A new pathway for the rapid decay of electronically excited adenine. J Chem Phys 122(10):10
59. Kistler KA, Matsika S (2008) Three-state conical intersections in cytosine and pyrimidinone bases. J Chem Phys 128(21):215102
60. Kistler KA, Matsika S (2007) Cytosine in context: a theoretical study of substituent effects on the excitation energies of 2-pyrimidinone derivatives. J Phys Chem A 111(35):8708–8716
61. Kistler KA, Matsika S (2007) Radiationless decay mechanism of cytosine: an ab initio study with comparisons to the fluorescent analogue 5-methyl-2-pyrimidinone. J Phys Chem A 111 (14):2650–2661
62. Yarasi S, Brost P, Loppnow GR (2007) Initial excited-state structural dynamics of thymine are coincident with the expected photochemical dynamics. J Phys Chem A 111 (24):5130–5135
63. Canuel C, Mons M, Piuzzi F, Tardivel B, Dimicoli I, Elhanine M (2005) Excited states dynamics of DNA and RNA bases: characterization of a stepwise deactivation pathway in the gas phase. J Chem Phys 122(7):074316–074317
64. Quinones E, Arce R (1989) Photochemistry and photophysics of purine free base and 6-methylpurine. J Am Chem Soc 111(21):8218–8223

65. Wilson RW, Callis PR (1980) Fluorescent tautomers and the apparent photophysics of adenine and guanine. Photochem Photobiol 31:323–327
66. Seefeld K, Brause R, Häber T, Kleinermanns K (2007) Imino tautomers of gas-phase guanine from mid-infrared laser spectroscopy. J Phys Chem A 111(28):6217–6221
67. Nachtigallova D, Hobza P, Spirko V (2008) Assigning the NH stretches of the guanine tautomers using adiabatic separation: CCSD(T) benchmark calculations. J Phys Chem A 112(9):1854–1856
68. Marian CM (2007) The guanine tautomer puzzle: quantum chemical investigation of ground and excited states. J Phys Chem A 111(8):1545–1553
69. Cerny J, Spirko V, Mons M, Hobza P, Nachtigallova D (2006) Theoretical study of the ground and excited states of 7-methyl guanine and 9-methyl guanine: comparison with experiment. Phys Chem Chem Phys 8(26):3059–3065
70. Kang H, Lee KT, Jung B, Ko YJ, Kim SK (2002) Intrinsic lifetimes of the excited state of DNA and RNA bases. J Am Chem Soc 124(44):12958–12959
71. Kistler KA, Matsika S (2007) The fluorescence mechanism of 5-methyl-2-pyrimidinone: an ab initio study of a fluorescent pyrimidine analog. Photochem Photobiol 83(3):611–624
72. Ullrich S, Schultz T, Zgierski MZ, Stolow A (2004) Electronic relaxation dynamics in DNA and RNA bases studied by time-resolved photoelectron spectroscopy. Phys Chem Chem Phys 6(10):2796–2801
73. Perun S, Sobolewski AL, Domcke W (2005) Ab initio studies on the radiationless decay mechanisms of the lowest excited singlet states of 9H-adenine. J Am Chem Soc 127 (17):6257–6265
74. Tomic K, Tatchen J, Marian CM (2005) Quantum chemical investigation of the electronic spectra of the keto, enol, and keto-imine tautomers of cytosine. J Phys Chem A 109 (37):8410–8418
75. Trygubenko SA, Bogdan TV, Rueda M, Orozco M, Luque FJ, Sponer J, Slavicek P, Hobza P (2002) Correlated ab initio study of nucleic acid bases and their tautomers in the gas phase, in a microhydrated environment and in aqueous solution - part 1. Cytosine. Phys Chem Chem Phys 4(17):4192–4203
76. Kobayashi R (1998) A CCSD(T) study of the relative stabilities of cytosine tautomers. J Phys Chem A 102(52):10813–10817
77. Szczesniak M, Szczepaniak K, Kwiatkowski JS, Kubulat K, Person WB (1988) Matrix-isolation infrared studies of nucleic-acid constituents. 5. Experimental matrix-isolation and theoretical abinitio scf molecular-orbital studies of the infrared-spectra of cytosine monomers. J Am Chem Soc 110:8319–8330
78. Brown RD, Godfrey PD, McNaughton D, Pierlot A (1989) Tautomers of cytosine by microwave spectroscopy. J Am Chem Soc 111:2308–2310
79. Schiedt J, Weinkauf R, Neumark DM, Schlag EW (1998) Anion spectroscopy of uracil, thymine and the amino-oxo and amino-hydroxy tautomers of cytosine and their water clusters. Chem Phys 239(1–3):511–524
80. Kosma K, Schroter C, Samoylova E, Hertel IV, Schultz T (2009) Excited-state dynamics of cytosine tautomers. J Am Chem Soc 131(46):16939–16943
81. Gonzalez-Vazquez J, Gonzalez L (2010) A time-dependent picture of the ultrafast deactivation of keto-cytosine including three-state conical intersections. ChemPhysChem 11 (17):3617–3624
82. Podolyan Y, Gorb L, Leszczynski J (2003) Ab initio study of the prototropic tautomerism of cytosine and guanine and their contribution to spontaneous point mutations. Int J Mol Sci 4 (7):410–421
83. Gorb L, Podolyan Y, Leszczynski J (1999) A theoretical investigation of tautomeric equilibria and proton transfer in isolated and monohydrated cytosine and isocytosine molecules. J Mol Struct Theochem 487(1–2):47–55

84. Chin W, Mons M, Dimicoli I, Piuzzi F, Tardivel B, Elhanine M (2002) Tautomer contributions to the near UV spectrum of guanine: towards a refined picture for the spectroscopy of purine molecules. Eur Phys J D 20(3):347–355

85. Nir E, Janzen C, Imhof P, Kleinermanns K, de Vries MS (2001) Guanine tautomerism revealed by UV-UV and IR-UV hole burning spectroscopy. J Chem Phys 115:4604–4611

86. Brown RD, Godfrey PD, Mcnaughton D, Pierlot AP (1989) A study of the major gas-phase tautomer of adenine by microwave spectroscopy. Chem Phys Lett 156(1):61–63

87. Brown RD, Godfrey PD, Mcnaughton D, Pierlot AP (1988) Microwave-spectrum of uracil. J Am Chem Soc 110(7):2329–2330

88. Vaquero V, Sanz ME, Lopez JC, Alonso JL (2007) The structure of uracil: a laser ablation rotational study. J Phys Chem A 111(18):3443–3445

89. Viant MR, Fellers RS, Mclaughlin RP, Saykally RJ (1995) Infrared-laser spectroscopy of uracil in a pulsed slit jet. J Chem Phys 103(21):9502–9505

90. Brown RD, Godfrey PD, Mcnaughton D, Pierlot AP (1989) Microwave-spectrum of the major gas-phase tautomer of thymine. J Chem Soc Chem Commun 1:37–38

91. Chin W, Mons M, Piuzzi F, Tardivel B, Dimicoli I, Gorb L, Leszczynski J (2004) Gas phase rotamers of the nucleobase 9-methylguanine enol and its monohydrate: optical spectroscopy and quantum mechanical calculations. J Phys Chem A 108(40):8237–8243

92. Abo-Riziq A, Crews B, Grace L, de Vries MS (2005) Microhydration of guanine base pairs. J Am Chem Soc 127(8):2374–2375

93. Smith VR, Samoylova E, Ritze HH, Radloff W, Schultz T (2010) Excimer states in microhydrated adenine clusters. Phys Chem Chem Phys 12(33):9632–9636

94. Ritze HH, Lippert H, Samoylova E, Smith VR, Hertel IV, Radloff W, Schultz T (2005) Relevance of pi sigma(*) states in the photoinduced processes of adenine, adenine dimer, and adenine-water complexes. J Chem Phys 122(22):224320

95. Saigusa H, Urashima S, Asami H, Ohba M (2010) Microhydration of the guanine-guanine and guanine-cytosine base pairs. J Phys Chem A 114(42):11231–11237

96. Saigusa H, Mizuno N, Asami H, Takahashi K, Tachikawa M (2008) Ultraviolet spectroscopy and theoretical calculations of mono- and dihydrated clusters of the guanine nucleosides: possibility of different hydration structures for guanosine and 2′-deoxyguanosine. Bull Chem Soc Jpn 81(10):1274–1281

97. Perun S, Sobolewski AL, Domcke W (2005) Photostability of 9H-adenine: mechanisms of the radiationless deactivation of the lowest excited singlet states. Chem Phys 313 (1–3):107–112

98. Sobolewski AL, Domcke W (2006) Photophysics of intramolecularly hydrogen-bonded aromatic systems: ab initio exploration of the excited-state deactivation mechanisms of salicylic acid. Phys Chem Chem Phys 8(29):3410–3417

99. Shemesh D, Hattig C, Domcke W (2009) Photophysics of the Trp-Gly dipeptide: role of electron and proton transfer processes for efficient excited-state deactivation. Chem Phys Lett 482(1–3):38–43

100. Shemesh D, Sobolewski AL, Domcke W (2009) Efficient excited-state deactivation of the gly-phe-ala tripeptide via an electron-driven proton-transfer process. J Am Chem Soc 131 (4):1374

101. Schultz T, Samoylova E, Radloff W, Hertel IV, Sobolewski AL, Domcke W (2004) Efficient deactivation of a model base pair via excited-state hydrogen transfer. Science 306 (5702):1765–1768

102. Sobolewski AL, Domcke W (2004) Ab Initio studies on the photophysics of the guanine–cytosine base pair. Phys Chem Chem Phys 6:2763–2771

103. Perun S, Sobolewski AL, Domcke W (2006) Role of electron-driven proton-transfer processes in the excited-state deactivation of the adenine-thymine base pair. J Phys Chem A 110:9031

104. Nir E, Kleinermanns K, de Vries MS (2000) Pairing of isolated nucleic-acid bases in the absence of the DNA backbone. Nature 408(6815):949–951

105. Nir E, Janzen C, Imhof P, Kleinermanns K, de Vries MS (2002) Pairing of the nucleobase guanine studied by IR-UV double-resonance spectroscopy and ab initio calculations. Phys Chem Chem Phys 4(5):740–750
106. Nolting D, Weinkauf R, Hertel IV, Schultz T (2007) Excited-state relaxation of protonated adenine. ChemPhysChem 8(5):751–755
107. Samoylova E, Lippert H, Ullrich S, Hertel IV, Radloff W, Schultz T (2005) Dynamics of photoinduced processes in adenine and thymine base pairs. J Am Chem Soc 127 (6):1782–1786
108. Ullrich S, Schultz T, Zgierski MZ, Stolow A (2004) Direct observation of electronic relaxation dynamics in adenine via time-resolved photoelectron spectroscopy. J Am Chem Soc 126(8):2262–2263
109. Samoylova E, Radloff W, Ritze HH, Schultz T (2009) Observation of proton transfer in 2-aminopyridine dimer by electron and mass spectroscopy. J Phys Chem A 113 (29):8195–8201
110. Samoylova E, Smith VR, Ritze HH, Radloff W, Kabelac M, Schultz T (2006) Ultrafast deactivation processes in aminopyridine clusters: excitation energy dependence and isotope effects. J Am Chem Soc 128(49):15652–15656
111. Nir E, Hünig I, Kleinermanns K, de Vries MS (2004) Conformers of guanosines and their vibrations in the electronic ground and excited states, as revealed by double-resonance spectroscopy and ab initio calculations. ChemPhysChem 5(1):131–137
112. Nir E, de Vries MS (2002) Fragmentation of laser-desorbed 9-substituted adenines. Int J Mass spectrom 219(1):133–138
113. Asami H, Yagi K, Ohba M, Urashima S, Saigusa H (2013) Stacked base-pair structures of adenine nucleosides stabilized by the formation of hydrogen-bonding network involving the two sugar groups. Chem Phys 419:84–89
114. Saigusa H, Lim EC (1996) Excimer formation in van der Waals dimers and clusters of aromatic molecules. Acc Chem Res 29(4):171–178
115. Schreier WJ, Schrader TE, Koller FO, Gilch P, Crespo-Hernandez CE, Swaminathan VN, Carell T, Zinth W, Kohler B (2007) Thymine dimerization in DNA is an ultrafast photoreaction. Science 315(5812):625–629
116. Crespo-Hernández CE, Cohen B, Kohler B (2005) Base stacking controls excited-state dynamics in A·T DNA. Nature 436:1141–1144
117. Takaya T, Su C, de La Harpe K, Crespo-Hernández CE, Kohler B (2008) UV excitation of single DNA and RNA strands produces high yields of exciplex states between two stacked bases. Proc Natl Acad Sci USA 105:10285–10290
118. Crespo-Hernández CE, de La Harpe K, Kohler B (2008) Ground-state recovery following UV excitation is much slower in G•C-DNA duplexes and hairpins than in mononucleotides. J Am Chem Soc 130:10844–10845

# Excitation of Nucleobases from a Computational Perspective I: Reaction Paths

**Angelo Giussani, Javier Segarra-Martí, Daniel Roca-Sanjuán, and Manuela Merchán**

**Abstract** The main intrinsic photochemical events in nucleobases can be described on theoretical grounds within the realm of non-adiabatic computational photochemistry. From a static standpoint, the *photochemical reaction path approach* (PRPA), through the computation of the respective *minimum energy path* (MEP), can be regarded as the most suitable strategy in order to explore the electronically excited isolated nucleobases. Unfortunately, the PRPA does not appear widely in the studies reported in the last decade. The main ultrafast decay observed experimentally for the gas-phase excited nucleobases is related to the computed barrierless MEPs from the bright excited state connecting the initial Franck–Condon region and a conical intersection involving the ground state. At the highest level of theory currently available (CASPT2//CASPT2), the lowest excited $^1(\pi\pi^*)$ hypersurface for cytosine has a shallow minimum along the MEP deactivation pathway. In any case, the internal conversion processes in all the natural nucleobases are attained by means of interstate crossings, a self-protection mechanism that prevents the occurrence of photoinduced damage of nucleobases by ultraviolet radiation. Many alternative and secondary paths have been proposed in the literature, which ultimately provide a rich and constructive interplay between experimentally and theoretically oriented research.

**Keywords** CASPT2//CASSCF · Conical intersection · DNA photochemistry · Minimum energy path · Quantum chemistry · Ultrafast radiationless decay

A. Giussani, J. Segarra-Martí, D. Roca-Sanjuán, and M. Merchán (✉)
Instituto de Ciencia Molecular Universitat de València, P.O. Box 22085, 46071 Valencia, Spain
e-mail: Manuela.Merchan@uv.es

## Contents

## Abbreviations

| | |
|---|---|
| A | Adenine |
| AC | Avoided crossing |
| ANO | Atomic natural orbital |
| aug-cc-pVDZ | Augmented correlation-consistent valence double-$\zeta$ plus polarization |
| C | Cytosine |
| CASPT2 | Complete active space second-order perturbation theory |
| CASSCF | Complete active space self-consistent field |
| CC | Coupled cluster |
| CC2-LR | Approximate coupled cluster singles and doubles linear response |
| cc-pVDZ | Correlation-consistent valence double-$\zeta$ plus polarization |
| CCSD(T) | Coupled cluster singles, doubles, and perturbative triples |
| CI | Conical intersection |
| CIS | Configuration interaction singles |
| CPU | Central processing unit |
| CR-EOM-CC | Completely renormalized equation of motion coupled cluster |
| DFT | Density functional theory |
| DNA | Deoxyribonucleic acid |
| DZP | Double-$\zeta$ plus polarization |
| EA | Electron affinity |
| EOMEE-CC | Equation-of-motion excitation-energy coupled cluster |
| FC | Franck Condon |
| G | Guanine |
| gs | Ground state |
| HL | Highest-occupied molecular orbital lowest-unoccupied molecular orbital |
| HOMO | Highest-occupied molecular orbital |
| IC | Internal conversion |

| | |
|---|---|
| IP | Ionization potential |
| IR | Infrared |
| IRC | Intrinsic reaction coordinate |
| ISC | Intersystem crossing |
| LIIC | Linear interpolation of internal coordinates |
| LUMO | Lowest-occupied molecular orbital |
| MECP | Minimum energy crossing point |
| MEP | Minimum energy path |
| min | Minimum |
| MO | Molecular orbital |
| MRCI | Multireference configuration interaction |
| MRCISD | Multireference configuration interaction singles and doubles |
| MS-CASPT2 | Multistate complete active space second-order perturbation theory |
| NAB | Nucleic acid base |
| NO | Natural orbital |
| OM2 | Orthogonalization model 2 |
| PCO | Projected constraint optimization |
| PEH | Potential energy hypersurface |
| PRPA | Photochemical reaction path approach |
| QCEXVAL | Quantum chemistry of the excited state of Valencia |
| RI-CC2 | Resolution of identity approximate coupled cluster singles and doubles |
| RNA | Ribonucleic acid |
| SOC | Spin-orbit coupling |
| STC | Singlet-triplet crossing |
| T | Thymine |
| TDDFT | Time-dependent density functional theory |
| TS | Transition state |
| TZVP | Valence triple-$\zeta$ plus polarization |
| U | Uracil |
| UDFT | Unrestricted density functional theory |
| UV | Ultraviolet |
| Vis | Visible |
| XMS-CASPT2 | Extended multistate complete active space second-order perturbation theory |

# 1 Introduction

When deoxyribonucleic/ribonucleic acid (DNA/RNA) is irradiated by ultraviolet (UV) light, population of the excited states of their basic chromophores, the nucleobases cytosine (C), thymine (T), uracil (U), adenine (A), and guanine (G), is expected to occur (see molecular structures in Fig. 1). In fact, the DNA
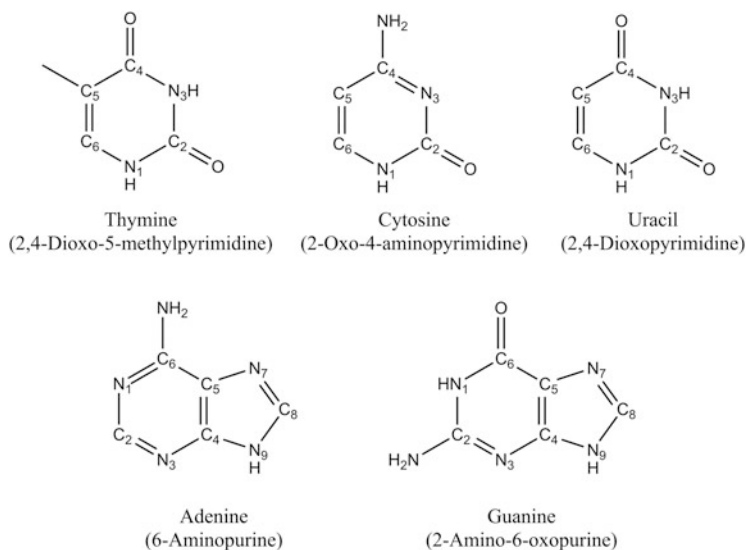
**Fig. 1** Chemical structure and labeling of DNA and RNA nucleobases with their conventional name and the IUPAC nomenclature (within parentheses)

absorption spectra closely resemble those of the building-block monomers, apart from the well-documented decrease of intensity (hypochromism). In principle, light absorption produces mainly excited states of singlet multiplicity. Thus, after the absorption process, what is the fate of the energy in the populated singlet excited states in the nucleobases? The present chapter is devoted to review the up-to-date detailed understanding of the properties, obtained on theoretical grounds, of the respective electronically excited-state species and to describe the knowledge gathered in the last decade on the underlying mechanisms controlling the photochemical evolution of the excited nucleobases.

According to modern computational photochemistry [1], the progression of the changes in the molecular structure of an excited state taking place upon light absorption can be monitored by means of the *photochemical reaction path approach* (PRPA) [2–6], which can be undertaken by computing the corresponding minimum energy path (MEP) [5, 7–12] along the $3N$-6 dimensional potential energy hypersurface (PEH), where $N$ represents the number of nuclei of the system. Consequently, the computational strategies related to the MEP computations are firstly addressed. A brief account of the quantum-chemical methods usually employed in connection with the MEP calculations is subsequently considered. The essentials of the photochemistry of the pyrimidine (T, C, U) and purine (A, G) nucleobases are in turn next considered. The conclusions and future perspectives derived from the global work performed within the framework of theoretical and computational photochemistry by so many different world-wide outstanding groups are finally outlined.

## 2   Computational Strategies in Photochemistry

Considering the excited and ground-state (gs) PEHs and the possible different reaction paths that a system might evolve through, molecular processes can be regarded in the realms of photophysics or photochemistry (adiabatic and non-adiabatic) [13–18]. Absorption and emission processes can be clearly identified as photophysical processes. From the theoretical standpoint they involve calculations at similar molecular structures. In an adiabatic reaction path, once the vertical absorption takes place, the system may proceed along the hypersurface of the excited state to reach usually a minimum, leading eventually to an emitting feature. In a non-adiabatic photochemical path, part of the reaction occurs on the excited state hypersurface and, after a non-radiative jump at the hypersurface crossing (or funnel), continues on the hypersurface of another state, normally the ground state. The process of a radiationless jump is denoted as internal conversion (IC) or intersystem crossing (ISC) depending on whether the spin multiplicity of the two hypersurfaces involved is the same or different, respectively. At the molecular level, the internal conversion may be mediated by an avoided crossing (AC) or a conical intersection (CI) [1, 19–22]. Among several researchers, the systematic work developed by Robb, Bernardi, Olivucci, Garavelli, and co-workers has repeatedly shown in the last 2 decades the important role that the CIs play in organic photochemistry, as well as in biochromophores (see, e.g., Olivucci [1] and references cited therein). Depending on the nature of the CI, the corresponding radiationless transition can yield specific photoproducts or relax energy towards the ground-state initial situation. The main photochemical events of the isolated nucleobases can be classified within the area of non-adiabatic photochemistry because the energy of the excited nucleobase is dissipated directly towards the ground-state at the original configuration. This fact has been related to the well-known photostability of the genetic material [6, 23, 24].

### 2.1   Photochemical Reaction Paths

In general, the photoinduced reaction can be studied by building and characterizing the photochemical reaction path [2–6]. It can be achieved by computing the MEP starting at the ground-state equilibrium geometry of the nucleic acid base (NAB) and evolving along the PEHs of the photochemically relevant excited states involved in the main electronic transitions bearing significant computed oscillator strength at the vertical absorption, the so-called spectroscopic or bright excited states [5, 6, 25–28]. Therefore, the requirements for computation of the pathways or simply paths can be systematized in the following steps:

- Determination of the ground-state equilibrium structure, that is, the Franck–Condon (FC) geometry at a given level of theory.
- MEP computation of the bright excited states from the FC region.
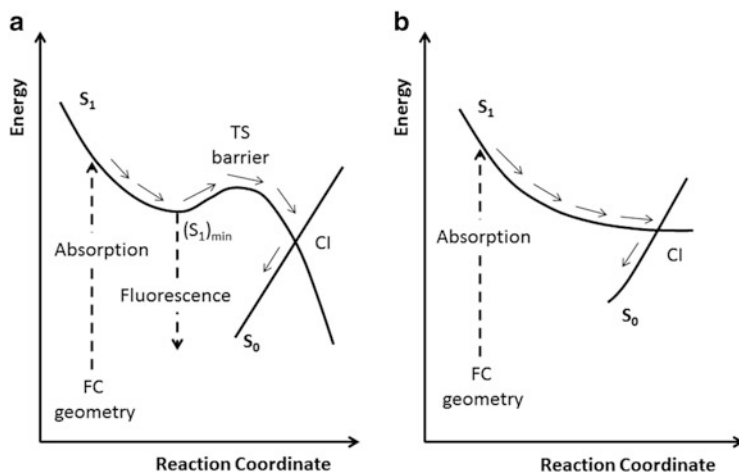
**Fig. 2** Schematic profiles based on MEP computations for the main photochemical reaction paths found in the literature for the decay of nucleobases: (**a**) passing through a minimum $(S_1)_{min}$ and (**b**) directly to the CI

- Analysis of the information provided by the MEP: geometrical changes, minima inferred, saddle points, and crossings between states.
- Check on the stability of the results and the conclusions from them derived upon higher levels of calculation.

The MEPs allow the rationalization on static grounds of different experimental data such as the excited-state lifetimes, the nature of the photoproducts (if present), as well as certain qualitative aspects related to quantum yields, transient absorption, and emission spectra. It is worth recalling that the information so obtained can be directly related to the motion of a vibrationally cold molecule with infinitesimal momentum. The approach is closely related to the method using the motion of wave packets or semi-classical trajectories on potential energy surfaces commonly used to describe ultrafast photochemical processes [5]. Based on actual MEP computations, two main profiles for the photochemical reaction path corresponding to the bright states have been found, depending on the nucleobase, nature of the excited state, and level of calculation employed. They are schematically depicted in Fig. 2.

As illustrated in Fig. 2, the mapping of the photochemical reaction path computed by following the MEP from the starting FC structure may lead to the ground state passing through a minimum $(S_1)_{min}$ and a transition state (TS) before reaching the CI (Fig. 2a) or directly to a CI in a barrierless way (Fig. 2b). Since the barrier heights are computed to be relatively small [26], the two situations are consistent with the ultrafast components detected experimentally, both in solution and in the gas phase. In this respect, it should be remembered that fluorescence lifetimes of DNA/RNA nucleosides and nucleotides recorded in solution fall in the sub-picosecond timescale, suggesting the

presence of an ultrafast internal conversion channel [23, 29, 30]. For gas-phase isolated purine and pyrimidine bases, very short lifetimes, in the picosecond regime have also been determined (see [31–34] and previous chapters about experimental studies). Thus, analysis of the reaction coordinate and relative energies obtained from the MEP computation yields useful information on the excited state lifetime and nature of the main deactivation path inherent in the internal conversion process.

As pointed out by Garavelli, Bernardi, and Cembran [5], and repeatedly emphasized by Michl [20, 35], well-recognized pioneers in the field, MEP mapping should be considered the preferred computational strategy in photochemical studies in contrast to standard geometry optimization of the excited states and/or determination of the lowest-energy CI. The MEP computation starting from the FC point offers information on the structure and accessibility of the photochemical reaction path, i.e., the driving forces responsible for the photoinduced nuclear motion. The MEP provides the intermediates, transition states, and interstate crossings directly accessible by the molecular system. Many other stationary points can be computed, thereby rendering a more complete view of the hypersurfaces. However, if those points are far away in terms of energy and geometry with respect to those of the MEP, they are not bound to become meaningful for the photochemical event of interest. For example, as seen below for G, the first decay crossing point intercepted by the MEP along $S_1$ differs from the minimum energy crossing point (MECP) (in practice the lowest-energy CI) [28]. The acronym CI should preferably be reserved just for those cases where the CI has been fully characterized by using the corresponding algorithms [1, 19–22]; otherwise the word crossing or MECP or related [9, 36] should be accordingly employed. In practice, for the sake of simplicity, the computed crossings are normally coined as CI, irrespective of the actual characterization.

In modern photochemistry, the efficiency of radiationless decay between different electronic states taking place in internal conversion and in intersystem crossing processes is usually associated with the presence of crossings involving hyperlines and hyperplanes, respectively, which behave as funnels where the probability for non-adiabatic jumps is high [20, 21]. A crossing seam occurs between two states of the same spin multiplicity when they intersect along an $(F - 2)$-dimensional hyperline as the energy is plotted against the $F$ nuclear coordinates, where $F$ is the number of internal degrees of freedom ($3N-6$). In any point of the $(F - 2)$-dimensional intersection space the energies of the two states are the same. The degeneracy is lifted along the two remaining linear independent coordinates, $x_1$ and $x_2$, that span the branching subspace corresponding to the gradient difference vector and the non-adiabatic coupling vector, respectively [20, 37]. Clearly, $x_1$ and $x_2$ do not have to be orthogonal to each other. The crossing seam can be seen as being formed by an infinite number of CI points. The corresponding PEHs at a CI point have the shape of a double cone when the energy of the upper and lower states is plotted against the $x_1$ and $x_2$ coordinates. Accordingly, the feature is denoted as "conical intersection." Great theoretical efforts have been focused on the localization of the

lowest-energy point in the intersection of two PEHs [22, 38–40]. The corresponding algorithms are based on Lagrange multipliers [10, 41–45] and on projected gradient techniques [46, 47]. These tools are currently available in popular software packages such as GAUSSIAN [48] and will not be further discussed here since they have been considered in detail in previous reviews [1, 19–22, 47, 49, 50]. Molecular structure optimization of stationary points as well as MEP computations on both the ground- and excited-state PEHs can be carried out using standard methods. Description of the crossing region requires, however, special algorithms as two potential energy hypersurfaces are degenerate and the gradient and Hessian cannot be unambiguously computed. Regarding the computation of MECPs as implemented in the MOLCAS software, the crossing searches are performed using the restricted Lagrange multipliers technique, in which the lowest-energy point is obtained under the restriction of degeneracy between the two states of interest [9]. No non-adiabatic coupling elements are calculated. On the other hand, MEPs are built as steepest descent paths in a procedure [10] based on a modification of the projected constrained optimization (PCO) algorithm of Anglada and Bofill [11] and follows the Müller–Brown approach [11, 12]. Each step requires the minimization of the energy on a hyperspherical cross section of the PEH centered on the initial geometry and characterized by a predefined radius. The optimized structure is taken as the center of a new hypersphere of the same radius, and the procedure is iterated until the bottom of the energy hypersurface is reached. The MEP coordinate corresponds to the so-called intrinsic reaction coordinate (IRC) [9] when mass-weighted coordinates are used [12]. It is anticipated that, to the best of our knowledge, despite the conceptual importance of MEP computations, only a few groups have computed MEPs using high-level correlated wave function methods for DNA/RNA nucleobase monomers [6, 25–28, 51–61]. In other studies, just simple geometry optimizations, linear interpolations between the FC region and an MECP, relaxed scans, or/and related techniques have been carried out. Unless wisely used, such strategies do not guarantee the presence or absence of energy barriers; they can even yield in certain cases unconnected profiles and therefore they may render useless information from a photochemical standpoint. Furthermore, the MECP might be irrelevant to understanding the non-adiabatic photochemistry of a given molecular system. A molecule that has reached the seam of a CI will fall to the lower hypersurface right away and will not have time to ride the seam looking for its lowest energy point. Only those interstate crossings that can be reached by the excited molecule in the short time available become relevant. From a photochemical standpoint, the effective funnel locations are those in which the seam is first reached and not the lowest-energy point in the intersection subspace. Therefore, the exploration of the deactivation pathways from the bright state at the FC region of the systems considered using the minimum energy path (MEP) approach has become mandatory nowadays.

## 2.2  Quantum-Chemical Methods

The improvement seen over the last few years in conceptual, programming, and technical aspects related to quantum-chemical software is certainly outstanding. It particularly holds true regarding the tools required for the correct treatment of excited states in molecular systems. Thanks to the efforts of so many colleagues devoted to basic research in method development and efficient software implementation, the interaction between the application-oriented researcher and the computer software may become really creative.

As proved by the joint efforts of different research groups, highly accurate multiconfigurational ab initio quantum-chemical methods [complete active space self-consistent field/complete active space second-order perturbation theory (CASSCF/CASPT2) and multireference configuration interaction (MRCI), basically] are needed to provide accurate reaction profiles able to identify the operative decay paths in nucleobases. We briefly describe here the most relevant aspects of the CASPT2//CASSCF approach as employed in the study of the decay processes in NABs and refer the reader to the available publications for further details on the theory and application of the CASSCF/CASPT2 [14, 18, 62–66] and the MRCI methods [67, 68].

The CASSCF method [69, 70] has been extensively employed to describe photochemical reaction paths. Nowadays, the computation of MEPs, excited-state minima, transition states, and crossing points can be run routinely at the CASSCF level because the analytical evaluation of gradients and second derivatives are available for CASSCF wave functions and it has been successfully implemented in well-known quantum-chemical packages such as GAUSSIAN [48], MOLCAS [71–73], and MOLPRO [74, 75], among others. To take into account the remaining electron correlation effects, multiconfiguration second-order perturbation methods, such as CASPT2, which employ the CASSCF wave function as zeroth-order wave function in the perturbation step, are subsequently applied to the nuclear arrangements computed at the CASSCF level. The protocol is known as CASPT2//CASSCF, being probably the CASPT2//CASSCF/6-31G* level of computation, the most widely used [76]. That is, geometries for the singular points of the PEH are obtained at the CASSCF level employing the 6-31G* basis set, whereas single-point CASPT2 calculations are performed at the structures thus obtained.

Since the bright spectroscopic state of the nucleobases, denoted generically as $^1(\pi\pi^*)$, involves a reorganization of the $\pi$ electronic system with respect to the ground state, the active space employed in the CASSCF computations has to include ideally the full $\pi$-valence molecular orbitals (MOs) with the respective $\pi$ electrons active. In practice, the full $\pi$-valence active space is not really required to describe accurately the lowest excited states of $\pi$ character. By using different criteria it can in fact be efficiently reduced. For instance, by inspection of the occupation of the natural orbitals (NOs) obtained at the second-order level, it is typically found that NOs topologically equivalent to the deepest occupied canonical $\pi$ MOs and the highest valence $\pi$ virtual canonical MOs do not play a significant

role in the description of the CASSCF wave function of the excited state. Their respective occupation numbers are close to two and zero, and therefore they can be safely treated as inactive and virtual MOs. Let us recall that, by definition, in the CASSCF method, the inactive and virtual (or secondary) MOs have in all configurations occupation number values of two and zero, respectively. The CASSCF wave function is formed by a linear combination of all possible configurations that can be built by distributing the active electrons among the active MOs (defined by the user) in all possible ways, consistent with the given spatial and spin symmetry constraints of the system under study. That is, in the configuration space spanned by the active orbitals, the CASSCF is complete (full). Within the framework of the variational method, the condition of stationary is searched for both the coefficients of the linear expansion and the MOs. In other words, the coefficients of the linear expansion and the orbitals implied in the description of the CASSCF wave function are optimized. The active space has to be properly enlarged with the lone-pair MOs and electrons in order to describe the dark states such as the $^1(n_o\pi^*)$ state, i.e., the electronically excited state mainly described in the CASSCF wave function by the one-electron promotion from the lone-pair localized on the oxygen atom to the corresponding $\pi^*$ NO [16, 77–79].

Experience has shown that by employing a given basis set, the CASPT2//CASSCF description of the photochemical reaction paths of pyrimidines may yield a completely different photochemical view with respect to that provided at the CASSCF level [15, 80]. Furthermore, the nature of the excited state involved in the decay towards the ground state also turns out to be different, which has been ascribed to the differential electron correlation between the ground state and the distinct possible excited states implied in the crossing. With the current possibility of performing MEP computations at the CASPT2 by using numerical gradients (MOLCAS) [72, 73] and CASPT2 geometry optimizations employing analytical gradients (MOLPRO) [81], the stability of the results obtained at the CASPT2//CASSCF level with respect to the CASPT2//CASPT2 findings can finally be evaluated for the nucleobases as has been recently carried out for models of the protonated Schiff base of retinal [76]. Certainly, MEP computations at the CASPT2 level represent a tremendous highly-demanding computational task, even for the current splendid standards in computer technology. Research efforts directed towards that target have already been started in different groups. Thus, the question arises as to whether MEP-CASPT2//CASPT2 computations support the MEP-CASPT2//CASSCF findings for nucleobases? At present that is really an open question, although recent preliminary results produced in our group seem to point out that it is actually the case for all the NABs. In fact, at the final preparatory stage of the present review, the first MEP computation at the CASPT2//CASPT2 level for C has been made available by Nakayama et al. (see supporting information in [61]). The findings support the presence of a minimum along the main decay path, thus validating the view gathered from previous results obtained at the CASPT2//CASSCF level, which are distinct from those found for T and U [26]. Nevertheless, the CASPT2 approach, as any other quantum-chemical method, is not free of limitations. It is inherent at its original formulation related to the

choice of the zeroth-order Hamiltonian. For instance, the open- and closed-shell electrons are not equally treated which causes a certain imbalance between electronic states which is reflected in the computed relative energies [82], as has been documented in the studies of the ionization potentials (IPs) [83–86] and electron affinities (EAs) [86, 87] of the nucleobases. On the other hand, in principle, the CASPT2 wave functions corrected up to first order might not be orthogonal, even though the zeroth-order wave functions used come from averaged-CASSCF calculations. For some time the multi-state extension of the CASPT2 method (MS-CASPT2) was believed to be a solution to solve this problem. In fact, the MS-CASPT2 [66] has been shown to be especially efficient in clearing up the valence-Rydberg mixing in spectroscopic applications [88, 89]. Photochemistry deals primarily with valence states. Therefore, the MS-CASPT2 is not suited for photochemical applications of medium-size molecular systems, such as the nucleobases, because the off-diagonal elements of the corresponding effective Hamiltonian matrix between valence states are much larger and more differential than those involving valence and Rydberg states. As a result, the MS-CASPT2 computations may sometimes lead to spurious results and artificial avoided crossings [36]. Recent advances in the extended MS-CASPT2 (XMS-CASPT2), however, certainly look promising to alleviate the problem considerably [76, 90, 91]. They are going to become especially relevant when the characterization of the lowest-energy CI is required. In practice, the CASPT2 can be confidently applied to locate, in a good approximation, the first interstate crossing point along an MEP computation [6, 36].

Much of the success of the CASPT2 method in earlier spectroscopic applications has been achieved because it has been used in conjunction with atomic natural orbital (ANO-type [92–94]) basis sets [6, 13–18, 62, 65, 80, 95–98]. Less flexible basis sets should be systematically checked with respect to the generally contracted ANO-L [94] basis sets or segmented basis sets including electron correlation in their construction (e.g., correlation consistent type). In order to maintain a balanced description along the different regions of the PEHs involved, the relative energy differences should be calculated with the same basis set and level of calculation as used for the geometry optimizations and structural MEP characterization with no symmetry restrictions when appropriate. In summary, the current state-of-the-art methodology for describing photochemical reaction paths can be denoted by CASPT2//CASSCF/6-31G* and preferably CASPT2//CASSCF/ANO C,N,O [$4s3p1d$]/H[$2s1p$] through actual MEP computations, either by using the original IRC formulation [7, 8] or the related improved algorithms [5, 9–11].

## 3 Non-Adiabatic Photochemistry of Pyrimidines

The non-adiabatic photochemistry of pyrimidine NABs is reviewed in this section, both in the singlet and triplet manifolds. Along the ultrafast IC of singlet-excited nucleobases, the lowest triplet state might also be populated by an ISC mechanism,

a possibility that has been explored by several groups. First, a brief overview of the theoretical absorption spectra will be outlined in order to underline the importance of determining the bright excited state, from which the photochemical decay originates. A chronological inspection about the studies focused on the subject shall be given next, describing in most cases the strategies employed and the main features determined on the PEHs of the ground and low-lying excited states, such as minima, TS, and crossings. The MEP computations available to characterize the main decay mechanisms capable of rationalizing the experimental findings are finally considered.

## 3.1 Photochemical Reaction Paths for Thymine

Several computational methods have been employed over the years to determine the vertical absorption energies of T, including time-dependent density functional theory (TDDFT) [99], coupled cluster (CC) [100, 101], DFT/MRCI [102], and CASPT2 [80, 103, 104]. The values for the bright $^1(\pi\pi^*)$ state stand in agreement with previous experimental data (4.8 eV [23]), yielding the values 4.95, 5.20, 5.15, 5.18, and 4.89–5.06 for the TDDFT, approximate coupled cluster singles and doubles linear response (CC2-LR), equation-of-motion excitation-energy coupled cluster singles, doubles, and perturbative triples [EOMEE-CCSD(T)], DFT/MRCI, and CASPT2 methods, respectively. It is also worth noting that the bright state of T corresponds to the second lowest-energy singlet state, or $S_2$, computed vertically. The excited state related to the lone-pair promotion is located at a lower vertical energy at the FC region and thus it will be considered a dark state due to its lower population upon irradiation. Since the bright state is described mainly by the one-electron promotion from the highest-occupied MO, HOMO-like, to the lowest-unoccupied MO, LUMO-like, the label $^1(\pi\pi^*$ HL) is used accordingly.

Holding the proper description of the absorption of the bright excited state, subsequent computations have been performed over the last decades in order to elucidate the photoinduced decay mechanisms prevailing in T. As can be seen below, distinct excited-state minima and crossings among the lowest-lying $\pi\pi^*$ and $n\pi^*$ singlet excited states and the ground state have been suggested to play an important role depending on the computational strategies employed.

In 2006, Perun et al. [105] found three different CIs, characterized by strongly out-of-plane distorted geometries. These crossings were described at the CASSCF/cc-pVDZ level of theory and connected to the FC geometry by using the linear interpolation of internal coordinates (LIIC) technique at that same level of theory. The lowest-lying CI involved the crossing between the lowest excited $^1(\pi\pi^*)$ state and the ground state, $(gs/\pi\pi^*)_{CI}$, being accessible in a barrierless manner from a previously found shallow minimum on the $^1(\pi\pi^*)$ hypersurface. In the same year, Merchán et al. [26] performed a CASPT2//CASSCF/ANO study on the photochemical pathways of T, C, and U, suggesting a unified model that contains the decay behavior of all three pyrimidines. MEP calculations on the bright $^1(\pi\pi^*)$ state from
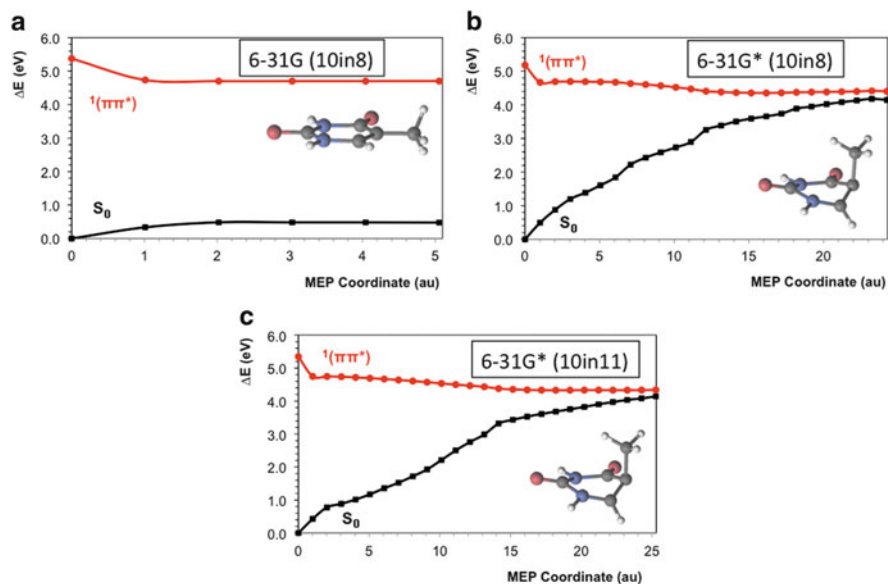
**Fig. 3** MEP computations of T at the CASPT2//CASSCF level of theory with the 6-31G and 6-31G* basis sets and including three extra correlating orbitals (10in11) in the active space

the FC geometry led the T molecule (and also U) to the ethene-like distorted $(gs/\pi\pi^*)_{CI}$ crossing with no barriers along the path. An equilibrium region on the $^1(\pi\pi^*)$ hypersurface, characterized by a planar geometry, was determined to be far from the MEP reaction path. Two distinct decays were then proposed involving direct and indirect paths. In the latter, the presence of the flat region on the $S_1$ might trap a certain percentage of the excitation energy before decay either by light emission or in a radiationless manner. The authors performed a theoretical analysis in order to ascertain the degree to which electronic correlation and the algorithm used to reach the $(gs/\pi\pi^*)_{CI}$ influenced the results of the calculation [26]. The main aspects of such analysis are next summarized.

Figure 3 shows the computed MEPs by using different basis sets and active spaces, increasing systematically the electron correlation. The calculations were performed using the full $\pi$-valence active space, and three extra virtual orbitals were subsequently added in order to check the results upon the enlargement of the active space. The $\pi$-valence active space comprises ten electrons in eight orbitals, namely 10in8. With three extra correlating orbitals added, the active space becomes 10in11. As can be seen in Fig. 3, the MEP computed with the 6-31G basis set leads to a planar minimum in the $^1(\pi\pi^*)$ hypersurface, as previously reported by Perun et al. [105]. However, employing the same active space but increasing the flexibility of the one-electron basis set employed yields a very different result (see the MEP at CASPT2//CASSCF/6-31G* level in Fig. 3). In this case, the system decays in a barrierless manner towards an ethene-like CI. The same result holds true after adding extra correlating orbitals to the active space, thus validating the previous

result obtained with the 6-31G* basis set. The illustration highlights the importance of the electronic correlation in order to give a proper description of the photochemical pathways actually accessible in a given molecular system. Moreover, the technique used to optimize the excited state also plays a key role in the result obtained in the calculation. Optimizing $^1(\pi\pi^*)$ with the 6-31G* basis set yields a planar minimum, identical to that found with the CASSCF/6-31G MEP, whereas the MEP at the CASSCF/6-31G* decays to the ethene-like CI as shown in Fig. 3. In other words, for T, determination of the different stationary points independently (geometry optimization for the ground state and the excited state, and CI search) at the CASSCF/6-31G* level, connecting those regions of the hypersurface subsequently by the LIIC procedure (*strategy 1*, hereafter), will offer a view of the photochemistry of the system similar to that displayed in Fig. 2a, i.e., through a minimum on the excited hypersurface. A similar situation occurs if the geometry optimizations are carried out at the MS-CASPT2 level [106, 107]. Nevertheless, CASPT2//CASSCF MEP computations employing a basis set with polarization functions on the C,N,O atoms (*strategy 2*) will lead to a scheme similar to that depicted in Fig. 2b, that is, a barrierless deactivation of the excited state towards the ground state. The available variety of results depending on the computational strategy employed is therefore not surprising. In fact, the conclusions derived from those studies are strongly dependent on the strategy used. It is especially crucial in dynamics simulations, where the outcomes become biased with respect to the static strategy chosen. The findings emphasize the importance of the systematic approach outlined in Sect. 2.1, the PRPA protocol, in order to unveil the photochemical decay upon light irradiation in molecular systems.

Continuing with the chronological review of the theoretical studies on the decay channels in T, in 2007 Hudock et al. [106] revisited the $S_2$ $^1(\pi\pi^*)$ bright state hypersurface, finding a minimum structure optimizing with the MS-CASPT2 method. The work is a clear representative study of *strategy 1*. The CI between the $S_2$ $^1(\pi\pi^*)$ and $S_1$ $^1(n\pi^*)$ states was also characterized at the CASSCF and CASPT2 levels of theory. On the basis of LIIC calculations between the FC, the $S_2$ minimum, and the $S_1/S_2$ CI, together with ab initio molecular dynamics at the CASSCF level, a two-step decay to the $^1(n\pi^*)$ state was suggested as the main mechanism, which differs from the direct decay towards a crossing with the ground state proposed in previous studies [26, 105]. The first step implied a fast relaxation to the $^1(\pi\pi^*)$ minimum on $S_2$, and next an energetic barrier had to be surmounted to reach the crossing $S_1/S_2$ CI. In that year, Serrano-Pérez et al. [56] studied at the CASPT2//CASSCF level the role of the triplet states in the decay channels of T and their population mechanisms mediated by the $^1(\pi\pi^*)$ bright state. Three different singlet-triplet crossing (STC) regions were characterized: (1) one located just after the FC region with the $^{1,3}(n\pi^*)$ states with a sizable spin-orbit coupling (SOC) that favors the population of the triplet state, which subsequently decays together with the also populated $^1(n\pi^*)$ state towards a $^{1,3}(n\pi^*)$ minimum, (2) a minimum that can be surmounted via both the singlet and triplet manifolds and that holds an extremely large SOC populating the triplet state and subsequently reaching a minimum in the $^3(\pi\pi^*)$ hypersurface, and (3) an extended STC region near the ethene-like CI

between the $^1(\pi\pi^*)$ and the ground state, with a relatively high SOC between the $^1(\pi\pi^*)$ and $^3(\pi\pi^*)$ states, which leads to the $^3(\pi\pi^*)$ minimum. From there, a small barrier was obtained to reach the $^3(\pi\pi^*)$ STC with the ground state, recovering the planarity of the molecule.

In 2008, Zechmann and Barbatti [108], within the framework of *strategy 1*, built on the results obtained by Hudock et al. [106] and considered the existence of a $^1(\pi\pi^*)$ minimum on the $S_2$ hypersurface, discarding the direct decay towards the ethene-like CI. Several $gs/S_1$-$^1(\pi\pi^*)$ and $gs/^1(n\pi^*)$ CIs were optimized in the study at the CASSCF and MRCI levels of theory and then the proposed decay paths from the $^1(n\pi^*)$ minimum on $S_1$ to the CIs were explored with the LIIC technique. The $(gs/n\pi^*)_{CI}$ structure was found higher in energy with respect to the $^1(n\pi^*)$ minimum, thus making unfavorable the IC process to the ground state. As for $(gs/\pi\pi^*)_{CI}$, the strategy used, LIIC, could not be conclusive on the barrier obtained. In contrast to this study, the direct path was again supported in a study carried out by González et al. [109], who employed the CASPT2//CASSCF approach to look for different arguments that might help explain the relative lifetimes experimentally found in T. The presence of tautomers and a $^1(\pi\sigma^*)$ dark state was evaluated and discarded, together with the possibility of a $^1(\pi\pi^*)$ minimum on the $S_2$ hypersurface, which was ascribed to a higher $^1(\pi\pi^*)$ state centered in an oxygen atom.

A year later (in 2009), Lan et al. [110] studied the photochemical decays of T with the semiempirical orthogonalization model 2 (OM2)/MRCI method, performing a series of excited state optimizations that led to the characterization of a minimum in the $^1(n\pi^*)$ state, and a $(n\pi^*/\pi\pi^*)_{CI}$ crossing was reached by optimizing the $^1(\pi\pi^*)$ bright state. Both $(gs/n\pi^*)_{CI}$ and $(gs/\pi\pi^*)_{CI}$ CIs were located, lying lower in energy than the $(n\pi^*/\pi\pi^*)_{CI}$ crossing. LIICs were performed between the different minima and the crossing points with the ground state, concluding that the $^1(n\pi^*)$ state was protagonist in the photochemical decay of T. Asturiol et al. [57] employed the MS-CASPT2//CASSCF method, taking into account different amounts of electron correlation in the CASSCF wave function, in order to characterize two decay paths from the FC region leading to the ethene-like $(gs/\pi\pi^*)_{CI}$ structure. The first involves the direct decay from the bright state towards the CI and corresponds to the path determined by Merchán et al. [26]. In contrast, the second is described as an indirect path that involves the minimum on the $^1(\pi\pi^*)$ state, suggested previously [26] as responsible for increasing the lifetime of the excited state. In this case, Asturiol et al. [57] also determined the most favorable decay channel from this minimum structure, yielding a small barrier to reach the CI between the $^1(\pi\pi^*)$ and $^1(n\pi^*)$ states, $(n\pi^*/\pi\pi^*)_{CI}$, and afterwards a barrierless profile to $(gs/\pi\pi^*)_{CI}$. Etinski et al. [111] studied the STC regions, reaching similar conclusions to those by Serrano-Pérez et al. [56], highlighting the possibility of a reaction path mediated by the lowest-lying triplet $T_1$ $^3(\pi\pi^*)$ state as a possible decay mechanism which would imply longer lifetimes. Szymczak et al. [112] carried out a study aiming at explaining the longer decay lifetime of T with respect to the other canonical NABs in the picosecond timescale [31, 32, 113]. The authors characterized the

$S_1/S_2$ seam at the CASSCF and MRCI singles and doubles (MRCISD) levels of theory, finding six different minima. Similar to the findings obtained by Hudock et al. [106], a minimum on the $S_2$ state of $\pi\pi^*$ character was also found featuring an elongation of the C4–O8 and C5–C6 bonds and shortening of the C4–C5 bond. This point was connected to the lowest $S_1/S_2$ crossing point. Two different possibilities were proposed from this CI: (1) going through the $S_1$ $^1(n\pi^*)$ state and towards a planar minimum, with a barrier that might be surmounted reaching the $(gs/n\pi^*)_{CI}$ or (2) going through the $^1(\pi\pi^*)$ state yielding an $S_2$ $^1(\pi\pi^*)$ pyramidalized minimum that might be overcome to reach the ethene-like $(gs/\pi\pi^*)_{CI}$. A characterization of the different CIs obtained was performed, finding an uphill feature for the $(gs/n\pi^*)_{CI}$, whereas the $(gs/\pi\pi^*)_{CI}$ was found to have a barrier that needed to be overcome. The possibility of trapping into the $S_2$ minima was confirmed performing dynamics based on PEHs at the CASSCF level and it was assigned to the effect of higher $S_3$ and $S_4$ states via avoided crossings, which reduces the direct decay. The delay to reach the $S_1/S_2$ crossing caused by the flatness of the $S_2$ hypersurface in the $^1(\pi\pi^*)$ minimum was proposed to be responsible for the longest excited-state lifetime in T [31, 32, 113]. During the same year, Serrano-Andrés and Merchán [6] analyzed and compared the most probable decay channels in the naturally occurring vs the modified NABs in order to find the particular decay patterns of the canonical nucleobases. MEP computations on the $^1(\pi\pi^*)$ PEH of 1-fluorothymine yielded a barrier along the path, thus hindering the direct deactivation towards the ethene-like CI with the ground state. As explained by the authors, these findings speak in favor of the choice of the biological nucleobases by natural selection based on their resistance to photochemical damage. On the other hand, methyl substitutes were found to have a photochemistry similar to that previously found for the canonical nucleobases.

In 2010, further exploration on the $S_1/S_2$ seam of intersection was performed by Asturiol et al. [114], yielding further insights into the topology of the seam. Direct quantum dynamics simulations were carried out with the same purpose, an interesting topic which will be covered in additional chapters of the present book. That same year, González-Luque et al. [55] completed the study on the triplet population mechanism in the DNA/RNA NABs, initiated previously in T [56], and compared the available channels for reaching the triplet manifold. T, together with A and U, displayed many ISC regions along the MEP of the bright state, related to the presence of low-lying singlet and triplet $^3(n\pi^*)$ states. These results may help to explain the prevalence of T and A components in the phosphorescence of DNA [115–117]. Barbatti et al. [118] also made a comparative analysis of NABs, focusing on the dynamical aspects of the lowest-lying $^1(\pi\pi^*)$ excited state using the CASSCF and MRCI methods to compute the energy gradients. In contrast to the predictions from MEP computations, the computational approach employed in the dynamics simulations did not show any activation of the direct pathway towards the crossing with the ground state. Instead, the shallow minimum in the second excited state of $^1(\pi\pi^*)$ character was pointed out to be the main feature on the photochemistry of T retaining the excitation for a few picoseconds.

   More recently (in 2012), Yamazaki and Taketsugu [107] published a paper alerting on the importance of including dynamical electron correlation to describe properly the critical points on the PEHs of the low-lying excited states of T, U, and 5-fluorouracil. *Strategy 1* was however used. In contrast to previous studies in which a $^1(\pi\pi^*)$ minimum was found on the $S_2$ hypersurface with an elongation of the C–O bond [106, 112, 119], here the $^1(\pi\pi^*)$ minimum was located on the $S_1$ PEH by using the MS-CASPT2 method. The disappearance of the $S_2$ minimum is explained as a result of further inclusion of dynamic electron correlation compared to the previous CASSCF and MS-CASPT2 calculations. The $S_1$ $^1(\pi\pi^*)$ minimum was found to be shallow, with a very small energy barrier along the connected LIIC path towards the ethene-like CI, $(gs/\pi\pi^*)_{CI}$. Fluoro-compounds were also computed showing larger barriers, in agreement with the results suggested by Serrano-Andrés and Merchán [6]. The hypothesis of a direct path to the crossing with the ground state involving only the lowest-lying $^1(\pi\pi^*)$ state is then supported by these results [107], although MEP computations (*strategy 2*) would be required to determine accurately the most relevant route in the decay process taking place in T.

   In general, many critical points on the PEHs of the lowest-lying excited state of T have been located, raising several hypothetical reaction pathways for non-radiative decay. Dynamics simulations have been performed with relatively fast methods such as ab initio CASSCF [57, 106, 112, 114, 118] or the semiempirical OM2/MRCI [110] methods, giving rise to lifetimes on the same timescale as the experimental data [31, 32, 113]. However, dynamics simulations employing highly accurate methods for the determination of the underlying PEHs, such as the CASPT2, are still prohibitive due to the high computational cost. Developments in this direction will surely help to evaluate the obtained data and provide converged results. Meanwhile, the PRPA and CASPT2//CASSCF computations provide the most efficient decay mechanisms present in the NAB [6, 26]. A direct relaxation of the $^1(\pi\pi^*)$ bright state towards an ethene-like CI with the ground state without barriers is predicted by such an approach as the main decay channel (see Fig. 4). This picture emerges after systematic analyses within the CASPT2//CASSCF approach [26]. In addition, preliminary results obtained in our group at the CASPT2//CASPT2 level also points to barrierless relaxation towards the ground-state PEH. Of course, accurate dynamics would be required for a direct comparison of the theoretical determined lifetimes with those derived experimentally. From the PRPA findings [6, 26], the direct and barrierless nature of this relaxation route can be related to very short lifetimes such as those observed in the molecular beams in the sub-picosecond timescale [23, 32–34]. Longer time signals might be attributed to the presence of a flat region far from the main decay, as displayed in Fig. 4. Moreover, other relaxation routes involving switches to the lowest-lying $^1(n\pi^*)$ state and barriers are also expected to increase the time spent in the excited state. Finally, the several STC regions with their large associated SOCs and singlet-triplet degeneracy imply the low-lying triplet states as main actors in one of the secondary decay routes [55, 56], which may provide a rationale for the experimental signals of longer time.

**Fig. 4** Scheme of the decay paths of T, C, and U on the basis of CASPT2 results. Reused with permission from Merchán et al. [26]. Copyright (2006) American Chemical Society
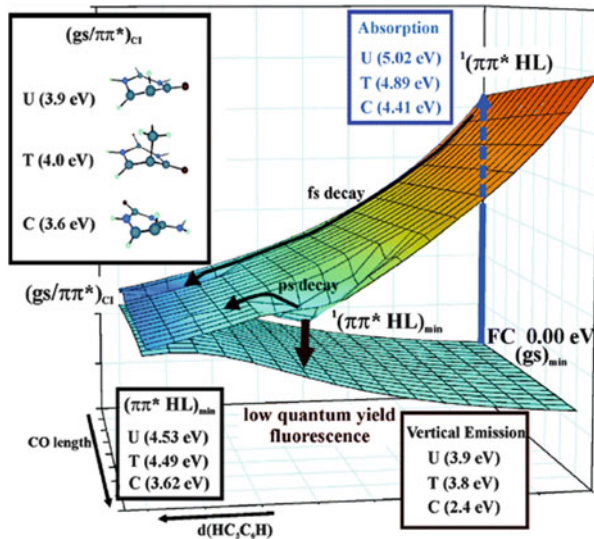
## 3.2   Photochemical Reaction Paths for Cytosine

In C, the $^1(\pi\pi^*$ HL) state is located vertically below the lower $^1(n_o\pi^*)$ state at the FC region. According to several ab initio methods, the molecule absorbs UV light at longer wavelengths as compared to the other NABs. In particular, the TDDFT [99], CC2-LR [100], EOMEE-CCSD(T) [101], DFT/MRCI [102], and CASPT2 [80, 104] methods estimate the vertical energies for the $^1(\pi\pi^*)$ state at 4.63, 4.66, 4.69, 4.62, and 4.41–4.68 eV, respectively. These values are in agreement with the gas-phase experimental data, 4.6 eV [23].

As for T (and the other NABs), several CIs have been determined in the theoretical studies on the photochemistry of C. To illustrate such diversity of crossings, we revise in this section the published works describing in more detail those aspects related to the distinct CIs. Special attention is also given to the different levels of theory and computational strategies used, which give rise in some cases to different decay mechanisms.

The first multiconfigurational ab initio quantum chemical study on the deactivation processes undertaken by C after absorption on the lowest singlet $^1(\pi\pi^*)$ excited state was reported in 2002 by Ismail et al. [77]. At the CASSCF/6-31G* level, the authors concluded on the basis of IRC calculations that the most probable decay of the $^1\pi\pi^*$ state was described by a barrierless path in which an adiabatic switch to the $^1(n_o\pi^*)$ state occurs, reaching subsequently a minimum region. From the equilibrium region, the system might reach a CI with the ground state by surmounting a barrier height of 3.6 kcal/mol (0.16 eV), and consequently decay back to the original ground state structure. An alternative decay path was also obtained, involving a population transfer from the $^1(n_o\pi^*)$ to the $^1(n_N\pi^*)$ state through a CI placed 9.8 kcal/mol (0.42 eV) above the minimum of the $^1(n_o\pi^*)$

ethene-like CI     amino-puckered CI     bond-inversion CI
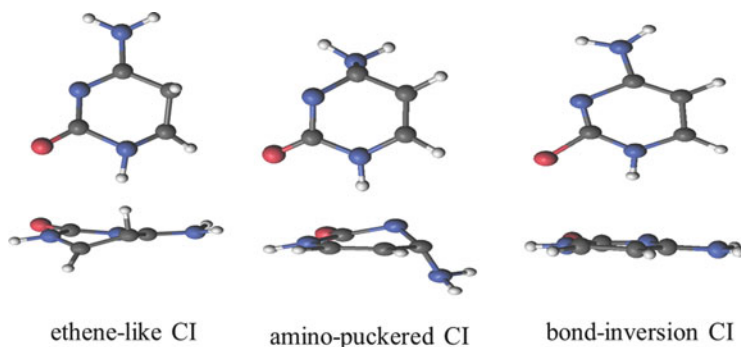
**Fig. 5** Frontal and side views of the structures for the distinct CIs characterized among the lowest-lying excited states and the ground state of C

state. The system may further decay towards a CI involving the $^1(n_N\pi^*)$ and the ground state.

Just one year later (in 2003), Merchán and Serrano-Andrés [78] showed that, in order to provide a correct description of the PEHs of the excited states of C, an adequate treatment of dynamic electron correlation (not considered previously) was mandatory. The authors in fact performed CASPT2 calculations on top of optimized CASSCF structures, demonstrating that the excited $^1(\pi\pi^*)$ state was directly connected through a CI with the ground state, and consequently the system might decay back through a mechanism that does not invoke the $^1(n_o\pi^*)$ state. From the FC region, the $^1(\pi\pi^*)$ state was described to evolve to a minimum structure and then to a CI with the ground state by surmounting a barrier height of 2.5 kcal/mol (0.11 eV). The path implying the $^1(n_N\pi)^*$ state described by Ismail et al. [77] was also studied at the CASPT2 level. A similar CI was identified, accessible from the minimum of the $^1(\pi\pi^*)$ state by surmounting a 12.0 kcal/mol (0.52 eV) barrier height. Such a description was obtained by using the LIIC strategy and the CASPT2//CASSCF approach. The 6-31G** basis set was used throughout. In both papers [77, 78], the CI mainly responsible for the radiationless deactivation of excited C was characterized by the interchange of the single-double bond character with respect to the ground state minimum geometry and a slight pyramidalization of the C6 atom. This type of CI will be further referred to as *bond-inversion* CI (see Fig. 5). In the CI involving the $^1(n_N\pi)^*$ and the ground state, the amino group suffers a pronounced out-of-plane distortion from the ring and it will consequently be denoted as *amino-puckered* CI (cf. Fig. 5).

In 2004, Blancafort and Robb [58] (see also [52]) proposed a decay mechanism based on CASPT2//CASSCF/6-31G* results in which the bright state would first decay to a minimum structure, then pass to a $S_1/S_2$ CI, and finally decay back to the ground state through a gs/$S_1$ crossing region by surmounting a small energy barrier. The key idea presented in the paper is that the $^1(\pi\pi^*)$ state decay is mediated by a three-state CI which involves the excited $^1(\pi\pi^*)$ and $^1(n_o\pi)^*$ states and the ground state. Due to the strong mixing related to such a

threefold degenerate situation, the state in that particular region is defined as a mixed $^1(n_o\pi)^*/^1(\pi\pi^*)$ state. This work showed the intrinsic difficulty to characterize unambiguously the nature of the states of C at the crossing region, a problem that will frequently emerge in future studies. IRC calculations were carried out at the CASPT2//CASSCF level.

Besides the description of the non-radiative decay mechanism responsible for the intrinsic photostability of the nucleobase, the processes leading to a possible population of the triplet states also started to be studied, due to their likely involvement in the photochemistry of C. In 2005, with the joint efforts of different groups, MEP CASPT2//CASSCF/6-31G** work appeared regarding the subject [51]. By connecting the $^1(\pi\pi^*)$ minimum to the bond-inversion CI, the system might pass through an STC region with the $^3(\pi\pi^*)$ state. That same year, Tomic et al. [120] studied the relaxation process of the $^1(\pi\pi^*)$ state of C using the DFT/MRCI//TDDFT/TZVP approach. A minimum structure was obtained by computing an unconstrained geometry optimization from the FC region. It was subsequently connected with a CI involving the ground state by a constrained minimum energy path calculation. The decay path so estimated is characterized by an energy barrier height of around 0.2 eV, and it was assigned as the main radiationless response of the bright state. A similar CI was firstly obtained in 2004 by Sobolewski and Domcke [121] by geometry optimization of a localized excited state of the G-C base pair system employing the configuration interaction singles (CIS) method. The crossing region, featuring a large elongation and twisting of the C5C6 double bond, is usually identified in the literature as *ethene-like* $(gs/\pi\pi^*)_{CI}$ crossing (see Fig. 5). A few months later, the importance of the $(gs/\pi\pi^*)_{CI}$ in C was further highlighted by Zgierski et al. [122] (see also [123, 124]). On the basis of completely renormalized equation of motion coupled cluster singles, doubles, and perturbative triples [CR-EOM-CCSD(T)] energy calculations at CIS/cc-pVDZ geometries, the authors showed that the initially excited $^1(\pi\pi^*)$ state might decay to $(gs/\pi\pi^*)_{CI}$, along a path involving a negligible energy barrier. The authors considered that the bright $^1(\pi\pi^*)$ state switches along such a decay path to an out-of-plane deformed singlet excited state of biradical character, which is the one that actually crosses with the ground state. The authors concluded that the $^1(n\pi)^*$ state will not play an important role in the ultrafast non-radiative decay mechanism of C, as previously pointed out by Merchán and Serrano-Andrés [78].

In 2006, Merchán et al. [26] (see also [6]) offered a unified study on the ultrafast decay of the pyrimidine NABs by computing CASPT2//CASSCF MEP calculations of the related bright states, testing different active spaces and basis sets. The authors showed that both T and U can decay along a barrierless path to an ethene-like CI with the ground state. Meanwhile, the C system seemed to decay to a minimum structure. Nevertheless, since the path obtained by an LIIC calculation in C at the CASPT2(14,10)/ANO-S C,N,O [3s,2p,1d]/H[2s1p] level of theory between the FC region and an ethene-like $(gs/\pi\pi^*)_{CI}$ crossing has a barrier height of only 2.5 kcal/mol (0.11 eV), it was suggested that the minimum described might be a spurious result probably due to the limited correlation employed in the geometry optimization approach, which was performed at the CASSCF level.

At the beginning of 2007, a new paper exploring the PEHs of C appeared, this time using the MRCI method in conjunction with three different types of expansions [125] (see also [126]) and the cc-pVDZ basis set. Kistler and Matsika concluded that the $^1(\pi\pi^*)$ state decays to a minimum region from which it may evolve along two different paths characterized by similar energy barrier heights of around 0.14 eV. One of them would lead the system to the ethene-like CI, $(gs/\pi\pi^*)_{CI}$, the other, to a crossing point characterized by an out-of-plane distortion of the N3 atom, whose geometry actually corresponds to that characterizing the amino-puckered CI. The latter crossing was claimed to involve the $^1(\pi\pi^*)$ and ground state and not the $^1(n_N\pi)^*$ state as was found previously [77, 78]. The paths described in the paper were obtained by a combination of mass-weighted gradient-directed and LIIC computations. In the same year (2007), Blancafort [59] further studied the system on the basis of IRC calculations at the CASPT2//CASSCF/6-31G* level, leading to the conclusion that from a minimum of the $^1(\pi\pi^*)$ state the system might decay to the ethene-like $(gs/\pi\pi^*)_{CI}$ by surmounting a barrier height of 0.11 eV or decay first to the $^1(n_N\pi)^*$ state and subsequently to the ground state along a path characterized by an energy barrier height of 0.21 eV. The CI involving the $^1(n_N\pi)^*$ state and the path connecting the FC region to such a crossing point closely resembles the one previously described [77, 78]. Due to the relatively small barrier found, it was suggested that the $^1(n_N\pi)^*$ state can contribute to the ultrafast decay of the system. On the other hand, Blancafort did disclaim the importance of the bond-inversion CI since, according to his new outcomes, it entails much higher energies [59].

In 2008, Kistler and Matsika [127] characterized three different three-state CIs and showed their connection with the previously described two-state CIs [125], which, according to the authors, still remain the main funnels back to the ground state. A computational strategy based on the MRCI method was employed, implemented in a similar fashion to that used by the same group in 2007 [125]. The paper did not present a new main deactivation mechanism of the system with respect to that reported in 2007, but provided some useful knowledge about the PEHs and the possible involvement and relevance of three-state CIs. Since 2008, different excited-state dynamics studies on C have been performed [118, 128–131], which will be discussed in another chapter of the book. One of the earlier dynamics studies was performed by Hudock and Martínez [128]. The energies of the populated regions of the PEHs during the dynamics simulation were determined at the CASSCF/6-31G* level. The three different CIs with the ground state depicted in Fig. 5, i.e., ethene-like CI, bond-inversion CI, and amino-puckered CI, were obtained. Such relevant regions were reoptimized with the MS-CASPT2//MS-CASPT2 approach, and the interpolated paths connecting them with the FC structure were computed. At the higher level of theory employed, the ethene-like and bond-inversion CIs were described to be reached by surmounting an energy barrier. Meanwhile, the path connecting the FC region and the $(gs/n_N\pi^*)_{CI}$ structure was found to be barrierless.

In 2009, Lan et al. [110] studied the photoinduced relaxation dynamics of C using the semiempirical OM2/MRCI method. The optimization of the bright

$^1(\pi\pi^*)$ state from the FC region led to the characterization of a minimum structure. Two CIs between the bright excited $^1(\pi\pi^*)$ state and the ground state were obtained. The first can be classified as an ethene-like CI, and is here considered the most relevant since it is placed at lower energies. The second is an amino-puckered CI, and its role in the deactivation process is believed to be less important due to its higher energy.

In 2010 a paper on the population of triplet states in NABs was published [55]. It was shown at the CASPT2//CASSCF/ANO-S C,N,O [3s,2p,1d]/H[2s1p] level that an accessible STC region was located near the ethene-like CI described in 2006 [26], which connects the singlet $^1(\pi\pi^*)$ and triplet $^3(\pi\pi^*)$ states. Once populated, the $^3(\pi\pi^*)$ might relax to a minimum structure, from where it might further decay to an STC region with the ground state.

In 2011, Barbatti et al. [130] (see also [118]) performed dynamics simulations computing the energy gradients with the CASSCF and MRCISD methods, employing the 6-31G* basis set. One minimum on the $S_1$ PEH and four different CIs with the ground state were obtained along the trajectories. The low-lying CIs are related to the ethene-like type, bond-inversion, and amino-puckered CIs. LIIC calculations were computed between the FC region and those CIs. The paths obtained both at the MRCISD and CASSCF level were found to be barrierless, with the exception of the CASSCF one related to the bond-inversion CI.

This year (2013), a study of C and its imino and enol tautomers has been reported by Nakayama et al. [61]. The picture obtained from MEP computations at the MS-CASPT2//MS-CASPT2/Sapporo-DZP level gives support to the scheme depicted in Fig. 2a.

In contrast to T (and also to U), CASPT2//CASSCF MEP computations from the bright state of C do not end in the ethene-like CI with the ground state [26]. According to the LIIC strategy between the FC and the ethene-like CI, a barrier height of 2.5 kcal/mol (0.11 eV) was found [26]. The different findings between the LIIC and MEP approaches were initially ascribed to a lack of geometry optimization at the highest level (CASPT2) including dynamic electron correlation. Nevertheless, preliminary results with the CASPT2//CASPT2 approach give rise to a well-identified minimum, distinct from the CI, which is consistent with the recent findings mentioned above [61]. In addition, new experimental studies have recently reported a dependence on temperature of the fluorescence [132], which supports the presence of a barrier to reach the CI. In any case, this barrier is estimated to be very small, thus preserving a fast decay process in C, provided a slight excess of energy. For these reasons, *strategy 1* outlined in the previous section may work out correctly for C, whereas for T it leads to a different picture with respect to the preferred MEP calculations. Thus, at the highest level of theory currently available, C reveals itself with an unparalleled behavior as compared to T and U, which brings a new question: what in C is the underlying source of such uniqueness? While the response to this question arises, let us also keep our minds open for further improvements in the treatment of dynamic electron correlation.

## 3.3  Photochemical Reaction Paths for Uracil

The computed vertical transition energies for U show a similar ordering as that found in T. The $^1(n\pi)^*$ state appears as the lowest-lying vertical excited state, below the $^1(\pi\pi^*$ HL) state. Transition to the latter accounts for the largest population after UV irradiation. The TDDFT [99], CC2-LR [100], DFT/MRCI [102], and CASPT2 [80, 104] methods produce the following vertical energies for the $^1(\pi\pi^*$ HL) state: 5.17, 5.34, 5.33, and 5.02–5.23 eV, respectively. The theoretical results are in agreement with the experimental band maximum of U compiled by Crespo-Hernández et al. at 5.1 eV [23].

For U, similar decay channels as in T have been found. Nevertheless, in certain studies small differences have been reported, as described next. In 2004, Matsika [133] performed the first ab initio quantum-chemical study on the deactivation processes undertaken by U after absorption of the bright singlet $^1(\pi\pi^*)$ excited state. On the basis of MRCI/cc-pVDZ calculations, the author proposed that the bright $^1(\pi\pi^*)$ state might decay back to the ground state along a barrierless path characterized by a CI between the $^1(\pi\pi^*)$ and $^1(n_o\pi)^*$ state and a second CI between the $^1(\pi\pi^*)$ and the ground state. From the FC structure a computed gradient-driven path led to a seam of intersection between the $^1(\pi\pi^*)$ and $^1(n_o\pi)^*$ state. The geometries of such a degenerate region have a relevant elongation of the C5C6 double bond, and at the energy-minimized point of the seam the ring was deformed in a boat arrangement. From that structure, a new gradient-driven path on the $^1(\pi\pi^*)$ PEH ended in a minimum structure, while a second gradient-driven path computed from a different point of the $(n_o\pi^*/\pi\pi^*)_{CI}$ seam connected it with a CI between the $^1(\pi\pi^*)$ and the ground state. The latter CI showed a strong pyramidalization of the C5 atom that led to quite a large value of the HC6C5H dihedral angle, referred to hereafter as ethene-like CI, $(gs/\pi\pi^*)_{CI}$.

In 2005, Matsika [134] further studied the U system at a similar level of computation, and obtained a three-state CI which is not predicted to be involved in the relaxation processes of the bright state of the system since it is placed 0.4 eV above the vertical excitation energy of the $^1(\pi\pi^*)$ state. In the same year, the joint efforts of different groups addressed the problem on the basis of CR-EOM-CCSD (T) energy calculations at CIS/cc-pVDZ geometries [123] (see also [124]). The authors proposed that the $^1(\pi\pi^*)$ state might decay along a barrierless path to the $(gs/\pi\pi^*)_{CI}$ crossing. From the FC region, the initially excited $^1(\pi\pi^*)$ state will switch to an out-of-plane deformed excited single state of biradical character, which was related to the one that actually crosses the ground state at the ethene-like CI. Such a picture of the photoreaction path experimented by U was obtained by performing two relaxed scan calculations on the $S_1$ PEH, one along the C4C5C6N1 dihedral angle and the second modifying the HC5C6H dihedral angle. Note, however, that those relaxed scans do not guarantee a connected path among the different stationary points produced.

In 2006, Merchán et al. [26] (see also [6]) studied the ultrafast decay of pyrimidine NABs performing CASPT2//CASSCF calculations. For U it was proven

that the MEP computation of the bright $^1(\pi\pi^*)$ state from the FC region, including an appropriate amount of electron correlation energy by enlarging the active space with a number of extra correlating MOs, leads directly to the ethene-like $(gs/\pi\pi^*)_{CI}$. The energies along the described path were computed at the CASPT2(14,10)/ANO-S C,N,O [$3s,2p,1d$]/H[$2s1p$] level of theory.

A year later (in 2007), a study of the triplet states of U based on CASPT2// CASSCF/6-31G** calculations was reported by Climent et al. [60] (see also [55]). It was shown that along the previously described decay path of the bright $^1(\pi\pi^*)$ state [26], two STC regions were accessible. The first was located at the beginning of the computed MEP of the $^1(\pi\pi^*)$ state, and involved the $^1(\pi\pi^*)$ and $^3(n_o\pi)^*$ states. From such a region the $^3(n_o\pi)^*$ state might further evolve to a minimum structure, in the vicinity of which a CI with the $^3(\pi\pi^*)$ state was found. The second is placed near the ethene-like CI, and mediates a population transfer from the $^1(\pi\pi^*)$ state to $^3(\pi\pi^*)$. The triplet state might further evolve to an equilibrium geometry. That region of the PEH is connected to a third STC region involving the $^3(\pi\pi^*)$ and the ground state by surmounting an energy barrier height of around 0.2 eV. In the same year (2007), Hudock et al. [106] analyzed the deactivation processes of the bright $^1(\pi\pi^*)$ state of U from a dynamic perspective, where the static description of the PEHs was provided on the basis of MS-CASPT2//MS-CASPT2/6-31G* outcomes. A minimum structure on the $S_2$ PEH and a CI between the $S_1$ and $S_2$ states were identified, and LIIC calculations were obtained connecting such structures with the FC region. The results showed that after excitation the system might decay without any energy barrier either to the $S_2$ minimum or to the $S_1/S_2$ CI. The PEH is the steepest descent along the path leading to the $S_2$ minimum. Dynamics simulations showed a predominance for this path. From the $S_2$ minimum the system might reach the $S_1/S_2$ CI overcoming a small energy barrier. Both the $S_2$ minimum and the $S_1/S_2$ CI display an elongated C5C6 double bond, but while the molecular ring in the equilibrium structure keeps its planarity, it is considerably folded along the C6-N3 axis in the crossing region.

In 2008, Mercier et al. [135] studied the radiationless decay processes of U at the MS-CASPT2//CASSCF/6-31G* level of theory and using the LIIC strategy. A barrierless profile was obtained on the PEH of the $^1(\pi\pi^*)$ state connecting the FC region to an ethene-like $(gs/\pi\pi^*)_{CI}$ crossing. Along such a path the $^1(n_o\pi)^*$ state crosses, and consequently part of the population might switch to such a state and further relax to the minimum structure. From the equilibrium geometry of the $^1(n_o\pi)^*$ state, the system might reach a CI with the ground state overcoming an energy barrier height of 36.7 kcal/mol (1.59 eV). The described critical points on the $^1(n_o\pi)^*$ PEH, the minimum structure, and the CI with the ground state presented significant elongations of the C4O8 and C5C6 bonds.

In 2009, Lan et al. [110] studied the U photophysics employing the semiempirical OM2/MRCI method. Performing an unconstrained optimization of the bright $^1(\pi\pi^*)$ state from the FC region, they obtained a barrierless profile leading to a CI with the $^1(n_o\pi)^*$ state. In this region, the ring kept its planarity and the C5C6 bond length increased. From the described CI the authors proposed that the system can further evolve along the PEH of the $^1(\pi\pi^*)$ state and decay to the ethene-like

$(gs/\pi\pi^*)_{CI}$ point or switch to the $^1(n_o\pi)^*$ state and decay via a crossing with the ground state $(gs/n_o\pi^*)_{CI}$. The latter crossing region features a strong distortion localized on the C4O8 bond, which is placed perpendicular to the plane of the molecular ring. In the same year, Etinski et al. [111] used the resolution of identity approximate coupled cluster singles and doubles (RI-CC2), the DFT, and the DFT/MRCI methods to study the decay of the bright state of U and in particular the mechanisms for triplet population. The work was mainly based on geometry optimizations of the lowest singlet and triplet excited states, and on the determination of spin-orbit coupling matrix elements (SOMEs), using a one-center mean-field approximation of the Breit–Pauli Hamiltonian. From the FC region, the optimization of the $^1(\pi\pi^*)$ state at the RI-CC2/cc-pVDZ level did not evolve towards a minimum structure, and in fact the calculation did not converge due to a root-flipping problem between the $^1(\pi\pi^*)$ and the $^1(n_o\pi)^*$ state. Such a result made the authors suspect the presence of a nearby CI involving these states. LIIC calculations at the DFT/MRCI/TZVP level of theory between the TDDFT- and unrestricted UDFT-optimized geometries of the $^1(n_o\pi)^*$ and the $^3(\pi\pi^*)$ states, respectively, showed the presence of a plausible path leading to the population of the $^3(\pi\pi^*)$ state. The path involved the passage from the $^1(\pi\pi^*)$ to the $^1(n_o\pi)^*$ state and the subsequent decay from the $^1(n_o\pi)^*$ to the $^3(\pi\pi^*)$ state.

In 2010, Delchev et al. [136] presented a paper comparing the relaxation mechanisms of U and the related 4-pyrimidinone heterocycle, by using the CC2, CASSCF, and CASPT2 methods and the 6-31G*, cc-pVDZ, and aug-cc-pVDZ basis sets. In agreement with the previous results of Matsika [133] and Merchán et al. [26], a barrierless path was obtained on the $^1(\pi\pi^*)$ hypersurface from the FC region to the ethene-like CI, $(gs/n_o\pi^*)_{CI}$ by means of coordinate-driven minimum energy path computations along the HC6C5H dihedral angle coordinate. A barrier was however obtained for 4-pyrimidinone.

In 2011, Nachtigallová et al. [119] (see also [118]) performed a study on the non-adiabatic dynamics of excited U. At the CASSCF/6-31G* and MRCISD/6-31G* levels a minimum structure on the $S_2$ PEH and different CIs between the $S_1$ and $S_2$ states and between the $S_1$ and the ground states were optimized. A LIIC path among different important regions of PEHs was obtained with the same methods. In this manner, a path from the FC region to a minimum of the $S_2$ PEH was described, connected to an $S_1/S_2$ CI by surmounting a small energy barrier (similar to those previously characterized in T) from which the system can finally decay along the $S_1$ PEH to $(gs/n_o\pi^*)_{CI}$. As for T, the dominant path was related to the indirect relaxation from the bright $^1(\pi\pi^*)$ state to the ground state via the $^1(n\pi^*)$ state. This decay channel was associated with the picosecond lifetime observed in the experiments [31, 32, 113]. Additional deactivation pathways were found in the dynamics, corresponding to the direct $^1(\pi\pi^*)$ decay to the ground state via $(gs/\pi\pi^*)_{CI}$, which was ascribed to the sub-picosecond lifetime [113]. In a fraction of trajectories, decay paths involving $^1(\sigma\pi^*)$ states and a ring-opening CI were also observed. The existence of these two additional channels in U, not found in T, was proposed to be responsible for the shorter lifetime of U compared to T.

The MS-CASPT2 method and the Sapporo-DZP basis set were used in 2012 by Yamazaki and Taketsugu [107] in order to address the problem. The authors concluded that the $^1(\pi\pi^*)$ state might decay to a minimum structure from the FC geometry and subsequently to a CI with the ground state. This CI was different from the previously described ethene-like CI [6, 26, 110, 118, 119, 123, 124, 133, 135, 136], since both the C5 and the C6 were slightly pyramidalized and the ring was a little folded along the C6N3 axis. Along the path leading to the $^1(\pi\pi^*)$ minimum structure, the $^1(n_o\pi)^*$ state might be populated by the presence of a CI between these states, from where the system might further relax to an equilibrium geometry. The MS-CASPT2 geometry optimization of the $^1(\pi\pi^*)$ state converged to a minimum structure. Starting at the minimum so obtained, a MS-CASPT2 relaxed scan calculation using the N1C6C5C4 dihedral angle up to a value of around 120° as a driving coordinate was computed. An LIIC path was then produced in order to connect the final point of the relaxed scan to the CI between the $^1(\pi\pi^*)$ and the ground state. No significant differences for the decay paths in U and T were found, concluding that the effect induced by the methyl substitution was weak, and pointing out other factors such as solvent effects for the longer lifetime of T. The biexponential decay of the excited-state signal observed experimentally was ascribed to the deactivation from both $^1(\pi\pi^*)$ and $^1(n_o\pi)^*$ minima.

As described for T above, it is worth noting that the results obtained from the application of *strategy 1* lead to the photochemical view of U according to the scheme depicted in Fig. 2a [106, 107, 118, 119]. Within *strategy 2*, the decay mechanism predicted by the PRPA in U is basically the same as that described for T [6, 26]. Briefly, after excitation to the $^1(\pi\pi^*\text{HL})$ state, the initially planar U molecule becomes deformed, increasing mainly the HC6C5H dihedral angle. The system evolves barrierless towards a CC-ethene-like crossing point $(\text{gs}/\pi\pi^*)_{\text{CI}}$ (see Fig. 4), in which the energy can be funneled to the ground state. A similar decay channel is obtained for 1-methyluracil, whereas barriers are found in 1-fluorouracil and 5-fluorouracil [6], in which an NH or CH is substituted by NF or CF, respectively. Comparison of these distinct findings obtained with the PRPA and the CASPT2//CASSCF approach allow rationalization of the different excited-state lifetime observed in the experiments for the canonical and modified U [137, 138]. Hence, almost identical decay times have been measured in water for U (96 fs) and 1-methyluracil (93 fs). Conversely, 5-fluorouracil displays a sevenfold increase in the state lifetime (694 fs) [137, 138].

## 4   Non-Adiabatic Photochemistry of Purines

As shall be seen below, A and G have a rich non-adiabatic photochemistry. Consequently, especially for the former, the reaction paths of electronically excited A have been actively studied, being quite often the research target of many different groups. In comparison, relatively less attention has been paid to G.

## 4.1 Photochemical Reaction Paths for Adenine

The A NAB has three low-lying singlet excited states, two of $\pi\pi^*$ nature (the $L_b$ and $L_a$ states) and a third $^1(n\pi^*)$ state. The $^1(\pi\pi^* L_a)$ state is related to the transition bearing the largest oscillator strength among the lowest-lying states. It is energetically higher than the $^1(\pi\pi^* L_b)$ state. The CC2-LR [100], EOMEE-CCSD(T) [101], DFT/MRCI [102], and CASPT2 [25, 27, 80, 104] methods estimate the vertical transition energy of the $^1(\pi\pi^* L_a)$ state at 5.25, 5.23, 5.15, and 5.30–5.35 eV, respectively. Meanwhile, the $^1(\pi\pi^* L_b)$ is predicted at 5.25, 5.04, 4.99, and 5.16–5.20 eV, respectively. The experimental band maximum is reported by Crespo-Hernández et al. at 5.2 eV [23]. The relative position of the $^1(n\pi^*)$ is, however, more controversial. It has been placed either above or below the $^1(\pi\pi^*)$ states. The multiconfigurational CASPT2//CASSCF approach establishes the following ordering of the $^1(n\pi^*)$, $^1(\pi\pi^* L_b)$, and $^1(\pi\pi^* L_a)$ states: 4.96, 5.16, and 5.35 eV, respectively [80].

The first PEH studies in A found different minima for the $^1(\pi\pi^* L_b)$ and $^1(n\pi^*)$ excited states [139, 140]. CIs were subsequently located in 2005 by the groups of Sobolewski, Domcke, Marian, Li, Sølling, and coworkers, characterized by out of plane distortions of the C2 and N1 atoms [141–144]. Three-state CIs were also found by Matsika [134]. Low barrier heights of the order of 0.1 eV were obtained from the minima on the $S_1$ hypersurface using LIIC and gradient- and coordinate-driven approaches together with the CASPT2//CASSCF, DFT/MRCI//TDDFT, and TDDFT//CASSCF protocols. The overall picture was that deactivation pathways in A imply the $^1(n\pi^*)$ state as key intermediate. Hence, the $^1(\pi\pi^* L_b)$ and $^1(\pi\pi^* L_a)$ states transfer the population energy to the $^1(n\pi^*)$ state on the $S_1$ hypersurface and next the molecule might evolve adiabatically on this PEH until reaching two types of crossings with the ground state, $(gs/n\pi^*)_{CI}$ or $(gs/\pi\pi^*)_{CI}$. Sobolewski, Domcke, and coworkers [145, 146] also located another type of CI involving $^1(\pi\sigma^*)$ states and hydrogen abstraction from the NH and $NH_2$ groups. However, this deactivation mechanism was predicted to compete only at higher energies, above 5 eV. In the same year (2005), Blancafort [53] computed MEPs at the CASPT2//CASSCF level to connect accurately the previously found minima and CIs. Two main paths were proposed for the non-radiative deactivation of the $^1(\pi\pi^* L_b)$ state: a direct decay to the ground state almost barrierless and an indirect decay via the $^1(n\pi^*)$ intermediate state in which a small barrier was also estimated for the population transfer from the $^1(n\pi^*)$ minimum to the ground state, in agreement with the aforementioned studies [141–144].

In 2006, Serrano-Andrés, Merchán, and Borin [25, 27] (see also [6]) published two comprehensive works focusing on the photophysics of A and two modified NABs: 2-aminopurine and 7H-adenine. The CASPT2//CASSCF approach was used to determine the most favorable evolution, as obtained by MEP calculations, for the bright excited states [$^1(\pi\pi^* L_a)$ in A]. A direct barrierless decay to the CN-methanamine-like crossing with the ground state was obtained. The $^1(\pi\pi^* L_b)$ and $^1(n\pi^*)$ states were shown to cross along the $^1(\pi\pi^* L_a)$ path. Hence, further

MEPs were computed along these states and from the corresponding crossings. The differences measured experimentally [32, 147–149] for the fluorescence and non-radiative quantum yields of those molecules were rationalized as the presence or absence of energy barriers along the MEPs from the spectroscopic state. Whereas a solely barrierless profile was obtained for the non-fluorescent A, significant energy barriers were found for the other non-canonical bases. Hence, the ultrafast decay was attributed to the barrierless profile of the bright $^1(\pi\pi^*\ L_a)$ state and the picosecond signal to crossings from the $^1(\pi\pi^*\ L_a)$ state to the $^1(n\pi^*)$ and $^1(\pi\pi^*\ L_b)$ states and barrier-based photochemical paths along the latter two states after direct light absorption. A year later (in 2007), Zgierski et al. [150] used the CR-EOM-CCSD(T)//CIS/cc-pVDZ level of theory to explore the PEHs of the lowest-lying states at different degrees of C2-puckering. As for pyrimidines, a biradical channel was suggested for the radiationless decay of A, involving the $(gs/\pi\pi^*)_{CI}$ as in previous studies [25, 27].

In 2008, Fabiano and Thiel [151] performed a dynamics study of the non-radiative deexcitation of A at the semiempirical OM2/MRCI level. The $(n\pi^*/\pi\pi^*\ L_a)_{CI}$, $(gs/\pi\pi^*\ L_a)_{CI}$, and $(gs/n\pi^*)_{CI}$ crossings were determined and, on the basis of the dynamics calculations, a two-step process was proposed characterized by an ultrashort transition from the $S_2$ hypersurface to $S_1$ followed by a subsequent transition to $S_0$. Later (in 2009), Conti et al. [54] reported an MEP study with the CASPT2//CASSCF and MS-CASPT2//CASSCF methodologies designed to treat homogenously all the previously proposed reaction paths, that is, the direct decay of the $^1(\pi\pi^*\ L_a)$ state to the CI with the ground state, the internal conversion from $^1(\pi\pi^*\ L_a)$ to the lower-lying $^1(\pi\pi^*\ L_b)$ and $^1(n\pi^*)$ states, and the decays involving the $^1(\pi\sigma^*)$ dissociative states. Great efforts were made to estimate the radiationless transitions rate constants for the distinct processes. Both sub-picosecond and picosecond signals [113, 147, 152] were attributed solely to the $^1(\pi\pi^*\ L_a)$ state, predicting longer lifetimes for the decay of the $^1(n\pi^*)$ and $^1(\pi\pi^*\ L_b)$ states.

In 2010, Barbatti et al. [118] obtained from ab initio CASSCF dynamics simulations a high predominance of the straightforward deactivation mechanism to the ground state, although it was not assigned to the shortest relaxation time observed experimentally in the order of 100 fs [32, 113, 147, 152, 153]. González-Luque et al. [55] also studied in 2010 at the CASPT2//CASSCF level the triplet population mechanism of A. As for T and U, three STC regions were found to be easily accessible from the singlet main decay pathway. Two of them were mediated by the presence of lowest-lying singlet and triplet $^3(n\pi^*)$ states, and the third was close to the end of the main MEP on the $^1(\pi\pi^*\ L_a)$ singlet excited state and the methanamine-like CI of this state with the ground state. More recently, Barbatti et al. [154] performed a detailed study of A dynamics in the gas phase in order to find the reason for the discrepancies obtained in previous studies on the dynamics [118, 151, 155–157] concerning the predominant mechanism. Simulations with the semiempirical (OM2) and ab initio MRCI methods predicted similar timescales, although through different IC channels. On the other hand, those computations carried out at the TDDFT level and employing different functionals failed to predict the ultrafast decay. A distinct topography of the PEHs was obtained depending on
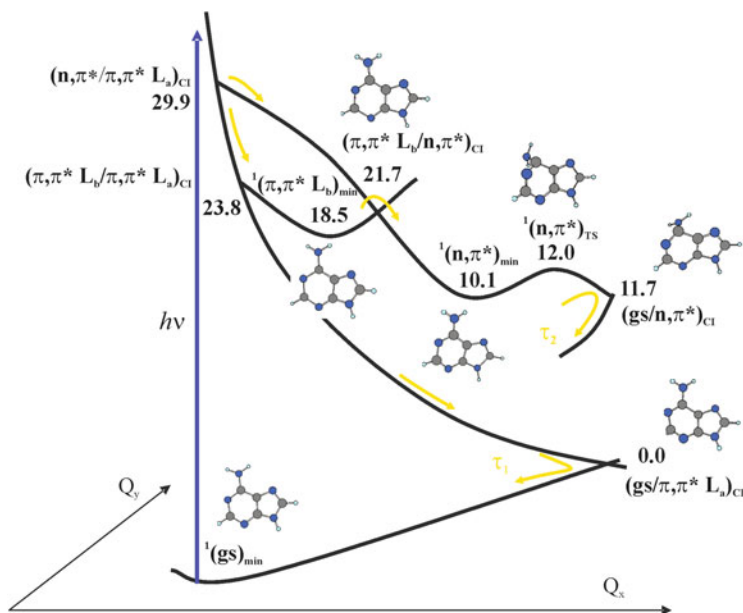
**Fig. 6** Scheme of the decay paths of A on the basis of CASPT2 results. Reused with permission from Serrano-Andrés et al. [27]. Copyright (2006) WILEY

the level of theory, which was proved to be the origin of the discrepancies. These findings are in line with previous theoretical results obtained for U and T and the outcomes of the analysis performed in Sect. 3.1 for T (see Fig. 3 and the related text).

   The application of the PRPA to study the photochemistry of A has allowed the establishment of two distinct decay mechanisms as displayed in Fig. 6 [6, 25, 27, 53, 54] which differ in the accessibility of the CIs between the excited and ground states. Population to the $^1(\pi\pi^* L_a)$ state deactivates the energy through a barrierless path to the $(gs/\pi\pi^* L_a)_{CI}$ crossing, thus providing a direct deactivation route. Considering that it involves the spectroscopic state, this is the primary deactivation pathway of excited A ($\tau_1$). Secondary decay ($\tau_2$) channels will depopulate the other two low-lying singlet excited states, $^1(n\pi^*)$ and $^1(\pi\pi^* L_b)$, activated through crossings along the $^1(\pi\pi^* L_a)$ MEP or by direct absorption. Regarding the crossings (shown in Fig. 6), two structures appear, $(n\pi^*/\pi\pi^* L_a)_{CI}$ and $(\pi\pi^* L_b /\pi\pi^* L_a)_{CI}$, from which the system evolves towards the minima of the $^1(n\pi^*)$ and $^1(\pi\pi^* L_b)$ states, respectively. From the $^1(n\pi^*)$ minimum, the system can decay to the ground state by surmounting the $^1(n\pi^*)_{TS}$ and via the $(gs/n\pi^*)_{CI}$. Other decay paths from the $^1(n\pi^*)$ minimum involve an adiabatic process to the $^1(\pi\pi^* L_a)$ hypersurface leading finally to the lowest $(gs/\pi\pi^* L_a)_{CI}$ (see Serrano-Andrés et al. [27]). No direct connection with the ground state occurs for the $^1(\pi\pi^* L_b)$ state from its minimum, $(\pi\pi^* L_b)_{min}$. Instead, a low-energy $S_1/S_2$ CI is present connecting the $^1(\pi\pi^* L_b)$ and $^1(n\pi^*)$ states, $(n\pi^*/\pi\pi^* L_b)_{CI}$. A not so clear scenario is found for the interpretation

of the experimental lifetimes [113, 147, 152], according to the different explanations proposed in the literature. Dynamics studies have begun in the last decade which can solve these problems. Nevertheless, the demands on time and central processing unit (CPU) power are nowadays still limiting systematic studies to find converged results upon increasing levels of theory for the description of the PEH.

## 4.2 Photochemical Reaction Paths for Guanine

The bright state of G computed vertically corresponds to the lowest-lying excited state $^1(\pi\pi^* L_a)$, being the $^1(n_o\pi^*)$, and $^1(\pi\pi^* L_b)$ states above it. Electronic transition to the latter state accounts for large oscillator strengths, similar to that related to $^1(\pi\pi^* L_a)$. Hence, both $^1(\pi\pi^* L_a)$ and $^1(\pi\pi^* L_b)$ states can be equally populated at higher energies. The CASPT2//CASSCF approach establishes the vertical energies at 4.93, 5.54, and 5.77 for the $^1(\pi\pi^* L_a)$, $^1(n_o\pi^*)$, and $^1(\pi\pi^* L_b)$ states, respectively [28, 80]. Other methods, such as TDDFT [99], CC2-LR [100], and EOMEE-CCSD (T) [101] also predict a $^1(\pi\pi^*)$ as the lowest excited state at 4.88, 4.98, and 4.86 eV, respectively, in agreement with the CASPT2//CASSCF findings and the gas-phase experimental data, 4.6 eV [23].

The location of excited-state minima and exploration of the PEHs through the LIIC strategy and using the CASPT2//CASSCF approach was first addressed by Chen and Li [158] in 2006. A $S_1$ $\pi\pi^*$ minimum was found in the proximity of the CI with the ground state. The two-step decay observed experimentally [32] was then attributed to the initial deactivation to the $S_1$ minimum and the subsequent energy barrier needed to reach the CI. Later (in 2007), Marian [159] employed the DFT// MRCI protocol to study the lowest-lying excited state of several tautomeric and rotameric forms of G, which for this NAB are close in energy in the gas phase. In this study, which was mainly focused on the proper assignment of the infrared (IR)-UV bands of the absorption spectrum, two CIs between the $S_0$ and $S_1$ states were located: $(gs/\pi\pi^*)_{CI}$ and $(gs/n_o\pi^*)_{CI}$. Zgierski et al. [160] (see also [124]) carried out a comparative study on G and a modified NAB, propanodeoxy-guanosine, in which the out-of-plane deformation of the six-membered ring at the C2 position is hindered. On the basis of CC2/cc-pVDZ computations and mapping of the PEHs of the lowest singlet states, an ultrafast internal conversion was proposed for G and not for the modified base.

In 2008, the role of the $^1(\pi\sigma^*)$ dissociative state was studied by Yamazaki et al. [161] at the CASPT2//CASSCF level of theory, exploring the PEHs of the ground and lowest-lying excited states along the coordinate-driven stretching of the NH bond. As for the other NABs, these paths are present at much higher energies than those involving non-reactive deformations of the ring and therefore they are relatively less relevant for the decay process of excited G. In the same year, Serrano-Andrés, Merchán, and Borin [28] (see also [6]) proposed a model for the photochemical decay mechanisms of G focusing on the $^1(\pi\pi^* L_a)$, $^1(\pi\pi^* L_b)$, and $^1(n_o\pi^*)$ states. MEP computations on the $S_1$ state at the CASPT2//CASSCF level

brought the population directly to the funnel with the ground state in a barrierless manner. Conversely, the deactivation of the $^1(n_o\pi^*)$ state showed energy barriers. In this study, the authors also presented an illustrative example highlighting the relevance of the crossing points obtained along the MEPs as compared to those obtained by geometry optimization techniques. Both types of crossing points were determined via MEP and MECP optimizations, respectively, and they were connected along the computed seam. An energy barrier was found from the former to the latter. As explained by Serrano-Andrés et al. [28], the excited G funnels the energy to the ground state already at the first point with a large probability for population transfer. Hence, decay does not take place at the MECP region, but at the first accessible crossing point along the reaction path. Serrano-Andrés et al. completed the work by including the first study on the dynamics of the excited-states of G, finding lifetimes of the order of <100 fs for the decay of the $S_1$. Further non-adiabatic dynamics simulations have been computed since then by Lan et al. [162] and Barbatti et al. [118, 163] at the semiempirical OM2/MRCI and ab initio MRCI levels of theory. The main role of the relaxation channel of the $^1(\pi\pi^*)$ state is also proposed in these works, although discrepancies appear in the pathways and the assignment of the lifetimes.

For G, the intrinsic population of the triplet mechanism was studied in 2010 by González-Luque et al. [55] at the CASPT2//CASSCF level of theory by performing MEP computations. ISC regions were obtained only in the surroundings of the $(gs/\pi\pi^* L_a)_{CI}$, as in C. From the STC point, the MEP led to the equilibrium structure of the $^3(\pi\pi^* L_a)$ state, which can further decay by phosphorescence light emission or in a radiationless manner through an STC with the ground state [55].

On the basis of the PRPA and CASPT2//CASSCF computations [6, 28], the most efficient decay channel in G at low excitation energies correspond to a barrierless evolution along the bright $^1(\pi\pi^* L_a)$ state towards an out-of-plane methanamine CN-like crossing with the ground state (see Fig. 7), thus explaining the ultrafast radiationless decay measured in molecular beams [32]. The direct and barrierless profile of such a relaxation pathway might be related to the shortest lifetime measured at 148 fs [32] ($\tau_1$ in Fig. 7). Secondary reaction paths are also predicted, which involve the evolution from the lowest-lying $^1(n_o\pi^*)$ minimum. Two possible decays are determined: (1) after surmounting a very low energy barrier represented by a transition state $^1(n_o\pi^*)_{TS}$, the system can reach the $(gs/n_o\pi^*)_{CI}$, in which the C6N1 bond twists and the six-membered ring distorts placing the oxygen atom almost perpendicular to the ring; (2) via the corresponding CI, the molecule can switch to the $L_a$ PEH and once there to the accessible $(gs/\pi\pi^* L_a)_{CI}$. Such indirect pathways are responsible for retaining the excited-state population and are therefore expected to be responsible for longer lifetimes measured with time-resolved spectroscopy [32], as displayed in Fig. 7 ($\tau_2$). At higher UV irradiation energies the $^1(\pi\pi^* L_b)$ may contribute with other decay channels involving first a decay towards a minimum structure, $^1(\pi\pi^* L_b)_{min}$, and then a population transfer to the $^1(\pi\pi^* L_a)$ or $^1(n_o\pi^*)$ states, mediated by the corresponding CIs. The triplet population mechanism is predicted in regions close to the main MEP and at low energies, close to the singlet-singlet CI, which is a common feature to all NABs [55]. On the other hand,
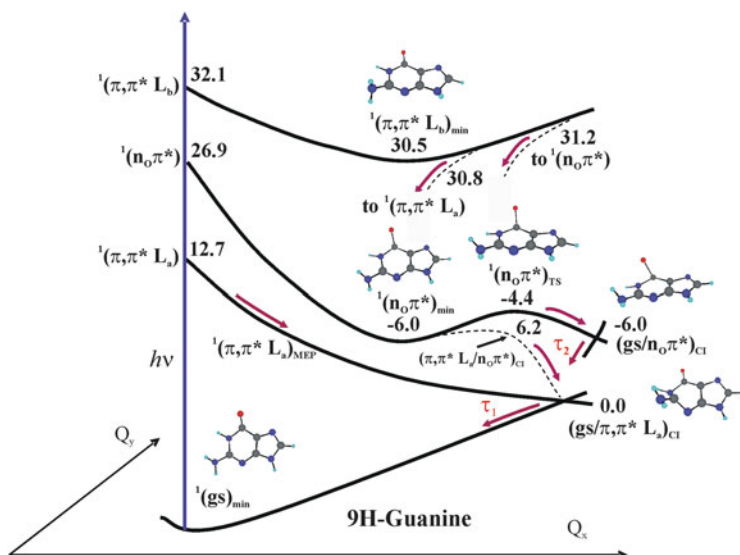
**Fig. 7** Scheme of the decay paths of G on the basis of CASPT2 results. Reused with permission from Serrano-Andrés et al. [28]. Copyright (2008) American Chemical Society

since G (and also C) have the low spectroscopic $^1(\pi\pi^*\ L_a)$ state below the $^1(n\pi^*)$ state, $n\pi^*$-mediated ISC mechanisms are not favorable, which is in contrast to the other NABs. These results explain the reported lower contribution of G and C to the phosphorescence of DNA [115–117].

# 5   Final Remarks and Future Perspective

In the present contribution we have reviewed the studies undergone in the last decade on the decay mechanisms of UV irradiated NABs. In particular, we have focused on the results obtained within the framework of a static description. The concepts and tools of modern theoretical photochemistry based on MEP computations and determination of the photochemically relevant CIs are extensively used. A large number of works have been carried out, reflecting the very rich and complex photochemistry of NABs. Figure 8 displays the results of the analysis of the literature, in which the prevalence of studies on pyrimidines is evident. Many photochemical channels have been drawn involving states of $\pi\pi^*$, $n_o\pi^*$, $n_o\pi^*$, and $\pi\sigma^*$ character and a large amount of two- and three-state CIs between them have been located. Among the different computational strategies employed, the most popular is the LIIC technique, which allows an inspection of the PEHs. Strategies such as constraint (or coordinate-driven) geometry optimizations have also been employed. In order to determine the most efficient decay mechanisms among all
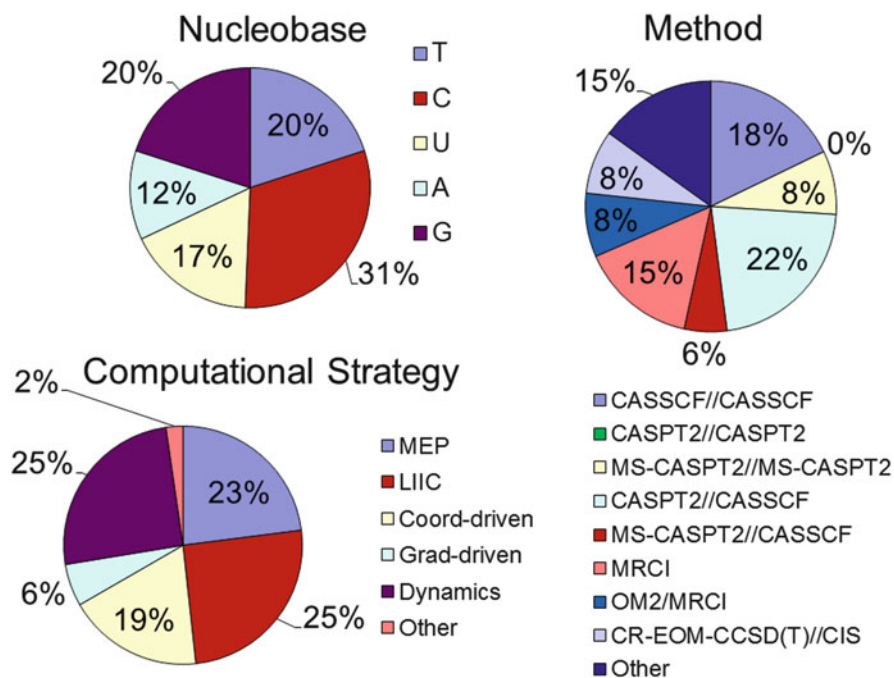
**Fig. 8** Statistical evaluation of published computational ab initio studies on the decay mechanisms of isolated nucleobases. Seventy five theoretical studies were considered in the analysis, in which only the main computational strategies and methods were taken into account

possible deactivation paths, we emphasize the importance of following a systematic approach in which, first, highly accurate multiconfigurational quantum chemical methods must be used together with theoretical strategies based on mapping the MEP for the efficient transit of the energy in the excited states toward accessible CIs, the so-called photochemical reaction path approach (PRPA), and, second, the stability of the conclusions derived from the results must be evaluated upon higher levels of theory. The findings obtained in such a manner determine the most probable decay mechanisms present in the UV irradiated NABs and at the same time build the basis for subsequent studies on the dynamics able to provide quantitative lifetimes and reaction rates. The CASPT2//CASSCF protocol and the CASSCF method are normally used in the static and dynamics studies, respectively. Regarding the former type of works, it is surprising that the MS-CASPT2//MS-CASPT2 approach has been preferred rather than the CASPT2//CASPT2 strategy, even when the MS-CASPT2 method can lead to unphysical results in the CI region.

On the basis of the PRPA results, a general picture has been drawn for the decay mechanism of the DNA and RNA bases. The photochemistry begins with the absorption of energy by the bright $^1(\pi\pi^*)$ state, computed vertically at energies in the range 4.41 (C)–5.35 (A) eV, in agreement with the gas-phase experimental data. In C and G, the electronic transition involves the lowest singlet excited state,

whereas the other NABs have close-lying or lower-lying $^1(n\pi^*)$ and $^1(\pi\pi^*\ L_b)$ excited states, whose direct absorption is expected to be relatively smaller. After photoexcitation, the most efficient evolution on the bright $^1(\pi\pi^*)$ state, as described by MEP computations, is essentially barrierless towards a CC ethene-like (U, T, C) or CN methanamine-like (A, G) crossing with the ground state, $(gs/\pi\pi^*)_{CI}$. Secondary paths have also been determined involving distinct decay channels: (1) population transfer along the MEP on the bright state to singlet $^1(n\pi^*)$ or triplet states, followed by further evolution until reaching a crossing with the ground state PEH, (2) direct absorption to the non-bright $^1(\pi\pi^*\ L_b)$ and $^1(n\pi^*)$ states and deactivation along these states, and (3) triplet population along the previous paths and decay on the triplet manifold. In addition other features of the low-lying states, such as $^1(\pi\pi^*)$ minima, have been determined, contributing to the indirect pathways. Those secondary pathways retain the population of the excited states to some extent due to non-efficient processes related to the presence of energy barriers or intersystem crossings.

The two types of decay mechanisms (main and secondary) determined within the PRPA might be related to the sub-picosecond and picosecond biexponential lifetime signals observed experimentally in the time-resolved spectroscopy. Nevertheless, other interpretations of the time-dependent aspects are possible based on the decay mechanisms provided by the PRPA. Hence, the twofold signal in adenine has been recently attributed only to the bright state. On the other hand, the most recent dynamical studies give rise to conclusions dramatically different from the scenario arising in the PRPA studies. In this respect, the development of more accurate strategies and the implementation of faster algorithms in the quantum-chemistry packages will hopefully help to rationalize these differences and provide an improved consensus for the photochemistry of NABs accomplished on theoretical grounds.

Experience in the theoretical studies of NABs photochemistry has shown that an accurate determination of the reaction paths of the low-lying states in NABs is a difficult task. This is especially true in pyrimidines, in which extended flat regions are typical and subtle changes in the computational approach may lead to different mechanisms, such as the presence of excited-state minima or barrierless profiles along the decay channels, which can induce different interpretations of the experimental data. In the present contribution we have illustrated these aspects in T, analyzing the effect of both the electron correlation, within the CASPT2//CASSCF approach, and the employed computational strategy to determine the decay paths. Inclusion of larger amounts of the electron correlation in the CASSCF reference function and the use of MEPs (vs geometry optimizations) lead to an accurate description of the decay of the bright state, supporting the ultrafast lifetimes observed experimentally. To evaluate further the convergence of the CASPT2//CASSCF results, additional studies must be focused on MEP computations at the CASPT2 level of theory, which has become possible only recently. Within the framework of the group *Quantum Chemistry of the Excited State of Valencia* (QCEXVAL), systematic research in this direction has begun, including calibration of further computational approaches within the CASPT2//CASSCF and CASPT2//CASPT2 protocols and additional technical aspects. The findings will be of great
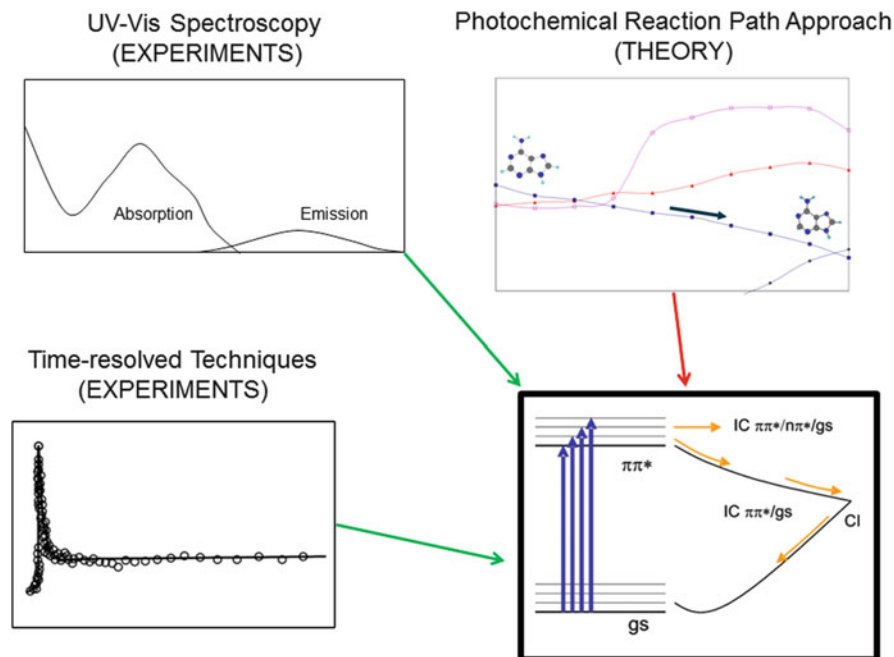
**Fig. 9** Comparative scheme of theoretical and experimental fingerprints of the decays of naturally occurring nucleobases

importance for studies on the dynamics of the systems in which an accurate characterization of the PEHs is essential to predict reliable time-dependent properties.

In perspective, the study of the photochemistry of the DNA/RNA constituents represents a beautiful example of a constructive interplay between experimental and theoretically oriented research. Figure 9 illustrates this fact by means of a comparative scheme of the photostable features determined in the computations and measured in the experiments on the photochemistry of NABs. Computed barrierless decay paths from the bright state connecting the initial FC region and the CI with the ground state can be directly related to the absence of emission or fluorescence quenching and very small (fs or ps) excited state lifetimes detected in the time-resolved experimental techniques. The UV-irradiated NABs funnel efficiently the excitation energy towards the ground state without retaining the excited state population for sufficient time to photoreact. The outlined fingerprints support the fact that internal conversion processes mediated by interstate crossings behave in the nucleobases as a self-protecting mechanism, preventing photochemical reactions induced by UV radiation.

# References

1. Olivucci M (2005) Computational photochemistry. Elsevier, Amsterdam
2. Fuß W, Lochbrunner S, Müller AM, Schikarski T, Schmid WE, Trushin SA (1998) Chem Phys 232:161. doi:10.1016/s0301-0104(98)00114-1
3. Robb MA, Garavelli M, Olivucci M, Bernardi F (2000) Rev Comput Chem 15:87. doi:10.1002/9780470125922.ch2
4. Olivucci M, Sinicropi A (2005) In: Olivucci M (ed) Theoretical and computational chemistry. Elsevier, Amsterdam, p 1
5. Garavelli M, Bernardi F, Cembran A (2005) In: Olivucci M (ed) Theoretical and computational chemistry. Elsevier, Amsterdam, p 191
6. Serrano-Andrés L, Merchán M (2009) J Photoch Photobio C-Photochem Rev 10:21. doi:10.1016/j.jphotochemrev.2008.12.001
7. Gonzalez C, Schlegel HB (1990) J Phys Chem 94:5523. doi:10.1021/j100377a021
8. Fukui K (1981) Acc Chem Res 14:363. doi:10.1021/ar00072a001
9. De Vico L, Olivucci M, Lindh R (2005) J Chem Theor Comput 1:1029. doi:10.1021/ct0500949
10. Anglada JM, Bofill JM (1997) J Comput Chem 18:992. doi:10.1002/(sici)1096-987x(199706)18:8<992::aid-jcc3>3.0.co;2-l
11. Müller K, Brown LD (1979) Theor Chim Acta 53:75. doi:10.1007/bf00547608
12. Truhlar DG, Steckler R, Gordon MS (1987) Chem Rev 87:217. doi:10.1021/cr00077a011
13. Serrano-Andrés L, Merchán M (2002) Encyclopedia of computational chemistry. Wiley, Chichester, p 1
14. Merchán M, Serrano-Andrés L (2005) In: Olivucci M (ed) Theoretical and computational chemistry. Elsevier, Amsterdam, p 35
15. Serrano-Andrés L, Merchán M (2005) J Mol Struc-Theochem 729:99. doi:10.1016/j.theochem.2005.03.020
16. Serrano-Andrés L, Serrano-Pérez JJ (2012) In: Leszczynski J (ed) Handbook of computational chemistry. Springer, The Netherlands, p 483
17. González L, Escudero D, Serrano-Andrés L (2012) Chemphyschem 13:28. doi:10.1002/cphc.201100200
18. Serrano-Andrés L, Roca-Sanjuán D, Olaso-González G (2010) Photochemistry. Roy Soc Chem 38:10
19. Domcke W, Yarkony D, Köppel H (2004) Conical intersections electronic structure, dynamics & spectroscopy. World Scientific. http://public.eblib.com/EBLPublic/PublicView.do?ptiID=238336
20. Klessinger M, Michl J (1995) Excited states and photochemistry of organic molecules. VCH, New York
21. Köppel H, Domcke W, Cederbaum LS (1984) Adv Chem Phys 57:59
22. Robb MA, Olivucci M, Bernardi F (1998) In: PvR S, Schreiner PR, Schaefer HF III, Jorgensen WL, Thiel W, Glen RC (eds) Encyclopedia of computational chemistry. Wiley, Chichester
23. Crespo-Hernández CE, Cohen B, Hare PM, Kohler B (2004) Chem Rev 104:1977. doi:10.1021/cr0206770
24. Friedberg EC, Walker GC, Siede W, Wood RD, Schultz RA, Ellenberger T (2006) DNA, repair and mutagenesis. ASM, Washington, DC
25. Serrano-Andrés L, Merchán M, Borin AC (2006) Proc Natl Acad Sci U S A 103:8691. doi:10.1073/pnas.0602991103
26. Merchán M, González-Luque R, Climent T, Serrano-Andrés L, Rodríguez E, Reguero M, Peláez D (2006) J Phys Chem B 110:26471. doi:10.1021/jp066874a
27. Serrano-Andrés L, Merchán M, Borin AC (2006) Chem-Eur J 12:6559. doi:10.1002/chem.200501515

28. Serrano-Andrés L, Merchán M, Borin AC (2008) J Am Chem Soc 130:2473. doi:10.1021/ja0744450
29. Middleton CT, de La Harpe K, Su C, Law YK, Crespo-Hernández CE, Kohler B (2009) Annu Rev Phys Chem 60:217. doi:10.1146/annurev.physchem.59.032607.093719
30. Kleinermanns K, Nachtigallová D, de Vries MS (2013) Int Rev Phys Chem 32:308. doi:10.1080/0144235x.2012.760884
31. Kang H, Lee KT, Jung B, Ko YJ, Kim SK (2002) J Am Chem Soc 124:12958. doi:10.1021/ja027627x
32. Canuel C, Mons M, Piuzzi F, Tardivel B, Dimicoli I, Elhanine M (2005) J Chem Phys 122:074316. doi:10.1063/1.1850469
33. Samoylova E, Lippert H, Ullrich S, Hertel IV, Radloff W, Schultz T (2005) J Am Chem Soc 127:1782. doi:10.1021/ja044369q
34. Kuimova MK, Dyer J, George MW, Grills DC, Kelly JM, Matousek P, Parker AW, Sun XZ, Towrie M, Whelan AM (2005) Chem Commun 1182. doi:10.1039/b414450c
35. Michl J (2005) In: Olivucci M (ed) Theoretical and computational chemistry. Elsevier, Amsterdam, p 9
36. Serrano-Andrés L, Merchán M, Lindh R (2005) J Chem Phys 122:104107. doi:10.1063/1.1866096
37. Klessinger M (1995) Angew Chem Int Edit 34:549. doi:10.1002/anie.199505491
38. Yarkony DR (2001) J Chem Phys 114:2601. doi:10.1063/1.1329644
39. Yarkony DR (1996) Rev Mod Phys 68:985. doi:10.1103/RevModPhys.68.985
40. Yarkony DR (2012) Chem Rev 112:481. doi:10.1021/cr2001299
41. Lischka H, Dallos M, Szalay PG, Yarkony DR, Shepard R (2004) J Chem Phys 120:7322. doi:10.1063/1.1668615
42. Koga N, Morokuma K (1985) Chem Phys Lett 119:371. doi:10.1016/0009-2614(85)80436-x
43. Farazdel A, Dupuis M (1991) J Comput Chem 12:276. doi:10.1002/jcc.540120219
44. Yarkony DR (1993) J Phys Chem 97:4407. doi:10.1021/j100119a026
45. Manaa MR, Yarkony DR (1993) J Chem Phys 99:5251. doi:10.1063/1.465993
46. Ragazos IN, Robb MA, Bernardi F, Olivucci M (1992) Chem Phys Lett 197:217. doi:10.1016/0009-2614(92)85758-3
47. Bearpark MJ, Robb MA, Schlegel HB (1994) Chem Phys Lett 223:269. doi:10.1016/0009-2614(94)00433-1
48. Frisch MJ, Trucks GW, Schlegel HB, Scuseria GE, Robb MA, Cheeseman JR, Scalmani G, Barone V, Mennucci B, Petersson GA, Nakatsuji H, Caricato M, Li X, Hratchian HP, Izmaylov AF, Bloino J, Zheng G, Sonnenberg JL, Hada M, Ehara M, Toyota K, Fukuda R, Hasegawa J, Ishida M, Nakajima T, Honda Y, Kitao O, Nakai H, Vreven T, Montgomery JA, Peralta JE, Ogliaro F, Bearpark M, Heyd JJ, Brothers E, Kudin KN, Staroverov VN, Kobayashi R, Normand J, Raghavachari K, Rendell A, Burant JC, Iyengar SS, Tomasi J, Cossi M, Rega N, Millam JM, Klene M, Knox JE, Cross JB, Bakken V, Adamo C, Jaramillo J, Gomperts R, Stratmann RE, Yazyev O, Austin AJ, Cammi R, Pomelli C, Ochterski JW, Martin RL, Morokuma K, Zakrzewski VG, Voth GA, Salvador P, Dannenberg JJ, Dapprich S, Daniels AD, Farkas Ő, Foresman JB, Ortiz JV, Cioslowski J, Fox DJ (2009) Gaussian 09, Revision D.01. Gaussian, Wallingford CT
49. Foresman JB, Aeleen F (1996) Exploring chemistry with electronic structure methods. Gaussian, Pittsburgh
50. Schlegel HB (1987) In: Lawley KP (ed) Ab initio methods in quantum chemistry II. Wiley, New York, p 249
51. Merchán M, Serrano-Andrés L, Robb MA, Blancafort L (2005) J Am Chem Soc 127:1820. doi:10.1021/ja044371h
52. Blancafort L, Cohen B, Hare PM, Kohler B, Robb MA (2005) J Phys Chem A 109:4431. doi:10.1021/jp045614v
53. Blancafort L (2006) J Am Chem Soc 128:210. doi:10.1021/ja054998f
54. Conti I, Garavelli M, Orlandi G (2009) J Am Chem Soc 131:16108. doi:10.1021/ja902311y

55. González-Luque R, Climent T, González-Ramírez I, Merchán M, Serrano-Andrés L (2010) J Chem Theor Comput 6:2103. doi:10.1021/ct100164m

56. Serrano-Pérez JJ, González-Luque R, Merchán M, Serrano-Andrés L (2007) J Phys Chem B 111:11880. doi:10.1021/jp0765446

57. Asturiol D, Lasorne B, Robb MA, Blancafort L (2009) J Phys Chem A 113:10211. doi:10.1021/jp905303g

58. Blancafort L, Robb MA (2004) J Phys Chem A 108:10609. doi:10.1021/jp046985b

59. Blancafort L (2007) Photochem Photobiol 83:603. doi:10.1562/2006-05-29-ra-903

60. Climent T, González-Luque R, Merchán M, Serrano-Andrés L (2007) Chem Phys Lett 441:327. doi:10.1016/j.cplett.2007.05.040

61. Nakayama A, Harabuchi Y, Yamazaki S, Taketsugu T (2013) Phys Chem Chem Phys 15 (29):12322–12339. doi:10.1039/C3CP51617B

62. Roca-Sanjuán D, Aquilante F, Lindh R (2012) WIREs Comput Mol Sci 2:585. doi:10.1002/wcms.97

63. Andersson K, Malmqvist PÅ, Roos BO, Sadlej AJ, Wolinski K (1990) J Phys Chem 94:5483. doi:10.1021/j100377a012

64. Andersson K, Malmqvist PÅ, Roos BO (1992) Adv Chem Phys 96:1218. doi:10.1063/1.462209

65. Roos BO, Andersson K, Fülscher MP, Malmqvist PÅ, Serrano-Andrés L, Pierloot K, Merchán M (1996) Adv Chem Phys 93:219. doi:10.1002/9780470141526.ch5

66. Finley J, Malmqvist PÅ, Roos BO, Serrano-Andrés L (1998) Chem Phys Lett 288:299. doi:10.1016/s0009-2614(98)00252-8

67. Buenker RJ, Sd P (1974) Theor Chim Acta 35:33. doi:10.1007/bf02394557

68. Marian CM, Gilka N (2008) J Chem Theor Comput 4:1501. doi:10.1021/ct8001738

69. Roos BO, Taylor PR, Siegbahn PEM (1980) Chem Phys 48:157. doi:10.1016/0301-0104(80)80045-0

70. Lawley KP (1987) Ab initio methods in quantum chemistry II. Wiley, New York

71. Andersson K, Barysz M, Bernhardsson A, Blomberg MRA, Carissan Y, Cooper DL, Cossi M, Fülscher MP, Gagliardi L, de Graaf C, Hess B, Hagberg G, Karlström G, Lindh R, Malmqvist PÅ, Nakajima T, Neogrády P, Olsen J, Raab J, Roos BO, Ryde U, Schimmelpfennig B, Schütz M, Seijo L, Serrano-Andrés L, Siegbahn PEM, Stålring J, Thorsteinsson T, Veryazov V, Widmark P-O (2006) Department of Theoretical Chemistry, Chemical Centre, University of Lund, Lund, Sweden

72. Aquilante F, De Vico L, Ferré N, Ghigo G, Malmqvist PÅ, Neogrády P, Pedersen TB, Pitoňák M, Reiher M, Roos BO, Serrano-Andrés L, Urban M, Veryazov V, Lindh R (2010) J Comput Chem 31:224. doi:10.1002/jcc.21318

73. Aquilante F, Pedersen TB, Veryazov V, Lindh R (2013) WIREs Comput Mol Sci 3:143. doi:10.1002/wcms.1117

74. Werner H-J, Knowles PJ, Knizia G, Manby FR, Schültz M, Celani P, Korona T, Lindh R, Mitrushenkov A, Rauhut G, Shamasundar KR, Adler TB, Amos RD, Bernhardsson A, Berning A, Cooper DL, Deegan MJO, Dobbyn AJ, Eckert F, Goll E, Hampel C, Hesselmann A, Hetzer G, Hrenar T, Jansen G, Höppl C, Liu Y, Lloyd AW, Mata RA, May AJ, McNicholas SJ, Meyer W, Mura ME, Nicklass A, O'Neill DP, Palmieri P, Peng D, Pflüger K, Pitzer R, Reiher M, Shiozaki T, Stoll H, Stone AJ, Tarroni R, Thorsteinsson T, Wang M (2012) MOLPRO, version 2012.1, a package of ab initio programs. Cardiff University, UK

75. Werner H-J, Knowles PJ, Knizia G, Manby FR, Schütz M (2012) WIREs Comput Mol Sci 2:242. doi:10.1002/wcms.82

76. Gozem S, Huntress M, Schapiro I, Lindh R, Granovsky AA, Angeli C, Olivucci M (2012) J Chem Theor Comput 8:4069. doi:10.1021/ct3003139

77. Ismail N, Blancafort L, Olivucci M, Kohler B, Robb MA (2002) J Am Chem Soc 124:6818. doi:10.1021/ja0258273

78. Merchán M, Serrano-Andrés L (2003) J Am Chem Soc 125:8108. doi:10.1021/ja0351600

79. Giussani A, Serrano-Andrés L, Merchán M, Roca-Sanjuán D, Garavelli M (2013) J Phys Chem B 117:1999. doi:10.1021/jp307200g
80. Serrano-Andrés L, Merchán M (2008) In: Shukla M, Leszczynski J (eds) Radiation induced molecular phenomena in nucleic acids. Springer, The Netherlands, p 435
81. Werner HJ, Knowles PJ, Knizia G, Manby FR, Schütz M (2012) WIREs Comput Mol Sci 2:242
82. Ghigo G, Roos BO, Malmqvist PÅ (2004) Chem Phys Lett 396:142. doi:10.1016/j.cplett.2004.08.032
83. Roca-Sanjuán D, Rubio M, Merchán M, Serrano-Andrés L (2006) J Chem Phys 125:084302
84. Rubio M, Roca-Sanjuán D, Merchán M, Serrano-Andrés L (2006) J Phys Chem B 110:10234
85. Rubio M, Roca-Sanjuán D, Serrano-Andrés L, Merchán M (2009) J Phys Chem B 113:2451
86. Roca-Sanjuán D, Olaso-González G, Rubio M, Coto PB, Merchán M, Ferré N, Ludwig V, Serrano-Andrés L (2009) Pure Appl Chem 81:743
87. Roca-Sanjuán D, Merchán M, Serrano-Andrés L, Rubio M (2008) J Chem Phys 129:095104
88. Crespo R, Merchán M, Michl J (2000) J Phys Chem A 104:8593
89. Rubio M, Serrano-Andrés L, Merchán M (2008) J Chem Phys 128:104305
90. Granovsky AA (2011) J Chem Phys 134:214113
91. Shiozaki T, Györffy W, Celani P, Werner H-J (2011) J Chem Phys 135:081106
92. Almlöf J, Taylor PR (1987) J Chem Phys 86:4070
93. Pierloot K, Dumez B, Widmark PO, Roos BO (1995) Theor Chim Acta 90:87. doi:10.1007/s002140050063
94. Widmark PO, Malmqvist PÅ, Roos BO (1990) Theor Chim Acta 77:291. doi:10.1007/bf01120130
95. Liu Y-J, Roca-Sanjuán D, Lindh R (2012) Photochemistry. Roy Soc Chem 40:42
96. Roos BO, Fülscher M, Malmqvist PÅ, Merchán M, Serrano-Andrés L (1995) In: Langhoff SR (ed) Quantum mechanical electronic structure calculations with chemical accuracy. Kluwer Academic Publishers, The Netherlands, p 357
97. Merchán M, Serrano-Andrés L, Fülscher M, Roos BO (1999) In: Hirao K (ed) Recent advances in multireference theory. World Scientific Publishing, Singapore, p 161
98. Serrano-Andrés L, Merchán M, Roca-Sanjuán D, Olaso-González G, Rubio M (2007) International conference on computational methods in science and engineering (AIP Conference Proceedings), vol 963. Corfu, GREECE, p 526
99. Shukla MK, Leszczynski J (2004) J Comput Chem 25:768. doi:10.1002/jcc.20007
100. Fleig T, Knecht S, Hättig C (2007) J Phys Chem A 111:5482
101. Szalay PG, Watson T, Perera A, Lotrich VF, Bartlett RJ (2012) J Phys Chem A 116:6702. doi:10.1021/jp300977a
102. Silva-Junior MR, Schreiber M, Sauer SPA, Thiel W (2008) J Chem Phys 129:104103. doi:10.1063/1.2973541
103. Lorentzon J, Fülscher MP, Roos BO (1995) J Am Chem Soc 117:9265
104. Schreiber M, Silva MR, Sauer SPA, Thiel W (2008) J Chem Phys 128:134110. doi:10.1063/1.2889385
105. Perun S, Sobolewski AL, Domcke W (2006) J Phys Chem A 110:13238. doi:10.1021/jp0633897
106. Hudock HR, Levine BG, Thompson AL, Satzger H, Townsend D, Gador N, Ullrich S, Stolow A, Martínez TJ (2007) J Phys Chem A 111:8500
107. Yamazaki S, Taketsugu T (2012) J Phys Chem A 116:491. doi:10.1021/jp206546g
108. Zechmann G, Barbatti M (2008) J Phys Chem A 112:8273. doi:10.1021/jp804309x
109. González L, González-Vázquez J, Samoylova E, Schultz T (2008) 5th international conference on radiation damage in biomolecular systems, vol 1080. Debrecen, Hungary, p 169
110. Lan Z, Fabiano E, Thiel W (2009) J Phys Chem B 113:3548. doi:10.1021/jp809085h
111. Etinski M, Fleig T, Marian CA (2009) J Phys Chem A 113:11809. doi:10.1021/jp902944a
112. Szymczak JJ, Barbatti M, Hoo JTS, Adkins JA, Windus TL, Nachtigallová D, Lischka H (2009) J Phys Chem A 113:12686

113. Ullrich S, Schultz T, Zgierski MZ, Stolow A (2004) Phys Chem Chem Phys 6:2796. doi:10.1039/b316324e
114. Asturiol D, Lasorne B, Worth GA, Robb MA, Blancafort L (2010) Phys Chem Chem Phys 12:4949. doi:10.1039/c001556c
115. Imakubo K (1968) J Physical Soc Japan 24:143. doi:10.1143/jpsj.24.143
116. Szerenyi P, Dearman HH (1972) Chem Phys Lett 15:81. doi:10.1016/0009-2614(72)87021-0
117. Arce R, Rodríguez G (1986) J Photochem 33:89
118. Barbatti M, Aquino AJA, Szymczak JJ, Nachtigallová D, Hobza P, Lischka H (2010) Proc Natl Acad Sci U S A 107:21453
119. Nachtigallová D, Aquino AJA, Szymczak JJ, Barbatti M, Hobza P, Lischka H (2011) J Phys Chem A 115:5247
120. Tomić K, Tatchen J, Marian CM (2005) J Phys Chem A 109:8410
121. Sobolewski AL, Domcke W (2004) Phys Chem Chem Phys 6:2763. doi:10.1039/b314419d
122. Zgierski MZ, Patchkovskii S, Lim EC (2005) J Chem Phys 123:081101
123. Zgierski MZ, Patchkovskii S, Fujiwara T, Lim EC (2005) J Phys Chem A 109:9384. doi:10.1021/jp054158n
124. Zgierski MZ, Fujiwara T, Lim EC (2008) Chem Phys Lett 463:289. doi:10.1016/j.cplett.2008.06.024
125. Kistler KA, Matsika S (2007) J Phys Chem A 111:2650. doi:10.1021/jp0663661
126. Kotur M, Weinacht TC, Zhou C, Kistler KA, Matsika S (2011) J Chem Phys 134:184309
127. Kistler KA, Matsika S (2008) J Chem Phys 128:215102
128. Hudock HR, Martínez TJ (2008) Chemphyschem 9:2486. doi:10.1002/cphc.200800649
129. González-Vázquez J, González L (2010) Chemphyschem 11:3617
130. Barbatti M, Aquino AJA, Szymczak JJ, Nachtigallová D, Lischka H (2011) Phys Chem Chem Phys 13:6145
131. Richter M, Marquetand P, González-Vázquez J, Solá I, González L (2012) J Phys Chem Lett 3:3090
132. Lobsiger S, Trachsel MA, Frey H-M, Leutwyler S (2013) J Phys Chem B 117:6106. doi:10.1021/jp401881b
133. Matsika S (2004) J Phys Chem A 108:7584. doi:10.1021/jp048284n
134. Matsika S (2005) J Phys Chem A 109:7538. doi:10.1021/jp0513622
135. Mercier Y, Santoro F, Reguero M, Improta R (2008) J Phys Chem B 112:10769. doi:10.1021/jp804785p
136. Delchev VB, Sobolewski AL, Domcke W (2010) Phys Chem Chem Phys 12:5007. doi:10.1039/b922505f
137. Gustavsson T, Bányász A, Lazzarotto E, Markovitsi D, Scalmani G, Frisch MJ, Barone V, Improta R (2006) J Am Chem Soc 128:607
138. Gustavsson T, Sarkar N, Lazzarotto E, Markovitsi D, Improta R (2006) Chem Phys Lett 429:551. doi:10.1016/j.cplett.2006.08.058
139. Broo A (1998) J Phys Chem A 102:526. doi:10.1021/jp9713625
140. Mennucci B, Toniolo A, Tomasi J (2001) J Phys Chem A 105:4749. doi:10.1021/jp0045843
141. Perun S, Sobolewski AL, Domcke W (2005) J Am Chem Soc 127:6257. doi:10.1021/ja044321c
142. Chen H, Li SH (2005) J Phys Chem A 109:8443. doi:10.1021/jp0537207
143. Marian CM (2005) J Chem Phys 122:104314
144. Nielsen SB, Sølling TI (2005) Chemphyschem 6:1276. doi:10.1002/cphc.200400644
145. Sobolewski AL, Domcke W (2002) Eur Phys J D 20:369. doi:10.1140/epjd/e2002-00164-5
146. Perun S, Sobolewski AL, Domcke W (2005) Chem Phys 313:107. doi:10.1016/j.chemphys.2005.01.005
147. Ullrich S, Schultz T, Zgierski MZ, Stolow A (2004) J Am Chem Soc 126:2262. doi:10.1021/ja030532q
148. Holmén A, Nordén B, Albinsson B (1997) J Am Chem Soc 119:3114

149. Santhosh C, Mishra PC (1991) Spectrochim Acta A 47:1685. doi:10.1016/0584-8539(91)80006-5
150. Zgierski MZ, Patchkovskii S, Lim EC (2007) Can J Chem 85:124. doi:10.1139/v07-006
151. Fabiano E, Thiel W (2008) J Phys Chem A 112:6859. doi:10.1021/jp8033402
152. Satzger H, Townsend D, Zgierski MZ, Patchkovskii S, Ullrich S, Stolow A (2006) Proc Natl Acad Sci U S A 103:10196. doi:10.1073/pnas.0602663103
153. Satzger H, Townsend D, Stolow A (2006) Chem Phys Lett 430:144. doi:10.1016/j.cplett.2006.08.122
154. Barbatti M, Lan ZG, Crespo-Otero R, Szymczak JJ, Lischka H, Thiel W (2012) J Chem Phys 137:22A503. doi:10.1063/1.4731649
155. Mitrić R, Werner U, Wohlgemuth M, Seifert G, Bonačić-Koutecký V (2009) J Phys Chem A 113:12700
156. Alexandrova AN, Tully JC, Granucci G (2010) J Phys Chem B 114:12116. doi:10.1021/jp103322c
157. Lei Y, Yuan S, Dou Y, Wang Y, Wen Z (2008) J Phys Chem A 112:8497. doi:10.1021/jp802483b
158. Chen H, Li SH (2006) J Chem Phys 124:154315
159. Marian CM (2007) J Phys Chem A 111:1545. doi:10.1021/jp068620v
160. Zgierski MZ, Patchkovskii S, Fujiwara T, Lim EC (2007) Chem Phys Lett 440:145. doi:10.1016/j.cplett.2007.04.017
161. Yamazaki S, Domcke W, Sobolewski AL (2008) J Phys Chem A 112:11965. doi:10.1021/jp806622m
162. Lan ZG, Fabiano E, Thiel W (2009) Chemphyschem 10:1225. doi:10.1002/cphc.200900030
163. Barbatti M, Szymczak JJ, Aquino AJA, Nachtigallová D, Lischka H (2011) J Chem Phys 134:014304

# Excitation of Nucleobases from a Computational Perspective II: Dynamics

**Sebastian Mai, Martin Richter, Philipp Marquetand, and Leticia González**

**Abstract** This chapter is devoted to unravel the relaxation processes taking place after photoexcitation of isolated DNA/RNA nucleobases in gas phase from a time-dependent perspective. To this aim, several methods are at hand, ranging from full quantum dynamics to various flavours of semiclassical or ab initio molecular dynamics, each with its advantages and its limitations. As this contribution shows, the most common approach employed up to date to learn about the deactivation of nucleobases in gas phase is a combination of the Tully surface hopping algorithm with on-the-fly CASSCF calculations. Different dynamics methods or, even more dramatically, different electronic structure methods can provide different dynamics. A comprehensive review of the different mechanisms suggested for each nucleobase is provided and compared to available experimental time scales. The results are discussed in a general context involving the effects of the different applied electronic structure and dynamics methods. Mechanistic similarities and differences between the two groups of nucleobases – the purine derivatives (adenine and guanine) and the pyrimidine derivatives (thymine, uracil, and cytosine) – are elucidated. Finally, a perspective on the future of dynamics simulations in the context of nucleobase relaxation is given.

**Keywords** DNA photochemistry · Ultrafast radiationless decay · Non-adiabatic dynamics · Excited-state lifetimes · Conical Intersections

S. Mai, M. Richter, P. Marquetand, and L. González (✉)
Institute of Theoretical Chemistry, University of Vienna, Währinger Str. 17, 1090 Vienna, Austria
e-mail: leticia.gonzalez@univie.ac.at

## Contents

## Abbreviations

| | |
|---|---|
| A | Adenine |
| AIMD | Ab initio molecular dynamics |
| AIMS | Ab initio multiple spawning |
| AM1 | (Semi-empirical) Austin model 1 |
| C | Cytosine |
| CASPT2 | Complete active space second-order perturbation theory |
| CASSCF | Complete active space self-consistent field |
| CI | Configuration interaction |
| CoIn | Conical intersection |
| CPMD | Car–Parrinello molecular dynamics |
| cs | Closed shell |
| DFT | Density functional theory |
| DFTB | Density functional-based tight binding |
| DNA | Deoxyribonucleic acid |
| DOF | Degree of freedom |
| FC | Franck–Condon |
| FMS | Full multiple spawning |
| G | Guanine |
| GS | Ground state |
| IC | Internal conversion |

| | |
|---|---|
| ISC | Intersystem crossing |
| MCH | Molecular Coulomb Hamiltonian |
| MCTDH | Multi-configurational time-dependent Hartree |
| MD | Molecular dynamics |
| MRCI | Multi-reference configuration interaction |
| MRCIS | Multi-reference configuration interaction with single excitations |
| NAC | Non-adiabatic coupling |
| OM2 | (Semi-empirical) Orthogonalization model 2 |
| PEH | Potential energy hypersurface |
| PM3 | (Semi-empirical) Parametrized model 3 |
| QD | Quantum dynamics |
| RNA | Ribonucleic acid |
| ROKS | Restricted open-shell Kohn–Sham |
| SHARC | Surface hopping including arbitrary couplings |
| SOC | Spin-orbit coupling |
| T | Thymine |
| TD-DFT | Time-dependent density functional theory |
| TD-DFTB | Time-dependent density functional-based tight binding |
| TDSE | Time-dependent Schrödinger equation |
| TRPES | Time-resolved photo-electron spectroscopy |
| TSH | Tully's surface hopping |
| TSH-CP | Tully's surface hopping coupled to Car–Parrinello dynamics |
| U | Uracil |
| UV | Ultraviolet |

# 1 Introduction

A wealth of reactions can occur after a molecule is excited by electromagnetic radiation. Especially important for all life on Earth is the interaction of nucleic acids with ultraviolet (UV) light. The reason is because the genetic information, which deoxyribonucleic acid (DNA) or ribonucleic acid (RNA) carry, can be damaged by photoreactions [1–6] leading, e.g., to skin cancer, which is the most frequent type of cancer [7]. DNA/RNA and in particular DNA/RNA nucleobases are photostable, meaning that they have mechanisms to return to the electronic ground state soon after light irradiation, thus avoiding detrimental excited-state reactions.

The question of how photostability is achieved on an atomistic level has motivated a large number of theoretical and experimental studies. On the microscopic scale, reactions are rearrangements of electrons and nuclei in time. Hence, the natural picture for an investigation of these processes is an approach where the instantaneous dynamics of the particles is described. This ansatz can be pursued computationally and constitutes the field of dynamics simulations [8–13]. Here, a detailed picture of the mechanisms underlying a photophysical and photochemical processes is obtained in an intuitive fashion. Important pathways along essential points of the reaction, like minima, transition states, or surface crossings, are

**Fig. 1** The chemical
structures and atom indices
of the five canonical
nucleobases of DNA/RNA.
In the *top row* the purine
bases are given, in the
*bottom row* the pyrimidine
bases



Adenine                    Guanine

Cytosine          Thymine          Uracil
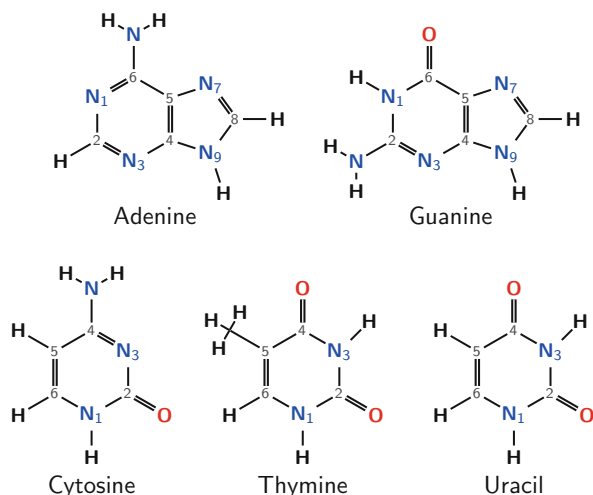
naturally identified. Of course, such reaction points can also be obtained with static quantum mechanical calculations, as illustrated in [118], and possible reaction routes can be suggested. Dynamics simulations, however, give an unequivocal answer regarding the regions which are de facto visited by the molecule after it gets electronically excited. Moreover, dynamics calculations naturally provide time scales and quantum yields that can be compared with time-resolved spectroscopic experiments.

The present chapter deals with dynamical simulations of isolated nucleobases electronically excited by UV light. Within the nucleic acids, the most important chromophores, i.e., the moieties which absorb the light, are the nucleobases adenine (A), guanine (G), cytosine (C), thymine (T), or uracil (U), which pairwise constitute the bridges of the well-known double helix structure [14]. They can be grouped into the purine bases (A and G) and the pyrimidine bases (C, T, and U). Their structures are given in Fig. 1. The study of the isolated nucleobases in the gas phase is only a small piece of a much larger field, but it can provide a unique insight into the behavior of matter and also leads to a general understanding of the relationship between structure and the fate of excited states.

In order to carry out dynamical simulations, the appropriate equations of motion have to be identified and then solved by suitable numerical tools. Therefore, this chapter starts with a short overview of the methods that can be employed to this end. A number of issues should be kept in mind when trying to connect the results from dynamical simulations and the available time-resolved experiments; these are discussed in Sect. 3. Afterwards, we review the different dynamical studies available on the isolated nucleobases (A, G, C, T, and finally U), each time starting with a short summary of the experimentally obtained relaxation lifetimes and followed by the different mechanisms that have been suggested to explain these lifetimes. In the conclusions, general trends for purine and pyrimidine bases are compared and the advances in this field are put into perspective.

## 2 Computational Approaches for Nuclear Dynamics

As pointed out above, understanding the photophysics of DNA nucleobases is not complete without a description of the dynamical processes triggered by UV excitation. In the following section we review the most popular computational approaches to describe chemical dynamics. The list of methods is not complete; rather, the focus is put on those methods which have been employed to calculate time-resolved properties in DNA nucleobases. It is nevertheless not the intention of this section to give a full description of the chosen methods, but only to provide a brief insight into their fundamentals in order to put the available simulations in context.

The study of chemical dynamics is the description of nuclear motion. Therefore, this section starts with the fundamental time-dependent Schrödinger equation and the Born–Oppenheimer approximation. Afterwards, the most accurate method to describe dynamics, i.e., the fully quantum-mechanical approach of wavepacket quantum dynamics (QD) is explained, followed by the multi-configurational time-dependent Hartree (MCTDH) method. Then we will motivate the use of a classical approximation to the nuclear motion, and from there add methodological features which improve the description of excited-state dynamics in full dimensionality. We will discuss the conceptually simple approach of mean-field (MF) dynamics, the widely employed trajectory surface hopping (TSH) scheme, and finally the full multiple spawning (FMS) approach.

### 2.1 The Schrödinger Equation and the Born–Oppenheimer Approximation

The time-dependent Schrödinger equation (TDSE) provides the exact quantum-mechanical and non-relativistic time evolution of a molecule. It reads as

$$\widehat{\mathcal{H}}|\Psi^{\text{tot}}\rangle = i\hbar \frac{\partial}{\partial t}|\Psi^{\text{tot}}\rangle. \tag{1}$$

Here, $|\Psi^{\text{tot}}\rangle$ is the total wavefunction and $\widehat{\mathcal{H}}$ is the total Hamiltonian, which contains the kinetic energy of all nuclei and electrons as well as the potential energy arising from the interactions of these particles:

$$\widehat{\mathcal{H}} = \widehat{\mathcal{T}}^{\text{nuc}} + \widehat{\mathcal{T}}^{\text{el}} + \widehat{\mathcal{V}}^{\text{nuc,nuc}} + \widehat{\mathcal{V}}^{\text{nuc,el}} + \widehat{\mathcal{V}}^{\text{el,el}}. \tag{2}$$

Since the motion of the particles is correlated by their mutual interactions, the Schrödinger equation can only be solved exactly for two-particle molecules (i.e., the hydrogen atom). Thus, several approximations are required to describe larger systems, such as molecules. The most important approximation is probably

the Born–Oppenheimer approximation, which allows one to separate the nuclear from the electronic motion.

The electronic wavefunction can be obtained by solving the time-independent electronic Schrödinger equation

$$\widehat{\mathcal{H}}^{\text{el}}\big|\Psi^{\text{el}}\big\rangle = E^{\text{el}}\big|\Psi^{\text{el}}\big\rangle, \tag{3}$$

where an electronic Hamiltonian – the so-called clamped-nuclei Hamiltonian – is given by

$$\widehat{\mathcal{H}}^{\text{el}} = \widehat{\mathcal{T}}^{\text{el}} + \widehat{\mathcal{V}}^{\text{nuc,nuc}} + \widehat{\mathcal{V}}^{\text{nuc,el}} + \widehat{\mathcal{V}}^{\text{el,el}}. \tag{4}$$

Solving (3) is the realm of quantum chemistry and a number of powerful electronic structure methods are available in different quantum chemistry codes. For the description of electronic excited states of nucleobases and related properties, the most popular methods have been described in [118]. In any case, the approximate solutions of the electronic Schrödinger equation deliver electronic wavefunctions and electronic energies which depend parametrically on the nuclear coordinates $\mathbf{R}$. The functions $E^{\text{el}}(\mathbf{R})$ are known as potential energy hypersurfaces (PEH).

Within the Born–Oppenheimer approximation the total wavefunction can be written as

$$\big|\Psi^{\text{tot}}\big\rangle = \sum_{\alpha} \big|\Psi^{\text{el}}_{\alpha}\big\rangle\big|\Psi^{\text{nuc}}_{\alpha}\big\rangle. \tag{5}$$

By inserting (5) and $\widehat{\mathcal{H}} = \widehat{\mathcal{T}}^{\text{nuc}} + \widehat{\mathcal{H}}^{\text{el}}$ in the TDSE (1), projecting on $\big\langle\Psi^{\text{el}}_{\beta}\big|$ and using (3) [15], the nuclear Schrödinger equation becomes

$$\left[\widehat{\mathcal{T}}^{\text{nuc}} + E^{\text{el}}_{\beta}\right]\big|\Psi^{\text{nuc}}_{\beta}\big\rangle + \sum_{\alpha} \widehat{\mathcal{T}}^{\text{NAC}}_{\beta\alpha}\big|\Psi^{\text{nuc}}_{\alpha}\big\rangle = \mathrm{i}\frac{\partial}{\partial t}\big|\Psi^{\text{nuc}}_{\beta}\big\rangle. \tag{6}$$

According to this equation, the nuclei move in the potentials $E^{\text{el}}(\mathbf{R})$ which are determined by the electronic motion in the field of the nuclei. The non-adiabatic coupling (NAC) operator

$$\widehat{\mathcal{T}}^{\text{NAC}}_{\beta\alpha} = \sum_{a} \frac{\hbar^2}{m_a}\left[\big\langle\Psi^{\text{el}}_{\beta}\big|\nabla^2_a\big|\Psi^{\text{el}}_{\alpha}\big\rangle - \big\langle\Psi^{\text{el}}_{\beta}\big|\nabla_a\big|\Psi^{\text{el}}_{\alpha}\big\rangle\nabla_a\right], \tag{7}$$

arising from the action of $\widehat{\mathcal{T}}^{\text{nuc}}$ on the electronic wavefunctions, describes the coupling between the electronic states in situations where the electronic wavefunction cannot adapt fast enough to the nuclear motion. Within the Born–Oppenheimer approximation, these couplings are completely neglected and the

nuclei move according to (6) in the potential corresponding to a single electronic state. This approximation is valid in many situations, especially if only the electronic ground state is involved, for example in thermal reactions. In photochemistry and photophysics, chemical reactions involve several electronic states and nuclear dynamics proceed on several PEHs which usually present crossings, where the Born–Oppenheimer approximation breaks down. In these cases, the couplings described in (7) can no longer be neglected.

## 2.2 Quantum Dynamics

The most accurate description of nuclear dynamics can be achieved by solving (6) numerically. This is known as wavepacket dynamics or full quantum dynamics, here abbreviated as QD.

In order to solve (6), the wavefunction $|\Psi^{\mathrm{nuc}}\rangle$ is linearly expanded in terms of time-independent basis functions $|\phi_\mu\rangle$ (usually in a grid, but not necessarily). In one dimension, this expansion reads

$$\left|\Psi^{\mathrm{nuc}}(t)\right\rangle = \sum_{\mu}^{N^{\mathrm{BF}}} c_\mu(t)\left|\phi_\mu\right\rangle, \tag{8}$$

with $N^{\mathrm{BF}}$ the number of basis functions. In several dimensions, the analogue expression is

$$\left|\psi^{\mathrm{nuc}}\left(R_1,\ldots,R_f,t\right)\right\rangle = \sum_{\mu_1}^{N_1^{\mathrm{BF}}}\cdots\sum_{\mu_f}^{N_f^{\mathrm{BF}}} c_{\mu_1\ldots\mu_f}(t)\prod_{\kappa=1}^{f}\left|\phi_{\mu_\kappa}^{(\kappa)}(R_\kappa)\right\rangle. \tag{9}$$

Here, $f$ is the number of degrees of freedom (DOF), $c_{\mu_1\ldots\mu_f}$ are the wavefunction expansion coefficients, and $|\phi_{\mu_\kappa}^{(\kappa)}(R_\kappa)\rangle$ are the time-independent basis functions for degree of freedom $\kappa$. By plugging this wavefunction into (6), the equations of motion for the coefficients are obtained and these equations can be solved numerically with standard matrix algebra computations. By solving the TDSE including the couplings described in (7), a rigorous description of photochemical processes can be carried out. QD simulations based on accurate PEHs provide the best description of a dynamical process and can deliver excellent accuracy. However, QD can only be afforded for small systems, since the calculation of the PEHs suffers from a very unfavorable exponential scaling with the number of DOF. Nowadays, QD simulations are able to treat at most six DOF with state-of-the-art techniques, which restricts these calculations to at most four-atomic molecules. For larger systems, such as DNA nucleobases, only simulations in reduced dimensionality would be feasible. Then the problem of choosing the appropriate DOF is

not trivial. Particularly, for DNA nucleobases – where a large number of degrees of freedom are involved along the many deactivation pathways (see [118]) – it is very challenging to choose a small subset of reaction coordinates which describe all deactivation pathways reasonably well. This problem motivates the use of more approximate approaches, as those presented below.

## 2.3  Multi-Configurational Time-Dependent Hartree

The multi-configurational time-dependent Hartree (MCTDH) method [16] is an approximation to full QD simulations that allows one to extend considerably the applicability of QD to systems with more than four atoms. MCTDH is still based on the exact nuclear Schrödinger equation, but approximations are introduced in the definition of the wavefunction. The general wavefunction is here given by

$$\left| \Psi^{\mathrm{nuc}}\left(R_1, \ldots, R_f, t\right) \right\rangle = \sum_{\mu_1}^{n_1^{\mathrm{BF}}} \cdots \sum_{\mu_f}^{n_f^{\mathrm{BF}}} c_{\mu_1 \ldots \mu_f}(t) \prod_{\kappa=1}^{f} \left| \phi_{\mu_\kappa}^{(\kappa)}(R_\kappa, t) \right\rangle. \tag{10}$$

The main difference to (9) is the time-dependence of the basis functions. Hence, the equations of motion in MCTDH have to be solved not only for the wavefunction coefficients $c_{\mu_1 \ldots \mu_f}(t)$, but also for the basis functions $|\phi_{\mu_\kappa}^{(\kappa)}(R_\kappa, t)\rangle$. This means, however, that the basis set expansion can be kept much smaller than in full QD calculations ($n_i^{\mathrm{BF}} \ll N_i^{\mathrm{BF}}$), since in MCTDH the basis functions can adapt during the dynamics. In some cases [16], only a handful of basis functions are necessary to obtain qualitatively correct results. Obviously, by increasing the number of basis functions, MCTDH approaches the accuracy of full QD calculations; however, in this limit MCTDH becomes as expensive as full QD.

The formal scaling of MCTDH remains exponential with respect to the number of DOF. However, through its definition of the basis functions, the method can be applied to systems involving between 20 and 50 DOF; see, e.g., [16]. Furthermore, related techniques such as Gaussian-based MCTDH [17], Multilayer MCTDH [18] and variational Multi-Configurational Gaussians (vMCG) [19] are very promising to treat much larger systems quantum-mechanically, exemplified by the simulation of the anthracene cation with 66 DOF [20].

## 2.4  Molecular Dynamics

While the above methods fully preserve the quantum-mechanical nature of the nuclear dynamics – describing all the quantum effects like interference, coherence, and tunneling – they suffer from an unfavorable scaling with system size, i.e., the number

of DOF. An alternative strategy to describing dynamics is to impose the classical approximation for the motion of the nuclei. Instead of being described by wavepackets moving according to the nuclear Schrödinger equation (6), the nuclei are treated as classical, point-like particles, which follow Newton's equation of motion

$$m_a\ddot{\mathbf{R}}_a = -\nabla_a E_\alpha^{\text{el}}. \tag{11}$$

The force acting on the nuclei is the gradient of the PEH of a single electronic state $\alpha$, in the frame of the Born–Oppenheimer approximation. Such a calculation is usually known as a molecular dynamics (MD) simulation. In the case where the energies $E_\alpha^{\text{el}}$ and driving forces $-\nabla_a E_\alpha^{\text{el}}$ are calculated by means of quantum-chemical electronic structure methods, the simulations are often called ab initio MD (AIMD) or semi-classical MD (since the electrons are described quantum-mechanically and the nuclei classically).

The *global* computation of the potential function $E_\alpha^{\text{el}}$ (prior to the dynamics simulation) still scales exponentially with the number of DOF. Thus, MD simulations are usually performed with "on-the-fly" calculations of the potential energy and nuclear forces at each time step of the simulation. In this way the simulation cost does not explicitly depend on the number of DOF anymore and thus there is no need to restrict the calculation to a certain subset of reaction coordinates.

## 2.5   Ehrenfest Dynamics

Without any further extension, semi-classical MD cannot describe excited-state dynamics because the classical nuclei are tied to one single Born–Oppenheimer PEH at all times. In photophysics and photochemistry, several electronic states are close in energy and interact via the NACs given in (7) during internal conversion (IC) close to conical intersections (CoIn), or during intersystem crossing (ISC) via spin-orbit coupling (SOC). At these interstate crossing points on the PEHs, population can be transferred from one state to the other, which is obviously not possible within MD simulations as explained above.

The Ehrenfest dynamics method, also called mean-field (MF) dynamics, is an extension of classical MD calculations which includes excited-state PEHs. Here, the electronic wavefunction is a linear combination of several electronic states:

$$\left|\Psi^{\text{el}}\right\rangle = \sum_\alpha c_\alpha |\Psi_\alpha\rangle. \tag{12}$$

The wavefunction coefficients are propagated along the trajectory according to the energies and the NACs of the electronic states. The potential energy for the MD simulation is substituted with the energy expectation value of the electronic wavefunction:

$$E^{\text{eff}} = \langle \Psi^{\text{el}} | \widehat{\mathcal{H}}^{\text{el}} | \Psi^{\text{el}} \rangle = \sum_\alpha |c_\alpha|^2 E_\alpha^{\text{el}}. \tag{13}$$

Thus, the nuclei are moving on an effective potential, which is the average of all adiabatic states of the same multiplicity, weighted by their state population, giving the method the name mean-field dynamics.

The mean-field approach suffers from the problem where the trajectory may follow a nonphysical mixed state after passing a non-adiabatic coupling region. A physically correct description would describe a splitting of the population into different reaction channels.

## 2.6   Trajectory Surface Hopping

As mentioned above, the main problem of the Ehrenfest dynamics is that it cannot describe a wavepacket splitting onto several PEHs. In order to get rid of this shortcoming, the trajectory surface hopping (TSH) scheme [21] was devised. Here, the mean-field trajectory is replaced by an ensemble of many trajectories, each following the classical equations of motion. Non-adiabatic effects are described by allowing the trajectories to switch stochastically between the PEHs, based on the strength of the NACs. Using a sufficiently large ensemble of trajectories, the splitting of a wavepacket due to non-adiabatic interactions can be approximated.

Similarly to (12), in the TSH approach the electronic wavefunction is expanded in the basis of the electronic states. The absolute square of the complex coefficients $|c_\alpha|^2$ can be interpreted as the probability of finding the trajectory in state $\alpha$. Thus, from the coefficients, one can derive an expression for the instantaneous probability $P_{\beta\rightarrow}$ of leaving the currently occupied classical state $\beta$. According to Tully's fewest switches criterion [22], this probability is given by

$$P_{\beta\rightarrow} = -\frac{2\Delta t}{|c_\beta|^2} \Re \left( c_\beta^* \frac{\partial}{\partial t} c_\beta \right). \tag{14}$$

The fewest switches criterion states that the surface hopping probabilities should minimize the number of hops while maintaining consistency between the population $|c_\alpha|^2$ and the fraction of trajectories assigned to the state $\alpha$.

The time-derivatives of the coefficients in (14) are directly obtained from the equation of motion of the coefficients

$$\frac{\partial}{\partial t} c_\beta = -\sum_\alpha \left[ \frac{i}{\hbar} H_{\beta\alpha} + \mathbf{v} \cdot T_{\beta\alpha}^{(1)} \right] c_\alpha, \tag{15}$$

where $\mathbf{v}$ is the nuclear velocity vector and where

$$\mathbf{v} \cdot T_{\beta\alpha}^{(1)} = \left\langle \psi_\beta \left| \frac{\partial}{\partial t} \right| \psi_\alpha \right\rangle. \tag{16}$$

The quantities $H_{\beta\alpha}$ and $T_{\beta\alpha}^{(1)}$ are calculated on-the-fly along with the gradient of the populated state. Equation (15) can be integrated by standard Runge–Kutta methods or unitary propagator methods, using small time steps $\Delta t$. Finally, by inserting (15) into (14), the probability $P_{\beta\rightarrow}$ can be written as a sum of $P_{\beta\rightarrow\alpha}$, the probability of switching from state $\beta$ to state $\alpha$.

Besides Tully's fewest switches criterion, there exist additional approaches to calculate the TSH probabilities, like coherent switching with decay of mixing [23] or fewest switches with time-uncertainty [24]; combination of Car–Parrinello molecular dynamics (CPMD) with TSH (TSH-CP) [25] and of TSH with mean-field dynamics [26] have also been reported.

The TSH scheme described above has only been employed to study the photo-chemical deactivation pathways involving PEHs of the same multiplicity, i.e., via internal conversion. Recently [27], the TSH scheme has been extended to treat ISC mediated by SOC. The SOC matrix elements appear as off-diagonal elements in $H_{\beta\alpha}$ in (15), which couple states of different multiplicity. Without any further changes, (15) could be propagated including SOC in $H_{\beta\alpha}$ (this is sometimes called "spin-diabatic approach" [28]), but this scheme is not rotationally invariant and neglects the effect of the SOC on the PEHs (zero-field splitting). Additionally, the TSH scheme is based on the assumption that the couplings between the electronic states are localized (as are the NACs around a CoIn), while SOCs are clearly not. Within the Surface Hopping including Arbitrary Couplings (SHARC) methodology [27], the Hamiltonian is diagonalized, yielding fully adiabatic, spin-mixed electronic states. In this spin-mixed basis, the non-local SOCs are transformed into localized non-adiabatic couplings, allowing use of the TSH method in the intended way. The diagonalization can be written in terms of a unitary transformation between the electronic states,

$$\mathbf{U}^\dagger \mathbf{H} \mathbf{U} = \mathbf{H}^{\text{diag}}. \tag{17}$$

Here, $\mathbf{H}$ is the Hamiltonian matrix represented in the basis of the eigenfunctions of the molecular Coulomb Hamiltonian (given in (2)), $\mathbf{H}^{\text{diag}}$ is the same matrix in diagonalized form, and $\mathbf{U}$ is the unitary transformation matrix. In order to include the non-adiabatic couplings consistently, they have to be transformed as well. This leads to a new equation of motion for the coefficients in the diagonal basis:

$$\frac{\partial}{\partial t} c_\beta^{\text{diag}} = -\sum_\alpha \left[ \frac{i}{\hbar} \left( \mathbf{U}^\dagger \mathbf{H} \mathbf{U} \right)_{\beta\alpha} + \mathbf{v} \cdot \left( \mathbf{U}^\dagger \mathbf{T}^{(1)} \mathbf{U} \right)_{\beta\alpha} - \left( \mathbf{U}^\dagger \frac{\partial \mathbf{U}}{\partial t} \right)_{\beta\alpha} \right] c_\alpha^{\text{diag}}. \tag{18}$$

From this equation, the surface hopping probabilities can be calculated, similar to the original TSH approach. Since in SHARC the nuclei follow spin-mixed PEHs,

the spin-mixed gradients have to be calculated from the gradients of the unmixed states and the eigenvectors given by the matrix **U**. In the current approach, this neglects the derivatives of the SOC elements with respect to the nuclear coordinates, but this is a reasonably good approximation because the SOC operator is of short-ranged nature [29]. Since in SHARC the gradients for several electronic states have to be calculated in order to evaluate the mixed gradient, this approach is slightly more expensive than regular TSH. The price is, however, worth the money, since the inclusion of ISC processes can be as relevant as those processes mediated by internal conversion, even in systems with light atoms such as nucleobases.

TSH, in any of many different flavors, is the most widely used method employed to perform excited-state dynamics of DNA nucleobases. Compared to QD methods, where the number of electronic structure calculations scales exponentially with the number of DOF, in TSH methods the energies, forces and couplings are evaluated on-the-fly, and thus the number of electronic structure only depends on the number of trajectories and the desired number of time steps. This gives TSH simulations the enormous advantage of being able to include all molecular degrees of freedom in the simulation, even for relatively large molecules. In fact, the cost of TSH simulations is basically only dependent on the cost of the on-the-fly electronic structure calculations as the cost of integrating (11) and (15) is almost negligible. An additional advantage of TSH methods is that – since the trajectories are all independent of each other – they can be executed in parallel, further increasing the efficiency of the approach.

Despite its attractiveness, one has to remember that, due to its semi-classical nature, TSH fails to properly describe a number of quantum effects. First, the method cannot account for tunneling of the intrinsically classical nuclei; however, a description of tunneling for selected DOF is still possible [30]. Another shortcoming of TSH methods is that quantum coherences between the electronic states are often not described correctly. One possibility is to add the so-called decoherence corrections [31, 32]. For more details on the TSH method see the excellent review in [8].

## 2.7 Full Multiple Spawning

The Full Multiple Spawning (FMS) methodology [33–35] could be considered a step from TSH towards full quantum-mechanical calculations. However, as it requires only local knowledge about the PEHs, it is still suited for on-the-fly calculations. FMS coupled to on-the-fly ab initio quantum chemistry is usually termed ab initio multiple spawning (AIMS). In a nutshell, in FMS the nuclear wavefunction is expanded in a basis of frozen Gaussians, whose centers follow classical trajectories. Non-adiabatic effects are described by population transfer between basis functions assigned to different electronic states. To minimize the size of the Gaussian basis set while accurately describing a wavepacket, new Gaussians are spawned whenever necessary.

Within FMS, the total wavefunction is expanded as in the Born–Oppenheimer ansatz (see (5)):

$$\left|\Psi^{\mathrm{tot}}(\mathbf{R}, \mathbf{r}, t)\right\rangle = \sum_{\alpha=1}\left|\Psi_{\alpha}^{\mathrm{el}}(\mathbf{r}; \mathbf{R})\right\rangle\left|\Psi_{\alpha}^{\mathrm{nuc}}(\mathbf{R}, t)\right\rangle \tag{19}$$

Each nuclear wavefunction is represented in a time-dependent basis set composed of Gaussian basis functions $G_{\mu}^{\alpha}$:

$$\left|\Psi_{\alpha}^{\mathrm{nuc}}(\mathbf{R}, t)\right\rangle = \sum_{\mu}^{N_{\alpha}(t)} c_{\mu}^{\alpha}(t) G_{\mu}^{\alpha}\left[\mathbf{R}; \overline{\mathbf{R}}_{\mu}^{\alpha}(t), \overline{\mathbf{P}}_{\mu}^{\alpha}(t), \gamma_{\mu}^{\alpha}(t)\right], \tag{20}$$

where $c_{\mu}^{\alpha}(t)$ are the complex coefficients, and there are $N_{\alpha}(t)$ basis functions for each electronic state $\alpha$ at time $t$. The Gaussian basis functions are specified by an average position $\overline{\mathbf{R}}(t)$, an average momentum $\overline{\mathbf{P}}(t)$, a phase factor $\gamma_{\mu}^{\alpha}(t)$, and by a set of time-independent width parameters for each degree of freedom (i.e., the basis functions are frozen Gaussians).

In FMS, the parameters $\overline{\mathbf{R}}(t)$ and $\overline{\mathbf{P}}(t)$ are propagated according to Newton's equation of motion (11), very similar to the surface hopping method. In a region of strong non-adiabatic coupling, new basis functions are spawned on the coupled surface. In this fashion, the splitting of a wavepacket and the involved population transfer in such a region can be modeled accurately.

Similar to TSH methods, the total cost of FMS calculations is primarily determined by the cost of the on-the-fly electronic structure calculations. However, since new basis functions are spawned every time a region of non-adiabatic effects is traversed, FMS is more expensive than TSH. On the positive side, FMS allows for the correct quantum-mechanical description of coherences between the different parts of the nuclear wavepacket and, combined with high-level correlated electronic structure methods [36], it may provide quantitatively correct results. According to Hack et al. [37], FMS delivers results which are as good as or better than TSH calculations.

## 3   Connection of the Dynamics Simulations to Experiment

The theoretical methods explained above aim at describing the real dynamical processes detected in an experiment. The complexity of these processes, however, affects what one can learn from both theory and experiments. On the one hand, simulations require approximations in order to be able to treat the considered systems and these approximations need to be validated by experiments. On the other, the experimental signals are extremely difficult to interpret without the help

of computational predictions. Theory and experiment therefore need to act in concert.

It might seem obvious that it is desirable to simulate all the processes induced in an experiment and yield directly comparable results. However, this simple wish is not easy to fulfill, as in most cases the measured observables and those calculated are not the same. Typically, only the evolution of the excited-state population is calculated. However, an experiment consists of excitation (pumping), evolution (excited-state dynamics), probing, side effects induced by the probing procedure like fragmentation, and finally detection of a signal. The interpretation of this signal by means of theoretical simulations requires knowledge of which of these phenomena are really simulated and how. To help in this task it is useful first to understand the different experimental setups and then make a connection with the particular computational approaches.

The different experimental approaches can be categorized on different levels. One can distinguish between gas phase and liquid phase experiments but also between ionization, transient absorption or fluorescence techniques. A detailed description can be found in reviews [1–6, 38, 39]. Here, we shall focus only on the elements needed to make a sensible connection between experiments and gas phase simulations. The common essence of all possible spectroscopic experiments is that the nucleobase is first excited by UV light, stemming typically from an ultrashort laser pulse. In this way, excited-state dynamics is initiated, which is probed after a variable delay. The different applicable experimental techniques will condition the information obtained about the excited-state populations.

In the following, we summarize several points that should be kept in mind when simulating dynamical processes.

## 3.1 Time Scale

Using the methods described in Sect. 2, only ultra-short dynamics (below a few picoseconds) can be computed. This limitation is given by the high computational cost of the electronic structure calculations at each time step. Additionally, over the course of many time steps, errors accumulate, making long simulations particularly error-prone.

## 3.2 System Size

The size of the system considered in the simulation plays an important role. A calculation of an isolated nucleobase strictly corresponds to a gas phase experiment but may also be used as an approximation for liquid phase experiments. Improvements to account for solvent effects are possible (see, e.g., [119]), but usually involve additional approximations and computational cost.

## 3.3   Excitation Process

In the majority of calculations, the UV excitation is not directly simulated but approached in an ad hoc fashion, i.e., by starting the simulation with a population in a carefully selected distribution of excited states. This implies the use of an infinitely short pump pulse (a $\delta$-pulse) while in reality the experimental pump pulse has a finite duration. This approximation is usually of little importance in comparison with other approximations, and thus the experimental pump process is reasonably well described.

## 3.4   Quality of the Potential Energy Hypersurfaces

The excited-state PEHs, on which the dynamics is simulated, are calculated with electronic structure methods that have an associated limited accuracy. A wide variety of methods exist, ranging from semi-empirical to high-level multi-reference (MR) approaches. Most of the computational studies on nucleic acids use one of the following methods: TD-DFT (time-dependent density functional theory), DFTB (density functional-based tight binding), CASSCF (complete active space self-consistent field), CASPT2 (complete active space perturbation theory of second order), MRCI (multi-reference configuration interaction), and CI methods based on semi-empirical Hamiltonians like OM2 or AM1. These methods differ in their ability to describe excited-state PEHs properly, with more accurate methods usually being more expensive; see, e.g., [40–44]. Even highly sophisticated methods involve approximations which need to be validated by experimental results. Commonly, this validation involves comparison of the calculated excitation energies at the ground state geometry with the experimental absorption spectrum. The experimental spectrum is often broad with overlapping bands, making the assignment of the computed excited-state energies far from straightforward. Additionally, one has to remember that a method giving good results at the equilibrium geometry still may perform badly at other non-equilibrium geometries. In most cases, a further validation using experimental data is not possible, apart from a comparison of the actual dynamics results. Another limiting factor when choosing a method is that some properties (e.g., gradients of the potential energy) needed in certain types of dynamics simulations may simply be unavailable for various sophisticated electronic structure methods. As a consequence, the choice of a method is a compromise between accuracy, method availability, and computational cost.
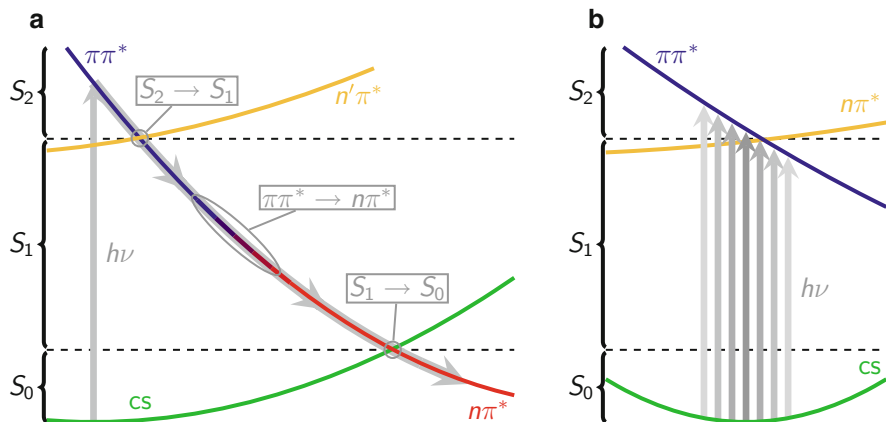
## 3.5 Representation

The choice of the representation, in which state populations are computed, be of great importance. The representation which arises naturally from the Born-Oppenheimer approximation and which is commonly used in electronic structure calculations, is termed "adiabatic" representation. Here, electronic states are ordered strictly according to energy, and population transfer between these states is introduced by the so-called NACs in the kinetic part of the Hamiltonian (here abbreviated as k-NAC). The adiabatic singlet states are usually referred to as $S_0, S_1$ and so on, with similar labels for other multiplicities. Adiabatic states do not preserve the wavefunction character. As a consequence, properties like the transition dipole moment may change drastically along a coordinate involving a fast change of wavefunction character.

In contrast to the adiabatic representation, states preserve their wavefunction character in the so-called "diabatic" representations (note that an infinite number of diabatic representations exist). In contrast to adiabatic states, PEHs of diabatic states can cross and molecular properties are usually smooth functions of the internal coordinates. The nomenclature of these states is often derived from the dominant excitation with respect to the ground state, e.g., $\pi\pi^*$ or $n\pi^*$. By changing from adiabatic to diabatic representation, the NACs in the kinetic part of the Hamiltonian are transformed into potential couplings (here p-NAC).

Quantum mechanically, both representations are strictly equivalent and correct as long as all couplings between all relevant states are considered. However, the state populations expressed in different representations can differ significantly. As a consequence, lifetimes obtained from fitting the excited-state populations are also dependent on the chosen representation. Since in the diabatic representation molecular properties change smoothly along a given coordinate, it is the most suitable representation for comparison with the experiment; here we term this representation "spectroscopic". As mentioned above, electronic structure calculations usually yield energies in the adiabatic representation and a transformation to the diabatic or spectroscopic picture is by no means trivial.

The problem of choosing the correct representation for dynamics simulations becomes more complicated if SOCs are involved. Then states of different multiplicity can mix and we can distinguish between representations where spin-orbit couplings are introduced either as potential couplings (p-SOC) or as kinetic couplings (k-SOC). The corresponding potentials are sometimes termed "spin-free" or "spin-diabatic" in the case of p-SOC and "spin-mixed" or "spin-adiabatic" in the case of k-SOC [27, 28]. The standard electronic structure programs yield p-SOC. Thus, the outcome of ab initio codes is usually adiabatic with respect to the NAC (k-NAC) but diabatic with respect to the SOC (p-SOC). To avoid confusion between the terms "diabatic" and "adiabatic," the following terminology [45] might be more convenient: In the "spectroscopic" (superscript spec) representation, the wavefunction character is preserved and the picture is closest to spectroscopic results. The "molecular Coulomb Hamiltonian" (MCH) representation is the

**Fig. 2** Comparing representations. (**a**) A relaxation pathway after photoexcitation (*gray arrows*) is shown in a simple model. The underlying potential energy curves are labeled according to their predominant state character ($\pi\pi^*$ *blue*, $n'\pi^*$ *yellow*, $n\pi^*$ *red*, *cs* (closed shell) *green*; spectroscopic representation) or their energetic ordering ($S_2$, $S_1$, $S_0$; note the *dashed separation lines*; MCH representation). Crossings are indicated with *circles* and labeled according to the involved states. (**b**) Photoexcitation involves several geometries and depending on the representation, different states can be excited, if a CoIn is located in the Franck–Condon region

standard output of quantum chemistry programs, where NACs are calculated as kinetic couplings and SOCs are off-diagonal terms of the potential when using a matrix form. Finally, the "diagonal" (diag) representation means that a fully diagonal potential matrix is obtained. Here, states of different multiplicity mix and terms like $S$ (singlet) and $T$ (triplet) might not be meaningful any longer. Instead, only the energetic ordering is unambiguous. For a distinction of the three representations, we write the corresponding total Hamiltonians in a simplified two-potential system:

$$\widehat{\mathcal{H}}^{\text{spec}} = \begin{pmatrix} T_1^{\text{spec}} & 0 \\ 0 & T_2^{\text{spec}} \end{pmatrix} + \begin{pmatrix} V_1^{\text{spec}} & \text{p-NAC} + \text{p-SOC} \\ \text{p-NAC} + \text{p-SOC} & V_2^{\text{spec}} \end{pmatrix} \tag{21}$$

$$\widehat{\mathcal{H}}^{\text{MCH}} = \begin{pmatrix} T_1^{\text{MCH}} & \text{k-NAC} \\ \text{k-NAC} & T_2^{\text{MCH}} \end{pmatrix} + \begin{pmatrix} V_1^{\text{MCH}} & \text{p-SOC} \\ \text{p-SOC} & V_2^{\text{MCH}} \end{pmatrix} \tag{22}$$

$$\widehat{\mathcal{H}}^{\text{diag}} = \begin{pmatrix} T_1^{\text{diag}} & \text{k-NAC} + \text{k-SOC} \\ \text{k-NAC} + \text{k-SOC} & T_2^{\text{diag}} \end{pmatrix} + \begin{pmatrix} V_1^{\text{diag}} & 0 \\ 0 & V_2^{\text{diag}} \end{pmatrix} \tag{23}$$

We note here that, in semiclassical simulations, the representations are not fully equivalent [22, 45] and thus special care is required.

In the following, we illustrate the general discussion on the representations with two examples. First, we focus on the difference between the spectroscopic and the MCH representation. In Fig. 2a, an exemplary excitation-relaxation pathway is

schematically depicted. Population is vertically excited from the ground state (closed-shell, cs) minimum and then evolves on different potentials. According to the MCH picture (typically employed in semiclassical calculations), the system follows an $S_2 \rightarrow S_1 \rightarrow S_0$ path. Analyzing dynamics results in this representation would result in two distinct time constants, with a small constant associated with the $S_2 \rightarrow S_1$ process and a larger one with $S_1 \rightarrow S_0$. When analyzing the dynamics instead in terms of spectroscopic states, the same path would be identified as $\pi\pi^* \rightarrow n\pi^*$ (indicated by the color gradient from blue to red). Accordingly, only one decay time of intermediate duration would be obtained. An experiment where $\pi\pi^*$ and $n\pi^*$ give rise to signals of different strengths would similarly only measure a single time constant. However, a direct comparison of the MCH populations with the experimental transient is not possible. Nevertheless, time constants derived from MCH populations can seemingly agree with experimental time constants due to error compensation. Moreover, the overlap of several competing processes can give rise to effective time constants which might coincide with time constants from MCH populations. In any case, the most straightforward comparison of simulation and experiment could be obtained by explicitly including the pump and probe processes in the simulation.

In the second example, one of the reasons for the above-mentioned occurrence of several simultaneous processes is illustrated (see Fig. 2b). The Franck–Condon (FC) region, from where excitation takes place, comprises several different geometries around the $S_0$ minimum. A simplification is often used and – especially in static simulations – only the ground state equilibrium geometry is considered (center arrow in the figure). At this specific geometry, the $S_2$ corresponds to the $\pi\pi^*$ in the present example. Here, the $\pi\pi^*$ is the bright state, where population is transferred from the ground state, while the dark $n\pi^*$ state corresponds to the $S_1$. If a CoIn between the two states is situated in the Franck–Condon region, other geometries exist, where the correspondence between $S_1, S_2$ and $\pi\pi^*, n\pi^*$ is reversed. In other words, the bright state, despite always being the $\pi\pi^*$ state, corresponds to $S_2$ for some geometries and to $S_1$ for others. Therefore a correct simulation must involve both states. To complicate things further, the oscillator strength of the $n\pi^*$ state may be small but non-zero. This again means that many starting geometries and states might be necessary to understand fully the dynamics of the system. Because all these initial conditions may lead to different processes and outcomes, the dynamical picture might be rather complicated.

## 3.6  Probe Process

Finally, the probe process is also often not simulated for several reasons. The focus of interest is the dynamics in the excited states, which can be observed only indirectly in an experiment by using a probe. In contrast, this information can be directly accessed in a calculation. Therefore, one might think the simulation of the probe process is superfluous. However, when one tries to compare theory and
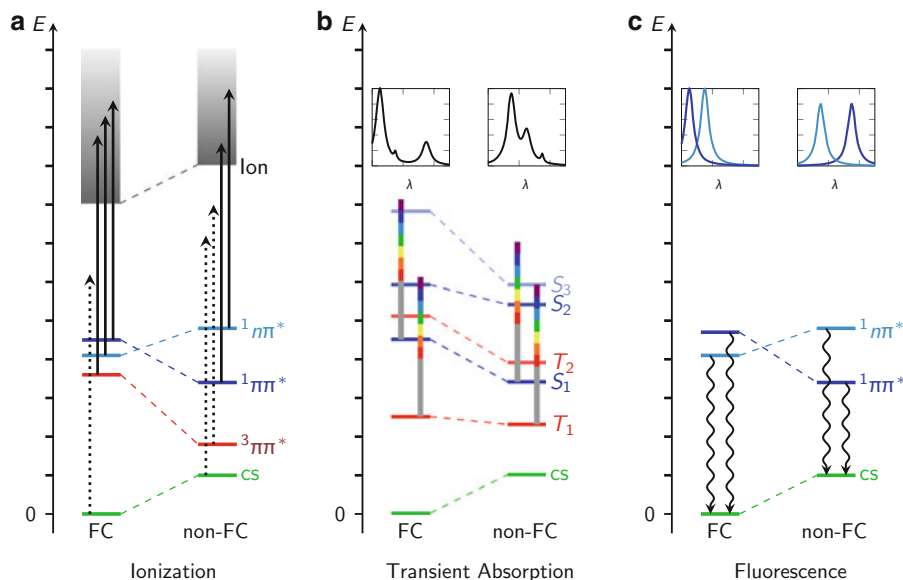
**Fig. 3** Basics of different experimental probing techniques. (**a**) Ionization. The probe pulse has to carry enough energy to ionize the molecule, which is the case for the excited states $^1n\pi^*$, $^1\pi\pi^*$ and $^3\pi\pi^*$ (ionization indicated by *solid* lines), but not for the closed-shell (cs) ground state (ionization not possible, *dotted* line). At geometries far from the FC region, even some excited states (here the $^3\pi\pi^*$) might be too low in energy to be ionized. (**b**) Transient absorption. The absorption of light by populated excited states leads to bands in the absorption spectrum. At another geometry, the energies of the excited states will have shifted, giving rise to a different spectrum. (**c**) After photoexcitation, the fluorescence is detected in a time-resolved way. During the dynamics, the fluorescence spectrum changes according to the state energies

experiment, computational state lifetimes are related to signal decay times. On the one hand, these signal decay times are usually "blind" for some molecular processes due to a specific experimental setup. Additionally, the probe process used for obtaining the decay times will have some intrinsic limitations, e.g., employing a limited energetic window. Therefore, a signal decay time can stem from different state lifetimes and setup-specific effects like running out of the probe window. On the other hand, the approximations made in the simulations may lead to errors in the computed state lifetimes. Hence, great care has to be taken when comparing experimental with theoretical results and it is desirable to simulate the probe process to arrive at really analogous outcomes.

In what follows, some key concepts of different probing schemes are illustrated and connections to possible simulations of such experiments are made. Here, we limit ourselves to setups using ionization, transient-absorption, or fluorescence (Fig. 3).

Ionization will be discussed first (Fig. 3a). After the pump pulse, the excited states get populated. Excited-state population can be detected by ionizing with a probe pulse carrying sufficient energy. Since the pulse does not carry enough

energy to ionize the ground state (indicated by the dotted arrow), the signal will be proportional to the population in the excited states only. By varying the delay between pump and probe, the evolution of the excited-state population can be tracked. However, depending on the geometry, additional states – here, for example, a $^3\pi\pi^*$ triplet – might be too low in energy to be ionized by the probe laser. Thus, a distinction between molecules relaxing to the ground state and molecules being trapped in the low-lying state is not possible any longer. The time constants extracted from the transient are hence an effective time constant including both processes. An additional issue to keep in mind is that the ionization probability depends not only on the energetic separation of the neutral and ionic states but also depends on the wavefunction character. However, a clear distinction between ionization from a triplet or from a singlet state is extremely difficult. Last, but not least, multiphoton processes are often employed in the experimental probing, so that the ionization probability is additionally influenced by the presence of intermediate states, which further complicates the connection between the signal obtained and the actual photo relaxation in the neutral states. While first attempts of simulating ionization yields have been made (see, e.g., [46]), a full simulation of multiphoton ionization is very demanding [47–50] and cannot be carried out on-the-fly during the excited-state dynamics computations.

As a second approach, particularly suited for liquid phase experiments, transient absorption detection will be briefly discussed (Fig. 3b). Here, the excited-state dynamics is ideally probed within a very wide spectral range (indicated by the vertical spectrally colored bars in the figure), i.e., by white light. The latter is absorbed by the excited molecules, and the amount and the frequency of the absorbed light is detected in a time-resolved fashion. During the relaxation, the transient absorption spectrum (given in the insets at the top) changes and the dynamics can be accurately mapped. Triplet states can also be detected in this way (e.g., by triplet-triplet absorption), but distinguishing singlet and triplet states is challenging. In general, assignment of transient absorption bands to specific processes is not an easy task and this is where theoretical simulations can help. It is in principle possible to calculate the excited-state absorption during the simulation of the dynamics. The bottleneck is caused by highly excited states which need to be computed and this can be difficult even for sophisticated methods, especially if accurate energetic differences are necessary in order to distinguish between all possible absorption pathways.

As a final case, we mention fluorescence experiments, where the fluorescence (excitation spectrum and fluorescence spectrum) of the excited-state population is detected time-dependently (Fig. 3c). Although fluorescence can be simulated in principle, the time scales are often beyond what can be investigated in quantum or semiclassical on-the-fly dynamics calculations, and therefore theoretical studies are rare.

In a nutshell, the description of the complex processes underlying photorelaxation is very challenging and the corresponding simulation methods are subject to ongoing developments. However, remembering all the pitfalls described above, extensive connections between theory and experiment are already possible today and a detailed picture of the photorelaxation dynamics of nucleic acids can be drawn.

# 4 Photodynamics of Nucleobases

In this section we shall discuss and analyze the photodynamics of each of the five DNA/RNA nucleobases in the gas phase, starting with the purine bases A and G, followed by the pyrimidine bases C, T, and U.

For each nucleobase we start by briefly summarizing the available experimental studies which report time scales and focus on the deactivation mechanism after light irradiation. These results will then be compared to the outcome of the theoretical studies. All relevant studies reporting excited-state dynamics simulations in the gas phase are discussed in chronological order. An effort has been made to compare the proposed relaxation paths and the CoIns encountered in the simulations. Comparison between the studies is enabled by schematic overviews of the proposed relaxation mechanisms. As the reader will soon recognize, different methods provide different results, which sometimes complement each other but sometimes conflict with each other. However, each dynamics method and each electronic structure method has different benefits and drawbacks, and it is often difficult to say *which method is better*. As such, each simulation contributes a small piece to the puzzle and advances a little further the interpretation of the experimental findings. An overall picture of the deactivation pathway for each nucleobase is summarized at the end of each section, assigning wherever possible the experimental time scales with the help of the molecular pathways obtained theoretically. All in all, this section shows the current state of knowledge of the deactivation processes occurring in isolated photoexcited DNA/RNA nucleobases.

## 4.1 Adenine

A is found in Watson–Crick pairs with T and U in DNA and RNA, respectively. Together with G, it is a purine derivative and therefore exhibits qualitatively different features compared to the pyrimidine bases C, T, or U. In water, A presents two different tautomers (see Fig. 4), the 7H and 9H forms, but 7H-A is the minor fraction with 15–23% of the population [51–55]. In the gas phase, 9H-A is the only tautomer at biologically relevant temperatures [56], although some studies also find 7H-A in the gas phase when vaporizing at high temperatures [57]. Theoretically, only the dynamics of the 9H tautomer has been investigated, and therefore by A we refer henceforth to this tautomer.

### 4.1.1 Experimental Time Scales

Table 1 summarizes the experiments that report time scales for the deactivation dynamics of A in the gas phase, specifying which pump and probe wavelengths have been employed to this purpose. The papers are listed in chronological order

**Fig. 4** The most important tautomers of A. 9H-A is the biologically relevant structure



9H          7H
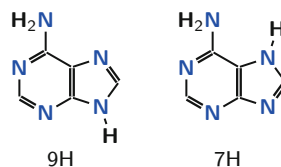
**Table 1** Experimentally observed decay times of A

| Setup | | Time constants | | | | |
|---|---|---|---|---|---|---|
| $\lambda_{pump}$ (nm) | $\lambda_{probe}$ (nm) | $\tau_1$ (fs) | $\tau_2$ (fs) | $\tau_3$ (ns) | References | Year |
| 267 | $n \times 800$ | | 1,000 | | Kang et al. [58, 59] | 2002, 2003 |
| 250–277 | 200 | <50 | 750–2,000 | 1 | Ullrich et al. [60, 61] | 2004 |
| 267 | $2 \times 400$ | 100 | 1,000 | | Canuel et al. [62] | 2005 |
| 267 | 200 | 40 | 1,200 | | Satzger et al. [63, 64] | 2006 |
| 262 | $n \times 780$ | 100 | 1,140 | | Kotur et al. [65] | 2012 |

and the time constants given in the corresponding publications have been classified *by us*. As will be seen, in all nucleobases different deactivation time scales have been found, typically spanning from femtoseconds to picoseconds, or even to nanoseconds. In A, $\tau_1$ is assigned to constants below 100 fs, $\tau_2$ is considered for hundreds of femtoseconds, and $\tau_3$ is a nanosecond time scale.

With this assignment in mind, all experiments show a fast deactivation ($\tau_2$) within the range 0.5–2 ps. Additionally, most studies reported another, shorter transient below 100 fs, while Ullrich et al. [60, 61] even observed a long-lived component ($\tau_3$) on the nanosecond time scale.

### 4.1.2 Deactivation Mechanism

Table 2 collects all the theoretical studies aimed at understanding the excited state deactivation dynamics of A in the gas phase. Figure 5 depicts schematically each of the paths predicted by theoretical calculations. Note these qualitative schemes collect several reaction coordinates in one dimension and are only intended for an at-first-glance comparison of the proposed relaxation pathways. For more detailed and precise information, the reader should consult the original reference. Colors indicate electronic state character, and are used consistently for all nucleobases. A color gradient indicates an adiabatic change of wavefunction character. If applicable, triplet states are given as dotted lines. Important geometries encountered by several studies are shown in Fig. 6. Atoms of characteristic geometrical features are given in gold. We note that in the dynamics the system does not hop exactly at the geometries shown, but at related geometries located on the same seam of intersection.

The first excited-state dynamics study on gas phase A was conducted in 2008 by Fabiano et al. [66] using TSH, three electronic states, and OM2/MRCI for the

**Table 2** Excited-state nuclear dynamics studies for isolated A in the gas phase

| Methodology | | Time constants | | | |
|---|---|---|---|---|---|
| Dyn. | El. Struct. | $\tau_1$ (fs) | $\tau_2$ (fs) | References | Year |
| TSH | OM2/MRCI | 15 | 560 | Fabiano et al. [66] | 2008 |
| TSH | CASSCF(12,10)/MRCIS(6,4)[a] | 22 | 538 | Barbatti et al. [67] | 2008 |
| MF | DFTB | | 1,050–1,360 | Lei et al. [68] | 2008 |
| TSH | TD-DFTB/B3LYP | 120 | 11,000 | Mitric et al. [69] | 2009 |
| TSH | CASSCF(12,10)/MRCIS(6,4)[a] | | 440–770 | Barbatti et al. [70] | 2010 |
| TSH | CASSCF(10,8)/MRCIS(6,4) | | 530 | Barbatti et al. [71] | 2012 |
| TSH | OM2/MRCI | | 900 | Barbatti et al. [71] | 2012 |
| TSH | TD-DFT[b] | | $\gg$1,000 | Barbatti et al. [71] | 2012 |

Time constants correspond to those given in the respective papers, classified as $\tau_1$ (below 120 fs) and $\tau_2$

[a]Different analysis of the same data

[b]Functionals: CAM-B3LYP, B3LYP, BHLYP, M06-HF, PBE, and PBE0
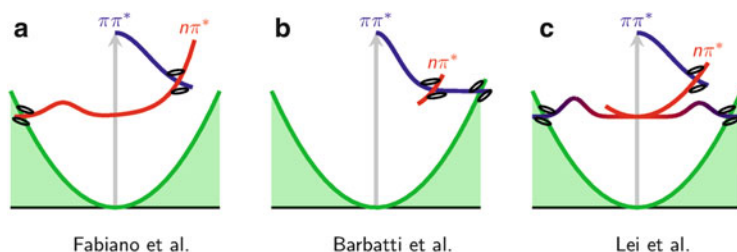


**Fig. 5** Schematic overview of the proposed relaxation mechanisms for A from the references: (**a**) [66], (**b**) [67, 70, 71], and (**c**) [68] (*left* to *right*)



**a** $S_2/S_1$
$\pi\pi^*/n\pi^*$
*ring torsion*
(Dihedral between
ring planes)

**b** $S_1/S_0$
$n\pi^*/cs$
$C_6$-*puckered*
($N_1$=$C_6$ torsion)

**c** $S_1/S_0$
$\pi\pi^*/cs$
$C_2$-*puckered*
($N_3$=$C_2$ torsion)
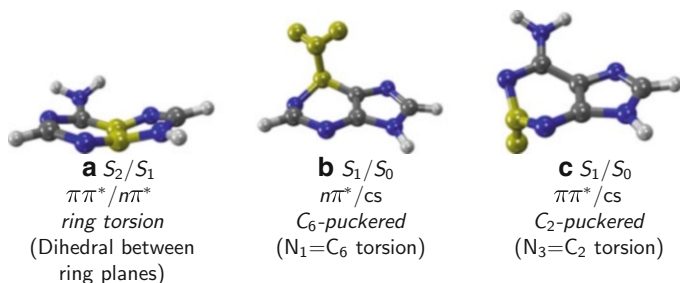
**Fig. 6** Geometries of important CoIns of A discussed in the text. The labels give the crossing states (adiabatic and state character) and the main geometrical feature, which are highlighted by golden atoms in the structures

underlying electronic structure calculations. They identified processes on two time scales, which they assigned as $\tau_1$ and $\tau_2$. The fast time scale was described as the relaxation of the initially populated bright $\pi\pi^*$ state within 15 fs to a dark $n\pi^*$ state through the CoIn depicted qualitatively in Fig. 6a. The CoIn is characterized by an

angle of about 15° between the planes of the two rings. Once in the $n\pi^*$, the deactivation to the ground state takes 560 fs via the $C_6$-puckered ($n\pi^*/cs$) CoIn, which features an out-of-plane distortion of the amino group (Fig. 6b). The overall path is depicted schematically in Fig. 5a.

In the same year, a TSH study based on CASSCF(12,10)/MRCIS(6,4) electronic properties was conducted by Barbatti et al. [67]. Their obtained time constants, $\tau_1 = 22$ fs. and $\tau_2 = 538$ fs, are very similar to those of Fabiano et al. [66] but the details of the deactivation mechanisms differ slightly. As in Fabiano et al. [66], the first constant arises from $S_2 \rightarrow S_1$ decay and the second constant is connected to the $S_1 \rightarrow S_0$ decay. However, and in contrast to the previous study [66], the CASSCF/MRCI-based dynamics employs the so-called $C_2$-puckered CoIn (Fig. 6c) as a major deactivation funnel. Note that even though the authors reported $S_2 \rightarrow S_1$ transitions, the system always stays in the $\pi\pi^*$ spectroscopic state.

Mean-field (MF) dynamics by Lei et al. [68] employing density functional-based tight binding (DFTB) observed a strong influence of the excitation energy on the relaxation path taken and hence on the relaxation times. Using an excitation energy of 5.0 eV, they observed that the $C_6$-puckered CoIn (Fig. 6b) is employed for relaxation. The excited-state lifetime in this case was 1,050 fs (note that in this mean-field dynamics only a single trajectory is computed). On the other hand, excitation at 4.8 eV activates the channel through the $C_2$-puckered CoIn (Fig. 6c), with an excited-state lifetime of 1,360 fs. In both cases the initial $\pi\pi^*$ state is reported to change to an intermediate $n\pi^*$ state before reverting to the $\pi\pi^*$ state and accessing the respective CoIn. Accordingly, the authors state that the final transition back to the ground state happens always from the $\pi\pi^*$ state (see Fig. 5c), even though previous studies report the $C_6$-puckered CoIn to be of $n\pi^*/cs$ character.

Mitrić et al. [69] investigated the decay of photoexcited A using TD-DFTB-based dynamics. Here, for the isolated nucleobase, a two-step relaxation process was observed, including a fast $S_2 \rightarrow S_1$ transition with a time constant of 120 fs and a slow deactivation back to the ground state within 11 ps. Unfortunately, since their study mainly focused on the photodynamics of micro-solvated A, they did not report on the details of the relaxation path taken by gas phase A.

In 2010, Barbatti et al. [70] published an overview article including all nucleobases, where the previously reported dynamics simulation [67] for A was reanalyzed in terms of the initial excitation energy of the trajectories. Here, a monoexponential decay with a lifetime of about 770 fs was observed after excitation at the band origin (low energy), which is equivalent to an excitation wavelength of 267 nm. Increasing the excitation energy (250 nm) reduces the excited-state lifetime to 440 fs. Despite the different time constant, no differences in the mechanistic details of the relaxation were found for the different excitation energies.

The latest dynamics simulations on gas phase A were also published by Barbatti et al. [71] in a compendium paper which compared the results of dynamics simulations based on different electronic structure methods. The simulations showed that TD-DFT was unable to describe the ultrafast decay of excited A, even though six different functionals were employed. In none of the TD-DFT-

based dynamics ground state relaxation was observed, except for very high initial energies. This is in strong contrast to the fast relaxation of A observed in the experiments. TD-DFT fails to describe the fast relaxation due to an overstabilization of planar distortions, which gives a general underestimation of the puckering modes. In contrast, OM2/MRCI and MRCIS dynamics show an ultrafast decay (900 or 530 fs, respectively) although via different deactivation channels which involve either puckering of the $C_6$ atom (OM2/MRCI) or the $C_2$ atom (MRCIS). Comparisons of these results to reaction paths calculated at the CASPT2 and CC2 level of theory suggest that MRCIS underestimates the ease of $C_6$ puckering, whereas OM2/MRCI overestimates it [71].

### 4.1.3   Final Discussion

Most of the dynamics studies of A in the gas phase assign the shortest time constant observed in the experiment ($\tau_1$ ) to $S_2 \rightarrow S_1$ or $\pi\pi^* \rightarrow n\pi^*$ transitions occurring within the excited-state manifold. For the longer time constant $\tau_2$ the theoretically predicted values [66–68, 70, 71] corresponding to ground state relaxation are in the range 440–1,120 fs, which is slightly shorter than the average of the experimental time constants. Nevertheless, given the good agreement, the assignment is plausible. The exception is provided by TD-DFT- [71] or TD-DFTB- [69] based TSH dynamics, which predict a significantly longer excited-state lifetime than observed experimentally, due to the limitations of these electronic structure methods to describe the excited-state PEHs.

Despite the fact that the time constants predicted by MRCIS- and OM2/MRCI-based dynamical studies [66, 67, 70, 71] are similar, the predominant relaxation pathways obtained are different. Depending on the level of theory, either the state character is preserved [67, 71], leading to the $C_2$-puckered CoIn, or it changes to $n\pi^*$ [66, 71], leading to a decay via the $C_6$-puckered CoIn. It remains unclear which puckering motion is of major importance until on-the-fly dynamics simulations at a more reliable level of theory become possible.

## 4.2   Guanine

G is another purine base; it is found in Watson–Crick pairs with C. G shows 36 different tautomers, of which the most important are shown in Fig. 7. Their experimental detection is very sensitive to the setup [72–74]. The most stable tautomers, 7H-keto-amino and 9H-keto-amino, show ultrafast decay. In DNA the 9H-keto-amino tautomer is dominant [75] and shows a first absorption band at a maximum of 284 nm [76].
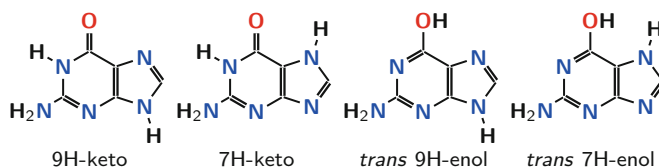
**Fig. 7** The most important tautomers of G. The biologically relevant form is the 9H-keto form

**Table 3** Experimentally observed decay times of G

| Setup | | Time constants | | | |
|---|---|---|---|---|---|
| $\lambda_{pump}$ (nm) | $\lambda_{probe}$ (nm) | $\tau_1$ (fs) | $\tau_2$ (fs) | References | Year |
| 267 | $n \times 800$ | | 800 | Kang et al. [59] | 2002 |
| 267 | $2 \times 400$ | 148 | 360 | Canuel et al. [62] | 2005 |

**Table 4** Excited-state nuclear dynamics studies for isolated G in the gas phase

| | Methodology | | Time constants | | | |
|---|---|---|---|---|---|---|
| G | Dyn. | El. Struct. | $\tau_1$ (fs) | $\tau_2$ (fs) | References | Year |
| 7H-e | TSH-CP | ROKS/BLYP | | | Langer et al. [78] | 2005 |
| 9H-k | TSH-CP | ROKS/BLYP | | 800 | Doltsinis et al. [79] | 2008 |
| 7H-k | TSH-CP | ROKS/BLYP | | 1,000 | Doltsinis et al. [79] | 2008 |
| 9H-k | TSH | OM2/MRCI(10,9) | 190 | 400 | Lan et al. [80] | 2009 |
| 9H-k | TSH | CASSCF(12,9)/MRCIS(10,7)[a] | | 280 | Barbatti et al. [70] | 2010 |
| 9H-k | TSH | CASSCF(12,9)/MRCIS(10,7)[a] | | 224 | Barbatti et al. [81] | 2011 |

The first column gives the tautomer (k: keto, e: enol). Time constants correspond to those given in the respective papers, classified as $\tau_1$ (below 100 fs) and $\tau_2$
[a]Same simulation, but different time constant reported

### 4.2.1 Experimental Observations

Table 3 collects the experimental decay times of G. Probably due to the large number of tautomers and associated difficulties, only a small number of experiments deal with the dynamics of photoexcited isolated G in the gas phase. The pump-probe transient ionization experiments of Kang et al. [59] found a monoexponential decay time of G after 267 nm excitation with a time constant of 800 fs in gas phase. Here, the cross-correlation of the pump and probe pulses of 400 fs (see [77]) was probably too large to find the second short component, which was observed later by Canuel et al. [62]. The latter authors reported $\tau_1 = 148$ fs and $\tau_2 = 360$ fs.

### 4.2.2 Deactivation Mechanism

Table 4 gives an overview of the different theoretical studies investigating gas phase dynamics of isolated G and Fig. 8 shows the corresponding deactivation paths.
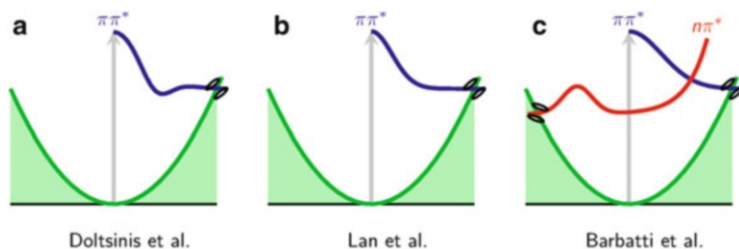
**Fig. 8** Schematic overview of the proposed relaxation mechanisms for 9H-keto G from (**a**) [79], (**b**) [80], and (**c**) [81]. Note that different reaction coordinates can be implied in the one-dimensional pictures



**a** *keto*: $S_1/S_0$      **b** *keto*: $S_1/S_0$      **c** *keto*: $S_1/S_0$
$\pi\pi^*$/cs              $\pi\pi^*$/cs              $n\pi^*$/cs
*$C_2$-perpendicular*      *$C_2$-parallel*           *oop-$O_6$*
($N_1=C_2$ torsion)       ($N_1=C_2$ torsion)        ($C_6$ pyramidalization)
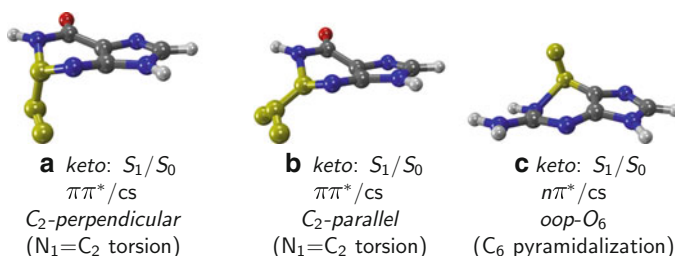
**Fig. 9** Geometries of important CoIns of G discussed in the text. The labels give the crossing states (adiabatic and state character) and the main geometrical feature

The first dynamics study on G in the gas phase was reported by Langer et al. [78] in 2005. The method used was a TSH approach coupled to Car–Parrinello dynamics (TSH-CP), based on PEHs from restricted open-shell Kohn–Sham (ROKS) with the BLYP functional. They investigated the possibility of O–H dissociation in the excited state dynamics of 7H-enol G. Since this reaction involves a rather high barrier, constrained dynamics was carried out in order to sample this barrier. It was found that in the gas phase the barrier is about 0.54 eV and thus is likely to be relevant only at high excitation energies. The abstraction of the hydrogen atom was accompanied by a non-adiabatic change to the $S_0$ state through an $S_1/S_0$ CoIn.

In 2008, Doltsinis et al. [79, 82] for the first time reported excited-state dynamics of G focused on understanding the photodeactivation. Using the same method as in [78], they reported a monoexponential decay for 9H-keto G with a time constant of 800 fs. Here, the system first relaxes to the $S_1(\pi\pi^*)$ minimum before reaching an $S_1/S_0$ CoIn, as shown schematically in Fig. 8a. The CoIn is characterized by $C_2$ puckering and an $N_2$–$C_2$–$C_4$–$C_5$ dihedral angle of 97° (see Fig. 9a). For the 7H-keto tautomer the $S_1$ minimum is very similar to the ground state minimum geometry. The decay dynamics are mostly driven by distortions of the imidazole ring and out-of-plane motions of the oxygen atom, resembling the oop-$O_6$ CoIn which is given in Fig. 9c for the 9H form. The excited-state population decays monoexponentially to the ground state with a time constant of 1,000 fs.

Simulations based on TSH and the semi-empirical OM2/MRCI electronic structure method by Lan et al. [80] find two different deactivation channels for 9H-keto G. The first channel involves the $C_2$-parallel CoIn given in Fig. 9b, which is stated to be responsible for a fast decay with a time constant of 190 fs. The second channel leads through the $C_2$-perpendicular CoIn, depicted in Fig. 9a. A 400 fs time constant was reported for this pathway. The two CoIns are distinguished by the angle between the $C_2$–amino bond and the ring plane. This angle is much larger for the $C_2$-parallel CoIn than for the $C_2$-perpendicular CoIn. Note that in this study the relaxation mechanism involved only the excited $\pi\pi^*$ state and the ground state (see Fig. 8b), even though an $n\pi^*$ state was included in the calculations.

In 2010, Barbatti et al. [70] published a TSH dynamics study based on the correlated CASSCF(12,9)/MRCIS(10,7) level of theory. They reported monoexponential decay for 9H-keto G with a time constant of 280 fs, caused by a single and direct decay via the two $C_2$-puckered CoIns (Fig. 9a, b). The authors stated that both CoIns involve an ethylene-like twisting of the $N_1=C_2$ bond, can be reached barrierless from the FC region, and connect the $\pi\pi^*$ state to the ground state. A more detailed analysis of the same simulations [81] revealed a slightly shorter time constant of 224 fs, which is a composite of a 97-fs delay and a 127-fs monoexponential decay of the excited-state population. The main route of deactivation follows the $\pi\pi^*$ state towards the $C_2$-parallel and $C_2$-perpendicular CoIns (Fig. 9a, b), which together account for 95% of all hops. Only 5% of the trajectories showed instead a transition to the $n\pi^*$ state, followed by out-of-plane motion of the oxygen atom, leading to the $S_1/S_0$ oop-$O_6$ CoIn (Fig. 9c).

### 4.2.3 Final Discussion

For G, less experimental and theoretical studies focused on the gas phase excited-state dynamics are available compared to the rest of the nucleobases.

The existing literature identifies G as the nucleobases showing the fastest relaxation to the ground state. Experimentally, a sub-picosecond decay is reported, which is also reproduced by all dynamics simulations. While the ROKS-based study [79] is consistent with the experimental transients of Kang et al. [59], the more recent simulations employing OM2/MRCI [80] or CASSCF/MRCIS [70, 81] show good agreement with the time constants of Canuel et al. [62]. All studies agreed on the dominance of the direct $\pi\pi^* \rightarrow S_0$ pathway, accessing the $C_2$-puckered CoIns. Relaxation involving the $n\pi^*$ state is likely to be of minor importance.

Based on the simulations of Doltsinis et al. [79], the 9H and 7H tautomers of G are expected to show decay on a very similar time scale. Nevertheless, in order to clarify the involvement of the 7H tautomer in the photodynamics of G, additional dynamics simulations based on reliable electronic structure methods are necessary.
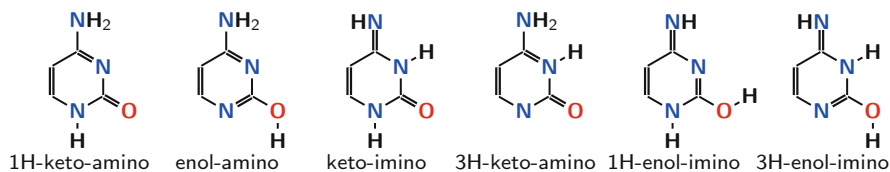
**Fig. 10** The six possible tautomers of C. The 1H-keto-amino form is found in DNA

## 4.3 Cytosine

C is a pyrimidine derivative, in contrast to A and G. In Watson–Crick pairs, C is hydrogen bonded to G. C can exist in different tautomers, which are shown in Fig. 10. The relative stability of the tautomers depends on the environmental conditions. While in DNA and in aqueous solution C only exists in the 1-H-keto-amino form (henceforth denoted as keto), in the gas phase other tautomers have been detected. A microwave spectroscopic study by Brown et al. [83] found a tautomer ratio of 0.44:0.44:0.12, for the keto, the enol-amino (enol), and the keto-imino (imino) tautomers, respectively. Tautomers other than keto, enol, and imino are very high in energy and have not been detected in the experiments. They are not discussed in the following. Two other matrix isolation infrared studies obtained ratios of 0.32:0.65:0.03 [84] and 0.22:0.70:0.08 [85]. Since the absorption spectra of the three tautomers overlap, it is expected that in gas phase experimental studies the signals of these three tautomers are measured simultaneously, giving rise to several time constants or effective time constants and making the assignment of time scales exceptionally difficult. For this reason, theoretical studies can be particularly helpful in assisting with the interpretation of the available time-resolved spectra. However, as will be discussed below, most theoretical gas phase studies have been focused only on the keto form, most likely because it is the biologically relevant tautomer. In the following, if no tautomer form is explicitly given, the keto form is implicitly assumed.

### 4.3.1 Experimental Observations

There are a number of experimental studies that have measured the excited-state lifetimes of C in the gas phase. Table 5 lists the exponential decay time constants reported in these studies. In most experiments a single pump wavelength [59, 61, 62, 65] has been used. Kosma et al. [86] and Ho et al. [87] employed arrays of excitation wavelengths ranging from 260 to 300 nm.

Generally, most of these papers report a time constant of about 1 ps ($\tau_2$) and a longer time constant of several ps ($\tau_3$). Interestingly, the shorter constant is present at all excitation wavelengths, but the longer time constant strongly increases with increasing excitation wavelength and vanishes for $\lambda_{\text{pump}} > 290$ nm. Besides these two time constants, some studies resolved another, very short decay constant ($\tau_1$).

**Table 5** Experimentally observed decay times of C

| Setup | | Time constants | | | | |
|---|---|---|---|---|---|---|
| $\lambda_{pump}$ (nm) | $\lambda_{probe}$ (nm) | $\tau_1$ (fs) | $\tau_2$ (fs) | $\tau_3$ (ps) | References | Year |
| 267 | $n \times 800$ | | | 3.2 | Kang et al. [59] | 2002 |
| 250 | 200 | <50 | 820 | 3.2 | Ullrich et al. [61] | 2004 |
| 267 | $2 \times 400$ | 160 | | 1.86 | Canuel et al. [62] | 2005 |
| 260–290 | $3 \times 800$ | 200–100 | 3,800–1,100 | up to 150 | Kosma et al. [86] | 2009 |
| 260–300 | $3 \times 800$ | | 200–1,200 | 2.7–45 | Ho et al. [87] | 2011 |
| 262 | $n \times 780$ | 50 | 240 | 2.36 | Kotur et al. [65] | 2012 |

**Table 6** Excited-state nuclear dynamics studies for isolated C in the gas phase

| | Methodology | | Time constants | | | | |
|---|---|---|---|---|---|---|---|
| C | Dyn. | El. Struct. | $\tau_1$ (fs) | $\tau_2$ (fs) | $\tau_3$ (ps) | References | Year |
| k | TSH-CP | ROKS/BLYP | | 700 | | Doltsinis et al. [79] | 2008 |
| k | FMS | CASSCF(2,2) | √ | | | Hudock et al. [88] | 2008 |
| k | TSH | OM2/MRCI | 40 | 370 | | Lan et al. [89] | 2009 |
| k | TSH | AM1/CI(2,2) | | | | Alexandrova et al. [90] | 2010 |
| k | TSH | CASSCF(12,9) | √ | √ | | González-Vázquez et al. [91] | 2010 |
| k | TSH | CASSCF (14,10) | 9 | 527 | 3.08 | Barbatti et al. [70, 92] | 2010, 2011 |
| k | SHARC | CASSCF(12,9) | √ | | | Richter et al. [93] | 2012 |
| k | TSH | CASSCF(12,9) | | √ | | Nakayama et al. [94] | 2013 |
| e | TSH | CASSCF(10,8) | | | √ | Nakayama et al. [94] | 2013 |
| i | TSH | CASSCF(12,9) | √ | | | Nakayama et al. [94] | 2013 |
| k | SHARC | CASSCF(12,9) | 7 | 270 | | Mai et al. [45] | 2013 |
| e | SHARC | CASSCF(12,9) | 40 | | 1.9 | Mai et al. [45] | 2013 |

The first column gives the tautomer (k: keto, e: enol, i: imino). Time constants correspond to those given in the respective papers, classified as $\tau_1$ below 100 fs, $\tau_2$ below 1 ps, and $\tau_3$ above 1 ps. A checkmark indicates that the authors discussed processes on these time scales without giving explicit values

In order to disentangle the deactivation pathways of each of the tautomers, Ho et al. [87] also carried out experiments for 1-methyl-C and 5-fluoro-C. In the former molecule, which cannot tautomerize to the enol form, they found essentially the same values for $\tau_2$ as in C but the longer time scale $\tau_3$ disappears. In 5-fluoro-C (which assumes the enol form), the dynamics was completely dominated by $\tau_3$.

### 4.3.2 Deactivation Mechanism

Table 6 reports a comprehensive list of all the excited-state dynamical studies performed in isolated C in the gas phase and Fig. 11 depicts schematically all the proposed mechanisms. They will be discussed in chronological order in the following.
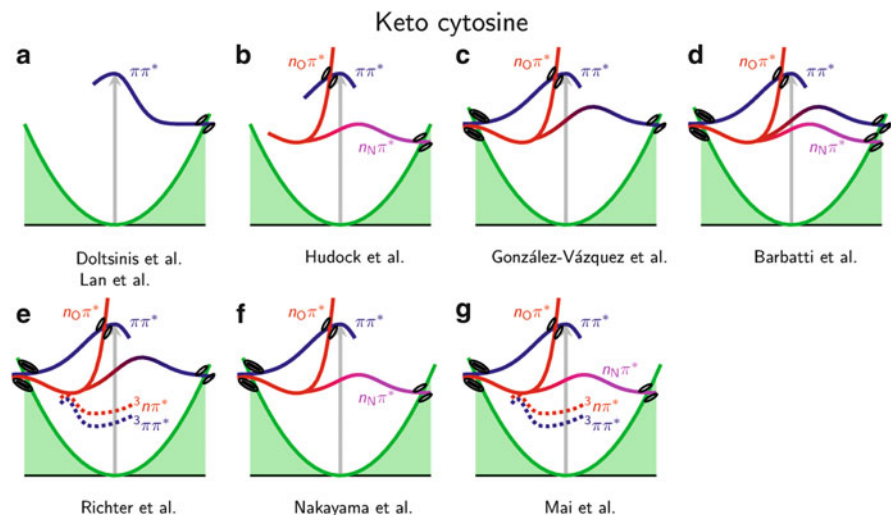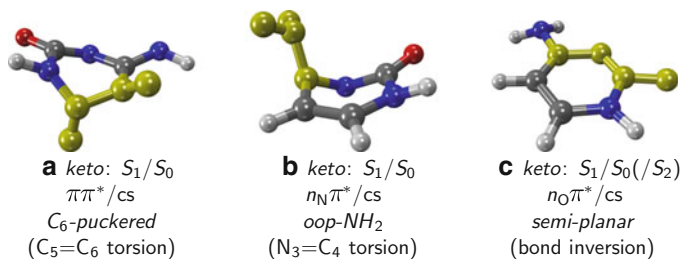
**Fig. 11** Schematic overview of the proposed relaxation mechanisms for keto C from (**a**) [79, 89], (**b**) [88], (**c**) [91], (**d**) [92], (**e**) [93], (**f**) [94], and (**g**) [45]. Note that different reaction coordinates can be implied in the one-dimensional picture

The first dynamics simulation for keto C was reported by the group of Doltsinis [79] in 2008, who employed the TSH methodology coupled to Car–Parrinello dynamics (TSH-CP). The underlying electronic structure calculations were performed with restricted open-shell Kohn–Sham (ROKS) [79] and the BLYP functional and included only the ground and first singlet excited state, which is of $\pi\pi^*$ character. The authors observed a monoexponential 700 fs lifetime of the excited state, in good agreement with the 820 fs transient observed experimentally by Ullrich et al. [61]. For the $S_1$ state no change of character was observed, as the $\pi\pi^*$ state was the only excited state involved in the calculations. The qualitative picture of the dynamics is summarized in Fig. 11a. The main relaxation mechanism involved variations of the $C_5=C_6$ bond length and the $H_5–C_5=C_6–H_6$ dihedral [82], as shown for the so-called $C_6$-puckered CoIn in Fig. 12a.

In the same year, Hudock et al. [88] performed an AIMS study in keto C based on CASSCF(2,2) calculations, also restricted to the ground and the first excited state. This two-state treatment does not allow a description of three-state CoIns, which had been suggested by Matsika and coworkers using quantum chemical calculations [95], but, based on [96], it was argued [88] that these CoIns are energetically inaccessible and therefore two states should suffice to describe the dynamics of C. As a first step in the dynamics, an adiabatic change of character from $\pi\pi^*$ to either $n_N\pi^*$ or $n_O\pi^*$ is predicted within the first 100 fs. Most of the population (65%) relaxed within 1 ps through a CoIn where $n_N\pi^*$ and ground state cross. This CoIn features a strong out-of-plane distortion of the amino group, and hence it is denoted as oop-$NH_2$ CoIn in the following (see Fig. 12b). A smaller number of basis functions also relaxed through the $C_6$-puckered CoIn (Fig. 12a) or

**a** *keto*: $S_1/S_0$
$\pi\pi^*$/cs
$C_6$-puckered
($C_5$=$C_6$ torsion)

**b** *keto*: $S_1/S_0$
$n_N\pi^*$/cs
*oop-NH$_2$*
($N_3$=$C_4$ torsion)

**c** *keto*: $S_1/S_0$(/$S_2$)
$n_O\pi^*$/cs
*semi-planar*
(bond inversion)

**Fig. 12** Geometries of important CoIns of keto C discussed in the text. The labels give the crossing states (adiabatic and state character) and the main geometrical feature. The geometry of the semi-planar CoIn shwon in figure part c is similar to the three-state CoIn mentioned in the text

the semi-planar CoIn (Fig. 12c). The latter CoIn connects the $n_O\pi^*$ with the ground state and shows a bond inversion of the $C_4$=$N_3$–$C_2$=O moiety, with stretching of the $C_4$=$N_3$ and $C_2$=O bonds and compression of the $N_3$–$C_2$ bond. Despite the fact that this study only considered two electronic states, it already reveals that keto C can follow a number of different pathways after excitation. Figure 11b summarizes the most prevalent: the relaxation from $\pi\pi^*$ to the $n_O\pi^*$ state, from which the system changes to the $n_N\pi^*$ character adiabatically (indicated by a color gradient) and later decays to the closed-shell ground state through the $n_N\pi^*$/cs CoIn.

One year later, Lan et al. [89] published a TSH study based on the semiempirical OM2/MRCI electronic structure method, including three electronic states – ground state, $\pi\pi^*$, and $n\pi^*$. For most trajectories the initial state was $S_1$; however, since at the Franck–Condon region both $\pi\pi^*$ and $n\pi^*$ states are very close, for some geometries the bright $\pi\pi^*$ state corresponded to $S_2$, as explained in Sect. 3. They obtained two time constants, $\tau_1 = 40$ fs for the $S_2 \rightarrow S_1$ decay and $\tau_2 = 370$ for the $S_1 \rightarrow S_0$ relaxation. The second time constant is too short – as the authors state – compared to the experimental value of 820 fs [61], but they ascribe the error to the approximations made in the calculations. Interestingly, even though the simulations included both the $\pi\pi^*$ and $n\pi^*$ states, the system exclusively relaxes to the ground state through the $\pi\pi^*$/cs $C_6$-puckered CoIn (Fig. 12a), and the $n\pi^*$ state was not reported to play a major role in the dynamics. Overall, this is a very similar mechanism to the one proposed by Doltsinis et al. [79] (see Fig. 11a), even though the time constants of Doltsinis et al. and Lan et al. differ by a factor of 2.

Alexandrova and coworkers [90] performed TSH simulations based on semiempirical AM1/MRCI(2,2) calculations on several nucleosides and DNA fragments, and also on isolated keto C. While they give time constants of 60–120 fs for cytidine, unfortunately, no time constants are reported for C. In their simulations, most of the trajectories relaxed with an out-of-plane motion of the $C_4$ atom, which might correspond to the oop-NH$_2$ CoIn shown in Fig. 12b. They also observed a very large stretch of the $N_1$–$C_2$ bond at hopping geometries.

Later TSH studies on C were done using CASSCF electronic structure calculations with relatively large active spaces. The first of these studies was carried out by our group [91] using CASSCF(12,9) PEHs, four singlet states, and a total

propagation time of 200 fs. After this time, it was found that 35% of the trajectories of keto C had already returned to the ground state, while 10% were trapped in the $S_2$. The former pathway was assigned as responsible for the fast ($\tau_1$) experimentally observed transients and the latter for the slower transients ($\tau_2$), although no decay constants were calculated because of the short propagation times. These calculations were superseded in later publications [45, 93], but very importantly in this work it was shown that the three-state CoIn reported much earlier by static calculations [95, 96] is a key ingredient in the deactivation pathway of C. At this CoIn the $\pi\pi^*$, $n_O\pi^*$ and ground state intersect. The geometry of this CoIn is comparable to the semi-planar $n_O\pi^*/cs$ CoIn (Fig. 12c), with additional pyramidalization of the $C_6$ atom [95]. The deactivation channel involving the semi-planar CoIn and the nearby three-state CoIn is shown qualitatively on the left side of Fig. 11c. The simulations [91] also found a decay pathway through the $C_6$-puckered CoIn (Fig. 12a), where deactivation was slightly slower than through the semi-planar CoIn. The path to this CoIn is shown on the right side of Fig. 11c.

   The later work of Barbatti et al. [70, 92] on keto C, based on TSH simulations built on CASSCF(14,10) calculations, reports three time constants, $\tau_1 = 9$ fs, $\tau_2 = 527$ fs, and $\tau_3 = 3.08$ ps, as a result of a triexponential fit of the ground state population of the first 1.2 ps. The time constants are in quite good agreement with those reported experimentally in [59, 61]; however, they represent the average over several different relaxation pathways. Similar to González-Vázquez et al. [91], the authors of [70, 92] find that the semi-planar CoIn (Fig. 12c) is the most relevant. During the first 10 fs, 16% of the ensemble returned to the ground state through this CoIn. Also, for later times, the main decay pathway involves the semi-planar CoIn, as indicated on the left side of Fig. 11d. Additional minor pathways involve either a switch to the $n_N\pi^*$ state and a relaxation through the oop-$NH_2$ CoIn (Fig. 12b) or a recrossing to the $\pi\pi^*$ state with subsequent decay through the $C_6$-puckered CoIn (Fig. 12a). Both paths are represented on the right side of Fig. 11d.

   The first study to include triplet states in the dynamics was performed in our group [93] in 2012 using the SHARC methodology. The simulations were done using CASSCF(12,9), as in [91], but propagating for 1 ps. A detailed analysis of the multiple pathways among the adiabatic states is done – most of them with time constants below 100 fs. After 1 ps, 90% of the ensemble returned to the ground state, as in the simulations of Barbatti et al. [92]. The reported hopping geometries also showed similarities with the $C_6$-puckered and semi-planar CoIns (Fig. 12a, c), but not with the oop-$NH_2$ CoIn. In this sense, the radiationless IC pathways involved the $\pi\pi^*$ and $n_O\pi^*$ states, as in our previous study [91]. Accordingly, Fig. 11e is the same for the singlet deactivation as Fig. 11c. However, and very interestingly, the remaining 10% of the ensemble underwent ISC on a sub-picosecond time scale. The doorway state is $S_1(n_O\pi^*)$, which interacts with the $^3\pi\pi^*$ and $^3n\pi^*$ states. According to the CASSCF on-the-fly calculations, ISC was found primarily between the $S_1$ and $T_2$ states. Subsequent triplet IC leads to the $T_1$ minimum, where the trajectories get trapped for the remainder of the simulations. This is also illustrated in Fig. 11e.
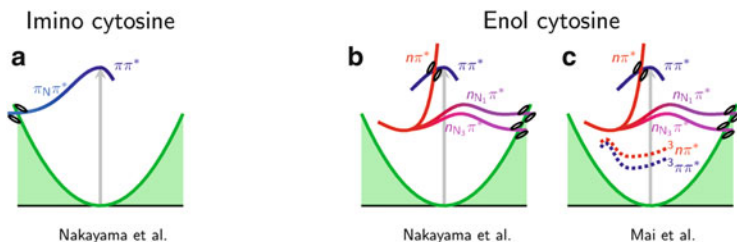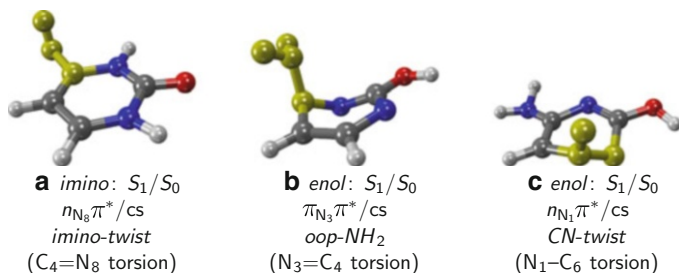
**Fig. 13** Qualitative overview over the proposed relaxation mechanisms for enol and imino C from the studies (**a**, **b**) of Nakayama et al. [94] and (**c**) of Mai et al. [45]

Up to this point, all the papers discussed have been concerned only with the keto form of C. However, as mentioned above, in the gas phase several tautomeric forms coexist, with the keto, enol, and imino tautomers being the most important. Thus, a comprehensive analysis of the reported experiments requires one to study the dynamics of the enol and imino tautomers as well. This fact was recognized in 2013 when two papers covering several tautomers were published [45, 94].

Nakayama et al. [94] performed TSH simulations on the keto, enol, and imino forms of C, taking into account only singlet states. For keto and imino, they used CASSCF(12,9) electronic structure calculations, while, for the enol tautomer, CASSCF(10,8) was employed. They found that the imino tautomer clearly shows the fastest decay of the three tautomers, with all trajectories returning to the ground state in less than 200 fs. The keto form showed a slower relaxation – 85% of the ensemble relaxed within 1 ps, which is comparable to the results obtained by Barbatti et al. [92] and Richter et al. [93]. The slowest decay was observed for the enol form, where only 10% of the population relaxed in the first ps. The assignment of intermediate time constants to keto and long time constants to enol is consistent with the experimental results of Ho et al. [87]. Nakayama et al. [94] showed that each tautomer relaxes through different pathways. The fast relaxation of the imino form is mediated by the rotation of the imino-hydrogen, as shown in Fig. 14a. This process is accompanied by a change of character to $\pi_{N_8}\pi^*$ (see Fig. 13a). Since the hydrogen atom is very light and there is no barrier, the relaxation is extremely efficient. In keto C, the authors find a strong predominance of the route involving the semi-planar CoIn (Fig. 12c), in agreement with similar previous CASSCF studies [91–93]. They also found a small number of trajectories relaxing via $n_N\pi^*$ through the oop-NH$_2$ CoIn, but no relaxation via $\pi\pi^*$ through the C$_6$-puckered CoIn (see Fig. 11f). For the enol form, they found a fast relaxation from the FC region ($\pi\pi^*$) to the $n\pi^*$ minimum. A small number of trajectories relaxed through two CoIns: the first is also of oop-NH$_2$ type (Fig. 14b) and the second is termed CN-twist CoIn, since it involves a puckering of N$_1$ and C$_6$ (Fig. 14c). The initial relaxation to the $n\pi^*$ minimum and the two decay pathways are depicted in Fig. 13b.

The most recent study covering different C tautomers has been conducted by our group [45], including both singlet and triplet states, by means of the SHARC method.

**a** *imino*: $S_1/S_0$
$n_{N_8}\pi^*/cs$
*imino-twist*
($C_4=N_8$ torsion)

**b** *enol*: $S_1/S_0$
$\pi_{N_3}\pi^*/cs$
*oop-NH$_2$*
($N_3=C_4$ torsion)

**c** *enol*: $S_1/S_0$
$n_{N_1}\pi^*/cs$
*CN-twist*
($N_1$–$C_6$ torsion)

**Fig. 14** Geometries of important CoIns of enol and imino C discussed in the text. The labels give the tautomer, crossing states (adiabatic and state character) and the main geometrical feature

The simulations considered the keto and the enol forms of C. For the keto tautomer, time constants of $\tau_1 = 7$ fs and $\tau_2 = 270$ fs were obtained. These time constants included both decay paths to the $S_0$ ground state and the deactivation into the $T_1$ minimum, explaining the smaller time constants compared to the other CASSCF dynamics simulations [91, 92]. For enol, a long time constant of 1,900 fs was found, which can be assigned to $\tau_3$. In the enol form, ISC was observed with very low efficiency and hence no time constant related to ISC was stated. The IC pathways of keto C were basically the same as in the study by Nakayama et al. [94]. The most important CoIn was the semi-planar one (Fig. 12c), but the oop-NH$_2$ CoIn (Fig. 12b) also played a significant role. In contrast, the $C_6$-puckered CoIn was unimportant in the dynamics. The ISC pathways are in general agreement with the ones previously calculated by Richter et al. [93]. The $S_1(n_O\pi^*)$ state is the precursor of the triplet states and ISC takes place mainly to the $T_2$ ($^3n\pi^*$) state, with higher efficiency when $T_1$ and $T_2$ are very close and mix. This mixing increases the otherwise small spin-orbit couplings between $S_1$ and $T_2$. The IC and ISC pathways are shown schematically in Fig. 11g. For enol, the dynamics observed is similar to that reported by Nakayama et al. [94]. However, Mai et al. found that the CN-twist CoIn (Fig. 14c) is the major relaxation funnel while the oop-NH$_2$ CoIn (Fig. 14b) plays a secondary role. Additionally, we found a rapid $\pi\pi^* \to n\pi^*$ transition with a time constant of 40 fs. ISC in the enol form was found to be much slower than in the keto tautomer, since the singlet-triplet gaps were larger. Additionally, SOCs in the enol form were considerably smaller than in the keto due to the protonation of the oxygen atom.

### 4.3.3 Final Discussion

Based on the considerable body of dynamical studies on C, the experimentally observed time constants can be assigned as follows.

The imino tautomer decays fastest according to Nakayama et al. [94]. CASSCF dynamics found a barrierless deactivation path involving the torsion of the imino group. The more accurate CASPT2 predicts the same path, lending high credibility

to the results concerning the imino form. Thus, at least part of the fastest time constants ($\tau_1$) obtained in the gas phase experiment could be explained by the decay of imino C, while this tautomer should not contribute to $\tau_2$ and $\tau_3$.

The enol form shows the slowest decay. Thus, it is tempting to assign the slowest experimental time constants to this tautomer. Indeed, the experiments of Kosma et al. [86] and Ho et al. [87] give evidence that the slowest transient vanishes for excitation wavelengths above 280 nm. Above this wavelength, the enol tautomer is no longer excited, explaining the vanishing transient. Additionally, 1-methyl-cytosine [87] – which does not possess the enol form – also does not show a slow transient, reinforcing the idea that the enol tautomer contributes to $\tau_3$. However, as pointed out by Nakayama et al. [94], the decay mechanism found in the dynamical studies is debatable, since CASSCF dynamics predicts decay via the oop-NH$_2$ CoIn (Fig. 14b) but static CASPT2 calculations show a rather high barrier for this CoIn. Instead, CASPT2 [94] favors decay through a CoIn analogue to the C$_6$-puckered CoIn of the keto form (Fig. 12a). Dynamics simulations based on CASPT2 electronic properties would be required to confirm this hypothesis. The simulations on this tautomer also show a fast component which might also contribute to $\tau_1$. Indeed, unpublished experimental work focusing on the transients of fragment ions specific to the enol tautomer found a transient on the 10 fs time scale (Weinacht TC (2013). Private communication).

Finally, according to all the dynamics simulations performed, it seems clear that the keto form is responsible for the intermediate $\tau_2$ time constant, although it also contributes to $\tau_1$. It is unclear whether the keto form also contributes to the $\tau_3$ transient. Interestingly, although most dynamical studies predict qualitatively correct time constants, the proposed mechanistic details differ dramatically – illustrating the importance of the choice of the level of theory. The mechanisms proposed are clearly grouped according to the electronic structure method used. The dynamical studies based on CASSCF employing relatively large active spaces [45, 91–94] predicted the semi-planar CoIn to be the most important pathway for ground state relaxation, while those based on OM2/MRCI [89] or ROKS/BLYP [79] favored the C$_6$-puckered CoIn. Indeed, high-level static investigations [94, 97, 98] also predict the C$_6$-puckered CoIn to be responsible for the fast decay of keto C. Since this CoIn involves changes at the C$_5$ and C$_6$ (recall Fig. 12a), substitution at C$_5$ should modify the time scales. Indeed, experiments carried out with 5-substituted cytosine derivates [4] show sensitivity of excited-state lifetimes, confirming the role of this CoIn in the deactivation of the keto form.

In addition to the deactivation pathways in the singlet manifold, the studies based on SHARC [45, 93] showed that ISC from the singlet to the triplet states is of ultrafast nature and contributes to $\tau_2$. This illustrates that $\tau_2$ is actually an average of a number of processes, including ground state relaxation via multiple pathways and ISC. Following ISC, the population gets trapped in the lowest triplet state and ISC from $T_1$ to $S_0$ then provides an explanation for the nanosecond transient observed by Nir et al. [99]. One should note that the proposed ISC mechanism found in the dynamics [45, 93] differs from the mechanism given by static calculations [100, 101]. While the static approach predicted the $^1\pi\pi^*$ state to be the precursor of

the triplet states, the dynamics showed instead that $^1n\pi^*$ might be the doorway state. Experimentally [4], there is evidence for ISC originating from $^1n\pi^*$. The main argument is that the $^1\pi\pi^*$ population decays too quickly to the ground state for ISC to occur from $^1\pi\pi^*$ [102].

## 4.4 Thymine

Like C, T is a pyrimidine derivative. In Watson–Crick pairs it is found attached to A. In RNA it is substituted by U, which is structurally similar, but lacks the methyl group in the 5-position. Although T can also exist in either keto (lactam) or enol (lactim) forms, the keto is the most stable and predominates both in the gas phase and in solution; therefore, here T always refers to the keto form.

From the dynamical point of view, T is believed to be the nucleobase with the slowest relaxation upon photoexcitation [59, 62].

### 4.4.1 Experimental Observations

Table 7 collects all the experimentally observed gas phase time scales. Up to four different time scales have been reported in T. Several studies [59, 61, 62, 105] report a time constants of several picoseconds (5–7 ps). In others [61, 62, 105] additional shorter time constants in the sub-picosecond region are found in the excited-state decay of T. Kang et al. [59] and Samoylova et al. [105] also observed a weak component in the 100 ps [59] or nanosecond [105] region. This is supported by He and coworkers [103, 104], who found a 22 ns decay.

### 4.4.2 Deactivation Mechanism

Table 8 collects all the excited-state dynamical studies performed in T in the gas phase and Fig. 15 summarizes the proposed mechanisms.

The first dynamics simulation on T was reported by Hudock et al. [46] in 2007. Their simulations employed the FMS methodology, coupled to CASSCF(8,6) calculations. This is one of the few papers where an effort is made to make an explicit connection to the experimental results by simulating a time-resolved photoelectron spectrum. The authors reported that, during the first 500 fs, the system relaxes from the FC region to an $S_2$ minimum. Based on their simulations the authors stated that the shortest time constant in the experiment ($\tau_1$) might be connected to the time the system takes to arrive at the minimum. Even though the study did not extend beyond 500 fs simulation time, they suggested that the experimentally observed picosecond decay might be related to $S_2 \rightarrow S_1$ transfer. The $S_2$ minimum was characterized by a stretching of the $C_5=C_6$ and $C_4=O_4$ bonds, relative to the FC geometry, and by pyramidalization of the $C_6$ atom (see Fig. 1 for

**Table 7** Experimentally observed decay times of T

| $\lambda_{pump}$ (nm) | $\lambda_{probe}$ (nm) | $\tau_1$ (fs) | $\tau_2$ (fs) | $\tau_3$ (ps) | $\tau_4$ (ns) | References | Year |
|---|---|---|---|---|---|---|---|
| Setup | | Time constants | | | | | |
| 267 | $n \times 800$ | | | 6.4 | >0.1 | Kang et al. [59] | 2002 |
| 250 | 200 | <50 | 490 | 6.4 | | Ullrich et al. [61] | 2004 |
| 267 | $2 \times 400$ | 105 | | 5.12 | | Canuel et al. [62] | 2005 |
| 250 | 220 | | | | 22 | He et al. [103, 104] | 2003, 2004 |
| 250 | 220 | 100 | | 7 | >1 | Samoylova et al. [105] | 2008 |

**Table 8** Overview over excited-state nuclear dynamics studies for isolated T in the gas phase

| Dyn. | El. Struct. | $\tau_1$ (fs) | $\tau_2$ (fs) | $\tau_3$ (ps) | References | Year |
|---|---|---|---|---|---|---|
| Methodology | | Time constants | | | | |
| FMS | CASSCF(8,6) | √ | | | Hudock et al. [46] | 2007 |
| TSH | OM2/MRCI | 17 | 420 | | Lan et al. [89] | 2009 |
| TSH | CASSCF(10,8) | 100 | | 2.6 | Szymczak et al. [106] | 2009 |
| | | | | | Barbatti et al. [70] | 2010 |
| TSH | CASSCF(8,6) | √ | | √ | Asturiol et al. [107] | 2009 |
| vMCG[b] | CASSCF(8,6) | | | | Asturiol et al. [108] | 2010 |
| TSH | AM1/CI(2,2) | | | | Alexandrova et al. [90] | 2010 |
| 3d-QD | TDDFT/PBE0 | √ | | | Picconi et al. [109] | 2011 |
| MCTDH, | HLVC model[a] | √ | | | Picconi et al. [109] | 2011 |
| TSH | CASPT2(2,2) | | 400 | | Nakayama et al. [110] | 2013 |

Time constants reported in the papers are given; a checkmark indicates that the authors discussed processes on these time scales without giving explicit values (classification: $\tau_1$ below 100 fs, $\tau_2$ below 1 ps, $\tau_3$ above 1 ps)

[a]Harmonic linear vibronic coupling

[b]Variational multi-configurational Gaussians (an MCTDH variant)

atom numbering). The geometry of the minimum is qualitatively depicted in Fig. 16a. A summary of the reported pathways is given schematically in Fig. 15a.

In their 2009 study based on TSH and the semi-empirical OM2/MRCI method, Lan et al. [89] observed a very fast $S_2 \rightarrow S_1$ decay (17 fs) and a slower $S_1 \rightarrow S_0$ one (420 fs), which correspond to $\tau_1$ and $\tau_2$, respectively. The slower time constant fits well with the 490 fs time constant of [61]. No explanation was offered, however, for the 5–7 ps time constants observed in many of the experimental studies [59, 62, 105]. The two relaxation paths are described as follows; see Fig. 15b. The fast relaxation of $S_2(\pi\pi^*)$ through a CoIn to $S_1$ operates via a planar geometry, which differs only slightly from the $S_2$ minimum (Fig. 16a) with a bond inversion of the $C_6=C_5-C_4=O_4$ moiety. The second and slower relaxation step is mediated by two different CoIns. In the major path, after the hop to $S_1$, the system changes to $n\pi^*$ character, which induces strong out-of-plane motion of the $O_4$ atom. This motion led to the oop-$O_4$ CoIn (Fig. 16b), which connects the $n\pi^*$ state with the ground state. A smaller number of trajectories (19%) relaxed via the direct $\pi\pi^* \rightarrow GS$ path, without intermediate change to $n\pi^*$ character. These trajectories decay via another
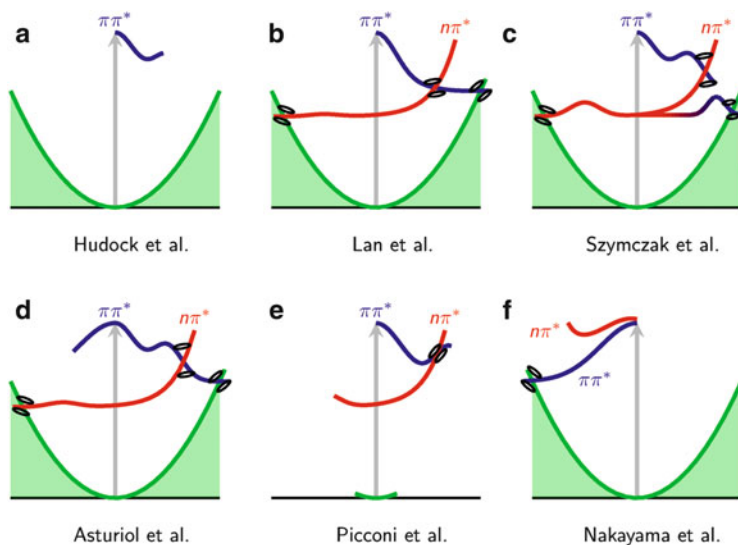
**Fig. 15** Qualitative overview over the proposed relaxation mechanisms for T from the studies (**a**) [46], (**b**) [89], (**c**) [106], (**d**) [107], (**e**) [109], and (**f**) [110]



**a** $S_2$ minimum
$\pi\pi^*$
(bond inversion and
$C_6$ pyramidalization)

**b** $S_1/S_0$
$n\pi^*/cs$
oop-$O_4$
($C_4$ pyramidalization)

**c** $S_1/S_0$
$\pi\pi^*/cs$
oop-$CH_3$
($C_5=C_6$ torsion)

**d** $S_2/S_1$
$\pi\pi^*/n\pi^*$
($C_6$ puckering and
short $C_4=O_4$)
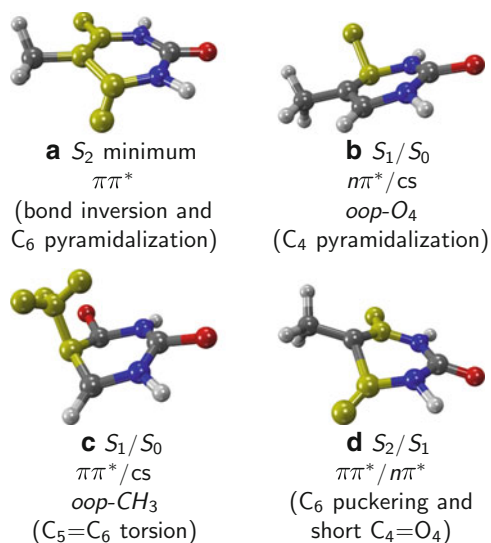
**Fig. 16** Geometries of important CoIns and minima of T discussed in the text. The labels give the crossing states (adiabatic and state character) and the main geometrical feature

CoIn, characterized by a strong out-of-plane displacement of the methyl group (Fig. 16c).

In the same year, Szymczak et al. [70, 106] performed TSH simulations based on CASSCF(10,8). As in the study of Hudock et al. [46], here the slow relaxation of T is found to be primarily related to the trapping of the system in the minimum of the $S_2$ state ($\pi_O\pi^*$ character). Two time constants were reported [106]: $\tau_1 = 100$ fs, attributed to the initial fast relaxation from the FC region to the $S_2$ minimum, and $\tau_2 = 2.6$ ps for the $S_2 \rightarrow S_1$ decay. Also in agreement with Hudock et al. [46], they described the $S_2$ minimum geometry with bond inversion of the $C_6 = C_5 - C_4 = O_4$ moiety (Fig. 15a). Because the barrier separating the $S_2$ minimum and the $S_2/S_1$ CoIn is rather high at the CASSCF level of theory, IC to $S_1$ is slow. Only after the system surmounts the barrier does IC quickly proceed to $S_1$. The $S_2/S_1$ CoIn (crossing of $\pi\pi^*$ and $n\pi^*$) is characterized by a shortening of the $C_4 = O_4$ bond and puckering of $C_6$ (Fig. 16d). After the IC process, the system further relaxes towards the $n\pi^*$ region of the PEH, and is possibly trapped again before ground state relaxation can take place. Consequently, only a small number of trajectories relaxed to the ground state within 3 ps. The additional slow step $S_1 \rightarrow S_0$ could explain the discrepancy between the simulated time constant of 2.6 ps and the experimental 5–7 ps time constants. Szymczak et al. reported that ground state relaxation could involve either the $\pi\pi^*/S_0$ or $n\pi^*/S_0$ crossing regions, but they did not discuss the geometries involved, so that a connection to the geometries discussed above is not possible. The deactivation paths proposed by Szymczak et al. [106] are summarized in Fig. 15c: trapping in the $\pi\pi^*$ minimum, transfer to $n\pi^*$, and ground state relaxation involving high barriers.

Asturiol et al. [107, 108] found two deactivation paths based on their TSH dynamics employing CASSCF energies. Since at the CASSCF level of theory the $S_2$ $\pi\pi^*$ minimum is separated from the CoIn by a barrier (which is not present at CASPT2 level [107]), they started the trajectories instead at the transition state between the minimum and the CoIn. Hence, their simulation does not include the initial trapping observed by Hudock et al. [46] and Szymczak et al. [106]. After going through the $S_2/S_1$ CoIn within 60 fs, the ensemble splits up, with some population continuing towards the $\pi\pi^*/S_0$ CoIn (oop-CH$_3$, Fig. 16c), and some going to the $n\pi^*$ state, finally reaching the $n\pi^*/S_0$ CoIn after some time. The latter CoIn was characterized by a long $C_4 = O_4$ bond, but no pyramidalization of the $C_4$ atom was mentioned. These results are shown schematically in Fig. 15d. They also noted that, at CASPT2 level of theory, there should be an additional, direct path from the FC region to the oop-CH$_3$ CoIn (without trapping in the $S_2$ minimum), which is not well described with CASSCF. On these grounds they proposed that the fast decay components ($\tau_1$ or $\tau_2$) are due to the direct path and the slow component ($\tau_3$) is due to the indirect path which involves $S_2$ trapping.

The second study by Asturiol et al. [108] strives to characterize the $S_1/S_2$ CoIn seam in order to investigate the efficiency of entering the $n\pi^*$ state coming from the $\pi\pi^*$ state. Using the variational multi-configurational Gaussians method in 39 DOFs (also based on CASSCF energies), they analyzed the intersection seam of $S_1$ and $S_2$ at regions of different topology. There is a region where the CoIn shows a peaked topology and the $\pi\pi^*$ character is preserved when passing the CoIn, and there is a region with a sloped topology allowing population transfer to $n\pi^*$.

Depending on the initial momentum when approaching the seam, either region can be entered, leading to different photophysical products.

In 2010, another TSH study based on AM1/CI(2,2) semiempirical calculations was published by Alexandrova et al. [90]. As with C, no time constants for isolated T were provided as they focused primarily on nucleosides. For thymidine, the times constants calculated are between 30 and 110 fs. They reported that the relaxation mechanism of T is dominated by ring puckering paths, with puckering at $C_4$ being the most important mechanism.

The work by Picconi et al. [109] focused exclusively on the $\pi\pi^* \rightarrow n\pi^*$ relaxation path (see Fig. 15e). They conducted two types of simulations, the first being a QD study in three dimensions, with PEHs based on TD-DFT with the PBE0 functional. Within this reduced-dimensionality model, the $n\pi^*$ state was already populated within the first 50 fs, in contrast to the findings of Hudock et al. [46], Szymczak et al. [106], and Asturiol et al. [107]. The second simulation of Picconi et al. [109] employed the MCTDH method. The PEHs were calculated with the harmonic linear vibronic coupling model [111] fitted to TD-DFT energies. These calculations agreed with the 50 fs transfer to the $n\pi^*$ state found in the QD simulations. The authors explained the faster $\pi\pi^* \rightarrow n\pi^*$ transfer as compared to the CASSCF-based dynamical studies with the smaller $n\pi^* - \pi\pi^*$ energy gap predicted by TD-DFT.

The most recent dynamics study on T has been performed by Nakayama et al. [110] in 2013. In this paper they reported the first dynamics based on accurate CASPT2 energies and gradients for a nucleobase, although with a small CAS(2,2) active space. To assess the quality of the CASPT2(2,2) calculations, every 50 fs the energies at the current geometry were recalculated with CASPT2(12,9). These calculations showed that the $n\pi^*$ state is above the $\pi\pi^*$ state throughout the simulation. Moreover, NACs were not included in the simulation, so the authors were only able to follow the dynamics on the $\pi\pi^*$ state until the system reached the $\pi\pi^*/S_0$ interaction region, without the possibility of actually hopping to the ground state surface. Interestingly, these calculations showed that in the gas phase the system is not trapped in the $\pi\pi^*$ state, since at CASPT2 level the $\pi\pi^*$ state does not exhibit a minimum. Instead (see Fig. 15f), the trajectories directly reach the $\pi\pi^*/S_0$ CoIn (oop-CH$_3$, Fig. 16c) after an average of 400 fs. Because the calculations did not include NACs, this time should be considered only a lower bound on the decay time constant (the trajectories could "miss" a hop and stay on the $S_1$ PEH for a longer time). It should also be noted that, because the simulation included only 10 trajectories and the active space is not flexible enough, it is uncertain whether additional CoIns could be involved in the excited-state dynamics of T.

### 4.4.3   Final Discussion

In T, much of the theoretical effort involving dynamics simulations has been devoted to studying the interplay of the excited $\pi\pi^*$ and $n\pi^*$ states. The available studies can be classified in two groups, depending whether the $S_2$ minimum is

involved or not. The first group includes all CASSCF-based dynamics studies [46, 106, 107], where trajectories quickly relax to the $S_2$ $\pi\pi^*$ minimum and get trapped for a considerable amount of time. After leaving the minimum well, the trajectories proceed to the $n\pi^*$ state, from where they eventually decay to the ground state [106]. In the second group [89, 109, 110], photoexcited T does not get trapped in the $\pi\pi^*$ minimum. However, none of the latter dynamics simulations provide an explanation for the experimentally observed 5–7 ps time constant ($\tau_3$). By combining the findings of dynamics and CASPT2 static calculations, Asturiol et al. [107] proposed that the biexponential decay could be explained by the bifurcation of the ensemble into a fast, direct relaxation path on the $\pi\pi^*$ state towards the oop-$CH_3$ CoIn and a slower, indirect path involving the $n\pi^*$ state.

A conclusive description of the excited-state dynamics thus might necessitate large-scale dynamics simulations based on highly accurate PEHs, e.g., from CASPT2 or MRCI calculations. The study by Nakayama et al. [110] is already a step in this direction, but the low number of trajectories and the restriction to two states and a small active space did not allow for complete elucidation of the dynamics of T.

## 4.5   Uracil

U is found in RNA exclusively. It is a pyrimidine derivative that forms Watson–Crick pairs with A. In DNA it is replaced by the closely related 5-methyl-U, or T. From the 13 different tautomers possible in U, the di-keto tautomer is the dominant form in the gas phase and in solution [112] and hence only this form will be discussed henceforth.

### 4.5.1   Experimental Observations

Table 9 collects experimental studies dealing with the relaxation of photoexcited U and the obtained decay times in the gas phase. While the early experiments of Kang et al. [59] only found a monoexponential decay of the excited population with a time constant of 2.4 ps, additional time constants were obtained later with the advent of better time resolution. In particular, and very similar to the other nucleobases, a very short transient ($\tau_1$) is found with constants between 50 and 130 fs. The study of Ullrich et al. [61] reported three transients for U; however, most experiments agree on a biexponential decay behavior. The recent experiments of Kotur et al. [65] and Matsika et al. [113] combine TOF-MS with strong-field ionization and thus can obtain insights into the differences of U and its fragments, most importantly the fragment with a mass/charge ratio of 69. By comparing the parent ion signal and the $m/Z = 69$ signal, they are able to disentangle different decay mechanisms.

**Table 9** Experimentally observed decay times of U

| Remark | Setup | | Time constants | | | References | Year |
|---|---|---|---|---|---|---|---|
| | $\lambda_{pump}$ (nm) | $\lambda_{probe}$ (nm) | $\tau_1$ (fs) | $\tau_2$ (fs) | $\tau_3$ (ps) | | |
| | 267 | $n \times 800$ | | | 2.4 | Kang et al. [59] | 2002 |
| | 250 | 200 | $<50$ | 530 | 2.4 | Ullrich et al. [61] | 2004 |
| | 267 | $2 \times 400$ | 130 | | 1.05 | Canuel et al. [62] | 2005 |
| | 262 | $n \times 780$ | 70 | | 2.15 | Kotur et al. [65] | 2012 |
| $m/z = 69$ | 262 | $n \times 780$ | 90 | | 3.21 | Kotur et al. [65] | 2012 |
| | 262 | $n \times 780$ | 70 | | 2.4 | Matsika et al. [113] | 2013 |
| $m/z = 69$ | 262 | $n \times 780$ | 90 | | 2.6 | Matsika et al. [113] | 2013 |

**Table 10** Excited-state nuclear dynamics studies for isolated U in the gas phase

| Methodology | | Time constants | | | References | Year |
|---|---|---|---|---|---|---|
| Dyn. | El. Struct. | $\tau_1$ (fs) | $\tau_2$ (fs) | $\tau_3$ (ps) | | |
| FMS | CASSCF(8,6) | √ | | | Hudock et al. [46] | 2007 |
| TSH-CP | ROKS/BLYP | | 551–608 | | Doltsinis et al. [79] | 2008 |
| | | | | | Nieber et al. [114] | 2008 |
| TSH | OM2/MRCI | 21 | 570 | | Lan et al. [89] | 2009 |
| TSH | CASSCF(10,8) | | 650–740 | 1.5–1.8 | Barbatti et al. [70] | 2010 |
| | | | | | Nachtigallova et al. [115] | 2011 |
| TSH | CASSCF(14,10) | √ | √ | | Fingerhut et al. [28] | 2013 |
| TSH | CASSCF(14,10) | √ | | √ | Richter et al. (2014) Unpublished | 2014 |

Time constants correspond to those given in the respective papers, classified as $\tau_1$ below 100 fs, $\tau_2$ below 1 ps, and $\tau_3$ above 1 ps. A checkmark indicates that the authors discussed processes on these time scales without giving explicit values

### 4.5.2 Deactivation Mechanism

Table 10 collects all the excited-state dynamical studies performed in U in the gas phase and Fig. 1 summarizes the proposed mechanisms.

The first dynamical study intending to understand the deactivation mechanism of U was carried out by Hudock et al. [46] by means of FMS simulations based on CASSCF(8,6) wavefunctions. Very similar to the case of T, after excitation U gets trapped in the $S_2$ minimum (see Fig. 17a). This relaxation pathway is accompanied by an increase of the $C_5=C_6$ bond length and a pyramidalization of the $C_6$ atom due to $sp^3$ hybridization. In their study they conclude that the ultrafast component $\tau_1$ found in the experiments is neither due to internal conversion via CoIns nor due to a change of character of the excited state. Instead, it is caused by an increase of energy of the ionic states while the system relaxes in the $S_2$, thus making ionization of the excited population less probable. The picosecond time constant is suggested to be caused by the subsequent barrier crossing from the $S_2$ minimum to a $S_2/S_1$ CoIn and further relaxation. However, the simulation time of 500 fs was too short to see a significant relaxation from the $S_2$ minimum.

One year later, Nieber, Doltsinis and coworkers [79, 114] reported a study using TSH coupled to Car–Parrinello dynamics (TSH-CP) on PEHs calculated with the
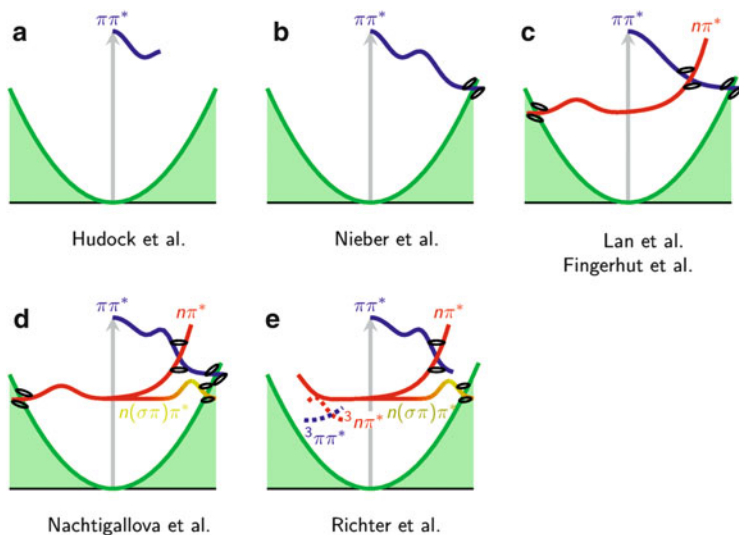
**Fig. 17** Schematic overview of the proposed relaxation mechanisms for U from (**a**) [46], (**b**) [114], (**c**) [89, 116], (**d**) [115], and (**e**) (Richter et al. (2014), unpublished). Note that different reaction coordinates can be implied in the one-dimensional picture

ROKS/BLYP approach. Their simulations find a sub-picosecond decay back to the ground state, driven only by $\pi\pi*/cs$ interactions with no other electronic states involved (see Fig. 17b). Although they could not reproduce the fast component below 100 fs, they assign this time constant to the initial relaxation from the FC region. They find a monoexponential decay of the excited state population with $\tau_2 = 608$ fs with non-zero initial velocities ($T = 300$ K). Reducing the initial velocities of the trajectories to zero ($T = 0$ K) seemed to accelerate the relaxation process to the ground state. Regardless of the initial velocities, the deactivation dynamics is driven by changes in the H–$C_5$=$C_6$–H dihedral angle as well as the $C_5$=$C_6$ and $C_4$–$C_5$ bond lengths, which give rise to the so-called ethylenic CoIn (see Fig. 18a).

The OM2/MRCI simulations of Lan et al. [89] from 2009 find two different relaxation mechanisms depicted in Fig. 17c. The first path directly connects the bright $\pi\pi*$ state with the ground state via the ethylenic CoIn, characterized by a strong out-of-plane motion of the $H_5$ atom; see Fig. 18a. The calculated decay time constant for this path is 21 fs. In the second, slower pathway, the initially excited $\pi\pi*$ population changes within 70 fs to a lower-lying $n\pi*$ state via a planar $S_2/S_1$ CoIn that is located close to the FC region. The trajectories spend some time in the $n\pi*$ state until finally reaching an $S_1/S_0$ CoIn, which was characterized by the authors by a strong out-of-plane motion of the $O_4$ atom (Fig. 18b). For this pathway the decay time constant was reported as 570 fs.

The TSH simulations at the CASSCF(10,8) level of theory, including three states, reported by Barbatti et al. [70], and later in more detail by Nachtigallova et al. [115] find multiple CoIns and three different deactivation pathways,

**a** $S_1/S_0$
$\pi\pi^*/cs$
*Ethylenic*
($C_5=C_6$ torsion)

**b** $S_1/S_0$
$n\pi^*/cs$
*oop-$O_4$*
($C_4$ pyramidalization)

**c** $S_1/S_0$
$\sigma\pi^*/cs$
*ring-opening*
($N_3$-$C_4$ cleavage)

**d** $S_1/S_0$
$n\pi^*/(\pi\pi^* + cs)$
*Ethylenic&oop-$O_4$*
($C_4$ pyramidalization
and $C_5=C_6$ torsion)
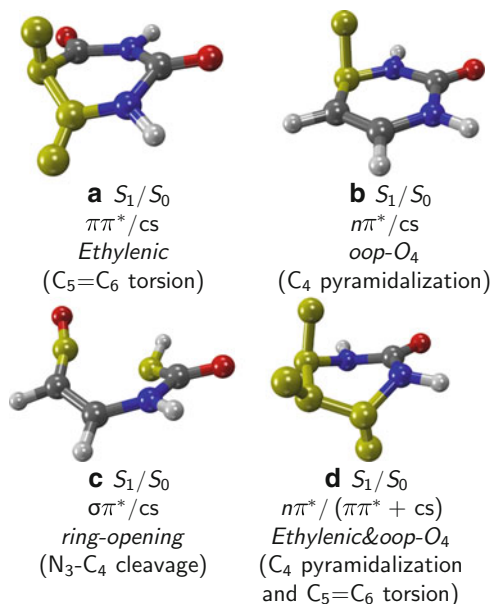
summarized in Fig. 17d. The first path agrees with the previous studies: it is found
that the fastest decay does not involve a state of another character apart from the
initially excited $\pi\pi^*$ state. After initial trapping in the $S_2$ minimum, the trajectories
proceed to a $\pi\pi^*/cs$ CoIn characterized by a twist of the $C_5=C_6$ bond, as shown in
Fig. 18a. Interestingly, this path is not observed in a comparable study made on T
[106], even though T and U have very similar PEHs and one could expect a very
similar dynamics. The authors [70, 115] argue that the efficiency of the direct
$\pi\pi^* \rightarrow S_0$ path in T is significantly reduced due to the heavy mass of the methyl
group. The second pathway found in U is also not observed in T. It involves
admixing of $n\pi^*$ character into the wavefunction, weakening the $N_3$–$C_4$ bond to
the point of breaking. The involved CoIn, termed ring-opening CoIn and depicted in
Fig. 18c, leads to the destabilization of the ground state as the ring breaks. In their
study it is stated that the $S_1$ wavefunction contains contributions of $\sigma$ orbitals, which
was described as $\sigma(n-\pi)\pi^*$ wavefunction character. The authors also noted this
pathway would probably lead to other photochemical products. Interestingly,
Buschhaus et al. [117] indeed observe ring opening after UV irradiation of nucle-
osides, although the detected isocyanates (R–N=C=O) cannot arise directly from
the $N_3$–$C_4$ bond cleavage predicted by Nachtigallova et al. [115]. The third deac-
tivation pathway described involves a change of character to $n\pi^*$ after initial
trapping and relaxation through the $S_2/S_1$ CoIn. The system gets trapped again in
the $n\pi^*$ minimum, delaying ground state relaxation. A distinction between $\pi\pi^*$
trapping and $n\pi^*$ trapping was reported, based on the significantly different $C_5$–$C_6$
bond lengths of the $\pi\pi^*$ and $n\pi^*$ minima. Two CoIns of $n\pi^*/cs$ character were
discussed. One involves an out-of-plane motion of the $O_4$ atom (see Fig. 18b), as

already reported by Lan et al. [89]. The second CoIn [70, 115] showed a combination of $C_5=C_6$ torsion and out-of-plane motion of the $O_4$ atom (see Fig. 18d), resulting in a mixed $n\pi^*/(\pi\pi^* + cs)$ character. A dependence of the decay times on the initial energy – corresponding to the excitation wavelengths – was also investigated by selecting trajectories with high (250 nm) and low (267 nm) initial energies. In both cases, a biexponential decay was observed with time constants of 650 fs and >1.5 ps for the high energy and 740 fs and >1.8 ps for the low energy trajectories. Here, higher excitation energies reduce the efficiency of trapping in the different excited-state minima, leading to a faster decay to the ground state.

The recent TSH simulations of Fingerhut et al. [116] are based on CASSCF (14,10) wavefunctions. At this level of theory, the two mechanisms described by Lan et al. [89] with semiempirical-based dynamics (see Fig. 17c) are found again. First, the initially populated $S_2$ state of $\pi\pi^*$ character decays to the $S_1$ ($n\pi^*$) state, which gains more than 20% of population within less than 100 fs. In the $n\pi^*$ state, trapping of the population before decay to the ground state can occur, leading to long relaxation times. Interestingly, this study shows much less pronounced trapping in the $S_2$ state than reported by Nachtigallova et al. [115], even though both studies use CASSCF. Fingerhut et al. [116] explained this to be an effect of the increased active space size. A second pathway involves the change to $S_1$ without changing the states character and subsequent $\pi\pi^* \rightarrow S_0$ relaxation through the ethylenic CoIn (Fig. 18a). In their simulations, all trajectories that reached the ground state within 1 ps followed the second pathway and only a few trajectories relaxed via the first pathway in longer runs of up to 2 ps.

TSH simulations performed in our group (Richter et al. (2014), unpublished) at the same CASSCF(14,10) level of theory, but including triplet states, show that after 1 ps a significant fraction of the population remains in the $S_2$ ($\pi\pi^*$) state. The relaxation process can be characterized by a biexponential decay. A fast component $\tau_1$ is attributed to the change of state character from the initially excited $\pi\pi^*$. The slower constant $\tau_3$ arises from ISC, directly competing with IC processes. The precursor for ISC was identified as the $S_1$ state, where population is trapped for a sufficiently long time to allow ISC to take place. In contrast to [116],within the first ps of the simulation only a very small number of trajectories relaxed to the ground state, showing that ground state relaxation might be quenched by ISC. Ground state relaxation is mediated by the ring-opening path previously observed by Nachtigallova et al. [115].

### 4.5.3   Final Discussion

As in the other nucleobases, most experimental studies report a very fast time constant $\tau_1$ and two longer time scales ($\tau_2$ and $\tau_3$). Based on the theoretical investigations, the fastest constant $\tau_1$ can be assigned to initial relaxation from the FC region, accompanied by a change of the wavefunction character and an increase in the ionization potential [46].

The slower transient ($\tau_2$) has been explained by ground state relaxation, according to dynamics based on ROKS/BLYP [79] or OM2/MRCI [89]. CASSCF-based dynamics [70, 115] (Richter et al. (2014), unpublished) additionally predict even slower processes ($\tau_3$) due to trapping in $S_2$ or $S_1$. The latter studies note that part of the population achieves a fast and direct decay to the ground state – accounting for $\tau_2$ – while the remaining fraction of the population causes $\tau_3$. The fact that CASSCF does predict a $\tau_3$ decay – while the other methods do not – emphasizes that the outcome of the dynamics is very sensitive to the electronic structure level of theory.

Due to their very similar molecular structure, T and U exhibit comparable excited-state PEHs and thus share some features of the observed dynamics. Studies reporting dynamics simulations of T and U using the same method [46, 70, 89] observe very similar dynamics in both nucleobases. In most of the studies, either the ethylenic CoIn (in T this is the oop-$CH_3$ CoIn) or the oop-$O_4$ CoIn is responsible for the ground state decay. However, it appears that the methyl group which is present in T but not in U might be responsible for the accelerated relaxation dynamics of U. While the ethylenic CoIn in U can be easily reached by torsion of the $C_5=C_6$ bond, in T this necessitates the rotation of the bulky methyl group out of the molecular plane.

# 5   Conclusions and Outlook

Upon UV excitation, the five nucleobases A, G, C, T, and U show ultrafast relaxation from the lowest bright $\pi\pi^*$ state to the ground state. This contribution has reviewed the dynamical behavior that accompanies this process from a dynamical perspective in an effort to interpret the time-resolved spectroscopic experiments from the last decade. While there is an enormous amount of static computations devoted to calculate excited states, potential energy surfaces, and conical intersections of the five molecules, the application of molecular dynamics to nucleobases took off only in 2007. In this chapter we have reviewed 28 publications which report a total of 35 distinct dynamics simulations. C and T are the bases with the largest number of papers and simulations reported. This fits with the fact that these bases have the slowest and most complex excited-state dynamics. U, which shows a dynamics similar to T has almost as many publications as C or T. The purine bases A and G have a smaller number of publications. For G, only four dynamics simulations have been reported in five papers, but G is also the nucleobase with the fastest and simplest dynamics. The number of simulations for A is relatively large, taking into account that [71] contains a comparative investigation using MRCIS, OM2/MRCI, and TDDFT with six different functionals.

Figure 19a gives the number of simulations performed in each nucleobase. From Fig. 19b it is obvious that TSH (including variants like SHARC or TSH-CPMD) is by far the most popular approach for nuclear dynamics simulations, accounting for 80% of all simulations. In Fig. 19c it is possible to appreciate that the most popular
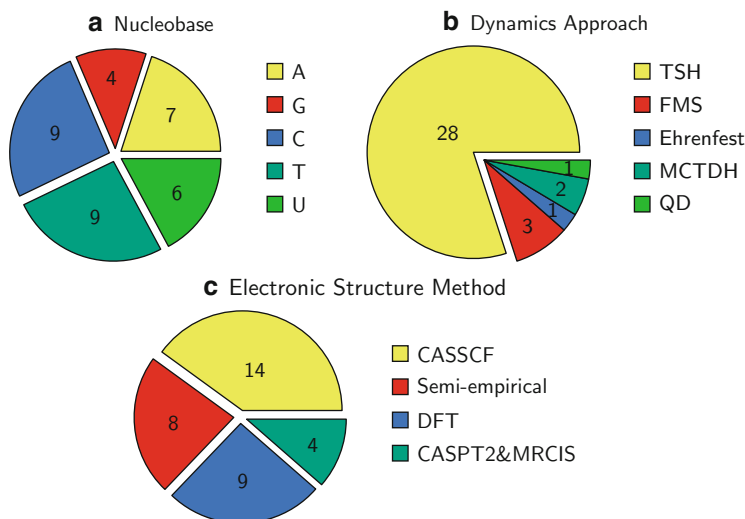
**Fig. 19** Summary of the number of published nuclear dynamics simulations of isolated nucleobases. (**a**) Number of simulations for each base. (**b**) Number of simulations using a given nuclear dynamics approach. (**c**) Number of simulations using a given electronic structure method. A total of 35 dynamics simulations from 28 publications were considered

electronic structure method underlying dynamics is CASSCF, with 40% of the simulations, followed by the semi-empirical multi-reference methods and DFT (including TDDFT, ROKS, and TDDFTB), each amounting to about 25%. Only a small number (about 10%) of the simulations used high-level ab initio methods (MRCIS, CASPT2), in contrast to the large number of static calculations that employ these methods in nucleobases.

All these calculations show that the ground state relaxation is – in agreement with experimental measurements – happening in all nucleobases within a few picoseconds after excitation. However, the common ultrafast relaxation is not due to a single deactivation mechanism for all nucleobases. There are some general geometrical motifs for the CoIns connecting the excited states to the ground state, like strong puckering of the six-membered rings and bond inversion of C=N–C=O moieties. Nevertheless, the details of the deactivation pathways are very sensitive to the form of the PEHs, which can differ considerably, even between tautomers of the same molecule (see, e.g., Sect. 4.3 about C).

Generally, the dynamics of the purine bases A and G is less complex and faster than the dynamics encountered in the pyrimidine bases C, T, and U. Experiments [58–62] report a biexponential decay for A, with a very fast (<100 fs) component and a component of about 1 ps. In G, time constants are even shorter [59, 62]. These findings are consistent with the theoretical dynamical predictions. Based on these simulations, the fast decay can be explained by the fact that the dynamics of A and G is determined by the $\pi\pi^*$ state. The $\pi\pi^*$ state facilitates in both systems a direct route to the CoIn with the ground state, leading to this rapid decay. In A, some

studies [66, 68] also predict involvement of the $n\pi^*$ state. Regardless of the underlying electronic structure method, in the purine bases all CoIns reported in the dynamics studies show a significant degree of ring puckering.

The dynamics of the pyrimidine bases is much slower and significantly more complex. Experimental time constants are around 1–3 ps for C and U and up to 7 ps for T [59, 61, 62]. This slower deactivation has been rationalized by a trapping in an $S_2$ ($\pi\pi^*$) minimum (T, U) or trapping in the $S_1$ ($n\pi^*$) state (C, T, U). The formation of a $\pi\pi^*$ minimum has been attributed to the interaction of different $\pi\pi^*$ states [46, 70, 106]. It was also found that different $n\pi^*$ states (e.g., located at the carbonyl oxygen or nitrogen atoms in the ring) may interact in certain regions of the PEHs. Even though some studies predicted trapping, there are also simulations which show relaxation to the ground state much faster (sub-picosecond), at least for part of the ensemble. The observed multiple time scales could thus be explained by a splitting of the wavepacket, with one part of the wavepacket decaying directly and another fraction getting trapped.

In general, the presented dynamics simulations still suffer on the one hand from the limited quality of the underlying electronic structure methods and on the other from lack of a proper description of the probe process in the simulations. Highly accurate correlated multi-reference methods are still too expensive and/or are not yet technically prepared to be employed efficiently in dynamics calculations of systems of the size of nucleobases. Yet, with the rapid advance of electronic structure codes, an impetuous development in the field dynamics is expected, allowing the delivery of quantitative or semi-quantitative results. The simulation of dynamical processes including the actual pump and probe laser pulses – as done in the experiment – is yet in its infancy. Progress in this direction will also be witnessed in the future, considerably increasing our understanding of the photophysics and photochemistry of nucleobases.

# References

1. Crespo-Hernández CE, Cohen B, Hare PM, Kohler B (2004) Ultrafast excited-state dynamics in nucleic acids. Chem Rev 104(4):1977–2020
2. Kleinermanns K, Nachtigallová D, de Vries MS (2013) Excited state dynamics of DNA bases. Int Rev Phys Chem 32(2):308–342
3. Markovitsi D, Gustavsson T, Talbot F (2007) Excited states and energy transfer among DNA bases in double helices. Photochem Photobiol Sci 6:717–724
4. Middleton CT, de La Harpe K, Su C, Law YK, Crespo-Hernández CE, Kohler B (2009) DNA excited-state dynamics: from single bases to the double helix. Ann Rev Phys Chem 60:217–239

5. Saigusa H (2006) Excited-state dynamics of isolated nucleic acid bases and their clusters. J Photoch Photobio C 7(4):197–210
6. Shukla MK, Leszczynski J (2007) Electronic spectra, excited state structures and interactions of nucleic acid bases and base assemblies: a review. J Biomol Struct Dyn 25(1):93–118
7. Leiter U, Garbe C (2008) Epidemiology of melanoma and nonmelanoma skin cancer - the role of sunlight. In: Reichrath J (ed) Sunlight, vitamin D and skin cancer, vol 624, Advances in experimental medicine and biology. Springer, New York, pp 89–103
8. Barbatti M (2011) Nonadiabatic dynamics with trajectory surface hopping method. WIREs Comput Mol Sci 1:620–633
9. Curchod BFE, Rothlisberger U, Tavernelli I (2013) Trajectory-based nonadiabatic dynamics with time-dependent density functional theory. ChemPhysChem 14(7):1314–1340
10. Martínez TJ (2006) Insights for light-driven molecular devices from ab initio multiple spawning excited-state dynamics of organic and biological chromophores. Acc Chem Res 39(2):119–126
11. Meyer HD, Worth GA (2003) Quantum molecular dynamics: propagating wavepackets and density operators using the multiconfiguration time-dependent Hartree method. Theor Chem Acc 109(5):251–267
12. Plasser F, Barbatti M, Aquino AJA, Lischka H (2012) Electronically excited states and photodynamics: a continuing challenge. Theor Chem Acc 131(1):1–14
13. Tannor D (2006) Introduction to quantum mechanics: a time-dependent perspective. University Science, Sausalito
14. Watson J, Crick F (1953) A structure for deoxyribose nucleic acid. Nature 171:737738
15. Doltsinis N (2006) Computational nanoscience: do it yourself! John von Neumann Institute for Computing. NIC Series, vol 31, Jülich
16. Meyer HD, Gatti F, Worth GA (2009) Multidimensional quantum dynamics. Wiley-VCH, Weinheim
17. Burghardt I, Meyer HD, Cederbaum LS (1999) Approaches to the approximate treatment of complex molecular systems by the multiconfiguration time-dependent Hartree method. J Chem Phys 111(7):2927–2939
18. Wang H, Thoss M (2003) Multilayer formulation of the multiconfiguration time-dependent Hartree theory. J Chem Phys 119(3):1289–1299
19. Lasorne B, Bearpark MJ, Robb MA, Worth GA (2006) Direct quantum dynamics using variational multi-configuration Gaussian wavepackets. Chem Phys Lett 432(4–6):604–609
20. Meng Q, Meyer HD (2013) A multilayer MCTDH study on the full dimensional vibronic dynamics of naphthalene and anthracene cations. J Chem Phys 138(1):014313
21. Tully JC, Preston RK (1971) Trajectory surface hopping approach to nonadiabatic molecular collisions: the reaction of H+ with D2. J Chem Phys 55(2):562–572
22. Tully JC (1990) Molecular dynamics with electronic transitions. J Chem Phys 93(2): 1061–1071
23. Zhu C, Nangia S, Jasper AW, Truhlar DG (2004) Coherent switching with decay of mixing: an improved treatment of electronic coherence for non-Born–Oppenheimer trajectories. J Chem Phys 121(16):7658–7670
24. Jasper AW, Stechmann SN, Truhlar DG (2002) Fewest-switches with time uncertainty: a modified trajectory surface-hopping algorithm with better accuracy for classically forbidden electronic transitions. J Chem Phys 116(13):5424–5431
25. Doltsinis NL, Marx D (2002) Nonadiabatic Car-Parrinello molecular dynamics. Phys Rev Lett 88:166402
26. Prezhdo OV, Rossky PJ (1997) Mean-field molecular dynamics with surface hopping. J Chem Phys 107(3):825–834
27. Richter M, Marquetand P, González-Vázquez J, Sola I, González L (2011) SHARC: ab initio molecular dynamics with surface hopping in the adiabatic representation including arbitrary couplings. J Chem Theory Comput 7(5):1253–1258

28. Granucci G, Persico M, Spighi G (2012) Surface hopping trajectory simulations with spin-orbit and dynamical couplings. J Chem Phys 137(22):22A501
29. Heß BA, Marian CM, Wahlgren U, Gropen O (1996) A mean-field spin-orbit method applicable to correlated wavefunctions. Chem Phys Lett 251((5â€"6)):365–371
30. Hammes-Schiffer S, Tully JC (1994) Proton transfer in solution: molecular dynamics with quantum transitions. J Chem Phys 101(6):4657–4667
31. Granucci G, Persico M (2007) Critical appraisal of the fewest switching algorithm for surface hopping. J Chem Phys 126(13):134114
32. Schwartz BJ, Bittner ER, Prezhdo OV, Rossky PJ (1996) Quantum decoherence and the isotope effect in condensed phase nonadiabatic molecular dynamics simulations. J Chem Phys 104(15):5942–5955
33. Ben-Nun M, Martínez TJ (2002) Ab initio quantum molecular dynamics. In: Advances in chemical physics, vol 121. John Wiley & Sons, New York, pp 439–512
34. Martínez TJ, Ben-Nun M, Levine RD (1996) Multi-electronic-state molecular dynamics: a wave function approach with applications. J Phys Chem 100(19):7884–7895
35. Martínez TJ, Ben-Nun M, Levine RD (1997) Molecular collision dynamics on several electronic states. J Phys Chem A 101(36):6389–6402
36. Coe JD, Levine BG, Martínez TJ (2007) Ab initio molecular dynamics of excited-state intramolecular proton transfer using multireference perturbation theory. J Phys Chem A 111(44):11302–11310
37. Hack MD, Wensmann AM, Truhlar DG, Ben-Nun M, Martínez TJ (2001) Comparison of full multiple spawning, trajectory surface hopping, and converged quantum mechanics for electronically nonadiabatic dynamics. J Chem Phys 115(3):1172–1186
38. Fischer I (2003) Time-resolved photoionisation of radicals, clusters and biomolecules: relevant model systems. Chem Soc Rev 32:59–69
39. Staniforth M, Stavros VG (2013) Recent advances in experimental techniques to probe fast excited-state dynamics in biological molecules in the gas phase: dynamics in nucleotides, amino acids and beyond. Proc R Soc A 469(2159):20130458
40. Cramer CJ (2004) Essentials of computational chemistry, 2nd edn. John Wiley & Sons, New York
41. Helgaker T, Jørgensen P, Olsen J (2000) Molecular electronic-structure theory. John Wiley & Sons, New York
42. Jensen F (2007) Introduction to computational chemistry, 2nd edn. John Wiley & Sons, New York
43. Levine IN (2001) Quantum chemistry. Prentice Hall, Upper Saddle River, New Jersey
44. Szabo A, Ostlund NS (1996) Modern quantum chemistry: introduction to advanced electronic structure theory. Dover, Mineola
45. Mai S, Marquetand P, Richter M, González-Vázquez J, González L (2013) Singlet and triplet excited-state dynamics study of the keto and enol tautomers of cytosine. ChemPhysChem 14:2920–2931
46. Hudock HR, Levine BG, Thompson AL, Satzger H, Townsend D, Gador N, Ullrich S, Stolow A, Martínez TJ (2007) Ab initio molecular dynamics and time-resolved photoelectron spectroscopy of electronically excited uracil and thymine. J Phys Chem A 111(34):8500–8508
47. Kotur M, Zhou C, Matsika S, Patchkovskii S, Spanner M, Weinacht TC (2012) Neutral-ionic state correlations in strong-field molecular ionization. Phys Rev Lett 109:203007
48. Spanner M, Patchkovskii S (2009) One-electron ionization of multielectron systems in strong nonresonant laser fields. Phys Rev A 80(6):063411
49. Spanner M, Patchkovskii S (2013) Molecular strong field ionization and high harmonic generation: a selection of computational illustrations. Chem Phys 414:10–19
50. Spanner M, Patchkovskii S, Zhou C, Matsika S, Kotur M, Weinacht TC (2012) Dyson norms in XUV and strong-field ionization of polyatomics: cytosine and uracil. Phys Rev A 86:053406

51. Chenon MT, Pugmire RJ, Grant DM, Panzica RP, Townsend LB (1975) Carbon-13 magnetic resonance. XXVI. Quantitative determination of the tautomeric opulations of certain purines. J Am Chem Soc 97(4636)
52. Cohen B, Hare PM, Kohler B (2003) Ultrafast excited-state dynamics of adenine and monomethylated adenines in solution: Implications for the nonradiative decay mechanism. J Am Chem Soc 125(13):594–13601
53. Dreyfus M, Dodin G, Bensaude O, Dubois JE (1975) Tautomerism of purines. I. N(7)H⇌N(9) H equilibrium in adenine. J Am Chem Soc 97:2369
54. Gonella NC, Nakanishi H, Holtwick JB, Horowitz DS, Kanamori K, Leonard NJ, Roberts JD (1983) Studies of tautomers and protonation of adenine and its derivatives by nitrogen-15 nuclear magnetic resonance spectroscopy. J Am Chem Soc 105:2050
55. Holmén A (1997) Vibrational transition moments of aminopurines: stretched film IR linear dichroism measurements and DFT calculations. J Phys Chem A 101:4361
56. Bravaya KB, Kostko O, Dolgikh S, Landau A, Ahmend M, Krylov AI (2010) Electronic structure and spectroscopy of nucleic acid bases: ionization energies, ionization-induced structural changes, and photoelectron spectra. J Phys Chem A 114(12):305–12317
57. Plützer C, Kleinermanns K (2002) Tautomers and electronic states of jet-cooled adenine investigated by double resonance spectroscopy. Phys Chem Chem Phys 4:4877–4882
58. Kang H, Jung B, Kim SK (2003) Mechanism for ultrafast internal conversion of adenine. J Chem Phys 118:6717–6719
59. Kang H, Lee KT, Jung B, Ko YJ, Kim SK (2002) Intrinsic lifetimes of the excited state of DNA and RNA bases. J Am Chem Soc 124(44):12958–12959
60. Ullrich S, Schultz T, Zgierski MZ, Stolow A (2004) Direct observation of electronic relaxation dynamics in adenine via time-resolved photoelectron spectroscopy. J Am Chem Soc 126:2262–2263
61. Ullrich S, Schultz T, Zgierski MZ, Stolow A (2004) Electronic relaxation dynamics in DNA and RNA bases studied by time-resolved photoelectron spectroscopy. Phys Chem Chem Phys 6:2796–2801
62. Canuel C, Mons M, Piuzzi F, Tardivel B, Dimicoli I, Elhanine M (2005) Excited states dynamics of DNA and RNA bases: characterization of a stepwise deactivation pathway in the gas phase. J Chem Phys 122(7):074316
63. Satzger H, Townsend D, Stolow A (2006) Reassignment of the low lying cationic states in gas phase adenine and 9-methyl adenine. Chem Phys Lett 430:144–148
64. Satzger H, Townsend D, Zgierski MZ, Patchkovskii S, Ullrich S, Stolow A (2006) Primary processes underlying the photostability of isolated DNA bases: adenine. Proc Natl Acad Sci 103(27):10196–10201
65. Kotur M, Weinacht TC, Zhou C, Matsika S (2012) Following ultrafast radiationless relaxation dynamics with strong field dissociative ionization: a comparison between adenine, uracil, and cytosine. IEEE J Sel Top Quant Electron 18(1):187–194
66. Fabiano E, Thiel W (2008) Nonradiative deexcitation dynamics of 9H-adenine: an OM2 surface hopping study. J Phys Chem A 112(30):6859–6863
67. Barbatti M, Lischka H (2008) Nonadiabatic deactivation of 9H-adenine: a comprehensive picture based on mixed quantum-classical dynamics. J Am Chem Soc 130(21):6831–6839
68. Lei Y, Yuan S, Dou Y, Wang Y, Wen Z (2008) Detailed dynamics of the nonradiative deactivation of adenine: a semiclassical dynamics study. J Phys Chem A 112(37):8497–8504
69. Mitrić R, Werner U, Wohlgemuth M, Seifert G, Bonačić-Koutecký V (2009) Nonadiabatic dynamics within time-dependent density functional tight binding method. J Phys Chem A 113(45):12700–12705
70. Barbatti M, Aquino AJA, Szymczak JJ, Nachtigallová D, Hobza P, Lischka H (2010) Relaxation mechanisms of UV-photoexcited DNA and RNA nucleobases. Proc Natl Acad Sci U S A 107(50):21453–21458

71. Barbatti M, Lan Z, Crespo-Otero R, Szymczak JJ, Lischka H, Thiel W (2012) Critical appraisal of excited state nonadiabatic dynamics simulations of 9H-adenine. J Chem Phys 117(22):22A503

72. Mons M, Piuzzi F, Dimicoli I, Gorb L, Leszczynski J (2006) Near-UV resonant two-photon ionization spectroscopy of gas phase guanine: evidence for the observation of three rare tautomer. J Phys Chem A 110(10):921–10924

73. Piuzzi F, Mons M, Dimicoli I, Tardivel B, Zhao Q (2001) Ultraviolet spectroscopy and tautomerism in the DNA base guanine and its hydrate formed in a supersonic jet. Chem Phys 270:205–214

74. Yamazaki S, Domcke W (2008) Ab initio studies on the photophysics of guanine tautomers: out-of-plane deformation and NH dissociation pathways to conical intersections. J Phys Chem A 112:7090–7097

75. Yamazaki S, Domcke W, Sobolewski AL (2008) Nonradiative decay mechanisms of the biologically relevant tautomer of guanine. J Phys Chem A 112(11):965–11968

76. Clark LB, Peschel GG, Tinoco I (1965) Vapor spectra and heats of vaporization of some purine and pyrimidine bases. J Phys Chem 69:3615–3618

77. Kang H, Lee KT, Kim SK (2002) Femtosecond real time dynamics of hydrogen bond dissociation in photoexcited adenine-water clusters. Chem Phys Lett 359:213–219

78. Langer H, Doltsinis NL, Marx D (2005) Excited-state dynamics and coupled proton-electron transfer of guanine. ChemPhysChem 6:1734–1737

79. Doltsinis NL, Markwick PRL, Nieber H, Langer H (2008) Ultrafast radiationless decay in nucleic acids: insights from nonadiabatic ab initio molecular dynamics. In: Shukla MK, Leszczynski J (eds) Radiation induced molecular phenomena in nucleic acids, vol 5, Challenges and advances in computational chemistry and physics. Springer, The Netherlands, pp 265–299

80. Lan Z, Fabiano E, Thiel W (2009) Photoinduced nonadiabatic dynamics of 9H-guanine. ChemPhysChem 10(8):1225–1229

81. Barbatti M, Szymczak JJ, Aquino AJA, Nachtigallová D, Lischka H (2011) The decay mechanism of photoexcited guanine – a nonadiabatic dynamics study. J Chem Phys 134(1):014304

82. Langer H (2006) Nichtadiabatische ab initio molekulardynamiksimulationen photo-angeregter nukleobasen. Ph.D. thesis, Ruhr-Universität Bochum

83. Brown RD, Godfrey PD, McNaughton D, Pierlot AP (1989) Tautomers of cytosine by microwave spectroscopy. J Am Chem Soc 111(6):2308–2310

84. Szczesniak M, Szczepaniak K, Kwiatkowski JS, KuBulat K, Person WB (1988) Matrix isolation infrared studies of nucleic acid constituents. 5. Experimental matrix-isolation and theoretical ab initio SCF molecular orbital studies of the infrared spectra of cytosine monomers. J Am Chem Soc 110(25):8319–8330

85. Bazsó G, Tarczay G, Fogarasi G, Szalay PG (2011) Tautomers of cytosine and their excited electronic states: a matrix isolation spectroscopic and quantum chemical study. Phys Chem Chem Phys 13(15):6799–6807

86. Kosma K, Schröter C, Samoylova E, Hertel IV, Schultz T (2009) Excited-state dynamics of cytosine tautomers. J Am Chem Soc 131(46):16939–16943

87. Ho JW, Yen HC, Chou WK, Weng CN, Cheng LH, Shi HQ, Lai SH, Cheng PY (2011) Disentangling intrinsic ultrafast excited-state dynamics of cytosine tautomers. J Phys Chem A 115(30):8406–8418

88. Hudock HR, Martínez TJ (2008) Excited-state dynamics of cytosine reveal multiple intrinsic subpicosecond pathways. ChemPhysChem 9(17):2486–2490

89. Lan Z, Fabiano E, Thiel W (2009) Photoinduced nonadiabatic dynamics of pyrimidine nucleobases: on-the-fly surface-hopping study with semiempirical methods. J Phys Chem B 113(11):3548–3555

90. Alexandrova AN, Tully JC, Granucci G (2010) Photochemistry of DNA fragments via semiclassical nonadiabatic dynamics. J Phys Chem B 114(37):12116–12128

91. González-Vázquez J, González L (2010) A time-dependent picture of the ultrafast deactivation of keto-cytosine including three-state conical intersections. ChemPhysChem 11(17): 3617–3624

92. Barbatti M, Aquino AJA, Szymczak JJ, Nachtigallová D, Lischka H (2011) Photodynamical simulations of cytosine: characterization of the ultrafast bi-exponential UV deactivation. Phys Chem Chem Phys 13(13):6145–6155

93. Richter M, Marquetand P, González-Vázquez J, Sola I, González L (2012) Femtosecond intersystem crossing in the DNA nucleobase cytosine. J Phys Chem Lett 3:3090–3095

94. Nakayama A, Harabuchi Y, Yamazaki S, Taketsugu T (2013) Photophysics of cytosine tautomers: new insights into the nonradiative decay mechanisms from MS-CASPT2 potential energy calculations and excited-state molecular dynamics simulations. Phys Chem Chem Phys 15(12):322–12339

95. Kistler KA, Matsika S (2008) Three-state conical intersections in cytosine and pyrimidinone bases. J Chem Phys 128(21):215102

96. Blancafort L, Robb MA (2004) Key role of a threefold state crossing in the ultrafast decay of electronically excited cytosine. J Phys Chem A 108(47):10609–10614

97. Blancafort L (2007) Energetics of cytosine singlet excited-state decay paths—a difficult case for CASSCF and CASPT2. Photochem Photobiol 83(3):603–610

98. Merchán M, González-Luque R, Climent T, Serrano-Andrés L, Rodríguez E, Reguero M, Peláez D (2006) Unified model for the ultrafast decay of pyrimidine nucleobases. J Phys Chem B 110(51):26471–26476

99. Nir E, Müller M, Grace L, de Vries M (2002) REMPI spectroscopy of cytosine. Chem Phys Lett 355(1–2):59–64

100. González-Luque R, Climent T, González-Ramírez I, Merchán M, Serrano-Andrés L (2010) Singlet and Triplet states interaction regions in DNA/RNA nucleobase hypersurfaces. J Chem Theory Comput 6(7):2103–2114

101. Merchán M, Serrano-Andrés L, Robb MA, Blancafort L (2005) Triplet-state formation along the ultrafast decay of excited singlet cytosine. J Am Chem Soc 127(6):1820–1825

102. Hare PM, Crespo-Hernández CE, Kohler B (2006) Solvent-dependent photophysics of 1-cyclohexyluracil: ultrafast branching in the initial bright state leads nonradiatively to the electronic ground state and a long-lived $^1n\pi^*$ state. J Phys Chem B 110(37):18641–18650

103. He Y, Wu C, Kong W (2003) Decay pathways of thymine and methyl-substituted uracil and thymine in the gas phase. J Phys Chem A 107(26):5145–5148

104. He Y, Wu C, Kong W (2004) Photophysics of methyl-substituted uracils and thymines and their water complexes in the gas phase. J Phys Chem A 108(6):943–949

105. Samoylova E, Schultz T, Hertel I, Radloff W (2008) Analysis of ultrafast relaxation in photoexcited DNA base pairs of adenine and thymine. Chem Phys 347(1–3):376–382

106. Szymczak JJ, Barbatti M, Soo Hoo JT, Adkins JA, Windus TL, Nachtigallová D, Lischka H (2009) Photodynamics simulations of thymine: relaxation into the first excited singlet state. J Phys Chem A 113(45):12686–12693

107. Asturiol D, Lasorne B, Robb MA, Blancafort L (2009) Photophysics of the $\pi$, $\pi^*$ and $n$, $\pi^*$ states of thymine: MS-CASPT2 minimum-energy paths and CASSCF on-the-fly dynamics. J Phys Chem A 113(38):10211–10218

108. Asturiol D, Lasorne B, Worth GA, Robb MA, Blancafort L (2010) Exploring the sloped-to-peaked S2/S1 seam of intersection of thymine with electronic structure and direct quantum dynamics calculations. Phys Chem Chem Phys 12:4949–4958

109. Picconi D, Barone V, Lami A, Santoro F, Improta R (2011) The interplay between $\pi\pi^*/n\pi^*$ excited states in gas-phase thymine: a quantum dynamical study. ChemPhysChem 12: 1957–1968

110. Nakayama A, Arai G, Yamazaki S, Taketsugu T (2013) Solvent effects on the ultrafast nonradiative deactivation mechanisms of thymine in aqueous solution: excited-state QM/MM molecular dynamics simulations. J Chem Phys 139(21):214304

111. Köppel H, Domcke W, Cederbaum LS (1984) Multimode molecular dynamics beyond the Born–Oppenheimer approximation. In: Adv Chem Phys, vol 57. Wiley, Chichester, pp 59–246

112. Rejnek J, Hanus M, Kabelac M, Ryjacek F, Hobza P (2005) Correlated ab initio study of nucleic acid bases and their tautomers in the gas phase, in a microhydrated environment and in aqueous solution. Part 4. Uracil and thymine. Phys Chem Chem Phys 7:2006–2017

113. Matsika S, Spanner M, Kotur M, Weinacht TC (2013) Ultrafast relaxation dynamics of uracil probed via strong field dissociative ionization. J Phys Chem A 117(12):796–12801

114. Nieber H, Doltsinis NL (2008) Elucidating ultrafast nonradiative decay of photoexcited uracil in aqueous solution by ab initio molecular dynamics. Chem Phys 347:405–412

115. Nachtigallová D, Aquino AJA, Szymczak JJ, Barbatti M, Hobza P, Lischka H (2011) Nonadiabatic dynamics of uracil: population split among different decay mechanisms. J Phys Chem A 115(21):5247–5255

116. Fingerhut B, Dorfman KE, Mukamel S (2013) Monitoring nonadiabatic dynamics of the RNA base uracil by UV pump-IR probe spectroscopy. J Phys ChemLett 4:1933–1942

117. Buschhaus L, Rolf J, Kleinermanns K (2013) DNA photoreacts by nucleobase ring cleavage to form labile isocyanates. Phys Chem Chem Phys 15(18):371–18377

118. Guissani A, Segarra-Martí J, Roca-Sanjuán D, Merchán M (2013) Excitation of nucleobases from a computation perspective I: reaction paths. In: Barbatti M, Borin A, Ullrich S (eds) Topics in current chemistry. Springer, Berlin Heidelberg. doi:10.1007/128_2013_501

119. Improta R, Barone V (2014) Excited states behavior of nucleobases in solution: insights from computational studies. In: Barbatti M, Borin A, Ullrich S (eds) Topics in current chemistry. Springer, Berlin Heidelberg. doi:10.1007/128_2013_524

# Photoionization Spectroscopy of Nucleobases and Analogues in the Gas Phase Using Synchrotron Radiation as Excitation Light Source

**Martin Schwell and Majdi Hochlaf**

**Abstract** We review here the photoionization and photoelectron spectroscopy of the gas phase nucleic acid bases adenine, thymine, uracil, cytosine, and guanine, as well as the three base analogues 2-hydroxyisoquinoline, 2-pyridone, and δ-valerolactam in the vacuum ultraviolet (VUV) spectral regime. The chapter focuses on experimental work performed with VUV synchrotron radiation and related ab initio quantum chemical calculations of higher excited states beyond the ionization energy. After a general part, where experimental and theoretical techniques are described in detail, key results are presented by order of growing complexity in the spectra of the molecules. Here we concentrate on (1) the accurate determination of ionization energies of isolated gas phase NABs and investigation of the vibrational structure of involved ionic states, including their mutual vibronic couplings, (2) the treatment of tautomerism after photoionization, in competition with other intramolecular processes, (3) the study of fragmentation of these molecular systems at low and high internal energies, and (4) the study of the evolution of the covalent character of hydrogen bonding upon substitution, i.e., examination of electronic effects (acceptor, donor, etc.).

M. Schwell (✉)
Laboratoire Interuniversitaire des Systèmes Atmosphériques (LISA), UMR 7583 CNRS, Universités Paris-Est Créteil et Paris Diderot, Institut Pierre et Simon Laplace, 61 Avenue du Général de Gaulle, 94010 Créteil, France
e-mail: martin.schwell@lisa.u-pec.fr

M. Hochlaf
Laboratoire Modélisation et Simulation Multi Echelle, Université Paris-Est, MSME UMR 8208 CNRS, 5 bd Descartes, 77454 Champs-sur-Marne, France

## Contents

## Abbreviations

| | |
|---|---|
| AE | Appearance energy |
| AIE | Adiabatic ionization energy |
| EI | Electron impact ionization |
| FEL | Free electron laser |
| IE | Ionization energy |
| NAB | Nucleic acid base |
| PE | Photoelectron |
| PES | Photoelectron spectroscopy |
| PI | Photoion |
| PIE | Photoionization efficiency |
| PIMS | Photoionization mass spectrometry |
| SPES | Slow photoelectron spectrum |
| SPI | Single photon ionization |
| SR | Synchrotron radiation |
| TOF | Time-of-flight |
| TPEPICO | Threshold photoelectron photoion coincidence |
| TPES | Threshold photoelectron spectroscopy |
| VIE | Vertical ionization energy |
| VUV | Vacuum ultraviolet |

# 1   Introduction

The study of large biomolecules, such as DNA and RNA, requires prior and extensive knowledge of the physicochemical properties of their smaller building blocks, for example, nucleobases and nucleosides. In particular, the investigation of ionized species of DNA or RNA has gained in importance during the last decades, because the damage produced by the interaction between ionizing radiation and
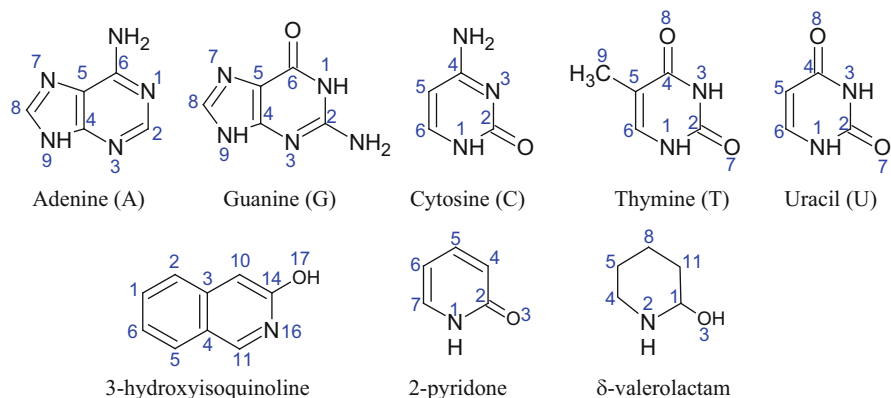
**Scheme 1** Chemical structures of the nucleic acid bases (with standard atom numbering) and three NAB analogues (with common numbering used in the literature, for non-H atoms only). The photoionization spectroscopy of these molecules is presented in this chapter

biological matter leads, for instance, to hazardous genetic mutations, potentially mediated by ions, with enhanced risk for cancer [1–3]. The mechanisms underlying DNA or RNA lesions are still under study and require the precise determination of thermochemical data and properties of the reactive species such as their ionization energy (IE), their spectroscopy, their nuclear dynamics, and a comprehensive understanding of their electronic structure. At the atomic level, a deep interpretation of induced radiation effects on the genetic material seems crucial with the growing development of cancer treatments by irradiation therapy. Since the electronic structure of DNA and RNA bases is complex, the comparison of their spectra to those of their analogues helps our understanding of the intrinsic processes occurring when these biologically relevant molecules are ionized and on the damage created when they are struck by ionizing radiation. Here we will indeed show how the complexity of the spectra increases gradually from 3-hydroxyisoquinoline (3-HQ) to 2-pyridone/2-hydroxypyridine, to δ-valerolactam, to thymine (T)/uracil (U), to adenine (A), to cytosine (C), and finally to guanine (G). In Scheme 1 we present the chemical structures of the nucleic acid bases (denoted hereafter as NABs) and three of their analogues whose photoionization spectroscopy will be presented in this chapter.

The question is why is complexity increasing? In fact, growing complexity is not linked to the skeletal structure of the molecules but rather it originates from the number of tautomers/rotamers and conformers that can be present in their neutral and ionic forms. Indeed, considering the analogues, 3-HQ presents a unique tautomeric form in the gas phase (the lactim) whereas, upon photoionization, two tautomeric cations (lactim$^+$/lactam$^+$) can be formed for 2-pyridone. For δ-valerolactam the situation is more complicated in spite of its simpler structure (cf. Scheme 1). For this base analogue we can count two tautomers, several conformers (boat/chair) and rotamers (*cis/trans*) which complicates matters

considerably, for example, the theoretical treatment of its VUV spectroscopy as depicted below. In this context, the case of guanine is particularly interesting and challenging to treat since the guanine cation is predicted to possess 36 tautomers/conformers lying close in energy. So how do these features influence the spectroscopy and the photoionization mechanisms of these species? The answer to this question may help to enlighten the still not well understood stability of DNA bases upon UV/VUV irradiation.

NABs are important building blocks of life. Therefore, their possible chemical genesis and survival, for example in an early Earth environment (or other "extreme" environments), has motivated many studies on the prebiotic formation and UV photophysics of these species. They were performed in the context of the study of the origin of life. It should be noted that these so-called astrobiological aspects of NAB photoionization and fragmentation are not the focus of the present chapter.

From the experimental point of view, photoion (PI) and photoelectron (PE) spectroscopies are powerful techniques for studying intramolecular photodynamics beyond the ionization energy. They have been extensively employed to study the single photoionization (SPI) of molecules that can be vaporized relatively easily. In order to ionize a molecule in the valence shell with a single photon, the wavelength of the photon falls generally in the vacuum ultraviolet (VUV) spectral domain. VUV radiation is roughly situated between 200 and 50 nm ($6.2 \text{ eV} < E_{\text{photon}} < 24.8 \text{ eV}$). It does not propagate in air due to the Schumann–Runge band transitions (between 200 and 170 nm) of molecular oxygen. In addition, lasers can be used as a light source in the VUV spectral domain in order to study photoinduced phenomena by SPI. Current advances are in very high resolution (sub-wavenumber). PI and PE spectroscopies using tunable VUV laser radiation generated by resonant four-wave mixing have been reviewed very recently by Ng [4]. Such experimental setups are costly since several lasers are needed for the photon mixing. Moreover, their proper alignment is an experimental challenge and is routinely performed in only a few laboratories in the world. Nucleobases have not been studied so far by SPI with tunable VUV lasers. Synchrotron radiation (SR), on the other hand, has been widely used as a light source in order to explore higher excited states in the VUV region, together with PI/PE spectroscopy. Recently, Qi and co-workers reviewed advances of VUV-SR photoionization mass spectrometry with particular attention to non-volatile molecules [5, 6]. Electron spectrometers are also operated routinely in connection with VUV-SR beamlines. They mainly work in the electron/ion coincidence regime and the most sophisticated ones also employ particle imaging techniques [7, 8]. SR offers a broad and continuous tunability which is its main advantage as compared to laser sources or VUV discharge lamps. Furthermore, at third generation synchrotron light sources, which are routinely operated today all over the world, the brilliance typically exceeds $10^{18}$ photons/s/mm$^2$/mrad$^2$/$10^{-3}$BW (where BW is the bandwidth around the light frequency), thus permitting the study of very small quantities.

With the advent of efficient vaporization techniques, such as laser desorption or nanoparticle desorption, photoionization and photoelectron spectroscopy were

applied to molecules that have very low vapor pressures at room temperature. Furthermore, enhancements of the sensitivity of detectors and of the efficiency of ion/electron collectors have led to the possibility of working with very small quantities inside the ion source. Consequently, even thermal vaporization of macroscopic samples in combination with effusive inlets or supersonic expansions can nowadays be used for the study of non-volatile (bio-) molecules by sophisticated gas phase spectroscopic methods. This is especially true for isolated nucleobases which possess a certain thermal stability in comparison with other, more fragile biomolecules (e.g., amino acids or peptides). In our opinion, the most notable examples of state-of-the-art VUV-SR spectroscopy applied to NABs and other related non-volatile biomolecules are found in [9–14].

The main objectives of the studies reviewed in this chapter are (1) accurate determination of ionization energies of isolated gas phase NABs and investigation of the vibrational structure of involved ionic states including their mutual vibronic couplings, (2) treatment of tautomerism after photoionization, in competition with other intramolecular processes, (3) study of fragmentation of these molecular systems at low and high internal energies, and (4) study of the evolution of the covalent character of hydrogen bonding upon substitution, i.e., examination of electronic effects (acceptor, donor, etc.).

The chapter is divided as follows: In Sect. 2, we detail the different experimental methodologies for studying the photoionization spectroscopy of NABs. In Sect. 3, we describe the quantum chemical methods used to analyze NABs photoionization and photoelectron spectra. Finally, in Sect. 4, we present key results of specific molecules.

## 2 Experimental Methodologies to Measure Photoionization and Photoelectron Spectra of NABs

### 2.1 Earlier Photoelectron (PE) Spectroscopy Experiments

HeI PE spectra of NABs have been measured since the mid-1970s by several groups [15–21]. One should note the high quality of the early pioneering experimental research, often carried out in combination with theoretical calculations. For example, using a commercial Perkin–Elmer photoelectron spectrometer and HeI emission at 21.21 eV, a spectral resolution down to 20–25 meV could be attained in the work of Dougherty et al. [16]. However, little evidence of vibrational structure could be revealed in these spectra. Only in the mid-2000s were these spectra interpreted in depth theoretically, including spectral intensity calculations [22–24]. In the 1990s, the zero kinetic energy electron (ZEKE) photoelectron spectroscopy technique was introduced and developed [25]. This technique is capable of recording PE spectra with spectral resolutions well below 1 meV, in the vicinity of the ionization threshold, by means of resonance enhanced

multiphoton ionization (REMPI) schemes and using lasers. Later on, REMPI (and also Laser Induced Fluorescence (LiF)) spectroscopy was widely used to measure high resolution optical spectra of NABs in the mid-UV where the intense $S_n \leftarrow S_0$ transitions are located (see the chapter by deVries et al.). However, it is difficult to apply REMPI to explore the photodynamics of higher excited states located well beyond the ionization energy. For those states, SPI with VUV synchrotron radiation or VUV lasers are favorably used.

## 2.2 Electron Impact Ionization Measurements on NABs

For the sake of completeness, we give here a short overview of experiments where electron impact ionization (EI) is used, generally in combination with mass spectrometry, to explore the photoion spectroscopy and dynamics of dissociative ionization beyond the ionization energy. We note that electron impact is a process which is physically completely different from photoabsorption (the latter process is sometimes called "photon impact", a term that might be misleading). The energetics of electron impact ionization can be well analyzed by energy and momentum conservation of the multiple interacting particles, whereas photoabsorption is a process where the photon energy is completely transferred to the molecule with the photon being annihilated. In earlier studies of dissociative ionization, it was found that the energy transferred to a molecule by electrons having 70 eV kinetic energy is grossly equivalent to photoabsorption of 35 eV photons [26]. We also note that photoionization cross sections are significantly greater than the EI ionization cross sections when incident electrons have a kinetic energy close to the photon quantum energy. In addition, the relative intensities of the bands by electron impact are different from those measured by photon impact because of different selection rules upon ionization. For instance, different threshold functions are measured and are widely used in the literature to deduce ionization energies from the corresponding spectra.

The kinetic energy of the impacting electrons can be scanned easily by changing the accelerating electric field of the electron source of the mass spectrometer. We note, however, that the experimental error of ionization and appearance energies is generally of the order of 0.2 eV and very often systematic errors are found when comparing threshold values measured by EI to those measured by photoionization using synchrotron radiation, for example. This is probably due to the accurate energy scale calibration using photon excitation where resonant transitions of rare gas absorption lines are used for that purpose. To our knowledge, the first EI mass spectra of NABs and their derivatives were recorded in 1965 by Rice et al. [27, 28], followed by others [29–32]. More recently, Denifl et al. used a hemispherical electron monochromator to study the threshold electron impact ionization of uracil and two of its chlorine derivatives [33, 34]. These authors measured the vertical ionization energy of uracil, found at 9.59 eV, with a precision of 0.08 eV. They also showed that the energy spread of the impinging electrons can be reduced to 35 meV

using such a monochromator, which is quite promising. We also mention that electron impact ionization has been used in experiments on NABs where the collisionally activated dissociation and gas phase tautomerization of NAB radical cations has been investigated [35, 36], in combination with extensive ab initio calculations.

## 2.3   Synchrotron Radiation (SR) as an Exciting Light Source

During the last decade, many excellent VUV-SR studies on gas phase nucleobases and related molecules were performed (see for example [9, 11–13, 37–45]). Generally, the white synchrotron light is monochromatized using normal incidence monochromators (NIM). In principle, the undulator of a synchrotron beamline can be used alone as a scanning device. In such experiments, the NIM grating would be set to its zero order, transmitting the maximum of number of photons without diffraction. The emission of VUV undulators has typical bandwidths of the order of 0.2–0.5 eV, which naturally limits the bandwidth of such spectra.

Since the density of the target molecules inside the ion source is usually very low for experiments with NABs, gratings with low groove numbers, which allow the transmission of more photons, are employed. Among them, the 200 g/mm grating integrated in the 6.65 m NIM at the undulator beamline DESIRS of the French SOLEIL synchrotron facility is used for such "flux-hungry" applications. Typical VUV bandwidths of the PI and PE spectra are on the order of 5–30 meV. Such spectral resolutions can be considered as state-of-the-art for VUV-SR experiments on NABs. Smaller bandwidths, below 1 meV, for example, can easily be achieved in principle with the current synchrotron-based PI and PE spectrometers. Nevertheless, the density of the target molecules would have to be further enhanced beyond what is possible today with current vaporization techniques. Furthermore, spectra of complex biomolecules could be congested and/or complicated by co-existing tautomers (or rotamers), so that high resolution spectrometers are not often of essential use.

From a perspective point of view, free electron lasers (FEL) operating in the VUV spectral regime will become more and more available in the near future. Such pulsed light sources should allow for pump-probe spectroscopy and thus the photodynamics of higher excited states could be studied directly using two synchronized VUV light pulses, combining, for example, FEL and VUV laser radiation. Moreover, FEL devices will have much higher brilliances compared to third generation SR sources (up to $10^{21}$ photons/s/mm$^2$/mrad$^2$/$10^{-3}$BW or even more). Thus, smaller sample quantities can be used. Further experimental developments are, however, needed because (1) these light sources are generally pulsed and their tunability is limited and (2) it is difficult to conduct electron/ion coincidence experiments (see below) with these FEL VUV light sources.

### 2.3.1   Vaporization Methods

At ambient pressure and temperature, NABs are solids with low vapor pressures. The sample can be placed directly in the ion source if the latter is completely heatable [37]. Nevertheless, most of the studies cited above have been conducted by heating the solid NAB sample in an oven prior to supersonic expansion into a molecular beam. Effusive inlets have also been used. Generally, macroscopic NAB samples have to be heated to about 130–250°C for a typical PI or PE spectroscopic experiment. The exact temperature needed for vaporization depends on the specific compound and on the sensitivity of the instrument used for PE and/or PI detection. The vapor pressure increases exponentially with temperature, and thus a few degrees more in the vaporization source can lead to a significant gain in signal-to-noise ratio. Eventually, thermal degradation may occur that is revealed easily in the mass spectrum by the presence of TOF peaks corresponding to $CO_2$, and/or other small, thermodynamically stable species (such as HCN or $NH_3$) eliminated upon pyrolysis. Whether a certain ion is indeed a parent ion formed by ionization of a pyrolysis product or a fragment formed by dissociation ionization of the parent NAB can generally be verified by measuring its appearance energy.

The technique of thermal vaporization of nanoparticles is applied to soft vaporization of NABs. Nowadays, such aerosol sources are operated routinely at the SOLEIL synchrotron (Saint Aubin, France) [10] and at the Advanced Light Source (Berkeley, USA) [45]. We show the experimental setup of the aerosol source operated at the DESIRS beamline at SOLEIL in Fig. 1. This technique has been shown to be a softer method of vaporization than simple heating of macroscopic samples [11]. Originally it was developed by the atmospheric physics community. In 2005 it was introduced at synchrotron beamlines by Mysak et al. [46]. Aerosol vaporization has been shown to work particularly well for amino acids which are more easily subject to thermal degradation upon heating than NABs [10, 47]. Within this method, an aqueous (or ethanolic) solution of approximately 1 g/L of the biological compound is nebulized, yielding a cloud of micrometer-sized droplets which are then dried efficiently by a diffusion dryer. The resulting nanoparticles, which consist chemically of the pure substance to be studied, are spatially focalized using an aerodynamic lens system providing a beam of nanoparticles with sub-millimeter dimensions and very low divergence. This beam is directed onto a hot tip where the nanoparticles are vaporized yielding a tiny vapor plume ideal for interfacing with a brilliant light beam. The source is continuous and, using a constant output atomizer (TSI) for nebulization, the density of the target molecules inside the ion source is stable for several hours. Consequently, spectroscopic studies can be performed.

Another notable advantage of the aerosol vaporization technique concerns the relatively low rate of sample consumption in a typical PE/PI spectroscopic experiment. Indeed, this rate is reduced by a factor of ~20 as compared to simple oven vaporization [11]. It can thus be an interesting alternative when samples are costly
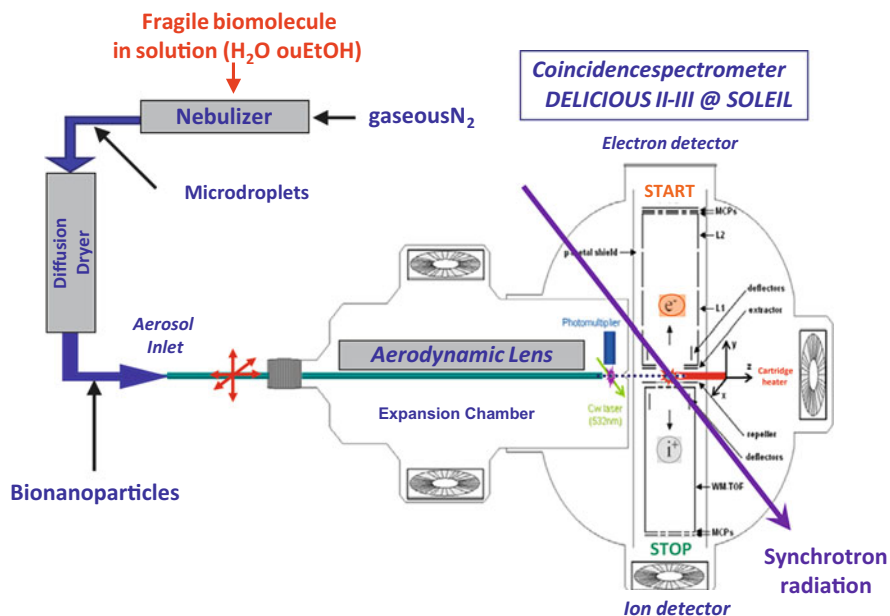
**Fig. 1** Thermal vaporization of bionanoparticles connected to coincidence photoelectron and photoion spectroscopy. These particles are produced by nebulization of an aqueous solution of the biomolecule and subsequent drying of the microdroplets. The nanoparticles, consisting of the pure biological compound to be studied, are spatially focused through an aerodynamic lens system. They impinge on a cartridge heater creating tiny vapor plumes ideal to be interfaced with brilliant SR. These kinds of aerosol sources for soft vaporization are operated today at the SOLEIL synchrotron and at the Advanced Light Source

or available only in very small quantities. A shortcoming is that the gas phase neutrals are formed at higher temperatures as compared to jet-cooled molecules.

Very recently, pulsed laser desorption was successfully used in combination with tunable (and continuous) VUV-SR, although the duty cycle of laser/synchrotron light interaction is unfavorable [5, 6, 48]. In these challenging experiments, the desorption and ionization processes are separated in space (and thus in time, since the desorbed molecules need to travel to the center of the ion source). The results are very encouraging. For example, Zhou et al. [6] succeeded in measuring PI mass spectra of the nucleoside uridine with a good signal-to-noise ratio at several photon energies close to the ionization threshold. Prior to ionization, the uridine molecules are desorbed using the fundamental emission of a nanosecond Nd:YAG laser at $\lambda = 1{,}064$ nm and operating at a repetition rate of 10 Hz. The focused laser beam hits the solid sample which is placed on a substrate located at variable distances, ranging from 1–4 mm, from the center of the ion source. The power density of the laser pulse is of the order of $10^7 \, \mathrm{W \cdot cm^{-2}}$ (power per unit of irradiated area). In each period between the laser pulses, ions formed by VUV-SR ionization of desorbed neutrals were collected by a home-made reflectron time-of-flight mass spectrometer

at the much higher repetition rate of 10 kHz. Using this technique, Zhou et al. also presented photoionization efficiency (PIE) spectra for the amino acid α-alanine.

The experimental approach of Kostko et al. [48] is quite different from that of Zhou et al. [6]. Indeed, Kostko et al. used an Nd:YLF laser emitting at $\lambda = 349$ nm and operating at a repetition rate of 2.5 kHz for desorption. This laser radiation is directed into a modified commercial time-of-flight secondary ion mass spectrometer (ToF-SIMS), which is commonly employed for mass spectrometric imaging experiments. This kind of mass spectrometer is normally operated using ion sputtering with fast, pulsed ion beams of nanosecond duration and several keV kinetic energy. Kostko et al. [48] were thus able to measure PI mass spectra of A, T, C, and U NABs. In their work, the laser desorption dynamics are studied and it is found that the internal temperature of laser-desorbed thymine is about 800 K whereas its translational temperature is well below, ranging from 216 to 346 K for the four NABs under study. Furthermore, the translational temperatures decrease with increasing laser power density (from $10^8$ to $4.5 \times 10^8$ W·cm$^{-2}$) which is deduced from the measurement and exploitation of the shape of the TOF mass peaks. As an explanation, these authors suggested efficient collisional cooling during the laser desorption process. Increasing the laser power leads in fact to the vaporization of more molecules per unit of surface area and thus the number of collisions is enhanced, leading to translational cooling. This effect is similar to the enhanced cooling in molecular beam experiments which is observed upon increasing the stagnation pressure.

More generally, we note that each vaporization method leads to different internal and translational energies of the produced parent and fragment cations. This aspect has been studied in depth in [10, 46–48] and the literature cited therein. The amount of internal energy $E_{int}$ imparted to the neutral upon vaporization is important to know for gas phase electronic spectroscopic studies of large molecules like NABs, since it directly affects their tautomer/conformer/rotamer distribution. The ionization energy cannot be used to get an estimate of $E_{int}$ since it is well known that the IE is not much affected by the temperature of the neutral molecule that undergoes photoionization. In rare cases, hot bands are observed below the experimental adiabatic ionization energy (AIE) but in many cases Franck–Condon factors are unfavorable for the appearance of such bands. In contrast, the appearance energies (AE) of fragments formed by dissociative photoionization are very much affected by the temperature of the parent neutral. In an "Arrhenius-like" behavior, the amount of internal energy can be deduced totally from the activation barrier, leading to a red shift of the AE that can be easily observed. For example, in the work of Gaie-Levrel et al. [10], a red shift of $0.57 \pm 0.1$ eV is observed for the formation of $m/z$ 130 from the dissociative photoionization of tryptophan when raising the temperature of the hot finger, used for the aerosol vaporization, from 423 to 558 K. An observed AE red shift can in turn be used to deduce $E_{int}$ by assuming that the latter is approximated by a collection of harmonic oscillators, as has been done in [47, 48]. In this context, one has to calculate vibrational frequencies of the molecule by theoretical chemistry methods. Consequently, this effect can be used in a straightforward manner to study the energy transfer during

vaporization with a particular method, by using VUV photoionization with tunable SR. Since tautomers, conformers, and rotamers produce in most cases the same fragment, the red shift is not affected by their distribution.

### 2.3.2 Spectroscopic Methods

Photoionization Mass Spectrometry (PIMS)

The first study of the photoionization of NABs, which combines VUV-SR with (quadrupole) mass spectrometry, was performed by Jochims et al. [37] on A, T, and U at the BESSY II synchrotron (Berlin). The spectral domain covered in this work was 6–22 eV and the measuring interval was 25 meV. The macroscopic neutral samples were placed and vaporized inside the heatable ion source. Ionization energies (IEs) of the NABs photoion parent and the appearance energies (AEs) of their photofragment cations were determined with accuracies ranging from 0.03 to 0.1 eV. The dissociative ionization pathways were discussed in depth using useful thermodynamical data from the literature (see also below). Astrophysical implications concerning the prospects and survival of NABs in interstellar media and meteorites were also discussed. We note here that IEs and AEs measured in this work must be considered as upper limits. To this end, experiments using threshold electrons (i.e., electrons with close to zero kinetic energy) are more powerful in determining more accurate IEs, AEs, and enthalpies of formation of the corresponding cations (see below). In principle, the thermal energy content of the parent neutral has to be subtracted from the measured IEs and AEs. On the other hand, activation barriers of photodissociation reactions often lead to the measurement of too-high AEs. These two effects might cancel out for simple single bond rupture reactions. In addition, a fragment AE can be subject to a substantial kinetic shift, $\Delta E_{kin}$ since at threshold, the reaction might be too slow to be observed. These effects were discussed in more detail by Schwell and co-workers in [49, 50]. Such kinetic shifts can be estimated by statistical models based on the possible existence of a transition state along the reactive pathways (see for example [51]).

   In the last decade, PIMS was widely used at the Chemical Dynamics beamline at the Advanced Light Source to study jet-cooled NABs. The use of molecular beams in these experiments enabled the study of small, homogeneous, and heterogeneous NAB clusters. For instance, Belau et al. [38] investigated the microhydration of A, T, G, and C by recording PIE curves in the 7.9–10.5 eV incident photon spectral domain. The typical scanning step of these PIE spectra was 50 meV. The authors mainly found that ionization energies of mixed NAB-$(H_2O)_n$ ($n = 1$–3) clusters decrease by ~0.3 eV when going from $n = 0$ to $n = 3$, except for guanine (see below). Later on, the same group studied proton transfer inside homogeneous and heterogeneous NAB clusters using PIMS in combination with electronic structure calculations on the shape of the potential energy surface along the reaction coordinate [13, 45]. NAB dimers have also been studied in depth using PIMS experiments complemented with extensive quantum-chemical calculations [12],

where the effects of π-stacking, H-bonding, and electrostatic interaction between the cluster forming molecules were deeply investigated.

## Electron/Ion Coincidence Spectroscopy and Imaging Techniques

This approach is currently pursued at the DESIRS beamline at the SOLEIL synchrotron. It concerns the use of electron/ion coincidence spectroscopy and particle imaging techniques in order to explore the photodynamics beyond the ionization energy of biological relevant molecules. The most recent instrument is called DELICIOUS III. It consists of a multipurpose double imaging particle coincidence spectrometer [8]. This spectrometer offers the possibility to analyze kinetic energies of coincident electrons and ions simultaneously and opens up the possibility to do state-selective threshold experiments, such as Threshold Photoelectron Spectroscopy (TPES) and Threshold Photoelectron and Photoion Coincidence (TPEPICO) spectroscopy with sub-meV resolution. In a typical experiment, the VUV photon energy is scanned and the electrons and ions formed are detected in coincidence. Typical count rates are on the order of $10^4$ per second for the electrons and $10^3$ for the ions. At the same time, the kinetic energy of the photoelectrons formed is analyzed using velocity map imaging. In a TPES spectrum, close to zero kinetic energy photoelectrons are plotted against the photon excitation energy. In a TPEPICO spectrum, the parent (or fragment) ion is detected in coincidence with zero kinetic energy photoelectrons. The coincidence counts are plotted against photon energy. In DELICIOUS III, an ion imaging is also performed, where the photoelectron images are correlated both to the mass and the ion kinetic energy and recoil directions. Among its attractive capabilities, this apparatus allows one to assess the electron spectroscopy of mass-selected species. We note that mass selection does not necessarily mean *species*-selective since in an ordinary mass spectrum a given mass can be either a fragment or a parent ion.

As discussed above, it is difficult to perform TPES or TPEPICO spectroscopy of NABs with very high resolution. This is mainly because of the low density of target molecules inside the ion source. Very recently, Hochlaf, Poisson and co-workers [9, 52] proposed an ingenious alternative where the photoelectrons are allowed to possess kinetic energies up to a certain value (e.g., 75 meV) in order to increase the signal-to-noise ratio of the spectrum. This technique is called "Slow Photoelectron Spectroscopy (SPES)." Basically, a SPES spectrum is very similar to a TPES spectrum. For instance, it permitted the measurement of the photoelectron spectrum of 2-pyridone, a model molecule for DNA nucleobases, with 9 meV resolution [9]. This allowed the resolution of the vibrational structure of the two co-existing tautomers of this molecule. In 2013, TPEPICO spectra of adenine and cytosine have been reported, with 40 meV spectral resolution, from 8 to 11 eV [11]. These experimental results are detailed below.

We note that a double imaging electron/ion coincidence spectrometer is also implemented at the VUV bending magnet beamline of the Swiss Light Source

(Villigen) [7]. However, biomolecules are not in the scientific focus of experiments performed at this beamline so far.

## 3 Theoretical Methods for the Analysis of Photoionization and Photoelectron Spectra

The full understanding of the photoionization reaction

$$\mathrm{M} + h\nu \rightarrow \mathrm{M}^* \rightarrow \mathrm{M}^+ + \mathrm{e}^- \rightarrow \text{fragments}$$

needs characterization of the neutral species (M), the intermediate (an electronically excited molecule, M*), the cation (M$^+$), and the fragments (neutral and cationic). During the first steps of this mechanism, the Franck–Condon principle is a priori in action. Since these species can be either closed or open shell molecular systems, we should use theoretical approaches that can describe both of them. In addition, their wavefunctions may be mono- or multiconfigurational in nature. To reach the so-called chemical accuracy, large computations should be performed. Such accurate theoretical calculations are of enormous help for assigning experimental spectra and for understanding the physico-chemical processes occurring after interaction of VUV light with NABs or their analogues. This concerns identification of the equilibrium structures of the neutral and cationic parent species and of their fragments, the pattern of their electronic states, the shape of their potential energy surfaces, fragmentation pathways, etc. In this section we review recent techniques applied for these purposes. Nowadays, most of these techniques are standard. They are implemented in several commercial ab initio quantum chemistry packages, e.g., Gaussian [53], Molpro (MOLPRO is a package of ab initio programs written by [54]), Molcas [55], Gamess [56], Turbomole [57], Columbus [58], and Aces II [59].

For monoconfigurational molecular systems, Hartree–Fock, conventional many-body [60], perturbation theory (Møller Plesset, MP2, MP4, . . .) [61, 62, and references therein; 63], coupled cluster approaches [64–66], and density functional theory based methods [67, 68] can be used. In 2000, Barone and co-workers [69] developed a hybrid Hartree–Fock/density functional model to optimize the equilibrium geometries of NABs and their radical cations. The computed structures and energetics (e.g., ionization energies) are in good agreement with available experimental data. This validated the use of their approach for the investigation of such open shell systems. These authors showed how this technique can be used for the assignment of experimental fragmentation mass spectra. Higher quality theoretical data can be obtained by coupled clusters approaches with perturbative treatment of triple excitations (RCCSD(T)) [64], which are, however, computationally demanding. Very recently, the use of newly implemented explicitly correlated methodologies [70–72], in addition to the inclusion of core-valence and scalar-relativistic

corrections, allowed accurate determination of ionization energies (IEs) of small and medium sized molecular systems such as NABs and analogues. Indeed, the differences between the calculated and the measured IEs are less than 1 meV. For such large sized molecular systems, these computations become feasible because of the reduction of CPU time and disk space by up to two orders of magnitude when using (R)CCSD(T)-F12 instead of (R)CCSD(T) for similar accuracy [73–76]. For explicitly correlated calculations, Peterson and co-workers developed an ensemble of explicitly correlated basis sets (cc-pVXZ-F12, X=D,T,Q)) to describe first and second raw atoms [77], in connection with their corresponding auxiliary basis sets and density fitting functions [78–81]. The core-valence effects are evaluated as the difference between electronic energies with only valence electrons correlated and electronic energies with all electrons correlated (e.g., at the (R)CCSD(T)/ cc-pwCVTZ level of theory [82, 83]). The scalar-relativistic energetic contributions correspond to the difference between electronic energies at the (R)CCSD(T) level where the atoms are described by Dunning's basis sets [84] without using the spin-free, one-electron Douglas–Kroll–Hess (DKH) Hamiltonian [85, 86] and at the (R) CCSD(T) level in connection with cc-pVXZ-DK basis sets [87] with the DKH Hamiltonian.

For multiconfigurational wavefunctions, configuration interaction techniques, such as multiconfiguration self-consistent field (MCSCF) and its variant, the complete active space self-consistent field (CASSCF) [88, 89] and the costly internally contracted multireference configuration interaction (MRCI) [90, 91] approaches are widely used. For NABs and their analogues, the choice of the CASSCF active space is not trivial, due to the computational hardware limitation. The best active space is chosen as a compromise between computational time and accuracy, where several tests should be performed to determine the appropriate size of active space without significant change in the order of electronic states of the NABs or analogues. Taking into account the size of the molecules under analysis, the good compromise (computational cost vs accuracy) corresponds to the inclusion of all molecular orbitals (MOs) from HOMO-$n$ to LUMO+$m$ where $n$ and $m$ equal 2–3 (cf. [92–98]). The lowest MOs are kept frozen. The CASSCF vectors are hence constructed using all configuration state functions (CSFs) obtained after excitations of all active electrons in these orbitals. This results in several thousands of CSFs to be treated. At the MRCI level only the configurations of the CASSCF wavefunction with coefficient modulus larger than a threshold (of 0.0–0.2) are included in the reference vector. The MRCI active space is constructed after single and double excitations of active electrons from the reference space into the virtual MOs. This usually results in more than ten million uncontracted configurations having to be considered. For better accuracy we generally quote the energies including the Davidson correction (MRCI+Q) that accounts for the contribution of higher order electron excitations [99]. Alternatively, one may perform multistate complete active space second-order perturbation theory (MS-CASPT2) [100] or CIPT2 [101] to consider dynamical electron correlation instead of the costly MRCI. In the MS-CASPT2 method the gradients are implemented [102]. Hence, this method may be used for the multidimensional mapping of the potential energy surfaces of

the neutral and the ionic electronic states close to and far from the molecular region, for instance for electronic excited states geometry optimizations, reaction pathways identifications, and computation of non-adiabatic transition characterizations, as illustrated in [103, 104].

For the investigation of the electronic excited states of ionized NABs, multiconfigurational techniques remain the methods of choice. Nevertheless, they are computationally demanding. In cases where the corresponding electronic wavefunctions are dominantly described by a unique determinant, time-dependent density functional theory (TD-DFT) [105, 106], equation-of-motion coupled clusters (EOM-CC), and third-order algebraic-diagrammatic construction approximation scheme (ADC(3)) for the one particle Green's function [107–109] all represent good approximations. Through a comparative study of the lowest electronic states of the 2-pyridone$^+$ cation (a NAB analog) using PBE0/6-311 + G(d,p) and CASSCF/MRCI/cc-pVDZ, Hammoutène et al. [94] showed that both TD-DFT and CASSCF/MRCI describe correctly the vertical excitation energies of these electronic states, whereas one should use multiconfiguration methods for mapping the evolution of the potential energy surfaces far from the molecular region and for treating the unimolecular decomposition processes undertaken by the 2-pyridone$^+$ cation. This is due to the possible change of the nature of the wavefunctions of these electronic states along the corresponding reactive coordinates not accounted for by TD-DFT methods.

The outer- and inner-valence photoelectron spectra (vertical ionization energies and spectral intensities) of NABs were computed using the ADC(3) scheme [23, 110], i.e., within the one-hole (h) and the two-hole one particle (2h–1p) configurations through third- and first-order, respectively, of the many-body perturbation theory. This technique allows the vertical ionization energies of electronic states to be correctly accounted for when the one-electron picture of ionization is valid [111]. Within this scheme and compared to configuration interaction (CI) treatments having equal accuracy, the ADC(3) method is a less expensive, more compact, and size-consistent method [112–114]. The simulated photoelectron spectra (both energy positions and relative intensities of the bands) issued from this treatment compare quite well with the measured spectra. This permits a correct interpretation for the structures occurring in the inner-valence region of the photoelectron spectrum of NABs [23].

In the last decade, Krylov and coworkers [42, 43] used EOM-IP-CCSD [115–119] and IP-CISD [120] to solve the problematic open-shell states in ionized NABs. These treatments require a "well-behaved" closed-shell neutral wave function. IP-CISD uses uncorrelated Hartree–Fock determinant as a reference, whereas EOM-IP-CCSD uses a correlated CCSD reference. EOM-IP-CCSD is of course more accurate than IP-CISD. These techniques have the advantage of being size-intensive and spin-pure. Through this treatment, several target states and interstate properties are derived. All are used to deduce the ionization energies and the ionization-induced structural changes, and to simulate the photoelectron spectra of NABs [42, 43].

# 4 Key Results

As mentioned in the introduction, the complexity of the optical spectra increases gradually when going from analogues to the natural NABs. That is why we start out with the presentation of key results for NAB analogues. The natural NABs are presented thereafter, by order of increasing complexity in the spectra.

## 4.1 NAB Analogues

In recent years, the investigation of ionized NAB analogues has attracted a lot of interest associated with understanding the effects of radiation damage of NABs after their interaction with ionizing radiation, atomic ion beams, and slow or energetic electrons. Here three examples will be treated (3-hydroxyisoquinoline, 2-pyridone/2-hydroxypyridine, and δ-valerolactam). We will show that the complexity of the spectra is related to their electronic structure, to the electronic states' mutual interaction, and to the possible contribution of several tautomers. This complexity increases gradually from 3-hydroxyisoquinoline, to 2-pyridone/2-hydroxypyridine, then to δ-valerolactam. The electronic structure of δ-valerolactam resembles those of adenine and of cytosine.

### 4.1.1 3-Hydroxyisoquinoline

3-Hydroxyisoquinoline (3-HQ) is a NAB analogue. It is considered to be a prototype for the lactam-lactim tautomerism of nitrogen-containing heteroaromatic systems and for studying the effect of electron delocalization on the aromatic ring as well as the electronic structure of NABs. There are a few experimental and theoretical studies on 3-hydroxyisoquinoline treating mainly the mechanisms of tautomerization in the ground and first excited states of this molecule [121–123]. The photoionization of 3-HQ was recently studied for the first time [98].

Scheme 2 displays the PBE0/6-311 + G(d,p) optimized equilibrium structures of neutral and charged forms of 3-HQ (lactim), and of its tautomer (lactam) as computed recently by Pan et al. [98]. The neutral lactim form is more stable than the lactam isomer, in good agreement with the QCISD/cc-pVDZ and QCISD(T)/cc-pVDZ results based on geometries at the B3LYP/cc-pVDZ level by Gerega et al. [123]. In contrast, the lactam$^+$ is favored with respect to the lactim$^+$. These tautomers are separated by transition states (TS and TS$^+$) where potential barriers for an intramolecular isomerization of more than 1 eV are computed. This is in line with the unique observation, in the experimental IR spectra, of the lactim form trapped in Ar matrices by Gerega et al. [123]. Therefore, jet cooled 3-hydroxyisoquinoline molecular beams are dominated by the lactim
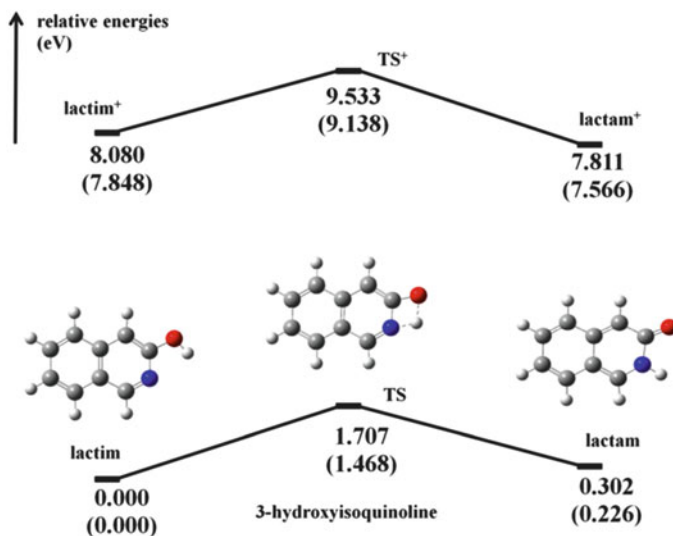
**Scheme 2** Structures of the lactim and lactam forms of neutral and cationic 3-hydroxyisoquinoline (lactim 3-HQ). We also give their energetic diagram computed at the (R) CCSD(T)-F12 level of theory including core-valence and scalar relativistic corrections using the equilibrium structure optimized at PBE0/6-311 + G(d,p) level. The relative energies obtained at PBE0 level are shown in parentheses. With permission of [98] Copyright (2013) American Chemical Society

(enol analogue) form unlike the case of 2-pyridone where both tautomers are present and contribute to the photoionization spectra (see below).

Figure 2 displays results obtained from a recent SPI study of gas phase 3-hydroxyisoquinoline measured with VUV light delivered by the SOLEIL synchrotron. The VUV radiation is coupled to the velocity map imaging electron/ion coincidence spectrometer DELICIOUS II as described in detail in [124]. The upper panel of this figure shows the full scale 2D spectrum of 3-hydroxyisoquinoline in the 7.4–9.8 eV photon energy range. The spectrum reveals that the photoionization is found to occur mainly via a direct process near the ionization threshold of 3-hydroxyisoquinoline. The middle panel of Fig. 2 presents the SPES of this lactim. This spectrum has been assigned with the help of theoretical calculations at the MRCI(+Q)/CASSCF/aug-cc-pVDZ level for the electronic states patterns and at the PBE0/6-311 + G(d,p) level for the harmonic and anharmonic wavenumbers of the lactim and lactam forms of 3-hydroxyisoquinoline and their cations.

As can be seen in Fig. 2, there is no electron signal around 7.5 eV where one may expect the formation of the lactam cationic form according to our theoretical value of 7.509 eV, predicted at the (R)CCSD(T)-F12/cc-pVTZ-F12 level and where core valence and scalar relativistic factors are also taken into consideration. Hence, there is no evidence for the formation of a lactam[+] isomer upon ionization of the lactim isomer, most likely because of the relatively high tautomerism barriers in both the neutral and ionic species (cf. Scheme 2). With the help of the explicitly correlated
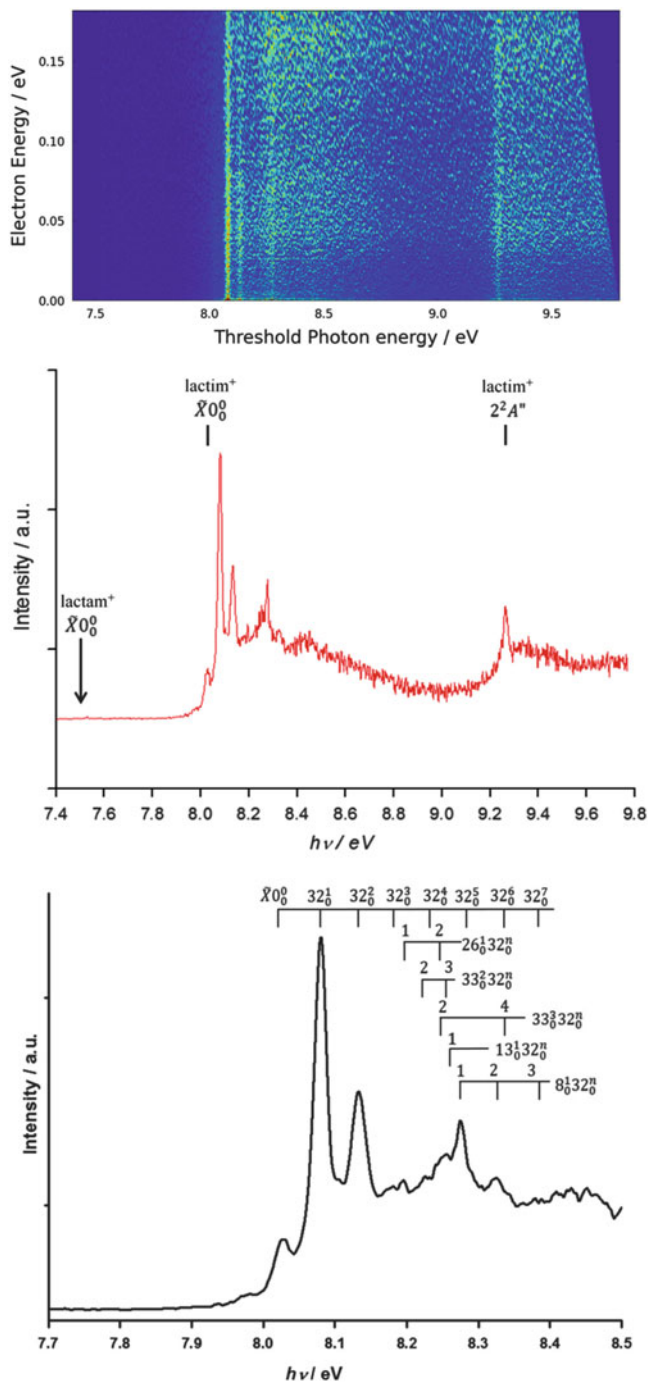
**Fig. 2** *Upper panel*: Full scale 2D spectrum of 3-hydroxyisoquinoline. This spectrum gives the photoelectron kinetic energies vs the photon energy. *Middle panel*: Slow photoelectron spectrum (SPES) (*red line*) deduced from the 2D spectrum. *Lower panel*: Blow-up of the SPES spectrum in

**Table 1** Dominant electron configurations and MRCI and MRCI + Q vertical excitation energies (in eV) of the ground and excited states of doublet lactim$^+$ (enol) of 3-hydroxyisoquinoline. These energies are given with respect to the $\widetilde{X}^1A'$ minimum of neutral 3-hydroxyisoquinoline lactim

| State | Electron configuration | MRCI | MRCI + Q |
|---|---|---|---|
| $\widetilde{X}^2A''$ | $0.92 \times \{(30a'')^2(31a')^2(32a')^2(4a'')^2(5a'')^2(6a'')^1\}$ | 7.40 | 7.55 |
| $2^2A''$ | $0.88 \times \{(30a')^2(31a')^2(32a')^2(4a'')^2(5a'')^1(6a'')^2\}$ | 9.30 | 9.30 |
| $1^2A'$ | $0.90 \times \{(30a')^2(31a')^2(32a')^1(4a'')^2(5a'')^2(6a'')^2\}$ | 11.04 | 10.26 |
| $3^2A''$ | $0.80 \times \{(30a')^2(31a')^2(32a')^2(4a'')^1(5a'')^2(6a'')^2\}$ | 10.84 | 10.84 |
| $4^2A''$ | $0.85 \times \{(30a')^2(31a')^2(32a')^2(4a'')^2(5a'')^2(7a'')^1\}$ | 11.95 | 11.69 |
| $2^2A'$ | $0.74 \times \{(30a')^2(31a')^2(32a')^1(4a'')^2(5a'')^2(6a'')^1(7a'')^1\}$ | 14.11 | 13.30 |
| $5^2A''$ | $0.59 \times \{(30a')^2(31a')^2(32a')^2(4a'')^2(5a'')^2(8a'')^1\}$ <br> $+0.57 \times \{(30a')^2(31a')^2(32a')^2(4a'')^2(5a'')^1(6a'')^1(7a'')^1\}$ | 14.04 | 13.43 |
| $3^2A'$ | $0.90 \times \{(30a')^2(31a')^2(32a')^2(33a')^1(4a'')^2(5a'')^2\}$ | 14.35 | 13.74 |
| $4^2A'$ | $0.90 \times \{(30a')^2(31a')^1(32a')^2(4a'')^2(5a'')^2(6a'')^2\}$ | 14.86 | 14.33 |
| $5^2A'$ | $0.91 \times \{(30a')^1(31a')^2(32a')^2(4a'')^2(5a'')^2(6a'')^2\}$ | 14.96 | 15.01 |

This table is adapted from [98]

computations results, the first dominant peak (at $h\nu = 8.028$ eV) is tentatively assigned as the band origin for the ionization transition of lactim. The corresponding theoretical IE (of 8.080 eV) coincides, within the theoretical and experimental error bars, with the experimental IE(lactim) = 8.028 eV value deduced from this SPES spectrum (cf. Fig. 2). In contrast, the theoretical DFT IE (of 7.848 eV) is off by ~0.2 eV as expected for such a level of theory. Moreover, a rich vibrational structure is observed that corresponds to vibrational transitions (single mode or combinations) populating the cationic lactim$^+$ ground state $\widetilde{X}$ vibrational levels. A key feature of the assignment is the strong transition at 8.08 eV. This transition is assigned to a vibrational mode ($\nu_{32}^+$) which corresponds mainly to the angular deformation (in-plane) involving the C10–C14–O17 and N16–C14–O17 angles, which represent the major geometrical differences between 3-hydroxyisoquinoline lactim and lactim$^+$ forms (cf. lower panel of Fig. 2 which illustrates tentative assignments of observed vibrational bands in the 7.7 to 8.5 eV region).

In addition, several weaker and complex bands are observed in the SPES spectrum above 9 eV. They correspond to the population of vibrational levels of the $\widetilde{A}$ electronically excited state of the cation. The $\widetilde{A}$ state is predicted to lie at these energies (cf. Table 1). At higher energies, a high density of electronic states is predicted (cf. Table 1) that will favor their mutual interaction by vibronic coupling. Vibronic coupling and predissociation will participate to congestion of the bands in this energy region.

**Fig. 2** (continued) the 7.7–8.5 eV region where the comb lines correspond to the tentative assignments. Reprinted with permission from Pan et al. [98]. Copyright (2013) American Chemical Society

**Scheme 3** 2-Pyridone (2-PY⁺) cation and its tautomer 2-hydroxypyridine (2-HP⁺)



**2-PY⁺**                                      **2-HP⁺**
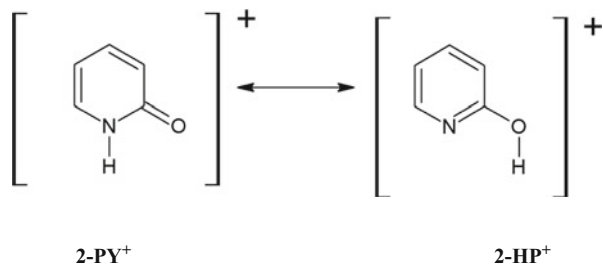
### 4.1.2 2-Pyridone

2-Pyridone (lactam, 2-PY), its tautomer 2-hydroxypyridine (lactim, 2-HP) (cf. Scheme 3), and their dimers together represent a model system to study NABs, isolated or paired, as well as the hydrogen bonding in their complexes. The neutral species were widely studied experimentally and theoretically as detailed in [9, 94]. Mainly, the work published in these references accurately characterized the equilibrium structure of both tautomers, their relative energies, and their electronic excited states. In contrast, only a few studies considered their cations.

In 2002, Trikoupis et al. [125] performed combined B3LYP/CBSB7 computations and mass spectrometric experiments on 2-HP⁺. They showed that the fragmentation pathways of the cationic species are very complex. Indeed, 2-HP⁺ undergoes decarbonylation to yield 3-H pyrrole ions and CO (pathway (b) in Scheme 4) after ring-opening. Alternatively, the reaction may proceed through the most stable form, 2-PY⁺, after 1,3-H transfer through a 28 kcal/mol ketonization barrier (pathway (a) in Scheme 4).

The IEs of 2-PY and of 2-HP were determined by electron impact ionization [126], photoelectron [127], resonance enhanced multiphoton ionization [128], zero kinetic energy (ZEKE) photoelectron, resonantly enhanced two-photon ionization, and mass analyzed threshold ionization (MATI) spectroscopies [129, 130], and more recently by slow photoelectron spectroscopy [9]. For 2-PY, ZEKE spectra provided an IE (2-PY) of $8.4479 \pm 0.0006$ eV and IE (2-HP) of $8.9384 \pm 0.0006$ eV [129], which were confirmed later by the SPES study of Poully et al. [9]. Of potential interest, the corresponding spectra (Figs. 3 and 4) present rich structures, which correspond to the population of the vibrational levels of the 2-PY⁺ cation in the $\widetilde{X}$ ground and $\widetilde{A}$ excited electronic states, as well as of the 2-HP⁺ cation in the electronic ground state. The SPES spectrum (Fig. 4) displays the assignment of these bands based on the PBE0/6-311 + G(d,p) computation results listed in Table 2. Because of symmetry selection rules, only the $a'$ cationic levels are populated by one photon ionization from the corresponding neutral ground state. These bands are mainly due to excitation of the cationic vibrational modes 18 and 20 together with weaker contributions of bands involving other vibrational modes and even numbers of quanta of the vibrational mode 21 (cf. Table 2). Moreover, the analysis of the SPES spectrum allows the determination of some fundamentals of 2-PY⁺,

**Scheme 4** Schematic representation of the unimolecular processes undertaken by 2-HP$^+$. Energies are in kcal/mol. The energetics of pathways a and b are unknown. With courtesy of [125]
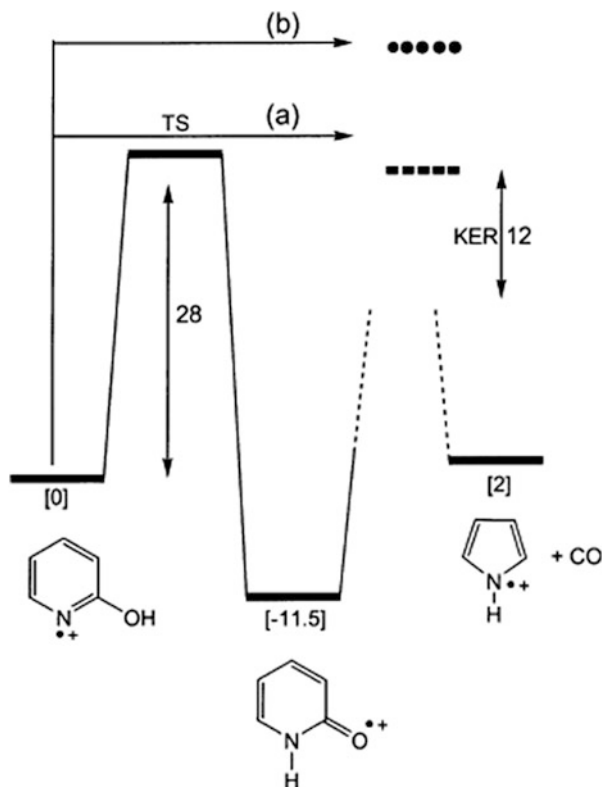
i.e., $\nu_{20}^+ = 521$, $\nu_{18}^+ = 739$, $\nu_{16}^+ = 1005$, $\nu_{13}^+ = 1223$, $\nu_{11}^+ = 1356$, $\nu_{10}^+ \approx \nu_9^+ = 1452$, and $\nu_8^+ \approx \nu_7^+ = 1573$ (all values are in cm$^{-1}$). The experimental values from ZEKE measurements are very close to those obtained using SPES spectroscopy since deviations between both sets of data are less than 4 cm$^{-1}$. For instance, the ZEKE $\nu_{20}^+$, $\nu_{16}^+$, $\nu_{13}^+$, $\nu_{10}^+ / \nu_9^+$, and $\nu_8^+ / \nu_7^+$ fundamentals were measured at 520, 1,010, 1,219, 1,457, and 1,572 (in cm$^{-1}$), respectively. Generally, the experimental and theoretical values agree quite well, which validates the use of the PBE0/6-311 + G(d,p) method for deduction of anharmonic frequencies of such classes of molecules. In addition, the 2D-SPES spectrum reveals that photoionization of 2-PY and of 2-HP molecules occurs mainly via a direct process close to their ionization thresholds, whereas the indirect route (autoionization) may contribute at higher energies.

Finally, the recent theoretical study [96] of the spectroscopy of methyl substituted 2-pyridones, tautomers and ions (denoted as xMe-2-PY$^{0/+1}$ and xMe-2-HP$^{0/+1}$, where x represents the relative position of the methyl group on the ring) and comparison to 2-PY$^{0/+1}$ and to 2-HP$^{0/+1}$ showed that there is a lowering of all vibrational frequencies upon ionization and that the substitution of an H by the methyl group enhances such reduction. Shifts for short wavelengths were computed, with the largest effect being predicted for 6Me-2-HP. The effects are large for the CO stretching mode, whereas the NH stretching mode varies only slightly.
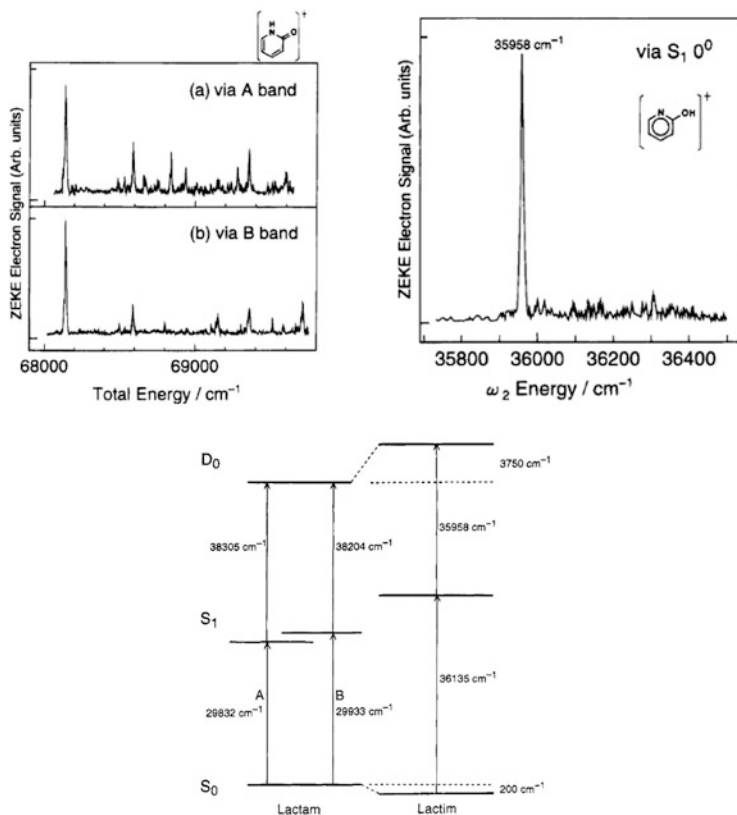
**Fig. 3** ZEKE photoelectron spectrum of 2-PY (lactam, *upper left panel*), of 2-HP (lactim) via the S1 neutral state (*upper right panel*), and energy diagram of 2-PY and of 2-HP (*lower panel*). Reprinted with permission from Ozeki et al. [129]. Copyright (1995) American Chemical Society

The computed frequency changes observed for the methyl compounds are large enough to be measurable by means of modern spectroscopic techniques.

The lowering of the frequencies upon ionization or methyl substitution is due to the perturbation of the $\pi$ electron distribution on the aromatic ring. Indeed, ionization induces a loss of $\pi$ electrons and the donor electronic effect of methyl leads to "excess" electrons on the ring. Both effects result on deviations from the $4n + 2$ electrons rule for perfect aromaticity.

### 4.1.3  δ-Valerolactam

δ-Valerolactam (piperidin-2-one) is a cyclic lactam (cf. Scheme 5). There are structural similarities between δ-valerolactam (saturated C–C bonds) and 2-pyridone (aromatic six ring cycle). δ-Valerolactam presents a small number of
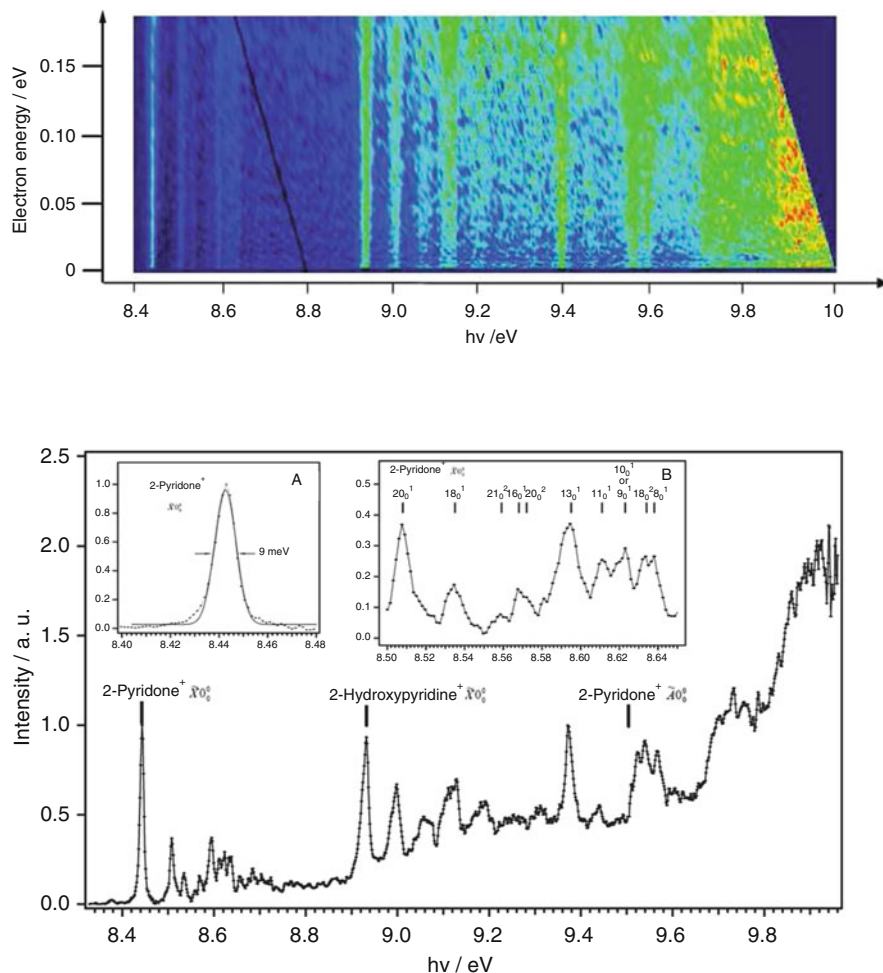
**Fig. 4** *Upper panel*: Full scale 2D SPES spectrum of 2-PY and of 2-HP. It gives the photo-electron kinetic energies vs the photon energy. *Lower panel*: Slow photoelectron spectrum (SPES) for electron kinetic energies from 0 to 75 meV. We highlight the experimentally-determined origin transitions for the ground state of 2-PY$^+$ and of 2-HP$^+$. The *insets* correspond to a zoom of this spectrum in the region 8.40–8.65 eV, where the vertical lines reproduce the assignments of the bands. Reproduced from [9] by permission of the PCCP Owner Societies

hydrogen bonding donor-acceptor sites. It represents an even simpler model for studying the pairing (hydrogen bonding) between NAB pairs since only the amide form predominates under laboratory conditions, whereas 2-pyridone possesses two tautomers (lactam and lactim forms). Several structural and spectroscopic studies were performed on the neutral δ-valerolactam molecule. They are reviewed in [95]. For the cation, Potapov et al. [131] and Treschanke and Rademacher [132, 133] determined the IEs of δ-valerolactam, at IE = 9.15 ± 0.02 and 9.30 eV,

**Table 2** PBE0/6-311 + G (d,p) fundamental harmonic and anharmonic frequencies (in cm$^{-1}$) of 2-PY$^+$ and 2-HP$^+$ cations [Hammoutène et al. Private communication]. For 2-PY$^+$, modes 1–21 are of $a'$ symmetry and modes 22–30 are of $a$ symmetry. For 2-HP$^+$, all modes are of $a$ symmetry

| Mode | 2-PY$^+$ | | 2-HP$^+$ | |
|---|---|---|---|---|
| | Harmonic | Anharmonic | Harmonic | Anharmonic |
| 1 | 3,547.4 | 3,385.4 | 3,782.4 | 3,579.7 |
| 2 | 3,243.7 | 3,123.8 | 3,236.2 | 3,108.6 |
| 3 | 3,237.6 | 3,113.6 | 3,225.6 | 3,098.9 |
| 4 | 3,224.3 | 3,085.0 | 3,204.2 | 3,076.0 |
| 5 | 3,220.3 | 3,091.9 | 3,196.6 | 3,062.5 |
| 6 | 1,637.5 | 1,596.8 | 1,631.7 | 1,589.4 |
| 7 | 1,595.6 | 1,568.3 | 1,571.1 | 1,540.1 |
| 8 | 1,581.6 | 1,561.5 | 1,500.6 | 1,466.8 |
| 9 | 1,491.1 | 1,458.4 | 1,474.6 | 1,450.1 |
| 10 | 1,484.2 | 1,454.8 | 1,445.8 | 1,412.7 |
| 11 | 1,388.5 | 1,355.9 | 1,396.4 | 1,365.7 |
| 12 | 1,270.0 | 1,243.2 | 1,359.7 | 1,329.0 |
| 13 | 1,241.8 | 1,212.3 | 1,178.3 | 1,148.5 |
| 14 | 1,180.8 | 1,165.1 | 1,158.9 | 1,120.7 |
| 15 | 1,098.4 | 1,081.3 | 1,119.4 | 1,096.0 |
| 16 | 1,037.0 | 1,018.9 | 1,011.8 | 1,015.0 |
| 17 | 994.0 | 983.3 | 1,009.9 | 992.6 |
| 18 | 789.1 | 770.3 | 989.1 | 981.4 |
| 19 | 604.4 | 596.2 | 985.7 | 965.5 |
| 20 | 538.3 | 531.9 | 864.4 | 845.1 |
| 21 | 452.4 | 448.6 | 827.0 | 829.6 |
| 22 | 1,022.5 | 1,015.6 | 776.6 | 748.7 |
| 23 | 1,011.1 | 1,016.9 | 675.8 | 656.9 |
| 24 | 919.4 | 913.6 | 602.9 | 575.2 |
| 25 | 813.9 | 810.6 | 601.2 | 588.3 |
| 26 | 766.9 | 762.1 | 552.0 | 533.5 |
| 27 | 670.9 | 670.1 | 448.0 | 436.5 |
| 28 | 450.1 | 451.7 | 431.6 | 427.3 |
| 29 | 350.1 | 348.4 | 353.6 | 352.1 |
| 30 | 177.8 | 175.6 | 124.1 | 124.7 |

respectively by means of HeI photoelectron spectroscopy. Their spectra are composed of well-resolved bands extending over ~1 eV each which were attributed to ionization from $\pi_N$, $n_O$ for the first two bands and to the inner valence shell ionization for the higher ones. Recently, Mahjoub et al. [95] studied the single photon ionization of gas phase δ-valerolactam and the state-to-state fragmentation of [δ-valerolactam]$^+$ by means of VUV synchrotron radiation coupled to a velocity map imaging electron/ion coincidence spectrometer [97]. These authors have also performed extensive state-of-the-art computations on equilibrium geometries, electronic state patterns, and evolutions, harmonic, and anharmonic frequencies of neutral and positively charged δ-valerolactam, and for over 170 possible dissociation channel products. The equilibrium structure computations were done at the PBE0/aug-cc-pVDZ and the MP2/aug-cc-pVTZ levels of theory. The mapping of

**Scheme 5** Structure of δ-valerolactam
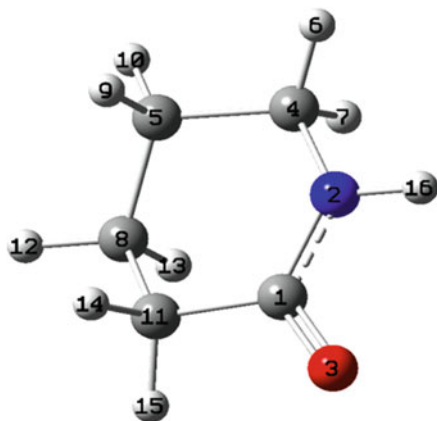


the electronic states of the cation was done at MRCI + Q/CASSCF/aug-cc-pVDZ level of theory.

We display in Fig. 5 the CASSCF/aug-cc-pVDZ one-dimensional evolutions of the potential energy surfaces of the lowest doublet electronic states of [δ-valerolactam]$^+$ along the planarization angle θ and along the normal coordinate relative to the out-of-plane torsion mode 41 [95]. This figure reveals that the ground electronic state $\widetilde{X}^2A$ and the first excited state $\widetilde{A}^2A$ become close to each other for θ ~ 190° and Δτ ~ 14°. An avoided crossing is visible at these nuclear configurations, i.e., close to the equilibrium molecular structure of the $\widetilde{A}^2A$ state. Consequently, both electronic states are coupled vibronically and their electronic wave functions are strongly mixed, resulting in complex and non-conventional rovibronic spectra for the $\widetilde{X}^2A$ and $\widetilde{A}^2A$ states in the vicinity of this avoided crossing (not sufficiently resolved in the SPES experimental study). Theoretically, accurate derivation of the spectrum of these states needs further development, where the potential energy surfaces of both states should be mapped in full dimensionality and a variational treatment of the nuclear motions is needed.

Figure 6 (upper panel) displays the full scale 2D spectrum of jet cooled δ-valerolactam providing the photo-electron kinetic energies vs the photon energy. This spectrum shows that photoionization of this molecule takes place mainly via a direct process close to the ionization thresholds whereas the indirect route (autoionization) contributes at higher energies. The SPES for electron kinet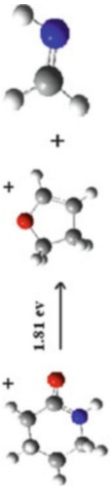ic energies from 0 to 57 meV as deduced from the 2D spectrum is also given (Fig. 6, middle panel). The vertical bars correspond to the theoretically-determined electronic state origin transitions. At the MRCI + Q/CASSCF/aug-cc-pVDZ level of theory, the $\widetilde{A}^2A, \widetilde{B}^2A, \widetilde{C}^2A,$ and $\widetilde{D}^2A$ states are computed to lie at 0.52, 2.90, 3.22, and 3.55 eV with respect to the [δ-valerolactam]$^+$ $\widetilde{X}^2A$ energy at equilibrium. These energies fit quite well with the origin bands of this SPES spectrum and compare quite well to those deduced from the HeI photoelectron spectrum of Treschanke and Rademacher [133] (at 0.5, 2.1, 2.8, and 3.0 eV, with respect to the ground state
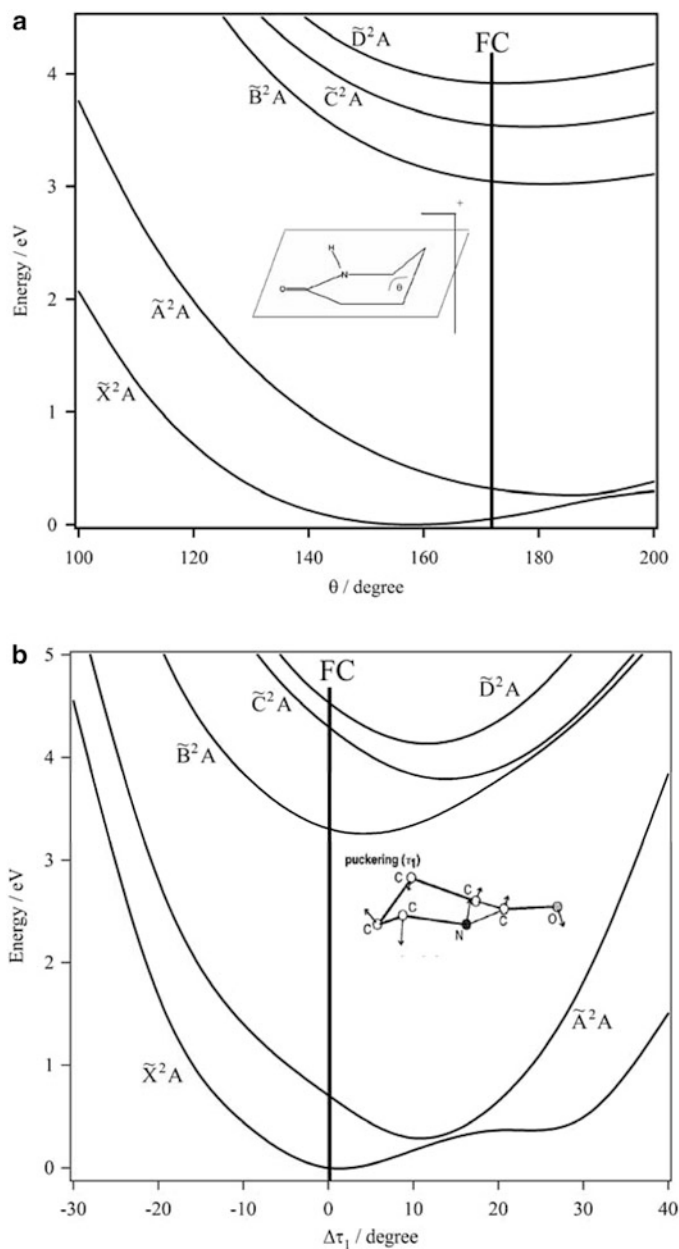
**Fig. 5** (**a**) CASSCF/aug-cc-pVDZ one-dimensional cuts of the potential energy surfaces of the lowest doublet electronic states of δ-valerolactam$^+$ along the planarization coordinate, θ. The remaining internal coordinates are kept fixed at their equilibrium values in δ-valerolactam$^+$ $\widetilde{X}$. (**b**) CASSCF/aug-cc-pVDZ one-dimensional cuts of the potential energy surfaces of the lowest doublet electronic states of δ-valerolactam$^+$ along the normal coordinate, $\Delta\tau_1$ (mode 41). These curves are given in energy with respect to the energy of δ-valerolactam$^+$ $\widetilde{X}$ at equilibrium. The *solid*

origin band of the cation). The synthetic spectrum in Fig. 6 illustrates the good agreement between experiment and theory.

The narrow bands at the left side of the slow photoelectron spectrum correspond to transitions populating vibrational levels of the cation $\widetilde{X}$ state. Moreover, several weaker and complex bands are observed, corresponding to population of vibrational levels (single or combination modes) of the electronically excited states of the cation arising from their mutual vibronic interactions. This is shown in the lower panel of Fig. 6 as an inset which corresponds to an enlargement of the SPES spectrum in the vicinity of the cationic ground state. The tentative assignment of the observed bands (vertical lines) is achieved with the help of the theoretical results [95].

After its formation, the [δ-valerolactam]$^{+}$ ion is subject to isolated state intramolecular unimolecular fragmentation processes. The time-of-flight mass spectra at different photon energies from 9 to 12 eV are displayed in Fig. 7. Various fragments of [δ-valerolactam]$^{+}$ parent cation are observed, corresponding to $m/z$ 30, 43, 56, 58, 70, 71, 82, and 98. Tentative identifications of the related fragmentation pathways based on ab initio computational results are given in Table 3. Generally, close analysis of the products shows that isolated state unimolecular decomposition of this NAB analogue leads mostly to nitriles and small heterocycles. These kinds of molecules can be qualified as "prebiotic" since they can themselves be precursors of the building blocks of life (amino acids and NABs). The reversed reactions of NAB dissociation may thus be of importance for the synthesis of these species in a prebiotic environment. Further experimental investigations in the laboratory are needed for confirmation.

## 4.2 NABs Occurring in Biological DNA and RNA

### 4.2.1 Thymine

The experimental adiabatic ionization energy of thymine (T) is found at AIE = 8.82 ± 0.03 eV by Jochims et al. [37]. PE spectra of thymine have been measured by several groups [15–17, 20, 23]. According to ab initio calculations, thymine, unlike cytosine, for example (see below), has no low-lying tautomers [134]. The most stable form is a diketo isomer followed by an enol form at ~45 kJ/mol higher in energy. Eleven other tautomers are identified, with energies up to 130 kJ/mol above the most stable one. The room temperature PE spectrum is therefore not complicated by the contribution of several tautomers prior to

---

**Fig. 5** (continued) thick vertical line corresponds to the middle of the Franck–Condon (FC) region accessible from δ-valerolactam $\widetilde{X}$ [95]. Copyright © Wiley-VCH Verlag GmbH & Co. KGaA, Weinheim
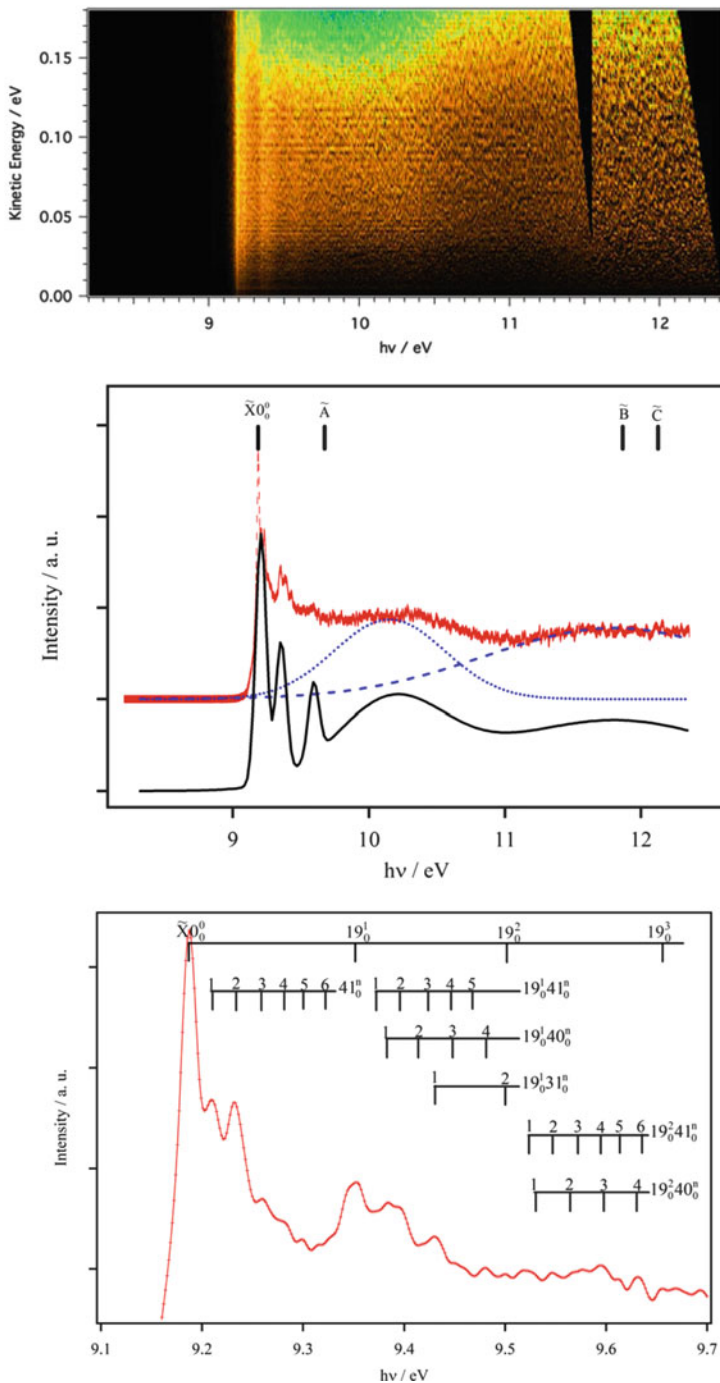
**Fig. 6** *Upper panel*: Full scale 2D spectrum of δ-valerolactam providing the photo-electron kinetic energies vs the photon energy. *Middle panel*: Slow photoelectron spectrum (SPES) (*red line*) for electron kinetic energies from 0 to 57 meV as deduced from the 2D spectrum.
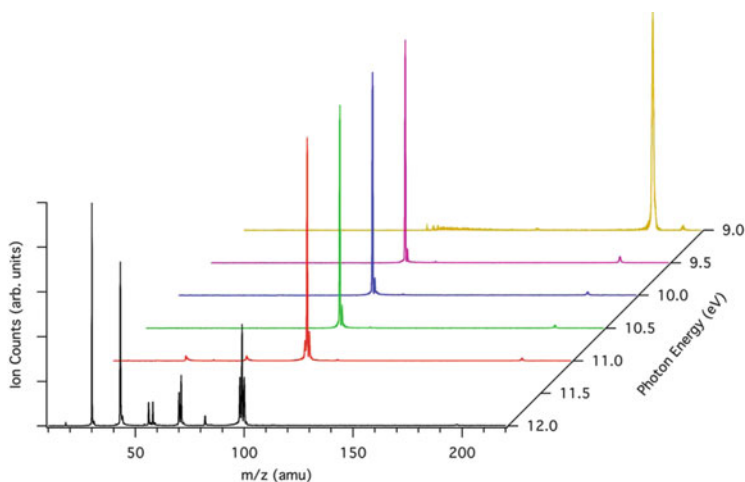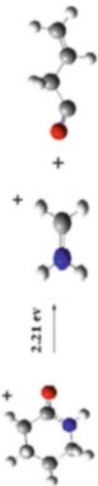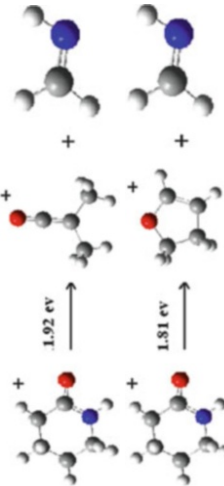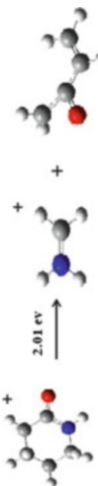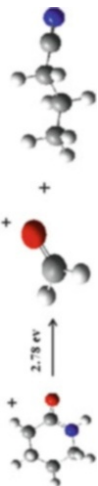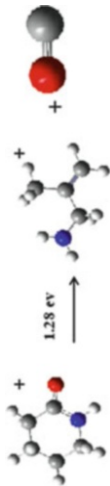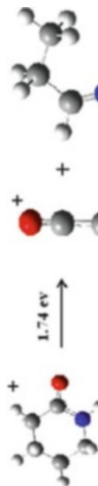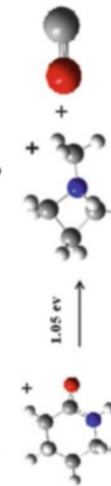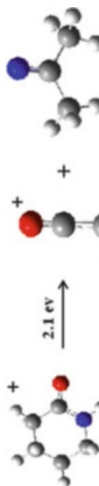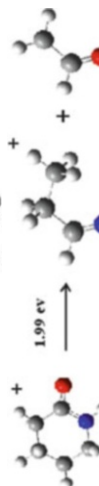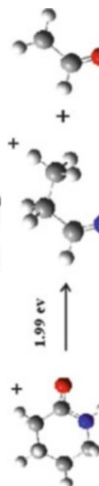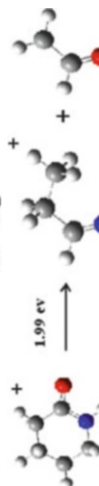
**Fig. 7** Time-of-flight (TOF) spectra of δ-valerolactam recorded at six fixed photon energies from 9.0 to 12.0 eV. Reprinted with permission from Mahjoub et al. [97]. Copyright (2012) American Chemical Society

ionization. However, rotation of the methyl group gives rise to two possible conformers, *cis* and *trans*. Trofimov et al. [23] have calculated the binding energies (BEs) and spectral band intensities in the 8.82 to 17.35 eV energy range using OVGF and ADC methods. Satisfactory agreement with their own and previous experimental spectra is achieved even though some of the electronic PE bands overlap and proper assignment, especially above 14 eV, becomes difficult. In their work, angle-dependent PE measurements helped to distinguish $\sigma$ from $\pi$ orbitals in the assignment. To give an extract from this excellent work, the lowest molecular orbitals of T have the following character and BE: $6a''(\pi_6)$, BE = 8.85 eV (OVGF, 6-311++G** basis set); $5a''(\pi_5)$, BE = 10.46 eV, $18a'(\sigma_{LP-O})$, BE = 10.46 eV; $17a'$ $(\sigma_{LP-O})$, BE = 11.36 eV; $4a''(\pi_4)$, BE = 12.52 eV. The following, more uncertain assignments can be found in [23].

Very shortly after this work, a Mass-Analyzed Threshold Ionization (MATI) spectrum was measured with high resolution (~0.1 meV). This spectrum (Fig. 8) corresponds to the photoionization of jet-cooled T close to the ionization threshold region, between its IE and IE + 1,800 $cm^{-1}$ (IE + 0.22 eV) [135]. It presents a rich structure that was attributed to the population of the lowest vibrational levels of the

---

**Fig. 6** (continued) We highlight the theoretically determined origin transitions with *vertical bars*. The synthetic spectrum (*black line*) is obtained after a rough adjustment of the experimental spectra assuming few Gaussian profiles: the narrow bands at the left side are for the ground state and the larger ones are for the two contributing autoionizing states (the *dotted* and *dashed blue lines*). *Lower panel*: SPES spectrum of delta-valerolactam$^+$ in the vicinity of the cationic ground state and its tentative assignment (*vertical lines*) by the help of the theoretical results [95]. Copyright © Wiley-VCH Verlag GmbH & Co. KGaA, Weinheim

**Table 3** Experimental linear extrapolated appearance energies (AE$_{exp}$, eV) for all the masses observed in the photodissociation of δ-valerolactam, along with their calculated fragmentation pathways

| Mass (amu) | AE$_{exp}$ | Calculated channel | Mass (amu) | AE$_{exp}$ | Calculated channel |
|---|---|---|---|---|---|
| 30 | 2.19 | 2.21 ev | 70 | 1.22<br>1.92 | 1.92 ev<br>1.81 ev |
| 43 | 1.42<br>1.96 | 2.01 ev<br>2.78 ev<br>1.74 ev<br>2.1 ev | 71 | 1.22<br>1.92 | 1.28 ev<br>1.05 ev |
| 56 | 2.00 | 1.99 ev | 82 | 1.99 | Several possibilities below 1.34 eV[a] |
|  |  |  | 98 | 1.07<br>1.85 | δ-Valerolactam$^+$ H loss (1.49 eV) |

1.95

58

2.29 ev

2.46 ev

1.80 ev

2.11 ev
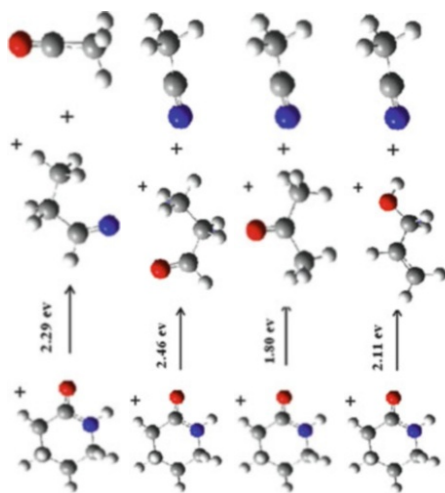
ᵃSee [97] for more details
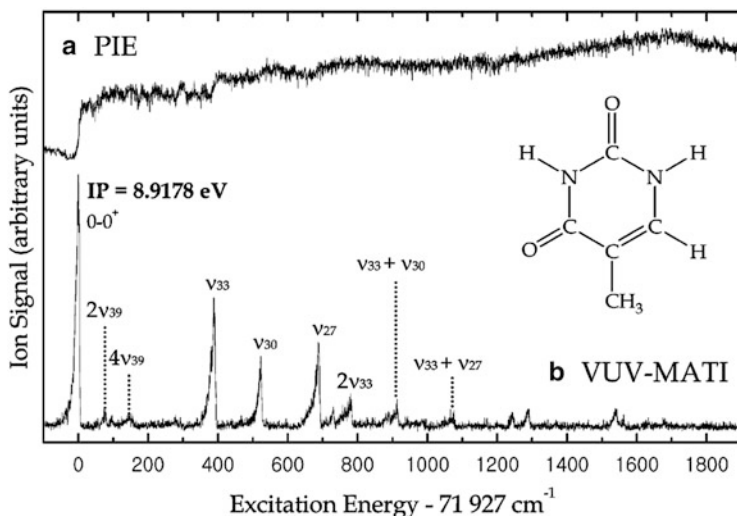
**Fig. 8** (**a**) Photoionization efficiency (PIE) and (**b**) VUV-MATI spectrum of thymine. Spectrum (**b**), recorded by nanosecond VUV laser spectroscopy (resolution ~0.8 cm$^{-1}$), can be regarded as a most highly resolved VUV spectrum in the IE + 1,800 cm$^{-1}$ region for a biological NAB. For the normal mode analysis of the S$_0$–D$_0$ transition of thymine please refer to [135]. Reprinted with permission from Choi et al. [135]. Copyright (2005) American Chemical Society

T$^+$ cation. The first normal-mode analysis of T$^+$ for the observed vibrational structure is also presented in the work of Choi et al. [135]. It is shown that the observed bands correspond to the population of the low frequency modes $\nu_{27}$, $\nu_{30}$, $\nu_{33}$, and $\nu_{39}$ of T$^+$. In addition, this spectrum is dominated by the 0–0 transition and the adiabatic IE is thus measured accurately to be AIE = 8.9178 $\pm$ 0.001 eV. The discrepancy with the value found by Jochims et al. [37], of the order of 0.1 eV, is most reasonably explained by the initial thermal energy content of the thymine neutrals produced by the source used in [37].

Later on, Bravaya et al. [43] presented a complete theoretical vibrational analysis of the S$_0$–D$_0$ transition between its origin and 9.7 eV. These authors used the high resolution MATI spectrum of Choi et al. [135] to test the quality of their calculations. In terms of accuracy in energy position, there is excellent agreement, since the theoretical AIE is computed at 8.89 eV, which differs by only ~0.02 eV from the AIE of [135]. The positions and relative intensities of the experimental vibrational bands are also nicely reproduced by the (blue-shifted) theoretical spectrum of [43] in the region between the AIE and AIE + 0.1 eV approximately (see Fig. 10 in [43]). This validates the approximation they used to compute the Franck–Condon Factors (FCF) for interpretation and prediction of experimental PESs. The authors of [43] then continue to calculate the full vibrational progression of the S$_0$–D$_0$ transition of the PES (up to AIE + 1 eV). However, in this spectral region there are considerable deviations to the experimental PES of [23]. They are explained by possible mixing with the S$_0$–D$_1$ progression, which makes sense, since
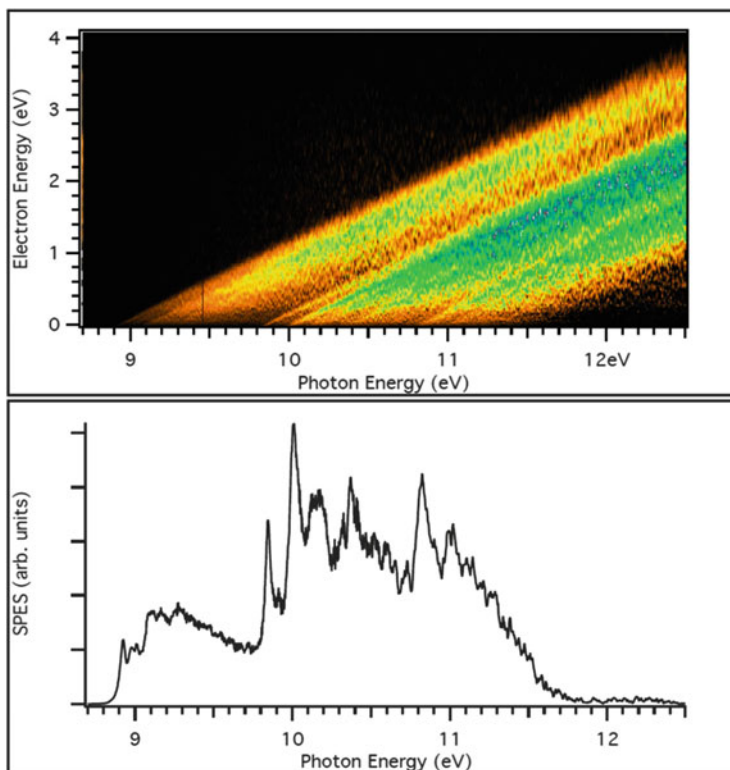
**Fig. 9** *Upper panel*: PES matrix corresponding to the thymine parent mass, obtained with oven vaporization. The energy step is 2.5 meV. *Lower panel*: SPES derived from the PES matrix by considering photoelectrons having kinetic energies less or equal 200 meV [136]

this transition is much more intense and its precise origin is not well known. Vertical ionization energies have also been calculated for the six lowest ionized electronic states of thymine by different methods. The order is found to be in agreement with the results of Trofimov et al. [23]. We note that experimental PES band positions are satisfactorily reproduced by the differentiated PIE spectrum (dPIE/dE) also presented in [43]; however, the relative spectral intensities of the experimental PES bands from [23] are not reproduced by the dPIE/dE curve.

Very recently, Majdi et al. [136] have recorded a thymine SPES spectrum at the SOLEIL synchrotron, under similar conditions to those depicted in [11] for adenine and cytosine. This spectrum is shown in Fig. 9. Strikingly, the SPES spectrum (Fig. 9, lower panel) presents rich and well-resolved structures that correspond to the electronic and vibrational structures of thymine[+] cation. This work extends the experimental spectrum of Choi et al. [135]. The full analysis of these bands is under investigation. The experimental work of Majdi et al. [136] reveals that the experimental capabilities at the DESIRS beamline of the SOLEIL synchrotron are powerful enough to get insight into the NABs cationic structure. It confirms our
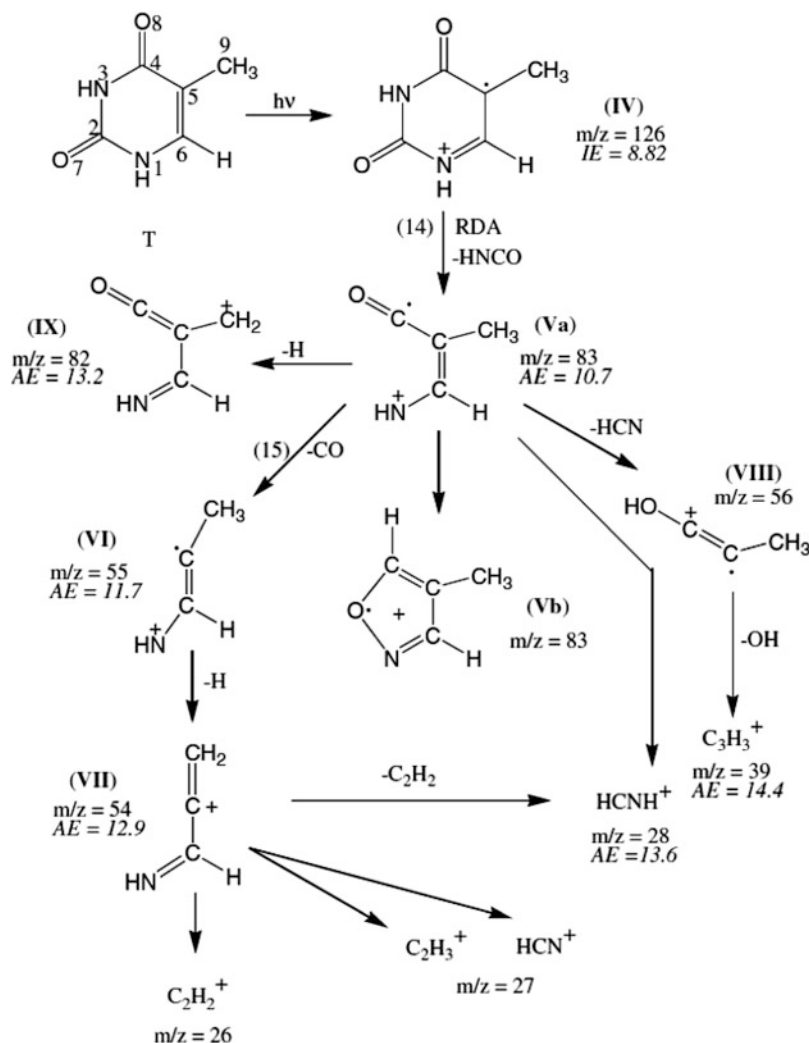
**Fig. 10** Principal fragmentation decay routes of the thymine radical cation. Measured appearance energy (AE) is given for each fragment (in eV). *Roman numerals* correspond to species discussed in [37]. Reprinted from Jochims et al. [37]. Copyright (2005), with permission from Elsevier

analysis for adenine and cytosine [11] where the congestion of the spectra resides in fact in the intrinsic complex electronic, tautomeric, and vibronic structure of adenine and cytosine (see also below).

The dissociative ionization of T was studied in detail by Jochims et al. [37]. The three main dissociation pathways, shown in Fig. 10, are as follows. (1) The loss of isocyanic acid (HNCO) by retro–Diels–Alder reaction from the thymine parent cation, to form the $m/z$ 83 residual fragment with an AE of $10.7 \pm 0.05$ eV. The loss

of HNCO involves rupture of two bonds, N3–C4 and C2–N1. The latter bond is shown to be weaker in the cation as compared to the neutral thymine [69]. (2) The subsequent loss of CO together with a fragment of $m/z$ 55 and AE $= 11.7 \pm 0.1$ eV. As was shown above, the loss of a CO is the lowest fragmentation channel of the 2-PY$^+$ and 2HP$^+$ analogues. (3) Another intense ion is seen at $m/z$ 28 (AE $= 13.6 \pm 0.1$ eV). It is assigned to the HCNH$^+$ ion (an ion observed in the interstellar medium). Other ions, with lower intensity are also detected. Possible assignments of the chemical structures of observed ions and corresponding neutral fragments, as well as formation pathways, are discussed in detail in [37].

### 4.2.2   Uracil

This RNA NAB has been less studied in the past decade than the other biological NABs. Early PE spectra are reported in [15–17, 20, 21]. As one can expect from the similarity of the chemical structure, the PE spectrum of uracil resembles closely the PE spectrum of thymine (see, for example, [20]). According to the analysis presented in [21], the four lowest lying molecular orbitals are of $\pi_1$, $n_1$, $\pi_2$, and $n_2$ character, respectively. They lie very close in energy (VIE (exptl.) = 9.53, 10.23, 10.57, and 10.99 in eV). Similar to thymine, the lowest energy tautomer of uracil is the diketo form and the second lowest tautomer is an enol form, lying 46.35 kJ/mol higher than the diketo tautomer according to high level ab initio calculations [134]. In all, 13 tautomers are identified in the work presented in [134], with relative energies up to 131 kJ/mol compared to the lowest lying diketo form. The room temperature PE spectrum of uracil thus consists of the contribution of a unique tautomer, for instance the diketo one. Experimentally, the adiabatic ionization energy of uracil was measured to be AIE $= 9.15 \pm 0.03$ eV [37], which is slightly higher than thymine's AIE. We can also mention the electron impact ionization value of VIE $= 9.59 \pm 0.08$ eV [33], in excellent agreement with the PES value obtained by Kubota et al. [21].

### 4.2.3   Adenine

The most stable tautomer of adenine is 9H-adenine, followed by two other tautomers, i.e., 3H-adenine and 7H-adenine at energies of 29 and 31 kJ/mol with respect to 9H-adenine. Both theoretical and experimental studies demonstrated that gas-phase adenine produced by heating and then followed by jet-cooling leads efficiently to the predominance of the 9H-adenine isomer in gas phase prior to ionization [43, 137–142]. Hence, the photoionization experimental spectra were fully assigned to the single tautomer 9H-adenine$^+$ + e$^-$ ← 9H-adenine + $h\nu$ transition.

The ionization of adenine has been widely studied since the 1970s using ultraviolet photoelectron spectroscopy [18, 20, 23, 143–145], photoionization mass spectrometry [146], electron impact mass spectrometry [28], and very

**Fig. 11** *Upper panel*: Differentiated PIE (*black line*) [43] and PES spectrum (*green line*) [23] of adenine. *Lower panel*: Vertical ionization energies and the corresponding MOs as computed at the EOM-IP-CCSD/cc-pVTZ level by Bravaya et al. [43]. Reprinted with permission from Bravaya et al. [43]. Copyright (2010) American Chemical Society
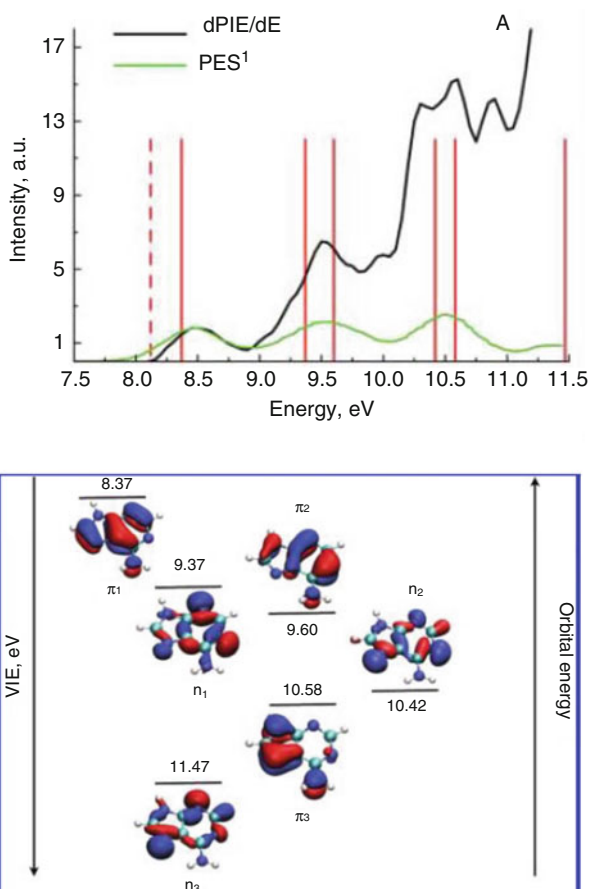


recently using slow photoelectron spectroscopy [11]. In the latter study, the close to zero kinetic energy photoelectrons and the corresponding photoions were measured in coincidence. The assignment of these experimental spectra was based on deep theoretical investigations of the structure and the electronic states of ionized adenine by means of modern theoretical methodologies [43, 147–150].

Below 8 eV, the experimental spectra of adenine present no signal and then the signals increase above $h\nu = 8$ eV [20, 23, 37, 43, 144]. This is exemplified in Fig. 11 where we show the PES spectrum of adenine measured by [23], the experimental dPIE/dE spectrum recorded at the Advanced Light Source, together with VIE calculations of [43] in the 7.5–11.5 eV energy range. Jochims et al. [37] used PIMS and SR from the BESSY synchrotron facility (Berlin-Adlershof) and proved that the fragmentation of the 9H-adenine$^+$ cation occurs for photon energies well above 11 eV. In 2013, this is confirmed by the threshold electron-ion coincidence measurements by Touboul et al. [11]. Therefore, the major contribution to the

photoelectron spectra in the energy range 8–11 eV corresponds to the 9H-adenine$^+$ radical cation.

In 2010, Krylov and coworkers computed an adiabatic ionization energy of adenine of AIE $=8.13$ eV using the equation-of-motion coupled-cluster method [43]. This value agrees well with the onset of their PIE curve found at $8.20 \pm 0.05$ eV [43] (Fig. 11, upper panel). The TPEPICO spectrum of adenine [11] shown in Fig. 12 presents a sharp peak at threshold, which is attributed by Touboul et al. to the 9H-adenine$^+$ $\widetilde{X}0_0^0 + e^- \leftarrow$ 9H-adenine $\widetilde{X}0_0^0 + h\nu$ photoionization transition. This allowed them to determine accurately the adiabatic IE of 9H-adenine as AIE $= 8.267 \pm 0.005$ eV. This value is in excellent agreement with previous ones obtained by photoionization mass spectrometry (PIMS) measurements of the relative intensity of the parent ion vs the photon energy ($8.20 \pm 0.03$ eV [37]; 8.26 eV [146]). The vertical ionization energy (VIE) of 9H-adenine corresponds to the maximum of the first band in the photoelectron spectra and was measured to be VIE $= 8.606 \pm 0.006$ eV [142], $8.44 \pm 0.03$ eV [143], and 8.48 eV [144] using photoionization techniques. The experimental VIE value of Nir et al. [142] is in excellent agreement with the maximum of the first electronic band of the TPEPICO spectrum shown in Fig. 12 (lower panel) [11]. The VIE is ~0.3 eV higher than the AIE. As established theoretically [43, 69, 151–153], this corresponds well to the Franck–Condon transition shift. Indeed, the geometrical changes between neutral and ionic 9H-adenine take place mainly on bond length and in-plane angles. In particular, ionized adenine does not lose its planarity. These precise ionization energies were used by Touboul et al. [11] to deduce an accurate heat of formation of the adenine radical cation $\Delta_f H_{298}$(adenine cation) of $1004 \pm 9$ kJ/mol. The photoionization mechanism close to and above the IEs is found to occur mainly via direct processes (Fig. 12). For the sake of completeness we mention that the IE values determined by electron impact ionization are less accurate and spread over 1 eV range [29, 154, 155].

In the 8–11 eV energy range, similar experimental spectra were measured for adenine as illustrated in Figs. 11, 12, and 13. They consist of broad bands due to the complex electronic structure of the cationic species. One can identify three broad bands centered at 8.6, 9.6, and 10.5 eV, respectively. These bands are structureless. Figure 11 displays the VIEs and the corresponding MOs as computed at the EOM-IP-CCSD/cc-pVTZ level by Krylov and coworkers [43]. According to these high level computations, these bands correspond to Koopmans-like ionization processes, where the first band is due to the ionization of the $\pi$-type HOMO, and the second and third bands are for the ionization from $\pi$- and $\sigma$-like molecular orbitals. In contrast to thymine and to the NAB analogues, the experimental spectra do not show any resolved vibrational structure in despite of a high enough experimental resolution. This is due to the complex electronic structure of 9H-adenine$^+$ as discussed widely by Krylov and coworkers [43]. For photon energies $\geq 11$ eV, the PE spectrum (Fig. 13) is composed of several bands that were attributed to the ionization from the outer-valence orbitals of adenine. The corresponding vertical
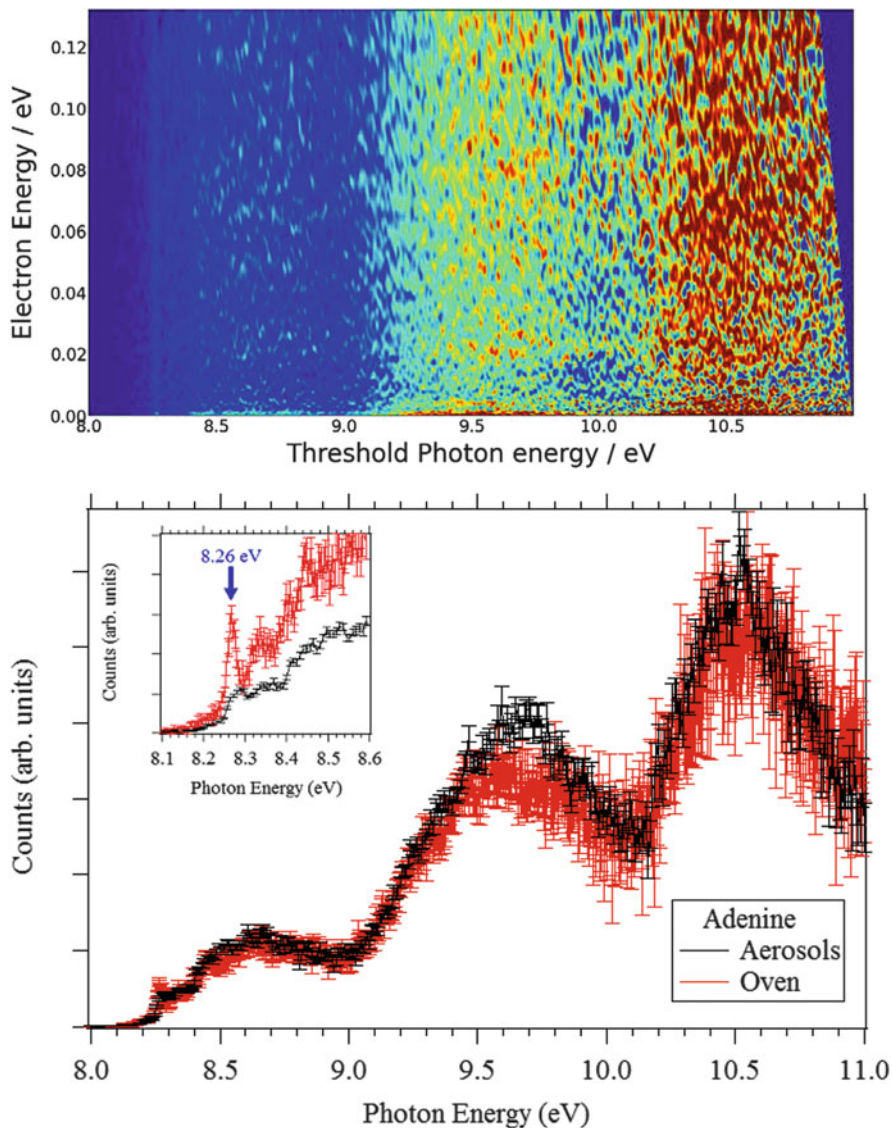
**Fig. 12** *Upper panel*: Full scale 2D spectrum of adenine obtained using oven vaporization providing the photo-electron kinetic energies as a function of the photon energy. *Lower panel*: TPEPICO spectra of the adenine parent obtained with 40 meV threshold electron resolution. The *black curve* is when adenine is vaporized with the aerosol source and the *red curve* is for in-vacuum oven. The *inset* presents an energy close up of the threshold region. Reprinted with permission from Touboul et al. [11]. Copyright (2013), AIP Publishing LLC
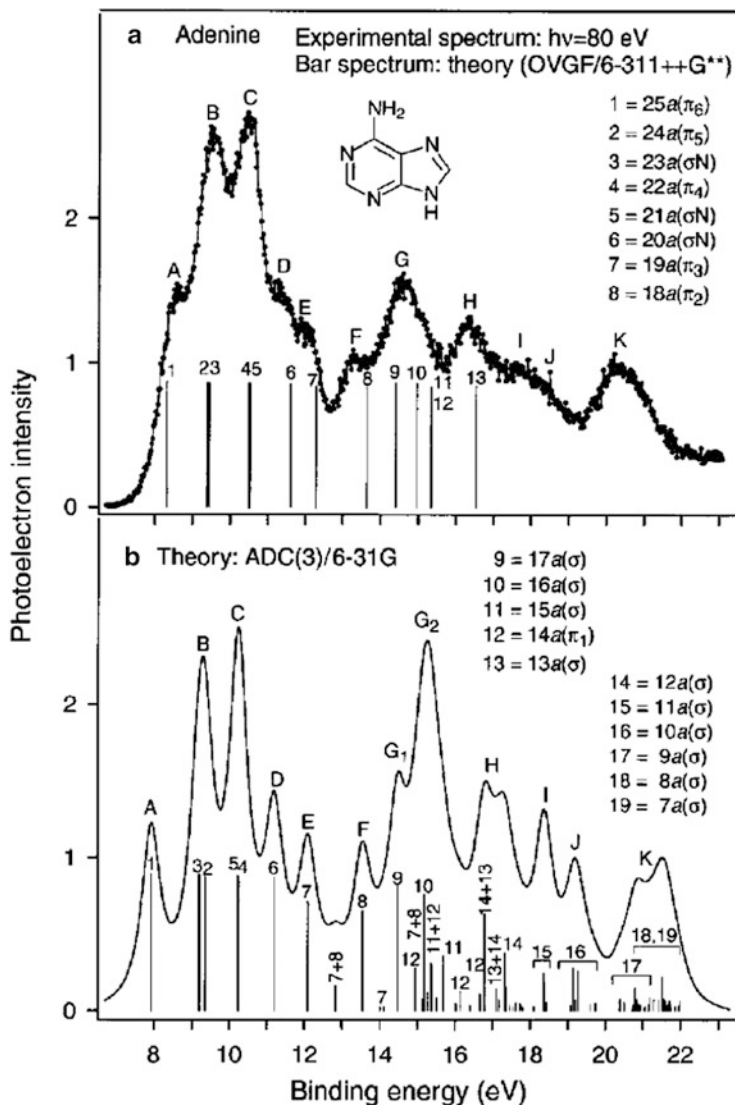
**Fig. 13** *Upper panel*: Photoelectron spectrum of adenine recorded for $h\nu = 80$ eV. *Lower panel*: synthetic theoretical spectrum obtained using the ADC(3) method Trofimov et al. [23] © IOP Publishing. Reproduced with permission. All rights reserved

ionization energies are listed in [23]. Some of the associated bands overlap significantly. This participates to the congestion of the experimental spectra.

The VUV photochemistry of adenine is very complex. For instance, Leach and coworkers [37, 156], who used a quadrupole mass spectrometer and VUV-SR for a PIMS study of adenine in the range of 6–22 eV, were able, with the help of

thermochemical data, to deduce dissociative ionization mechanisms in detail. The recent experiments of Pilling et al. [157], using a photoelectron-photoion coincidence technique (PEPICO), confirmed such a complex chemistry upon ionization of adenine. Both groups showed that the adenine cation fragments at energies between 10.7 and 22 eV. However, the most abundant ion, even at $h\nu = 21$ eV, is still the parent ion $C_5H_5N_5^+$. This confirms the high stability of adenine upon absorption of a VUV photon. Both groups also observed other intense fragment ions such as $C_4H_4N_4^+$, $C_3H_3N_3^+$, $C_2H_2N_2^+$ (corresponding to successive losses of HCN), $NH_2CNH^+$, as well as $HCNH^+$. Through the analysis of the relative abundances for each ionic fragment and their mean kinetic energy release, they found that the production of the neutral HCN fragment represents up to 40% of the dissociative channels for this molecule as induced by VUV photons. Interestingly, some of these products are also observed after unimolecular decomposition of the δ-valerolactam cation as illustrated above.

### 4.2.4 Cytosine

In the literature there exist several ab initio computations of the equilibrium structures, the relative energies, and the ionization energies of the tautomers of cytosine [36, 42, 43]. These studies showed that these tautomers are close in energy. Five of them (for instance, C1, C2a, C2b, C3a, and C3b) are located within energy differences less than 11.5 kJ/mol (cf. Fig. 14). Accordingly, molecular beams of cytosine are most likely composed of a mixture of several tautomers prior to ionization. The composition of the neutral gas depends strongly on the techniques used for vaporization (gas temperature, oven vaporization, aerosols, etc., see our discussion in Sect. 2.3.1). The three most stable forms (for instance C1, C2b, and C3a) are expected to prevail. Analysis of the recent experimental photoionization spectra mainly considers the contribution of these three tautomers. This makes the situation more complicated for cytosine than for adenine.

Photoionization of cytosine was studied using mass spectrometry coupled to VUV rare gas lamps for excitation [39] and VUV-SR sources at the Advanced Light Source [38, 42], at the Daresbury Laboratory storage ring [23], and very recently at Synchrotron SOLEIL [11]. The 2D spectrum of the cytosine⁺ cation, of photoelectrons having kinetic energies from 0 to 140 meV is displayed in Fig. 15 (upper panel) [11]. This 2D matrix reveals that the single photoionization of cytosine occurs mainly by a direct process in the energy ranges of interest, so that autoionization processes can be neglected. We present in Fig. 14 the PES and the differentiated PIE curve (upper panel) up to 3 eV above the IE and in Fig. 15 (lower panel) the TPEPICO spectrum of cytosine from threshold up to 2 eV above the IE. This is the spectral region covering the excitation of the lowest lying electronic excited states of the ion. Within the TPEPICO measurement scheme, the mass selection ensures that only the photoelectrons associated with the cytosine ion are detected in coincidence, ruling out the contribution of eventual fragments. All these experimental spectra are similar. They start by a sharp increase of the signal close to the IE of cytosine.
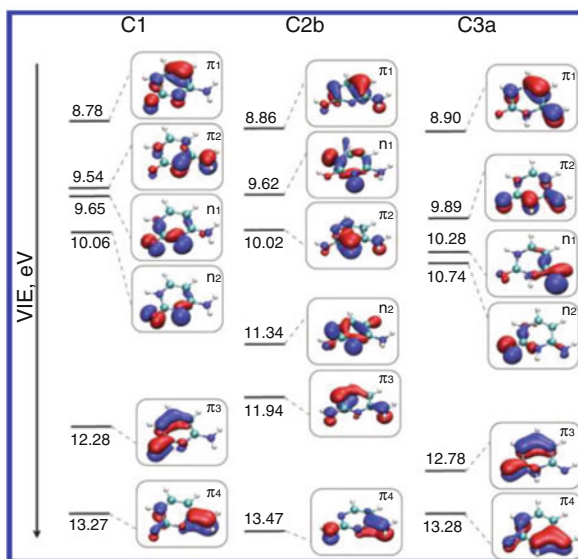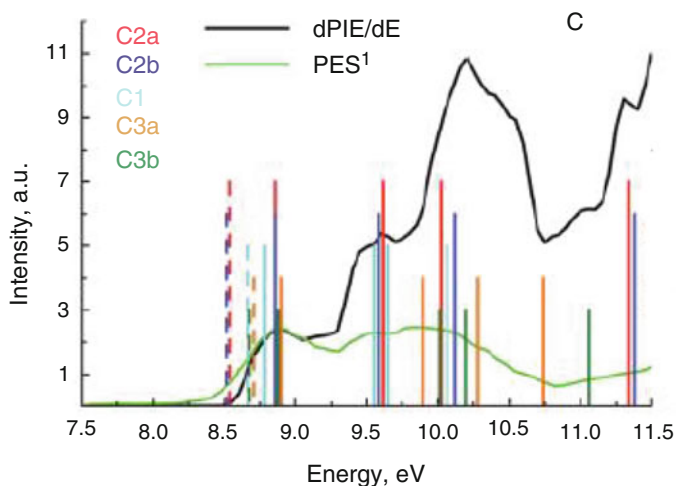
**Fig. 14** *Upper panel*: Differentiated experimental PIE spectrum (*black line*) of cytosine [43] and experimental PES spectrum (*green line*) [23] of cytosine. *Lower panel*: Vertical ionization energies and the corresponding MOs as computed at the EOM-IP-CCSD/cc-pVTZ level by Krylov and coworkers [43]. C1, C2b, and C3a correspond to the most stable forms of the neutral cytosine. See [23] for more details. Reprinted with permission from Bravaya et al. [43]. Copyright (2010) American Chemical Society

The ionization energy of cytosine has been determined experimentally by several methods. Using electron impact ionization, the IE is found to be $IE = 9.0 \pm 0.1$ eV [154]. Using PIMS in combination with a hydrogen discharge lamp, values of $AIE = 8.68$ eV and $VIE = 8.94$ eV have been obtained [146]. With
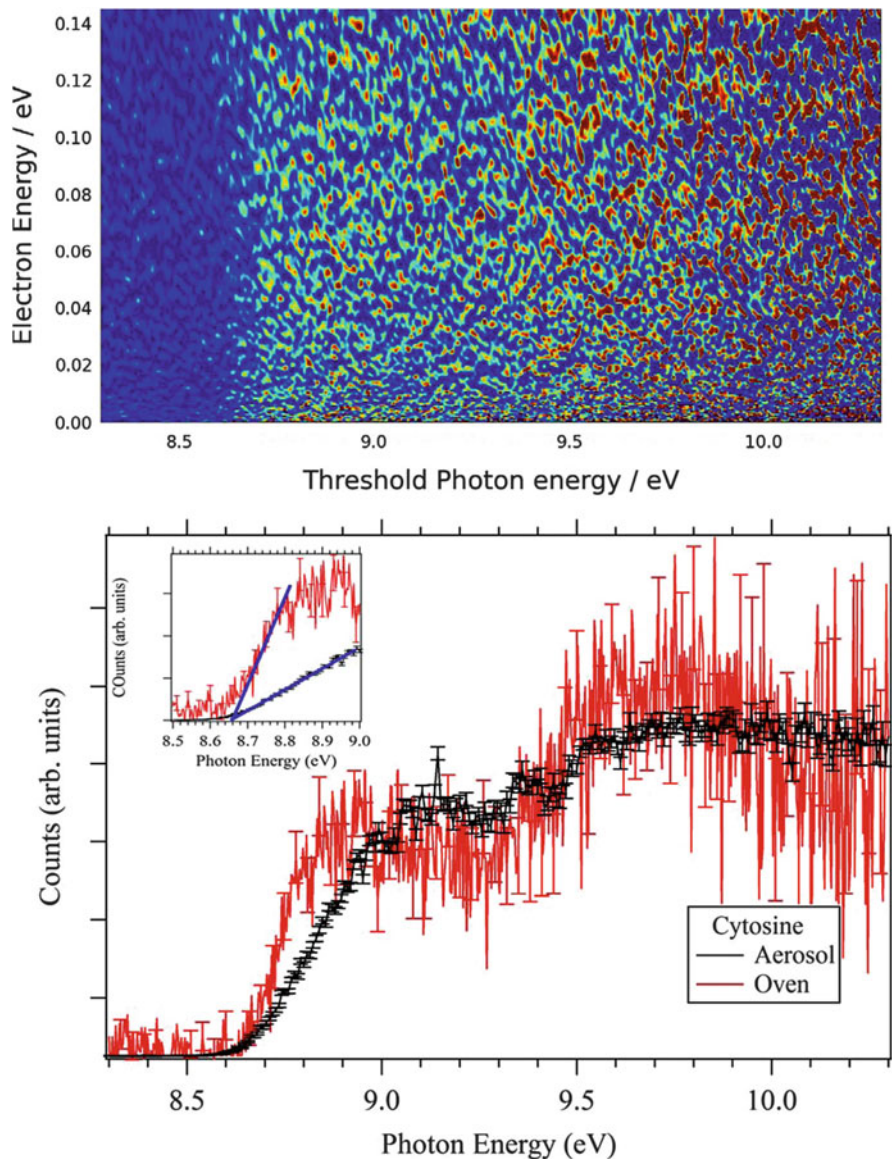
**Fig. 15** *Upper panel*: Full scale 2D spectrum of cytosine obtained using oven vaporization providing the photo-electron kinetic energies vs the photon energy. *Lower panel*: TPEPICO spectra of the cytosine parent obtained with 40 meV threshold electron resolution when using the aerosol source (*black curve*) and with 80 meV (*red curve*) when using the in-vacuum oven. The *inset* is an enlargement for the threshold ionization energy where the *oblique lines* are to enlighten the slopes at the ionization threshold. Reprinted with permission from Touboul et al. [11]. Copyright (2013), AIP Publishing LLC

PES, IE = 8.45 eV [19] and VIE = $8.94 \pm 0.03$ eV [143] are obtained. Finally, very recently, the AIE of cytosine has been determined to be AIE = $8.66 \pm 0.01$ eV using TPEPICO [11]. Since there is no clear adiabatic transition in the TPEPICO spectrum of [11], the latter value was deduced by linear extrapolation of the first onset of the TPEPICO spectrum as illustrated in the inset in Fig. 15. This recent AIE value agrees very well with the measurements of Kostko et al. ($8.60 \pm 0.05$ eV [42]), whereas some deviations are observed with the earlier PES values which can be partially explained by different compositions of the cytosine tautomer distribution in the gas jet prior to photoionization. The spectra are composed of several overlapped bands corresponding to the population of the ground and the first two electronic excited states of this cation. For energies >11 eV, the PE spectrum (Fig. 16) shows several bands due to ionization of the outer-valence molecular orbitals of cytosine.

Similar to adenine, the VUV photochemistry of cytosine upon ionization is complex. For illustration, we mention the combined theoretical and neutralization–reionization mass spectrometric study performed by Wolken et al. [36] (cf. Fig. 17). Interestingly, these authors observed that metastable cytosine cation–radicals undergo ring-cleavage dissociations by eliminations of CO (major) and HNCO (minor). The production of CO was also discussed for the fragmentation of thymine$^+$, 2-pyridone$^+$, and 2-hydroxypyridone$^+$ cations (see above).

## 4.2.5   Guanine

Guanine has been a little less studied in the past than the other biological NABs, most probably because it is more difficult to bring this compound into the gas phase as compared to the other NABs whose molecular weight is lower. The compound has to be heated up to more than 300°C, which is close to its melting point, in order to have sufficient vapor pressure to perform gas phase measurements. Using SR-PIMS, Zaytseva et al. showed that, even at these high temperatures, guanine is not thermally degraded [24]. Furthermore, guanine is insoluble in water, in contrast to all other biological NABs, which hinders the use of the soft aerosol desorption technique described above. PE spectra are presented in [19, 24]. In the article of Hush and Cheung [143], an ionization energy determined by PES is reported. Electron impact ionization studies are given in [28, 158]. Plekan et al. recorded PI mass spectra using rare gas lamp radiation at five spectral lines between 8.43 and 21.2 eV [39]. Jet-cooled guanine and G-$(H_2O)_n$ ($n = 1$–3) clusters have also been studied at the Advanced Light Source, using PIMS [38, 41]. The most comprehensive theoretical studies of higher excited states of neutral and ionic guanine are detailed in [24, 147, 148, 159]. Briefly, they mainly concern the simulations of its PE spectrum [24], ab initio calculations of the ionization energies [147, 148] and of the relative energies of the numerous guanine tautomers [159].

Guanine has four nitrogen-bonded hydrogen atoms that can potentially migrate. According to the ab initio calculations presented in [159], the four lowest lying tautomers are within 0.1 eV of each other. Four other tautomers lie within 0.28 eV
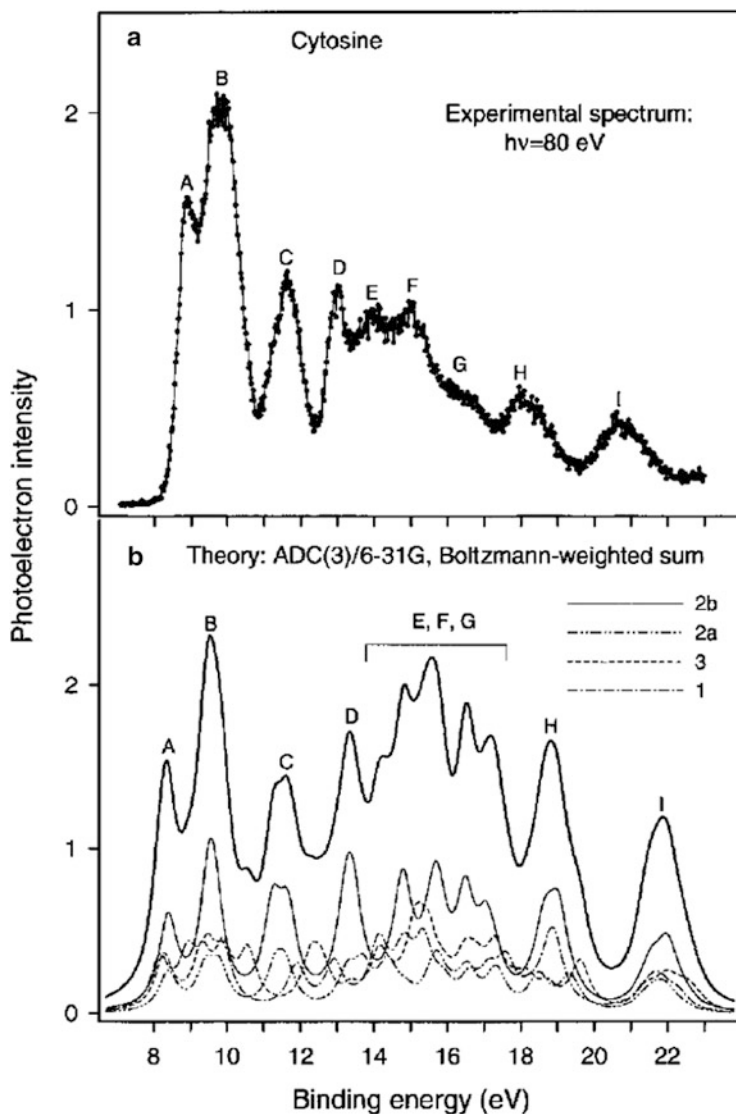
**Fig. 16** *Upper panel*: Photoelectron spectrum of cytosine recorded for $h\nu = 80$ eV. *Lower panel*: synthetic theoretical spectrum obtained using the ADC(3) method (Trofimov et al. [23]) © IOP Publishing. Reproduced with permission. All rights reserved

above the lowest. Gas phase guanine, even if jet-cooled, is therefore necessarily a mixture of these different molecules. According to IE calculations reviewed in [41], their respective AIEs lie between 7.80 and 8.17 eV, and their VIEs between 8.16 and 8.44 eV. These values agree well with experimental PE spectra [19, 24]. Zhou et al. [41] tried to relate the experimental photoionization efficiency curve recorded
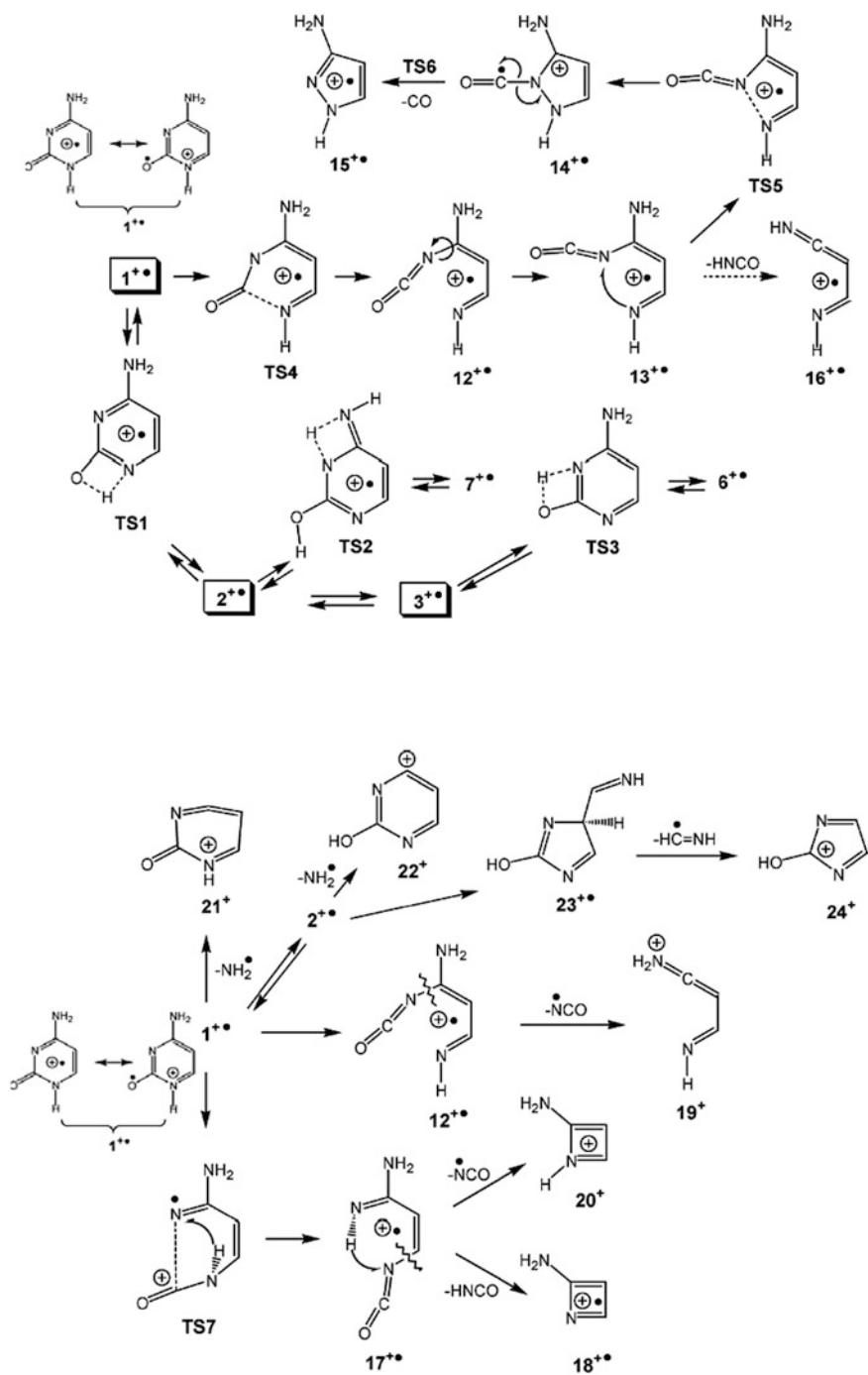
**Fig. 17** Schematic representation of the unimolecular decomposition processes undertaken by the cytosine[+]radical cation. Reprinted from Wolken et al. [36] Copyright (2007), with permission from Elsevier

by PIMS in combination with VUV-SR to the theoretical VIEs. Comparing thermal vaporization and laser desorption by an Nd:YLF laser (operating at $\lambda = 527$ nm), they were able to show that different tautomer populations are produced with these two different vaporization methods. In the comprehensive theoretical and experimental study of Zaytseva et al. [24], full valence shell PE spectra from the IE up to 24 eV are presented. In their calculations, the four most stable guanine tautomers are considered. The composite theoretical spectrum, constructed from a Boltzmann distribution of the four tautomers at $T = 600$ K, reproduces the experimental PE spectrum quite well (see Fig. 18).

The dissociative photoionization of guanine has been studied by Plekan et al. [39], using rare gas lines for excitation and time-of-flight PIMS, at 8.43, 10.0, 11.62, 16.67, and 21.2 eV incident photon energies. These authors measured a dominating mass peak corresponding to the parent ion of guanine, $C_5H_5N_5O^+$, for all photon energies (even at 21.2 eV). Similar to adenine$^+$, the guanine$^+$ cation shows a remarkable stability against VUV radiation-induced fragmentation. For $h\nu = 11.62$ eV the PI mass spectrum of guanine is almost fragment-free. Fragmentation develops at higher energies. At $h\nu = 21.2$ eV the main fragment ions are $m/z$ 43 and 44, which have, however, less than half the intensity of the parent ion. Many other ions with low intensity are also observed. For the sake of completeness, we mention the earlier EI mass spectrometric studies [28, 158]. Rice and Dudek [28] have made suggestions for fragmentation mechanisms of guanine (and three different methyl derivatives) upon electron impact ionization. However, a detailed study of the photoionization fragmentation mechanisms, taking advantage of accurate thermochemical data of the implied cationic and neutral fragments, is still missing. Nowadays, such thermochemical data can be calculated in a relatively easy way.

## 4.3   Complexes of NABs

The investigation of NABs complexes of increasing size can mimic the transition from the isolated molecules to the solution (or bulk) phase. For instance, the microhydration of the NABs T, A, C, and G has been studied recently at the Advanced Light Source [38, 44]. The experimental PIE spectra of mono-, di-, and tri-hydrates are used to gain insight into the computation of the FCF of such hydrogen-bonded aggregates. These authors found that ionization energies of mixed NAB-$(H_2O)_n$ ($n = 1$–3) clusters decrease by 0.3 eV approximately when going from $n = 0$ to $n = 3$, except for guanine. For the latter, the onset of the PIE curve of the monomer $C_5H_5N_5O^+$ is found at $E = 8.1 \pm 0.1$ eV (see our discussion above). The onsets of the PIE curves of the three water clusters G-$(H_2O)_n$ ($n = 1$–3) are all found at $8.0 \pm 0.1$ eV, indicating that the shift in ionization energy upon microhydration is only about 0.1 eV for this molecule. However, one must note the poor signal-to-noise ratio of the G-$(H_2O)_n$ ($n = 1$–3) PIE curves in these difficult experiments. In a related topic, the combined theoretical and SPES studies of the
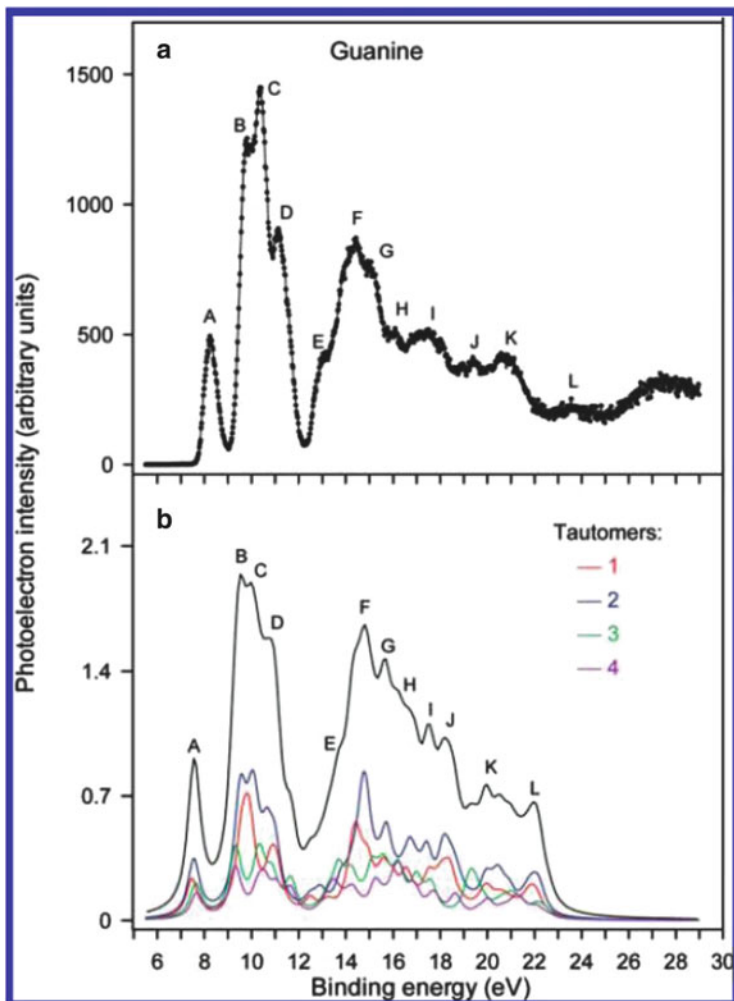
**Fig. 18** (**a**) Experimental valence shell photoelectron spectrum of guanine, photon energy 100 eV. (**b**) Composite theoretical spectrum of guanine, constructed from the Boltzmann-weighted sum for $T = 600$ K of the individual spectra representing the 1–4 forms. The individual contributions are also shown. Reprinted with permission from Zaytseva et al. [24]. Copyright (2009) American Chemical Society

δ-valerolactam dimer [95, 97] revealed that (δ-valerolactam)$_2^+$ cation is subject to an intramolecular isomerization, H-transfer, and further unimolecular fragmentation processes. These unimolecular processes occur either along the ground or the excited state potential energy surfaces of (δ-valerolactam)$_2^+$.

Thymine dimers and the binary adenine–thymine aggregate have also been thoroughly studied, both experimentally and theoretically. For instance, theoretical binding energies (between monomers in the dimer) of different geometries and the

computed AIEs and VIEs of these aggregates are reported and analyzed in [12]. It was found there that the non-covalent interactions strongly affect the ionization energies, both AIE and VIE. The origin of the experimental PIE curve agrees well with the calculated AIE of a π-stacked TT dimer. The observed IE shifts in AA and AT clusters are smaller relative to TT, probably due to a less efficient overlap of the highest molecular orbitals, the smaller dipole of A, and the larger energy gap between ionized states of A and T monomers in the case of AT.

## 5 Conclusions and Perspectives

The present chapter reviews the most recent theoretical and experimental methodologies and results on the photoionization of NABs and their analogues in the VUV spectral regime. The electron spectroscopy of the ions and their unimolecular decomposition processes were mainly covered. It turns out from this presentation that the complexity of the spectra is due to the complex electronic structure of the cationic species and to the possible contribution of more than one tautomer. Thymine apparently represents an exception with a vibrationally resolved spectrum. The fragmentation of NAB cations leads to the formation of CO, HCN, and other prebiotic units. As stated above, the reverse reactions in prebiotic media may be at the origin of the formation of biological building blocks in these media.

In the field of theoretical chemistry, new developments for treating the nuclear dynamics beyond the adiabatic approximation should be undertaken. Indeed, the experimental spectra of the NABs and of their analogues show strong vibronic coupling between the cationic electronic states. These couplings induce mixing of the electronic wave functions of the corresponding electronic states in the vicinity of their avoided crossings or crossing. Hence, they strongly disturb the pattern of rovibrational levels of these states and result in nontrivial nuclear dynamics. In this case, the system behavior can be revealed by time-dependent multidimensional wave packet simulations, while taking into account coupling between the electronic states, and so exploring the dynamics beyond the Born–Oppenheimer or adiabatic approximation. Such types of simulation are still challenging and should be developed. This is also essential for studying pairing between DNA base pairs and damage of the hydrogen bonding systems by X-ray radiation.

The interaction of DNA and RNA bases and analogs with soft and hard X-ray light can result in ultrafast physico-chemical processes more complex than direct photoionization. These ultrafast processes induced by core-hole or valence ionization may also be studied in the near future. Inner-shell excitation or ionization of isolated molecules leads to the formation of highly excited species, which have been shown to decay on a very short timescale (order of femtosecond) by electronic decay and/or nuclear motion or dissociation. Following the excitation or ionization of electrons from the K (1s), L (2p), or M (3d) electronic shells of light elements constituting the DNA bases (C, N, O), electronic decay of the system will most probably occur (~99% of the decay events) by non-radiative electronic decay

(so called Auger decay), producing ions in a broad range of excited electronic and rovibrational states. The resonant processes form single charged cations, while non-resonant inner-shell ionization results in the formation of dications. The cross-sections for these channels depend on the frequency of the X-ray radiation, on transition dipole moments, as well as on the potential energy surface of the core-hole and cationic states. These scattering processes are described essentially as one-step processes. They may result in unusual molecular decomposition, ultrafast dissociation, or unexpected molecular reactivity, and have to be taken into account in order to obtain the global picture of photo-induced reaction and damage of the DNA base prototypes. Investigation of these processes can be done with the help of time-dependent wave packet scattering through intermediate core-hole states and, experimentally, by X-FEL sources.

From an experimental point of view, different vaporization methods have been applied to study gas phase NABs. They all proved to be successful. Their respective advantages and disadvantages have been discussed in this chapter. Their efficiency will probably be further enhanced in the future but substantial progress (by orders of magnitude) is currently not expected from this side. Concerning VUV beamlines coupled to third generation VUV-SR sources, we are today probably close to the limit to what can be done in terms of experimental spectroscopy of NABs with these sources, in combination with the connected state-of-the-art ion and electron spectrometers (considering for instance the problem of spectral congestion). In the field of experimental molecular VUV photophysics, a promising new step is the advent of VUV FEL sources developed in parallel at several places in the world (Germany, Italy, China, USA), with brilliances well above third generation SR sources. Although the tunability of these sources will be limited (in the beginning), their pulsed time structure will allow (1) for pump-probe spectroscopy well above the ionization threshold and (2) the straightforward combination with pulsed laser desorption. This will open up a whole new research field of experimental and theoretical VUV photophysics.

# References

1. Hagen U (1986) Radiat Environ Biophys 25:261
2. Kumar A, Sevilla MD (2010) Chem Rev 110:7002
3. Shikazono N, Noguchi M, Fujii K, Urushibara A, Yokoya A (2009) J Radiat Res 50:27
4. Ng CY (2014) Annu Rev Phys Chem 2014:65
5. Pan Y, Zhang L, Guo H, Deng L, Qi F (2010) Int Rev Phys Chem 29:369
6. Zhou Z, Guo H, Qi F (2011) Trends Anal Chem 30:1400
7. Bodi A, Hemberger P, Gerber T, Sztáray B (2012) Rev Sci Instr 83:083105
8. Garcia GA, Cunha de Miranda BK, Tia M, Daly S, Nahon L (2013) Rev Sci Instr 84:053112
9. Poully JC, Schermann JP, Nieuwjaer N, Lecomte F, Grégoire G, Desfrançois C, Garcia GA, Nahon L, Nandi D, Poisson L, Hochlaf M (2010) Phys Chem Chem Phys 12:3566
10. Gaie-Levrel F, Garcia GA, Schwell M, Nahon L (2011) Phys Chem Chem Phys 13:7024
11. Touboul D, Gaie-Levrel F, Garcia GA, Nahon L, Poisson L, Schwell M, Hochlaf M (2013) J Chem Phys 138:094203
12. Bravaya BS, Kostko O, Ahmed M, Krylov AI (2010) Phys Chem Chem Phys 12:2292
13. Golan A, Bravaya KB, Kudirka R, Kostko O, Leone SR, Krylov AI, Ahmed M (2012) Nat Chem 4:323
14. Golan A, Ahmed M (2012) J Vis Exp 68:e50164
15. Lauer G, Schäfer WW, Schweig A (1975) Tetrahedron Lett 45:3942
16. Dougherty D, Wittel K, Meeks J, McGlynn SP (1976) J Am Chem Soc 98:3815
17. Padva A, O'Donnell TJ, LeBreton PR (1976) Chem Phys Lett 41:278
18. Peng S, Padva A, LeBreton PR (1976) Proc Natl Acad Sci USA 73:2966
19. Dougherty D, Younathan ES, Voll S, Abdulnur S, McGlynn SP (1978) J Electron Spectrosc Relat Phenom 13:379
20. Urano S, Yang X, LeBreton PR (1989) J Mol Struct 214:315
21. Kubota M, Kobayashi T (1996) J Electron Spectrosc Relat Phenom 82:61
22. Dolgounitcheva O, Zakrzewski VG, Ortiz JV (2002) J Phys Chem A 106:8411
23. Trofimov AB, Schirmer J, Kobychev VB, Potts AW, Holland DMP, Karlsson L (2006) J Phys B At Mol Opt Phys 39:305
24. Zaytseva IL, Trofimov AB, Schirmer J, Plekan O, Feyer V, Richter R, Coreno M, Prince KC (2009) J Phys Chem A 113:15142
25. Müller-Dethlefs K, Schlag EW (1998) Angew Chem Int Ed 37:1346
26. Leach S, Eland JHD, Price SD (1989) J Phys Chem 93:7575
27. Rice JM, Dudek GO, Barber M (1965) J Am Chem Soc 87:4569
28. Rice JM, Dudek GO (1967) J Am Chem Soc 89:2719
29. Lifschitz C, Bergmann ED, Pullman B (1967) Tetrahedron Lett 46:4583
30. Ulrich J, Teoule R, Massot R, Cornu A (1969) Org Mass Spectrom 2:1183
31. Barrio MG, Scopes DIC, Holtwick JB, Leonard NJ (1981) Proc Natl Acad Sci USA 78:3986
32. Sethi SK, Gupta SP, Jenkins EE, Whitehead CW, Townsend LB, McCloskey JA (1982) J Am Chem Soc 104:3349
33. Denifl S, Sonnweber B, Hanel G, Scheier P, Märk TD (2004) Int J Mass Spectrom 238:47
34. Denifl S, Ptasińska S, Gstir B, Scheier P, Märk TD (2004) Int J Mass Spectrom 232:99
35. Turecek F, Wolken JK (2001) J Phys Chem A 105:8740
36. Wolken JK, Yao C, Turecek F, Polce MJ, Wesdemiotis C (2007) Int J Mass Spectrom 267:30
37. Jochims HW, Schwell M, Baumgärtel H, Leach S (2005) Chem Phys 314:263
38. Belau L, Wilson KR, Leone SR, Ahmed M (2007) J Phys Chem A 111:7562
39. Plekan O, Feyer V, Richter R, Coreno M, de Simone M, Prince KC (2007) Chem Phys 334:53
40. Feyer V, Plekan O, Richter R, Coreno M, Prince KC (2009) Chem Phys 358:33
41. Zhou J, Kostko O, Nicolas C, Tang X, Belau L, de Vries MS, Ahmed M (2009) J Phys Chem A 113:4829
42. Kostko O, Bravaya KB, Krylov AI, Ahmed M (2010) Phys Chem Chem Phys 12:2860

43. Bravaya KB, Kostko O, Dolgikh S, Landau A, Ahmed M, Krylov AI (2010) J Phys Chem A 114:12305
44. Khistyaev K, Bravaya KB, Kamarchik E, Kostko O, Ahmed M, Krylov AI (2011) Faraday Discuss 150:313
45. Khistyaev K, Golan A, Bravaya KB, Kamarchik E, Orms N, Krylov AI, Ahmed M (2013) J Phys Chem A 117:6789
46. Mysak E, Wilson KR, Jiminez-Cruz M, Ahmed M, Baer T (2005) Anal Chem 77:5953
47. Wilson KR, Jiminez-Cruz M, Nicolas C, Belau L, Leone SR, Ahmed M (2006) J Phys Chem A 110:2106
48. Kostko O, Takahashi LK, Ahmed M (2011) Chem Asian J 6:3066
49. Gaie-Levrel F, Gutlé C, Jochims HW, Rühl E, Schwell M (2008) J Phys Chem A 112:5138
50. Leach S, Schwell M, Garcia GA, Benilan Y, Fray N, Gazeau MC, Gaie-Levrel F, Champion N, Guillemin JC (2013) J Chem Phys 139:184304
51. Baer T, Mayer PM (1997) J Am Soc Mass Spectrom 8:103–115
52. Briant M, Poisson L, Hochlaf M, de Pujo P, Gaveau MA, Soep B (2012) Phys Rev Lett 109:193401
53. Gaussian, Revision A, Frisch MJ, Trucks GW, Schlegel HB, Scuseria GE, Robb MA, Cheeseman JR Scalmani G, Barone V, Mennucci B, Petersson GA, Nakatsuji H, Caricato M, Li X, Hratchian HP, Izmaylov AF, Bloino J, Zheng G, Sonnenberg JL, Hada M, Ehara M, Toyota K, Fukuda R, Hasegawa J, Ishida M, Nakajima T, Honda Y, Kitao O, Nakai H, Vreven T, Montgomery JA Jr, Peralta JE, Ogliaro F, Bearpark M, Heyd JJ, Brothers E, Kudin KN, Staroverov VN, Kobayashi R, Normand J, Raghavachari K, Rendell A, Burant JC, Iyengar SS, Tomasi J, Cossi M, Rega N, Millam NJ, Klene M, Knox JE, Cross JB, Bakken V, Adamo C, Jaramillo J, Gomperts R, Stratmann RE, Yazyev O, Austin AJ, Cammi R, Pomelli C, Ochterski JW, Martin RL, Morokuma K, Zakrzewski VG, Voth GA, Salvador P, Dannenberg JJ, Dapprich S, Daniels AD, Farkas Ö, Foresman JB, Ortiz JV, Cioslowski J, Fox DJ (2009) Gaussian, Inc., Wallingford CT
54. Werner H-J, Knowles PJ, Knizia G, Manby FR, Schütz M, Celani P, Korona T, Lindh R, Mitrushenkov A, Rauhut G, Shamasundar KR, Adler TB, Amos RD, Bernhardsson A, Berning A, Cooper DL, Deegan MJO, Dobbyn AJ, Eckert F, Goll E, Hampel C, Hesselmann A, Hetzer G, Hrenar T, Jansen G, Köppl C, Liu Y, Lloyd AW, Mata RA, May AJ, McNicholas SJ, Meyer W, Mura ME, Nicklaß A, O'Neill DP, Palmieri P, Pflüger K, Pitzer R, Reiher M, Shiozaki T, Stoll H, Stone AJ, Tarroni R, Thorsteinsson T, Wang M, Wolf A. See http://www.molpro.net for more details (versions 2008, 2010 and 2012)
55. Karlström G, Lindh R, Malmqvist PA, Roos BO, Ryde U, Veryazov V, Widmark PO, Cossi M, Schimmelpfennig B, Neogrady P, Seijo L (2003) Comput Mater Sci 28:222
56. Schmidt MW, Baldridge KK, Boatz JA, Elbert ST, Gordon MS, Jensen JH, Koseki S, Matsunaga N, Nguyen KA, Su S, Windus TL, Dupuis M, Montgomery JA Jr (1993) J Comput Chem 14:1347
57. Ahlrichs R, Bar M, Haser M, Horn H, Kolmel C (1989) Chem Phys Lett 162:165
58. Lischka H, Shepard R, Shavitt I, Pitzer RM, Dallos M, Mueller T, Szalay PG, Brown FB, Ahlrichs R, Boehm HJ, Chang A, Comeau DC, Gdanitz R, Dachsel H, Ehrhardt C, Ernzerhof M, Hoechtl P, Irle S, Kedziora G, Kovar T, Parasuk V, Pepper MJM, Scharf P, Schiffer H, Schindler M, Schueler M, Seth M, Stahlberg EA, Zhao J-G, Yabushita S, Zhang Z, Barbatti M, Matsika S, Schuurmann M, Yarkony DR, Brozell SR, Beck EV, Blaudeau J-P (2006) COLUMBUS: an ab initio electronic structure program, release 5.9.1: www.univie.ac.at/columbus
59. Stanton JF, Gauss J, Watts JD, Lauderdale WJ, Bartlett RJ (1992) Int J Quantum Chem S 26:879
60. Pople JA, Krishnan R, Schlegel HB, Binkley JS (1978) Int J Quantum Chem XIV:545
61. Møller C, Plesset MS (1934) Phys Rev 46:618
62. Hampel C, Peterson K, Werner HJ (1992) Chem Phys Lett 190:1
63. Amos RD, Andrews JS, Handy NC, Knowles PJ (1991) Chem Phys Lett 185:256

64. Knowles PJ, Hampel C, Werner HJ (1993) J Chem Phys 99:5219
65. Knowles PJ, Hampel C, Werner HJ (2000) J Chem Phys 112:3106
66. Raghavachari K, Trucks GW, Pople JA, Head-Gordon M (1989) Chem Phys Lett 157:479
67. Parr RG, Yang W (1998) Density functional theory of atoms and molecules. Oxford University Press, New York
68. Chong DP (ed) (1995) Recent advances in density functional methods. World Scientific, Singapore, p 287
69. Improta R, Scalmani G, Barone B (2000) Int J Mass Spectrom 201:321
70. Adler TB, Knizia G, Werner HJ (2007) J Chem Phys 127:221106
71. Werner HJ, Knizia G, Manby FR (2011) Mol Phys 109:407
72. Knizia G, Adler TB, Werner HJ (2009) J Chem Phys 130:054104
73. Brites V, Hochlaf M (2009) J Phys Chem A 113:11107
74. Lique F, Klos J, Hochlaf M (2010) Phys Chem Chem Phys 12:15672
75. Rauhut G, Knizia G, Werner HJ (2009) J Chem Phys 130:054105
76. Hochlaf M (2013) Phys Chem Chem Phys 15:9967
77. Peterson KA, Adler TB, Werner HJ (2008) J Chem Phys 128:084102
78. Weigend FA (2002) Phys Chem Chem Phys 4:4285
79. Hättig C (2005) Phys Chem Chem Phys 7:59
80. Klopper W (2001) Mol Phys 99:481
81. Yousaf KE, Peterson KA (2008) Chem Phys 129:184108
82. Watts JD, Gauss J, Bartlett RJ (1993) J Chem Phys 98:8718
83. Peterson KA, Dunning TH (2002) J Chem Phys 117:10548
84. Dunning TH (1989) J Chem Phys 90:1007
85. Douglas M, Kroll NM (1974) Ann Phys 82:89
86. Jansen G, Hess BA (1989) Phys Rev A 39:6016
87. de Jong WA, Harrison RJ, Dixon DA (2001) J Chem Phys 114:48
88. Knowles PJ, Werner HJ (1985) Chem Phys Lett 115:259
89. Werner HJ, Knowles PJ (1985) J Chem Phys 82:5053
90. Werner HJ, Knowles PJ (1988) J Chem Phys 89:5803
91. Knowles PJ, Werner HJ (1988) Chem Phys Lett 145:514
92. Sobolewski AL, Adamowicz L (1996) J Phys Chem 100:3933
93. Sobolewski AL, Adamowicz L (1996) Chem Phys 213:193
94. Hammoutène D, Hochlaf M, Ciofini I, Adamo C (2010) Int J Quant Chem 110:498
95. Mahjoub A, Hochlaf M, Poisson L, Nieuwjaer N, Lecomte F, Schermann JP, Grégoire G, Manil B, Garcia GA, Nahon L (2011) ChemPhysChem 12:1822
96. Ben Messaouda M, Abderrabba M, Mahjoub A, Chambaud G, Hochlaf M (2012) Comput Theor Chem 990:94
97. Mahjoub A, Hochlaf M, Garcia GA, Nahon L, Poisson L (2012) J Phys Chem A 116:8706
98. Pan Y, Lau KC, Poisson L, Garcia GA, Nahon L, Hochlaf M (2013) J Phys Chem A 117:8095
99. Langhoff SR, Davidson ER (1974) Int J Quantum Chem 8:61
100. Finley J, Malmqvist P, Roos BO, Serrano-Andrès L (1998) Chem Phys Lett 288:299
101. Celani P, Stoll H, Werner HJ, Knowles PJ (2004) Mol Phys 102:2369
102. Celani P, Werner HJ (2003) J Chem Phys 119:5044
103. Hudock HR, Levine BG, Thompson AL, Satzger H, Townsend D, Gador N, Ullrich S, Stolow A, Martinez TJ (2007) J Phys Chem A 111:8500
104. Poisson L, Nandi D, Soep B, Hochlaf M, Boggio-Pasqua M, Mestdagh JM (2014) Phys Chem Chem Phys 16:581
105. Bauernschmitt R, Ahlrichs R (1996) Chem Phys Lett 256:454
106. Furche F, Ahlrichs R (2002) J Chem Phys 117:7433
107. von Niessen W, Schirmer J, Cederbaum LS (1984) Comput Phys Rep 1:57
108. Schirmer J, Cederbaum LS, Walter O (1983) Phys Rev A 28:1237
109. Schirmer J, Angonoa G (1989) J Chem Phys 91:1754

110. Potts AW, Holland DMP, Trofimov AB, Schirmer J, Karlsson L, Siegbahn K (2003) J Phys B At Mol Opt Phys 36:3129
111. Cederbaum LS, Domcke W, Schirmer J, von Niessen W (1986) Adv Chem Phys 65:115
112. Schirmer J, Cederbaum LS, Walter O (1983) Phys Rev A 28:1237
113. Mertins F, Schirmer J (1996) Phys Rev A53:2140
114. Schirmer J, Mertins F (1996) Int J Quantum Chem 58:329
115. Pieniazek PA, Arnstein SA, Bradforth SE, Krylov AI, Sherrill CD (2007) J Chem Phys 127:164110
116. Pal S, Rittby M, Bartlett RJ, Sinha D, Mukherjee D (1987) Chem Phys Lett 137:273
117. Stanton JF, Gauss J (1994) J Chem Phys 101:8938
118. Kamiya M, Hirata SJ (2006) Chem Phys 125:074111
119. Pieniazek PA, Bradforth SE, Krylov AI (2008) J Chem Phys 129:074104
120. Golubeva AA, Pieniazek PA, Krylov AI (2009) J Chem Phys 130:124113
121. Wei CY, Yu WS, Chou PT, Hung FT, Chang CP, Lin TC (1998) J Phys Chem B 102:1053
122. Ramos AF, Smedarchina Z, Zgierski MZ (2000) J Chem Phys 113:2662
123. Gerega A, Lapinski L, Nowak MJ, Furmanchuk A, Leszczynski J (2007) J Phys Chem A 111:4934
124. Garcia GA, Soldi-Lose H, Nahon L (2009) Rev Sci Instrum 80:023102
125. Trikoupis MA, Gerbaux P, Lavorato DJ, Flammang R, Terlouw JK (2002) Int J Mass Spectrom 217:1
126. Stefanovic D, Grutzmacher HF (1974) Org Mass Spectrom 9:1052
127. Cook MJ, El-Abbady S, Katritzky AR, Guimon C, Pfister-Guillouzo GJ (1977) Chem Soc Perkin Trans 2:1652
128. Trembreull R, Sin CH, Pang HM, Lubman DM (1985) Anal Chem 57:2911
129. Ozeki H, Cockett MCR, Okuyama K, Takahashi M, Kimura K (1995) J Phys Chem 99:8608
130. Lee D, Baek SJ, Choi KW, Choi YS, Kim SK (2002) Bull Korean Chem Soc 23:277
131. Potapov VK, Filyugina AD, Shigorin DN, Ozerova GA (1968) Dokl Akad Nauk SSSR 180:398
132. Treschanke L, Rademacher P (1985) J Mol Struct (Theochem) 122:35
133. Treschanke L, Rademacher P (1985) J Mol Struct 122:47
134. Rejnek J, Hanus M, Kabeláč M, Ryjáček F, Hobza P (2005) Phys Chem Chem Phys 7:2006
135. Choi KW, Lee JH, Kim SK (2005) J Am Chem Soc 127:15674
136. Majdi Y, Garcia GA, Nahon L, Schwell M, Poisson L, Hochlaf M Manuscript in preparation
137. Wang S, Schaefer HF III (2006) J Chem Phys 124:044303
138. Guerra CF, Bickelhaupt FM, Saha S, Wang F (2006) J Phys Chem A 110:4012
139. Hanus M, Kabelàc M, Rejnek J, Ryjacek F, Hobza P (2004) J Phys Chem B 108:2087
140. Piacenza M, Grimme S (2004) J Comput Chem 25:83
141. Plützer C, Nir E, de Vries MS, Kleinermanns K (2001) Phys Chem Chem Phys 3:5466
142. Nir E, Plützer C, Kleinermanns K, de Vries MS (2002) Eur Phys J D 20:317
143. Hush NS, Cheung AS (1975) Chem Phys Lett 34:11
144. Lin J, Yu C, Peng S, Akiyama I, Li L, Li KL, LeBreton PR (1980) J Am Chem Soc 102:4627
145. Satzger H, Townsend D, Stolow A (2006) Chem Phys Lett 430:144
146. Orlov VM, Smirnov AN, Varshavsky YM (1976) Tetrahedron Lett 17:4377
147. Roca-Sanjuan D, Rubio M, Merchan M, Serrano-Andrés LJ (2006) J Chem Phys 125:084302
148. Cauët E, Dehareng D, Liévin L (2006) J Phys Chem A 110:9200
149. Dolgounitcheva O, Zakrzewski VG, Ortiz JV (2000) Int J Quantum Chem 80:831
150. Dolgounitcheva O, Zakrzewski VG, Ortiz JV (2009) J Phys Chem A 113:14630
151. Colson AO, Besler B, Close DM, Sevilla MD (1992) J Phys Chem 96:661
152. Wetmore SD, Boyd RJ, Eriksson LA (1998) J Phys Chem B 102:10602
153. Reynisson J, Steenken S (2002) Phys Chem Chem Phys 4:527
154. Verkin BI, Sukodub LF, Yanson IK (1976) Dokl Akad Nauk SSSR 228:1452
155. Kim SK, Lee W, Herschbach DR (1996) J Phys Chem 100:7933
156. Schwell M, Jochims HW, Baumgärtel H, Dulieu F, Leach S (2006) Planet Space Sci 54:1073

157. Pilling S, Lago AF, Coutinho LH, de Castilho RB, de Souza GGB, Naves de Brito A (2007) Rapid Commun Mass Spectrom 21:3646
158. Zavilopulo AN, Shepnik OB, Agafanova AS (2009) J Phys B At Mol Opt Phys 42:025101
159. Hanus M, Ryjáček F, Kabeláč M, Kubar T, Bogdan TV, Trygubenko SA, Hobza P (2003) J Am Chem Soc 125:7678

# Modified Nucleobases

**Spiridoula Matsika**

**Abstract**   Various molecules which are similar to the natural nucleobases exist in
nature or have been synthetically developed. In this chapter we review work on the
photophysical properties of several modified nucleobases, focusing particularly on
how these properties differ from those of the natural nucleobases. We discuss
studies that give physical insight into how the molecular structure can be related
to photophysical properties with many of these studies being theoretical. One useful
photophysical property is the ability to fluoresce with high quantum yields. Natural
bases practically do not fluoresce, so being able to design molecules that fluoresce is
a goal of practical importance. Many of the modified nucleobases discussed in this
review are fluorescent analogues, analogues that have very different fluorescent
properties from the natural bases. The studies reviewed here may provide ways to
design other analogues with a set of desired properties.

## Contents

S. Matsika (✉)
Spiridoula Matsika Temple University, 1901 N.13th Street, Philadelphia, PA 19122, USA
e-mail: smatsika@temple.edu

# 1   Introduction

Nucleic acids are built using five building blocks consisting of purine and pyrimidine bases (shown in Fig. 1). There are, however, many other structures related to these natural bases, either already existing in nature or having been synthesized, which could substitute the natural nucleobases in the nucleic acids. In fact, artificially expanding the genetic code is a task that many scientists have tried to tackle [1]. Although there are many properties and functions that unnatural nucleobases could be used for, in this chapter we will discuss photoinitiated processes in selected modified nucleobases, focusing particularly on the question of how modifying the structure affects the behavior of the molecules after they absorb light. The photophysical properties are in line with the focus of the remainder of the volume, which is about photoinduced phenomena in nucleic acids and their five building blocks. The field of physical chemistry dealing with this topic has exploded in the last decade. As a result, the related area of photophysical properties of modified nucleobases is also expanding constantly, and many of the studies reviewed here have been published in recent years. Further progress in this area is expected in the near future.

There are a few reasons why we should focus on the photoinitiated behavior of modified nucleobases and their comparison with the natural bases. Modified nucleobases can help us understand the development of the genetic building blocks in prebiotic earth. The very short excited state lifetimes observed in natural nucleobases [2–5] make them more photostable, since they do not live for sufficient time in the excited state for photochemistry to occur. It has been suggested that the bases were naturally selected to be the building blocks in the nucleic acids among many other existing molecules based on their photostability, as well as other reasons such as the ability to form Watson–Crick base pairs. Some theories also suggest that before the current bases there were also other alternative bases which existed in the pre-RNA world. Photostability was very important for any base surviving because of the intense UV radiation present on Earth prior to formation of the stratospheric ozone layer. Studying modified bases provides a way to find which of these molecules have ultrafast decay and photostability [5–13].

A more practical motivation to focus on modified nucleobases is being able to develop alternatives to the bases which will be able to fluoresce. Fluorescence is a very important technique for studying nucleic acid dynamics and interactions with other biomolecules. It is very sensitive, easily available, versatile, and fast, and thus
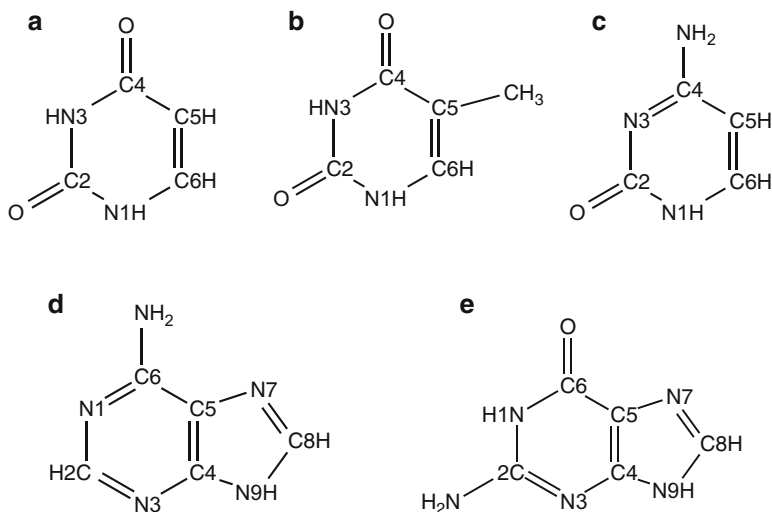
**Fig. 1** The structure and labeling of the natural nucleobases: (**a**) uracil, (**b**) thymine, (**c**) cytosine, (**d**) adenine, and (**e**) guanine in their canonical form

preferred over other techniques [14]. Natural nucleic acids have very low quantum yields for fluorescence, so artificial chromophores have to be introduced. These fluorophores can be introduced in DNA and RNA either noncovalently via intercalation or covalently. There are many commercially available fluorescent probes, such as fluorescein, Alexa, and cyanine dyes, which are used widely in fluorescent studies. These probes have advantages since they are highly fluorescent but they also have major disadvantages in that they perturb the natural structure of the oligonucleotides when incorporated in them. So, an attractive alternative is to develop probes that are very similar to the natural nucleobases and thus cause minimal perturbation to the secondary structure. Understanding how the photophysical properties of modified nucleobases are related to their structure is very important in the development of new and improved fluorescent base analogues.

Finally, from a fundamental knowledge point of view, it is quite interesting that various, diverse, and often minimal structural modifications can dramatically alter the photophysical characteristics of the chromophores. Can we obtain a better understanding of the relation between structure and photophysical properties? Can we learn more about what governs the photophysical behavior of molecules if we examine a series of molecules with controlled modifications?

Because of these fundamental and practical questions related to modified nucleobases and their photophysical properties, there has been a lot of work in this area, especially during the last decade, and in parallel with work on natural nucleobases. There have been several recent reviews summarizing work on fluorescent nucleobases [15–21], as well as a special issue of *Tetrahedron* [22]. These reviews mainly focus on the synthesis and properties of fluorescent analogues.

In the present review the focus is on studies that try to elucidate the mechanisms and intrinsic properties that make these molecules fluorescent as opposed to the similar natural nucleobases which have very low fluorescence quantum yields and very short excited state lifetimes. It is not possible here, nor is it our aim, to review all the compounds that have been synthesized as modified nucleobases. We are primarily interested in their photophysical properties and how they relate to the photophysics of natural nucleobases. So, we will discuss in more detail selected modified bases and studies which focus on the mechanisms for the photophysical properties and how they compare with the natural bases. It should be noted that in this work we use the words modified nucleobases or nucleobase analogues interchangeably.

## 2 Fluorescent Nucleobase Analogues

Since fluorescent analogues are central to the discussion of photophysical properties of modified nucleobases, we will briefly discuss some basics about this group of molecules. The types of molecules that we will discuss here range from molecules that only differ from the natural bases by a single substituent to molecules that are quite different from the natural bases. Some of these molecules have been designed systematically so that the effect of the modification on the photophysics will be examined. Other molecules, however, have existed as fluorescent probes for years, and the reason they have such different properties compared to the natural bases is the question to be addressed.

In general, the desired properties of any fluorescent analogue are:

- Red-shifted absorption compared to the absorption of the natural bases, so that the analogue can be selectively excited when it is incorporated in nucleic acids.
- Increased quantum yield for fluorescence.
- Some dependence of the fluorescence on the environment, so that the environment can be probed based on fluorescence techniques.

The current probes have these characteristics in various degrees. Values of fluorescence quantum yields spread over a wide range. The environmental influence can be varied even more, and it is actually desirable to have probes that show different responses to the environment. For example, there are many probes whose fluorescence is quenched when they are π-stacked, and this has been utilized to probe stacking in DNA and RNA. However, it is also useful to have other probes whose fluorescence is not quenched in these circumstances. How to design molecules that have the desired characteristics is not trivial, and understanding how to accomplish this would be useful.

A review by Sinkeldam et al. includes extended tables with more than 100 nucleobase fluorescent analogues and their properties [19]. According to that review the fluorescent analogues of nucleobases can be categorized as following: (1) chromophoric base analogues, (2) pteridines, (3) expanded nucleobases,
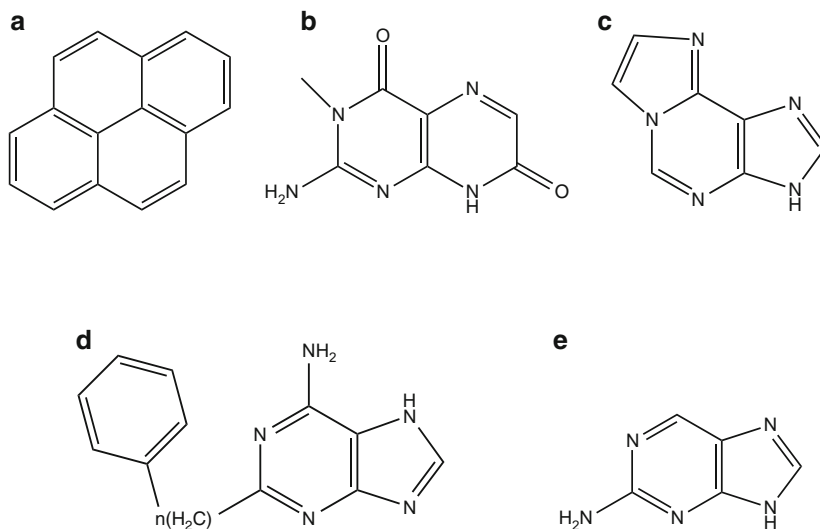
**Fig. 2** Examples of fluorescent base analogues: (**a**) pyrene, (**b**) 6MI, (**c**) ethenoadenine, (**d**) 2-phenylpropyl adenine, (**e**) 2-aminopurine

(4) extended nucleobases, and (5) isomorphic nucleobases. These categories help navigate through the increased number of fluorescent probes that have been developed. A brief description of the type of molecules included in each category follows:

1. One strategy to utilize fluorescence when studying DNA/RNA is to replace the bases with already established fluorophores, typically polycyclic aromatic hydrocarbons [23, 24], such as pyrene, shown in Fig. 2a. These probes do not form Watson–Crick hydrogen bond pairs, but they can have high emission quantum yields and be selectively excited. They have been used in various applications, such as the investigation of enzyme-substrate recognition and electron transfer in DNA [19, 25, 26].

2. Pteridines are naturally occurring chromophores that have similar structure to the natural bases, but they fluoresce [18, 27]. They usually consist of two six-membered rings, and the most promising members of this group are analogues of guanine (3-methyl isoxanthopterin (3MI) and 6-methylisoxanthopterin (6MI), Fig. 2b) or adenine (4-amino-6-methyl-8-(2-deoxy-β-D-ribofuranosyl)-7(8H)-pteridone (6MAP) and (4-amino-2,6-dimethyl-8-(2-deoxy-β-D-ribofuranosyl)-7(8H)-pteridone (DMAP)). They can be selectively excited by absorption at around 300 nm and have high quantum yields for fluorescence. Incorporation of these modified nucleosides into nucleic acids, except for 6MI, typically results in some sequence-dependent destabilizing effects.

3. Another way to generate chromophores that fluoresce and absorb to the red of the natural bases is to expand the aromatic system by fusing aromatic rings between the pyrimidine and purine systems. These chromophores are naturally

red-shifted since they have a larger conjugated system. The reason why they may fluoresce is not clear a priori but some of the theoretical studies to be discussed later may shed light onto that property as well. Early attempts to design fluorescent probes was inspired by natural occurring fluorescent nucleobases such as the wyosine bases, which use an ethenobridge in guanine to form a third ring. Ethenoadenosine is a useful analogue that was developed early on using an etheno bridge (Fig. 2c) [28]. A very recent new analogue is quadracyclic adenine, an adenine analogue with four rings [29]. Unlike many others, it maintains or even increases the stability of the duplex, it can be selectively excited, and it displays a fluorescence quantum yield of 6.8%. 1,3-Diaza-2-oxophenothiazine (tC) is another molecule in this category which will be discussed later.

4. Extended analogues differ from the expanded ones in that known chromophores are connected to the bases via electronically nonconjugating linkers. This yields nucleobase analogues with photophysical features that are relatively more similar to those of the parent nucleobases compared to the properties of the expanded ones, which may differ a lot from those of the nucleobases. As an example, 2-substituted adenine analogues, 2-phenylpropyl adenine (Fig. 2d) and 2-phenylbutyl adenine, have been developed, which have increased fluorescence yield when incorporated in RNA hairpins [30].

5. The category that is more relevant to what we are discussing here is isomorphic nucleobases. These are the analogues with structures closely resembling the natural bases in terms of overall dimensions, hydrogen bonding patterns, and ability to form Watson–Crick base pairs. The advantage of these analogues is that they minimally perturb the structure of oligonucleotides when incorporated in them. However, it is quite difficult to obtain all the desired characteristics of fluorescent analogues while retaining minimum perturbation. Several of these systems will be discussed in later sections. 2-Aminopurine (2AP) (see Fig. 2e) and 5-methyl-2-pyrimidinone (5M2P) to be discussed later are other examples of analogues belonging to this category.

# 3  Theoretical Approach for Studying Photoinitiated Processes

Here we introduce the framework which is used to explore and understand the photophysical properties in molecules. The events that can occur after the absorption of light can be divided into radiative or radiationless. Radiative events include emission of light either as fluorescence or as phosphorescence or even chemiluminescence. Radiationless events include internal conversion, intersystem crossing, or other photochemical reactions. In order to understand what isolated molecules may do when they absorb light we need to know the Potential Energy Surfaces (PESs) of their ground and excited states and explore how they affect the excited state dynamics.

The radiationless processes in isolated molecules depend on the accessibility of regions of nuclear configurational space where PESs between different electronic states approach each other, and these processes become optimal when the gap between the PESs goes to zero and conical intersections (CIs) exist. CIs are points where the energies of two or more states become degenerate [31–42]. These are not isolated points but hypersurfaces of dimension $n − 2$, where $n$ is the number of vibrational modes in the molecule ($n = 3N − 6$ or $3N − 5$, where $N$ is the number of atoms in the molecule), called seams. Even though the existence of CIs was known in the 1930s [43, 44], their importance and prevalence in molecular systems was realized only in the 1990s and later when algorithms were developed for their location [45–55]. Without algorithms it is practically impossible to locate CIs in polyatomic molecules without any symmetry present, so before these technological advances they were thought to be rare.

PESs provide the available pathways for dynamics. Usually multiple pathways and processes exist and there is competition between them, so the faster rates determine which processes prevail. Considering the rates and lifetimes associated with the radiative and radiationless processes gives more insight into the outcome of the competitions. Phosphorescence is a very slow process since it involves change of spin, and it takes milliseconds to seconds, speeding up when heavy atoms are involved since the spin-orbit coupling increases. Fluorescence is much faster with lifetimes of nanoseconds to microseconds. Radiationless processes depend on the accessibility to CIs and avoided crossings, and if they can occur faster than nanoseconds then they compete effectively with fluorescence. Thus fluorescence efficiency mainly depends on the competition of fluorescence with the available radiationless pathways, and one of the most important factors in determining what makes molecules fluoresce or not is the accessibility of fast radiationless paths. Consequently, the task of explaining the efficiency or lack of fluorescence in nucleobases and their analogues is often translated into finding minimum energy points on CI seams and the pathways towards them. This approach involves studying a single isolated molecule, and it does not include interactions with other molecules which can also lead to radiationless events and can quench fluorescence, especially in condensed phases. It is, however, a good first step to understanding the intrinsic photophysical properties of molecules.

Since predicting PESs for polyatomic molecules such as the modified nucleobases is not an easy task, there are several studies that try to predict or explain the photophysical behavior based mainly on the initial absorption spectra and location of excited states. More advanced studies, especially in recent years, include more information on the PESs.

# 4   Why Natural Nucleobases Do Not Fluoresce

Natural nucleobases are discussed extensively throughout this volume. A summary of their photophysical properties and underlying mechanistic explanations is given to be used to contrast their properties to those of the fluorescent analogues.

The objective would be to use this information in order to design other fluorescent probes with the required properties in an intelligent way. Extensive reviews of these studies can be found elsewhere in this volume. Figure 1 shows the natural nucleobases with numbering labels which will be used in the text.

It has been shown by an extensive body of work that all natural nucleobases have ultrashort excited state lifetimes because ultrafast decay occurs through conical intersections [56–58]. The electronically excited states in the nucleobases are generated either by excitations from the $\pi$ orbitals to $\pi^*$ leading to bright $\pi\pi^*$ states, or from the lone pair orbitals localized on the nitrogen or oxygen atoms to $\pi^*$ leading to dark $n\pi^*$ states. $\pi\sigma^*$ states with excitations to diffuse orbitals have also been found, although they are usually higher in energy; they may play a role in the purine bases but have not been found to be important in the pyrimidine bases. The initial events often involve radiationless transitions between excited states, especially if the bright absorbing state is not the first excited state, or if higher energies are populated upon excitation, while the final relaxation occurs through CIs between the first excited state, $S_1$, and the ground state, $S_0$.

All three pyrimidine bases have conical intersections between $S_0$ and $S_1$ in geometries where the C5–C6 double bond twists [56–58]. These CIs involve an $S_1$ state which has $\pi\pi^*$ character, and, as the double bond twists and breaks, a biradical is formed. In addition, there are conical intersections involving the $n_O\pi^*$ excited state and the ground state, and in this case the geometry shows elongation of the carbonyl bond [59]. In cytosine a third CI exists involving distortion/puckering along the N3–C4 bond [60]. Experiments suggest that the dynamics are an interplay between ultrafast decay through the $S_1/S_0$ CIs and slower decay when the dark $n\pi^*$ states are reached.

Purine bases also have $\pi\pi^*$ and $n\pi^*$ states. In particular there are two $\pi\pi^*$ states (historically labeled as $L_a$ and $L_b$) which are excited upon absorption of UV radiation. In purine bases the major conical intersections involve distortion in the six-membered ring, with two main CIs playing the major role, one involving out-of-plane motion along the C2–N3 and another along the N1–C6 bonds. Pathways involving the $\pi\sigma^*$ states have also been found for the purine bases in the gas phase [61]. These can be accessed when higher energy photons are used.

A major issue when studying the natural, as well as modified, nucleobases is the possibility that different tautomers may exist at room temperature. Often multiple tautomers have comparable energies and they can coexist either in the gas phase or in solution. In order to be able to interpret the experimentally observed lifetimes and spectra, one should examine the photoinitiated processes for all the tautomers that are present at a given temperature.
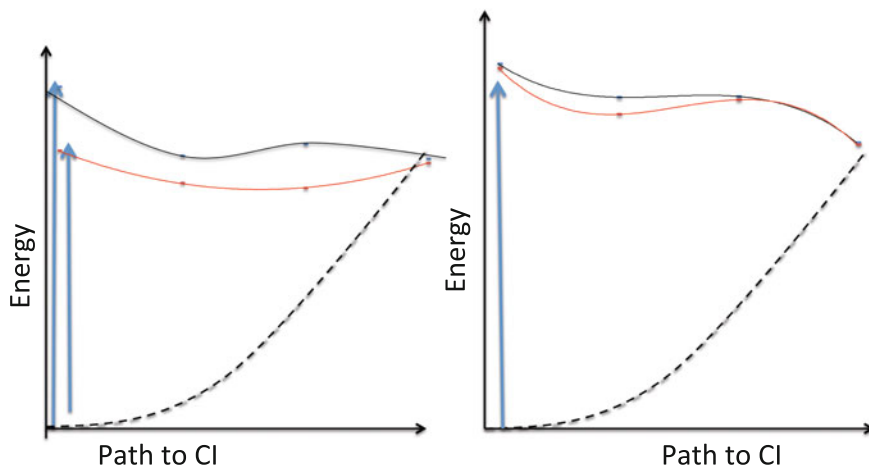
**Fig. 3** PES of a natural base (*black line*) and a modified base (*red line*). *Left panel*: Diagram is based on results from comparison between cytosine and 5M2P from [60]. *Right panel*: Diagram is based on results from comparison between uracil and 5-fluorouracil from [81]

# 5  Pyrimidine Analogues

## *5.1  Adding Substituents to the Natural Pyrimidine Bases*

Before going into details of how specific substituents have been found to affect the photophysical properties of bases, some general principles can be mentioned. In general, the PESs of substituted bases have several features  similar to those of the natural bases such as CIs between the ground and first excited state, even if the substituted bases have much longer lifetimes. The primary reason for the changes in lifetimes is that the substituents shift different parts of the PESs in different ways, creating or removing barriers, and this leads to changes in the photophysical properties. Figure 3 shows diagrams which illustrate this behavior. On the left panel of the figure a situation is illustrated where the PES of the modified base has a stable minimum below the CI while the PES of the natural base has a low barrier between the CI and the minimum. On the right panel, the barrier increases for the modified base. Furthermore, the left panel shows a pronounced red shift in absorption for the modified base while the right panel does not. As can be seen in these diagrams, a variety of changes can occur with the modification of the structure. These changes will depend on the structure and the specific interactions in each molecule, and it is not easy (or even possible) to predict the changes in the PESs. In some cases some simple rules may be established, but in most cases this will not be possible. Below we focus on a few studies of bases and try to rationalize the findings whenever possible.

As it is known that an important coordinate for the decay in pyrimidine bases involves the C5–C6 double bond, a natural first step to create molecules with different photophysical properties is to modify this part of the molecule and restrict the twisting of the bond. Several studies focused on substitutions on the C5 and/or C6 carbons in order to affect the decay rates.

Initial studies were done on 5-fluorocytosine, 5-methylcytosine, and N4-acetylcytosine in solution using transient absorption complemented by Complete Active Space Self-Consistent Field (CASSCF) and perturbation theory corrected CASSCF (CASPT2) calculations [62, 63]. Femtosecond transient absorption measurements show that replacement of the C5 hydrogen of cytosine by fluorine increases the excited-state lifetime by two orders of magnitude. The CASSCF/ CASPT2 calculations were used to explain the difference between fluorocytosine and cytosine [62]. These calculations did not show dramatic changes in the electronic structure and PES, but these early studies did not take into account all the possible decay pathways, which were revealed later.

The transient absorption findings were similar to findings by steady-state fluorescence measurements which also show that fluorescence is much weaker for 6-fluorocytosine as compared to 5-fluorocytosine [64]. Zgierski and coworkers studied several derivatives of the nucleobases in an effort to show how substitution affects the photophysical properties [64–70]. As part of this effort they studied 5- or 6-fluoro substituted uracil and cytosine. Configuration Interaction Singles (CIS) and Equation of Motion Coupled Cluster singles doubles and perturbative triples (CR-EOM-CCSD(T)) calculations were used to examine pathways to the CIs, and the C5–C6 twisting pathway was considered in detail. The calculations revealed that C5 substitution has a much stronger effect on the decay mechanism compared to the C6 substitution. These results agree with what would be expected from the distortion at the CI for the unmodified bases, since distortion on C5 is larger at the CIs.

More recently, Ho et al. studied 5-fluorocytosine in the gas phase [71]. In the gas phase, however, one has to worry about different tautomers and calculations show that 5-fluorocytosine exists mainly in the enol tautomeric form. So the measurements correspond to deactivation of the enol tautomer, which is longer than the keto tautomer.

N4-Acetylcytosine has much longer lifetimes compared to cytosine [63, 66]. According to calculations the excited state lifetime is longer for this molecule because the barrier on the way to the CI increases through the formation of a weak intramolecular CH:O hydrogen bond between the acetyl carbonyl group and the C5H group [66].

The experiments on 5-methylcytosine show a modest increase in lifetime [63, 66]. A recent study on 5-methylcytosine shows that the decay will take a longer time compared to cytosine because the barrier to the CI is higher (ca. 0.3 eV) and dynamical simulations showed a slower decay [72]. Other studies however do not show differences in the PES with the addition of a methyl group [73].

Similarly to cytosine, substitution of uracil at C5 has an effect on the dynamics. The excited-state lifetimes of several uracil derivatives in solution of water or
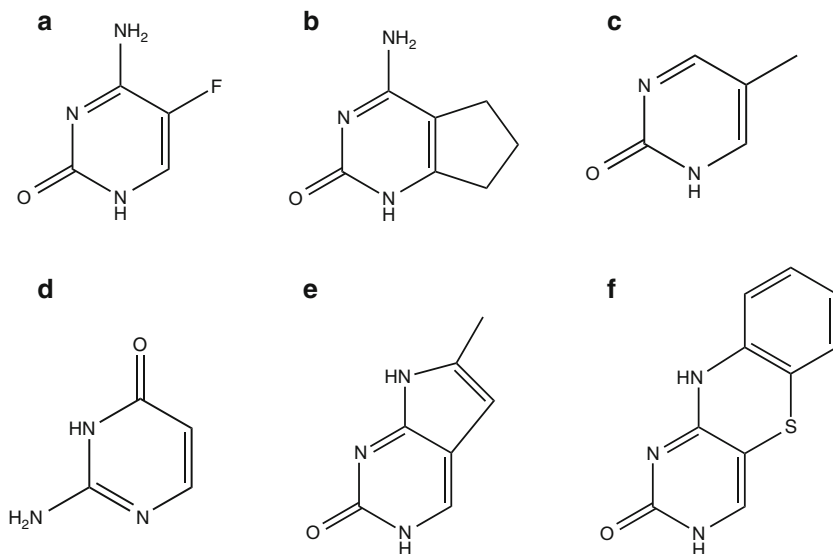
**Fig. 4** Cytosine analogues: (**a**) 5-fluorocytosine, (**b**) 5,6-trimethylenecytosine, (**c**) 5-methyl-2-pyrimidinone, (**d**) isocytosine, (**e**) pyrrolocytosine, (**f**) tC

acetonitrile were measured using femtosecond fluorescence upconversion in the UV, and Time-Dependent Density Functional Theory (TDDFT) calculations were used to explain the results [74–79]. Substituents (–CH$_3$, F, Cl, and CF$_3$) in positions N1, N3, C5, and C6 were examined, and it was found that substitution of F in the C5 position of uracil leads to a sevenfold increase in the lifetime. Several theoretical calculations explained the longer lifetime in 5-fluorouracil by the existence of a barrier on the pathway towards the CI [64, 73, 76–78, 80, 81]. Figure 3 shows this effect on the PESs. In recent sophisticated studies, Yamazaki and Taketsugu used Multi-State CASPT2 (MS-CASPT2) to compare uracil, 5-methyluracil (thymine), and 5-fluorouracil in order to examine the effect of substitution at the 5 position for uracil [81]. Their calculations showed that the barrier of 5-fluorouracil in the bright $\pi\pi^*$ state is higher than similar barriers in uracil and thymine, and suggests that the elongation of the excited-state lifetime of uracil by fluorine substitution is significantly affected by intrinsic electronic effects of the molecule. However, their electronic structure calculations do not reveal any difference between uracil and thymine, i.e., methyl substitution does not change the PESs. In general, almost all theoretical studies agree that methyl substitution does not cause large electronic effects and changes in the PESs of the pyrimidine molecules. Differences in lifetimes are likely due to the different effective mass when the methyl group moves along the reaction coordinate [82].

A more aggressive way to block the twisting of the C5–C6 bond occurs when using cyclic groups, as in 5,6-trimethylenecytosine (see Fig. 4b) and 5,6-trimethyleneuracil, which were studied by Zgierski and coworkers [65]. Here

a closed ring blocks the large amplitude motion of the C5–C6 twisting, and, as expected, these systems do not exhibit the subpicosecond excited-state lifetime characteristic of the naturally occurring pyrimidine bases.

Amino substituted uracils, 5-aminouracil and 5-dimethylaminouracil, have been studied by steady-state and time-resolved fluorescence spectroscopy and theoretical TDDFT calculations [83]. These studies showed that the amino substitution leads to the emitting states of both molecules being substantially longer-lived than that of uracil. 5-Aminouracil is about five times more fluorescent than the DNA bases, while 5-dimethylaminouracil is about two orders of magnitude more fluorescent. In these molecules the bright $\pi\pi^*$ state is red-shifted compared to that in uracil and it shows a stable emitting minimum.

## 5.2  Replacing the Amino or Oxo Substituents

A more invasive way to produce analogues is to replace completely one of the substituents already present in the pyrimidine bases. When the amino group in cytosine or the oxo group from C4 in uracil is removed, the remaining system is 2-pyrimidinone. This system has an absorption which is red-shifted compared to the natural pyrimidine bases and it also fluoresces more than they do [87, 88]. These facts lead to an interest in studying more systematically the role of the substituent on C4. In a systematic theoretical study of a series of substituted pyrimidinone systems various substituents were placed in position C4 [60, 84, 89, 90]. When the substituent is an amino group cytosine is formed and when it is oxo group uracil is formed. So this series of molecules naturally includes the nucleobases, while it allows for a systematic study of the photophysical properties. It was found that electron-donating substituents blue shift the absorption compared to the parent molecule while electron-withdrawing substituents cause a red shift. The effect can even be quantified as there is a linear correlation between excitation energies and the Hammet parameter for each substituent. Hammet parameter is a number that quantifies the electron-donating or -withdrawing ability of a substituent [91]. This linear correlation exists for both experimental absorption maxima and theoretically calculated excitation energies with the same slope. As a result, one could predict the absorption maximum of a new molecule using the Hammet parameter of the substituent. This is important for building molecules with red-shifted absorption, a property needed for selective excitation. The shifts in absorption can be understood by simple frontier molecular orbital arguments by examining the HOMO and LUMO of the chromophores, and, in principle, one could use the same ideas to predict substituent effects on absorption of other molecules.

Interestingly, the red-shifted absorption can be linked to fluorescence properties as well. Many of the red-shifted chromophores show increased fluorescence. A reasonable explanation for this correlation has been made clear in a comparison between cytosine and 5-methyl-2-pyrimidinone (5M2P). 5M2P differs from
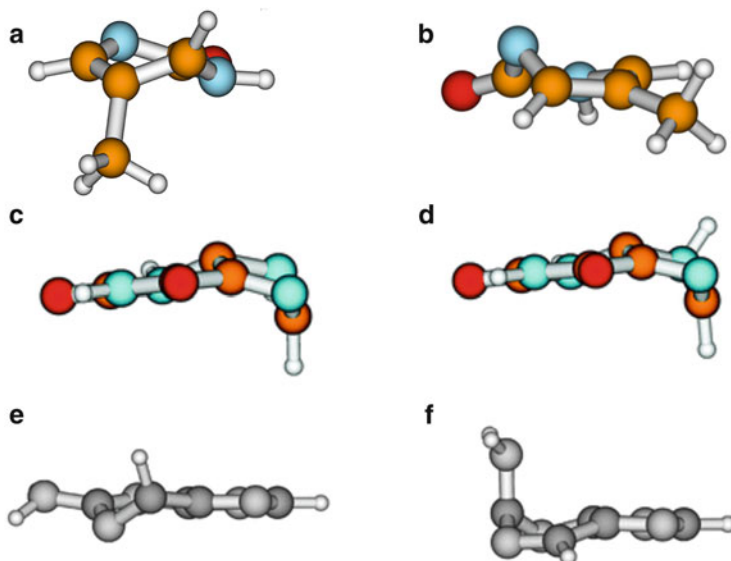
**Fig. 5** Structures of conical intersections between $S_1$ and $S_0$ for: (**a**, **b**) 5-methyl-2-pyrimidinone, (**c**, **d**) xanthine, (**e**, **f**) 2-aminopurine. Structures for (**a**, **b**) are taken from [84], for (**c**, **d**) from [85], and for (**e**, **f**) from [86]

cytosine in the fact that it does not have an amino group in position 4 but it has a methyl group in position 5 of the pyrimidinone ring (see Fig. 4c). This different substitution changes the vertical absorption with 5M2P absorbing at 4 eV compared to cytosine at 4.7 eV. Furthermore, 5M2P fluoresces in aqueous solution [92]. It has been shown by Multi-Reference Configuration Interaction (MRCI) calculations that qualitatively 5M2P has similar excited state PESs as cytosine [60, 84]. Specifically the same types of conical intersections are present, since these CIs are determined by the ring system rather than the substituents. The main CIs between $S_0$ and $S_1$ are shown in Fig. 5a,b where it is seen that one of them involves the C5–C6 familiar twisting (termed 'twist' in [60, 84] and Fig. 6) while the other one involves a N3–C4 puckering (termed 'sofa' in [60, 84] and Fig. 6) similar to that found in cytosine. However, the observed differences in the photophysical properties are due to quantitative differences in the PES. Figure 6 shows the calculated PESs for cytosine and 5M2P superimposed, so that the differences can be seen. The excited state PES of 5M2P is in general red-shifted compared to cytosine. However, the red shift is very pronounced initially and it becomes much smaller as the molecule deviates from planarity and travels along the PES towards the CI. Eventually at the CI the energies of the two molecules are very similar. This means that for 5M2P the pathway to reach the CI is uphill while in cytosine it is downhill. As a result the excited state lifetime in 5M2P increases. Qualitative changes in the PESs around the CI lead to changes in the topology of the CI as well, which can be more 'sloped' or 'peaked' [34, 93]. Peaked CIs (which are downhill from the upper surface)
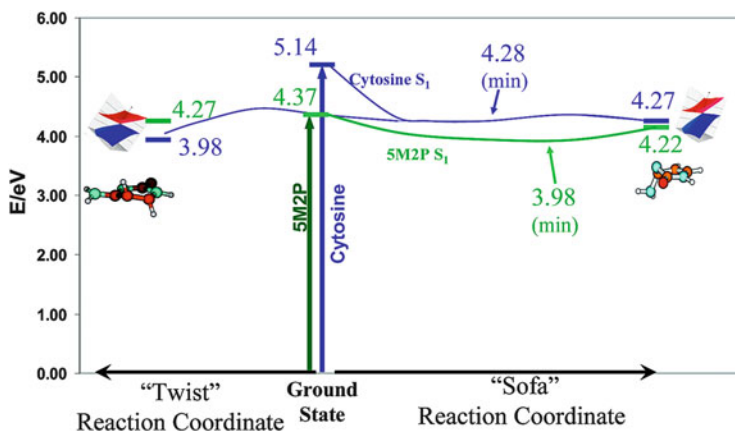
**Fig. 6** Photophysically important regions of the $S_1$ surfaces of cytosine and 5M2P are shown for comparison. Energies of vertical excitations, conical intersections, and the $S_1$ minimum for 5M2P are in eV, referenced to the ground-state minimum for each base. *Blue* and *green lines* represent $S_1$ $\pi\pi^*$ minimum energy paths calculated using MRCI, for cytosine and 5M2P, respectively. "Sofa" refers to the N3–C4 CI discussed in the text. Reproduced from [89]

facilitate radiationless decay from the upper surface to the lower while sloped ones can facilitate the opposite transitions, i.e., transitions from the lower to the upper surface. The qualitative changes in the PESs of cytosine vs 5M2P can also lead to changes in the topology of the corresponding CIs which may also affect the effectiveness of the decay.

The enol form of 5-methyl-2-pyrimidinone has been studied in the gas phase [94]. Its vibronic spectrum is well structured and its excited state $S_1$ lifetime is approximated to be 55 ps, much longer than the natural bases. This state is identified as $n\pi^*$. It is obvious that the photophysical properties of different tautomers can be very different.

The presence of the methyl group in the 5 position is not very important, so 2-pyrimidinone is also expected to show slower decay compared to cytosine and uracil. The photophysics of 1-methyl-2-pyrimidinone in water has been investigated by steady-state and time-resolved fluorescence, UV/vis absorption, and IR spectroscopy [95]. The experiments have shown that the lowest in energy state exhibits a lifetime on the 100 ps timescale.

Related to 2-pyrimidinone is 4-pyrimidinone. This is an analogue of uracil where the oxo group of uracil at C2 is removed instead of the one at C4. As with 2-pyrimidinone, the lack of the second substituent leads to a red-shifted absorption to the $\pi\pi^*$ state. The absorption maximum of uracil in the gas phase is at 5.08 eV, while matrix-isolated 4-pyrimidinone absorbs at 4.51 eV [96]. Theoretical work has focused on comparison between 4-pyrimidinone and uracil [97]. Unlike uracil, 4-pyrimidinone has two double bonds on the ring which can be twisted, leading to more photophysical pathways. The calculations show that relaxation of the $\pi\pi^*$ state of 4-pyrimidinone via the regular C5–C6 twisting is hindered by a barrier.

On the other hand, twisting along the C–N double-bond indicates that the formation of the Dewar form may represent a photochemical channel in 4-pyrimidinone.

Isocytosine is an isomer of cytosine where the amino and oxo groups have switched positions (Fig. 4d). It has been shown that, upon absorption of UV irradiation, matrix-isolated isocytosine undergoes tautomerization of the amino-oxo tautomer to the amino-hydroxy form [98]. The excited-state behavior of isocytosine has been studied theoretically [99, 100]. Although earlier studies had reported the minima of ground and excited states [99], more recent studies [100] used high level CASSCF methods to locate conical intersections and found that after photoexcitation the amino-oxo tautomer of isocytosine isomerizes to the amino-hydroxy form through a $\pi\sigma^*$ state, while it can also relax back to the ground amino-oxo form through CIs similar to those found in cytosine.

## 5.3   Expanded Cytosine Analogues

We now discuss some other, more complicated, pyrimidine analogues which have been developed and used as fluorescent probes.

Pyrrolocytosine is an environmentally sensitive fluorescent analogue of cytosine [101–104]. It has an ethylenic group connecting the nitrogen on the amino group to C5, forming a second five-membered ring (see Fig. 4e). Substituted derivatives of pyrrolocytosine have also been synthesized and tested [101], such as phenylpyrrolocytosine, which is exceptionally bright and environmentally sensitive, and [bis-ortho-(aminoethoxy)phenyl]pyrrolocytosine (boPhpC), which is designed for tight binding to guanine and for its hybridization performance in PNA [105]. Pyrrolocytosine has an absorption which is red-shifted from the natural bases (350 nm) and a visible emission (460 nm) with a fluorescence quantum yield ca. 0.2. Fluorescence is significantly quenched upon incorporation into single stranded oligonucleotides and further quenched upon duplex formation.

Theoretical studies of pyrrolocytosine have so far focused on the vertically excited states, while there are no detailed studies of the excited state PESs beyond the Franck–Condon region. The excited states have been calculated at the CIS, TDDFT, and MRCI levels [89, 103]. The theoretical studies showed that the spacing between the first $\pi\pi^*$ state and the first $n\pi^*$ state is significantly larger in the case of pyrrolocytosine compared to cytosine. This fact has been used as a rationale for the higher fluorescence quantum yield of the former, since it makes interaction of the bright state with the dark more difficult and this could prevent quenching through the dark state [103]. The mechanisms for decay in cytosine and the other bases, however, are a lot more complicated, so merely looking at the spacing of the initial states may not be sufficient explanation. Another explanation that can be speculated is that the ethylenic group blocks the distortion of the ring and prevents easy access to the CIs.

Another cytosine analogue which consists of multiple rings is 1,3-diaza-2-oxophenothiazine (denoted tC), originally synthesized by Matteucci and coworkers

[106]. Its structure is shown in Fig. 4. It forms Watson–Crick base pairs with guanine and, unlike most other fluorescent nucleobases, its quantum efficiency is not reduced dramatically upon incorporation into PNA or DNA. tC, and similar molecules $tC^0$ (which has O instead of S in the middle ring) and $tC_{nitro}$ (which has an extra $NO_2$ substituent added to tC), base-pair selectively with guanine and stabilize the B-DNA double helix in contrast to natural cytosine [107–110]. $tC^0$ is on average the brightest fluorescent nucleobase analogue inside the DNA double-helix [109]. In contrast to the strong fluorescence of tC and $tC^0$, the nitro-substituted $tC_{nitro}$ is virtually non-fluorescent in polar solvents at room temperature. Its absorption is red-shifted compared to tC and $tC^0$ and, as a result, it can be used as a FRET acceptor with tC and $tC^0$ being donors.

Some early studies used semiempirical methods to calculate absorption energies and properties of tC [107]. More recently Preus et al. [111, 112] used high level DFT and TDDFT to study the PESs of all three molecules, tC, $tC^0$, and $tC_{intro}$. Temperature-dependent fluorescence quantum yield measurements were also made in this work. The calculations showed that the ground state of $tC^0$ is planar while those of tC and $tC_{nitro}$ have two equivalent minima corresponding to geometries folded along the middle S–N axis separated by an energy barrier of 0.05 eV. The $S_1$ equilibrium geometries of all three base analogues are predicted to be planar. The calculations predict that the stronger fluorescence of $tC^0$ compared to tC is due to a larger oscillator strength of the lowest energy electronic transition. The authors suggest that the nonradiative decay process dominating the fast deactivation of $tC_{nitro}$ is an internal conversion which may involve rotational or vibrational modes of the $NO_2$ group. There are no detailed calculations of the PESs that could explain radiationless decay in any detail.

In summary, it appears that more theoretical work should be done to explore these more complicated pyrimidine analogues.

## 6  Purine Analogues

Natural purine bases have one or two substituents in positions C2 and C6. The first absorption band consists of two bright $\pi\pi^*$ states, $L_a$ and $L_b$, and there is at least one $n\pi^*$ state nearby. Figure 7 shows the main orbitals participating in the excited states in purine. $L_a$ and $L_b$ are linear combinations of $H \rightarrow L$, $H \rightarrow L + 1$, $H - 1 \rightarrow L$ and $H - 1 \rightarrow L + 1$. Although the main coordinates that lead to the CIs have been identified, it is not always as straightforward to predict what needs to be done to block radiationless decay. For example, in adenine the most efficient CI involves puckering of C2, and this may lead to a simple explanation as to why 2AP is fluorescent, since it has a substituent on C2. Guanine, however, also has a substituent on C2 but it decays very fast. So, simple substituent effects which were useful in pyrimidine bases are not always as useful in purine bases.
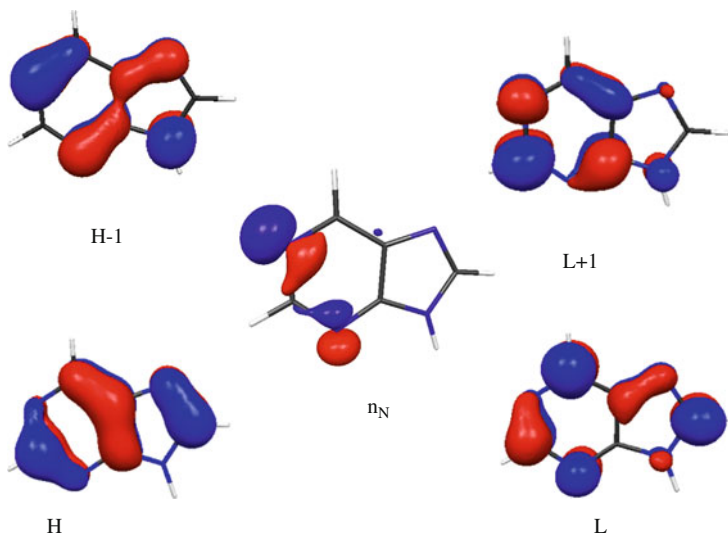
**Fig. 7** Orbitals of purine participating in the main excited state configurations. H, H-1, L, and L+1 stand for HOMO, HOMO-1, LUMO, and LUMO+1, respectively. Reproduced from [113]

## 6.1 Tautomers and/or Adding Substituents to Natural Purine Bases

All purine derivatives have at least two tautomers, the 9H and 7H ones, where the hydrogen is on N9 or N7, respectively. The biologically relevant one is the 9H tautomer since this bond is used to bond to the sugar. Radiationless decay processes on different tautomers of guanine and adenine have been studied spectroscopically and computationally [114–121]. Quite interestingly, even such a small change in the structure can lead to major differences in the excited state dynamics. As an example, 7-methyladenine and the 7H-tautomer of adenine have much longer lifetimes than adenine [114].

Serrano-Andrés and coworkers studied several modified purine nucleobases (7H-adenine, 9H-2AP, 9H-iminoadenine, 7H-guanine, 9H-2-amino-6-hydroxypurine, 7H-2-amino-6-hydroxypurine, 9-methylguanine), either by means of tautomerization or substitution [73]. They found that these modified nucleobases, except the methylated ones, should be less photostable because they display energy barriers along the lowest-energy paths.

Zgierski and coworkers examined carefully designed derivatives of adenine and guanine to see if affecting the coordinate leading to radiationless decay in adenine would slow the decay [68]. *N,N*-Dimethyladenine, which has the amino group methylated, was found to have a slightly longer lifetime compared to adenine. The nucleoside of propanoguanine, where the out-of-plane deformation of the six-membered ring of the guanine moiety is hindered (see Fig. 8b), does not exhibit the subpicosecond internal conversion characteristic of the naturally occurring purine bases [67].
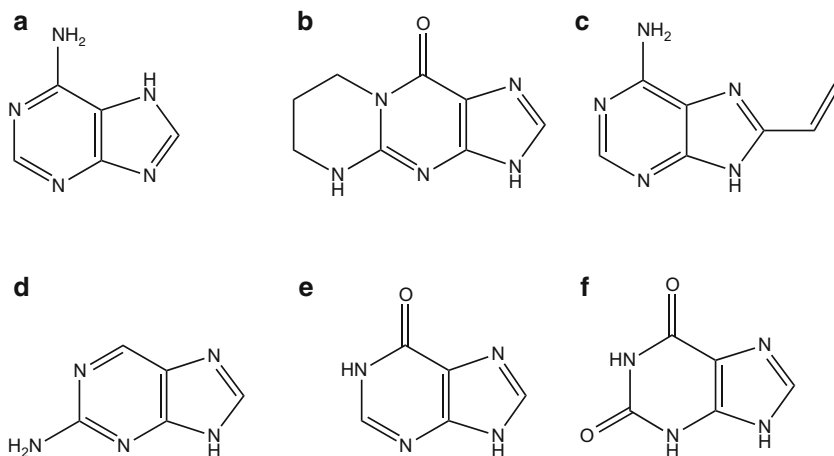
**Fig. 8** Purine analogues: (**a**) 7H-adenine, (**b**) propanoguanine, (**c**) 8-vinyladenine, (**d**) 2-aminopurine, (**e**) hypoxanthine, (**f**) xanthine

8-Vinyladenine (see Fig. 8c) is a recently developed adenine analogue that has an additional vinyl substituent to the ring in a position (C8) that does not affect base pairing with thymine in duplex DNA [122, 123]. It has a red-shifted absorption band centered around 290 nm and fluorescence centered at 370 nm. The fluorescence quantum yield is sensitive to base stacking as in many other analogues, making it an effective reporter of DNA structure and dynamics. Its excited state properties have been studied with Stark spectroscopy, cyclic voltammetry, and theoretical calculations [124–126], with the aim of understanding whether the charge transfer character of the excited states is responsible for quenching in π-stacking arrangements. The redox potentials suggest that electron transfer to or from 8-vinyladenine may not be the dominant mechanism of quenching when π-stacked with natural bases. Thymine, however, may be an effective electron acceptor. Less attention has been paid to the monomer behavior and why it is so different from adenine. PESs have not been calculated for this molecule, although it is very interesting that a substituent on the five-membered ring affects the fluorescence behavior to such a degree, given the fact that the CIs in adenine distort the six-membered ring. Very recently, the equivalent analogue of guanine, 8-vinylguanine has also been synthesized and incorporated in DNA and PNA [127–129]. Detailed studies of its properties have not yet been performed.

## 6.2 Amino and Oxo Substituted Purines

Common purines, which have been studied a lot, are the purines created by the purine ring system using the same substituents as those used in the natural bases, the amino and oxo groups. One can create analogues with only one of these groups.

If the amino group is used in C6 it leads to adenine, while in C2 it leads to 2AP. The oxo group in C6 gives hypoxanthine and in C2 it gives 2-oxopurine. When two substituents are used, 2,6-diaminopurine (with two amino groups), xanthine (with two oxo groups), guanine and isoguanine (with one amino and one oxo groups) are formed. Figure 8 shows some of these derivatives. Several of these molecules have been studied in detail for their photophysical properties. A theoretical study has calculated the excitation energies for all of them and compared them in order to get some insight into how the substituents affect vertical excitations [113]. Some conclusions that were observed are: substitution at the C2 position decreases the energy of the first $\pi\pi^*$ state considerably whereas substitution at the C6 position has a much smaller effect; the carbonyl group has in general a stronger effect than the amino group; $n\pi^*$ states for all substituted purines are blue-shifted compared to purine. The origins of electronic transitions for several purines have been reported by de Vries and coworkers [130–134]. Below we will discuss selected systems in this family whose photophysical properties have been studied in more detail.

### 6.2.1 Amino-Purines: 2-Aminopurine and 2,6-Diaminopurine

One of the earliest reports on fluorescent nucleobase analogues was about adenine analogues formycin, 2-aminopurine, and 2,6 diaminopurine [135]. 2-Aminopurine is one of the first and most widely utilized fluorescent nucleobase analogues (see Fig. 8). It is an isomer of adenine with the amino group moved from the 6 position to the 2 position. This simple change leads to substantially enhanced fluorescence. In aqueous solutions it has a fluorescence quantum yield of 0.68 and a long excited state lifetime of 11.8 ns [135]. In the gas phase two tautomers of 2AP exist, 9H-2AP and 7H-2AP, though the former is dominant [136]. Laser induced fluorescence and resonance enhanced two photon ionization (R2PI) on jet-cooled 2AP, show that the 9H-2AP tautomer exhibits only weak fluorescence in the gas phase [137, 138].

Previous theoretical studies have shown that 2AP and adenine possess at least two pathways leading to CIs, which allow for ultrafast nonradiative excited state decay [86, 119, 139]. The structures of the molecule at the CIs are shown in Fig. 5e, f. In 2AP, barriers on the $S_1$ surface hinder access to the nearby CIs [86], while in adenine there are no high barriers to prevent access to the CIs, so ultrafast radiationless decay takes place much more readily [86, 136, 139]. Figure 9 summarizes the findings of CASPT2 calculations by Domcke and coworkers [86]. One can see that the $\pi\pi^*$ minimum in 2AP is about 0.5 eV below the barrier to either CI, while in adenine the $\pi\pi^*$ minimum is energetically higher. 2AP photophysics has also been studied theoretically in aqueous solution using a sequential Monte Carlo quantum mechanics approach [140]. It was found that the barrier to access the CI (only one CI was studied in this work) increases in aqueous environment, leading to increased fluorescence. These results are in agreement with experimental findings.

2,6-Diaminopurine, similarly to 2AP, fluoresces and absorbs at longer wavelengths than the natural nucleobases. R2PI and IR-UV double resonance spectra were measured for gas phase 2,6-diaminopurine and it was shown that the excited
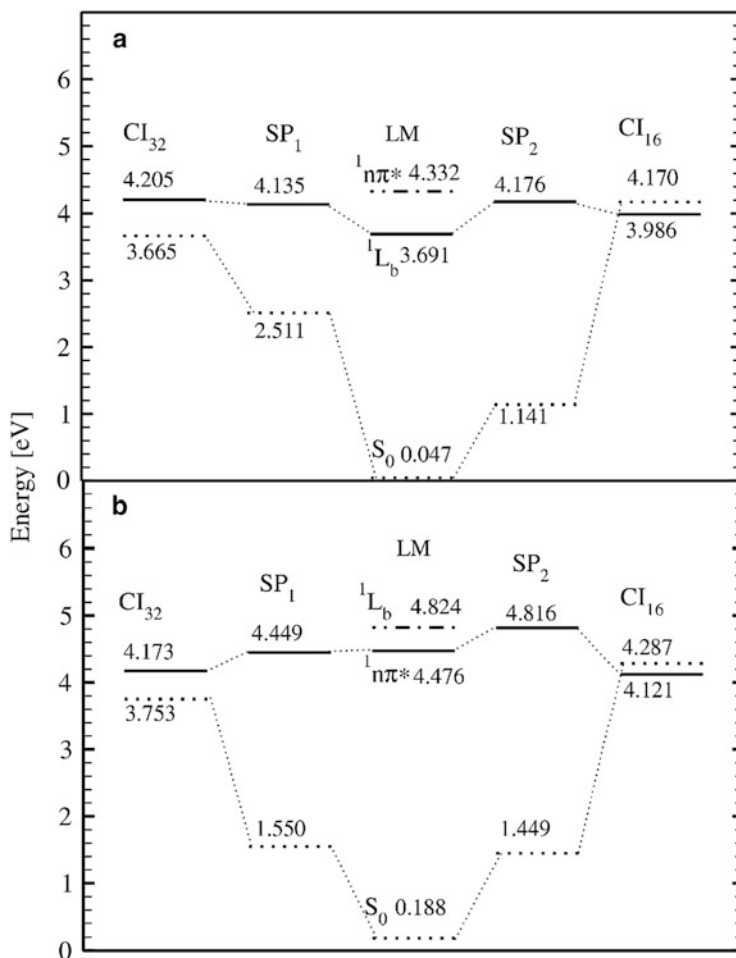
**Fig. 9** Energy-level diagram (in eV) of the S0 (*dotted line*) and S1 (*solid line*) excited states of 2AP (**a**) and 9H-adenine (**b**), obtained by single-point CASPT2 calculations. LM denotes local minima of the excited states in the Franck Condon region. The *dashed-dotted line* gives the minimum energy of the S2 state. CI32 and CI16 are the minimum energies of the S1S0 CI seams associated with the twisting of the N3C2 and N1C6 bonds, respectively. SP1 and SP2 are the saddle points of the corresponding reaction paths, separating the local minima from the CIs. Reproduced from [86]

state lifetimes were nanoseconds, so even in the gas phase this molecule has a slow decay [141]. Comparisons with 4-aminopyrimidine give an idea of how the five-membered ring affects the dynamics. 4-Aminopyrimidine decays in times between picoseconds and nanoseconds, showing a faster decay component. Theoretical studies on 2,4-diaminopyrimidine showed that there exist pathways to CIs, and it was proposed that the addition of the five-membered ring in 2,6-diaminopurine blocks some of these pathways and makes the decay more unlikely to occur. This proposal has also been made by comparing 4-aminopyrimidine with adenine [142].

### 6.2.2   Oxo-Purines: Hypoxanthine and Xanthine

Analogues of the natural purine bases with only oxo groups as substituents are xanthine and hypoxanthine. These molecules may have been available organic compounds in the prebiotic world, and an interesting question is whether they have efficient deactivation pathways that could have protected them from the increased UV radiation at that time. There have been some very recent studies that address this question for both molecules.

Hypoxanthine has been recently studied experimentally by fluorescence up-conversion and transient absorption in solution [143–145]. It has one of the shortest decay times among purines, shorter than guanine and similar to adenine. Hypoxanthine has two tautomers, keto-N7H and keto-N9H, which co-exist in aqueous solution. Nevertheless, unlike adenine, it does not show a biexponential decay in solution indicating that both tautomers decay with similar rates. Ab initio calculations were performed for both tautomers and showed that CIs similar to those found in guanine and adenine exist here as well, involving the C2N3 puckering [143]. Access to the CIs is barrierless and this is expected to lead to a very fast decay. More recent nonadiabatic dynamic simulations were also performed on the two tautomers of hypoxanthine [146] which also show barrierless decay through multiple different CIs. Earlier theoretical studies of hypoxanthine focused on the vertical excitation energies and ground- and excited-state proton transfer in the isolated and monohydrated forms of hypoxanthine [147, 148].

Various methylated xanthines have been studied using femtosecond transient absorption spectroscopy in aqueous and acetonitrile solution [144]. The parent compound, xanthine, is poorly soluble in water at neutral pH and that is why only the methylated ones were studied. This work showed that the decay of these compounds was ultrafast after absorption of UV radiation [144]. Gas phase xanthine and methylated xanthines have also been studied with R2PI, UV–UV, and IR–UV double resonance spectroscopy [131, 149]. These spectra only show one tautomer of xanthine present, which the authors suggest is the N7H one. The lack of other tautomers could be either because one is much more stable than the others or because other tautomers decay too fast to be observed in the spectra.

Xanthine and methylated xanthines cannot decay via the same mechanisms as adenine and guanine because there is no double bond along C2–N3 or N1–C6 of the six-membered ring (see Fig. 8f). Twisting along these bonds leads to the main deformation coordinates for adenine, guanine, and several of their analogues, such as hypoxanthine and 2AP. It has been shown, however, that xanthine has different CIs where the geometry is distorted on the five-membered ring [85]. Yamazaki et al. studied the deactivation pathways for the two most stable tautomers of xanthine, 7H-diketo and 9H-diketo tautomers. They found that for both of them there are CIs between $S_1$ and $S_0$ where the five-membered ring is deformed. The structures of the minimum points on the CI seams are shown in Fig. 5c, d. A different decay pathway which involves CIs between the $\pi\sigma^*$ states and the ground state has also been reported in the same study [85]. According to the calculations the
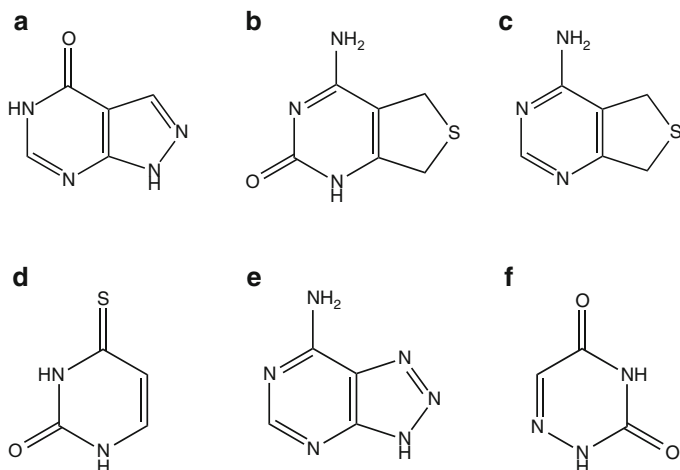
**Fig. 10** Modified nucleobases: (**a**) allopurinol, (**b**) thiophene analogue of cytosine ($^{th}$C), (**c**) thiophene analogue of adenine ($^{th}$A), (**d**) 4-thiouracil, (**e**) 8-azaadenine (**f**) 6-azauracil

pathway through the πσ* state is efficient for the 9H tautomer, but not for the 7H one. On the contrary, the pathway involving deformation of the five-membered ring is more efficient for the 7H-diketo tautomer but is blocked by high energy barriers on the 9H tautomer. This work supports the experimental finding that in the R2PI spectrum only the 7H-diketo tautomer of xanthine is observed by attributing the missing 9H tautomer to efficient nonradiative deactivation via a low-energy dissociative πσ* state. The out-of-plane pathways calculated could be those involved in the experimental ultrafast decay of methylated xanthines.

In all purine bases except xanthine the five-membered ring does not seem to participate in the deactivation pathways. In order to test how the five-membered ring affects deactivation, the imidazole ring can be substituted. Allopurinol is a derivative which is similar to hypoxanthine except that the five-membered ring is pyrazole instead of imidazole (see Fig. 10a). Experimental and theoretical studies showed that this change in the five-membered ring does not cause major changes in the photophysics [150]. Specifically fluorescence upconversion showed an ultrafast decay of the fluorescence signal in water ($\tau < 0.2$ ps), similar to hypoxanthine and guanine. Ab initio calculations reveal similar CIs to the other bases as well, involving only the six-membered ring [150].

## 7   Sulfur and Aza Substituted Nucleobases

As a final group of modified nucleobases we discuss some which use sulfur or substitution of additional nitrogen atoms in the ring. A group of modified analogues, recently synthesized and studied, can be obtained by replacing the

imidazole moiety of purine nucleobases with thiophene or by adding a second ring, thiophene, to pyrimidine bases. The structures of the thiophene analogues of cytosine, $^{th}C$, and adenine, $^{th}A$, are shown in Fig. 10b, c. Thiophene analogues were recently synthesized as emissive RNA nucleobases [151] and have been studied theoretically at the TDDFT level using PCM to account for the solvents of water and dioxane which were used experimentally [152, 153]. All thiophene analogues have excited states red-shifted compared to the natural bases, and thus they can be selectively excited. Furthermore, they have lifetimes of several nanoseconds, much longer than those of the natural bases. Although the theoretical studies so far have not directly computed PESs which could explain these long-lived states, one can speculate on the reasons based on the structures and the calculations on vertical excited states. The pyrimidine analogues $^{th}C$ and $^{th}U$ have the C5–C6 double bond blocked from being able to twist, so the twisting CI will not be easily accessible. Furthermore, in $^{th}U$ the first excited state is $\pi\pi^*$ while in natural U it is a dark $n\pi^*$ state, so the decay pathway present in uracil which leads from the bright $S_2$ state to the dark $S_1$ is not present in $^{th}U$.

When sulfur is used to substitute oxygen in the oxo groups of natural bases, intersystem crossing increases as one would expect based on the heavy atom effect. This has indeed been observed experimentally [154, 155]. The singlet and triplet excited states of several thioanalogues have been studied theoretically [156–159]. It has been shown that the excitation energies for both the singlet and the triplet states in thioanalogues are lower than the respective energies in the regular bases. In 2-thiothymine, besides excitation energies, several crossing have also been computed to find the pathways for the intersystem crossing observed experimentally [159].

Finally, modified nucleobases where a C atom is substituted by N have also been studied. Azapurines have been found to exhibit interesting fluorescence properties in aqueous medium [160–162]. Often fluorescence is found to originate from the anionic species as it increases at high values of pH. Intersystem crossing in aza-nucleobases has been observed, and mechanisms have been found for these processes through theoretical calculations [163–166]. In some cases intersystem crossing is found to compete with internal conversion from the bright $\pi\pi^*$ state to a dark $n\pi^*$ state [164].

# 8   Effects of $\pi$ Stacking on the Photophysical Properties

All of the discussion so far has focused on isolated modified nucleobases. Much of their functionality, however, depends on their properties when they are incorporated into oligonucleotides and interact with other bases. Most of the fluorescent analogues developed exhibit quenched fluorescence when incorporated in oligonucleotides. The effect of neighboring bases on photophysical properties is a very important issue in natural bases as well. Experimental work has shown that excited states in DNA polymers and oligomers have slower decay times compared to the excited states of the individual bases, revealing that the environment plays a

crucial role [6, 167–170]. Specifically, it is shown that π-stacking plays a big role in introducing the longer lived states. This is quite interesting since the behavior is the opposite of what is seen in the fluorescent probes where the radiationless excited state decay becomes much faster in oligonucleotides. Understanding the effects of the environment on both natural and modified nucleobases is an important goal and further work is needed to address this problem.

Here we will focus on the modified base 2AP for which detailed experimental information exists. The processes that lead to the fluorescence quenching of 2AP when incorporated in oligonucleotides are still under investigation, although it has been shown that the quenching arises mostly from base stacking rather than base pairing [171]. Several mechanisms have been proposed based on experimental evidence, in particular photoinduced electron transfer and the presence of dark states [172–176]. Photoinduced electron transfer between neighboring bases, especially guanine, has been championed by Barton and coworkers [172–175], while other workers attribute quenching to the presence of a dark state [171, 176, 177].

Theoretical studies have also contributed to investigations of the underlying reason for the quenching [178–183]. Initially dimers and trimers of 2AP π-stacked with natural bases were used to calculate vertical excitation energies at geometries corresponding to a regular B-DNA conformation. In these studies dark charge-transfer (CT) states were found below the bright $\pi\pi^*$ states and it was suggested that these dark states are responsible for the quenching [178, 184]. These studies, however, used TDDFT, and it is well known now that TDDFT methods fail to compute CT states accurately [185–187], so these results should be viewed with skepticism. Other studies have shown that the CT states are higher energetically and are not expected to be the dominant states upon absorption [179–183].

More recent studies examined the excited state landscape beyond the vertical excitation energies using perturbation theory corrected CIS [181–183]. These studies enabled a more accurate and complete picture of the photoinitiated dynamics. Dimers of 2AP with all four natural DNA bases were included in the studies. Furthermore, since the intermolecular interactions depend on the position of 2AP with respect to the natural base, for every base two initial conformations were included, one where 2AP was at the $3'$ and one where it was at the $5'$ position. It was found that these intermolecular interactions are crucial and there are a number of possible mechanisms that can lead to quenching. The neighboring base seems to be very important for the photophysical behavior. The most interesting pathways that can lead to quenched fluorescence involve the formation of exciplexes and bonded exciplexes. Figure 11 shows a diagram of how the PESs are in these two cases. In an exciplex a minimum on the excited state of the dimer exists which does not exist in any of the monomers. The wavefunction of the state at that minimum has CT character and the oscillator strengths are considerably decreased compared to the oscillator strength of isolated 2AP. These properties of the exciplexes can lead to the observed quenching of fluorescence. Exciplexes were found in dimers of 2AP with guanine and adenine. A bonded exciplex is formed when the minimum on the excited state is stabilized considerably through bonding
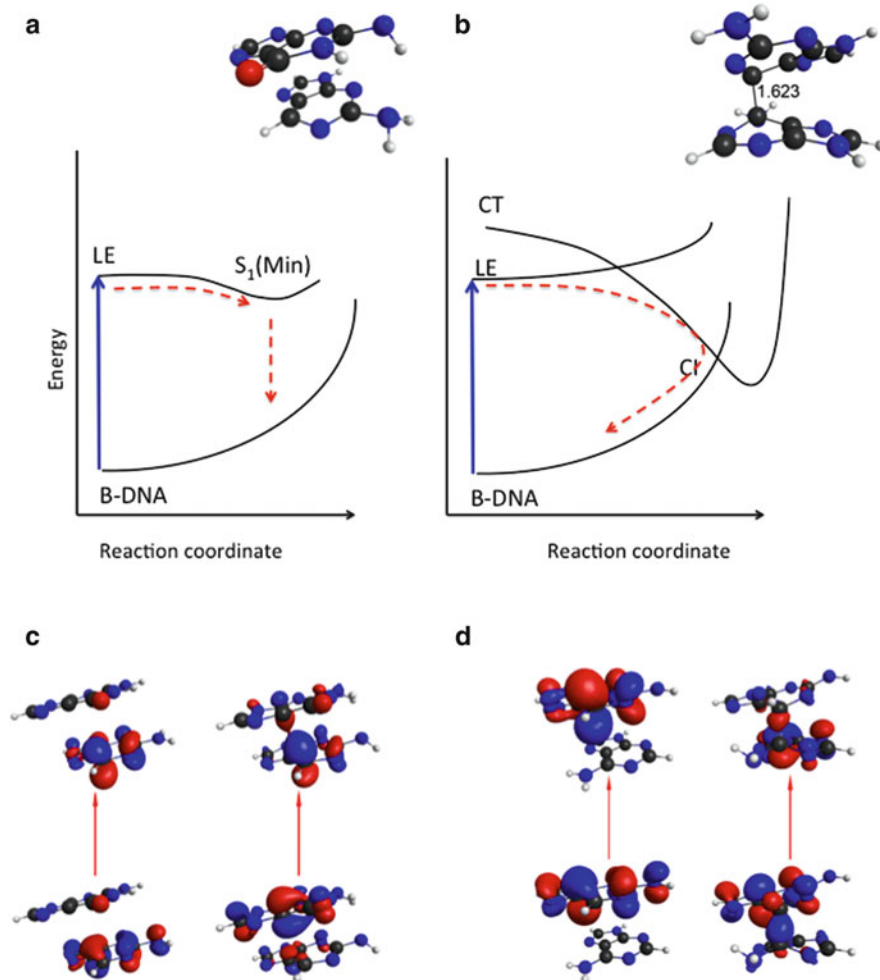
**Fig. 11** Diagram showing (**a**) a regular exciplex and (**b**) a bonded exciplex. (**a**) Summarizes the findings for 5′-adenine-2AP-3′ and 5′-guanine-2AP-3′ while (**b**) summarizes the finding for 5′-2AP adenine-3′ (from [183]). LE stands for locally excited state, in this case on 2AP, and CT stands for charge-transfer state. (**c, d**) Orbitals for the initial and final wavefunctions in (**a**) and (**b**), respectively

interactions between the monomers. This concept was first introduced by Wang and co-workers [188, 189]. When the excited state is stabilized it can reach the ground state surface forming a CI with it. In this case quenching occurs through radiationless decay through the CIs. Bonded exciplexes were found in dimers of 2AP with cytosine, thymine, and adenine. The structure of the dimers at the CIs involves

bonding interactions between the bases (see Fig. 11). Whether these structures can exist when the dimers are incorporated in a larger single or double stranded sequence is not clear and needs further investigation.

Dimers of modified nucleobases have been studied in the gas phase as well. de Vries and coworkers examined methylated xanthines in the gas phase [149]. They observed dimers of 7-methylxanthine and theobromine (3,7-dimethylxanthine). They determined that in the case of 7-methylxanthine the dimer was a hydrogen bonded one, but in the case of theobromine it was a π-stacked structure. It appears that increased methylation enhances the likelihood of getting stable π-stacked structures in the gas phase. Theoretical studies of the methylated xanthine dimers have also been carried out [190]. The calculations focused on various relative orientations of the monomers within the dimers. It was found that the excited state minima of the dimers are stabilized compared to the minima of the monomers. Several CIs were also found, including some with structures similar to the bonded exciplexes discussed for 2AP dimers. Most of the CIs were determined to be energetically inaccessible, but the bonded exciplex type ones were accessible. These CIs could explain the absence of the corresponding dimers in the R2PI spectra.

The studies mentioned here for the π-stacking systems are very recent and indicate the beginning of investigations on interacting systems. It is certain that work in this area will continue to provide more insight into the photophysical properties of modified nucleobases, as well as natural bases, when they are incorporated in oligonucleotides.

# 9   Concluding Remarks

This review showcases how the photophysical properties of modified nucleobases are very sensitive to their structure. Very simple alterations can cause great changes in photophysical properties. In recent years we have gained significant insight into how the structure is related to these properties. The hope is that we can use this knowledge to design more modified molecules with desired properties. In particular, we would like to design molecules with increased fluorescence compared to the natural bases. A lot more work is needed to understand better fluorescence properties when the bases are interacting with other bases. In particular, the observed fluorescence quenching of fluorescent analogues when they are incorporated into single or double strands is an area that needs more work in order to elucidate the mechanisms involved.

# References

1. Bag SS, Heemstra JM, Saito Y, Chenoweth DM (2012) Expansion of the genetic alphabet: unnatural nucleobases and their applications. J Nucleic Acids 2012:718582
2. Callis PR (1983) Electronic states and luminescence of nucleic acid systems. Ann Rev Phys Chem 34:329
3. Daniels M, Hauswirth W (1971) Fluorescence of the purine and pyrimidine bases of the nucleic acids in neutral aqueous solution at 300 k. Science 171:675
4. Daniels M (1976) In: Wang SY (ed) Photochemistry and photobiology of nucleic acids, vol 1. Academic, New York, p 23
5. Crespo-Hernandez CE, Cohen B, Hare PM, Kohler B (2004) Ultrafast excited-state dynamics in nucleic acids. Chem Rev 104:1977
6. Middleton CT, de La Harpe K, Su C, Law YK, Crespo-Hernandez CE, Kohler B (2009) DNA excited-state dynamics: from single bases to the double helix. Annu Rev Phys Chem 60:217–239
7. Sobolewski AL, Domcke W (2006) The chemical physics of the photostability of life. Europhys News 37:20–23
8. Shapiro R (1995) The prebiotic role of adenine: a critical analysis. Origins Life Evol Biosph 25:83–98
9. Levy M, Miller SL (1998) The stability of the RNA bases: implications for the origin of life. Proc Natl Acad Sci U S A 95:7933–7938
10. Orgel LE (2004) Prebiotic chemistry and the origin of the RNA world. Crit Rev Biochem Mol Biol 39:99–123
11. Ehrenfreund P, Rasmussen S, Cleaves J, Chen LH (2006) Experimentally tracing the key steps in the origin of life: the aromatic world. Astrobiology 6:490–520
12. Limbach PA, Crain PF, McCloskey JA (1994) Summary: the modified nucleosides of RNA. Nucleic Acids Res 22:2183–2196
13. Cockell CS, Horneck G (2001) The history of the UV radiation climate of the Earth – theoretical and space-based observations. Photochem Photobiol 73:447–451
14. Lakowicz JR (2006) Principles of fluorescence spectroscopy. Springer, New York
15. Asseline U (2006) Development and applications of fluorescent oligonucleotides. Curr Org Chem 10:491–518
16. Rist M, Marino J (2002) Fluorescent nucleotide base analogs as probes of nucleic acid structure, dynamics and interactions. Curr Org Chem 6:775–793
17. Hall KB (2009) 2-Aminopurine as a probe of RNA conformational transitions. Methods Enzymol 469:269–285
18. Hawkins ME, Brand L, Michael LJ (2008) Fluorescent pteridine probes for nucleic acid analysis. Methods Enzymol 450:201
19. Sinkeldam RW, Greco NJ, Tor Y (2010) Fluorescent analogs of biomolecular building blocks: design, properties, and applications. Chem Rev 110:2579–2619
20. Wilhelmsson LM (2010) Fluorescent nucleic acid base analogues. Q Rev Biophys 43:159–183
21. Tanpure AA, Pawar MG, Srivatsan SG (2013) Fluorescent nucleoside analogs: probes for investigating nucleic acid structure and function. Isr J Chem 53:366–378
22. Tor Y (2007) Fluorescent nucleoside analogs: synthesis, properties and applications. Tetrahedron 63:3415–3614
23. Kool ET (2002) Replacing the nucleobases in DNA with designer molecules. Acc Chem Res 35:936
24. Wilson JN, Kool ET (2006) Fluorescent DNA base replacements: reporters and sensors for biological systems. Org Biomol Chem 4:4265
25. Matray TJ, Kool ET (1999) A specific partner for abasic damage in DNA. Nature 399:704
26. Grigorenko NA, Leumann CJ (2009) 2-Phenanthrenyl-DNA: synthesis, pairing, and fluorescence properties. Chem Eur J 15:639

27. Hawkins ME (2001) Fluorescent pteridine nucleoside analogs. Cell Biochem Biophys 34:257

28. Leonard NJ, Tolman GL (1975) Fluorescent nucleosides and nucleotides. Ann N Y Acad Sci 255:43

29. Dierckx A, Miannay F-A, Ben Gaied N, Preus S, Bjorck M, Brown T, Wilhelmsson LM (2012) Quadracyclic adenine: a non-perturbing fluorescent adenine analogue. Chem Eur J 18:5987–5997

30. Zhao Y, Knee JL, Baranger AM (2008) Characterization of two adenosine analogs as fluorescence probes in RNA. Bioorg Chem 36:271–277

31. Yarkony DR (1998) Conical intersections: diabolical and often misunderstood. Acc Chem Res 31:511–518

32. Yarkony DR (1996) Diabolical conical intersections. Rev Mod Phys 68:985–1013

33. Yarkony DR (1996) Current issues in nonadiabatic chemistry. J Phys Chem 100:18612–18628

34. Yarkony DR (2001) Conical intersections: the new conventional wisdom. J Phys Chem A 105:6277–6293

35. Bernardi F, Olivucci M, Robb MA (1990) Predicting forbidden and allowed cycloaddition reactions: potential surface topology and its rationalization. Acc Chem Res 23:405–412

36. Bernardi F, Olivucci M, Robb MA (1996) Potential energy surface crossings in organic photochemistry. Chem Soc Rev 25:321–328

37. Robb MA, Garavelli M, Olivucci M, Bernardi F (2000) A computational strategy for organic photochemistry. In: Lipkowitz KB, Boyd DB (eds) Reviews in computational chemistry, vol 15. Wiley-VCH, New York, pp 87–146

38. Barckholtz TA, Miller TA (1998) Quantitative insights about molecules exhibiting Jahn-Teller and related effects. Int Rev Phys Chem 17:435–524

39. Domcke W, Yarkony DR, Köppel H (2004) Conical intersections. World Scientific, Singapore

40. Jasper AW, Zhu C, Nangia S, Truhlar DG (2004) Introductory lecture: nonadiabatic effects in chemical dynamics. Faraday Discuss 127:1–22

41. Matsika S (2007) Conical intersections in molecular systems. In Lipkowitz KB, Cundari TR (eds) Reviews in computational chemistry, vol 23. Wiley-VCH, New Jersey, pp 83–124

42. Matsika S, Krause P (2011) Nonadiabatic events and conical intersections. Annu Rev Phys Chem 62:621–643

43. von Neumann J, Wigner EP (1929) On the behaviour of eigenvalues in adiabatic processes. Physik Z 30:467–470

44. Teller E (1937) The crossing of potential surfaces. J Phys Chem 41:109–116

45. Koga N, Morokuma K (1985) Determination of the lowest energy point on the crossing seam between two potential surfaces using the energy gradient. Chem Phys Lett 119:371–374

46. Farazdel A, Dupuis M (1991) On the determination of the minimum on the crossing seam of two potential energy surfaces. J Comput Chem 12:276–282

47. Yarkony DR (1990) On the characterization of regions of avoided surface crossings using an analytic gradient based method. J Chem Phys 92:2457–2463

48. Manaa MR, Yarkony DR (1993) On the intersection of two potential energy surfaces of the same symmetry. Systematic characterization using a Lagrange multiplier constrained procedure. J Chem Phys 99:5251–5256

49. Anglada JM, Bofill JM (1997) A reduced-restricted-quasi-Newton-Raphson method for locating and optimizing energy crossing points between two potential energy surfaces. J Comput Chem 18:992–1003

50. Ragazos IN, Robb MA, Bernardi F, Olivucci M (1992) Optimization and characterization of the lowest energy point on a conical intersection using an MC-SCF Lagrangian. Chem Phys Lett 119:217–223

51. Bearpark MJ, Robb MA, Schlegel HB (1994) A direct method for the location of the lowest energy point on a potential surface crossing. Chem Phys Lett 223:269–274

52. Zilberg S, Hass Y (1999) Molecular photochemistry: a general method for localizing conical intersections using the phase-change rule. Chem Eur J 5:1755–1765

53. Ciminelli C, Granucci G, Persico M (2004) The photoisomerization mechanism of azobenzene: a semiclassical simulation of nonadiabatic dynamics. Chem Eur J 10:2327–2341

54. De Vico L, Olivucci M, Lindh R (2005) New general tools for constrained geometry optimizations. J Chem Theory Comput 1:1029–1037

55. Levine BG, Coe JD, Martinez TJ (2008) Optimizing conical intersections without derivative coupling vectors: application to multistate multireference second-order perturbation theory (MS-CASPT2). J Phys Chem B 112:405–413

56. Kistler KA, Matsika S (2009) Quantum mechanical studies of the photophysics of DNA and RNA Bases. In Lee T-S, York DM (eds) Challenges and advances in computational chemistry and physics: multi-scale quantum models for biocatalysis: modern techniques and applications, vol 7. Springer, The Netherlands, pp 285–339

57. Merchán M, Gonzalez-Luque R, Climent T, Serrano-Andrés L, Rodriuguez E, Reguero M, Pelaez D (2006) Unified model for the ultrafast decay of pyrimidine nucleobases. J Phys Chem B 110:26471–26476

58. Barbatti M, Aquino AJA, Szymczak JJ, Nachtigallova D, Hobza P, Lischka H (2010) Relaxation mechanisms of UV-photoexcited DNA and RNA nucleobases. Proc Natl Acad Sci U S A 107:21453–21458

59. Ismail N, Blancafort L, Olivucci M, Kohler B, Robb MA (2002) Ultrafast decay of electronically excited singlet cytosine via $\pi, \pi^*$ to $n\pi^*$ state switch. J Am Chem Soc 124:6818

60. Kistler KA, Matsika S (2007) Radiationless decay mechanism of cytosine: an ab initio study with comparisons to the fluorescent analogue 5-methyl-2-pyrimidinone. J Phys Chem A 111:2650–2661

61. Sobolewski AL, Domcke W (2002) On the mechanism of nonradiative decay of DNA bases: ab initio and TDDFT results for the excited states of 9H-adenine. Eur Phys J D 20:369

62. Blancafort L, Cohen B, Hare P, Kohler B, Robb M (2005) Singlet excited-state dynamics of 5-fluorocytosine and cytosine: an experimental and computational study. J Phys Chem A 109:4431–4436

63. Malone RJ, Miller AM, Kohler B (2003) Singlet excited-state lifetimes of cytosine derivatives measured by femtosecond transient absorption. Photochem Photobiol 77:158–164

64. Zgierski MZ, Patchkovskii S, Fujiwara T, Lim EC (2005) On the origin of the ultrafast internal conversion of electronically excited pyrimidine bases. J Phys Chem A 109:9384–9387

65. Zgierski MZ, Fujiwara T, Kofron WG, Lim EC (2007) Highly effective quanching of the ultrafast radiationless decay of photoexcited pyrimidine bases by covalent modification: photophysics of 5,6-trimethylenecytosine and 5,6-trimethyleneuracil. Phys Chem Chem Phys 9:3206–3209

66. Zgierski MZ, Patchkovskii S, Lim EC (2005) Ab initio study of a biradical radiationless decay channel of the lowest excited electronic state of cytosine and its derivatives. J Chem Phys 123:081101

67. Zgierski MZ, Patchkovskii S, Fujiwarab T, Lim EC (2007) The role of out-of-plane deformations in subpicosecond internal conversion of photoexcited purine bases: absence of the ultrafast decay channel in propanodeoxyguanosine. Chem Phys Lett 440:145–149

68. Zgierski MZ, Patchkovskii S, Lim EC (2007) Biradical radiationless decay channel in adenine and its derivatives. Can J Chem 85:124

69. Zgierski MZ, Fujiwara T, Kofron WG, Lim EC (2007) Highly effective quenching of the ultrafast radiationless decay of photoexcited pyrimidine bases by covalent modification: photophysics of 5,6-trimethylenecytosine and 5,6-trimethyleneuracil. Phys Chem Chem Phys 9:3206–3209

70. Zgierski MZ, Fujiwara T, Kofron WG, Lim EC (2008) Conical intersections and ultrafast intramolecular excited-state dynamics in nucleic acid bases and electron donoracceptor molecules. Chem Phys Lett 463:289–299

71. Ho J-W, Yen H-C, Chou W-K, Weng C-N, Cheng L-H, Shi H-Q, Lai S-H, Cheng P-Y (2011) Disentangling Intrinsic ultrafast excited-state dynamics of cytosine tautomers. J Phys Chem A 115:8406–8418

72. Yuan S, Ma J, Zhang W-Y, Shu K-X, Dou Y-S (2012) Semiclassical dynamics simulation and CASSCF calculation for 5-methyl cytosine and cytosine. Acta Phys Chim Sin 28:2803–2808

73. Serrano-Andrés L, Merchán M (2009) Are the five natural DNA/RNA base monomers a good choice from natural selection? A photochemical perspective. J Photoch Photobiol C Photochem Rev 10:21–32

74. Gustavsson T, Banyasz A, Sarkar N, Markovitsi D, Improta R (2008) Assessing solvent effects on the singlet excited state lifetime of uracil derivatives: a femtosecond fluorescence upconversion study in alcohols and D2O. Chem Phys 350:186–192

75. Gustavsson T, Sarkar N, Banyasz A, Markovitsi D, Improta R (2007) Solvent effects on the steady-state absorption and fluorescence spectra of uracil, thymine and 5-fluorouracil. Photochem Photobiol 83(3):595–599

76. Gustavsson T, Banyasz A, Lazzarotto E, Markovitsi D, Scalmani G, Frisch M, Barone V, Improta R (2006) Singlet excited-state behavior of uracil and thymine in aqueous solution: a combined experimental and computational study of 11 uracil derivatives. J Am Chem Soc 128(2):607–619

77. Santoro F, Barone V, Gustavsson T, Improta R (2006) Solvent effect on the singlet excited-state lifetimes of nucleic acid bases: a computational study of 5-fluorouracil and uracil in acetonitrile and water. J Am Chem Soc 128(50):16312–16322

78. Gustavsson T, Sarkar N, Lazzarotto E, Markovitsi D (2006) Solvent effect on the singlet excited-state dynamics of 5-fluorouracil in acetonitrile as compared with water. J Phys Chem B 110:12843

79. Santoro F, Improta R, Barone V (2009) Three-dimensional diabatic models for the pi pi*– > n pi* excited-state decay of uracil derivatives in solution. Theor Chem Acc 123:273

80. Mercier Y, Reguero M (2011) Comparison of the deactivation mechanism of 5-fluorouracil with that of its parent system, uracil: the need of the use of the MS-CASPT2 method. Int J Quantum Chem 111:3405

81. Yamazaki S, Taketsugu T (2012) Nonradiative deactivation mechanisms of uracil, thymine, and 5-fluorouracil: a comparative ab initio study. J Phys Chem A 116:491

82. Hudock HR, Levine BG, Thompson AL, Satzger H, Townsend D, Gador N, Ullrich S, Stolow A, Martinez TJ (2007) Ab initio molecular dynamics and time-resolved photoelectron spectroscopy of electronically excited uracil and thymine. J Phys Chem A 111:8500–8508

83. Gustavsson T, Improta R, Banyasz A, Vaya I, Markovitsi D (2012) The effect of methylation on the excited state dynamics of aminouracils. J Photochem Photobiol A Chem 234:37–43

84. Kistler KA, Matsika S (2007) The fluorescence mechanism of 5-methyl-2-pyrimidinone: an ab initio study of a fluorescent pyrimidine analog. Photoch Photob 83:611–624

85. Yamazaki S, Sobolewski AL, Domcke W (2009) Photophysics of xanthine: computational study of the radiationless decay mechanisms. Phys Chem Chem Phys 11:10165–10174

86. Perun S, Sobolewski AL, Domcke W (2006) Ab initio studies of the photophysics of 2-aminopurine. Mol Phys 104:1113–1121

87. Beak P, Fry FSJ, Lee J, Steele F (1975) Equilibration studies. Protomeric equilibria of 2- and 4-hydroxypyridines, 2- and 4-hydroxypyrimidines, 2- and 4-mercaptopyridines, and structurally related compounds in the gas phase. J Am Chem Soc 98:171

88. Kaluzhny DN, Mikhailov SN, Efimtseva EV, Borisova OF, Florentiev VL, Shchyolkina AK, Jovin TM (2003). Fluorescent 2-pyrimidinone nucleoside in parallel-stranded DNA. Nucleosides Nucleotides and Nucleic Acids 22:1499–1503

89. Kistler KA, Matsika S (2007) Cytosine in context: a theoretical study of substituent effects on the excitation energies of 2-pyrimidinone derivatives. J Phys Chem A 111:8708–8716

90. Kistler KA, Matsika S (2008) Three-state conical intersections in cytosine and pyrimidinone bases. J Chem Phys 128:215102

91. Krygowski TM, Stepien BT (2005) Sigma- and pi-electron delocalization: focus on substituent effects. Chem Rev 105:34823512

92. Laland SG, Serck-Hanssen G (1964) Synthesis of pyrimidin-2-one deoxyribosides and their ability to support the growth of the deoxyriboside-requiring organism Lactobacillus acidophilus R26. Biochem J 90:76–81

93. Atchity GJ, Xantheas SS, Ruedenberg K (1991) Potential energy surfaces near intersections. J Chem Phys 95:1862

94. Lobsiger S, Frey H-M, Leutwyler S, Morgan P, Pratt D (2011) S-0 and S-1 state structure, methyl torsional barrier heights, and fast intersystem crossing dynamics of 5-methyl-2-hydroxypyrimidine. J Phys Chem A 115(46):13281–13290

95. Ryseck G, Schmierer T, Haiser K, Schreier W, Zinth W, Gilch P (2011) The excited-state decay of 1-methyl-2(1H)-pyrimidinone is an activated process. ChemPhysChem 12:1880

96. Nowak MJ, Szczepaniak K, Barski A, Shugar D (1980) Tautomeric equilibria of 2(4)-monooxopyrimidines in the gas-phase, in low-temperature matrices and in solution. J Mol Struct 62:47–69

97. Delchev VB, Sobolewski A, Domcke W (2010) Comparison of the non-radiative decay mechanisms of 4-pyrimidinone and uracil: an ab initio study. Phys Chem Chem Phys 11:5007–5015

98. Vranken H, Smets J, Maest G, Lapinski L, Nowak MJ, Adamowicz L (1994) Infrared-spectra and tautomerism of isocytosine - an ab-initio and matrix-isolation study. Spectrochim Acta A 50:875–889

99. Shukla M, Leszczynski J (2000) Investigations of the excited-state properties of isocytosine: an ab initio approach. Int J Quantum Chem 77:240–254

100. Bakalska RI, Delchev VB (2012) Comparative study of the relaxation mechanisms of the excited states of cytosine and isocytosine. J Mol Model 18:5133–5146

101. Hudson RHE, Dambenieks AK, Viirre RD (2004) Fluorescent 7-deazapurine derivatives from 5-iodocytosine via a tandem cross-coupling-annulation reaction with terminal alkynes. Synlett 13:2400–2402

102. Berry DA, Jung K-Y, Wise DS, Sercel AD, Pearson WH, Mackie H, Randolph JB, Somers RL (2004) Pyrrolo-dC and pyrrolo-C: fluorescent analogs of cytidine and 2′-deoxycytidine for the study of oligonucleotides. Tetrahedron Lett 45:2457–2461

103. Thompson KC, Miyake N (2005) Properties of a new fluorescent cytosine analogue, pyrrolocytosine. J Phys Chem B 109:6012–6019

104. Hardman SJO, Botchway SW, Thompson KC (2008) Evidence for a nonbase stacking effect for the environment-sensitive fluorescent base pyrrolocytosine-comparison with 2-aminopurine. Photochem Photobiol 84:1473–1479

105. Wojciechowski F, Hudson RHE (2008) Fluorescence and hybridization properties of peptide nucleic acid containing a substituted phenylpyrrolocytosine designed to engage guanine with an additional H-bond. J Am Chem Soc 130:1257412575

106. Lin K-Y, Jones RJ, Matteucci M (1995) Tricyclic 2′-deoxycytidine analogs: syntheses and incorporation into oligodeoxynucleotides which have enhanced binding to complementary RNA. J Am Chem Soc 117:38733874

107. Wilhelmsson LM, Sandin P, Holmén A, Albinsson B, Lincoln P, Nordén B (2003) Photophysical characterization of fluorescent DNA base analogue, tC. J Phys Chem B 107:9094–9101

108. Engman KC, Sandin P, Osborne S, Brown T, Billeter M, Lincoln P, Nordén B, Albinsson B, Wilhelmsson LM (2004) DNA adopts normal b-form upon incorporation of highly fluorescent DNA base analogue tC: NMR structure and UV-vis spectroscopy characterization. Nucleic Acids Res 32:5087–5095

109. Sandin P, Brjesson K, Li H, Mårtensson J, Brown T, Wilhelmsson LM, Albinsson B (2008) Characterization and use of an unprecedentedly bright and structurally non-perturbing fluorescent DNA base analogue. Nucleic Acids Res 36:157

110. Börjesson K, Preus S, El-Sagheer AH, Brown T, Albinsson B, Wilhelmsson LM (2009) Nucleic acid base analog FRET-pair facilitating detailed structural measurements in nucleic acid containing systems. J Am Chem Soc 131:4288

111. Preus S, Borjesson K, Kilsa K, Albinsson B, Wilhelmsson L (2010) Characterization of nucleobase analogue FRET acceptor tC(nitro). J Phys Chem B 114:1050–1056

112. Preus S, Kilsa K, Wilhelmsson L, Albinsson B (2010) Photophysical and structural properties of the fluorescent nucleobase analogues of the tricyclic cytosine (tC) family. Phys Chem Chem Phys 12:8881–8892

113. Mburu E, Matsika S (2008) An ab initio study of substituent effects on the excited states of purine derivatives. J Phys Chem A 112:12485–12491

114. Cohen B, Hare P, Kohler B (2003) Ultrafast excited-state dynamics of adenine and monomethylated adenines in solution: implications for the nonradiative decay mechanism. J Am Chem Soc 125:13594

115. Marian CM (2007) The guanine tautomer puzzle: quantum chemical investigation of ground and excited states. J Phys Chem A 111:1545–1553

116. Mons M, Piuzzi F, Dimicoli I, Gorb L, Lesczynski J (2006) Near-UV resonant two-photon ionization spectroscopy of gas phase guanine: evidence for the observation of three rare tautomers. J Phys Chem A 110:10921–10924

117. Chen H, Li SH (2006) Theoretical study on the excitation energies of six tautomers of guanine: evidence for the assignment of the rare tautomers. J Phys Chem A 110:12360–12362

118. Serrano-Andres L, Merchan M, Borin AC (2008) A three-state model for the photophysics of guanine. J Am Chem Soc 130:2473–2484

119. Serrano-Andrés L, Merchán M, Borin AC (2006) Adenine and 2-aminopurine: paradigms of modern theoretical photochemistry. Proc Natl Acad Sci U S A 103:8691–8696

120. Marian CM, Kleinschmidt M, Tatchen J (2008) The photophysics of 7H-adenine: a quantum chemical investigation including spin-orbit effects. Chem Phys 347:346–359

121. Serrano-Andres L, Merchan M, Borin AC (2006) A three-state model for the photophysics of adenine. Chem A Eur J 12:6559–6571

122. Lang P, Gerez C, Tritsch D, Fontecave M, Biellmann J-F, Burger A (2003) Synthesis of 8-vinyladenosine 50-di- and 50-triphosphate: evaluation of the diphosphate compound on ribonucleotide reductase. Tetrahedron 59:7315–7322

123. Gaied NB, Glasser N, Ramalanjaona N, Beltz H, Wolff P, Marquet R, Burger A, Mly Y (2005) 8-Vinyl-deoxyadenosine, an alternative fluorescent nucleoside analog to 2′-deoxyribosyl-2-aminopurine with improved properties. Nucl Acids Res 33:1031–1039

124. Kenfack CA, Burger A, Mély Y (2006) Excited-state propertes and transitions of fluorescent 8-vinyl adenosine in DNA. J Phys Chem A 110:26327–26336

125. Kodali G, Kistler KA, Narayanan M, Matsika S, Stanley RJ (2010) Change in electronic structure upon optical excitation of 8-vinyladenosine: an experimental and theoretical study. J Phys Chem A 114:256–267

126. Narayanan M, Kodali G, Singh VR, Velvadapu V, Stanley RJ (2010) Oxidation and reduction potentials of 8-vinyladenosine measured by cyclic voltammetry: implications for photoinduced electron transfer quenching of a fluorescent adenine analog. J Phys Chem A 114:256–267

127. Nadler A, Strohmeier J, Diederichsen U (2011) 8-Vinyl-2′-deoxyguanosine as a fluorescent 2′-deoxyguanosine mimic for investigating DNA hybridization and topology. Angew Chem Int Ed 50:5392–5396

128. Muellar S, Strohmeier J, Diederichsen U (2012) 8-Vinylguanine nucleo amino acid: a fluorescent PNA building block. Org Lett 14(6):1382–1385

129. Holzberger B, Strohmeier J, Siegmund V, Diederichsen U, Marx A (2012) Enzymatic synthesis of 8-vinyl- and 8-styryl-2′-deoxyguanosine modified DNA-novel fluorescent molecular probes. Bioorg Med Chem Lett 22(9):3136–3139

130. Nir E, Kleinermanns K, Grace L, de Vries MS (2001) On the photochemistry of purine nucleobases. J Phys Chem A 105:5106

131. Callahan MP, Crews B, Abo-Riziq A, Grace L, de Vries MS, Gengeliczki Z, Holmes TM, Hill GA (2007) IR-UV double resonance spectroscopy of xanthine. Phys Chem Chem Phys 9:4587–4591

132. Nir E, Grace LI, Brauer B, de Vries MS (1999) REMPI spectroscopy of jet-cooled guanine. J Am Chem Soc 121:4896–4897

133. Crews B, Abo-Riziq A, Grace LI, Callahan M, Kabeláč M, Hobza P, de Vries MS (2005) IR-UV double reonance spectroscopy of guanine-$H_2O$ clusters. Phys Chem Chem Phys 7:3015–3020

134. Abo-Riziq A, Crews BO, Compagnon I, Oomens J, Meijer G, Helden GV, Kabeláč M, Hobza P, de Vries MS (2007) The mid-IR spectra of 9-ethyl guanine, guanosine, and 2-deoxyguanosine. J Phys Chem A 111:7529–7536

135. Ward DC, Reich E, Stryer L (1969) Fluorescence studies of nucleotides and polynucleotides. J Biol Chem 244:1228

136. Seefeld KA, Plützer C, Löwenich D, Häber T, Linder R, Kleinermanns K, Tatchen J, Marian CM (2005) Tautomers and electronic states of jet-cooled 2-aminopurine investigated by double resonance spectroscopy and theory. Phys Chem Chem Phys 7:3021–3026

137. Feng K, Engler G, Seefeld K, Kleinermanns K (2009) Disperesed fluorescence and delayed ionizaton of jet-cooled 2-aminopurine: relaxation to a dark state causes weak fluorescence. ChemPhysChem 10:886–889

138. Lobsiger S, Sinha RK, Trachsel M, Leutwyler S (2011) Low-lying excited states and nonradiative processes of the adenine analogues 7H- and 9H-2-aminopurine. J Chem Phys 134:114307

139. Perun S, Sobolewski AL, Domcke W (2005) Ab Initio studies on the radiationless decay mechanisms of the lowest excited singlet states of 9H-adenine. J Am Chem Soc 127:6257–6265

140. Ludwig V, do Amaral M, da Costa Z, Borin A, Canuto S, Serrano-Andres L (2008) 2-Aminopurine non-radiative decay and emission in aqueous solution: a theoretical study. Chem Phys Lett 463:201–205

141. Gengeliczki Z, Callahan MP, Svadlenak N, Pongor CI, Sztaray B, Meerts L, Nachtigallova D, Hobza P, Barbatti M, Lischka H, de Vries MS (2010) Effect of substituents on the excited-state dynamics of the modified DNA bases 2,4-diaminopyrimidine and 2,6-diaminopurine. Phys Chem Chem Phys 12:5375–5388

142. Barbatti M, Lischka H (2007) Can the nonadiabatic photodynamics of aminopyrimidine be a model for the ultrafast deactivation of adenine? J Phys Chem A 111:2852–2858

143. Peon J, Villabona-Monsalve J, Noria R, Matsika S (2012) On the accessibility to conical intersections in purines: hypoxanthine and its singly protonated and deprotonated forms. J Am Chem Soc 134:7820–7829

144. Chen J, Kohler B (2012) Ultrafast nonradiative decay by hypoxanthine and several methyl-xanthines in aqueous and acetonitrile solution. Phys Chem Chem Phys 14:10677–10682

145. Röttger K, Siewertsen R, Temps F (2012) Ultrafast electronic deactivation dynamics of the rare natural nucleobase hypoxanthine. Chem Phys Lett 536:140146

146. Guo X, Lan Z, Cao Z (2013) Ab initio insight into ultrafast nonadiabatic decay of hypoxanthine: keto-N7H and keto-N9H tautomers. Phys Chem Chem Phys 15:10777–10782

147. Shukla M, Leszczynski J (2003) Electronic spectra, excited-state geometries, and molecular electrostatic potentials of hypoxanthine: a theoretical investigation. J Phys Chem A 107(29):5538–5543

148. Shukla M, Leszczynski J (2005) Time-dependent density functional theory (TD-DFT) study of the excited state proton transfer in hypoxanthine. Int J Quantum Chem 105(4):387–395

149. Callahan MP, Gengeliczki Z, Svadlenak N, Valdes H, Hobza P, de Vries MS (2008) Non-standard base pairing and stacked structures in methyl xanthine clusters. Phys Chem Chem Phys 10:2819–2826

150. Villabona-Monsalve JP, Islas RE, Rodríguez-Córdoba W, Matsika S, Peón J (2013) Ultrafast excited state dynamics of allopurinol, a modified DNA base. J Phys Chem A 117:898–904

151. Shin RD, Sinkeldam YT (2011) Emissive RNA alphabet. J Am Chem Soc 133:14912–14915

152. Samanta PK, Manna AK, Pati SK (2012) Thieno analogues of RNA nucleosides: a detailed theoretical study. J Phys Chem B 116:7618–7626

153. Gedik M, Brown A (2013) Computational study of the excited state properties of modified RNA nucleobases. J Photochem Photobiol A Chem 259:25–32

154. Harada Y, Suzuki T, Ichimura T, Xu Y (2007) Triplet formation of 4-thiothymidine and its photosensitization to oxygen studied by time-resolved thermal lensing technique. J Phys Chem B 111:5518–5524

155. Kuramochi H, Kobayashi T, Suzuki T, Ichimura T (2010) Excited-state dynamics of 6-aza-2-thiothymine and 2-thiothymine: highly efficient intersystem crossing and singlet oxygen photosensitization. J Phys Chem B 114:8782–8789

156. Shukla M, Leszczynski J (2004) Multiconfigurational self-consistent field study of the excited state properties of 4-thiouracil in the gas phase. J Phys Chem A 108:72417246

157. Shukla M, Leszczynski J (2004) Electronic transitions of thiouracils in the gas phase and in solutions: time-dependent density functional theory (TD-DFT) study. J Phys Chem A 108:10367–10375

158. Gedik M (2009) TDDFT study of nucleobase thioanalogues and oxo-derivatives excited states. J Theor Comput Chem 8:71–83

159. Cui G, Fang WH (2013) State-specific heavy-atom effect on intersystem crossing processes in 2-thiothymine: a potential photodynamic therapy photosensitizer. J Chem Phys 138:044315

160. Wierzchowski J, Wielgus-Kutrowska B, Shugar D (1996) Fluorescence emission properties of 8-azapurines and their nucleosides, and application to the kinetics of the reverse synthetic reaction of PNP. Biochim Biophys Acta 1290:9–17

161. Seela IMF, Javelakar AM (2005) Replacement of canonical dna nucleobases by benzotriazole and triazolo[4,5-d]pyrimidine: synthesis, fluorescence and ambiguous base pairing. Helv Chim Acta 88:751–765

162. Budowa S, Seela F (2010) 2-Azapurine nucleosides: synthesis, properties, and base pairing of oligonucleotides. Chem Biodivers 7:2145–2190

163. Kobayashi T, Harada Y, Suzuki T, Ichimura T (2008) Excited state characteristics of 6-azauracil in acetonitrile: drastically different relaxation mechanism from uracil. J Phys Chem A 112:13308–13315

164. Kobayashi T, Kuramochi H, Harada Y, Suzuki T, Ichimura T (2009) Intersystem crossing to excited triplet state of aza analogues of nucleic acid bases in acetonitrile. J Phys Chem A 113:12088–12093

165. Gobbo JP, Borin AC, Serrano-Andrés L (2011) On the relaxation mechanisms of 6-azauracil. J Phys Chem B 115:6243–6251

166. Gobbo JP, Borin AC (2012) On the mechanisms of triplet excited state population in 8-azaadenine. J Phys Chem B 116:14000–14007

167. Crespo-Hernandez CE, Cohen B, Kohler B (2005) Base stacking controls excited-state dynamics in A-T DNA. Nature 436:1141–1144

168. Crespo-Hernandez CE, de La Harpe K, Kohler B (2008) Ground-state recovery following UV excitation is much slower in G.C-DNA duplexes and hairpins than in mononucleotides. J Am Chem Soc 130:19844–10845

169. Kwok W-M, Ma C, Phillips DL (2006) Femtosecond time- and wavelength-resolved fluorescence and absorption spectroscopic study of the excited states of adenosine and an adenine oligomer. J Am Chem Soc 128:11894–11905

170. Buchvarov I, Wang Q, Raytchev M, Trifonov A, Fiebig T (2007) Electronic energy delocalization and dissipation in single- and double-stranded DNA. Proc Natl Acad Sci U S A 104:4794–4797

171. Rachofsky EL, Osman R, Ross JBA (2001) Probing structure and dynamics of DNA with 2-aminopurine: effects of local environment on fluorescence. Biochemistry 40:946–956

172. Wan C, Fiebig T, Schiemann O, Barton J, Zewail A (2000) Femtosecond direct observation of charge transfer between bases in DNA. Proc Natl Acad Sci U S A 97(26):14052–14055

173. Kelley SO, Barton JK (1999) Electron transfer between bases in double helical DNA. Science 283:375

174. Fiebig T, Wan C, Zewail A (2002) Femtosecond charge transfer dynamics of a modified DNA base: 2-aminopurine in complexes with nucleotides. Chem Phys Chem 3(9):781–788

175. O'Neill MA, Becker H-C, Wan C, Barton JK, Zewail AH (2003) Ultrafast dynamics in DNA-mediated electron transfer: base gating and the role of temperature. Angew Chem Int Ed 42:5896–5900

176. Larsen O, van Stokkum I, de Weerd F, Vengris M, Aravindakumar C, van Grondelle R, Geacintov N, van Amerongen H (2004) Ultrafast transient-absorption and steady-state fluorescence measurements on 2-aminopurine substituted dinucleotides and 2-aminopurine substituted DNA duplexes. Phys Chem Chem Phys 6(1):154–160

177. Somsen OJG, Keukens LB, Niels de Keijzer M, van Hoek A, van Amerongen H (2005) Structural heterogeneity in DNA: temperature dependence of 2-aminopurine fluorescence in dinucleotides. Chem Phys Chem 6:1622–1627

178. Jean JM, Hall KB (2001) 2-Aminopurine fluorescence quenching and lifetimes: role of base stacking. Proc Natl Acad Sci U S A 98:37–41

179. Hardman SJO, Thompson KC (2006) Influence of base stacking and hydrogen bonding on the fluorescence of 2-aminopurine and pyrrolocytosine in nucleic acids. Biochemistry 45:9145–9155

180. Hardman SJO, Thompson KC (2007) The fluorescence transition of 2-aminopurine in double- and single-stranded DNA. Int J Quantum Chem 107:20922099

181. Liang J, Matsika S (2011) Pathways for fluorescence quenching in 2-aminopurine π-stacked with pyrimidine nucleobases. J Am Chem Soc 133:6799–6808

182. Liang J, Matsika S (2012) Pathways for fluorescence quenching in 2-aminopurine pi-stacked with pyrimidine nucleobases (vol 133, pg 6799, 2011). J Am Chem Soc 134(25):10713–10714

183. Liang J, Nguyen Q, Matsika S (2013) Exciplexes and conical intersections lead to fluorescence quenching in π-stacked dimers of 2-aminopurine with purine nucleobases. Photochem Photobiol Sci 12:1387–1400

184. Jean JM, Hall KB (2002) 2-Aminopurine electronic structure and fluorescence properties in DNA. Biochemistry 41:13152–13161

185. Dreuw A, Head-Gordon M (2005) Single-reference ab Initio methods for the calculation of excited states of large molecules. Chem Rev 105:4009–4037

186. Dreuw A, Weisman JL, Head-Gordon M (2003) Long-range charge-transfer excited states in time-dependent density functional theory require non-local exchange. J Chem Phys 119:2943

187. Lange A, Rohrdanz M, Herbert JM (2008) Charge-transfer excited states in a π-stacked adenine dimer, as predicted using long-range-corrected time-dependent density functional theory. J Phys Chem B 112:6304

188. Wang Y, Haze O, Dinnocenzo JP, Farid S, Farid RS, Gould IR (2007) Bonded exciplexes. A new concept in photochemical reactions. J Org Chem 72(18):6970–6981

189. Wang Y, Haze O, Dinnocenzo JP, Farid S, Farid RS, Gould IR (2008) Bonded exciplex formation: electronic and stereoelectronic effects. J Phys Chem A 112(50):13088–13094

190. Nachtigallova D, Aquino AJA, Horn S, Lischka H (2013) The effect of dimerization on the excited state behavior of methylated xanthine derivatives: a computational study. Photochem Photobiol Sci 12:1496

# Photochemistry of Nucleic Acid Bases and Their Thio- and Aza-Analogues in Solution

**Marvin Pollum, Lara Martínez-Fernández, and Carlos E. Crespo-Hernández**

**Abstract** The steady-state and time-resolved photochemistry of the natural nucleic acid bases and their sulfur- and nitrogen-substituted analogues in solution is reviewed. Emphasis is given to the experimental studies performed over the last 3–5 years that showcase topical areas of scientific inquiry and those that require further scrutiny. Significant progress has been made toward mapping the radiative and nonradiative decay pathways of nucleic acid bases. There is a consensus that ultrafast internal conversion to the ground state is the primary relaxation pathway in the nucleic acid bases, whereas the mechanism of this relaxation and the level of participation of the $^1\pi\sigma^*$, $^1n\pi^*$, and $^3\pi\pi^*$ states are still matters of debate. Although impressive research has been performed in recent years, the microscopic mechanism(s) by which the nucleic acid bases dissipate excess vibrational energy to their environment, and the role of the N-glycosidic group in this and in other nonradiative decay pathways, are still poorly understood. The simple replacement of a single atom in a nucleobase with a sulfur or nitrogen atom severely restricts access to the conical intersections responsible for the intrinsic internal conversion pathways to the ground state in the nucleic acid bases. It also enhances access to ultrafast and efficient intersystem crossing pathways that populate the triplet manifold in yields close to unity. Determining the coupled nuclear and electronic pathways responsible for the significantly different photochemistry in these nucleic acid base analogues serves as a convenient platform to examine the current state of knowledge regarding the photodynamic properties of the DNA and RNA bases from both experimental and computational perspectives. Further investigations

Lara Martínez-Fernández participated as a visiting graduate research assistant.

M. Pollum and C.E. Crespo-Hernández (✉)
Department of Chemistry and Center for Chemical Dynamics, Case Western Reserve University, 10900 Euclic Avenue, Cleveland, OH 44106, USA
e-mail: cxc302@case.edu

L. Martínez-Fernández
Departamento de Química, Universidad Autónoma de Madrid, 28049 Cantoblanco, Madrid, Spain

should also aid in forecasting the prospective use of sulfur- and nitrogen-substituted base analogues in photochemotherapeutic applications.

**Keywords** Azabases • DNA and RNA analogues • DNA and RNA monomers • Excited singlet and triplet states • Excited-state dynamics • Femtochemistry • Fluorescence up-conversion • Photochemistry • Pump-probe transient absorption • Quantum-chemical calculations • Thiobases

## Contents

## Abbreviations

| | |
|---|---|
| 2tCyd | 2-Thiocytidine |
| 2tCyt | 2-Thiocytosine |
| 2t-dThd | 2-Thiodeoxythymidine |
| 2tThd | 2-Thiothymidine (ribose) |
| 2tThy | 2-Thiothymine |
| 2tUra | 2-Thiouracil |
| 2tUrd | 2-Thiouridine |
| 4t-dThd | 4-Thiodeoxythymidine |
| 4tThy | 4-Thiothymine |
| 4tUra | 4-Thiouracil |
| 4tUrd | 4-Thiouridine |
| 5azaCyt | 5-Azacytosine |

| | |
|---|---|
| 6aza-2tThy | 6-Aza-2-thiothymine |
| 6azaUra | 6-Azauracil |
| 6azaUrd | 6-Azauridine |
| 6Me-tGua | 6-Methylthioguanine |
| 6Me-tPur | 6-Methylthiopurine |
| 6tGua | 6-Thioguanine |
| 6tGuo | 6-Thioguanosine |
| 6tIno | 6-Thioinosine |
| 6tPur | 6-Thiopurine |
| 7Me-8azaGua | 7-Methyl-8-azaguanine |
| 8azaAde | 8-Azaadenine |
| 8azaAdo | 8-Azaadenosine |
| 8azaGua | 8-Azaguanine |
| 8azaGuo | 8-Azaguanosine |
| 8azaIno | 8-Azainosine |
| 8Me-8azaGua | 8-Methyl-8-azaguanine |
| Ac | 2′-3′-5′-Tri-$O$-acetylated ribose |
| ACN | Acetonitrile |
| Ade | Adenine |
| Ado | Adenosine |
| AMP | Adenosine 5′-monophosphate |
| Br-4tUrd | 5-Bromo-4-thiouridine (2′-3′-5′-tri-$O$-acetylated ribose) |
| CASPT2 | Complete Active Space Perturbation Theory |
| CASSCF | Complete Active Space Self-Consistent Field |
| CD$_3$-4tUra | 1-Methyl-3-trideuteriomethyl-4-thiouracil |
| CIS | Configuration Interaction Singles |
| Cl-4tUrd | 5-Chloro-4-thiouridine (2′-3′-5′-tri-$O$-acetylated ribose) |
| CMP | Cytidine 5′-monophosphate |
| COSMO | COnductor-like Screening MOdel |
| CPCM | Conductor-like Polarizable Continuum Model |
| Cyd | Cytidine |
| Cyt | Cytosine |
| dAdo | 2′-Deoxyadenosine |
| dAMP | 2′-Deoxyadenosine 5′-monophosphate |
| DCM | Dichloromethane |
| dCMP | 2′-Deoxycytidine 5′-monophosphate |
| dCyd | 2′-Deoxycytidine |
| dGMP | 2′-Deoxyguanosine 5′-monophosphate |
| dGuo | 2′-Deoxyguanosine |
| DMTU | 1,3-Dimethyl-4-thiouracil |
| dThd | 2′-Deoxythymidine |
| dTMP | 2′-Deoxythymidine 5′-monophosphate |
| dtUra | 2,4-Dithiouracil |
| dtUrd | 2,4-Dithiouridine |

| dUrd | 2′-Deoxyuridine |
| Em | Emission |
| EOM-CC2 | Equation Of Motion Coupled Cluster |
| F-4tUrd | 5-Fluoro-4-thiouridine (2′-3′-5′-tri-$O$-acetylated ribose) |
| Fl | Fluorescence |
| FU | Fluorescence Up-conversion |
| GMP | Guanosine 5′-monophosphate |
| Gua | Guanine |
| Guo | Guanosine |
| I-4tUrd | 5-Iodo-4-thiouridine (2′-3′-5′-tri-$O$-acetylated ribose) |
| Ino | Inosine |
| LIOAS | Laser-Induced OptoAcoustic Spectroscopy |
| MRCI | MultiReference Configuration Interaction |
| NE | Non-Emissive |
| NR | Non-Radiative |
| PBS | Phosphate Buffer Solution |
| Pch | Photochemical |
| PFDMCH | Perfluoro-1,3-dimethylcyclohexane |
| Ph | Phosphorescence |
| Pr-4tThy | 1-Propyl-4-thiothymine |
| Pr-4tUra | 1-Propyl-4-thiouracil |
| Pr-6tPur | 9-Propyl-6-thiopurine |
| Pur | Purine |
| Sh | Shoulder |
| TAS | Transient Absorption Spectroscopy |
| TCSPC | Time-Correlated Single Photon Counting |
| TD-DFT | Time-Dependent Density Functional Theory |
| Thd | Thymidine (ribonucleoside) |
| THF | Tetrahydrofuran |
| Thy | Thymine |
| TMP | Thymidine 5′-monophosphate (ribonucleotide) |
| TQP | Two-Quanta Photolysis |
| TRF | Time-Resolved Fluorescence |
| TRIS | Tris(hydroxymethyl)aminomethane buffer |
| TRL | Time-Resolved Luminescence |
| TRPES | Time-Resolved PhotoElectron Spectroscopy |
| TRTL | Time-Resolved Thermal Lensing |
| Ura | Uracil |
| Urd | Uridine |
| UVA | UltraViolet, electromagnetic radiation subtype A (400 to 315 nm) |
| UVC | UltraViolet, electromagnetic radiation subtype C (280 to 100 nm) |

# 1 Introduction

Interest in the photochemistry of DNA has long been the motivation for investigating the excited-state dynamics of its component nucleic acid bases. Examining the steady-state and time-resolved photochemistry at the monomer level is important because population of electronic excited states in the nucleobases is the first step in a complex cascade of events leading to UV-induced DNA damage. In particular, the flurry of investigations witnessed during the last 15 years have shown that it is crucial to comprehend the excited-state dynamics of the nucleic acid bases before a firm, mechanistic understanding of the photochemistry of DNA and RNA polymers can be established [1–9]. These investigations have revealed how subtle intra- and intermolecular environmental or structural changes modulate the photochemistry and dynamics of DNA.

Among the key revelations, the photochemical and dynamical properties of the natural bases have been shown to be exquisitely sensitive to minor structural modifications, such as substitution of a single atom or small groups of atoms or movement of substituents around the main UV chromophore core. These structural modifications can impose restrictions on the base's access to key deactivation pathways that lead to the efficient dissipation of deleterious electronic energy to potentially less harmful vibrational energy into the environment. Consequently, photochemical investigations of DNA and RNA base analogues can provide a wealth of valuable mechanistic information that can be used to understand on a fundamental level the delicate balance between the nuclear and electronic relaxation pathways responsible for the remarkable photostability of DNA.

In particular, a growing interest in the photochemistry and excited-state dynamics of the sulfur- and nitrogen-substituted nucleobases has been witnessed in recent years [10–33]. The single (or double) substitution of an atom in a nucleic acid base by a sulfur, generating a thiobase, or a nitrogen, generating an azabase, often causes a redshift in the absorption spectrum, moving the strongly allowed absorption band in the nucleic acid monomers from the UVC to the UVA region of the electromagnetic spectrum. Although these nucleobase analogues share the common photochemical property of negligible fluorescence at room temperature, as observed in the natural nucleic acid, the well-known intrinsic relaxation pathways in the nucleic acid monomers are dramatically altered by a single atom substitution. Thio- and aza-substitution often inhibits ultrafast internal conversion to the ground state and enhances intersystem crossing to the triplet manifold, which leads to near unity triplet yields in these nucleic acid base analogues.

Besides their fundamental relevance, thio- and azabase analogues frequently hold photochemical properties that have tremendous practical uses in biological and medical applications [34–56]. However, patients treated with some of these drugs for prolonged periods of time can develop severe sunlight-induced side effects [36, 43, 57–64]. As reviewed in this chapter, the efficient population of the triplet state often leads to the generation of singlet oxygen, which could have important implications regarding the phototoxic activity of these drugs.

Section 2 reviews some of the most important photochemical features that the natural DNA and RNA nucleic acid bases exhibit in solution, whereas those shown by the thiobase and azabase analogues are discussed in Sects. 3 and 4, respectively. Also given throughout this chapter is a compilation of key steady-state and time-resolved properties for the nucleic acid bases and their sulfur- and nitrogen-substituted analogues in solution. This latter approach permits a convenient and straightforward comparison of their photochemistry. Final remarks and future perspectives are presented in Sect. 5.

## 2 Nucleic Acid Bases

The photochemistry of the nucleic acid bases and their derivatives has been continuously reviewed over the past 10 years [1–9]. Hence, the chief aim of this section is to summarize some of the key steady-state and time-resolved photochemical properties of the nucleic acid bases in solution, with particular emphasis on studies that have appeared during the last 3–5 years. These latter works embody current topics of ongoing controversy and/or hint toward research issues that still need further scrutiny and development. We note from the outset that the focus is limited to experimental work on the natural nucleobases and their nucleosides and nucleotides in aqueous and acetonitrile solutions, as it is thought these compounds and solvents exemplify some of the most important features found in the photochemistry of the DNA and RNA bases in solution. The structures and standard ring numbering for the five nucleic acid bases and their nucleosides and nucleotides are shown in Scheme 1. These compounds are collectively designated as nucleic acid monomers (or simply monomers) hereafter, following contemporary practices in the literature [1, 4].

A key feature in all the natural DNA and RNA monomers is the very small fluorescence yield [65], a property which hints at the accessibility of highly efficient nonradiative decay pathways in the photochemistry of nucleic acid monomers. Indeed, the need to invoke very high rates of nonradiative decay in the DNA/RNA monomers in solution was already ingrained in the literature in the early 1970s [65–67]. The first femtosecond pump-probe experiments on the nucleic acid bases were performed by Reuther et al. in 1996 [68, 69]. However, the first self-consistent set of measurements on these fleeting events was reported in a groundbreaking femtosecond study by Kohler and co-workers [70]. In their work, Pecourt et al. [70] successfully probed the weak singlet excited-state absorption signals of the nucleic acid monomers, presenting direct evidence of relaxation of the initially-populated $^1\pi\pi^*$ state to the ground state on a sub-picosecond time scale. Fluorescence decay lifetimes on the order of hundreds of femtoseconds were reported soon after by the groups of Zewail and Gustavsson and Markovitsi [71–73]. These investigations paved the way for what has now become an exciting area of scientific inquiry into the ultrafast excited-state dynamics of DNA. As documented in this book, the excited-state dynamics of DNA currently traverses experimental and computational

## Purines
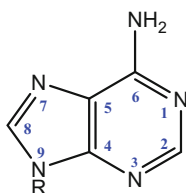


**Adenine** (R = H)
Adenosine (R = ribose)
Deoxyadenosine (R = 2'-deoxyribose)
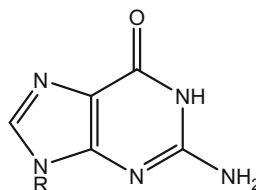
**Guanine** (R = H)
Guanosine (R = ribose)
Deoxyguanosine (R = 2'-deoxyribose)

## Pyrimidines
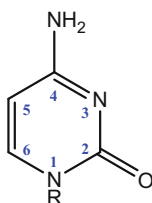


**Cytosine** (R = H)
Cytidine (R = ribose)
Deoxycytidine
  (R = 2'-deoxyribose)
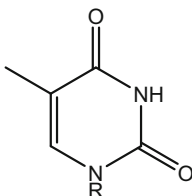
**Thymine** (R = H)
Thymidine (R=ribose)
Deoxythymidine
  (R = 2'-deoxyribose)
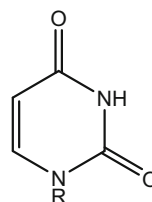
**Uracil** (R = H)
Uridine (R = ribose)
Deoxyuradine
  (R = 2'-deoxyribose)
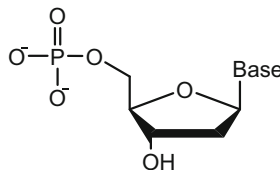
## Nucleobases          Nucleosides

R = H          R = ribose          R = 2'-deoxyribose
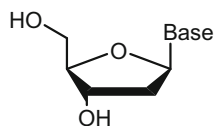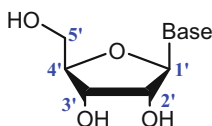


## Nucleotides

R = ribose 5'-monophosphate          R = 2'-deoxyribose 5'-monophosphate
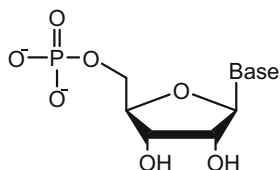


**Scheme 1** Structures of the nucleic acid bases, their nucleosides and nucleotides. Common ring numbering of the bases and of the sugar substituent are given

work in both the gas and condensed phases, with both areas of research being tremendously informed by one another. In particular, the application of a wide range of time-resolved spectroscopic techniques with femtosecond time resolution and the use of increasingly more sophisticated methods in static and dynamic quantum-chemical calculations have led to a richer and deeper understanding of this chemistry.

## 2.1   Steady-State Photophysics of the Nucleic Acid Monomers

The lowest-energy absorption band near 260 nm in the nucleic acid monomers arises from strongly allowed $\pi\pi^*$ electronic transitions [67, 74]. As shown in Tables 1 and 2, the molar absorptivity coefficients of the $\pi\pi^*$ transitions are on average ca. 30% larger in magnitude for the purine monomers than for the pyrimidine monomers in aqueous solution, which makes the purine monomers more efficient absorbers of UV radiation. In addition, the absorption spectra of adenine and guanine in this spectral region show two absorption bands at approximately 260 nm and 270 nm and at 250 nm and 275 nm, respectively. These $\pi\pi^*$ electronic transitions are often labeled as the $^1L_a$ and $^1L_b$ states using the Platt–Murrell nomenclature [75, 76], where the $L_a$ label represents the singlet state with the highest HOMO $\rightarrow$ LUMO contribution. N-Glycosidic bond formation brings these two absorption bands closer together, resulting in the observation of a single absorption band in the adenine nucleosides or an absorption band with a band shoulder in the guanine nucleosides.

On the other hand, a single $\pi\pi^*$ electronic transition is observed in the lowest-energy absorption band of the pyrimidine bases (Table 2). This absorption band redshifts in going from the nucleobase to the nucleoside by 2–3 nm, with the absorption maximum at approximately 260 nm in uridine and 270 nm in cytidine. In addition to the intense $\pi\pi^*$ electronic transitions, the lone pairs in the heteroatoms of the purine and pyrimidine bases give rise to $n\pi^*$ electronic transitions that often overlap with the $\pi\pi^*$ ones. However, the $n\pi^*$ absorption bands in the DNA and RNA monomers have been characterized to a lesser extent because of their reduced absorption cross sections and their strong overlap with the $\pi\pi^*$ absorption bands in solution [1, 67].

Tables 1 and 2 also show that all the nucleic acid monomers exhibit fluorescence quantum yields of ca. $10^{-4}$ at room temperature, with emission maxima in the spectral region ca. 310–330 nm [1, 65, 67, 78–80, 84, 85, 87]. In general, the fluorescence yield of the nucleic acid monomers appears to be independent of the excitation wavelength and experimental conditions used within the reported uncertainties, with the exception of the adenine and guanine monomers, in which either tautomerization from N9H to N7H contributes to the total fluorescence yield [73, 88] or the yield is excitation-wavelength dependent [81, 82, 89]. The small fluorescence yields, together with the small photodegradation [90–96] and triplet quantum yields of ca. $10^{-2}$ in aqueous solution [12, 97–102], show that most of the excited-state population decays nonradiatively back to the ground state.

**Table 1** Steady-state properties and quantum yields of the natural purine bases

| | $\lambda_{max}$ (nm)[a] | $\varepsilon_{max}$ ($M^{-1}$ $cm^{-1}$)[b] | $\lambda_{em}$ (nm)[c] | $\Phi_{Fl} \times 10^{-4}$ ($\lambda_{ex}$)[d] | Experimental conditions |
|---|---|---|---|---|---|
| Ade | 262[e], 270sh[e] | 13,500[e], 11,500[e] | – | – | $H_2O$ [77] |
| | 261 | – | 321 | 2.6 (261) | $H_2O$, pH 7.3 [65] |
| Ado | 262[e] | – | 311[e] | 0.08 (250) | $H_2O$, pH 6.2 [78] |
| | – | – | 310 | 0.5 (265) | $H_2O$ [67] |
| dAdo | 259.7 | 14,930 | 307 | $0.86 \pm 0.15$ (255) | $H_2O$ [79] |
| | 260 | – | 319 | 0.6 (265) | $H_2O$ [80] |
| | 258 | – | 310 | 0.84 (265) | ACN [80] |
| Gua | 250[e], 272[e] | 10,500[e], 8,200[e] | – | – | $H_2O$ [77] |
| | 249[e], 276 | – | 328[e] | 3.0 (276) | $H_2O$, pH 6.3 [65] |
| Guo | 252[e], 272sh[e] | – | 345[e] | 0.06 (250) | $H_2O$, pH 6.2 [78] |
| dGuo | 253, 273sh[e] | 13,850, 9,100[e] | 334 | $0.97 \pm 0.08$ (255) | $H_2O$ [79] |
| | 253 | 13,500 | 334 | – | PBS, pH 7.0 [81] |
| | 252 | – | 327 | 1.0 (265) | $H_2O$ [80] |
| | 253 | 13,500 | 334 | – | $H_2O$ [81] |
| | 253[f] | 13,500[f] | 334[f] | 0.868 (245)[f] | $H_2O$ [81] |
| | – | – | – | 1.23 (267)[f] | $H_2O$ [81] |
| | – | – | – | 1.38 (285)[f] | $H_2O$ [81] |
| | 250[f], 270sh[f] | – | 334[f] | $1.03 \pm 0.07$ (250)[f] | $H_2O$ [82] |
| | – | – | – | $1.31 \pm 0.07$ (265)[f] | $H_2O$ [82] |
| | – | – | – | $1.45 \pm 0.14$ (275)[f] | $H_2O$ [82] |
| | – | – | – | $1.51 \pm 0.14$ (285)[f] | $H_2O$ [82] |
| | 254 | – | 317 | 1.2 (265) | ACN [80] |

[a]Wavelength of maximum absorption in the spectral region above ~230 nm; wavelength of red-most absorption peak also given if not the overall maximum
[b]Extinction coefficient of the maximum and red-most absorption bands
[c]Wavelength of maximum fluorescence emission
[d]Fluorescence quantum yield; excitation wavelength given in parenthesis
[e]Extrapolated from graph
[f]Measured for the nucleotide form

## 2.2 Time-Resolved Photophysical Properties of the Nucleic Acid Monomers

Femtosecond transient absorption and fluorescence up-conversion experiments have shown that the $^1\pi\pi^*$ states in the nucleic acid monomers decay primarily to the ground state on a sub-picosecond time scale. These experiments have further revealed that multiple relaxation processes contribute to the ultrafast depopulation of the optically populated excited states [73, 81, 103–108]. There is still debate regarding the specific assignment of the multiexponential decay components. Some authors have assigned the relaxation pathways to nonadiabatic transitions among multiple electronic states [1, 4, 109], whereas others have assigned them to diabatic relaxation pathways occurring on a single potential energy surface [82, 89, 110–112].

**Table 2** Steady-state properties and quantum yields of the natural pyrimidine bases

| | $\lambda_{max}$ (nm)[a] | $\varepsilon_{max}$ ($M^{-1}$ $cm^{-1}$)[b] | $\lambda_{em}$ (nm)[c] | $\Phi_{Fl} \times 10^{-4}$ ($\lambda_{ex}$)[d] | Experimental conditions |
|---|---|---|---|---|---|
| Cyt | 267[e] | 5,800[e] | – | – | $H_2O$ [77] |
| | 266 | 6,200 | – | – | PBS, pH 7.0 [83] |
| | 267 | – | 314 | 0.82 (267) | $H_2O$, pH 6.5 [65] |
| Cyd | 270 | 8,830 | – | – | PBS, pH 7.0 [83] |
| | 269[e] | – | 329[e] | 0.4 (250) | $H_2O$, pH 6.2 [78] |
| | – | – | 324 | 0.7 (265) | $H_2O$ [67] |
| dCyd | 270.7 | 9,300 | 328 | $0.89 \pm 0.10$ (255) | $H_2O$ [79] |
| Thy | 265[e] | 7,600[e] | – | – | $H_2O$ [77] |
| | 265 | 8,400 | 329 | 1.02 (255) | $H_2O$ [84] |
| | 265 | – | 337.8 | 1.04 (265) | $H_2O$, pH 6.7 [85] |
| | – | – | 325 | 1.0 (265) | $H_2O$ [67] |
| | 261 | – | 315 | – | ACN [86] |
| | – | – | – | 1.12 | ACN [87] |
| dThd | – | – | 327 | 1.0 (265) | $H_2O$ [67] |
| | 267.0 | 9,860 | 330 | $1.32 \pm 0.07$ (255) | $H_2O$ [79] |
| | 265[e] | – | 330[e] | 0.4 (250) | $H_2O$, pH 6.7 [78] |
| Ura | 259[e] | 8,000[e] | – | – | $H_2O$ [77] |
| | 259 | 8,200 | – | – | PBS, pH 7.0 [83] |
| | 259 | 9,100 | 312 | 0.35 (255) | $H_2O$ [84] |
| | 258.4 | – | 309 | 0.45 (258.4) | $H_2O$, pH 6.8 [65] |
| | 256 | – | 311 | – | ACN [86] |
| Urd | 262 | 9,820 | – | – | PBS, pH 7.0 [83] |
| | 259[e] | – | 315[e] | 0.1 (250) | $H_2O$, pH 6.3 [78] |

[a]Wavelength of maximum absorption in the spectral region above ~230 nm
[b]Extinction coefficient of the maximum absorption
[c]Wavelength of maximum fluorescence emission
[d]Fluorescence quantum yield; excitation wavelength given in parenthesis
[e]Extrapolated from graph

Another general observation is that conical intersections, i.e., points of degeneracy between two or more potential energy surfaces in the nuclear coordinate space of the molecule [113–116], play a key role in the ultrafast deactivation of the excited-state electronic energy in all the nucleic acid monomers [109, 110, 116–124]. These conical intersections are often accessed from near the Franck–Condon region via near-barrierless, out-of-plane deformations that lead to ultrafast internal conversion pathways connecting the excited states to the ground state. In simple terms, the relaxation pathway for the purine monomers involves the twist of the C2–N3 bond, leading to an out-of-plane bending of the C2 substituent. For the pyrimidine monomers, the relaxation pathways involve a pyramidalization of the C5 and/or torsion about the C5–C6 bond, accompanied by out-of-plane motion of the C5 substituent. These nuclear relaxation pathways are supported by resonant Raman experiments, which report on the initial excited-state structural dynamics in the DNA and RNA monomers [125–130]. Importantly, in all natural DNA and

RNA monomers, the ultrafast and efficient transfer of excited-state electronic energy into vibrational energy in the ground state is followed by the transfer of the intramolecular vibrational energy into high-frequency vibrational modes of the solvent molecules [4, 131]. This electronic-to-heat energy transfer mechanism is thought to protect the DNA and RNA monomers from UV-induced damage [4, 9].

### 2.2.1   Adenine and Guanine Monomers

Tables 3 and 4 collect the singlet-state lifetimes for the adenine and guanine monomers in aqueous solution and in acetonitrile. Lifetime assignments are given as footnotes in each table. As discussed in Sect. 2.1, two low-lying $^1\pi\pi^*$ states ($^1L_a$ and $^1L_b$) are populated simultaneously upon ca. 267 nm excitation in the adenine and guanine monomers, which complicates the assignment of the multiexponential decays. In the case of adenine, there is agreement that the biexponential decay components of ca. 0.2 ps and 8.4 ps in aqueous solution should be assigned to the decay of the singlet state in the N9H and N7H tautomers, respectively [73, 88, 132, 133]. Transient absorption experiments show that these lifetimes are solvent-dependent, increasing to ca. 0.4 ps and 11 ps in acetonitrile [132].

The excited-state decay mechanism in the adenine and guanine nucleosides and nucleotides has been a matter of dispute. Several groups have reported a monoexponential decay component assigned to ultrafast internal conversion from the excited singlet state to the ground state [71, 88, 133–135], whereas others have reported biexponential decay signals [73, 79, 89, 108, 136]. Kwok et al. [136] proposed a biexponential deactivation mechanism where the fast decay component in adenosine was assigned to internal conversion from the $^1L_a$ to the $^1L_b$ state, followed by ultrafast internal conversion to the ground state (i.e., $^1L_a \rightarrow {}^1L_b \rightarrow S_0$). Lan et al. [120] reached a different conclusion using nonadiabatic semi-empirical calculations. Their calculations predict a sequential decay mechanism to the ground state on an ultrafast time scale (i.e., $^1L_a \rightarrow {}^1n\pi^* \rightarrow S_0$). More recently, the multiexponential decays observed in the adenine and guanine nucleosides have been explained by ultrafast internal conversion from the $^1L_b$ state to the $^1L_a$ state in sub-100 fs, followed by a diabatic evolution along the $^1L_a$ state potential energy surface towards a planar-like plateau ($^1L'_a$; $\tau_1 \sim 0.1$ ps). The $^1L'_a$ plateau in turn leads to a conical intersection with the ground state ($\tau_2 \sim 0.3$–0.5 ps) [89, 111]. CASPT2 and TD-DFT calculations [112, 137, 138] and recent time-resolved photoelectron spectroscopy results for adenine and adenosine in solution [133] are in agreement with this interpretation (i.e., $^1L_b \rightarrow {}^1L_a \rightarrow {}^1L'_a \rightarrow S_0$). This interpretation highlights the fact that multiexponential decay signals are not always indicative of nonadiabatic transitions among multiple electronic states.

Interestingly, low yields of the triplet state and of singlet oxygen have been reported in the adenine and guanine monomers [98, 139], even though the population of their $^1n\pi^*$ and $^3\pi\pi^*$ states has not been detected in solution [89, 140–142]. Nikogosyan and co-workers [98] used two-step laser excitation to

**Table 3** Singlet lifetimes for the adenine monomers

|  | Singlet-state lifetimes (ps) | Technique, time resolution | Experimental conditions |
|---|---|---|---|
| Ade | $0.23 \pm 0.05$[a], $8.0 \pm 0.3$[b] | FU, 100 fs | $H_2O$ [73] |
|  | $0.34 \pm 0.07$[a,c], $8.4 \pm 0.8$[b] | FU, 200 fs | $H_2O$ [88] |
|  | $0.18 \pm 0.03$[a], $8.8 \pm 1.2$[b] | TAS, 200 fs | $H_2O$, pH 6.8 [132] |
|  | $0.064 \pm 0.002$[a], $8.5 \pm 1.7$[b,d] | TRPES, 80 fs | TRIS, pH 8 [133] |
|  | $0.44 \pm 0.07$[a], $11 \pm 5$[b] | TAS, 200 fs | ACN [132] |
| Ado | $0.31 \pm 0.05$ | FU, 200 fs | $H_2O$ [88] |
|  | $0.53 \pm 0.12$ | FU, 360 fs | PBS, pH 7 [71] |
|  | $0.29 \pm 0.04$ | TAS, 200 fs | $H_2O$, pH $\sim$7 [134] |
|  | $0.215 \pm 0.020$[e] | TRPES, 80 fs | TRIS, pH 8 [133] |
|  | $0.52 \pm 0.16$[f] | FU, 360 fs | PBS, pH 7 [71] |
|  | $0.37 \pm 0.04$[f] | TAS, 200 fs | PBS, pH 6.8 [135] |
| dAdo | $0.1$[g], $0.5 \pm 0.1$ | FU, 100 fs | $H_2O$ [73] |
|  | $0.10$[g], $0.42 \pm 0.10$[h] | FU, 100 fs | $H_2O$ [79] |
|  | $0.11 \pm 0.02$[i] | FU, 80 fs | $H_2O$ [89] |
|  | $0.13$[j], $0.45$[k] | TRF, 300 fs/TAS, 200 fs | $H_2O$ [136] |
|  | $0.1$[f,g], $0.5 \pm 0.1$[f] | FU, 100 fs | $H_2O$ [73] |
|  | $\leq 0.10$[f,j], $0.34 \pm 0.11$[f] | FU, 150 fs | PBS [108] |
|  | $\leq 0.5$[f,l] | TAS, 50 fs | PBS [108] |
|  | $0.10$[f,g], $0.52 \pm 0.10$[f, h] | FU, 100 fs | $H_2O$ [79] |
|  | $0.18 \pm 0.02$[i] | FU, 80 fs | ACN [89] |

[a]Attributed to the N9H tautomer
[b]Attributed to the N7H tautomer
[c]Excitation wavelength dependent
[d]Dependent on probe energy
[e]Independent of probe energy, but higher pump energies decrease this lifetime attributed to greater access to the $S_1/S_0$ conical intersection
[f]Measured for the nucleotide form
[g]Limited by time-resolution of the experimental set-up
[h]No specific assignment was given to these lifetimes
[i]Reported as average of $^1L_a$ and $^1L_b$ $\pi\pi^*$ excited-state lifetimes at 310 nm, lifetime increases as the observed wavelength increases to 380 nm
[j]Attributed to lifetime of $^1L_a$ $\pi\pi^*$
[k]Attributed to lifetime of $^1L_b$ $\pi\pi^*$
[l]Assigned to internal conversion to the ground state

high-lying electronic states and kinetic modeling to estimate triplet yields in adenine and guanine of ca. $10^{-3}$ in aqueous solution (Table 5). Bishop et al. [139] measured a singlet oxygen yield of $0.030 \pm 0.005$ for adenine in acetonitrile after 248 nm nanosecond laser excitation by detecting singlet oxygen emission decay signals at 1,270 nm. However, for guanine and guanosine 5′-monophosphate, the authors were unable to detect singlet oxygen emission quantifiably in deuterated water, and estimated the yield to be lower than 0.005 (Table 6). Although, the experiments by Nikogosyan and Bishop, taken together, suggest the triplet state in adenine and guanine may be populated in solution, the triplet state has not been observed in more recent transient absorption experiments based on one-photon excitation. Furthermore, even if the triplet state is populated in the adenine and

**Table 4** Singlet lifetimes for the guanine monomers

|      | Singlet-state lifetimes (ps) | Technique, time resolution | Experimental conditions |
|------|------------------------------|----------------------------|-------------------------|
| Guo  | $0.69 \pm 0.10$              | FU, 360 fs                 | PBS, pH 7 [71]          |
|      | $0.46 \pm 0.04$              | TAS, 200 fs                | $H_2O$, pH $\sim 7$ [134] |
|      | $0.86 \pm 0.10^a$            | FU, 360 fs                 | PBS, pH 7 [71]          |
|      | $0.2^{a,b}$, $0.9^{a,c}$, $2.5^{a,d}$ | TAS, 100 fs       | PBS, pH 7 [111]         |
| dGuo | $0.16 \pm 0.02^e$, $0.78 \pm 0.05^e$ | FU, 100 fs        | $H_2O$ [79]             |
|      | $0.22 \pm 0.02^b$, $0.77 \pm 0.02^c$, $1.99 \pm 0.11^f$ | TRF, 300 fs / TAS, 200 fs | PBS, pH 7.0 [81] |
|      | $0.20 \pm 0.02^{a,e}$, $0.89 \pm 0.06^{a,e}$ | FU, 100 fs | $H_2O$ [79]             |
|      | $0.16 \pm 0.02^{a,g}$, $0.94 \pm 0.09^{a,g}$ | FU, 300-350 fs | $H_2O$ [82]            |
|      | $0.20 \pm 0.03^{a,b}$, $0.79 \pm 0.04^{a,c}$, $1.98 \pm 0.10^{a,f}$ | TRF, 300 fs / TAS, 200 fs | PBS, pH 7.0 [81] |
|      | $0.12 \pm 0.07^{a,h}$, $0.68 \pm 0.11^{a,c}$ | FU, 150 fs | PBS [108]               |
|      | $\sim 2^{a,i}$               | TAS, 50 fs                 | PBS [108]               |

[a]Measured for the nucleotide form
[b]Attributed to lifetime of $^1L_a$ $\pi\pi^*$
[c]Attributed to movement across a plateau-like region ($^1L'_a$ $\pi\pi^*$)
[d]Attributed to vibrational cooling in the ground state
[e]No specific assignment was given to these lifetimes
[f]Attributed to lifetime of a weakly emissive $^1\pi\sigma^*$ state
[g]Emission wavelength dependent
[h]Attributed to relaxation of $^1L_b$ $\pi\pi^*$ to $^1L_a$ $\pi\pi^*$
[i]Assigned to vibrational cooling in the ground state

guanine nucleobases, it is unclear whether its population originates from the N7H or N9H tautomers in solution. Nevertheless, the results from Nikogosyan et al. and Bishop et al. need to be revisited before any conclusion can be reached.

The participation of $\pi\sigma^*$ states in the excited-state dynamics of the monomers is a matter of intense debate [1, 4, 6, 7, 81, 88, 111, 145–149]. The population of $^1\pi\sigma^*$ states has been proposed to play a role in the excited-state dynamics of adenine and guanine monomers in solution, particularly at high excitation energies [81, 88, 145–147]. A recent study by Cheng and co-workers [81] continues to add fuel to this discussion. The authors presented experimental evidence for the co-existence of two nonradiative decay pathways in 2′-deoxyguanosine and 2′-deoxyguanosine 5′-monophosphate in solution. The dynamics depend on the solvent and excitation wavelength used, but not on the presence of the 5′-monophosphate moiety. The deactivation mechanism is similar to that proposed previously by others [89, 111], except for the suggestion that the $^1\pi\sigma^*$ state is also populated; either directly upon 285 nm excitation or indirectly from the $^1L_b$ and the $^1L_a$ states upon either 245 nm or 267 nm excitation. Furthermore, Cheng et al. [81] proposed that the population in the $^1\pi\sigma^*$ state decays back to the ground state with a solvent-dependent fluorescence lifetime of ~2 ps in water, ~2.3 ps in deuterated water, and ~4.1 ps in methanol. An example of the spectral evolution can be observed in Fig. 1. This figure shows the femtosecond time-resolved fluorescence spectra and fluorescence decay traces for 2′-deoxyguanosine after excitation at 267 nm and 285 nm in

**Table 5**  Triplet yields of the natural bases

|       | $\Phi_T{}^a$ | Technique, time resolution | Experimental conditions[b] |
|-------|--------------|----------------------------|------------------------------|
| Ade   | 0.0023       | TQP, 20 ns                 | $H_2O$, $O_2$, pH 6.3, 30 $\mu$M [98] |
| Gua   | 0.0012       | TQP, 20 ns                 | $H_2O$, $O_2$, pH 6.3, 30 $\mu$M [98] |
| Cyt   | 0.0127       | TQP, 20 ns                 | $H_2O$, $O_2$, pH 6.3, 30 $\mu$M [98] |
| Thy   | 0.0123       | TQP, 20 ns                 | $H_2O$, $O_2$, pH 6.3, 30 $\mu$M [98] |
|       | 0.0062       | TAS, 30 ns                 | $H_2O$, Ar, ~1 mM [99] |
|       | $0.06 \pm 0.012$ | TAS, 30 ns             | ACN, Ar [99] |
|       | 0.18         | TAS, <10 $\mu$s            | ACN, Degassed, 2 mM [100] |
| dThd  | 0.014        | TAS, 30 ns                 | $H_2O$, Ar [101] |
|       | $0.014 \pm 0.001^c$ | TAS, 8 ns           | PBS, $N_2$ [102] |
|       | $0.015^c$    | TAS, 30 ns                 | $H_2O$, Ar [101] |
|       | 0.069        | TAS, 30 ns                 | ACN, Ar [101] |
| Ura   | 0.0144       | TQP, 20 ns                 | $H_2O$, pH 6.3, $O_2$, 30 $\mu$M [98] |
|       | 0.023        | TAS, 30 ns                 | $H_2O$, Ar, ~1 mM [99] |
|       | $0.21 \pm 0.02$ | TAS, 20 ns              | ACN, Ar [12] |
|       | 0.20         | TAS, 30 ns                 | ACN, Ar [101] |
|       | $0.20 \pm 0.04$ | TAS, 30 ns              | ACN, Ar [99] |
|       | 0.40         | TAS, <10 $\mu$s            | ACN, Degassed, 1.3 mM [100] |
| Urd   | 0.015        | TAS, 30 ns                 | $H_2O$, Ar [101] |
|       | $0.011^c$    | TAS, 30 ns                 | $H_2O$, Ar [101] |
|       | 0.078        | TAS, 30 ns                 | ACN, Ar [101] |
|       | 0.30         | TAS, <10 $\mu$s            | ACN, Degassed, 1.8 mM [100] |

[a]Quantum yield of $T_1$ state formation
[b]Concentration of the DNA and RNA monomers in a given solvent along with the purging gas used
[c]Measured for the nucleotide form

aqueous buffer solution. According to the authors, the ($^1L_a \rightarrow {}^1L'_a \rightarrow S_0$) decay pathway reported previously [89, 111] is associated with the fluorescence band that redshifts from 335 nm to 345 nm in less than 1 ps, whereas the $^1\pi\sigma^* \rightarrow S_0$ decay path is associated with the red-most fluorescence band observed at decay times equal to or larger than ~2.75 ps. The latter decay pathway is suggested to be responsible for the red tail in the steady-state fluorescence spectra of the guanine monomers. It should be noted, however, that calculations have consistently predicted a negligible oscillator strength for the $^1\pi\sigma^*$ state of the guanine monomers in gas phase [150] and in solution [111], which makes the possibility of detecting emission from this state in time-resolved experiments questionable.

Cheng et al. further proposed that the transient absorption decay signal that they measured probing at 305 nm after excitation of 2′-deoxyguanosine at 267 nm should be assigned to excited-state absorption by the $^1\pi\sigma^*$ state. This absorption signal decays in lock-step with the ground-state recovery signal at 253 nm in aqueous buffer solution, deuterated water, and methanol [81]. The authors observed a significant solvent isotope effect in the transient absorption signals at 305 nm and 253 nm, which they took as evidence of the $^1\pi\sigma^*$ state decay. Other authors have previously assigned this same picosecond decay component to vibrational cooling dynamics in the ground state [70, 111, 134] or to the diabatic decay of a fraction of

**Table 6** Singlet oxygen yields of the natural bases and some thio and aza analogues

| | $\Phi_\Delta$[a] | Experimental conditions[b] |
|---|---|---|
| Ade | $0.03 \pm 0.005$ | ACN, 10–100 mM [139] |
| Gua | $<0.005$[c] | $D_2O$, 10–100 mM [139] |
| GMP | $<0.005$[c] | $D_2O$, 10–100 mM [139] |
| Cyt | $0.02 \pm 0.005$ | ACN, 10–100 mM [139] |
| Thy | ~0.01[c] | $D_2O$, 10–100 mM [139] |
| | $0.07 \pm 0.010$ | ACN, 10–100 mM [139] |
| TMP | ~0.01[c] | $D_2O$, 10–100 mM [139] |
| Ura | $0.13 \pm 0.010$ | ACN, 10–100 mM [139] |
| | $0.15 \pm 0.02$ | ACN, O2 [15] |
| 6tGua | $0.56 \pm 0.18$ | $D_2O$, TRIS, pH 7.4, <0.1 mM [23] |
| | $0.58 \pm 0.08$ | $NaOH/D_2O$, pH 10, <0.1 mM [23] |
| 6tGuo | $0.55 \pm 0.08$ | $D_2O$, TRIS, pH 7.4, <0.1 mM [23] |
| | $0.49 \pm 0.09$ | $NaOH/D_2O$, pH 10, <0.1 mM [23] |
| 6Me-tGua | $0.46 \pm 0.05$ | $NaOH/D_2O$, pH 10, $O_2$ < 0.1 mM [24] |
| 6tPur | $0.52 \pm 0.05$ | $NaOH/D_2O$, pH 10, $O_2$ < 0.1 mM [24] |
| 6Me-tPur | $0.36 \pm 0.05$ | $NaOH/D_2O$, pH 10, $O_2$ < 0.1 mM [24] |
| 2tThy | $0.36 \pm 0.02$ | ACN, $O_2$, <0.1 mM [16] |
| 4 t-dThd | $0.50 \pm 0.10$ | ACN, $O_2$, 60 μM [11] |
| 4tUrd | 0.7 | $H_2O$ [143] |
| | $0.18 \pm 0.04$ | $H_2O$, $O_2$, 50 μM [144] |
| | $0.50 \pm 0.20$ | ACN, $O_2$, 50 μM [144] |
| 8azaAde | $0.15 \pm 0.02$ | ACN [14] |
| 8azaGua | $<0.01$ | ACN [14] |
| 5azaCyt | $<0.01$ | ACN [14] |
| 6azaUra | 0.34 | ACN [12] |
| | $0.63 \pm 0.03$[d] | ACN, $O_2$ [15] |
| | $0.54 \pm 0.02$[e] | ACN, $O_2$ [15] |
| 6azaUrd | $0.49 \pm 0.01$[d] | ACN, $O_2$ [15] |
| 6aza-2tThy | $0.69 \pm 0.02$ | ACN, $O_2$ [15] |

[a]Singlet oxygen quantum yield
[b]Concentrations given are of the DNA and RNA monomers and their analogues in solution; solutions were under air-saturated conditions unless otherwise noted
[c]Estimation, signal lower than instrument's limit of quantitation
[d]Excited at 248 nm
[e]Excited at 308 nm

the $^1L_a$ state population to the $^1L'_a$ plateau [82, 89, 111], as discussed above. In fact, Miannay et al. [82] proposed that emission from the $^1L'_a$ region of the potential energy surface is responsible for the weak red tail in the steady-state fluorescence spectra of the guanine monomers, in contrast to Cheng et al. [81].

The authors further suggested that the $^1\pi\sigma^*$ state can act as a "dark trap state" to which most of the $^1L_a$ state population decays, thus making its deactivation the predominant relaxation pathway in the nonadiabatic relaxation of 2′-deoxyguanosine and 2′-deoxyguanosine 5′-monophosphate in solution [81]. However, this proposal seems unlikely. Experimental and computational results have

**Fig. 1** Time-resolved fluorescence spectra of 2′-deoxyguanosine in aqueous buffer solution (pH 7) following 267 nm and 285 nm excitation (*top panel*) along with normalized decay traces at the indicated fluorescence emission wavelengths (*bottom panel*). Reproduced from [81] with permission of The Royal Society of Chemistry (RSC) on behalf of the Centre National de la Recherche Scientifique (CNRS) and the RSC
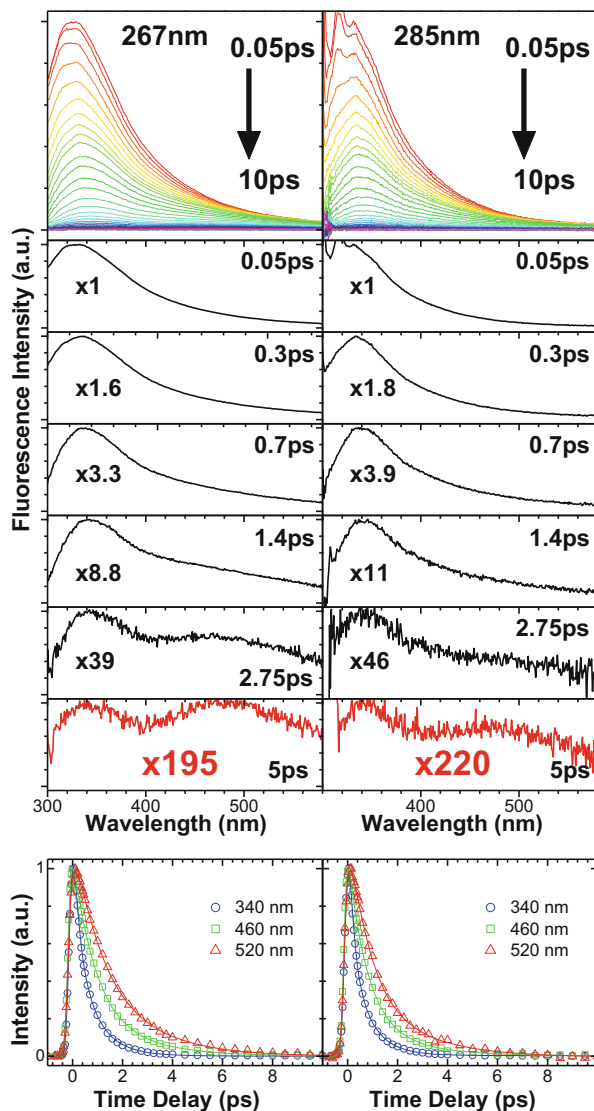
overwhelmingly shown that ultrafast internal conversion to populate hot ground states is the primary relaxation pathway in all the nucleic acid bases upon 267 nm excitation [1, 4, 5, 9, 70, 109, 134, 151]. It seems unlikely that the guanine nucleosides and nucleotides are the exception. Furthermore, as will be discussed in more detail in Sect. 2.3, femtosecond transient absorption experiments probing the ground-state recovery dynamics in the mid-infrared spectral region have provided compelling evidence that vibrational cooling is the main relaxation pathway in 2′-deoxyguanosine and guanosine 5′-monophosphate [86, 152–154].

The ground-state recovery lifetimes for the $\nu_{N3C4} + \nu_{amino}$ (1,517 cm$^{-1}$) and the $\nu_{CO}$ (1,662 cm$^{-1}$) vibrational modes of guanosine 5'-monophosphate in deuterated water reported by Zhang et al. [152, 154] are $2.7 \pm 0.3$ ps and $3.1 \pm 0.3$ ps, respectively. These values are in excellent agreement with the $2.25 \pm 0.05$ ps lifetime reported by Cheng et al. [81] for the transient absorption trace at the 253 nm probe wavelength in the same solvent. In addition, Kohler and co-workers [131, 152] have previously observed similar solvent and solvent isotope effects in the ground state recovery signals of several purine bases to those reported by Cheng et al. [81], but have explained them in terms of mode-specific, high-frequency intermolecular energy transfer events in the ground state between the solute and the solvent. Nevertheless, the observation of a weakly emissive state in the time-resolved fluorescence spectra of 2'-deoxyguanosine and 2'-deoxyguanosine 5'-monophosphate and the dependence of the excited-state dynamics on the solvent and excitation wavelength warrant further investigation.

### 2.2.2 Cytosine, Thymine, and Uracil Monomers

Tables 7 and 8 collect the singlet state lifetimes of the cytosine, thymine, and uracil monomers in aqueous solution and in acetonitrile. Lifetime assignments are given as footnotes in each table. There is agreement in the literature that the $^1\pi\pi^*$ state population in the pyrimidine monomers decays on an ultrafast time scale. Excitation with ultraviolet radiation overwhelmingly populates the bright $^1\pi\pi^*$ states in solution, while the $^1n\pi^*$ and $^3\pi\pi^*$ states can subsequently be reached through internal conversion and intersystem crossing decay pathways, respectively [105, 140, 153, 155–158]. The lifetime of the $^1n\pi^*$ state is highly sensitive to the solvent used [159], varying by approximately an order of magnitude in going from water to acetonitrile solution. Experimental observations have shown that the population of the $^1n\pi^*$ state increases when the sugar is covalently linked to the base (see Sect. 2.4) [140, 156, 158]. The long-lived $^1n\pi^*$ and $^3\pi\pi^*$ excited states are thought to decay primarily back to the ground state [140], but they might also play a key role in the small but quantifiable photochemistry of the pyrimidine bases [97, 105, 160–162]. This is particularly evident for the $^3\pi\pi^*$ state, which has long been recognized to be involved in the formation of the cyclobutane pyrimidine dimers in dilute aqueous solutions [97, 105, 160–162]. The triplet yields and triplet lifetimes of the pyrimidine monomers are reported in Tables 5 and 9, respectively.

The characterization of the intersystem crossing dynamics in the pyrimidine monomers has been a challenging task because the triplet yields are small (ca. 10$^{-2}$) in aqueous solution, whereas much greater yields are observed in less polar and aprotic solvents (Table 5) [101, 159]. The higher triplet yields in aprotic solvents correlate with the reported singlet oxygen yields in Table 6. Experimental evidence has been accumulating over recent years that the intersystem crossing should occur within a few picoseconds or less in order to be competitive with ultrafast internal conversion [105, 140, 157, 159, 168], although direct measurement of the intersystem crossing rate constants in solution is still lacking for all the monomers

**Table 7** Singlet lifetimes for the cytosine monomers

|  | Singlet-state lifetimes (ps) | Technique, time resolution | Experimental conditions |
|---|---|---|---|
| Cyt | $0.20 \pm 0.02$[a], $1.30 \pm 0.07$[a] | FU, 100 fs | $H_2O$ [163] |
|  | 0.72 | TAS, 200 fs | $H_2O$, pH 6.8 [164] |
|  | $1.0 \pm 0.2$ | TAS, 320 fs | PBS, pH 6.8 [165] |
|  | $2.9 \pm 0.7$[b], $12 \pm 3$[c] | TAS, 200 fs | PBS, pH 7 [140] |
|  | 0.251, 3.970 | TAS, <10 fs | $H_2O$ [104] |
| Cyd | $0.76 \pm 0.12$ | FU, 360 fs | PBS, pH 7 [71] |
|  | $0.72 \pm 0.04$ | TAS, 200 fs | $H_2O$, pH ∼ 7 [134] |
|  | $1.0 \pm 0.1$ | TAS, 320 fs | PBS, pH 6.8 [165] |
|  | $0.95 \pm 0.12$[d] | FU, 360 fs | PBS, pH 7 [71] |
|  | $3.7 \pm 0.8$[b,d], $34 \pm 3$[c,d] | TAS, 200 fs | PBS, pH 7 [140] |
| dCyd | $0.18 \pm 0.02$[a], $0.92 \pm 0.06$[a] | FU, 100 fs | $H_2O$ [79] |
|  | $0.27 \pm 0.02$[a,d], $1.38 \pm 0.11$[a,d] | FU, 100 fs | $H_2O$ [79] |

[a]No specific assignment was given to these lifetimes
[b]Assigned to vibrational cooling from the hot $S_0$ state
[c]Assigned to the lifetime of the lowest-energy $^1n\pi^*$ state
[d]Measured for the nucleotide form

except possibly 2′-deoxythymidine [105]. The proposal of ultrafast intersystem crossing dynamics is supported by static and dynamical calculations [169–175]. However, the mechanism by which intersystem crossing occurs is still poorly understood, and there is no agreement in the literature on the nuclear and electronic factors that promote crossing to the triplet state or on the electronic states that play a key role.

The vibrationally-excited $^1n\pi^*$ state has been proposed to act as a doorway state in the intersystem crossing to the $^3\pi\pi^*$ state, but this does not appear to be the case for the vibrationally-relaxed $^1n\pi^*$ state [140, 159]. Additional evidence supporting the idea that the $^3\pi\pi^*$ state is populated from the non-equilibrated $^1n\pi^*$ state might come from the study by Kwok et al. [105]. These authors presented spectroscopic evidence for the ultrafast population of the $^3\pi\pi^*$ state ($\tau_{ISC} = 0.76$ ps) in deoxythymidine in aqueous solution. However, according to them, the efficient population of the $^3\pi\pi^*$ state is a result of variations in the mixed character of the doorway state, labeled $S_n'$ in their work, caused by the strong vibrational coupling between the $^1n\pi^*$ and the $^1\pi\pi^*$ states as a function of solvation dynamics.

The magnitude of the spin-orbit coupling interaction between the doorway state and the receiver triplet state should play an important role, but it is also necessary to identify the vibrational modes and structural features that most significantly contribute to the intersystem crossing pathway. Recently, the group of González performed the first molecular dynamics simulations that include nonadiabatic interactions and spin-orbit interactions for a DNA base [173, 174]. The authors investigated the singlet and triplet excited-state dynamics in cytosine by using ab initio surface-hopping dynamics. Although the calculations were performed in vacuum, the important new insights that the study brings about regarding the electronic and nuclear factors that facilitate intersystem crossing in cytosine are worth briefly discussing here. According to their calculations, excitation of cytosine

**Table 8** Singlet lifetimes for the thymine and uracil monomers

|  | Singlet-state lifetimes (ps) | Technique, time resolution | Experimental conditions |
|---|---|---|---|
| Thy | $0.195 \pm 0.017^a$, $0.633 \pm 0.018^b$ | FU, 330 fs | $H_2O$ [84] |
|  | $<0.15^{c,d}$, $0.58 \pm 0.05^d$ | FU, 150 fs | $H_2O$ [72] |
|  | $2.8 \pm 0.4^e$, $30 \pm 13^b$ | TAS, 200 fs | PBS, pH 7 [140] |
|  | $0.140^f$, $1.220^b$ | TAS, <10 fs | $H_2O$ [166] |
|  | $0.190^f$, $1.100^b$ | FU, 100 fs | ACN [86] |
| dThd | $0.70 \pm 0.12$ | FU, 360 fs | PBS, pH 7 [71] |
|  | $<0.15^{c,d}$, $0.69 \pm 0.05^d$ | FU, 150 fs | $H_2O$ [72] |
|  | $0.15 \pm 0.02^d$, $0.72 \pm 0.03^d$ | FU, 100 fs | $H_2O$ [79] |
|  | $0.15^g$, $0.76^h$ | TRF, 300 fs / TAS, 200 fs | $H_2O$ [105] |
|  | $0.54 \pm 0.04$ | TAS, 200 fs | $H_2O$, pH ~ 7 [134] |
|  | $0.98 \pm 0.12$ | FU, 360 fs | PBS, pH 7 [71] |
|  | $0.20 \pm 0.05^{d,i}$, $1.10 \pm 0.10^{d,i}$ | FU, 150 fs | $H_2O$ [72] |
|  | $0.21 \pm 0.03^{d,i}$, $1.07 \pm 0.06^{d,i}$ | FU, 100 fs | $H_2O$ [79] |
|  | $2.2 \pm 0.1^{e,i}$, $127 \pm 15^{b,i}$ | TAS, 200 fs | PBS, pH 7 [140] |
| Ura | $0.096 \pm 0.003$ | FU, 330 fs | $H_2O$ [84] |
|  | $1.9 \pm 0.1^e$, $24 \pm 2^b$ | TAS, 200 fs | PBS, pH 7 [140] |
|  | $0.100^c$ | FU, 100 fs | ACN [86] |
| Urd | $0.21 \pm 0.03$ | TAS, 200 fs | PBS, pH 6.8 [167] |
|  | $2.3 \pm 0.2^{e,i}$, $147 \pm 7^{d,i}$ | TAS, 200 fs | PBS, pH 7 [140] |

[a]Assigned to the lifetime of moving through a conical intersection from the $^1\pi\pi^*$ state to the $S_0$ state

[b]Assigned to the lifetime of the $^1n\pi^*$ state

[c]Limited by the time resolution of the experimental setup

[d]No specific assignment was given to this lifetime

[e]Assigned to vibrational cooling from the hot $S_0$ state

[f]Assigned to the lifetime of the $^1\pi\pi^*$ state

[g]Assigned to internal conversion from $^1\pi\pi^*$ to the $^1n\pi^*$ state

[h]Assigned to intersystem crossing from the $^1n\pi^*$ to the $^3\pi\pi^*$ state

[i]Measured for the nucleotide form

with UV radiation results in a biexponential decay with lifetimes of 7 fs and 270 fs. The two lifetimes are associated with a number of competing internal conversion and intersystem crossing pathways, respectively, which are discussed in detail elsewhere [174]. Relevant to the discussion here, the intersystem crossing mechanism was found to involve a three-state near-degeneracy between the $S_1$, $T_2$, and $T_1$ states, whereas no singlet–triplet crossings involving only two states were observed. The $S_1$ and $T_2$ states have predominantly $n\pi^*$ character, but it was observed that the spin-orbit coupling interaction between them is enhanced by up to $40 \text{ cm}^{-1}$ because of strong mixing of these states with states of $\pi\pi^*$ character and the small energy gap (0.01 eV) in the vicinity of the crossing. More importantly, and in contrast to the intersystem crossing mechanism proposed by Merchán et al. previously [169], the analysis of all the geometries in which intersystem crossing takes place reveals that elongation of the C2=O bond and shortening of the C2–N3 bond are the key features of the singlet–triplet crossing [174], whereas the early proposal [173] that pyramidalization of the N1 atom plays an essential role was reconsidered.

**Table 9** Triplet state properties in the natural pyrimidine monomers

| | $\lambda_T$ (nm)[a] | $\varepsilon_T$ ($M^{-1}\,cm^{-1}$)[b] | Triplet lifetime ($\mu s$) | Technique, time resolution | Experimental conditions[c] |
|---|---|---|---|---|---|
| Thy | – | – | 1.3[d] | TAS, 20 ns | $H_2O$, Ar, 0.2–0.3 mM [194] |
| | 320 | 5,200[e] | 0.60[d] | TAS, 30 ns | $H_2O$, Ar, 1 mM [99] |
| | 290, 360sh | – | 2[d] | TAS, 20 ns | ACN, Ar, 0.2–0.3 mM [194] |
| | 340 | 4,000 | 10[f,g] | TAS, 30 ns | ACN, Ar [99] |
| dThd | – | – | 0.004[h] | TAS, 200 fs | $H_2O$, 4–5 mM [105] |
| | – | – | 4[d] | TAS, 20 ns | $H_2O$, Ar, 0.2–0.3 mM [194] |
| | 380[e] | 3,750[e] | 25[i] | TAS, 30 ns | $H_2O$, Ar [101] |
| | 360[j] | – | 5[j] | TAS, 8 ns | PBS, $N_2$ [102] |
| | 375[e,j] | 2,700[e,j] | – | TAS, 30 ns | $H_2O$, Ar [101] |
| | 295, 380sh | – | 2.0[d] | TAS, 20 ns | ACN, Ar, 0.2–0.3 mM [194] |
| | 370 | 3,600 | – | TAS, 30 ns | ACN, Ar [101] |
| Ura | – | – | 0.9[d] | TAS, 20 ns | $H_2O$ Ar, 0.2–0.3 mM [194] |
| | 360 | 2,750[e] | 0.35[d] | TAS, 30 ns | $H_2O$, Ar, 1 mM [99] |
| | – | – | 0.58[f] | TAS, 7 ns | ACN, Ar, 0.6 mM [176] |
| | – | – | $1.43 \pm 0.04$ | TAS, 20 ns | ACN, Ar [12] |
| | 290, 370 | – | 1.1[d] | TAS, 20 ns | ACN, Ar, 0.2–0.3 mM [194] |
| | 340 | 2,750 | 2[f,k] | TAS, 30 ns | ACN, Ar [99] |
| Urd | – | – | 2[d] | TAS, 20 ns | $H_2O$, Ar, 0.2–0.3 mM [194] |
| | 410[e] | 6,875[e] | 2[l] | TAS, 30 ns | $H_2O$, Ar [101] |
| | 415[e,j] | 10,000[e,j] | 3.3[j] | TAS, 30 ns | $H_2O$, Ar [101] |
| | 300, 410 | – | 1.2[d] | TAS, 20 ns | ACN, Ar, 0.2–0.3 mM [194] |
| | 370 | 6,400 | – | TAS, 30 ns | ACN, Ar [101] |
| dUrd | 290, 380sh | – | 1.0[d] | TAS, 20 ns | ACN, Ar, 0.2–0.3 mM [194] |

[a]Wavelength of triplet absorption band maximum

[b]Extinction coefficient at triplet absorption band maximum

[c]DNA and RNA monomer concentrations are given; solutions were under air-saturated conditions unless otherwise noted

[d]Triplet lifetime was not corrected for self-quenching

[e]Extrapolated from graph

[f]Calculated to infinite dilution

[g]Self-quenching rate constant of $6 \times 10^8\ M^{-1}\ s^{-1}$

[h]Assigned to relaxation of the $T_1$ state to a biradical intermediate involved in a $T_1$ self-quenching reaction

[i]Self-quenching rate constant of $1 \times 10^8\ M^{-1}\ s^{-1}$

[j]Measured for the nucleotide form

[k]Self-quenching rate constant of $20 \times 10^8\ M^{-1}\ s^{-1}$

[l]Self-quenching rate constant of $8 \times 10^8\ M^{-1}\ s^{-1}$

An important reminder from this study is that near-degeneracy between singlet and triplet states can often compensate for small spin-orbit coupling interactions. Because of the proposed key participation of the triplet state in the photochemistry of DNA and its components [97, 105, 176], further work is urgently needed to scrutinize the intersystem crossing mechanism in the DNA and RNA monomers in solution.

## 2.3    Vibrational Cooling Dynamics in the Ground State

It is now accepted that ultrafast internal conversion to the ground state transfers more than 4 eV of energy to the vibrational modes of the DNA and RNA monomers in solution [4, 9, 70]. The vibrationally-excited modes of the bases in the ground state return to thermal equilibrium in several picoseconds in solution, but the role that intramolecular and intermolecular energy transfers play in the dissipation of the excess energy is currently a topic of significant interest. Understanding the mechanism by which the vibrationally-excited monomers in the ground state dissipate excess energy is also important because thermal reactions after electronic-energy relaxation to the ground state could lead to product formation [97, 160]. Pioneer transient absorption experiments by Middleton [131] investigated the solvent and solvent isotope effects on the vibrational cooling dynamics in 9-methyladenine. It was observed that the vibrational cooling lifetimes increased from 2.4 ps in water to 13.1 ps in acetonitrile, with the lifetimes in deuterated water and methanol showing intermediate values of 4.2 ps and 4.5 ps, respectively. These results led the authors to conclude that the number and strength of the solute–solvent hydrogen bonds affect the rate of vibrational cooling. Solvents with a dense network of hydrogen bonds enhance the rate of vibrational cooling by facilitating energy transfer from the solute to the solvent. The authors rationalized the pronounced solvent isotope effect as caused by a large portion of the excess vibrational energy being transferred to relatively high-frequency solvent librational modes in the 700–1,000 cm$^{-1}$ range because the vibrational friction spectra of water and deuterated water are nearly identical at frequencies below ~700 cm$^{-1}$ [177–179].

Zhang et al. [152] recently used femtosecond pump-probe transient absorption spectroscopy in the 1,500–1,725 cm$^{-1}$ probe region to learn more about the factors that influence the rate of vibrational cooling dynamics in several purine monomers in solution. Figure 2 shows the ground-state recovery signals for six different purine derivatives probed at the specified vibrational modes in deuterated water solution. The authors selected those monomers because all of them undergo ultrafast internal conversion to the ground state [180], and because the extent of methylation determines the number and types of hydrogen bonds with the solvent (see Scheme 2). As can be observed in Fig. 2 and Scheme 2, the rate of vibrational cooling correlates with the number of hydrogen bond donors (N–D) the purine base has, but not with the number of hydrogen bond acceptors. Adenine, guanine, and hypoxanthine each have at least two N–D bonds and exhibit the shortest vibrational
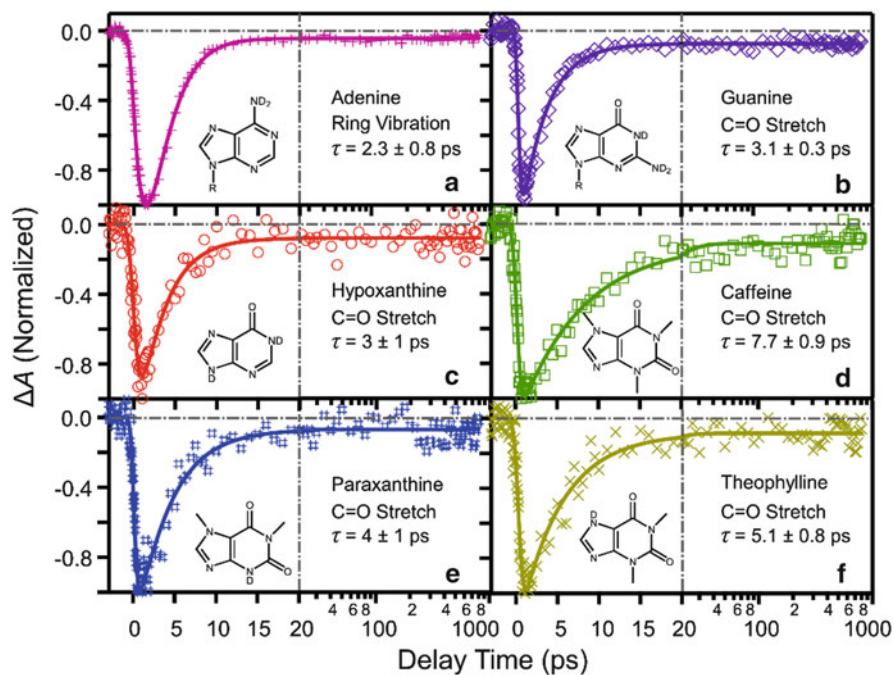
**Fig. 2** Bleach recovery kinetics for (**a**) adenine ring vibration at 1,623 cm$^{-1}$; (**b**) guanine carbonyl stretch at 1,662 cm$^{-1}$; (**c**) hypoxanthine carbonyl stretch at 1,673 cm$^{-1}$; (**d–f**) the carbonyl stretch for methylated xanthines at ~1,640 cm$^{-1}$. All data were obtained in D$_2$O. The points are experimental data. The lines are the best exponential decay fits determined in Igor Pro. Only time constants ($\tau$) larger than 1 ps are reported. Uncertainties associated with the time constants are 2× standard deviation. *Vertical dashed–dotted lines* denote the linear–logarithmic break. Reprinted with permission from [152]. Copyright 2013 American Chemical Society

cooling lifetimes in deuterated water. Paraxanthine and theophylline have only one N–D bond and exhibit longer vibrational cooling lifetimes, whereas caffeine has no N–D bonds and shows the longest lifetime. Thus, the authors concluded that hydrogen bond donation sites in the base accelerate intermolecular vibrational energy transfer via direct coupling of the N–D modes of the base with the relatively high frequency O–D modes of the solvent. Their results further suggest that strong solute–solvent couplings caused by hydrogen bonds and near resonances with solvent modes are two factors that facilitate intermolecular energy transfer. The importance of resonant energy transfer was emphasized by the observation of slower and approximately equal vibrational cooling lifetimes for caffeine, paraxanthine, and theophylline in acetonitrile, a solvent in which resonant energy transfer pathways and high-frequency acceptor modes are absent.

Further structural impacts on vibrational cooling dynamics were investigated by Nielsen and co-workers [155, 181], who recently showed that the phosphate group in the adenine, guanine, and cytosine nucleotides does not significantly contribute to the vibrational relaxation process. The authors also used femtosecond broadband
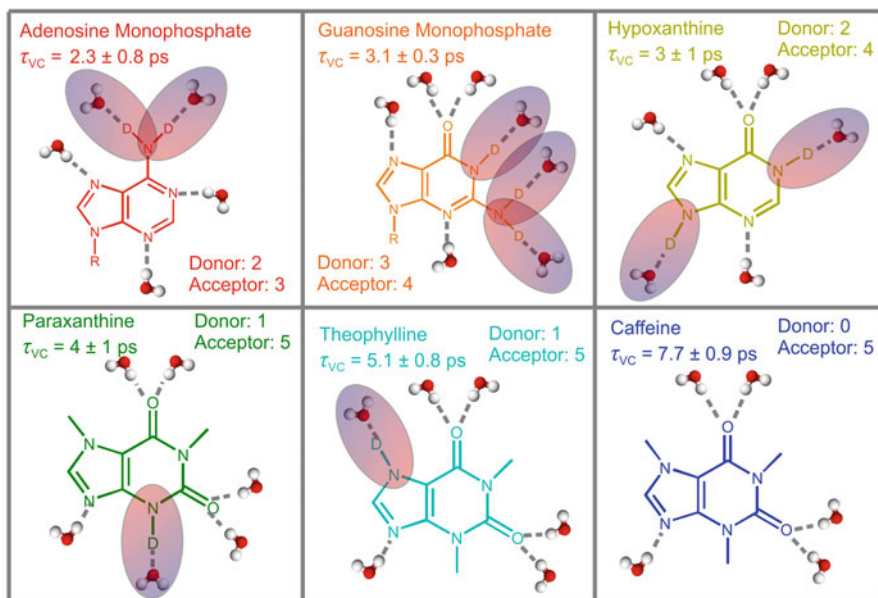
**Scheme 2** The structures of adenosine monophosphate, guanosine monophosphate, and a series of methylated xanthines. Hydrogen bond donor sites are *highlighted* to emphasize their inverse relationship with the molecule's vibrational cooling lifetime ($\tau_{vc}$), i.e. the fewer the hydrogen bond donor sites the longer the lifetime. Note that the hydrogen bond counts do not consider the ribose and phosphate groups of AMP and GMP. Adapted with permission from [152]. Copyright 2013 American Chemical Society

transient absorption spectroscopy to probe the vibrational regions pertinent to the aromatic rings from $1,500$ cm$^{-1}$ to $1,800$ cm$^{-1}$ and the phosphate groups from $1,025$ cm$^{-1}$ to $1,175$ cm$^{-1}$. Weak and featureless transient absorption signals were observed in the phosphate fingerprint region of the three nucleotides, which led the authors to conclude that the phosphate group is not involved in the vibrational relaxation process. The authors further proposed that the electronic excitation energy is primarily contained within the aromatic vibrational modes of the base with negligible coupling to either the sugar or the phosphate components of the nucleotides [155, 181]. The negligible role of the sugar in the vibrational relaxation process was inferred by noticing, according to these authors, that the vibrational relaxation times of the ring and amide modes are similar in cytosine (5.0 ps and 3.3 ps) and its nucleotide (2.8 ps and 3.3 ps) [155]. Altogether, these observations led the authors to conclude that the vibrational relaxation dynamics cannot be explained using the anharmonic coupling model [182–186], but rather that their results suggest that a mode-specific dissipation of the vibrational energy to the solvent takes place at a rate faster than the intramolecular redistribution of energy. In the anharmonic coupling model, the vibrational population obeys a Boltzmann distribution at all experimentally accessible delay times. In the second model, which is known as the non-thermal relaxation model [187–189], the vibrational

populations of a small number of high-frequency modes are non-statistical for times that are long enough to be experimentally measured. Thus, the authors proposed that the vibrational energy transfer to the solvent in the ground state is more efficient than intramolecular vibrational redistribution, such that the sugar and phosphate groups are never vibrationally excited.

The mode-specific vibrational energy transfer model proposed by Nielsen and co-workers [155, 181] is further supported by the recent studies of Kohler and co-workers [152, 154]. These authors investigated the vibrational relaxation dynamics of guanosine 5′-monophosphate by femtosecond broadband transient absorption spectroscopy in the 1,400–1,750 cm$^{-1}$ probe region in deuterated aqueous buffer solution (pD = 7.2) [154]. In agreement with earlier studies [153, 181, 190], the authors found that the bleach recovery signals of the $\nu_{N3C4} + \nu_{amino}$ (1,517 cm$^{-1}$) and the $\nu_{CO}$ (1,662 cm$^{-1}$) vibrational modes are dominated by dynamics that occur on the ground state potential energy surface. Evidence was presented for mode-specific vibrational relaxation in the electronic ground state of several medium-frequency modes, such as ring in-plane stretching and carbonyl stretching modes. This observation lends further support to the idea that vibrational energy distribution in the ground state of the nucleic acid monomers is non-statistical in nature [152, 155, 181]. Furthermore, by complementing the experiments with quantum-chemical calculations at the density functional level of theory, Zhang et al. were able to associate the excitation of those vibrational modes with structural changes occurring when the excited-state population goes from the Franck–Condon region of the $^1\pi\pi^*$ potential energy surface to the conical intersection with the ground state. The authors concluded that vibrational cooling dynamics in the ground state are dominated by solute-to-solvent intermolecular vibrational energy relaxation, in agreement with other investigations [131, 152, 155, 181].

Alternatively, West et al. [191, 192] performed transient grating and two-dimensional electronic spectroscopy in the deep UV to investigate vibrational energy transfer in thymine and 9-methyladenine at temperatures of 100–300 K. The experiments were performed in a mixture of 85% methanol and 15% water as the solvent. It was observed that the rate of vibrational cooling in these bases is independent of temperature in the range 100–300 K. According to their model calculations, the insensitivity of the vibrational cooling rates to temperature originates from a combination of two effects. In the first effect, vibrational energy transfer from the base to the solvent initiates directly from intramolecular modes of the base with frequencies greater than 300 cm$^{-1}$, in which both translational and librational modes of the solvent are involved. In the second effect, the vibrational relaxation induces an increase in the effective temperature of the solvent surrounding the base, which reduces the sensitivity of vibrational cooling to the temperature at which the system was set before excitation. However, the authors acknowledged that to explain fully the insensitivity of the vibrational cooling to the temperature of the system they needed to invoke the direct transfer of vibrational energy into high-frequency librational modes of the solvent, which is in agreement with the leading interpretations [131, 152, 155, 181]. Additionally, it is possible that the high methanol content used in their experiments could slow intermolecular energy

transfer enough for intramolecular energy transfer via low frequency modes to become competitive, as recently noted by Kohler and co-workers [152].

## 2.4 The Role of the N-Glycosidic Group in the Rates of Internal Conversion and Vibrational Cooling

We define throughout this chapter (for the lack of a better term) the N-glycosidic group or substituent as the group or atom that is covalently-linked to the N9 and N1 atom of the purine and pyrimidine bases, respectively.[1] The covalent incorporation of the deoxyribose or ribose sugar group at the N1 position of the pyrimidine monomers has a significant effect on the excited-state dynamics of the nucleobase [129, 140, 155, 156, 158]. Hare et al. [140] first reported that the magnitude of the $^1n\pi^*$ state lifetime increases significantly when the hydrogen in the N1 position of the pyrimidine bases is substituted by a sugar. The authors hypothesized that the hydrogen bonding sites of the sugar group promote the efficient relaxation of the excess vibrational energy in the $^1n\pi^*$ state to the solvent. This in turn decreases the probability of barrier crossing to access the ground state nonradiatively and thus increases the $^1n\pi^*$ state lifetime. Keane et al. [158] arrived at a similar conclusion in their picosecond transient infrared study of the cytosine monomers in deuterated aqueous buffer solution. Nielsen et al. [155], on the other hand, proposed that N-glycosidic bond formation does not actively contribute to vibrational relaxation in the excited state, but might still alter the excited-state dynamics of cytosine by either shifting the relative energies of the $^1\pi\pi^*$ and $^1n\pi^*$ states or by opening a conical intersection between these states which is not available in the cytosine base.

West et al. [193] also explored the interplay between ultrafast internal conversion to the ground state and the associated vibrational cooling dynamics in thymine and its nucleoside and dinucleotide. The authors found that vibrational cooling is enhanced as the molecular size of the system increases from the base to the dinucleotide. Two separate vibrational energy transfer pathways were proposed to explain this behavior: (1) vibrational energy transfer from the base to the deoxyribose sugar and (2) vibrational energy transfer between neighboring units in the dinucleotide. According to these authors, the increase in the rate of vibrational energy transfer is driven by the increase in the density of vibrational states on the substituent with an increase in molecular size, which increases the number of states that can effectively couple to those on the base.

Figure 3a shows the effect of temperature on the $^1\pi\pi^*$ lifetimes. The lifetimes below 300 K were estimated indirectly from the transient grating experiments.

---

[1] This is contrary to the accepted use of the term. See, for instance, International Union of Pure Applied Chemistry. Division of Organic Chemistry. Commission on Nomenclature of Organic Chemistry. A Guide to IUPAC Nomenclature of Organic Compounds, Recommendations 1993; R. Panico, W. H. Powell, J.-C. Richer, eds.; Blackwell Scientific Publications, Oxford, UK (1993).

**Fig. 3** (**a**) ππ* lifetimes obtained for the thymine family of systems at temperatures ranging from 100 K to 300 K. The lifetimes show a definite increase with decreasing temperature for thymidine and its dinucleotide. (**b**) Arrhenius plots for internal conversion rates ($k_{IC}$) for this series of thymine-based molecules. Reprinted with permission from [193]. Copyright 2013 American Chemical Society
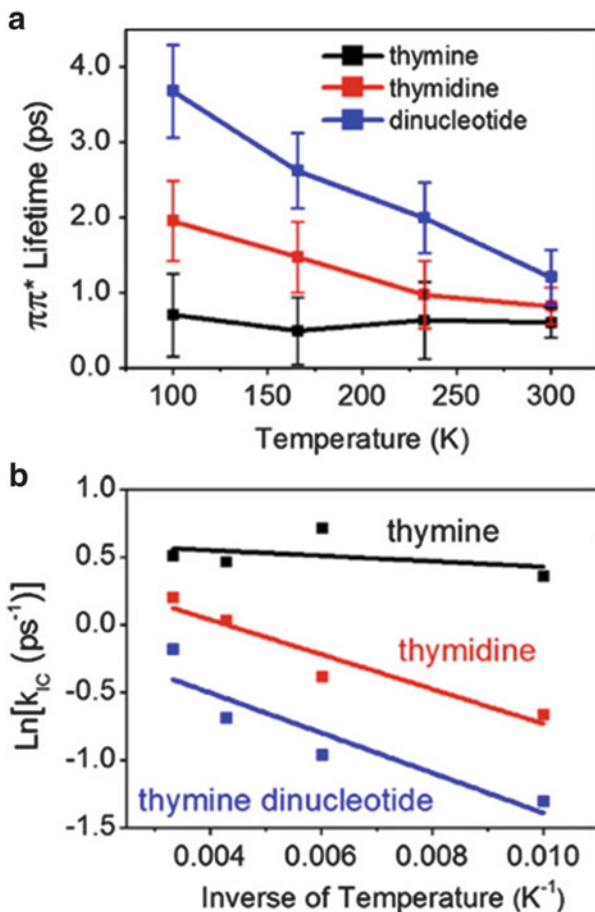


This was done by solving the coupled differential equations for a two-step sequential kinetic model (i.e., $^1\pi\pi^* \rightarrow S_0(\text{hot}) \rightarrow S_0$) and assuming that the vibrational cooling rates in the range 100–300 K are independent of temperature for the nucleoside and dinucleotide, as previously observed for thymine [191]. Hence, according to this model, the $^1\pi\pi^*$ lifetimes of thymidine and its dinucleotide increase with decreasing temperature, whereas that of thymine does not change within experimental error. The reason for the increase in the $^1\pi\pi^*$ lifetimes with a decrease in temperature was suggested to be the enhanced ability of the excess vibrational energy on the base to transfer to the substituent.

The analysis of the data using the Arrhenius expression is shown in Fig. 3b. The magnitude of the slope was associated with the presence of an energy barrier between the Franck–Condon region of the $^1\pi\pi^*$ potential energy surface and the conical intersection that leads to internal conversion to the ground state (Scheme 3). According to this model, thymine has the smallest energy barrier because it lacks a
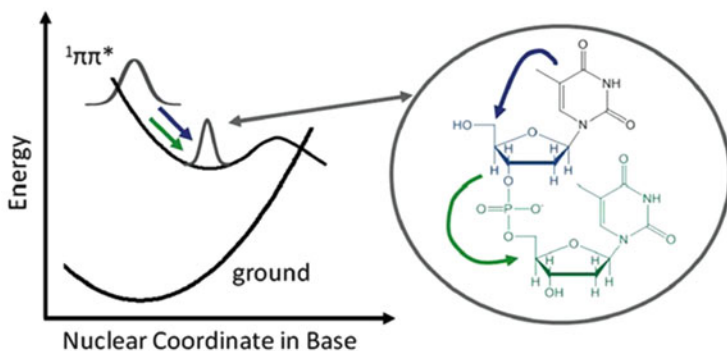
**Scheme 3** Photoexcitation producing a vibrationally "hot" wavepacket, which relaxes through vibrational energy transfer (VET) onto the substituent of the thymine base. This loss of heat causes the wavepacket to narrow and sink deeper into the potential energy well, thereby suppressing internal conversion. The two VET channels indicated on the PES are drawn on the molecular structure of the thymine dinucleotide. Vibrational energy first flows into the deoxyribose ring and then to the adjacent unit. Reprinted with permission from [193]. Copyright 2013 American Chemical Society

substituent onto which the base can rapidly transfer vibrational energy. Hence, excess vibrational energy promotes motion over the energy barrier, as depicted in Scheme 3. The $^1\pi\pi^*$ lifetime of thymine is insensitive to temperature because the base is not coupled to an intramolecular bath and the solute-to-solvent vibrational energy transfer is slower than internal conversion [191]. In contrast, intramolecular vibrational energy transfer can compete effectively with internal conversion in thymidine and the thymine dinucleotide, thereby necessitating thermal activation to proceed through the conical intersection (Scheme 3). The authors concluded that the transfer of vibrational energy from the thymine base to the sugar (or nucleotide substituent) influences the internal conversion rate by increasing the time it takes the population in the $^1\pi\pi^*$ state to access the conical intersection with the ground state [193].

At first glance it might appear that the model proposed by West et al. [193] is analogous to that proposed by Hare et al. [140, 159] to explain the role of the sugar substituent in reducing the excess vibrational energy that promotes nonradiative decay in the $^1n\pi^*$ state. However, West et al. propose that an increase in the low-frequency solute–solvent vibrational modes is the key feature in the energy transfer event. On the other hand, Hare et al. attribute the transfer to relatively high-frequency vibrational modes between the sugar and the water solvent that can increase intermolecular vibrational energy transfer to the solvent. As in the case of 9-methyladenine above, Zhang et al. [152] proposed that the observations by West et al. [193] could be related to the use of a mixture of 85% methanol and 15% water as the solvent in their study. The high methanol content could slow the intermolecular energy transfer enough to increase the importance of energy dissipation via low frequency modes.

Zhang et al. [152] further noticed that a simple increase in the vibrational cooling rates with the number of vibrational degrees of freedom fails to explain the vibrational cooling rates they measured for the purine derivatives in deuterated water solution at room temperature. Hypoxanthine and caffeine have 36 and 66 normal modes, respectively, whereas adenosine 5′-monophosphate has an even greater number of modes. Hence, according to the model of West et al., vibrational cooling should speed up on going from hypoxanthine to caffeine to adenosine 5′-monophosphate. However, experiments show that hypoxanthine and adenosine 5′-monophosphate have similar vibrational cooling lifetimes in deuterated water, whereas caffeine cools more slowly than hypoxanthine [152]. More work is needed to gather a firm, microscopic understanding of the experiments reported by West et al. [193]. Regardless, evidence is accruing linking the N-glycosidic group to changes in the rates of internal conversion in the DNA and RNA monomers in solution.

## 2.5 Role of the N-Glycosidic Group in the Population of the Triplet State

N-Glycosidic bond formation also seems to play a role in the population (Table 5) and lifetime (Table 9) of the $^3\pi\pi^*$ state in the pyrimidine bases. Table 9 shows that the triplet lifetimes depend on the monomer concentration and solvent used. Caution must be exercised in attempting to interpret these results since most of the triplet lifetimes reported in this table have not been corrected for triplet self-quenching and only a few values have been obtained at infinite-dilution conditions. Hare et al. put forward the idea that intersystem crossing from the $^1n\pi^*$ state to the $^3\pi\pi^*$ state occurs efficiently only when the $^1n\pi^*$ state has sufficient excess vibrational energy [140, 157, 159]. The hypothesis that N-glycosidic bond formation modulates the triplet yield seems to be supported by the triplet yields reported in Table 5 for uracil and uridine in aqueous solution [99, 101] and in acetonitrile [100, 101]. The results presented in Table 5 consistently show higher triplet yields in uracil than in uridine under similar experimental conditions. Similarly, the triplet yield of thymine in acetonitrile solution is ~30% higher than that of thymidine under similar experimental conditions [100]. Unfortunately, the triplet yields and lifetimes reported in Table 5 and 9 are too inconclusive to permit generalization of this idea and further systematic and quantitative work is needed to understand fully the dependence of the triplet yields on the N-glycosidic group and on the concentration and solvent used.

## 2.6   Summary

Investigations using femtosecond laser spectroscopies have shown that the optically populated $^1\pi\pi^*$ states in the DNA and RNA monomers decay to other low-lying electronic states, primarily the ground state, on multiple time scales ranging from tens of femtoseconds to tens of picoseconds and beyond [1–9]. The specific nuclear dynamics that couple to the electronic relaxation pathways are coming into focus and consensus has now been reached regarding the key participation of conical intersections in the excited-state dynamics of the DNA and RNA monomers in solution. There is still uncertainty regarding (1) the specific assignment of the multiexponential decay components, (2) the microscopic mechanism by which excess vibrational energy is redistributed and its dependence on solvent and temperature, and (3) the mechanism by which the functional group in the N-glycosidic bond modulates the different nonradiative relaxation pathways. In addition, the rate of intersystem crossing to the triplet state and details about its mechanism for the different nucleic acid monomers in solution are still unknown.

## 3   Thiobases

The photochemistry of natural DNA and RNA monomers is intricately sensitive to minor structural modifications to the nucleobase core. These structural modifications often alter the excited-state potential energy surfaces in a manner which restricts access to one or more of the ultrafast and efficient electronic relaxation pathways, which are the hallmarks of the DNA and RNA monomers. Hence, investigations of DNA and RNA base analogues can be used as a *testbed* to benchmark our mechanistic understanding of the intrinsic relaxation pathways observed in DNA from both experimental and computational perspectives. For instance, a single substitution of an oxygen atom by a sulfur atom in a carbonyl group of the nucleobase, generating a so-called thiobase, leads to a dramatic change in the photochemical properties of the DNA and RNA monomers. The absorption spectra shift from the UVC region in the nucleic acid monomers out to the UVA region in the thiobases. Furthermore, sulfur substitution inhibits ultrafast internal conversion to the ground state and dramatically increases the rate of intersystem crossing to the triplet manifold by enhanced spin-orbit coupling [11, 17, 18, 27, 33], which leads to near-unity triplet yields in these nucleic acid base analogues [11, 16, 18, 22, 31, 144, 195, 196].

In addition to their relevance as convenient proxies to gauge our understanding of the photochemical properties in the DNA and RNA monomers, thiobases are naturally found in transfer RNA [197–199] and have been used as intrinsic photoaffinity probes of DNA and RNA structures and DNA/RNA-protein interactions by exploiting their strong absorption in the UVA region, which permits their selective excitation [34, 35]. Thiobases also belong to a family of molecules known

## Thiopurines
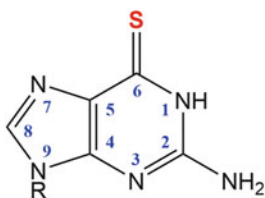


**6-thioguanine** (R=H)
6-thioguanosine
(R = ribose or 2'-deoxyribose)
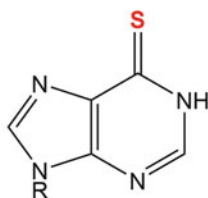
**6-thiopurine** (R=H)
6-thioinosine
(R = ribose or 2'-deoxyribose)

## Thiopyrimidines
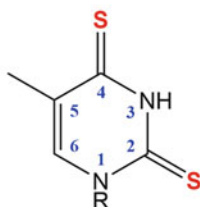


**2,4-dithiothymine** (R = H)
2,4-dithiothymidine
(R = ribose or 2'-deoxyribose)
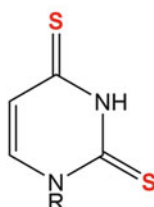
**2,4-dithiouracil** (R = H)
2,4-dithiouridine
(R = ribose or 2'-deoxyribose)
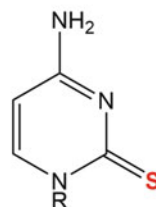
**2-thiocytosine** (R=H)
2-thiocytidine
(R = ribose or 2'-deoxyribose)

**Scheme 4** Structures and common ring numbering of the thiobases

as prodrugs, which are commonly prescribed as immunosuppressants for organ transplant patients [36] and as maintenance therapy for acute lymphoblastic leukemia, inflammatory bowel disease [37], and gliomas [38, 39]. They are also widely used as cytotoxic agents of clinical relevance [35, 40, 41] and in photochemotherapeutic applications to treat skin disorders [42], superficial tumors [43, 44], and bladder cancer [45]. However, their prolonged use in patients often leads to phototoxic side effects and skin cancer [26, 36, 43, 62]. Hence, understanding their steady-state and time-resolved photochemistry is intrinsically important.

This section reviews the current state of knowledge regarding the steady-state and time-resolved photochemistry of the sulfur-substituted DNA and RNA analogues and recent efforts to understand their excited-state relaxation mechanisms using quantum-chemical methods. The structures and standard ring numbering of the thiobases are shown in Scheme 4.

## 3.1   Steady-State and Time-Resolved Photochemistry of the 4-Thiouracil Derivatives

A single substitution of the oxygen by a sulfur atom in the carbonyl group found at the four position of the uracil or thymine (5-methyluracil) ring results in dramatic changes to the steady-state and time-resolved photochemical properties of the nucleic acid bases. The absorption spectra of the 4-thiouracil derivatives reveal an intense band ($\varepsilon_{max} \sim 1.8$–$2.1 \times 10^4 \, M^{-1} \, cm^{-1}$) with absorption maximum in the UVA region (~330–340 nm), which depends only weakly on the solvent used (Table 10). A tail that develops into a weak absorption band ($\varepsilon_{max} \sim 40$–$60 \, M^{-1} \, cm^{-1}$) in nonpolar solvents is also observed on the red edge of the absorption spectra (~410–440 nm) [34]. This absorption band is not observed in the absorption spectra of the pyrimidine bases (Table 2). Figure 4 shows the absorption spectra of 1,3-dimethyl-4-thiouracil in CCl$_4$ [200] and 4-thiothymine deoxyribonucleoside in aqueous buffer solution at pH 7.4 [18] as representative examples. The red-most absorption bands have been assigned to the $S_0 \rightarrow S_2(\pi\pi^*)$ and the $S_0 \rightarrow S_1(n\pi^*)$ electronic transitions, respectively [10, 18, 19, 34, 200, 201]. These assignments are supported by quantum chemical calculations [11, 17, 18, 196, 202–204]. Additional absorption bands are observed closer to 200 nm (see, for example, Fig. 4b), related to weak- to moderate-intensity $n\pi^*$ and $\pi\pi^*$ electronic transitions, which at present have not been fully characterized. It is also worth noting that not is only the lowest-energy $\pi\pi^*$ electronic transition significantly red-shifted, but the magnitude of the absorption coefficients reported in Table 10 for the 4-thiouracil derivatives is significantly higher than that of the pyrimidine bases (Table 2).

A common photophysical property of the 4-thiouracil derivatives is the observation of dual emission at room temperature (Fig. 4 and Table 10). These emission bands have been characterized as the $S_2(\pi\pi^*) \rightarrow S_0$ and $T_1(\pi\pi^*) \rightarrow S_0$ radiative transitions in the 4-thione, 2-keto uracil derivatives and exhibit fluorescence and phosphorescence quantum yields in the ranges of (0.4–1.5) $\times 10^{-4}$ and (0.2–123) $\times 10^{-4}$, respectively, depending on the solvent and the concentration of the solute used [10, 13, 34, 200, 201, 203]. In addition, some of the photophysical properties have been measured at infinite dilution in order to determine intrinsic triplet decay lifetimes and phosphorescence quantum yields (Tables 10, 12, 13, and 14) [200, 203]. It is clear from those experiments that the concentration of the thiobase plays an important role in the quenching of the triplet state population in the thiobase monomers in solution.

### 3.1.1   Singlet-State Dynamics

The first investigation of the fluorescence properties of a 4-thiouracil derivative was reported in 2002 by Skalski and co-workers [200]. The authors used steady-state and picosecond laser spectroscopies to determine the fluorescence yield and

**Table 10** Steady-state absorption and emission properties of the 4-thiouracil derivatives

| | $\lambda_{max}$ (nm)[a] | $\varepsilon_{max}$ (M$^{-1}$ cm$^{-1}$)[b] | $\lambda_{em}$ (nm)[c] | $\Phi_{em} \times 10^{-4}$ [d] | Experimental conditions[e] |
|---|---|---|---|---|---|
| 4tUra | 330 | 21,000 | NE (Fl)<br>530 (Ph) | –<br>2.8 (Ph) | H$_2$O [34] |
| | 328 | 16,700 | – | – | H$_2$O, pH 7 [205] |
| | 327 | 12,800 | – | – | ACN [205] |
| 4tUrd | 331 | 23,000 | – | – | H$_2$O, ~pH 7 [205] |
| | 331 | 11,900 | – | – | ACN [205] |
| | 412[f] | 40–60[f] | – | – | DCM [34] |
| Ac-4tUrd | 328 | 20,600 | 420 (Fl)<br>550 (Ph) | 1.0 (Fl)<br>2.0 (Ph) | ACN [10] |
| | – | – | – | 25 (Ph)[g] | ACN, Ar [13] |
| | 330 | 20,600 | 420 (Fl) | – | CCl$_4$, He [201] |
| | 420[f] | 40[f] | 540 (Ph) | 123 (Ph)[g] | |
| Pr-4tUra | 326 | – | – | 46 (Ph)[g] | PFDMCH, Ar [203] |
| DMTU | 329 | 18,800 | 420 (Fl)<br>535 (Ph) | 0.4 (Fl)[g]<br>– | H$_2$O [200] |
| | 330 | | 530 (Ph) | 2.7 (Ph) | H$_2$O [34] |
| | 330 | 19,800 | 410 (Fl) | 0.60 (Fl)[g] | CCl$_4$, He [200] |
| | 427[f] | 38[f] | 540 (Ph) | 14 (Ph)[g] | |
| | – | – | 410 (Fl)<br>535 (Ph) | 1.50 (Fl)[g]<br>25 (Ph)[g] | PFDMCH, He [200] |
| | 412[f] | 40–60[f] | – | – | DCM [34] |
| CD3-4tUra | 317 | – | – | 32 (Ph)[g] | PFDMCH, Ar [203] |
| 4tThy | – | – | 540 (Ph) | 4 (Ph) | H$_2$O [34] |
| 4t-dThd | 335 | – | 400 (Fl)<br>542 (Ph) | –<br>2.8 ± 0.3 (Ph)[g] | PBS, pH 7.4 [Dunn and Crespo-Hernández, unpublished results] |
| | 337 | 19,440 | NE | – | ACN [11] |
| | 337 | – | 410 (Fl)<br>550 (Ph) | – | ACN [19] |
| Pr-4tThy | 332 | – | – | 42 (Ph)[g] | PFDMCH, Ar [203] |

[a]Wavelength of maximum absorption in the spectral region above ~230 nm; attributed to the S$_2$($\pi\pi^*$) state unless otherwise noted

[b]Extinction coefficient, attributed to S$_2$($\pi\pi^*$) maximum unless otherwise noted

[c]Peak emission wavelength, fluorescence (Fl) or phosphorescence (Ph) noted in parenthesis

[d]Emission quantum yield of fluorescence or phosphorescence as noted in parenthesis

[e]Under air-saturated conditions unless otherwise noted

[f]Property of the S$_1$($n\pi^*$) state absorption maximum

[g]Calculated to infinite dilution

lifetime of 1,3-dimethyl-4-thiouracil in perfluoro-1,3-dimethylcyclohexane (PFDMCH), CCl$_4$, hexane, and water. In organic solvents, a monoexponential fluorescence decay lifetime was reported, with a value of 2.5 ps and 7.5 ps in CCl$_4$ and in PFDMCH, respectively. The authors concluded that the S$_2$($\pi\pi^*$) state decays primarily through intra- and intermolecular nonradiative pathways with a quantum yield of $\Phi_{NR} > 0.99$. Among the nonradiative decay processes, a
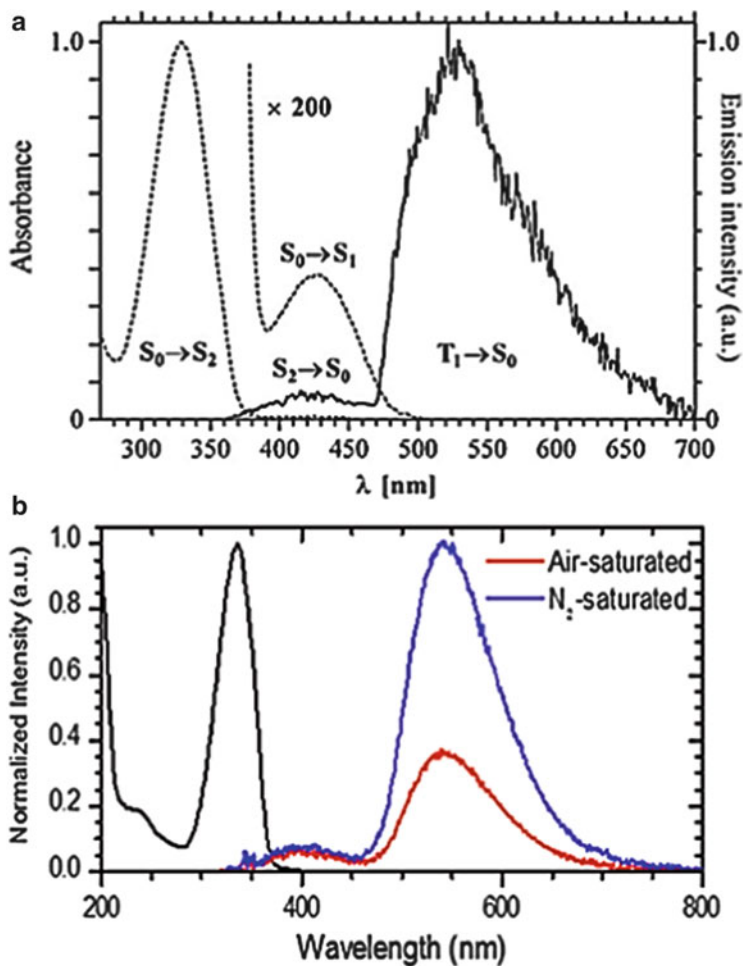
**Fig. 4** (**a**) Normalized absorption and emission spectra of 1,3-dimethyl-4-thiouracil in carbon tetrachloride. The state transitions responsible for each absorption and emission band are labeled on the graph. Adapted from [200]. Copyright 2002 American Society for Photobiology. (**b**) Normalized absorption and emission spectra of 4-thiodeoxythymidine in aqueous buffer solution (pH 7.4). The red-most emission band is attributed to phosphorescence because of the quenching of its intensity by the presence of oxygen. Adapted with permission from [18]. Copyright 2010 American Chemical Society

reversible, intramolecular H-abstraction pathway, in which the excited thiocarbonyl group abstracts a H-atom from the methyl group in the *ortho* position of the 1,3-dimethyl-4-thiouracil ring, was proposed to be the fastest decay channel of the $S_2(\pi\pi^*)$ state with an estimated rate constant of $1.2 \times 10^{11}$ s$^{-1}$ in PFDMCH and CCl$_4$. This intramolecular relaxation pathway has been put into question more recently [203]. $S_2(\pi\pi^*)$ to $S_1(n\pi^*)$ internal conversion was estimated to be an

order of magnitude slower, with a rate constant of $1.5 \times 10^{10}$ s$^{-1}$ and $2.8 \times 10^{10}$ s$^{-1}$ in PFDMCH and CCl$_4$, respectively. The twofold shorter lifetime of the S$_2(\pi\pi^*)$ state in CCl$_4$ relative to the lifetime in PFDMCH is thought to be a consequence of intermolecular quenching by the solvent, with a rate constant of $2.5 \times 10^{11}$ s$^{-1}$.

On the other hand, the fluorescence decay of 1,3-dimethyl-4-thiouracil in doubly-distilled and deionized water results in biexponential decay with 7.5 ps and 118 ps lifetimes and fractional coefficients of 0.3 and 0.7, respectively [200]. No assignments were given regarding the particular excited-state pathways or species responsible for these fluorescence decay lifetimes. Time-resolved investigations using the deuterated 1,3-dimethyl-4-thiouracil or deuterated water as solvent might be able to provide some useful insights regarding this additional decay component.

Wenska and co-workers [10] reported changes in the intensity and band shape of the fluorescence spectrum of 2′,3′,5′-tri-O-acetyl-4-thiouridine in acetonitrile as a function of laser irradiation time at 365 nm. Analysis of the fluorescence decay signals at 400 nm, 430 nm, and 450 nm before and after different intervals of laser irradiation revealed the presence of three emitting species with lifetimes of $(5 \pm 1)$ ps, $(80 \pm 20)$ ps, and $(600 \pm 100)$ ps. The three lifetimes did not depend on the irradiation time or on the probe wavelength used, whereas the fractional coefficients of each of the fluorescence components depended on the irradiation time, suggesting the presence of three different emitting species.

An intramolecular phototautomerization mechanism was proposed to explain these observations. According to these authors, direct excitation to the S$_2(\pi\pi^*)$ state of the 2-keto, 4-thione tautomeric form leads to the formation of the 2-enol, 4-thione tautomer in the S$_2$ state and of the 2-keto, 4-thiol tautomer in the S$_1$ state [10]. Thus, the authors assigned the first lifetime to fluorescence emission from the S$_2(\pi\pi^*)$ state of 2′,3′,5′-tri-O-acetyl-4-thiouridine in its 2-keto, 4-thione tautomeric form, whereas the other two lifetimes were assigned to fluorescence emission from the S$_2$ state of the 2-enol, 4-thione tautomer and from the S$_1$ state of the 2-keto, 4-thiol tautomer, respectively.

Interestingly, Favre previously estimated a fluorescence lifetime of 5 ps for the 2-keto, 4-thione tautomeric form of 4-thiouridine in the S$_1(n\pi^*)$ state in acetonitrile at room temperature [34]. This value agrees remarkably well with the first fluorescence lifetime measured by Wenska and co-workers for 2′,3′,5′-tri-O-acetyl-4-thiouridine in the same solvent, which the authors assigned to S$_2(\pi\pi^*)$ state emission instead [10]. Regardless, most of the S$_2(\pi\pi^*)$ population in 2′,3′,5′-tri-O-acetyl-4-thiouridine decays by nonradiative relaxation pathways, as fluorescence emission amounts to only $1 \times 10^{-4}$ in acetonitrile [10]. Therefore, the relevance of this phototautomerization mechanism to the photochemistry of the 4-thiouracil derivatives is expected to be minor at best.

Recently, Gustavsson and co-workers (Gustavsson and Crespo-Hernández, unpublished results) performed the first femtosecond fluorescence up-conversion study on a thiobase (IRF = 325 fs, 76 MHz, 40 mW). They investigated 4-thiodeoxythymidine in aqueous buffer solution exciting at 267 nm. Figure 5 shows the fluorescence decay signals at 380 nm and 420 nm. Preliminary analysis

**Fig. 5** Decay traces obtained from fluorescence up-conversion for 4-thiodeoxythymidine following 267 nm excitation. The traces observed at 380 nm and 420 nm yield the same biexponential decay lifetimes for the compound (Gustavsson and Crespo-Hernández, unpublished results)
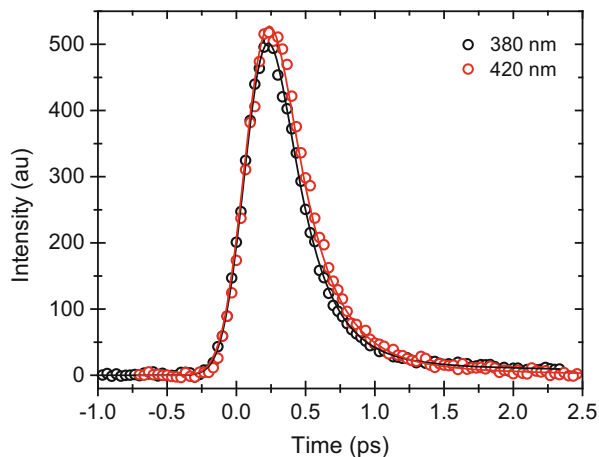
of the data indicates that two exponentials are needed to fit the fluorescence decay signals. The first lifetime has a value of $(0.23 \pm 0.03)$ ps and its amplitude accounts for 97% of the total fluorescence intensity. The magnitude of this lifetime is in excellent agreement with the intersystem crossing lifetime of $(0.24 \pm 0.02)$ ps reported earlier by Reichardt and Crespo-Hernández for 4-thiodeoxythymidine upon 340 nm excitation in the same solvent (see below) [18]. The second lifetime has a value of a few picoseconds and accounts for only 3% of the total fluorescence intensity. Evidently, more experimental and computational work is needed to understand the origin of the multiexponential fluorescence decay lifetimes in the 4-thiouracil derivatives in solution [10, 200].

### 3.1.2 Triplet State Dynamics

The photophysical properties of the $T_1$ state of the 4-thiouracil derivatives at room temperature have been investigated using time-resolved phosphorescence spectroscopy and transient absorption spectroscopy with nanosecond and femtosecond time resolution (Tables 11, 12, and 13) [11, 13, 17–19, 34, 35, 196, 200, 201, 203, 206, 207]. Calculations [17, 18, 196, 203] and experimental results agree that the $T_1$ state has primarily $\pi\pi^*$ character and can decay by radiative (minor pathway; $\Phi_{Ph} \sim 10^{-2}$ to $10^{-4}$) and nonradiative (major pathway; $\Phi_{NR} \geq 0.99$) processes (Table 11). Most experimental work shows that the $T_1$ state of the 4-thiouracil derivatives is populated with near-unity triplet yield. In addition, experimental results show that a fraction of the $T_1(\pi\pi^*)$ state population can be quenched (1) by the solvent, (2) by bimolecular collision with another solute molecule in the ground state at diffusion-controlled rates (i.e., by triplet self-quenching), and (3) by molecular oxygen, resulting in the generation of high yields of singlet oxygen (Tables 9 and 13). The $T_1(\pi\pi^*)$ state of the 4-thiouracil derivatives is also quenched by (or reacts with) nucleic acid bases and amino acids and is involved in photooxidation,

**Table 11** Radiative and nonradiative decay properties and photochemical quantum yields of some thiobase derivatives

| | $k_{Ph} \times 10^2$ $(s^{-1})^a$ | $\Phi_{NR}^b$ | $k_{NR} \times 10^5$ $(s^{-1})^c$ | $\Phi_{Pch} \times 10^{-3\ d}$ | Technique, time resolution | Experimental conditions[e] |
|---|---|---|---|---|---|---|
| 4tUra | – | – | – | 1 | – | H$_2$O, pH 6 [34] |
| 4tUrd | – | – | – | 1 | – | H$_2$O [34] |
| Ac-4tUrd | 12.5 | >0.99 | >4.9 | – | TAS, 8 ns | ACN, Ar [13] |
| | 8.1 | 0.99 | 0.6 | 8 | TAS, 8 ns | CCl$_4$, He [201] |
| 4tThy | – | – | – | 2 | – | H$_2$O pH 6 [34] |
| 4 t-dThd | – | – | 2.4 ± 1.0 | – | TRTL, 30 ns | ACN, Ar [11] |
| F-4tUrd | 2.6 | 0.99 | 0.7 | 10 | TAS, 8 ns | CCl$_4$, He [201] |
| Cl-4tUrd | 5.3 | 0.99 | 2.0 | 1 | TAS, 8 ns | CCl$_4$, He [201] |
| Br-4tUrd | 20.5 | 0.99 | 5.2 | 5 | TAS, 8 ns | CCl$_4$, He [201] |
| I-4tUrd | 125 | 0.98 | 408 | 21 | TAS, 8 ns | CCl$_4$, He [201] |
| Pr-4tUra | 2.7 | – | 0.6 | <1 | TAS, 8 ns | PFDMCH, Ar [203] |
| Pr-4tThy | 1.9 | – | 0.4 | <1 | TAS, 8 ns | PFDMCH, Ar [203] |
| DMTU | – | – | – | 0.7 | – | H$_2$O, Ar [34] |
| | 4.2 | >0.99 | – | <10 | TCSPC, 2 ps | CCl$_4$ [200] |
| | 2.8 | >0.99 | 1.9 | <10 | TCSPC, 2 ps | PFDMCH [200] |
| CD3-4tUra | 5.3 | – | 1.6 | <1 | TAS, 8 ns | PFDMCH, Ar [203] |
| 2tThy | 1.2 | ~0.9 | 1 | 8 | TAS, 300 fs | ACN, Ar [31] |
| 2tThd | <2.8 | ~0.9 | 25 | 2 | TAS, 300 fs | ACN, Ar [31] |
| 2 t-dThd | <1.7 | ~0.9 | 15 | 2 | TAS, 300 fs | ACN, Ar [31] |
| 6tPur | – | – | – | 0.6 ± 0.1 | TAS, 8 ns | PBS, pH 5.8, Ar [208] |
| Ac-6tIno | 0.60 | >0.99 | >3.1 | <1 | TAS, 8 ns | ACN, Ar, [13] |

[a]Phosphorescence rate constant
[b]Quantum yield of non-radiative decay
[c]Non-radiative decay rate constant
[d]Photochemical quantum yield
[e]Under air-saturated conditions unless otherwise noted

photoreduction, and photoaddition reactions [34]. Those reactions will not be discussed further in this chapter. Triplet–triplet annihilation and triplet self-quenching in tens to hundreds of picoseconds have also been proposed for aggregates or weakly-interacting ground-state complexes of 4-thiodeoxythymidine [18, 19]; however, the evidence gathered for such molecular complexes is still inconclusive and further scrutiny is warranted.

Because of the high physical and chemical reactivity of the T$_1$($\pi\pi^*$) state of 4-thiouracil derivatives in solution, a property which is also shared by other thiobases in general, attempts have been made to use weakly interacting, chemically inert solvents and extrapolation of the photophysical results to infinite dilution conditions in order to determine the primary intramolecular decay pathways. In general, solvent quenching dominates the deactivation of the T$_1$($\pi\pi^*$) state in

**Table 12** Intersystem crossing lifetimes and quantum yields of some thiobase derivatives

| | $\tau_{ISC}$ (ps)[a] | $\Phi_{ISC}$[b] | Technique, time resolution | Experimental conditions[c] |
|---|---|---|---|---|
| 4tUrd | – | $0.90 \pm 0.1$ | TAS, 7 ns | $H_2O$, Ar, 20 μM [196] |
| | – | $0.67 \pm 0.17$ | LIOAS, 15 ns | $H_2O$, Ar, 50 μM [144] |
| | – | $0.61 \pm 0.15$ | LIOAS, 15 ns | ACN, Ar, 50 μM [144] |
| | – | 0.02 [d] | TAS, 25 ns | ACN, Ar [207] |
| 4tThd | – | $0.85 \pm 0.15$ | TAS, 200 fs | PBS, pH 7.4, 400 μM [18] |
| | – | $1.0 \pm 0.1$ | TRTL, 30 ns | ACN, Ar [11] |
| 4 t-dThd | $0.24 \pm 0.02$ | – | TAS, 200 fs | PBS, pH 7.4, 400 μM [18] |
| | $0.54 \pm 0.01$ | – | TAS, 200 fs | ACN, 250 μM [19] |
| DMTU | | $1.0 \pm 0.1$ | TAS, 7 ns | $H_2O$, Ar, 20 μM [196] |
| 2tUra | $0.35 \pm 0.06$ | – | TAS, 200 fs | PBS, pH 7.4, <2 mM [32] |
| | $0.34 \pm 0.09$ | – | TAS, 200 fs | ACN, <2 mM [32] |
| 2tThy | $0.62 \pm 0.07$ | – | TAS, 200 fs | PBS, pH 7.4, <2 mM [32] |
| | $0.32 \pm 0.09$ | – | TAS, 200 fs | ACN, <2 mM [32] |
| | – | $1.00 \pm 0.05$ | TAS, 20 ns | ACN, Ar [16] |
| | – | $0.9 \pm 0.1$ | TAS, 300 fs | ACN, Ar [31] |
| 2tThd | – | $0.9 \pm 0.1$ | TAS, 300 fs | ACN, Ar [31] |
| 2 t-dThd | – | $0.9 \pm 0.1$ | TAS, 300 fs | ACN, Ar [31] |
| 6tGuo | $0.31 \pm 0.05$ | $0.8 \pm 0.2$ | TAS, 200 fs | PBS, pH 7.0, 200 μM [22] |
| | $0.36 \pm 0.04$ | – | TAS, 200 fs | ACN, 50 μM [22] |
| 6tPur | – | 0.99 | TAS, 6 ns | ACN [195] |

[a]Lifetime of intersystem crossing
[b]Intersystem crossing quantum yield
[c]Thiobase derivative concentrations are given; solutions were under air-saturated conditions unless otherwise noted
[d]Calculated to infinite dilution

polar solvents, whereas triplet self-quenching plays an important role in less polar solvents, even at low concentrations ($<10^{-5}$ M, see Table 13).

Wenska and co-workers [203] also investigated the intramolecular decay pathways of the triplet state in a group of 4-thiouracil derivatives in PFDMCH. The authors used steady-state absorption and emission spectroscopy, *ab initio* calculations in vacuum at the EOM-CC2/aug-cc-pVDZ level of theory, and time-resolved emission spectroscopy. The set of compounds was comprised of 1-propyl-4-thiouracil, 1-propyl-4-thiothymine, 1,3-dimethyl-4-thiouracil, and 1-methyl-3-trideuteriomethyl-4-thiouracil (Tables 12 and 13). In the absence of triplet self-quenching and solvent-induced deactivation, the $T_1(\pi\pi^*)$ state was shown to decay overwhelmingly by an intramolecular nonradiative pathway ($T_1 \rightarrow S_0$). It was observed that the trend of the rate of nonradiative decay correlates with the magnitude of the $T_2(n\pi^*) - T_1(\pi\pi^*)$ energy gap; the smaller the energy gap the larger the rate. This led the authors to propose that mixing of the $T_2(n\pi^*)$ and $T_1(\pi\pi^*)$ states via vibronic coupling involving out-of-plane vibrational modes can explain the trend of nonradiative decay rate constants in these 4-thiouracil derivatives. It was concluded that the methyl substituents at both the N3 and C5 positions of the 4-thiouracil ring influence, to different extents, the energy and electronic

**Table 13** Triplet state lifetime and self-quenching rate of the 4-thiouracil derivatives

| | $\tau_{T \to S_0}$ (μs)[a] | $k_{SQ} \times 10^9$ $(M^{-1} s^{-1})$[b] | Technique, time resolution | Experimental conditions[c] |
|---|---|---|---|---|
| 4tUrd | 0.32[d] | – | TAS, 7 ns | $H_2O$, Ar, 20 μM [196] |
| | 0.20 | – | TCSPC | $H_2O$ [35] |
| | 0.31 | – | TCSPC/LIOAS, 15 ns | $H_2O$, Ar, 50 μM [144] |
| | 0.25[e] | 2 | TAS, 25 ns | $H_2O$, Ar [207] |
| | 1.06 | – | TCSPC/LIOAS, 15 ns | ACN, Ar, <50 μM [144] |
| | 0.29 | – | TAS, 7 ns | ACN, Ar, 20 μM [196] |
| | 2.0[e] | 5 | TAS, 25 ns | ACN, Ar [207] |
| Ac-4tUrd | 2.0[e] | 5.1[e] | TAS, 8 ns | ACN, Ar [13] |
| | 15.2[e] | 5.0[e] | TAS, 8 ns | $CCl_4$, He [201] |
| DMTU | 0.22[f] | – | TAS, 7 ns | $H_2O$, Ar, 20 μM [196] |
| | 0.15 | – | TAS, 7 ns | ACN, Ar, 20 μM [196] |
| | 3.6[e] | 5.2[e] | TAS, 8 ns | $CCl_4$ [200] |
| | 5.3[e] | 8.0[e] | TAS, 8 ns | PFDMCH [200] |
| CD3-4tUra | 6.0[e] | 8.0[e] | TAS, 8 ns | PFDMCH, Ar [203] |
| Pr-4tUra | 17.2[e] | 8.0[e] | TAS, 8 ns | PFDMCH, Ar [203] |
| 4 t-dThd | $4.2 \pm 3.0$[e,g] | $7.8 \pm 0.4$[e] | TRTL, 30 ns | ACN, Ar [11] |
| Pr-4tThy | 22.2[e] | 8.0[e] | TAS, 8 ns | PFDMCH, Ar [203] |
| F-4tUrd | 13.2[e] | 4.7[e] | TAS, 8 ns | $CCl_4$, He [201] |
| Cl-4tUrd | 4.9[e] | 3.4[e] | TAS, 8 ns | $CCl_4$, He [201] |
| Br-4tUrd | 1.9[e] | 4.4[e] | TAS, 8 ns | $CCl_4$, He [201] |
| I-4tUrd | 0.024[e] | – | TAS, 8 ns | $CCl_4$, He [201] |

[a]Lifetime of triplet state
[b]Self-quenching rate constant
[c]Concentrations given are of the thiobase derivatives in solution; solutions were under air-saturated conditions unless otherwise noted
[d]$T_1$ absorption band maximum at 540 nm with an extinction coefficient of 2,400 $M^{-1}$ $cm^{-1}$
[e]Calculated to infinite dilution
[f]$T_1$ absorption band maximum at 590 nm with an extinction coefficient of 2,500 $M^{-1}$ $cm^{-1}$
[g]$T_1$ absorption band maximum at 520 nm with an extinction coefficient of 2,800 $M^{-1}$ $cm^{-1}$

configuration of the $T_1(\pi\pi^*)$ state [203]. In related work [201], an increase in the nonradiative rate constant (Table 11) was observed with increasing atomic number of the halogen atom in the $2',3',5'$-tri-$O$-acetyl-4-thio-5-halogenouridine series (i.e., with C5–X=F, Cl, Br, or I). This trend with increasing atomic number of the halogen was also embodied by a corresponding decrease in phosphorescence quantum yield and shortening of triplet state lifetime (Table 13). These observations were explained as a result of the heavy atom effect imparted by the halogen.

Taras-Goślińska et al. [200] reported an intrinsic triplet decay lifetime for 1,3-dimethyl-4-thiouracil of $\tau_{T_1}^0 = 5.3$ μs at infinite dilution in a PFDMCH solution, while an intrinsic triplet decay lifetime of $\tau_{T_1}^0 = 3.6$ μs was measured for the same compound in $CCl_4$. The longest intrinsic triplet decay lifetime measured thus far is for $2',3',5'$-tri-$O$-acetyl-4-thiouridine ($\tau_{T_1}^0 = 15.2$ μs) using $CCl_4$ as a solvent

[201]. This value is about four times longer than the intrinsic lifetime reported above for 1,3-dimethyl-4-thiouracil in the same solvent (Table 13). The striking difference in the intrinsic triplet lifetimes between these two compounds was proposed to be a result of reversible intramolecular hydrogen abstraction in the $T_1(\pi\pi^*)$ state of 1,3-dimethyl-4-thiouracil from the ortho methyl group to the sulfur atom of the thiocarbonyl group [201]. However, recent work [203] using the deuterated compound (1-methyl-3-trideuteriomethyl-4-thiouracil) in PFDMCH has shown that the reversible intramolecular H-abstraction pathway is insignificant. These results provide clear evidence of the limitations of using solution phase experiments to uncover the intrinsic excited-state properties of thiobases in general. Another major limitation of using weakly interacting, chemically inert solvents to characterize intramolecular relaxation pathways is that most of the thiobase derivatives are not soluble (or not soluble enough) in these solvents. It is evident that more experimental and computational work is necessary to unravel the intramolecular relaxation pathways in these 4-thiouracil derivatives and other thiobases. Spectroscopic experiments in the gas phase, as those performed successfully for a wide variety of the DNA and RNA nucleobase derivatives [1, 3, 9], are expected to be particularly informative.

### 3.1.3 Excited-State Deactivation Mechanism in 4-Thiouracil Derivatives

Suzuki and co-workers [11] investigated the excited-state dynamics of 4-thiodeoxythymidine by using a combination of time-dependent density functional theory (TD-DFT) calculations, time-resolved thermal lensing, and nanosecond transient absorption spectroscopy. Excitation was performed using 6-ns laser pulses at 355 nm. A triplet quantum yield of $1.0 \pm 0.1$ was reported in acetonitrile. Based on vertical TD-DFT calculations, the authors proposed a kinetic model in which internal conversion from the $S_2(\pi\pi^*)$ to the $S_1(n\pi^*)$ state is followed by intersystem crossing to the $T_1(\pi\pi^*)$ state with a quantum yield of unity [11]. However, the authors were unable to corroborate the proposed mechanism because of the nanosecond time resolution of their experimental setup.

Harada et al. [17] and Reichardt and Crespo-Hernández [18, 19] performed the first femtosecond transient absorption experiments on a thiobase in an effort to rationalize the efficient population of the triplet state in 4-thiodeoxythymidine. Harada et al. [17] performed the time-resolved experiments in aqueous solution, exciting at 263 nm with a time resolution of 0.5 ps. The transient absorption signals were measured at 500 nm and 570 nm probe wavelengths. As shown in Fig. 6, the signal at 570 nm appears within the time resolution of the instrument and then partially decays during the first 10 ps. A fraction of the absorption signal at 500 nm is also observed within the instrument response function, but at this probe wavelength the amplitude continues to grow with a lifetime that corresponds to the partial decay observed at 570 nm. No further changes were observed in transient spectra after 10 ps, suggesting that the relaxation processes were completed within

**Fig. 6** Time profiles measured at (**a**) 500 nm and (**b**) 570 nm for the transient absorption of 4-thiodeoxythymidine in phosphate buffer solution (pH 7.4) following 263 nm excitation. Adapted with permission from [17]. Copyright 2010 American Chemical Society
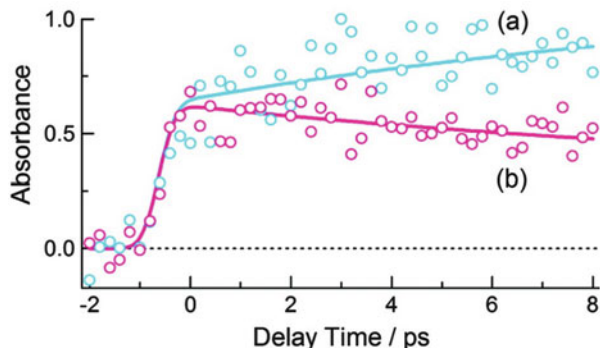


that time interval. After 10 ps, the transient spectrum resembles that assigned previously to the triplet state of the 4-thiodeoxythymidine in acetonitrile [11], which led the authors to propose that population of the $T_1(\pi\pi^*)$ state is completed within the initial 10 ps.

Harada et al. [17] presented two plausible kinetic models to explain the relaxation process leading to the population of the $T_1(\pi\pi^*)$ state. In the first model, the 10 ps relaxation pathway was assigned to vibrational cooling in the $T_1(\pi\pi^*)$ state, populated on an ultrafast time scale from the $S_2(\pi\pi^*)$ or the $S_1(n\pi^*)$ state. In the second model, the 10 ps relaxation pathway was assigned to slow internal conversion from the $S_2(\pi\pi^*)$ state to the $S_1(n\pi^*)$ state. According to the authors, the large energy gap (10,000 cm$^{-1}$) between these two states, determined from TD-B3LYP/6-31G($d,p$) vertical excitation energies, support this assignment, and the 10 ps relaxation process should be assigned to the lifetime of the $S_2(\pi\pi^*)$ state [17]. Regardless of which pathway explains the 10 ps relaxation process, the authors concluded that intersystem crossing from the $S_1(n\pi^*)$ state to the $T_1(\pi\pi^*)$ state should be more favorable than from the $S_2(\pi\pi^*)$ state to the $T_2(n\pi^*)$ state, based on the spin-orbit coupling interaction energies calculated at the CASSCF (16,11)/cc-pVDZ levels of theory [17].

Reichardt and Crespo-Hernández [18, 19] also investigated the excited-state dynamics of 4-thiodeoxythymidine, but arrived at quantitatively different conclusions than Harada et al. [17]. The authors used a broadband transient absorption setup with an instrument response function of $(200 \pm 50)$ fs. The experiments were performed exciting at 340 nm or 360 nm in aqueous buffer solution (pH 7.4), in acetonitrile, and in an ionic liquid. Figure 7 shows the changes in the transient absorption spectra in aqueous buffer solution after excitation at 340 nm. At delay times shorter than 170 fs, the transient absorption spectra show three transient absorption bands. The two bands with negative amplitudes ($\Delta A$) were assigned to ground-state bleaching (short-wavelength band) and stimulated emission (long-wavelength band) from the $S_2(\pi\pi^*)$ state, in agreement with the steady-state spectra shown in Fig. 4b [18]. The absorption band with positive amplitude above 520 nm develops in less than 2 ps to a transient spectrum that was assigned to triplet state absorption. This intersystem crossing relaxation pathway has a lifetime of
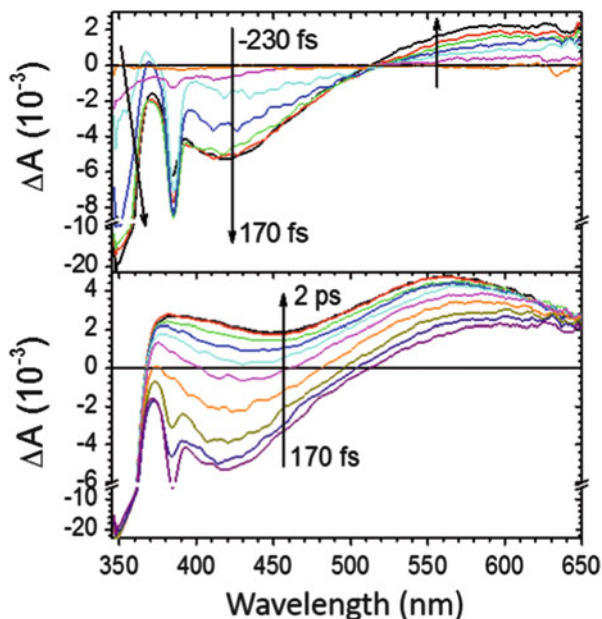
$(0.24 \pm 0.02)$ ps, which results in the population of the $T_1(\pi\pi^*)$ state with an 85% yield in aqueous solution [18]. After a 2 ps time window, the authors proposed that the $T_1(\pi\pi^*)$ state decays on multiple time scales to repopulate the ground state [18]. Similar results were obtained in acetonitrile and in an ionic liquid, but the magnitudes of the lifetimes are solvent dependent [19].

The following kinetic model was proposed to explain the excited-state dynamics of 4-thiodeoxythymidine in the three solvents investigated. Excitation at 340 nm or 360 nm results in population of the spectroscopic $S_2(\pi\pi^*)$ state. Most of the $S_2(\pi\pi^*)$ state population decays through a barrierless path which connects the $S_2(\pi\pi^*)$ state to the $T_1(\pi\pi^*)$ state. A negligibly small fraction of the $S_2(\pi\pi^*)$ state population decays back to the ground state by fluorescence emission, whereas no evidence of ultrafast $S_2(\pi\pi^*) \to S_0$ internal conversion was observed. The efficient and ultrafast intersystem crossing pathway was proposed to result from enhanced spin–orbit coupling interactions and increased vibrational overlap between the singlet and triplet states caused by the presence of a sulfur atom and the small energy gap between the singlet and triplet states [18, 19]. A fraction of the $T_1(\pi\pi^*)$ state population was proposed to return back to the ground state in tens to thousands of picoseconds depending on the viscosity of the solvent used [19]. Triplet self-quenching by weakly-interacting ground-state complexes and triplet–triplet annihilation were proposed to explain this fractional quenching of the $T_1(\pi\pi^*)$ state [18, 19]. However, more work is needed to identify this pathway unequivocally.

The kinetic model presented by Reichardt and Crespo-Hernández [18, 19] upon excitation of 4-thiothymine deoxyribonucleoside at 340 nm or 360 nm can be compared to that proposed by Harada et al. [17] upon excitation at 263 nm. Harada

et al. [17] proposed that intersystem crossing to the $T_1(\pi\pi^*)$ state occurs on an ultrafast time scale and in high yield, in agreement with the results by Reichardt and Crespo-Hernández [18, 19]. However, Harada et al. [17] were unable to measure the intersystem crossing rate constant and the stimulated emission process reported by Reichardt and Crespo-Hernández [18, 19], likely because of the limited time resolution of their setup. In addition, Harada et al. [17] reported a 10 ps relaxation pathway, which was assigned to either vibrational cooling in the $T_1(\pi\pi^*)$ state or to slow $S_2(\pi\pi^*) \rightarrow S_1(n\pi^*)$ internal conversion. This relaxation pathway was not observed by Reichardt and Crespo-Hernández in their work [18, 19]. In contrast, direct excitation of the $S_2(\pi\pi^*)$ state with either 340 nm or 360 nm did not provide evidence for a slow $S_2(\pi\pi^*) \rightarrow S_1(n\pi^*)$ internal conversion. Although unequivocal evidence of vibrational cooling dynamics in the $T_1(\pi\pi^*)$ state was not obtained, excitation at 263 nm may open up another relaxation pathway not accessed at 340 nm, which could lead to the population of the $T_1(\pi\pi^*)$ state with excess vibrational energy. The fluorescence up-conversion experiments reported by Gustavsson and co-workers (Gustavsson and Crespo-Hernández, unpublished results) for 4-thiodeoxythymidine exciting at 267 nm show that most of the radiative decay occurs in ~230 fs, but a minor fraction of the emissive state seems to decay on the picosecond time scale. Additional experimental and computational work is needed to characterize the 10 ps relaxation pathway reported by Harada et al. [17] upon 263 nm excitation.

## 3.2 Steady-State and Time-Resolved Photochemistry of 2-Thio- and 2,4-Dithio-Pyrimidine Derivatives

There is insufficient spectroscopic information regarding the steady-state and time-resolved photochemistry of the 2-thiouracil, 2-thiocytosine, and 2,4-dithiouracil derivatives at room temperature. Table 14 shows that substitution of the oxygen atom in position 2 of the pyrimidine ring by a sulfur atom redshifts the absorption band associated with the lowest-energy $\pi\pi^*$ electronic transition of the pyrimidine base by only ~10–35 nm. However, substitution of the oxygen atom in position 4 of the uracil or thymine ring by a sulfur atom redshifts the lowest-energy $\pi\pi^*$ electronic transition by more than 60 nm (Table 11). Similarly, the 2,4-dithiouracil derivatives show a redshift in the absorption spectra that is roughly the linear combination of the redshifts observed in the 2- and 4-thiouracil derivatives. Generally speaking, these observations are obviously related to the different mixings of the atomic orbitals involved in the electronic transitions, which lead to diverse structures of the electronic states. However, quantum-chemical calculations are required to provide a quantitative explanation of the dependence of the spectral shift of the absorption spectra on the position at which the sulfur atom is substituted.

The different electronic structures of these thiobases also have small but measurable effects on other photophysical properties, as reported in Tables 11, 12, 13,

**Table 14** Steady-state absorption properties and emission quantum yields of the 2- and 2,4-thiopyrimidine derivatives

|  | $\lambda_{max}$ (nm)[a] | $\varepsilon_{max}$ ($M^{-1}$ $cm^{-1}$)[b] | $\lambda_{em}$ (nm)[c] | $\Phi_{Ph} \times 10^{-4}$ [d] | Experimental conditions[e] |
|---|---|---|---|---|---|
| 2tUra | 274 | 14,500 | – | – | $H_2O$, pH ~ 7 [205] |
|  | 268 | 11,900 | – | – | ACN [205] |
| 2tUrd | 275 | 16,700 | – | – | $H_2O$, pH ~ 7 [205] |
|  | 268 | 10,400 | – | – | ACN [205] |
| 2tThy | 300 | 11,600 | NE | – | ACN [16] |
|  | 290 | 12,400 | NE(Fl) | – | ACN, Ar [31] |
|  |  |  | 480(Ph) | 9.8[f] |  |
| 2tThd | 285 | 14,500 | NE | <1 | ACN, Ar [31] |
| 2t-dThd | 285 | 14,100 | NE | <1 | ACN, Ar [31] |
| dtUra | 351 | 4,600 | – | – | $H_2O$, pH ~ 7 [205] |
|  | 351 | 1,000 | – | – | ACN [205] |
| dtUrd | 345 | 11,400 | – | – | $H_2O$, pH ~ 7 [205] |
|  | 351 | 10,000 | – | – | ACN [205] |
| 2tCyt | 270 | 18,200 | – | – | $H_2O$, pH ~ 7 [205] |
| 2tCyd | 270 | 14,000 | – | – | $H_2O$, pH ~ 7 [205] |

[a]Wavelength of maximum in the spectral region above ~230 nm, attributed to the $S_2(\pi\pi^*)$ state
[b]Extinction coefficient of maximum $S_2(\pi\pi^*)$ absorption
[c]Peak emission wavelength, fluorescence (Fl) or phosphorescence (Ph) noted in parenthesis
[d]Phosphorescence quantum yield
[e]Under air-saturated conditions unless otherwise noted
[f]Calculated to infinite dilution

14, and 15. For instance, both fluorescence and phosphorescence emission at room temperature have been reported for several 4-thiouracil derivatives, albeit in very small yields, whereas only phosphorescence emission has been observed in 2-thiothymine at room temperature thus far. In addition, 2-thiothymine seems to be less effective at sensitizing singlet oxygen than the 4-thiouracil derivatives. On the other hand, the few 2-thiouracil derivatives investigated thus far show ultrafast intersystem crossing lifetimes, near-unity triplet quantum yields, and triplet self-quenching, as observed in the 4-thiouracil derivatives. In addition, the 2- and 4-thiouracil derivatives show very small photochemical degradation yields and their triplet state population decays nonradiatively back to the ground state in near-unity yield at infinite dilution conditions. Currently, it is unclear whether some of the photophysical values reported in Tables 11 and 12, or in Tables 13 and 15 are different simply because of experimental errors or because of quantitative differences in the electronic structure of the 2- and 4-thiouracil derivatives. More systematic experiments are needed before any firm conclusion can be reached regarding the steady-state and time-resolved photochemistry of these thiobases. Below, we summarize the few works that have been recently published regarding the excited-state dynamics in 2-thiouracil derivatives.

**Table 15** Triplet state properties of the 2-thioura derivatives

| | $\lambda_T$ (nm)[a] | $\varepsilon_T$ (M⁻¹ cm⁻¹)[b] | $\tau_{T \to S_0}$ (μs)[c] | $k_{SQ} \times 10^9$ (M⁻¹ s⁻¹)[d] | Technique, time resolution | Experimental conditions[e] |
|---|---|---|---|---|---|---|
| 2tUra | – | – | 0.07 | – | TAS, 10 ns | ACN, N$_2$ [209] |
| 2tThy | – | – | 2.3 | – | TAS, 10 ns | ACN, N$_2$ [209] |
| | 615 | 3,560 | 2.7 ± 0.5[f] | – | TAS, 20 ns | ACN, Ar [16] |
| | 700 | 4,800 | 9.00 ± 0.03[f] | 1.53 ± 0.05[f] | TAS, 300 fs | ACN, Ar [31] |
| | 420 | 1,600 | | | | |
| 2tThd | 700 | 4,500 | 0.40 ± 0.03[f] | 12.16 ± 2.05[f] | TAS, 300 fs | ACN, Ar [31] |
| | 420 | 1,500 | | | | |
| 2t-dThd | 700 | 4,200 | 0.64 ± 0.07[f] | 11.08 ± 1.40[f] | TAS, 300 fs | ACN, Ar [31] |
| | 420 | 1,700 | | | | |

[a]Maximum wavelength(s) of triplet absorption band

[b]Extinction coefficients of corresponding triplet absorption maximum

[c]Lifetime of triplet state

[d]Self-quenching rate constant

[e]Purging gas is noted

[f]Calculated to infinite dilution

### 3.2.1 Excited-State Deactivation Mechanism in 2-Thiouracil Derivatives

Suzuki and co-workers [16] investigated the excited-state dynamics of 2-thiothymine using the time-resolved thermal lensing technique, nanosecond transient absorption spectroscopy, and calculations at the B3LYP/6-31 + G($d$,$p$)/ PCM level of theory in acetonitrile. Excitation was performed using 20-ns laser pulses at 308 nm. The authors determined a triplet quantum yield of unity for 2-thiothymine and reported that the triplet state can sensitize singlet oxygen with a $0.36 \pm 0.02$ yield. The efficient population of the triplet state was attributed to enhanced intersystem crossing caused by the heavy-atom effect of the sulfur atom [16]. In particular, the authors proposed that substitution of the oxygen atom of the carbonyl group in position 2 of the ring by a sulfur atom leads to larger spin-orbit coupling. It also results in localization of the electron density into the HOMO or HOMO − 1 orbitals of the sulfur atom, which can increase the efficiency of intersystem crossing because of the larger overlap of the corresponding orbitals associated with the $n \to \pi$ or $\pi \to n$ one-electron transitions. Based on TD-DFT calculations, the authors presented a kinetic model in which internal conversion from the $S_2(\pi\pi^*)$ to the $S_1(n\pi^*)$ state occurs along the C=S bond elongation axis toward the $S_1$ minimum, which then intersystem crosses to the $T_1(\pi\pi^*)$ state with a quantum yield of unity [16]. As described below, the key role of the $S_1(n\pi^*)$ state in the efficient and ultrafast population of the $T_1(\pi\pi^*)$ state has been corroborated recently by experimental [32] and computational methods [29].

Taras-Goślińska et al. [31] investigated the radiative and nonradiative decay pathways of the $T_1(\pi\pi^*)$ state in 2-thiothymine and of its DNA and RNA nucleosides in acetonitrile. The authors used absorption, emission, and circular dichroism spectroscopic techniques, as well as nanosecond ($\lambda_{exc} = 266$ nm) and femtosecond

transient absorption ($\lambda_{exc}$ = 266 or 303 nm; IRF = 300 fs) spectroscopic techniques. As suggested by Suzuki and co-workers for 2-thiothymine earlier [16], the authors proposed that intersystem crossing occurs on an ultrafast time scale and with near-unity quantum yields, independent of the substituent in the N1 position (i.e., H, riboside, or deoxyriboside). In addition, it was shown that, in the absence of triplet self-quenching, nonradiative decay of the $T_1(\pi\pi^*)$ state is the primary relaxation pathway (Table 11). Noticeably, substitution of the H1 atom for a ribose or deoxyribose group results in an enhanced nonradiative decay of the $T_1(\pi\pi^*)$ state in 2-thiothymine. The enhanced nonradiative decay of the $T_1(\pi\pi^*)$ state hinders phosphorescence emission in the nucleosides, whereas a weak phosphorescence was detected in 2-thiothymine at room temperature (Table 14). It was suggested that addition of the sugar results in an increased number of vibrational and torsional modes in the nucleosides, which increases the Franck–Condon factors for nonradiative decay [31]. However, it is not clear if covalent addition of a sugar group at position 1 of 4-thiouracil or 4-thiothymine also reduces the phosphorescence emission because the values reported in Table 10 were obtained by different groups and under different experimental conditions. The role of the N-glycosidic group on the nonradiative decay mechanism of the 2-thiothymine derivatives echoes that presented in Sect. 2.4 for the nucleic acid bases, but more work is needed before making direct comparisons or arriving at any major conclusion.

The femtosecond laser experiments performed by Taras-Goślińska et al. were unable to determine the intersystem crossing rate of 2-thiothymine because of their limited time resolution [31], but did reveal small changes in the transient absorption spectra over a 1–20 ps time window in acetonitrile. The amplitude of the absorption bands from ~350 nm to 600 nm decreases during this time window, whereas the amplitude of the absorption band from ~600 nm to 650 nm (the highest probe wavelength used) increases during the same time scale. The authors suggested that these changes are associated with vibrational cooling dynamics in the $T_1(\pi\pi^*)$ state with a lifetime of 3.4 ps, but no evidence was provided to support this.

Pollum and Crespo-Hernández [32] presented the first experimental report providing evidence of the involvement of the $S_1(n\pi^*)$ state in the ultrafast and efficient population of the $T_1(\pi\pi^*)$ state in 2-thiothymine and 2-thiouracil. These experiments were performed exciting at 316 nm in aqueous buffer solution and in acetonitrile (Fig. 8). The authors used a global and target analysis method based on a sequential kinetic model to extract the lifetimes and the decay-associated spectra from the multidimensional transient absorption data. Two lifetimes plus a time-independent offset were required to fit the time-resolved spectra during the initial ~3 ns time window. The first, sub-picosecond lifetime was assigned to intersystem crossing from the $S_1(n\pi^*)$ to the $T_1(\pi\pi^*)$ state, which depends on the thiobase and the solvent used (Table 15). The second, tens-of-picoseconds lifetime was tentatively assigned to triplet self-quenching by weakly bound ground-state complexes. Its magnitude depends on the solvent and concentration used, as has previously been reported for 4-thiodeoxythymidine [18, 19]. This pathway only accounts for a small fraction of the $T_1(\pi\pi^*)$ state decay in 2-thiothymine and 2-thiouracil, while
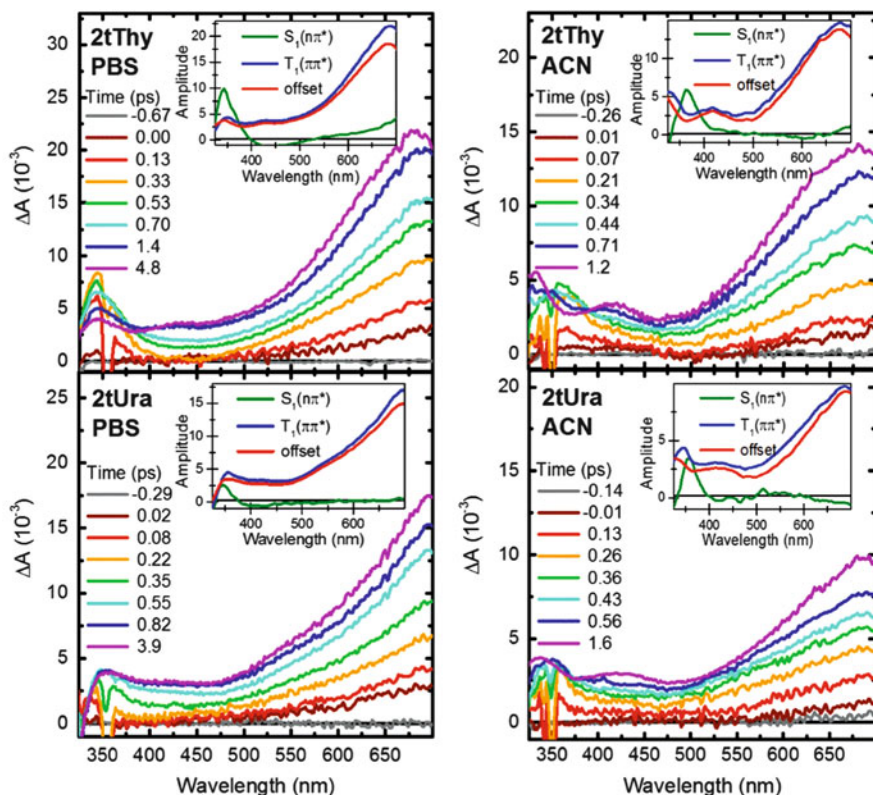
**Fig. 8** Transient absorption spectra of 2-thiothymine (2tThy) and 2-thiouracil (2tUra) in pH 7.4 buffer solution (PBS) and acetonitrile (ACN) following 316 nm excitation. Spectra are given from time zero to the peak of the band in the visible. Stimulated Raman emission is observed around 350 nm at short time delays (negative-amplitude peak centered at 350 nm). The decay-associated spectra for each sample are *inset* in their respective graphs. Modified with permission from [32]. Copyright 2014, AIP Publishing LLC

most of the triplet state population decays nonradiatively to the ground state on the microsecond time scale [31].

In contrast to the report by Taras-Goślińska et al. [31] with 2-thiothymine, no evidence of vibrational cooling in the $T_1(\pi\pi^*)$ state was reported by these authors [32]. Instead, the authors proposed that excitation at 316 nm results in the direct population of the spectroscopic $S_2(\pi\pi^*)$ state in both 2-thiouracil derivatives. The $S_2(\pi\pi^*)$ state internally converts through a conical intersection [29] to populate the $S_1(n\pi^*)$ state with a lifetime which is faster than the time resolution of their experimental setup (i.e., $\tau < 200$ fs). The population in the $S_1(n\pi^*)$ state intersystem crosses in hundreds of femtoseconds to populate the $T_1(\pi\pi^*)$ state with a near-unity yield, as observed by others [16, 31]. The insets of Fig. 8 show the $S_1(n\pi^*)$ and $T_1(\pi\pi^*)$ decay associated spectra of 2-thiothymine and 2-thiouracil reported by

these authors [32]. The resemblance of the decay-associated spectra assigned to the $S_1(n\pi^*)$ state absorption to the transient absorption spectra reported for the $S_1(n\pi^*)$ state in uracil and thymine monomers [105, 140, 159] lends support to their assignment.

The sequential kinetic model proposed by Pollum and Crespo-Hernández [32] is also supported by the high-level, multiconfigurational calculations performed by Cui and Fang [29]. The authors reported the excited-state relaxation pathways for 2-thiouracil in vacuum at the CASPT2/cc-pVDZ//CASSCF(16,11)/6-31 + G* level of theory, used as the archetypal chromophore of 2-thiothymine [29]. Optimized minimum energy structures, crossing points, and conical intersections between the three lowest-energy singlet and triplet states were reported. On the basis of the computed potential energy profiles and spin-orbit couplings, the authors presented three competitive nonadiabatic relaxation pathways that can lead to the efficient population of the $T_1(\pi\pi^*)$ state from the initially populated $S_2(\pi\pi^*)$ state: (1) $S_2(\pi\pi^*) \rightarrow S_1(n\pi^*) \rightarrow T_1(\pi\pi^*)$; (2) $S_2(\pi\pi^*) \rightarrow T_2(n\pi^*) \rightarrow T_1(\pi\pi^*)$; and (3) $S_2(\pi\pi^*) \rightarrow T_3(n\pi^*) \rightarrow T_2(n\pi^*) \rightarrow T_1(\pi\pi^*)$. The relaxation pathways proposed by these authors are shown in Fig. 9. Cui and Fang [29] also found a conical intersection between the $S_1/S_0$ states, but calculations suggest that this relaxation pathway cannot be accessed because it is too high in energy (136.0 kcal/mol) compared to the vertical energy of the $S_2(\pi\pi^*)$ state (102.9 kcal/mol).

According to the authors, the primary nonadiabatic relaxation pathway involves ultrafast internal conversion from the $S_2(\pi\pi^*)$ state to the $S_1(n\pi^*)$ state, which is mediated by an $S_2/S_1$ conical intersection (Fig. 9a) [29]. The population reaching the $S_1(n\pi^*)$ state then decays to the $T_1(\pi\pi^*)$ state through a minimum energy crossing point which has a spin-orbit coupling interaction of 121.01 cm$^{-1}$. The second decay pathway involves intersystem crossing to the $T_2(n\pi^*)$ state directly from the $S_2(\pi\pi^*)$ potential energy surface. Once the population has arrived at the $T_2(n\pi^*)$ state, it can internally convert to the $T_1(\pi\pi^*)$ state through a $T_2/T_1$ conical intersection (Fig. 9b). The third relaxation pathway predicted by the calculations is intersystem crossing from the $S_2(\pi\pi^*)$ state to the $T_3(n\pi^*)$ state via an $S_2/T_3$ crossing minimum (Fig. 9c). The authors suggest that internal conversion from the $T_3(n\pi^*)$ to the $T_2(n\pi^*)$ state should be efficient because the energy gap between these states is high (3 kcal/mol) at the avoided crossing, through which the $T_3(n\pi^*)$ state can directly arrive at the $T_2/T_1$ conical intersection. Based on the magnitude of the spin-orbit coupling interactions and the relative energy of minimum crossing points calculated between the singlet and triplet states above, the authors proposed that pathways (2) and (3) should not be as efficient as pathway (1), but could also play a role in the population of the $T_1(\pi\pi^*)$ state in solution [29]. The experimental results presented by Pollum and Crespo-Hernández [32] suggest that pathway (1) plays a major role in the efficient population of the $T_1(\pi\pi^*)$ state in solution. Further mechanistic insights on the extent of participation of the nonadiabatic pathways predicted by the static calculations of Cui and Fang are necessary. Here quantum dynamical calculations are expected to play a leading role.

**Fig. 9** Possible relaxation pathways from the $S_2(\pi\pi^*)$ of 2-thiouracil proposed by CASPT2 calculations: (**a**) $S_2(\pi\pi^*) \rightarrow S_1(n\pi^*) \rightarrow T_1(\pi\pi^*)$; (**b**) $S_2(\pi\pi^*) \rightarrow T_2(n\pi^*) \rightarrow T_1(\pi\pi^*)$; (**c**) $S_2(\pi\pi^*) \rightarrow T_3(n\pi^*) \rightarrow T_2(n\pi^*) \rightarrow T_1(\pi\pi^*)$. Adapted with permission from [29]. Copyright 2013, AIP Publishing LLC
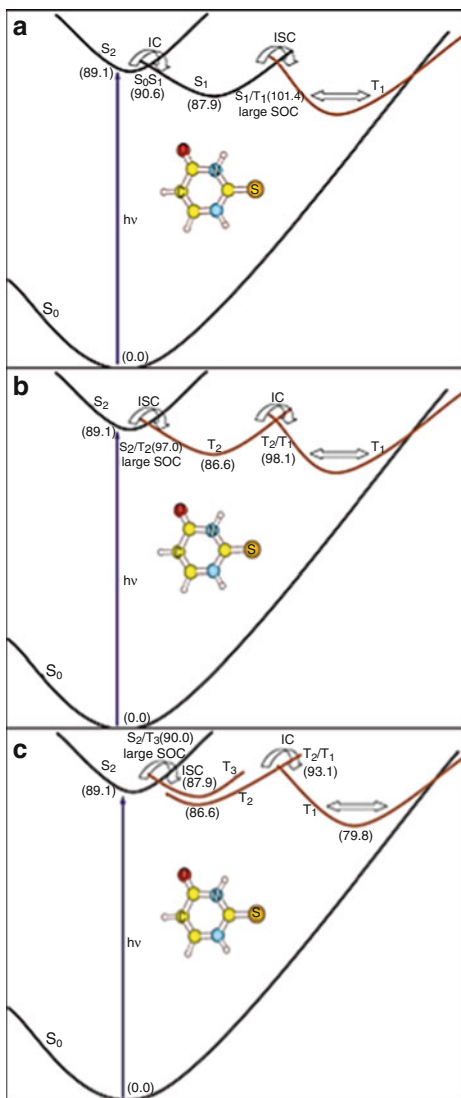


## 3.3 Steady-State and Time-Resolved Photochemistry of 6-Thiopurine Derivatives

Similar to the 2-thiopyrimidine derivatives, few investigations have been performed regarding the photophysics and excited-state dynamics of the 6-thiopurine derivatives. As in 4-thiouracil derivatives, the absorption spectrum of 6-thiopurine in the UVA spectral region shows an intense band with maximum at 331 nm and a weak absorption shoulder at ca. 430 nm in tetrahydrofuran [195]. These absorption bands

were assigned to electronic transitions from the ground state to the $S_2(\pi\pi^*)$ and the $S_1(n\pi^*)$ states, respectively. In general, the $\pi\pi^*$ electronic transition of the 6-thiopurine derivatives shifts from ca. 290 nm to 346 nm depending on the solvent used (Table 16). The $n\pi^*$ transition appears as an absorption tail to the red of the lowest-energy $\pi\pi^*$ transition. The absorption spectra shift to higher energies in basic pH, which correlates with the $pK_a$ of the 6-thiopurine chromophore and has been attributed to tautomerization from the N9H to the N7H form [210, 211].

The fluorescence spectra and fluorescence lifetimes of 6-mercaptopurine and 6-thioguanine have been reported at neutral, acidic, and basic pHs [212]. Tautomerization seems to play a role in the photophysics at different pHs [212]. The fluorescence decay of 6-thiopurine upon excitation at 365 nm is characterized by two lifetimes with values of $1.215 \pm 0.006$ ns and $17.3 \pm 0.6$ ns, with fluorescence amplitudes of 0.933 and 0.005,[2] respectively. In the case of 6-thioguanine, the fluorescence decay is characterized by two lifetimes of $1.4 \pm 0.3$ ns and $24.1 \pm 0.5$ ns, with fluorescence amplitudes of 0.48 and 0.94 (see footnote 2), respectively [212]. The two lifetimes were assigned to emission originating from the lowest-energy $^1\pi\pi^*$ states of the 6-thione (N9H) and (N7H) tautomers. The N9H and N7H tautomers have been previously reported to exist in 21% and 79% amounts in neutral aqueous solutions [210, 211], respectively. The significance of the fluorescence decay pathway in the overall excited-state electronic relaxation mechanism is unclear, however, since fluorescence quantum yields have not been reported.

On the other hand, fluorescence emission was not observed in 6-thiopurine in tetrahydrofuran at room temperature, which suggests that most of the excited-state dynamics in this solvent environment occur through nonradiative decay pathways. Lack of fluorescence emission was also reported for 6-thioguanosine and 2′,3′,5′-tri-O-acetyl-thioinosine in neutral aqueous solution and acetonitrile (Table 16). Room-temperature phosphorescence with emission maximum at 485 nm was observed in 2′,3′,5′-tri-O-acetyl-thioinosine in acetonitrile, with a phosphorescence quantum yield of $2 \times 10^{-4}$ at infinite dilution [13].

As observed recently for the 2-thiothymine derivatives [31], the results reproduced in Table 17 suggest that the covalent addition of a sugar or an alkyl group to the N9 position of the 6-thiopurine chromophore increases the rate of triplet state decay. The increase in nonradiative decay upon covalent substitution at the N9 position could explain why the yield of singlet oxygen generation decreases by more than 10% on going from 6-thioguanine to 6-thioguanosine under similar experimental conditions [23, 24]. As we describe next, however, the excited-state dynamics in 6-thiopurine derivatives is poorly understood and the role played by covalent substitutions at the N9 position deserves further scrutiny.

---

[2] Usually fractional amplitudes are reported. The fluorescence amplitudes stated here are taken as given in [212].

**Table 16** Steady-state absorption and emission properties of the 6-thiopurine derivatives

| | $\lambda_{\max}$ (nm)[a] | $\varepsilon_{\max}$ (M$^{-1}$ cm$^{-1}$)[b] | $\lambda_{\mathrm{em}}$ (nm)[c] | Experimental conditions[d] |
|---|---|---|---|---|
| 6tGua | 340 | 21,000 | – | TRIS, pH 7.4 [23] |
| | 337 | 18,000 | – | NaOH , pH 10 [23] |
| | 340 | – | 400(Fl) | H$_2$O, pH 2.3 [212] |
| | 340 | – | 400(Fl), 500(Fl) | H$_2$O, pH 7.8 [212] |
| | 320 | – | 400(Fl) | H$_2$O, pH 12.3 [212] |
| 6tGuo | 342 | 23,000 | NE | PBS, pH 7.0 [22] |
| | 342 | 20,000 | – | TRIS, pH 7.4 [23] |
| | 320 | 18,000 | – | NaOH, pH 10 [23] |
| | 346 | 22,000 | NE | ACN [22] |
| 6Me-tGua | 310 | 12,000 | – | NaOH, pH 10 [24] |
| 6tPur | 321 | 17,000 | – | NaOH, pH 10 [24] |
| | 320 | – | 510(Fl) | H$_2$O, pH 2.3 [212] |
| | 320 | – | 460 to 510(Fl) | H$_2$O, pH 7.8 [212] |
| | 300 | – | 380(Fl) | H$_2$O, pH 12.3 [212] |
| | 331, 430[e] | 18,000, 20–30[e] | NE | THF, Ar [195] |
| 6tIno | 320 | 22,500 | NE[f] | PBS, pH 5.8, Ar [208] |
| Ac-6tIno | 325 | 22,500 | 485(Ph)[g] | ACN, Ar [13] |
| 6Me-tPur | 292 | 12,000 | – | NaOH, pH 10 [24] |
| Pr-6tPur | 320[h] | 25,200[h] | – | PBS, pH 5.8, Ar [21] |

[a]Wavelength of maximum absorption in the spectral region above ~230 nm, corresponds to the S$_2$($\pi\pi$*) state unless otherwise noted

[b]Extinction coefficient of maximum absorption corresponding to S$_2$($\pi\pi$*) unless otherwise noted

[c]Peak emission wavelength, fluorescence (Fl) or phosphorescence (Ph) noted in parenthesis

[d]Under air-saturated conditions unless otherwise noted

[e]Property of the S$_1$($n\pi$*) state absorption

[f]Fluorescence quantum yield $<1 \times 10^{-4}$

[g]Phosphorescence quantum yield of $2 \times 10^{-4}$ determined at infinite dilution

[h]Extrapolated from graph

### 3.3.1 Excited-State Deactivation Mechanism in 6-Thiopurine Derivatives

Early works investigated the transient absorption spectra of 6-thiopurine, also known as 6-mercaptopurine, in aqueous buffer solution at different pHs ($\lambda_{\mathrm{exc}} = 266$ nm) and in tetrahydrofuran ($\lambda_{\mathrm{exc}} = 355$ nm) using laser flash photolysis and nanosecond and picosecond transient absorption spectroscopy, respectively [13, 195, 213]. The primary photochemical processes in aqueous solution are triplet state population and photoionization. Prompt population of the triplet state was also observed in tetrahydrofuran, with a yield of 0.99. Rate constants for triplet decay, triplet self-quenching, triplet–triplet annihilation, H-abstraction by the triplet state, and triplet quenching by molecular oxygen and by other triplet quenchers in different organic solvents were reported [195]. Intrinsic triplet lifetimes and rate

**Table 17** Triplet state properties of the 6-thiopurine derivatives

| | $\lambda_T$ (nm)[a] | $\varepsilon_T$ (M$^{-1}$ cm$^{-1}$)[b] | $\tau_{T \to S_0}$ (µs)[c] | $k_{SQ} \times 10^9$ (M$^{-1}$ s$^{-1}$)[d] | Technique, time resolution | Experimental conditions [e] |
|---|---|---|---|---|---|---|
| 6tGuo | 520 | 3,400 | $0.72 \pm 0.01$ | – | TAS, 200 fs | PBS, pH 7.0, 0.2 mM [22] |
| 6tPur | – | – | 1.25[f] | 5.1[f] | TAS, 8 ns | PBS, pH 5.8, Ar [208] |
| | – | – | 4.48[f] | 4.9[f] | TAS, 6 ns | ACN [195] |
| Ac-6tIno | 675 | 3,850 | 3.2[f] | 7.4[f] | TAS, 8 ns | ACN, Ar [13] |
| Pr-6tPur | 500 | 2,800 | $1.16 \pm 0.05$[f] | $4.4 \pm 0.2$[f] | TAS, 8 ns | PBS, pH 5.8, Ar [21] |

[a]Maximum wavelength of triplet absorption band
[b]Extinction coefficient of triplet absorption maximum
[c]Lifetime of triplet state
[d]Self-quenching rate constant
[e]Concentrations given are of the thiobase derivatives in solution; solutions were under air-saturated conditions unless otherwise noted
[f]Calculated to infinite dilution

constants for self-quenching in tetrahydrofuran, 2-propanol, ethanol, and acetonitrile were reported, some of which are reproduced in Table 17. The self-quenching constants depend on the viscosity of the solvent, suggesting they are close to the diffusion-controlled limit [195]. Similar results were obtained more recently for 6-thiopurine [208] and 9-propyl-6-thiopurine [21] upon nanosecond laser excitation at 355 nm in aqueous buffer solution at pH 5.8. Attempts to determine the intersystem crossing rate constant of 6-thiopurine by using picosecond transient absorption spectroscopy (35 ps pulse duration) were unsuccessful [195] and the authors concluded that it must have a value greater than $1.3 \times 10^{10}$ s$^{-1}$.

Wenska and co-workers investigated the relaxation pathways that lead to the deactivation of the triplet state in the acetylated 6-thiopurine nucleoside, 2′,3′,5′-tri-*O*-acetyl-thioinosine, in acetonitrile. Excitation at 355 nm with 8 ns laser pulses results in the prompt population of the triplet state [13]. It was determined that nonradiative processes play a major role in the deactivation of the triplet state (Table 11), with a fraction of the triplet state population decaying by self-quenching (Table 17) [13], as observed previously in 6-thiopurine [195, 208]. Based on the El-Sayed propensity rules [214, 215] and on vertical excited-state calculations performed in acetonitrile at the CIS/CPCM/aug-cc-pVTZ level of theory, the authors proposed that intersystem crossing should occur from the $S_1(n\pi^*)$ state to the $T_1(\pi\pi^*)$ state upon direct excitation of the $S_2(\pi\pi^*)$ state, i.e., $S_2(\pi\pi^*) \to S_1(n\pi^*) \to T_1(\pi\pi^*)$. However, direct experimental evidence supporting this model was not obtained because of the limited time-resolution of their experimental setup. In addition, the authors were unable to rule out the possibility that direct intersystem crossing from the $S_2(\pi\pi^*)$ state to a high-energy triplet state could

compete with internal conversion from the $S_2(\pi\pi^*)$ state to the $S_1(n\pi^*)$ state, as has been proposed recently for 6-thioguanosine [22].

The first time-resolved investigation of a 6-thiopurine derivative with femtosecond time resolution (IRF of $200 \pm 50$ fs) was reported by Reichardt et al. in 2011 [22]. The authors investigated the excited-state dynamics of 6-thioguanosine in aqueous buffer solution (pH 7) and in acetonitrile. Excitation was performed at 340 nm. Figures 10 and 11 show the transient absorption spectra and the decay signals at representative probe wavelengths in aqueous buffer solution. The transient absorption spectra show an absorption band with negative amplitude below ~350 nm, while two bands with positive amplitudes are observed above this probe wavelength. The kinetics of the three absorption bands were fitted globally, revealing two components during the first 100 ps, with lifetimes of $0.31 \pm 0.05$ ps and $80 \pm 15$ ps in aqueous solution and $0.36 \pm 0.04$ ps and $32 \pm 5$ ps in acetonitrile. The absorption band with negative amplitude was assigned to ground state bleaching since it matches the steady-state absorption spectrum of 6-thioguanosine. The transient absorption bands with positive amplitudes are quenched by molecular oxygen and were assigned to the $T_1(\pi\pi^*)$ state absorption spectrum. The authors show that the triplet state decays back to the ground state nonradiatively, with a pseudo-first-order rate constant of $1.4 \times 10^6$ s$^{-1}$ under $N_2$-saturated conditions, for a 6-thioguanosine concentration of ca. $2 \times 10^{-4}$ M. In addition, a triplet yield of $0.8 \pm 0.2$ was reported in aqueous solution.

Figures 10 and 11 also show that a small fraction of the triplet state population (~15%) repopulates the ground state on a time scale represented by the second lifetime. Guided by vertical excited-state calculations performed at the TD-PBE0/IEFPCM/6-311++G($d,p$) level of theory, the authors proposed that the initial population in the $S_2(\pi\pi^*)$ state bifurcates in ~300 fs ($\tau_1$) to populate a high-energy triplet state (i.e., the $T_3(n\pi^*)$ state at this level of theory) and the $S_1(n\pi^*)$ state. The authors proposed that the population in the $S_1(n\pi^*)$ state decays back to the ground state in tens of picoseconds ($\tau_2$) in both solvents, explaining the fractional repopulation of the ground state on that time scale. The majority of the initial excited-state population in the $S_2(\pi\pi^*)$ state (80%) was proposed to intersystem cross to populate the $T_1(\pi\pi^*)$ state in a few hundred femtoseconds [22]. As has now been shown in a few thiobases [18, 19, 32], intersystem crossing on the femtosecond time scale is an intrinsic property also observed in other 6-thiopurine derivatives. The ultrafast intersystem crossing dynamics, together with the lack of any significant internal conversion process to the ground state (see below) [22, 27, 33], explains the near unity triplet yield and the high yield of singlet oxygen generation reported for several 6-thiopurine derivatives in Tables 12 and 6, respectively [13, 195].

The kinetic model proposed by Reichardt et al. [22] to explain the excited-state dynamics in 6-thioguanosine was scrutinized recently by Martínez-Fernández et al. [27, 33]. These authors used 6-thioguanine as a model compound and investigated its deactivation mechanism in vacuum at the MS-CASPT2//SA-CASSCF(14,12)/ANO-L level of theory [27] using a mixed quantum-classical surface hopping dynamics approach [33]. A schematic representation of the static
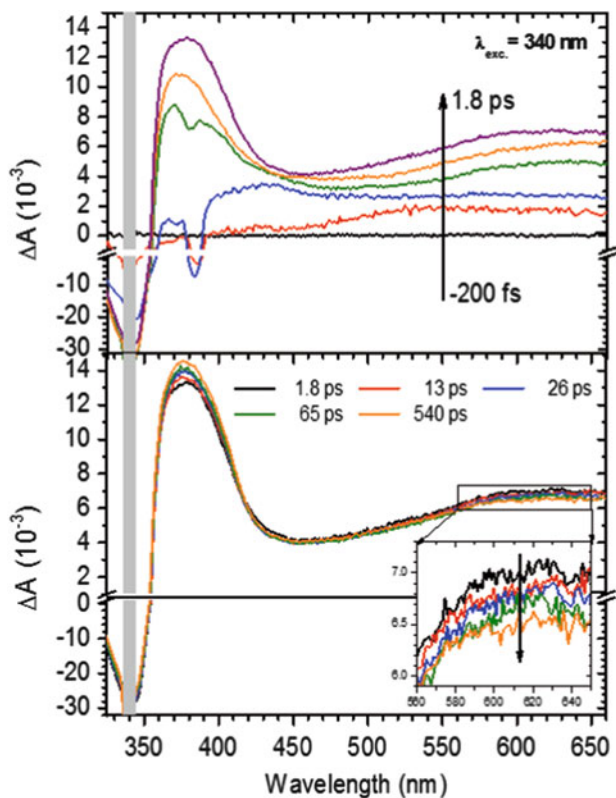
**Fig. 10** Femtosecond transient absorption spectra for 6-thioguanosine in aqueous buffer solution (pH 7.4) from −200 fs to 1.8 ps (*upper panel*) and 1.8–540 ps (*lower panel*). Stimulated Raman emission is observed around 385 nm at short time delays (negative-amplitude peak centered at 385 nm) Adapted with permission from [22]. Copyright 2011 American Chemical Society
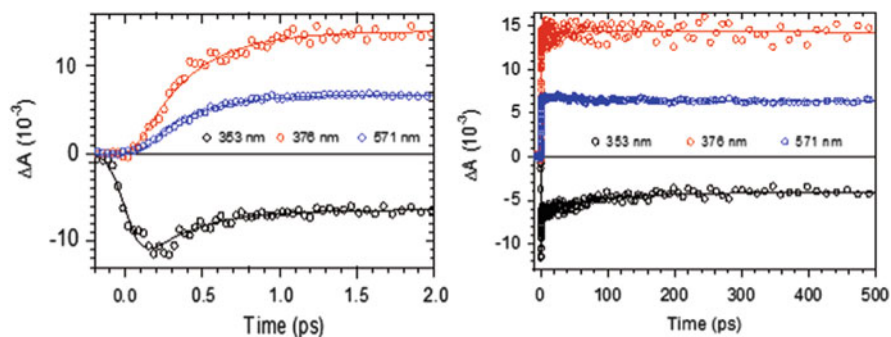


**Fig. 11** Decay profiles for 6-thioguanosine in aqueous buffer solution (pH 7.4) at 353 nm, 376 nm, and 571 nm. The early time decays are expended (*left*) for clarity. Adapted with permission from [22]. Copyright 2011 American Chemical Society
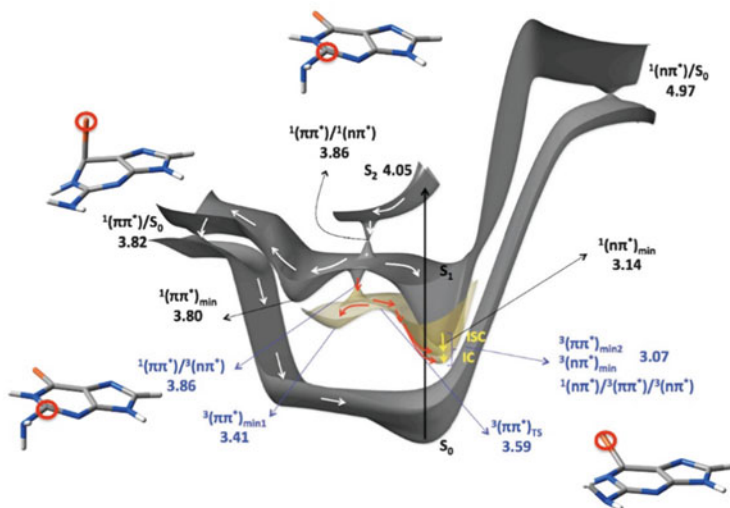
**Fig. 12** Proposed deactivation mechanism for 6-thioguanine starting from the $S_2(\pi\pi^*)$ state. Relaxation pathways proceeding in the singlet manifold are represented by *white arrows*, whereas those populating the triplet manifold are depicted with *red* and *yellow arrows*. The reported energies are relative to the optimized ground-state energy of 6-thioguanine. Adapted from [27] with permission of The Royal Society of Chemistry

excited-state deactivation mechanism predicted by these calculations is shown in Fig. 12. According to these calculations, the $^1\pi\pi^*$ state can internally convert to the $^1n\pi^*$ state through a $^1\pi\pi^*/^1n\pi^*$ conical intersection. This conical intersection, which is located at 3.86 eV relative to the energy of the optimized ground state geometry, requires stretching of the C=S bond, twisting of the $NH_2$ group, slight pyramidalization of the C2, and a small reorganization of the purine skeleton. According to the static calculations, the population reaching the $^1n\pi^*$ state can relax into two local minima in the singlet manifold: the $^1(\pi\pi^*)_{min}$ and the $^1(n\pi^*)_{min}$, which are located at 3.80 eV and at 3.14 eV, respectively. Relaxation into the $^1(\pi\pi^*)_{min}$ requires further pyramidalization and twisting of the C2 and the $NH_2$ group. On the other hand, relaxation into the $^1(n\pi^*)_{min}$ is accompanied by the synchronized stretching and out-of-plane movement of the C=S bond and by the recovery of the amino group to its Franck–Condon orientation. The molecular dynamics simulations reveal that the $^1\pi\pi^*$ state decays through $^1\pi\pi^*/^1n\pi^*$ conical intersection to the $^1n\pi^*$ state almost instantaneously, with 45% of the initial population decaying during the first 10 fs (see Fig. 13), to reach primarily the $^1(n\pi^*)_{min}$ [33]. The ultrafast decay of the $^1\pi\pi^*$ state is in agreement with the experimental results by Reichardt et al. [22].

Importantly, as first proposed by Reichardt et al. [22], the calculations also revealed that intersystem crossing to the triplet manifold in 6-thioguanine competes favorably with internal conversion to the ground state [27, 33]. Static calculations predict that the probability of intersystem crossing to the triplet manifold is high at

**Fig. 13** Population of the singlet states as a function of time, i.e., surface hopping simulations with only singlet states (*upper panel*). Population of the spin-diabatic states as a function of time, i.e., surface hopping simulations including singlet and triplet states (*lower panel*). Adapted from [33] with permission of The Royal Society of Chemistry
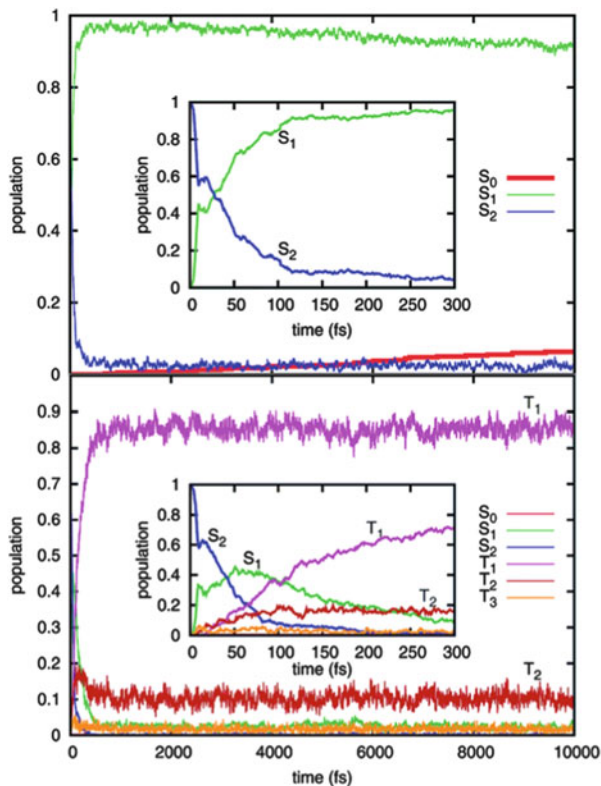


both $^1\pi\pi^*$ and $^1n\pi^*$ local minima. The spin-orbit coupling interaction between these two singlet minima and the $^3n\pi^*$ state exceeds 200 cm$^{-1}$, with corresponding energy gaps of less than 0.2 eV at the MS-CASPT2//SA-CASSCF(14,12)/ANO-L level of theory. Furthermore, as shown in Fig. 12, the minimum-energy $^1\pi\pi^*/^3n\pi^*$ and $^1n\pi^*/^3n\pi^*$ singlet-triplet crossing points are located very close to the $^1\pi\pi^*/^1n\pi^*$ conical intersection and the $^1(n\pi^*)_{min}$, respectively. These results led the authors to propose that intersystem crossing to the triplet manifold can proceed through two parallel relaxation pathways, which are represented by red and yellow arrows in Fig. 12. In the first intersystem crossing pathway (red arrows), population transfer through the $^1\pi\pi^*/^3n\pi^*$ crossing leads to a nonadiabatic distribution of population into three different minima in the triplet manifold: $^3(\pi\pi^*)_{min1}$, $^3(\pi\pi^*)_{min2}$, and $^3(n\pi^*)_{min}$. In the second pathway (yellow arrows), population transfer through the $^1n\pi^*/^3\pi\pi^*$ crossing leads to the $^3(\pi\pi^*)_{min2}$ in the T$_2$ state potential energy surface, which internally converts to the $^3(n\pi^*)_{min}$ in the T$_1$ state potential energy surface through a three-state crossing point. Indeed, the simulations show multiple recrossings along this trajectory, consistent with the closeness of these potential energy surfaces in the region of the $^1(n\pi^*)_{min}$ [33].

Thus, according to the calculations [27, 33], the transient absorption reported by Reichardt et al. [22] during the first 10 ps is caused by the mixture of $T_1$ and $T_2$ states, with most of the population in the former state. Assuming the $T_1$ state to be responsible for the transient absorption, a rise time of ~170 fs is predicted to be primarily associated with the sequence of transitions $S_2 \rightarrow S_1 \rightarrow T_2 \rightarrow T_1$, with a minor contribution from the more direct pathway $S_2 \rightarrow S_1 \rightarrow T_1$. This intersystem crossing lifetime, which is calculated for the 6-thioguanine in vacuum, compares favorably with the ~300 fs lifetime measured by Reichardt et al. [22] for 6-thioguanosine in solution. The simulations also reveal that the intersystem crossing pathway to the triplet manifold involves significant movement of the C=S bond out of the plane of the molecule, the rotation of the amino group around the C7N7 bond, and minor deformations of the purine ring concentrated in the puckering of the C7 atom [33].

On the other hand, the ground-state repopulation observed experimentally in tens of picoseconds in Fig. 11 [22] was assigned to internal conversion from the $^1\pi\pi^*$ state to the $S_0$ state [27], instead of internal conversion from the $^1n\pi^*$ state to the $S_0$ state. This is represented by white arrows in Fig. 12. The $^1\pi\pi^*/S_0$ crossing requires the folding of the C=S bond to a perpendicular conformation relative to the purine skeleton. Although conical intersections were found between both singlet states and the ground state, the energy of the $^1\pi\pi^*/S_0$ conical intersection was 3.82 eV, whereas that of the $^1n\pi^*/S_0$ conical intersection was 4.97 eV. In solution, the $^1n\pi^*/S_0$ conical intersection should be inaccessible from the $^1\pi\pi^*$ state minimum because it is expected to be found at even higher energies [27]. In fact, the nonadiabatic dynamics simulations predict that a statistically-insignificant fraction of the population returns to the ground state (Fig. 13) [33].

Even though internal conversion from the $S_2(\pi\pi^*)$ state to the ground state [27] is a reasonable hypothesis to explain the fractional ground-state recovery in tens of picoseconds in 6-thioguanosine [22], the simulations for 6-thioguanine suggest that internal conversion to the ground state should be insignificant (Fig. 13) [33]. Triplet self-quenching is another hypothesis which could explain the partial ground-state recovery shown in Fig. 11 for 6-thioguanosine. Fractional quenching of the triplet state in tens of picoseconds from excited aggregates that are in equilibrium with the monomers in the ground state has been proposed previously for 4-thiodeoxythymidine [18, 19]. Triplet self-quenching could explain the partial decay of the triplet absorption spectrum observed in the visible region in Fig. 10. It could also explain why a triplet yield of only 80% was measured for 6-thioguanosine in aqueous solution [22], while a triplet yield of unity has been reported for the 6-thiopurine base in organic solvent [195]. The dynamical calculations shown in Fig. 13 also suggest that most of the excited-state population should intersystem cross to the triplet manifold, as experimentally observed.

## 3.4 Summary

There is growing interest in the photochemistry and excited-state dynamics of the thiobases. Sulfur substitution in the nucleobases causes a remarkable redshift in the absorption spectra, moving the strongly allowed absorption observed in the nucleic acid monomers in the UVC all the way to the UVA region of the electromagnetic spectrum. Although the nucleic acid monomers and thiobases share the common photochemical property of negligible fluorescence, the well-known intrinsic relaxation pathways in the nucleic acid monomers are dramatically modified by the single replacement of a carbonyl oxygen atom with a sulfur atom. The main deactivation mechanism in both thiopurine and thiopyrimidine monomers is characterized by an ultrafast internal conversion from the spectroscopic $^1\pi\pi^*$ state to a lower-energy $^1n\pi^*$ state, which is followed by population of the lowest-energy $^3\pi\pi^*$ state. Thio-substitution inhibits ultrafast internal conversion to the ground state and enhances intersystem crossing to the triplet manifold. The majority of the triplet state population decays back to the ground state nonradiatively in the absence of molecular oxygen and at infinitely low dilution, but a small fraction can decay by emission of photons. Room-temperature phosphorescence has now been reported in 4-thiodeoxythymidine [18], 2′,3′,5′-tri-O-acetyl-thioinosine [13], 2-thiothymine [31], and a variety of 4-thiouracil derivatives [10, 13, 34, 200, 201, 203] in solution, while several thiobases show dual emission at room temperature in small yields [10, 18, 200]. A fraction of the triplet state population can also decay through diffusion-controlled self-quenching with other thiobases in the ground state, and perhaps by triplet self-quenching in ground-state complexes. Formation of an N-glycosidic bond seems to enhance nonradiative decay of the triplet state population, at least in the 2-thiothymine derivatives [31].

   Evidence is accruing showing that key electronic-structure factors controlling the ultrafast intersystem crossing lifetimes in the thiobase monomers are (1) the topology of the singlet and triplet potential energy surfaces (near barrierless decay pathway), (2) the small singlet-triplet energy gap (near degeneracy), and (3) the large magnitude of the spin-orbit coupling interaction in the intersystem crossing region. Indeed, femtosecond intersystem crossing dynamics seems to be a general property of the thiobase derivatives, which results in the efficient population of the $^3\pi\pi^*$ state in yields approaching unity. This unique property leads to the generation of singlet oxygen and other reactive species [11, 16, 23, 24, 64, 143, 144] and can explain the UVA-photosensitization efficacy of the thiobase derivatives and their extensive use in medical and photo-chemotherapeutic applications [36, 42]. Generation of Type I and/or Type II photosensitized reactions can explain why thiobase derivatives are effective at damaging DNA and killing cells [36, 42, 216, 217], which can ultimately lead to a 200-fold increase in UVA-induced skin cancer in patients treated with these drugs for prolonged periods of time [36]. Whether Type I or Type II photosensitization reactions play the leading role in this damage when the thiobases are incorporated into DNA is still unknown and requires urgent scrutiny.

## 4  Azabases

Azabases represent another family of intriguing DNA and RNA analogues with interesting photochemical properties and important biological implications. Substitution of a carbon atom with a nitrogen atom at position 8 of adenine and guanine, position 5 of cytosine, or position 6 of thymine and uracil leads to the formation of the azabases. The structures and standard ring numbering for the azabases are shown in Scheme 5. These nucleic acid analogues have useful properties as antiviral and anticancer drugs [46, 47] and in the treatment of several diseases [48, 49]. They are known to halt the spread or development of cancer [50–53] and to inhibit the growth of tumors [54]. Azabases have been used in a variety of cancer treatments [49, 55, 56], often administered simultaneously with chemotherapy and photodynamic therapy [51]. However, photosensitivity to these drugs has also been reported [63, 64]. As observed in the thiobases and other nucleobase analogues, the photochemical properties of the azabases are noticeably different from those of the natural bases [12, 14–16]. Therefore, it is both fundamentally informative and important to examine how a single nitrogen substitution affects the photophysical properties and excited-state dynamics observed in the nucleic acid bases.

## 4.1  *Steady-State and Time-Resolved Photochemistry of the Azabases*

The photophysics of several azabase derivatives in aqueous solution and at different pHs have been studied to some extent [218–223] and reviewed recently [224]. The interpretation of the photophysical results is complicated by the fact that aza-substitution lowers the $pK_a$ of the bases significantly, thus resulting in a mixture of tautomers in the ground state and at different pHs (Table 18) [224]. The nitrogen atom in place of the methine group at position 6 (C6H) of the uracil or thymine ring of the nucleosides lowers the $pK_a$ of the N3 hydrogen considerably relative to its $pK_a$ in uridine and thymidine [225–230]. Hence, unlike the uracil and thymine nucleosides that are found as neutral species at pH 7, 6-azauridine and 6-azathymidine are significantly deprotonated at neutral pH. Evidence for excited-state proton transfer and phototautomerism has been presented [224], but further experimental (particularly time-resolved) and computational work are needed to understand fully their photochemistry in aqueous solution. On the other hand, the photophysics of the azabase derivatives can be significantly simplified by using acetonitrile as the solvent. Suzuki and co-workers [12, 14–16] have recently performed the first steady-state and time-resolved experiments with azabase analogues in acetonitrile solution. These studies will be reviewed briefly below.

## Azapurines
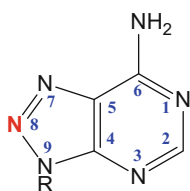


**8-azaadenine** (R = H)
8-azaadenosine (R = ribose or 2'-deoxyribose)
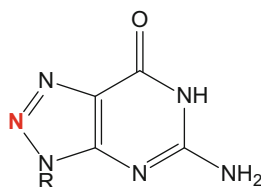
**8-azaguanine** (R = H)
8-azaguanosine (R = ribose or 2'-deoxyribose)

## Azapyrimidines
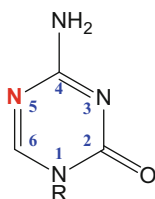


**5-azacytosine** (R = H)
5-azacytidine
(R = ribose or 2'-deoxyribose)
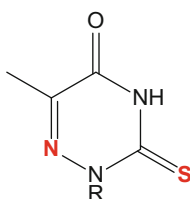
**6-aza-2-thiothymine** (R = H)
6-aza-2-thiothymidine
(R = ribose or 2'-deoxyribose)
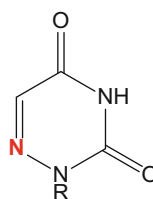
**6-azauracil** (R = H)
6-azauridine
(R = ribose or 2'-deoxyribose)

**Scheme 5** Structures and common ring number of the azabases

   The steady-state absorption and emission properties of the azabases in acetonitrile, including 6-azauridine and 6-aza-2-thiothymine, were investigated by Suzuki and co-workers [12, 14–16]. In general, the absorption spectra of the azabase derivatives shift slightly to the red compared to those of the natural bases, with the largest redshift observed in 6-aza-2-thiothymine, presumably because of the additional sulfur substitution (Table 18). Figure 14 shows a comparison of the absorption spectra of uracil and 6-azauracil nucleobases and nucleosides in acetonitrile. The lowest-energy absorption band of the aza-nucleobase (259 nm) and aza-nucleoside (266 nm) is red-shifted and broadened compared to that of uracil and uridine, respectively, whereas the absorption cross sections are lowered by ~30–40%. In addition, a small absorption tail is observed to the red of the lowest-energy absorption band in 6-azauracil and 6-azauridine, indicative of a low-lying electronic transition with reduced oscillator strength. This is in agreement with TD-B3LYP/PCM/6-31G($d,p$) calculations performed by Kobayashi et al. [12, 15] in acetonitrile, which show that the two lowest-energy electronic transitions in the 6-azauracil nucleobase and nucleoside have $S_2(\pi\pi^*)$ and $S_1(n\pi^*)$ electronic configurations, with a larger energy gap than the corresponding electronic transitions in uracil and uridine in the same solvent. The calculations further show that the oscillator strength of the $S_2(\pi\pi^*)$ state in 6-azauridine is ~33% smaller than in uridine, in good agreement with the experimental observations (Fig. 14). A shoulder

**Table 18** Steady-state properties and quantum yields of the aza-base derivatives

| | $\lambda_{max}$ (nm)[a] | $\varepsilon_{max}$ (M$^{-1}$ cm$^{-1}$)[b] | $\lambda_{em}$ (nm)[c] | $\Phi_{Fl} \times 10^{-3}$ ($\lambda_{ex}$)[d] | Experimental conditions[e] |
|---|---|---|---|---|---|
| 8azaGua | 249 | 11,200 | 395 | 54 (280); 330 (300) | Neutral, pH < 6.5 [218] |
| | 278 | 6,170 | 355 | ~30 (280) | Monoanion, pH > 6.5 and < 10.8 [218] |
| | 280 | 7,900 | 360 | ~120 (280) | Dianion, pH > 10.8 [218] |
| | 258[f] | – | NE | 98 ± 11 (248)[g] | ACN [14] |
| 7Me-8azaGua | 297 | 5,100 | 390 | 90 (300) | Neutral, pH < 8.25 [218] |
| | 299 | 5,890 | 405 | 70 (300) | Monoanion, pH > 8.25 [218] |
| 8Me-8azaGua | 293 | 6,600 | 400 | 510 (300) | Neutral, pH < 8.6 [218] |
| | 298 | 7,980 | 410 | 450 (300) | Monoanion, pH > 8.6 [218] |
| 8azaGuo | 256 | 12,900 | 347 | < 10[h] | Neutral, pH < 8.05 [218] |
| | 278 | 11,700 | 362 | 550[h] | Anion, pH > 8.05 [218] |
| 8azaIno | 254 | 10,000 | NE | < 1[h] | Neutral, pH < 7.9 [218] |
| | 275 | 10,700 | 357 | 18[h] | Anion, pH > 7.9 [218] |
| 8azaAde | 263 | 10,700 | NE | < 1 (280) | Cation, pH < 2.7 [218] |
| | 273 | 10,500 | 345 | 8 (280) | Neutral, pH > 2.7 and < 6.3 [218] |
| | 275 | 10,800 | ~328 | 2 (280) | Anion, pH > 6.3 [218] |
| | 275 | – | 350 | 3.2 ± 0.4 (248) | ACN [14] |
| 8azaAdo | 263 | 13,300 | NE | < 1[h] | Cation, pH < 2.2 [218] |
| | 278 | 12,000 | 352 | 68[h] | Neutral, pH > 2.2 [218] |
| 5azaCyt | 260[i] | – | NE | – | ACN [14] |
| 6azaUra | 259 | 5,500 [15][j] | 420 | NE (248) 4.2 ± 0.4 (308) | ACN, Ar [12] |
| 6azaUrd | 266 | 6,100 [j] | NE | NE[h] | ACN, Ar [15] |
| 6aza-2tThy | 310[i] | 4,260[i] | NE | – | ACN [16] |
| | 350[f] | 640[f] | | | |

[a]Wavelength(s) of maximum absorption in the spectral region above ~230 nm
[b]Extinction coefficient of absorption maximum (maxima)
[c]Peak wavelength of fluorescence emission
[d]Fluorescence quantum yield, excitation wavelength given in parenthesis
[e]Under air-saturated condition unless otherwise noted; protonation state charge of azabase is given in aqueous solution at different pHs
[f]Property of $S_1$ state absorption band
[g]Fluorescence from the N8H tautomer
[h]Independent of excitation wavelength
[i]Property of $S_2$ state absorption band
[j]Extrapolated from graph

was also observed to the red of the lowest-energy absorption band of 6-aza-2-thiothymine at 350 nm which was assigned to the $S_0 \rightarrow S_1(n\pi^*)$ electronic transition [16].
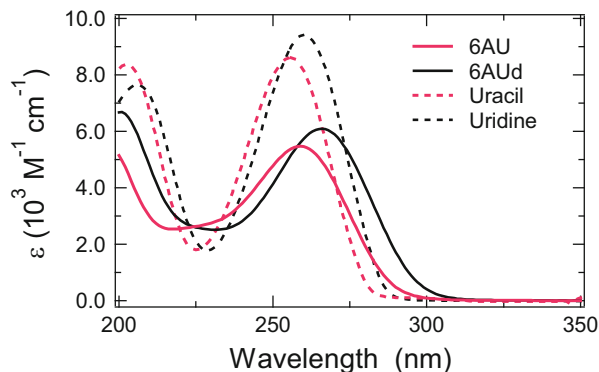
Fluorescence emission has not been detected in 5-azacytosine, 6-azauridine, or 6-aza-2-thiothymine in acetonitrile, but a fluorescence yield of ca. $10^{-2}$ to $10^{-3}$ was measured in 8-azaadenine, 8-azaguanine, and 6-azauracil (Table 18). Fluorescence emission in 8-azaguanine was assigned to the N8H tautomer, whereas it was assigned to the N9H tautomer in 8-azaadenine [14]. In the case of 6-azauracil [12], the fluorescence emission is excitation-wavelength-dependent. Excitation at 308 nm results in weak fluorescence emission, whereas no fluorescence was observed upon excitation at 248 nm. This observation led the authors to propose that fluorescence emission in 6-azauracil originates from the $S_1(n\pi^*)$ state, which is supported by the measurement of the excitation spectrum and by the calculation of vertical excitation energies at the TD-B3LYP/PCM/6-31G(d,p) level of theory in acetonitrile [12].

## 4.2 Excited-State Deactivation Mechanism in the Azabase Derivatives

Suzuki and co-workers [12, 14–16] also studied the excited-state dynamics of several azabase derivatives using nanosecond laser flash photolysis, time-resolved thermal lensing, and near IR single-photon counting spectroscopy. The reported transient properties and quantum yields of the triplet state and of singlet oxygen generation are compiled in Table 19 and Table 6, respectively. As observed in the thiobase derivatives in Sect. 3, 6-aza-2-thiothymine shows a near-unity triplet quantum yield. Gobbo and Borin [30] performed CASPT2//CASSCF calculations and predicted that multiple relaxation pathways lead to efficient population of the $T_1(\pi\pi^*)$ state in 6-aza-2-thiothymine, which is in agreement with the unity triplet yield experimentally measured by Kuramochi et al. [16]. According to these authors, ultrafast internal conversion from the $S_2(\pi\pi^*)$ to the $S_1(n\pi^*)$ state occurs through a conical intersection. Once in the $S_1(n\pi^*)$ state, the system evolves to its minimum, where an efficient and accessible singlet-triplet crossing with a

**Table 19** Time-resolved properties and quantum yields of azabase derivatives

| | $\lambda_T$ (nm)[a] | $\varepsilon_T$ (M$^{-1}$ cm$^{-1}$)[b] | $\tau_{Tn \to S_0}$ (ns)[c] | $\Phi_{ISC}$[d] | Experimental conditions[e] |
|---|---|---|---|---|---|
| 8azaGua | – | – | – | [f] | ACN [14] |
| 8azaAde | 455 | – | $240 \pm 5$ | – | ACN [14] |
| 5azaCyt | – | – | – | [f] | ACN [14] |
| 6azaUra | 320[g] | – | $190 \pm 10$[g] | $1.00 \pm 0.10$[g] | ACN, Ar [15] |
| | 320[h] | – | $180 \pm 10$[h] | $0.93 \pm 0.04$[h] | ACN, Ar [15] |
| | 320 | $1{,}100 \pm 100$ | – | $1.00 \pm 0.10$ | ACN, Ar [12] |
| | 600 | $320 \pm 30$ | | | |
| 6azaUrd | 320[g] | – | $130 \pm 10$[g] | $1.00 \pm 0.07$[g] | ACN, Ar [15] |
| | 320[h] | $810 \pm 40$ | $130 \pm 10$[h] | $0.78 \pm 0.05$[h] | ACN, Ar [15] |
| | 600[h] | $260 \pm 20$ | | | |
| 6aza-2tThy | 615 | 1,460 | $7{,}500 \pm 300$[i] | $1.00 \pm 0.02$ | ACN [16] |

[a]Wavelength of triplet absorption band maxima
[b]Extinction coefficients of corresponding triplet absorption band maxima
[c]Triplet lifetime
[d]Intersystem crossing quantum yield
[e]Under air-saturated conditions unless otherwise noted; all values measured using 20 ns TAS
[f]No transient species with triplet character were observed
[g]Excited at 248 nm
[h]Excited at 308 nm
[i]The intersystem crossing lifetime was estimated to be <1 ps and a self-quenching rate constant of $(6.6 \pm 0.8) \times 10^8$ M$^{-1}$ s$^{-1}$ was measured

spin-orbit coupling of 169 cm$^{-1}$ populates the T$_1$($\pi\pi$*) state. Meanwhile, in a second relaxation pathway, the S$_2$($\pi\pi$*) state transfers its population to the triplet manifold facilitated by a crossing point between the S$_2$($\pi\pi$*) state and the T$_3$($n\pi$*) state with a spin-orbit coupling of 130 cm$^{-1}$. Once in the T$_3$($n\pi$*) state, the population can be transferred to the T$_1$($\pi\pi$*) state through a conical intersection between these two states. An additional conical intersection was located between the S$_2$($\pi\pi$*) state and the ground state, but the authors suggest that it should have a minor relevance in the deactivation mechanism since most of the population is transferred to the triplet manifold.

As observed in 6-aza-2-thiothymine, Kobayashi et al. [12, 15] reported a near-unity triplet quantum yield for 6-azauracil and 6-azauridine in acetonitrile. Based on previous reports for uracil derivatives [84, 86, 110, 140, 159, 170, 231–233], and making use of vertical singlet–triplet energy gap arguments for 6-azauracil, the authors proposed two mechanisms to explain the efficient population of the triplet state. The first mechanism is direct population of a triplet state with $n\pi$* character from the initially excited $^1\pi\pi$* state. The second involves ultrafast internal conversion from the $^1\pi\pi$* to the vibrationally excited $^1n\pi$* state, which is followed by intersystem crossing to the $^3\pi\pi$* before the excess vibrational energy can relax in the S$_1$($n\pi$*) state. This intersystem crossing event is proposed to be in competition with internal conversion of the relaxed S$_1$($n\pi$*) state to the ground state, as shown previously by Hare et al. [140, 159] in other uracil derivatives. The high triplet yield provides strong evidence that intersystem crossing to the triplet state is the primary

relaxation pathway in 6-azauracil and 6-azauridine, whereas internal conversion to the ground state, from either the $S_1(n\pi^*)$ or $S_2(\pi\pi^*)$ states, is inefficient.

Calculations performed by the groups of Marian [20] and Borin [25] at the DFT/MRCI/COSMO/cc-pVDZ and CASPT2//CASSCF/ANO-L levels of theory, respectively, support the above mechanism. Etinski and Marian [20] concluded that the $S_1(n\pi^*)$ state acts as a doorway state in the population of the $T_1(\pi\pi^*)$ state, where the $S_2(\pi\pi^*)$ state population is transferred nearly quantitatively to the $S_1(n\pi^*)$ state. The authors estimated that the $T_1(\pi\pi^*)$ state is populated within 30 ps in acetonitrile. However, in contrast to Kobayashi et al. [14, 15] and to Gobbo et al. [25], Etinski and Marian [20] proposed that intersystem crossing from the $S_2(\pi\pi^*)$ state to the $T_2(n\pi^*)$ state is not competitive with internal conversion from the $S_2(\pi\pi^*)$ state to the $S_1(n\pi^*)$ state.

Kobayashi et al. [12] also reported that the triplet yield and fluorescence emission in 6-azauracil and 6-azauridine depend on the excitation wavelength (Table 18). The triplet yield in 6-azauracil and 6-azauridine is unity when exciting at 248 nm and 0.93 and 0.78, respectively, when exciting at 308 nm [12]. This dependence was attributed to an increase in excess vibrational energy in the $S_1(n\pi^*)$ state upon 248 nm excitation, which results in a more efficient population transfer to the $T_1(\pi\pi^*)$ state compared to excitation at 308 nm. It is often observed that vibrational cooling occurs more slowly when the excess of vibrational energy is greater [234, 235]. As discussed in Sect. 2.5, an analogous mechanism was previously proposed by Hare et al. [140, 159] to explain intersystem crossing to the triplet state in other uracil derivatives. The slowdown in vibrational cooling to the $S_1(n\pi^*)$ state minimum upon 248 nm vs 308 nm excitation can also explain why fluorescence emission is not detected when 6-azauracil is excited at 248 nm, but weak emission is observed upon 308 nm excitation. The relaxation mechanism proposed by Etinski and Marian fails to explain the dependence of the triplet yield and fluorescence emission on the excitation wavelength [20].

Gobbo et al. [25] ascribed the excitation-wavelength dependence in 6-azauracil to the accessibility of an additional relaxation pathway when excitation is performed at 248 nm vs 308 nm. Scheme 6 presents the most relevant relaxation pathways computed by these authors. According to them, excitation at 308 nm leads to the direct population of the $S_1(n\pi^*)$ state. Most of its energy is transferred to the $T_1(\pi\pi^*)$ state via a $^1n\pi^*/^3\pi\pi^*$ crossing region located near the $S_1(n\pi^*)$ state minimum, whereas a small fraction can be emitted as fluorescence, as observed experimentally by Kobayashi et al. [12]. On the other hand, excitation at 248 nm to the $S_2(\pi\pi^*)$ state leads to the population of the $S_2(\pi\pi^*)$ state minimum through a barrierless pathway, where crossings with the $S_1(n\pi^*)$ and $T_2(n\pi^*)$ states can occur. Both pathways lead to the efficient population of the $T_1(\pi\pi^*)$ state, which reduces even more the already low fluorescence emission observed upon 308 nm excitation according to these authors. In addition, internal conversion from the $S_2(\pi\pi^*)$ state or the $S_1(n\pi^*)$ state to the ground state via conical intersections was found to be unlikely because of the high energy required to access the corresponding conical intersections, in agreement with the experimental findings of Kobayashi et al. [12].
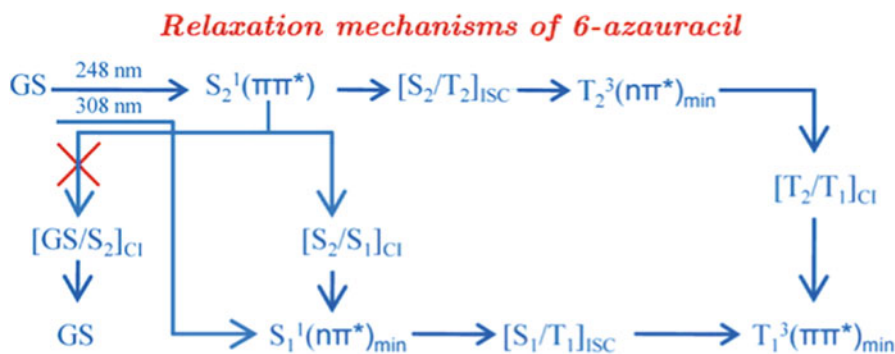
**Scheme 6** Proposed relaxation mechanisms of 6-azauracil depicting the multiple pathways that lead to the $T_1(\pi\pi^*)$ state. Reprinted with permission from [25]. Copyright 2011 American Chemical Society

In contrast to Hare's mechanism [140, 159], in which it was proposed that intersystem crossing in the uracil derivatives from the relaxed $S_1(n\pi^*)$ state to the triplet state should be inefficient because of small spin-orbit coupling interactions, Kobayashi et al. [12] proposed that intersystem crossing from the relaxed $S_1(n\pi^*)$ state is competitive with internal conversion to the ground state in 6-azauracil and 6-azauridine because of the high triplet yields observed upon excitation at 308 nm. Hence, according to these authors, the accompanying loss in planarity of the 6-azauracil ring upon relaxation to the $S_1(n\pi^*)$ state does not lead to a decrease in the spin-orbit coupling interaction in the 6-azauracil and 6-azauridine, as was proposed in the case of the uracil derivatives by Hare et al. [140, 159]. Gobbo et al. [25] found an $S_1(n\pi^*)/T_1(\pi\pi^*)$ crossing near the $S_1(n\pi^*)$ state minimum with a spin-orbit coupling of 64.7 cm$^{-1}$. However, the $S_1(n\pi^*)/T_1(\pi\pi^*)$ spin-orbit coupling at the position of the $S_1(n\pi^*)$ state minimum was not reported.

Kobayashi et al. [12] proposed that population of the vibrationally-relaxed $S_1(n\pi^*)$ state increases the probability of internal conversion to the ground state in 6-azauridine vs 6-azauracil. This idea is supported by the observation that direct excitation of the $S_1(n\pi^*)$ state at 308 nm leads to a triplet yield of 0.78 in 6-azauridine, whereas it leads to a 0.93 yield in 6-azauracil under similar experimental conditions. According to these authors, the additional degrees of freedom introduced by the sugar group increase the vibrational modes and intramolecular vibrational energy redistribution in the nucleoside, thus accelerating the population to the vibrationally-relaxed $S_1(n\pi^*)$ state. This in turn seems to increase the probability of internal conversion to the ground state in the 6-azauridine, explaining its lower triplet yield vs that of 6-azauracil upon 308 nm excitation. Kobayashi et al. [15] proposed that the intramolecular hydrogen bond between the base and the ribose should potentially enhance the intramolecular vibrational energy redistribution, explaining the lower triplet yield in 6-azauridine vs 6-azauracil. As discussed in Sect. 2.5, lower triplet yields have also been reported for uridine vs uracil in acetonitrile upon 254 nm and 265 nm excitation [99–101]. The increase in the

internal conversion rate from the $S_1(n\pi^*)$ state to the ground state caused by intramolecular vibrational energy relaxation in 6-azauridine vs 6-azauracil [15] is in agreement with the relaxation model proposed by West et al. [193], but in contrast to that by Hare et al. [140, 159]. A potential way to lessen this apparent discrepancy is by assuming that low-frequency intramolecular vibrational modes play a more important role when acetonitrile is used as a solvent, whereas the relatively high-frequency solute–solvent intermolecular modes could dominate in aqueous solution. See Sects. 2.3–2.5 for an account of this lively debate. Regardless, more experimental and computational work is needed to scrutinize this mechanism and to provide more insight on the nuclear and electronic factors that lead to the increased rate of internal conversion in 6-azauridine vs 6-azauracil in acetonitrile.

Kobayashi et al. [12] compared the relaxation mechanism of 6-azauracil with that of uracil. The authors proposed two different mechanisms to explain the impact of C6 aza-substitution on the dynamics of uracil: (1) acceleration of intersystem crossing and (2) the inhibition of the ultrafast internal conversion to the ground state. In the first mechanism, the substitution of the methine group for a nitrogen atom, is proposed to accelerate intersystem crossing to the triplet manifold caused by the additional lone pair orbitals, which can enhance $S_1(n\pi^*)$ to $T_1(\pi\pi^*)$ nonradiative transition. This mechanism is supported by DFT/MRCI calculations performed by Etinski and Marian [20]. The second mechanism is based on the hypothesis that the rigidity of the C5$=$N6 double bond should affect the internal conversion process to the ground state. This idea is supported by the observation that ultrafast internal conversion to the ground state in uracil occurs via a conical intersection in which a nonplanar deformation equivalent to a twist around the double bond of C5$=$C6 is suggested to be important [84, 86, 140, 231, 232, 236]. Hence, the increased rigidity of the C5$=$N6 double bond could decrease the probability of accessing this conical intersection, allowing the efficient population of the triplet state in 6-azauracil [12]. This mechanism is supported by CASPT2// CASSCF calculations [25], where it was observed that an energy barrier of ~13 kcal/mol must be surmounted from the $S_2(\pi\pi^*)$ state minimum in order to reach a conical intersection with the ground state. The substitution of the methine group for the nitrogen atom prevents the stretching and twisting of the C5$=$N6 bond, which is a key deformation in allowing the development of the ethene-like out-of-plane conical intersection structure.

The key role of the $S_1(n\pi^*)$ state in the intersystem crossing to the triplet state is supported by the investigations of Kobayashi et al. [14] on the excited-state relaxation pathways in 8-azaguanine and 5-azacytosine. Transient absorption experiments show that triplet state population in these compounds is inefficient and quantum yields for singlet oxygen generation are less than $10^{-2}$. Vertical excitation energies at the TD-B3LYP/PCM/6-31G($d$,$p$) level of theory suggest that the first $^1n\pi^*$ state in these azabases is actually higher in energy than the first two $^1\pi\pi^*$ states in acetonitrile. This observation led the authors to propose that there are two types of azabase derivatives. 6-Azauracil and 8-azaadenine derivatives are members of the type A group, in which the $^1n\pi^*$ state is the lowest-energy excited-

singlet state. Type A derivatives have large triplet and singlet oxygen yields. On the other hand, in the type B derivatives, 8-azaguanine and 5-azacytosine, the $^1n\pi*$ state is higher in energy than the first two $^1\pi\pi*$ excited states in the Franck–Condon region. These type B derivatives show negligible triplet and singlet oxygen yields.

Gobbo and Borin [28] investigated the electronic-energy relaxation mechanism in 8-azaadenine using the CASPT2//CASSCF/ANO-L protocol and proposed a more detailed picture. According to their calculations, excitation of the spectroscopic $S_2(\pi\pi*)$ state results in bifurcation of the initial excited-state population. In the first pathway, the $S_2(\pi\pi*)$ state evolves barrierlessly toward its minimum. Once the population reaches the $S_2(\pi\pi*)$ state minimum, it can internally convert to the $S_1(n\pi*)$ state minimum or to the ground state via $^1\pi\pi*/^1n\pi*$ or $^1\pi\pi*/S_0$ conical intersections, respectively, or it can intersystem cross to the $T_2(n\pi*)$ state through a $^1\pi\pi*/^3n\pi*$ crossing with a spin-orbit coupling of 10 cm$^{-1}$. After 8-azaadenine reaches the $T_2(n\pi*)$ state, it can evolve barrierlessly to the $T_2(n\pi*)$ state minimum, where a conical intersection with the $T_1(\pi\pi*)$ state was found, resulting in efficient internal conversion to the $T_1(\pi\pi*)$ state minimum. The calculations suggest that reaching the $^1\pi\pi*/S_0$ conical intersection is unlikely because of the high energy barrier that must be surmounted. According to these authors, internal conversion to the $S_1(n\pi*)$ state minimum can lead to the weak fluorescence emission observed experimentally by Suzuki and co-workers [14] or could lead to additional population of the $T_1(\pi\pi*)$ state via a $^1n\pi*/^3\pi\pi*$ crossing point. In the second pathway, the population in the Franck–Condon region of the $S_2(\pi\pi*)$ potential energy surface can evolve barrierlessly to a planar conical intersection with the $S_1(n\pi*)$ state, causing an ultrafast depopulation of the $S_2(\pi\pi*)$ state. Once the system reaches the $S_1(n\pi*)$ state surface, it evolves through a barrierless path to its minimum, from which it can fluoresce weakly or intersystem cross to the $T_1(\pi\pi*)$ state with computed spin-orbit coupling of ~13 cm$^{-1}$, as described above in the first pathway.

According to Gobbo and Borin [28], excitation of 8-azaadenine to the $S_2(\pi\pi*)$ state always finds a relaxation path that reaches the $T_1(\pi\pi*)$ state, suggesting that a near-unity triplet yield should be observed in 8-azaadenine. However, taking into consideration the available experimental and computational data for uracil, 6-azauracil, and 8-azaadenine, it appears as if the triplet yield of 8-azaadenine should be much smaller than unity and comparable to that of uracil. Suzuki and co-workers [14] did not report the triplet yield of 8-azaadenine. However, they measured the yield of singlet oxygen generation to be $0.15 \pm 0.02$ under $O_2$-saturated conditions. While this singlet oxygen yield is significant, it is much smaller than the figure reported by the same authors for 6-azauracil under identical experimental conditions (Table 6). This is so regardless of the fact that the two azabases have comparable triplet decay lifetimes and that 8-azaadenine has an approximately fourfold greater rate constant of triplet quenching by $O_2$. In addition, Suzuki and co-workers determined that the singlet oxygen yield of uracil is identical to that of 8-azaadenine and that their triplet quenching rate constants by $O_2$ are comparable, yet the triplet yield of uracil is only $0.21 \pm 0.02$ under the equivalent experimental conditions [12]. Moreover, the calculated triplet state energies for 8-azaadenine, 6-azauracil, and uracil are all similar and the triplet

state of each has mostly $\pi\pi^*$ character at the CASSCF/CASPT2 level of theory [25, 28, 170]. Taken together, these observations suggest that the triple yield of 8-azaadenine should be comparable to that of uracil instead of near unity as predicted by the calculations [28], assuming that the pathways to populate the triplet state are similar for the three compounds.

One possible explanation for this apparent discrepancy is that the electronic configuration of the triplet state of 8-azaadenine is significantly different from that of 6-azauracil; however, the calculations predict that both have $\pi\pi^*$ character. Moreover, the comparable triplet decay lifetimes observed experimentally for these two azabases suggest that their triplet states have similar electronic configurations. Another possible explanation is that the singlet oxygen photosensitization mechanism by 8-azaadenine is significantly different from that of 6-azauracil. It is known that the involvement of a partial charge–transfer complex in singlet oxygen production increases the rate constant of the triplet state quenching by oxygen, while simultaneously reducing the number of triplet states quenched to form singlet oxygen ($S_\Delta$) by approximately 75% [237]. This could explain how 8-azaadenine has a fourfold higher rate of triplet quenching by oxygen while still generating far less singlet oxygen than 6-azauracil. The $S_\Delta$ value for 6-azauracil and uracil has been reported to be 0.8, but, unfortunately, the $S_\Delta$ value for 8-azaadenine is currently unknown. Further experimental and computational work is necessary before a definitive conclusion can be reached.

## 4.3 Summary

Azabase derivatives are characterized by slightly red-shifted absorption spectra compared to the natural DNA and RNA monomers. These nitrogen-substituted analogues also exhibit a small fluorescence yield and show no phosphorescence at room temperature. Photophysical investigation of the azabases in aqueous solution is problematic because of the presence of multiple tautomers around neutral pHs. Hence, the time-resolved studies to date have been performed in acetonitrile solution. Two distinct groups of azabases have been identified. The first group consists of 6-azauracil and 8-azaadenine, and their triplet states are populated in high yields, whereas triplet yields are negligible in the second group of azabases consisting of 8-azaguanine and 5-azacytosine. The $^1n\pi^*$ state has been proposed to play a key role in modifying the photochemistry of these azabases. 6-Azauracil and 8-azaadenine have received most attention from both experimental and computational perspectives, but there is still a relatively small body of work on the azabase derivatives in general. Nonetheless, these early studies provide another example of the ability of a single atom substitution to tune the photochemistry of the nucleic acid monomers over a broad range – from bases showing no measurable triplet yield all the way to bases possessing near unity triplet yields and high levels of singlet oxygen generation. As shown in Sect. 3 for the thiobases, azabases show

promise for advancing the fundamental understanding of the excited-state dynamics in the natural DNA and RNA monomers.

## 5    Final Remarks and Future Perspective

Ultraviolet excitation of nucleic acid monomers and their thiobase and azabase analogues populates strongly allowed $^1\pi\pi^*$ states, the dynamics of which are tightly coupled to a large number of competitive relaxation pathways. Investigating the underlying dynamics is crucial toward understanding the photochemistry of not only the monomers but also of the DNA and RNA polymers.

Undeniably, major progress has been made toward understanding the steady-state and time-resolved photochemistry of DNA and RNA monomers in solution. The primary radiative and nonradiative decay pathways have been reported, as well as the nuclear dynamics that are coupled to them. However, further research is needed to gather a firm understanding of the mechanism by which excess vibrational energy is redistributed to the solvent and how this mechanism is affected by environmental factors such as solvent composition and temperature. It is now evident that the substituent in the N-glycosidic bond has an important, but poorly understood, effect on the dissipation of excess vibrational energy coupled to several nonadiabatic decay pathways. In particular, the precise role of the N-glycosidic group in the intersystem crossing dynamics and in modulating the internal conversion processes in the singlet and triplet manifolds warrants further scrutiny.

In contrast to the nucleic acid monomers, only a handful of experiments and high-level electronic-structure calculations have been performed for the thiobase and azabase derivatives to date. It is evident that further experimental and computational investigations of the excited-state dynamics in these analogues should provide meaningful information to scrutinize current kinetic models that couple specific conical intersections and excited-state potential energy surfaces to the photochemistry of the nucleic acid bases in solution. The intrinsic ultrafast internal conversion process well-known in the nucleic acid monomers is dramatically overshadowed by intersystem crossing to the triplet state when a single oxygen or carbon atom in the nucleobase skeleton is replaced with a sulfur or a nitrogen atom. Indeed, all the thiobases and most of the azabases investigated thus far exhibit near-unity triplet yields. To put the significance of these results in perspective, the triplet yields of the DNA counterparts are approximately two orders of magnitude smaller in aqueous solution [97]. This unique property can lead to the generation of singlet oxygen and other reactive species in high yields [11, 16, 23, 24, 64]. All the thiobase analogues reviewed in this chapter and several azabases exhibit approximately a fivefold higher yield of singlet oxygen than the DNA/RNA monomers in aqueous solution and acetonitrile, which could explain the UVA-photosensitization efficacy of the thiobase derivatives and their extensive use in medical and photo-chemotherapeutic applications [36, 42, 45]. Still, it is necessary to investigate the excited-state dynamics and to measure the triplet state and singlet oxygen yields in

other thio- and azabase derivatives. There are still many gaps in our knowledge regarding their photochemistry and excited-state dynamics in solution. Filling these gaps is essential for the discovery of prospective drugs with desirable phototherapeutic properties, as well as for furthering the understanding of dynamics in natural DNA and RNA monomers. More fundamentally, these studies can clarify whether the rate of intersystem crossing and the triplet and singlet-oxygen yields depend on general changes in the chemical structure (i.e., structural isomers), or on specifically which atom is replaced in the nucleobase skeleton.

Importantly, all of the thiobase monomers (except for those substituted at the 2 position) have significantly larger absorption cross sections in the UVA region than the azabase and nucleic acid base monomers. Ninety-five percent of the solar UV energy incident on the skin derives from the deeply-penetrating UVA region of the electromagnetic spectrum, and photodamage of the skin, photoaging, and carcinogenesis by UVA radiation are rapidly emerging as important areas of research [238–242]. In general, precise knowledge about the electronic decay mechanisms in sensitizers and how these sensitizers damage DNA at the molecular level is lacking. In this regard, thiobase derivatives can be thought of as model compounds of biologically-important photosensitizers. Laboratory experiments have shown that human cells can metabolize and incorporate thiobases into their native DNA [26, 36, 43, 57–61, 243], especially 6-thiodeoxyguanosine and 4-thiodeoxythymidine. This incorporation results in cell death upon exposure to doses of UVA irradiation that would otherwise be nonlethal [43]. More importantly, the skin of patients treated with these drugs is sensitive to UVA radiation and long-term treatment results in up to a 200-fold increase in incidence of sunlight-induced skin cancer [26, 36, 62]. A key reason for the increase in skin cancer is that UVA irradiation of DNA containing thiobases results in DNA oxidation, breakage, and crosslinking [26, 34–36, 43]. It has been proposed that Type II photosensitization reactions by thiobases play a key role in damaging DNA [26, 36, 42]. However, to support a Type II photosensitization mechanism, one needs to know how the yields of triplet state population and singlet oxygen generation measured for the thiobase monomers in solution are affected when these compounds are incorporated in the DNA polymers. Although damage to DNA is manifested as structural modifications to the DNA itself, unraveling the electronic decay pathways and the mechanisms by which these sensitizers damage DNA are crucial steps toward understanding how skin is damaged. Further experimental and computational studies are essential to determine how the physico-chemical interactions between the nucleobases and the thiobases within DNA modulate the photosensitization mechanism by which DNA is damaged.

Equally important, ultrafast intersystem crossing dynamics seem to be a general property of thiobase derivatives. Understanding ultrafast intersystem crossing dynamics is of fundamental and biological relevance because ultrafast intersystem crossing often, but not always as in thymidine [105], leads to high triplet yields, which play a leading role in determining the damage to DNA and other cellular components. While the intersystem crossing lifetimes for the azabases have not been measured, it is also expected that they are on the ultrafast time scale.

This raises the question: *Why does intersystem crossing occur on the femtosecond time scale and with near-unity yields in these compounds?* Clearly, the topology of the singlet and triplet potential energy surfaces, as well as the small energy gaps and strong spin-orbit coupling interactions in the singlet-triplet crossing regions, are expected to play a major role, but these are not necessarily the only phenomena at work. Examples of ultrafast intersystem crossing in organic molecules are well-documented in the literature [159, 244–248], which may include the thymine nucleobase [105]. Nevertheless, the traditional view that the rate of internal conversion is always larger than that of intersystem crossing in organic molecules still persists [249–251]. A quantitative understanding of the ultrafast intersystem crossing dynamics in nucleic acid bases and their analogues is necessary to rigorously examine an alternative paradigm.

It is important to answer the following question from an both experimental and computational perspective: *What electronic and nuclear factors control the electronic decay mechanisms in these compounds?* From a computational point of view, it is necessary to determine the topology of the potential energy surfaces and the nuclear dynamics associated with the excited states that participate in the relaxation mechanisms. High-level *ab initio* calculations in combination with molecular dynamics simulations that include non-adiabatic and spin-orbit coupling interactions are necessary to accomplish this quantitatively. On the one hand, high-level *ab initio* calculations can describe the topology of the singlet and triplet potential energy surfaces and their nonadiabatic interactions, allowing for characterization of the major relaxation pathways in great detail. However, these calculations alone cannot determine the time required for populating an excited state or which conical intersections in the singlet or triplet manifolds are relevant. On the other hand, only dynamical studies can elucidate which pathways are operative and what regions of the potential energy surface are visited. However, dynamical simulations based on fully quantum-mechanical approaches are (currently) incredibly demanding for molecules of this size, let alone inclusion of solvent effects. Thus, the use of approximations or semi-empirical methods is often necessary.

From an experimental standpoint, femtosecond pump-probe transient absorption, probing the spectral region from the deep-UV to the mid-IR, and femtosecond fluorescence up-conversion spectroscopies have been the workhorse techniques during the last 15 years for the investigation of the excited-state dynamics of the DNA and RNA monomers in solution. These techniques often offer complementary but limited information about the relaxation pathways. More recently, four-wave mixing spectroscopies in the deep-UV [107, 192] and time-resolved photoelectron spectroscopy [133] have been applied, but there are still technical challenges to overcome with these approaches [252]. Even so, the ever-close synergism between experimentalists and theoreticians in this field is expected to continue to throw light on our understanding of the photochemistry of nucleic acids and their analogues for years to come.

**Authors' note** Space limitations preclude a comprehensive review, and it is unfitting to include all references to relevant work from many research groups working in this area (particularly in Sect. 2). We apologize for any unintentional omissions.

# References

1. Crespo-Hernández CE, Cohen B, Hare PM, Kohler B (2004) Ultrafast excited-state dynamics in nucleic acids. Chem Rev 104:1977–2019
2. Saigusa H (2006) Excited-state dynamics of isolated nucleic acid bases and their clusters. J Photochem Photobiol C 7:197–210
3. de Vries MS, Hobza P (2007) Gas-phase spectroscopy of biomolecular building blocks. Annu Rev Phys Chem 58:585–612
4. Middleton CT, de La Harpe K, Su C, Law YK, Crespo-Hernández CE, Kohler B (2009) DNA excited-state dynamics: from single bases to the double helix. Annu Rev Phys Chem 60:217–239
5. Towrie M, Doorley GW, George MW, Parker AW, Quinn SJ, Kelly JM (2009) ps-TRIR covers all the bases – recent advances in the use of transient IR for the detection of short-lived species in nucleic acids. Analyst 134:1265–1273
6. Gustavsson T, Improta R, Markovitsi D (2010) DNA/RNA: building blocks of life under UV irradiation. J Phys Chem Lett 1:2025–2030
7. Kohler B (2010) Nonradiative decay mechanisms in DNA model systems. J Phys Chem Lett 1:2047–2053
8. Markovitsi D, Gustavsson T, Akos B (2012) DNA fluorescence. In: Griesbeck A, Oelgemoller M, Ghetti F (eds) CRC handbook of organic photochemistry and photobiology, vol 2. CRC, Boca Raton, pp 1057–1079
9. Kleinermanns K, Nachtigallová D, de Vries MS (2013) Excited state dynamics of DNA bases. Int Rev Phys Chem 32:308–342
10. Wenska G, Taras-Goślińska K, Skalski B, Maciejewski A, Burdziński G, Karolczak J (2006) Putative phototautomerization of 4-thiouridine in the $S_2$ excited state revealed by fluorescence study using picosecond laser spectroscopy. J Photochem Photobiol A 181:12–18
11. Harada Y, Suzuki T, Ichimura T, Xu Y-Z (2007) Triplet formation of 4-thiothymidine and its photosensitization to oxygen studied by time-resolved thermal lensing technique. J Phys Chem B 111:5518–5524
12. Kobayashi T, Harada Y, Suzuki T, Ichimura T (2008) Excited state characteristics of 6-azauracil in acetonitrile: drastically different relaxation mechanism from uracil. J Phys Chem A 112:13308–13315
13. Wenska G, Koput J, Burdziński G, Taras-Goslinska K, Maciejewski A (2009) Photophysical and photochemical properties of the $T_1$ excited state of thioinosine. J Photochem Photobiol A 206:93–101
14. Kobayashi T, Kuramochi H, Harada Y, Suzuki T, Ichimura T (2009) Intersystem crossing to excited triplet state of aza analogues of nucleic acid bases in acetonitrile. J Phys Chem A 113:12088–12093
15. Kobayashi T, Kuramochi H, Suzuki T, Ichimura T (2010) Triplet formation of 6-azauridine and singlet oxygen sensitization with UV light irradiation. Phys Chem Chem Phys 12:5140–5148

16. Kuramochi H, Kobayashi T, Suzuki T, Ichimura T (2010) Excited-state dynamics of 6-aza-2-thiothymine and 2-thiothymine: highly efficient intersystem crossing and singlet oxygen photosensitization. J Phys Chem B 114:8782–8789
17. Harada Y, Okabe C, Kobayashi T, Suzuki T, Ichimura T, Nishi N, Xu Y-Z (2010) Ultrafast intersystem crossing of 4-thiothymidine in aqueous solution. J Phys Chem Lett 1:480–484
18. Reichardt C, Crespo-Hernández CE (2010) Room-temperature phosphorescence of the DNA monomer analogue 4-thiothymidine in aqueous solution after UVA excitation. J Phys Chem Lett 1:2239–2243
19. Reichardt C, Crespo-Hernández CE (2010) Ultrafast spin crossover in 4-thiothymidine in an ionic liquid. Chem Commun 46:5963–5965
20. Etinski M, Marian CM (2010) Overruling the energy gap law: fast triplet formation in 6-azauracil. Phys Chem Chem Phys 12:15665–15671
21. Wenska G, Filipiak P, Taras-Goślińska K, Sobierajska A, Gdaniec Z (2011) Orientation-dependent quenching of the triplet excited 6-thiopurine by nucleobases. J Photochem Photobiol A 217:55–61
22. Reichardt C, Guo C, Crespo-Hernández CE (2011) Excited-state dynamics in 6-thioguanosine from the femtosecond to microsecond time scale. J Phys Chem B 115:3263–3270
23. Zhang Y, Zhu X, Haygood MT, Gao R (2011) Direct observation and quantitative characterization of singlet oxygen in aqueous solution upon UVA excitation of 6-thioguanines. J Phys Chem B 115:1889–1894
24. Zhang Y, Barnes AN, Zhu X, Campbell NF, Gao R (2011) Quantification of thiopurine/UVA-induced singlet oxygen production. J Photochem Photobiol A 224:16–24
25. Gobbo JP, Borin AC, Serrano-Andrés L (2011) On the relaxation mechanisms of 6-azauracil. J Phys Chem B 115:6243–6251
26. Brem R, Karran P (2012) Multiple forms of DNA damage caused by UVA photoactivation of DNA 6-thioguanine. Photochem Photobiol 88:5–13
27. Martínez-Fernández L, González L, Corral I (2012) An *ab initio* mechanism for efficient population of triplet states in cytotoxic sulfur substituted DNA bases: the case of 6-thioguanine. Chem Commun 48:2134–2136
28. Gobbo JP, Borin AC (2012) On the mechanisms of triplet excited state population in 8-azaadenine. J Phys Chem B 116:14000–14007
29. Cui G, Fang W (2013) State-specific heavy-atom effect on intersystem crossing processes in 2-thiothymine: a potential photodynamic therapy photosensitizer. J Chem Phys 138:044315
30. Gobbo JP, Borin AC (2013) On the population of triplet excited states of 6-aza-2-thiothymine. J Phys Chem A 117:5589–5596
31. Taras-Goślińska K, Burdziński G, Wenska G (2014) Relaxation of the $T_1$ excited state of 2-thiothymine, its riboside and deoxyriboside - enhanced nonradiative decay rate induced by sugar substituent. J Photochem Photobiol A 275:89–95
32. Pollum M, Crespo-Hernández CE (2014) Communication: the dark singlet state as a doorway state in the ultrafast and efficient intersystem crossing dynamics in 2-thiothymine and 2-thiouracil. J Chem Phys 140:071101
33. Martinez-Fernandez L, Corral I, Granucci G, Persico M (2014) Competing ultrafast intersystem crossing and internal conversion: a time resolved picture for the deactivation of 6-thioguanine. Chem Sci 5:1336–1347
34. Favre A (1990) 4-Thiouridine as intrinsic photoaffinity probe of nucleic acid structure and nucleic acid-protein interactions. In: Morrison H (ed) Bioorganic photochemistry. Wiley, New York, pp 379–425
35. Favre A, Saintomé C, Fourrey J-L, Clivio P, Laugâa P (1998) Thionucleobases as intrinsic photoaffinity probes of nucleic acid structure and nucleic acid-protein interactions. J Photochem Photobiol B 42:109–124
36. Attard NR, Karran P (2012) UVA photosensitization of thiopurine and skin cancer in organ transplant recipients. Photochem Photobiol Sci 11:62–68

37. Kaba SE, Kyritsis AP (1997) Recognition and management of gliomas. Drugs 53:235–244
38. Massey A, Xu Y-Z, Karran P (2002) Ambiguous coding is required for the lethal interaction between methylated DNA bases and DNA mismatch repair. DNA Repair 1:275–286
39. Ren X, Li F, Jeffs G, Zhang X, Xu Y-Z, Karran P (2010) Guanine sulphinate is a major stable product of photochemical oxidation of DNA 6-thioguanine by UVA irradiation. Nucleic Acids Res 38:1832–1840
40. Zheng Q, Xu Y-Z, Swann PF (1997) Photochemical cross-linking of λ-Cro repressor to operator DNA containing 4-thiothymine or 6-thioguanine. Nucleos Nucleot 16:1799–1803
41. Wang Z, Rana TM (1998) RNA-protein interactions in the Tat-trans-activation response element complex determined by site-specific photo-cross-linking. Biochemistry 37:4235–4243
42. Reelfs O, Karran P, Young AR (2012) 4-Thiothymidine sensitization of DNA to UVA offers potential for a novel photochemotherapy. Photochem Photobiol Sci 11:148–154
43. Massey A, Xu Y-Z, Karran P (2001) Photoactivation of DNA thiobases as a potential novel therapeutic option. Curr Biol 11:1142–1146
44. Zhang X, Jeffs G, Ren X, O'Donovan P, Montaner B, Perrett CM, Karran P, Xu Y-Z (2007) Novel DNA lesions generated by the interaction between therapeutic thiopurines and UVA light. DNA Repair 6:344–354
45. Prodgeon SW, Heer R, Taylor GA, Newell DR, O'Toole K, Robinson M, Xu Y-Z, Karran P, Boddy AV (2011) Thiothymidine combined with UVA as a potential novel therapy for bladder cancer. Br J Cancer 104:1869–1876
46. Roblin R, Lampen J, English JP, Cole QP, Vaughan JR (1945) Studies in chemotherapy. VIII Methionine and purine antagonists and their relation to the sulfonamides. J Am Chem Soc 67:290–294
47. Skoda J (1963) Mechanism of action and application of azapyrimidines. Prog Nucl Acid Res 2:197
48. Broughton BJ, Chaplen P, Knowles P, Lunt E, Pain DL, Wooldridge KRH, Ford R, Marshall S, Walker JL, Maxwell DR (1974) New inhibitor of reagin-mediated anaphylaxis. Nature 251:650–652
49. El-Brollosy NR (2008) Synthesis and antimicrobial evaluation of 6-azauracil non-nucleosides. Monatsh Chem 139:1483–1490
50. Schindler R, Welch AD (1957) Ribosidation as a means of activating 6-azauracil as an inhibitor of cell reproduction. Science 125:548–549
51. Shnider BI, Frei E III, Tuohy JH, Gorman J, Freireich EJ, Brindley CO Jr, Clements J (1960) Clinical studies of 6-azauracil. Cancer Res 20:28–33
52. Handschumacher RE, Skoda J, Sorm F (1963) Metabolic and biochemical effects of 6-azacytidine in mice with Ehrlich ascites carcinoma. Collect Czech Chem Commun 28:2983–2990
53. Raska K, Juroycik M, Sormoya Z, Sorm F (1965) On the metabolism of 5-azacytidine and 5-aza-2′-deoxycytidine in mice. Collect Czech Chem Commun 30:3001–3006
54. Kozlowski DL, Singh P, Hodgson DJ (1974) Aza analogs of nucleic acid constituents. V. The crystal and molecular structure of 8-azaguanine hydrochloride monohydrate. Acta Crystallogr B 30:2806–2811
55. Montgomery JA (1959) The relation of anticancer activity to chemical structure. A review. Cancer Res 19:447–463
56. Spremulli EN, Crabtree GW, Dexter DL, Chu SH, Farineau DM, Ghoda LY, McGowan DL, Diamond I, Parks REJ, Calabresi P (1982) Biochemical pharmacology and toxicology of 8-azaadenosine alone and in combination with 2'-deoxycoformycin (pentostatin). Biochem Pharmacol 31:2415–2421
57. Penn I (1994) The problem of cancer in transplant patients: an overview. Transplant Sci 4:23–32
58. Swann PF, Waters TR, Moulton DC, Xu Y-Z, Edwards M, Mace R (1996) Role of postreplicative DNA mismatch repair in the cytotoxic action of thioguanine. Science 273:1109–1111

59. Karran P (2006) Thiopurines, DNA damage, DNA repair and therapy-related cancer. Br Med Bull 79–80:153–170
60. Perrett CM, Walker SL, O'Donovan P, Warwick J, Harwood CA, Karran P, McGregor JM (2008) Azathioprine treatment sensitizes human skin to ultraviolet A radiation. Br J Dermatol 159:198–204
61. Karran P, Attard N (2008) Thiopurines in current medical practice: molecular mechanisms and contributions to therapy-related cancer. Nat Rev Cancer 8:24–36
62. Cooke MS, Duarte TL, Cooper D, Chen J, Nandagopal S, Evans MD (2008) Combination of azathioprine and UVA irradiation is a major source of cellular 8-oxo-7,8-dihydro-2'-deoxyguanosine. DNA Repair 7:1982–1989
63. Chen MS, Chang PK, Prusoff WH (1976) Photochemical studies and ultraviolet sensitization of Escherichia coli thymidylate kinase by various halogenated substrate analogs. J Biol Chem 251:6555–6561
64. O'Donovan P, Perrett CM, Zhang X, Montaner B, Xu Y-Z, Harwood CA, McGregor JM, Walker SL, Hanaoka F, Karran P (2005) Azathioprine and UVA light generate mutagenic oxidative DNA damage. Science 309:1871–1874
65. Daniels M, Hauswirth W (1971) Fluorescence of the purine and pyrimidine bases of the nucleic acids in neutral aqueous solution at 300 K. Science 171:675–677
66. Callis PR (1979) Polarized fluorescence and estimated lifetimes of the DNA bases at room temperature. Chem Phys Lett 61:563–567
67. Callis PR (1983) Electronic states and luminescence of nucleic acid systems. Annu Rev Phys Chem 34:329–357
68. Reuther A, Nikogosyan DN, Laubereau A (1996) Primary photochemical processes in thymine in concentrated aqueous solution studied by femtosecond UV spectroscopy. J Phys Chem 100:5570–5577
69. Reuther A, Iglev H, Laenen R, Laubereau A (2000) Femtosecond photo-ionization of nucleic acid bases: electronic lifetimes and electron yields. Chem Phys Lett 325:360–368
70. Pecourt J-ML, Peon J, Kohler B (2000) Ultrafast internal conversion of electronically excited RNA and DNA nucleosides in water. J Am Chem Soc 122:9348–9349
71. Peon J, Zewail AH (2001) DNA/RNA nucleotides and nucleosides: direct measurement of excited-state lifetimes by femtosecond fluorescence up-conversion. Chem Phys Lett 348:255–262
72. Gustavsson T, Sharonov A, Markovitsi D (2002) Thymine, thymidine and thymidine 5'-monophosphate studied by femtosecond fluorescence upconversion spectroscopy. Chem Phys Lett 351:195–200
73. Gustavsson T, Sharonov A, Onidas D, Markovitsi D (2002) Adenine, deoxyadenosine and deoxyadenosine 5'-monophosphate studied by femtosecond fluorescence upconversion spectroscopy. Chem Phys Lett 356:49–54
74. Voet D, Gratzer WB, Cox RA, Doty P (1963) Absorption spectra of nucleotides, polynucleotides, and nucleic acids in the far ultraviolet. Biopolymers 1:193–208
75. Platt JR (1949) Classification of spectra of cata-condensed hydrocarbons. J Chem Phys 17:484–495
76. Murrell JN (1971) The theory of the electronic spectra of organic molecules. Chapman and Hall, London
77. Bensasson RV, Land EJ, Truscott TG (1983) Flash photolysis and pulse radiolysis, vol 1. Pergamon, New York
78. Vigny P (1971) Fluorescence of nucleosides and nucleotides at ambient temperature. C R Acad Sci Ser D 272:3206–3209
79. Onidas D, Markovitsi D, Marguet S, Sharonov A, Gustavsson T (2002) Fluorescence properties of DNA nucleosides and nucleotides: a refined steady-state and femtosecond investigation. J Phys Chem B 106:11367–11374
80. Ababneh AM, Large CC, Georghiou S (2007) Electronic excited-states properties of the purine nucleoside bases of DNA at room temperature. J Appl Sci Res 3:1288–1295

81. Cheng CC-W, Ma C, Chan CT-L, Ho KY-F, Kwok W-M (2013) The solvent effect and identification of a weakly emissive state in nonradiative dynamics of guanine nucleosides and nucleotides – a combined femtosecond broadband time-resolved fluorescence and transient absorption study. Photochem Photobiol Sci 12:1351–1365

82. Miannay F-A, Gustavsson T, Banyasz A, Markovitsi D (2010) Excited-state dynamics of dGMP measured by steady-state and femtosecond fluorescence spectroscopy. J Phys Chem A 114:3256–3263

83. Ploeser JM, Loring HS (1949) The ultraviolet absorption spectra of the pyrimidine ribonucleosides and ribonucleotides. J Biol Chem 178:431–437

84. Gustavsson T, Banyasz A, Lazzarotto E, Markovitsi D, Scalmani G, Frisch MJ, Barone V, Improta R (2006) Singlet excited-state behavior of uracil and thymine in aqueous solution: a combined experimental and computational study of 11 uracil derivatives. J Am Chem Soc 128:607–619

85. Hauswirth WW, Daniels M (1971) Fluorescence of thymine in aqueous solution at 300 K. Photochem Photobiol 13:157–163

86. Gustavsson T, Sarkar N, Lazzarotto E, Markovitsi D, Improta R (2006) Singlet excited state dynamics of uracil and thymine derivatives: a femtosecond fluorescence upconversion study in acetonitrile. Chem Phys Lett 429:551–557

87. Daniels M (1976) Excited states of the nucleic acids: bases, mononucleosides, and mononucleotides. In: Wang SY (ed) Photochemistry and photobiology of nucleic acids, vol 1. Academic, New York, pp 23–108

88. Pancur T, Schwalb NK, Renth F, Temps F (2005) Femtosecond fluorescence up-conversion spectroscopy of adenine and adenosine: experimental evidence for the $\pi\sigma^*$ state? Chem Phys 313:199–212

89. Gustavsson T, Sarkar N, Vayá I, Jiménez MC, Markovitsi D, Improta R (2013) A joint experimental/theoretical study of the ultrafast excited state deactivation of deoxyadenosine and 9-methyladenine in water and acetonitrile. Photochem Photobiol Sci 12:1375–1386

90. Görner H (1994) Photochemistry of DNA and related biomolecules - quantum yields and consequences of photoionization. J Photochem Photobiol B 26:117–139

91. Crespo-Hernández CE, Martínez L, González-Sierra AE, Robles-Irizarry L, Díaz-Vázquez A, Arce R (2002) The 254 nm low intensity and 266 nm laser photochemistry of adenosine – effect of pH and concentration on the reactive precursors of the principal products, adenine and FAPyAde. J Photochem Photobiol A 152:123–133

92. Arce R, Martínez L, Danielsen E (1993) The photochemistry of adenosine: intermediates contributing to its photodegradation mechanism in aqueous solution at 298 K and characterization of the major product. Photochem Photobiol 58:318–328

93. Crespo-Hernández CE, Flores S, Torres C, Negrón-Encarnación I, Arce R (2000) Part I. Photochemical and photophysical studies of guanine derivatives: intermediates contributing to its photodestruction mechanism in aqueous solution and the participation of the electron adduct. Photochem Photobiol 71:534–543

94. Fisher GJ, Johns HE (1973) Thymine hydrate formed by ultraviolet and gamma irradiation of aqueous solutions. Photochem Photobiol 18:23–27

95. Brown IH, Johns HE (1968) Photochemistry of uracil. Intersystem crossing and dimerization in aqueous solution. Photochem Photobiol 8:273–286

96. Swenson PA, Setlow RB (1963) Kinetics of dimer formation and photohydration in ultraviolet-irradiated polyuridylic acid. Photochem Photobiol 2:419–434

97. Cadet J, Vigny P (1990) The photochemistry of nucleic acids. In: Morrison H (ed) Bioorganic photochemistry, vol 1. New York, pp 1–272

98. Nikogosyan DN, Angelov DA, Oraevsky AA (1982) Determination of parameters of excited states of DNA and RNA bases by laser UV photolysis. Photochem Photobiol 35:627–635

99. Salet C, Bensasson R (1975) Studies on thymine and uracil triplet excited state in acetonitrile and water. Photochem Photobiol 22:231–235

100. Lamola AA, Mittal JP (1966) Solution photochemistry of thymine and uracil. Science 154:1560–1561
101. Salet C, Bensasson R, Becker RS (1979) Triplet excited states of pyrimidine nucleosides and nucleotides. Photochem Photobiol 30:325–329
102. Marguet S, Markovitsi D (2005) Time-resolved study of thymine dimer formation. J Am Chem Soc 127:5780–5781
103. Canuel C, Elhanine M, Mons M, Piuzzi F, Tardivel B, Dimicoli I (2006) Time-resolved photoelectron and photoion fragmentation spectroscopy study of 9-methyladenine and its hydrates: a contribution to the understanding of the ultrafast radiationless decay of excited DNA bases. Phys Chem Chem Phys 8:3978–3987
104. Miyazaki J, Kida Y, Kobayashi T (2013) Electronic excited state and vibrational dynamics of water solution of cytosine observed by time-resolved transient absorption spectroscopy with sub-10fs deep ultraviolet laser pulses. EPJ Web Conf 41:05017
105. Kwok W-M, Ma C, Phillips DL (2008) A doorway state leads to photostability or triplet photodamage in thymine DNA. J Am Chem Soc 130:5131–5139
106. Gustavsson T, Bányász Á, Sarkar N, Markovitsi D, Improta R (2008) Assessing solvent effects on the singlet excited state lifetime of uracil derivatives: a femtosecond fluorescence upconversion study in alcohols and $D_2O$. Chem Phys 350:186–192
107. Tseng C-H, Sándor P, Kotur M, Weinacht TC, Matsika S (2012) Two-dimensional Fourier transform spectroscopy of adenine and uracil using shaped ultrafast laser pulses in the deep UV. J Phys Chem A 116:2654–2661
108. Stuhldreier MC, Temps F (2013) Ultrafast photo-initiated molecular quantum dynamics in the DNA dinucleotide d(ApG) revealed by broadband transient absorption spectroscopy. Faraday Discuss 163:173–178
109. Serrano-Andrés L, Merchán M (2009) Are the five natural DNA/RNA base monomers a good choice from natural selection? A photochemical perspective. J Photochem Photobiol C 10:21–32
110. Hudock HR, Levine BG, Thompson AL, Satzger H, Townsend D, Gador N, Ullrich S, Stolow A, Martínez TJ (2007) *Ab initio* molecular dynamics and time-resolved photoelectron spectroscopy of electronically excited uracil and thymine. J Phys Chem A 111:8500–8508
111. Karunakaran V, Kleinermanns K, Improta R, Kovalenko SA (2009) Photoinduced dynamics of guanosine monophosphate in water from broad-band transient absorption spectroscopy and quantum-chemical calculations. J Am Chem Soc 131:5839–5850
112. Conti I, Garavelli M, Orlandi G (2009) Deciphering low energy deactivation channels in adenine. J Am Chem Soc 131:16108–16118
113. Domcke W, Yarkony DR, Koppel H (2004) Conical intersections: electronic structure, dynamics & spectroscopy. Adv Ser Phys Chem, vol 15. World Scientific, Singapore
114. Domcke W, Yarkony DR (2012) Role of conical intersections in molecular spectroscopy and photoinduced chemical dynamics. Annu Rev Phys Chem 63:325–352
115. Matsika S (2005) Three-state conical intersections in nucleic acid bases. J Phys Chem A 109:7538–7545
116. Matsika S, Krause P (2011) Nonadiabatic events and conical intersections. Annu Rev Phys Chem 62:621–643
117. Shukla MK, Leszczynski J (2007) Elelctronic spectra, excited state structures and interactions of nucleic acid bases and bases assemblies: a review. J Biomol Struct Dyn 25:93–118
118. Asturiol D, Lasorne B, Robb MA, Blancafort L (2009) Photophysics of the π, π* and n, π* states of thymine: MS-CASPT2 minimum-energy paths and CASSCF on-the-fly dynamics. J Phys Chem A 113:10211–10218
119. Szymczak JJ, Barbatti M, Hoo JTS, Adkins JA, Windus TL, Nachtigallová D, Lischka H (2009) Photodynamics simulations of thymine: relaxation into the first excited singlet state. J Phys Chem A 113:12686–12693
120. Lan Z, Fabiano E, Thiel W (2011) QM/MM nonadiabatic decay dynamics of 9H-adenine in aqueous solution. ChemPhysChem 12:1989–1998

121. Lan Z, Fabiano E, Thiel W (2009) Photoinduced nonadiabatic dynamics of pyrimidine nucleobases: on-the-fly surface-hopping study with semiempirical methods. J Phys Chem B 113:3548–3555
122. Asturiol D, Lasorne B, Worth GA, Robb MA, Blancafort L (2010) Exploring the sloped-to-peaked $S_2/S_1$ seam of intersection of thymine with electronic structure and direct quantum dynamics calculations. Phys Chem Chem Phys 12:4949–4958
123. Hudock HR, Martínez TJ (2008) Excited-state dynamics of cytosine reveal multiple intrinsic subpicosecond pathways. ChemPhysChem 9:2486–2490
124. Improta R, Barone V, Lami A, Santoro F (2009) Quantum dynamics of the ultrafast $\pi\pi*/n\pi*$ population transfer in uracil and 5-fluoro-uracil in water and acetonitrile. J Phys Chem B 113:14491–14503
125. Billinghurst BE, Loppnow GR (2006) Excited-state structural dynamics of cytosine from resonance Raman spectroscopy. J Phys Chem A 110:2353–2359
126. Billinghurst BE, Oladepo SA, Loppnow GR (2012) Initial excited-state structural dynamics of thymine derivatives. J Phys Chem B 116:10496–10503
127. Yasari S, Brost P, Loppnow GR (2007) Initial excited-state structural dynamics of thymine are coincident with the expected photochemical dynamics. J Phys Chem A 111:5130–5135
128. Ng SS, Teimoory F, Loppnow GR (2011) Mass-tuned initial excited-state structural dynamics of DNA nucleobases from UV resonance Raman spectroscopy: 5-deuterouracil. J Phys Chem Lett 2:2362–2365
129. Zhu X-M, Wang H-G, Zheng X, Phillips David L (2008) Role of ribose in the initial excited state structural dynamics of thymidine in water solution: a resonance Raman and density functional theory investigation. J Phys Chem B 112:15828–15836
130. El-Yazbi AF, Palech A, Loppnow GR (2011) Initial excited-state structural dynamics of 2′-deoxyguanosine determined via UV resonance Raman spectroscopy. J Phys Chem A 115:10445–10451
131. Middleton C, Cohen B, Kohler B (2007) Solvent and solvent isotope effects on the vibrational cooling dynamics of a DNA base derivative. J Phys Chem A 111:10460–10467
132. Cohen B, Hare PM, Kohler B (2003) Ultrafast excited-state dynamics of adenine and monomethylated adenines in solution: implications for the nonradiative decay mechanism. J Am Chem Soc 125:13594–13601
133. Buchner F, Ritze H-H, Lahl J, Lübcke A (2013) Time-resolved photolectron spectroscopy of adenine and adenosine in aqueous solution. Phys Chem Chem Phys 15:11402–11408
134. Pecourt J-ML, Peon J, Kohler B (2001) DNA excited-state dynamics: ultrafast internal conversion and vibrational cooling in a series of nucleosides. J Am Chem Soc 123:10370–10378
135. Crespo-Hernández CE, Kohler B (2004) Influence of secondary structure on electronic energy relaxation in adenine homopolymers. J Phys Chem B 108:11182–11188
136. Kwok W-M, Ma C, Phillips DL (2006) Femtosecond time- and wavelength-resolved fluorescence and absorption spectroscopy study of the excited states of adenosine and an adenine oligomer. J Am Chem Soc 128:11894–11905
137. Serrano-Andrés L, Merchán M, Borin AC (2006) Adenine and 2-aminopurine: paradigms of modern theoretical photochemistry. Proc Natl Acad Sci U S A 103:8691–8696
138. Santoro F, Improta R, Fahleson T, Kauczor J, Norman P, Coriani S (2014) Relative stability of the $L_a$ and $L_b$ excited states in adenine and guanine: direct evidence from TD-DFT calculations of MCD spectra. J Phys Chem Lett 5:1806–1811
139. Bishop SM, Malone M, Phillips D, Parker AW, Symons MCR (1994) Singlet oxygen sensitisation by excited state DNA. J Chem Soc Chem Commun 7:871–872
140. Hare PM, Crespo-Hernández CE, Kohler B (2007) Internal conversion to the electronic ground state occurs via two distinct pathways for pyrimidine bases in aqueous solution. Proc Natl Acad Sci USA 104:435–440

141. Crespo-Hernández CE, de La Harpe K, Kohler B (2008) Ground-state recovery following UV excitation is much slower in G·C-DNA duplexes and hairpins than in mononucleotides. J Am Chem Soc 130:10844–10845

142. Takaya T, Su C, De La Harpe K, Crespo-Hernández CE, Kohler B (2008) UV excitation of single DNA and RNA strands produces high yields of exciplex states between two stacked bases. Proc Natl Acad Sci USA 105:10285–10290

143. Foote CS, Dobrowolski DC (1984) In: Bors W, Saran M, Tait D (eds) Oxygen radicals in chemistry and biology. Walter de Gruyter, West Berlin, pp 467–470

144. Heihoff K, Redmond RW, Braslavsky SE, Rougee M, Salet C, Favre A, Bensasson RV (1990) Quantum yields of triplet and $O_2(^1\Delta g)$ formation of 4-thiouridine in water and acetonitrile. Photochem Photobiol 51:635–641

145. Nosenko Y, Kunitski M, Riehn C, Harbach PHP, Drew A, Brutschy B (2010) The structure of adenine monohydrates studied by femtosecond multiphoton ionization detected IR spectroscopy and quantum chemical calculations. Phys Chem Chem Phys 12:863–870

146. Sobolewski AL, Domcke W (2002) On the mechanism of nonradiative decay of DNA bases: *ab initio* and TDDFT results for the excited states of 9H-adenine. Eur Phys J D 20:369–374

147. Yamazaki S, Domcke W, Sobolewski AL (2008) Nonradiative decay mechanisms of the biologically relevant tautomer of guanine. J Phys Chem A 112:11965–11968

148. Roberts GM, Stavros VG (2014) The role of πσ* states in the photochemistry of heteroaromatic biomolecules and their subunits: insights from gas-phase femtosecond spectroscopy. Chem Sci 5:1698–1722

149. Wells KL, Hadden DJ, Nix MGD, Stavros VG (2010) Competing πσ* states in the photodissociation of adenine. J Phys Chem Lett 1:993–996

150. Chen H, Li S (2006) *Ab initio* study on deactivation pathways of excited 9H-guanine. J Chem Phys 124

151. Barbatti M, Aquino AJA, Szymczak JJ, Nachtigallová D, Hobza P, Lischka H (2010) On the relaxation mechanisms of UV-photoexcited DNA and RNA nucleobases. Proc Natl Acad Sci USA 107:21453–21458

152. Zhang Y, Chen J, Kohler B (2013) Hydrogen bond donors accelerate vibrational cooling of hot purine derivatives in heavy water. J Phys Chem A 117:6771–6780

153. Kuimova MK, Dyer J, George MW, Grills DC, Kelly JM, Matousek P, Parker AW, Sun ZX, Towrie M, Whelan AM (2005) Monitoring the effect of ultrafast deactivation of the electronic excited states of DNA bases and polynucleotides following 267 nm laser excitation using picosecond time-resolved infrared spectroscopy. Chem Commun 9:1182–1184

154. Zhang Y, Improta R, Kohler B (2014) Mode-specific vibrational relaxation of photoexcited guanosine 5′-monophosphate and its acid form: a femtosecond broadband mid-IR transient absorption and theoretical study. Phys Chem Chem Phys 16:1487–1499

155. Nielsen JB, Thøgersen J, Jensen SK, Keiding SR (2013) Photo protection of RNA building blocks: adenosine 5′-monophosphate, cytidine 5′-monophosphate and cytosine. Chem Phys Lett 567:50–54

156. Quinn S, Doorley GW, Watson GW, Cowan AJ, George MW, Parker AW, Ronayne KL, Towrie M, Kelly JM (2007) Ultrafast IR spectrscopy of the short-lived transients formed by UV excitation of cytosine derivatives. Chem Commun 21:2130–2132

157. Hare PM, Middleton CT, Mertel KI, Herbert JM, Kohler B (2008) Time-resolved infrared spectroscopy of the lowest triplet state of thymine and thymidine. Chem Phys 347:383–392

158. Keane PM, Wojdyla M, Doorley GW, Watson GW, Clark IP, Greetham GM, Parker AW, Towrie M, Kelly JM, Quinn SJ (2011) A comparative picosecond transient infrared study of 1-methylcytosine and 5'-dCMP that sheds further light on the excited states of cytosine derivatives. J Am Chem Soc 133:4212–4215

159. Hare PM, Crespo-Hernández CE, Kohler B (2006) Solvent-dependent photophysics of 1-cyclohexyluracil: ultrafast branching in the initial bright state leads nonradiatively to the electronic ground state and a long-lived $^1n\pi^*$ state. J Phys Chem B 110:18641–18650

160. Fisher GJ, Johns HE (1976) Pyrimidine Photodimers. In: Wang SY (ed) Photochemistry and photobiology of nucleic acids, vol 1. Academic, New York, pp 225–294

161. Ruzsicska BP, Lemaire DGE (1995) DNA photochemistry. In: Horspool WM, Song P-S (eds) CRC handbook of organic photochemistry and photobiology. CRC, Boca Raton, pp 1289–1317

162. Cuquerella MC, Lhiaubet-Vallet V, Bosca F, Miranda MA (2011) Photosensitised pyrimidine dimerisation in DNA. Chem Sci 2:1219–1232

163. Sharonov A, Gustavsson T, Carre V, Renault E, Markovitsi D (2003) Cytosine excited state dynamics studied by femtosecond fluorescence upconversion and transient absorption spectroscopy. Chem Phys Lett 380:173–180

164. Blancafort L, Cohen B, Hare PM, Kohler B, Robb MA (2005) Singlet excited-state dynamics of 5-fluorocytosine and cytosine: an experimental and computational study. J Phys Chem A 109:4431–4436

165. Malone RJ, Miller AM, Kohler B (2003) Singlet excited-state lifetimes of cytosine derivatives measured by femtosecond transient absorption. Photochem Photobiol 77:158–164

166. Kobayashi T, Kida Y (2012) Ultrafast spectroscopy with sub-10 fs deep-ultraviolet pulses. Phys Chem Chem Phys 14:6200–6210

167. Cohen B, Crespo-Hernández CE, Kohler B (2004) Strickler-Berg analysis of excited singlet state dynamics in DNA and RNA nucleosides. Faraday Discuss 127:137–147

168. Kosma K, Schröter C, Samoylova E, Hertel IV, Schultz T (2009) Excited-state dynamics of cytosine tautomers. J Am Chem Soc 131:16939–16943

169. Merchán M, Serrano-Andrés L, Robb MA, Blancafort L (2005) Triplet-state formation along the ultrafast decay of excited singlet cytosine. J Am Chem Soc 127:1820–1825

170. Climent T, González-Luque R, Merchán M, Serrano-Andrés L (2007) On the intrinsic population of the lowest triplet state of uracil. Chem Phys Lett 441:327–331

171. Marian CM, Schneider F, Kleinschmidt M, Tatchen J (2002) Electronic excitation and singlet-triplet coupling in uracil tautomers and uracil-water complexes A quantum chemical investigation. Eur Phys J D 20:357–367

172. Etinski M, Fleig T, Marian CM (2009) Intersystem crossing and characterization of dark states in the pyrimidine nucleobases uracil, thymine, and 1-methylthymine. J Phys Chem A 113:11809–11816

173. Richter M, Marquetand P, González-Vázquez J, Sola I, González L (2012) Femtosecond intersystem crossing in the DNA nucleobase cytosine. J Phys Chem Lett 3:3090–3095

174. Mai S, Marquetand P, Richter M, González-Vázquez J, González L (2013) Singlet and triplet excited-state dynamics study of the keto and enol tautomers of cytosine. ChemPhysChem 14:2920–2931

175. Climent T, González-Ramírez I, González-Luque R, Merchán M, Serrano-Andrés L (2010) Cyclobutane pyrimidine photodimerization of DNA/RNA nucleobases in the triplet state. J Phys Chem Lett 1:2072–2076

176. Yang C, Yu Y, Song D, Wu L, Su H (2011) [2+2] Photocycloaddition reaction dynamics of triplet pyrimidines. J Phys Chem A 115:5335–5345

177. Chorny I, Vieceli J, Benjamin I (2002) Molecular dynamics study of the vibrational relaxation of OClO in bulk liquids. J Chem Phys 116:8904–8911

178. Shiga M, Okazaki S (1999) Molecular dynamics study of vibrational energy relaxation of $CN^-$ in $H_2O$ and $D_2O$ solutions: an application of path integral influence functional theory to multiphonon processes. J Chem Phys 111:5390–5401

179. Lim M, Gnanakaran S, Hochstrasser RM (1997) Charge shifting in the ultrafast photoreactions of $ClO^-$ in water. J Chem Phys 106:3485–3493

180. Chen J, Kohler B (2012) Ultrafast nonradiative decay by hypoxanthine and several methylxanthines in aqueous and acetonitrile solution. Phys Chem Chem Phys 14:10677–10682

181. Nielsen JB, Thøgersen J, Jensen SK, Nielsen SB, Keiding SR (2011) Vibrational dynamics of deoxyguanosine 5′-monophosphate following UV excitation. Phys Chem Chem Phys 13:13821–13826

182. Szyc Ł, Yang M, Nibbering ETJ, Elsaesser T (2010) Ultrafast vibrational dynamics and local interactions of hydrated DNA. Angew Chem Int Ed 49:3598–3610
183. Botan V, Hamm P (2008) Intramolecular vibrational energy relaxation in nitrous acid (HONO). J Chem Phys 129:164506
184. Backus EHG, Nguyen PH, Botan V, Pfister R, Moretto A, Crisma M, Toniolo C, Stock G, Hamm P (2008) Energy transport in peptide helices: a comparison between high- and low-energy excitations. J Phys Chem B 112:9091–9099
185. Huse N, Bruner BD, Cowan ML, Dreyer J, Nibbering ETJ, Miller RJD, Elsaesser T (2005) Anharmonic couplings underlying the ultrafast vibrational dynamics of hydrogen bonds in liquids. Phys Rev Lett 95:147402
186. Hamm P, Ohline SM, Zinth W (1997) Vibrational cooling after ultrafast photoisomerization of azobenzene measured by femtosecond infrared spectroscopy. J Chem Phys 106:519–529
187. Bolinger JC, Hayes SC, Reid PJ (2004) Time resolved infrared absorption studies of geminate recombination and vibrational relaxation in OClO photochemistry. J Chem Phys 121:4795–4803
188. Thomsen CL, Thøgersen J, Keiding SR (2001) Vibrational relaxation of aqueous $CS_2$. J Chem Phys 114:4099–4106
189. Poulsen JA, Thomsen CL, Keiding SR, Thøgersen J (1998) Vibrational relaxation of $ClO_2$ in water. J Chem Phys 108:8461–8471
190. McGovern DA, Quinn S, Doorley GW, Whelan AM, Ronayne KL, Towrie M, Parker AW, Kelly JM (2007) Picosecond infrared probing of the vibrational spectra of transients formed upon UV excitation of stacked G-tetrad structures. Chem Commun 48:5158–5160
191. West BA, Womick JM, Moran AM (2011) Influence of temperature on thymine-to-solvent vibrational energy transfer. J Chem Phys 135:114505
192. West BA, Womick JM, Moran AM (2011) Probing ultrafast dynamics in adenine with mid-UV four-wave mixing spectroscopies. J Phys Chem A 115:8630–8637
193. West BA, Womick JM, Moran AM (2013) Interplay between vibrational energy transfer and excited state deactivation in DNA components. J Phys Chem A 117:5865–5874
194. Görner H (1990) Transients of uracil and thymine derivatives and the quantum yields of electron ejection and intersystem crossing upon 20 ns photolysis at 248 nm. Photochem Photobiol 52:935–948
195. Alam MM, Fujitsuka M, Watanabe A, Ito O (1998) Photochemical properties of excited triplet state of 6H-purine-6-thione investigated by laser flash photolysis. J Phys Chem A 102:1338–1344
196. Milder SJ, Kliger DS (1985) Spectroscopy and photochemistry of thiouracils: implications for the mechanism of photocrosslinking in tRNA. J Am Chem Soc 107:7365–7373
197. Lipsett MN (1965) The isolation of 4-thiouridylic acid from the soluble ribonucleic acid of Escherichia coli. J Biol Chem 240:3975–3978
198. Zachau HG (1969) Transfer ribonucleic acids. Angew Chem Int Ed 8:711–727
199. Pleiss MG, Cerutti PA (1971) Phototransformation of 4-thiouridine in Escherichia coli valine transfer ribonucleic acid to uridine, cytidine, and $N^4$-methylcytidine. Biochemistry 10:3093–3099
200. Taras-Goślińska K, Wenska G, Skalski B, Maciejewski A, Burdziński G, Karolczak J (2002) Intra- and intermolecular electronic relaxation of the second excited singlet and the lowest excited triplet states of 1,3-dimethyl-4-thiouracil in solution. Photochem Photobiol 75:448–456
201. Taras-Goślińska K, Wenska G, Skalski B, Maciejewski A, Burdziński G, Karolczak J (2004) Spectral and photophysical properties of the lowest excited triplet state of 4-thiouridine and its 5-halogeno derivatives. J Photochem Photobiol A 168:227–233
202. Gomzi V (2009) TDDFT study of nucleobase thioanalogues and oxo-derivatives excited states. J Theo Comp Chem 8:71–83

203. Wenska G, Taras-Goślińska K, Łukaszewicz A, Burdziński G, Koput J, Maciejewski A (2011) Mechanism and dynamics of intramolecular triplet state decay of 1-propyl-4-thiouracil and its α-methyl-substituted derivatives studied in perfluoro-1,3-dimethylcyclohexane. Photochem Photobiol Sci 10:1294–1302

204. Shukla MK, Leszczynski J (2004) Electronic transitions of thiouracils in the gas phase and in solution: time-dependent density functional theory (TD-DFT) study. J Phys Chem A 108:10367–10375

205. Igarashi-Yamamoto N, Tajiri A, Hatano M, Shibuya S, Ueda T (1981) Ultraviolet absorption, circular dichroism and magnetic circular dichroism studies of sulfur-containing nucleic acid bases and their nucleosides. Biochim Biophys Acta 656:1–15

206. Meisenheimer KM, Koch TH (1997) Photocross-linking of nucleic acids to associated proteins. Crit Rev Biochem Mol Biol 32:101–140

207. Salet C, Bensasson RV, Favre A (1983) Studies on the triplet excited state of 4-thiouridine. Photochem Photobiol 38:521–525

208. Wenska G, Filipiak P, Burdzinski G, Pedzinski T, Hug GL, Gdaniec Z (2009) Photocycloaddition of the $T_1$ excited state of thioinosine to uridine and adenosine. Photochem Photobiol Sci 8:1379–1388

209. Vendrell-Criado V, Sáez JA, Lhiaubet-Vallet V, Cuquerella MC, Miranda MA (2013) Photophysical properties of 5-substituted 2-thiopyrimidines. Photochem Photobiol Sci 12:1460–1465

210. Chenon M-T, Pugmire RJ, Grant DM, Panzica RP, Townsend LB (1975) Carbon-13 magnetic resonance. XXV. A basic set of parameters for the investigation of tautomerism in purines established from carbon-13 magnetic resonance studies using certain purines and pyrrolo [2,3-d]pyrimidines. J Am Chem Soc 97:4627–4636

211. Chenon M-T, Pugmire RJ, Grant DM, Panzica RP, Townsend LB (1975) Carbon-13 magnetic resonance. XXVI A quantitative determination of the tautomeric populations of certain purines. J Am Chem Soc 97:4636–4642

212. Santhosh C, Mishra PC (1993) Electronic structures and spectra of 6-mercaptopurine and 6-thioguanine. Spectrochim Acta 49A:985–993

213. Hemmens VJ, Moore DE (1986) Photochemical sensitization by azathioprine and its metabolites—I. 6-Mercaptopurine. Photochem Photobiol 43:247–255

214. El-Sayed MA (1962) The radiationless processes involving change of multiplicity in the diazenes. J Chem Phys 36:573–574

215. El-Sayed MA (1963) Spin-orbit coupling and the radiationless processes in nitrogen heterocycles. J Chem Phys 38:2834–2838

216. Peak MJ, Peak JG, Carnes BA (1987) Induction of direct and indirect single-strand breaks in human cell DNA by far- and near-ultraviolet radiation: action spectrum and mechanisms. Photochem Photobiol 45:381–387

217. Komeda K, Iwamoto S, Kominami S, Ohnishi T (1997) Induction of cell killing, mutation and *umu* gene expression by 6-mercaptopurine or 2-thiouracil with UVA irradiation. Photochem Photobiol 65:115–118

218. Wierzchowski J, Wielgus-Kutrowska B, Shugar D (1996) Fluorescence emission properties of 8-azapurines and their nucleosides, and application to the kinetics of the reverse synthetic reaction of purine nucleoside phosphorylase. Biochim Biophys Acta 1290:9–17

219. Mędza G, Wierzchowski J, Kierdaszuk B, Shugar D (2009) Fluorescence emission properties of 8-aza analogues of caffeine, theophylline, and related *N*-alkyl xanthines. Bioorg Med Chem 17:2585–2591

220. Jiang D, Seela F (2010) Oligonucleotide duplexes and multistrand assemblies with 8-aza-2′-deoxyisoguanosine: a fluorescent isoGd shape mimic expanding the genetic alphabet and forming ionophores. J Am Chem Soc 132:4016–4024

221. Wierzchowski J, Mędza G, Sepioł J, Szabelski M, Shugar D (2012) Fluorescence emission properties of 8-azaisoguanine and its N-methyl derivatives: ground- and excited-state tautomerism. J Photochem Photobiol A 237:64–70

222. Wierzchowski J, Sepioł J, Sulikpwski D, Kierdaszuk B, Shugar D (2006) Fluorescence emission properties of 8-azaxanthine and its *N*-alkyl derivatives: excited-state proton transfer, and potential applications in enzymology. J Photochem Photobiol A 179:276–282

223. Mishra PC, Pandey KS (1989) Electronic spectra of 8-azaguanine in solution: evidence for double-vell potential surface and effect of dissolved oxygen. Proc Ind Acad Sci (Chem Sci) 101:65–74

224. Wierzchowski J (2010) Excited-state proton transfer in nucleic acids bases, nucleosides, and their analogues: a mini-review. Curr Top Biophys 33:9–16

225. Kára J, Šorm F (1963) Study of the substrate specificity of deoxynucleoside phosphokinases. Phosphorylation of $^3$H-thymidine, 6-azathymidine, deoxyuridine, 6-azadeoxyuridine and 5-hydroxymethyldeoxyuridine labelled with $^{14}$C, by enzymes from normal and malignant mammalian tissues in vitro. Collect Czech Chem Commun 28:1441–1448

226. Holý A, Cech D (1974) Synthesis of 2′-deoxythymidine, 2′-deoxy-5-fluorouridine, and 2′-deoxy-6-azauridine from ribonucleosides. Collect Czech Chem Commun 39:31857–33167

227. Drašar P, Hein L, Beránek J (1976) 2′,3′-O-Carbonyl derivatives of uridine and 6-azauridine. Synthesis of 2′-deoxyuridine, 2′-deoxy-6-azauridine and 2′-deoxy-6-azacytidine. Collect Czech Chem Commun 41:2110–2123

228. Freskos JN (1989) Synthesis of 2′-deoxypyrimidine nucleosides via copper(I) iodine catalysis. Nucleos Nucleot 8:549–555

229. Seela F, Chittepu P (2007) Oligonucleotides containing 6-aza-2′-deoxyuridine: synthesis, nucleobase protection, pH-dependent duplex stability and metal-DNA formation. J Org Chem 72:4358–4366

230. Sanghvi Y, Hoke GD, Freier SM, Zounes MC, Gonzalez C, Cummins L, Sasmor H, Cook PD (1993) Antisense oligodeoxynucleotides: synthesis, biophysical and biological evaluation of oligodeoxynucleotides containing modified pyrimidines. Nucleic Acids Res 21:3197–3203

231. Matsika S (2004) Radiationless decay of excited states of uracil through conical intersections. J Phys Chem A 108:7584–7590

232. Zgierski MZ, Patchkovskii S, Fujiwara T, Lim EC (2005) On the origin of the ultrafast internal conversion of electronically excited pyrimidine bases. J Phys Chem A 109:9384–9387

233. Merchán M, González-Luque R, Climent T, Serrano-Andrés L, Rodríguez E, Reguero M, Peláez D (2006) Unified model for the ultrafast decay of pyrimidine nucleobases. J Phys Chem B 110:26471–26476

234. Laermer F, Elsaesser T, Kaiser W (1989) Ultrashort vibronic and thermal relaxation of dye molecules after femtosecond ultraviolet excitation. Chem Phys Lett 156:381–386

235. Elsaesser T, Kaiser W (1991) Vibrational and vibronic relaxation of large polyatomic molecules in liquids. Annu Rev Phys Chem 42:83–107

236. Santoro F, Barone V, Gustavsson T, Improta R (2006) Solvent effect on the singlet excited-state lifetimes of nucleic acid bases: a computational study of 5-fluorouracil and uracil in acetonitrile and water. J Am Chem Soc 128:16312–16322

237. Schweitzer C, Schmidt R (2003) Physical mechanisms of generation and deactivation of singlet oxygen. Chem Rev 103:1685–1758

238. Gasparro FP (2000) Sunscreens, skin photobiology, and skin cancer: the need for UVA protection and evaluation of efficacy. Environ Health Perspect 108:71–78

239. Wondrak GT, Jacobson MK, Jacobson EL (2006) Endogenous UVA-photosensitizers: mediators of skin photodamage and novel targets for skin photoprotection. Photochem Photobiol Sci 5:215–237

240. Cadet J, Douki T, Ravanat J-L, Mascio PD (2009) Sensitized formation of oxidatively generated damage to cellular DNA by UVA radiation. Photochem Photobiol Sci 8:903–911

241. Mouret S, Baudouin C, Charveron M, Favier A, Cadet J, Douki T (2006) Cyclobutane pyrimidine dimers are predominant DNA lesions in whole human skin exposed to UVA radiation. Proc Natl Acad Sci USA 103:13765–13770

242. Haywood R, Andrady C, Kassouf N, Sheppard N (2011) Intensity-dependent direct solar radiation- and UVA-induced radical damage to human skin and DNA, lipids and proteins. Photochem Photobiol 87:117–130
243. Weinshilboum R (2001) Thiopurine pharmacogenetics: clinical and molecular studies of thiopurine metabolism. Drug Metab Dispos 29:601–605
244. Cavaleri JJ, Prater K, Bowman RM (1996) An investigation of the solvent dependence on the ultrafast intersystem crossing kinetics of xanthone. Chem Phys Lett 259:495–502
245. Aloïse S, Ruckebusch C, Blanchet L, Réhault J, Buntinx G, Huvenne J-P (2008) The benzophenone $S_1(n, \pi^*) \to T_1(n, \pi^*)$ states intersystem crossing reinvestigated by ultrafast absorption spectroscopy and multivariate curve resolution. J Phys Chem A 112:224–231
246. Reichardt C, Vogt RA, Crespo-Hernández CE (2009) On the origin of ultrafast nonradiative transitions in nitro-polycyclic aromatic hydrocarbons: excited-state dynamics in 1-nitronaphthalene. J Chem Phys 131:224518
247. Yang C, Su H, Sun X, George MW (2012) Ultrafast formation of the benzoic acid triplet upon ultraviolet photolysis and its sequential photodissociation in solution. J Chem Phys 136:204507
248. Vogt RA, Gray TG, Crespo-Hernández CE (2012) Subpicosecond intersystem crossing in mono- and di-(organophosphine)gold(I) naphthalene derivatives in solution. J Am Chem Soc 134:14808–14817
249. Turro NJ, Ramamurthy V, Scaiano JC (2009) Principles of molecular photochemistry: an introduction. University Science Books, Sausalito
250. Wardle B (2009) Principles and applications of photochemistry. Wiley, Chichester
251. Klán P, Wirz J (2009) Photochemistry of organic compounds: from concepts to practice. Wiley, Chichester
252. West BA, Molesky BP, Giokas PG, Moran AM (2013) Uncovering molecular relaxation processes with nonlinear spectroscopies in the deep UV. Chem Phys 423:92–104

# Excited States Behavior of Nucleobases in Solution: Insights from Computational Studies

**Roberto Improta and Vincenzo Barone**

**Abstract** We review the most significant results obtained in the study of isolated nucleobases in solution by quantum mechanical methods, trying to highlight also the most relevant open issues. We concisely discuss some methodological issues relevant to the study of molecular electronic excited molecular states in condensed phases, focussing on the methods most commonly applied to the study of nucleobases, i.e. continuum models as the Polarizable Continuum Model and explicit solvation models. We analyse how the solvent changes the relative energy of the lowest energy excited states in the Franck–Condon region, their minima and the Conical Intersections among the different states, interpreting the experimental optical spectra, both steady state and time-resolved. Several methods are available for accurately including solvent effects in the Franck–Condon region, and for most of the nucleobases the solvent shift on the different excited states can be considered assessed. The study of the excited state decay, both radiative and non-radiative, in solution still poses instead significant theoretical challenges.

**Keywords** Ab initio calculation · Adenine · Cytosine · Guanine · Optical spectra · Photophysics · Solvent effect · Thymine · Uracil

## Contents

R. Improta (✉)
Istituto Biostrutture e Bioimmagini-CNR, Via Mezzocannone 16, 80134 Naples, Italy
e-mail: robimp@unina.it

V. Barone
Scuola Normale Superiore, piazza dei Cavalieri 7, 50126 Pisa, Italy

# 1 Introduction

Nucleic acids (NA) strongly absorb ultraviolet (UV) light and this process has several important biological implications, since it can trigger a cascade of dangerous photochemical events, potentially leading to apoptosis and to the damage of genetic code [1, 2]. The photophysical and photochemical behavior of NAs after absorption at 200–320 nm (a region biologically relevant since its red-wing falls in the solar radiation spectrum) is ruled by the excited states of pyrimidinic (thymine/uracil and cytosine) and purinic (adenine and guanine) nucleobases, which, in contrast to the other NA's constituents (phosphate and (deoxy)ribose moieties) strongly absorb in this spectral window [3–9]. On the other hand, the high photostability of nucleobases (the fluorescence quantum yield is very low, and the excited state lifetime is in the sub-picosecond time scale) calls for the existence of very fast and effective non-radiative deactivation routes [3–9]. Their remarkable photostability, providing a "natural" protection towards radiation induced damage, has likely contributed to the selection of these molecules as building blocks of the NAs, especially when taking into account that most of the prebiotic chemistry probably occurred under intense UV irradiation [3–9]. The most recent studies have also shown that, besides its intrinsic interest, a detailed knowledge of the nucleobase behavior is also fundamental to understand the photophysics and photochemistry of NAs. Experiments and calculations agree in predicting that monomer-like decay channels, i.e., those exhibiting features similar to those found for isolated nucleobases, exist in single and double strand oligonucleotides [10–13]. Furthermore the long-living components in NAs have been assigned to excited states deriving from the interaction of nucleobase excited states (excimers, exciplexes, etc.) and, in some cases, also to excited states localized on a single base [13–19]. As a consequence, a continuously growing number of studies, both experimental and computational, have been devoted to assess the static and dynamic behavior of nucleobase excited states [20–25]. Theoretical studies (too many for being exhaustively reviewed here) have been very useful, since they have shown that, for all the bases, barrierless paths exist on the Potential Energy Surfaces (PES) of the lowest

energy ππ* states connecting the Franck–Condon (FC) region to Conical Intersections (CoIs) with the ground electronic state ($S_0$), thus allowing a fast and effective non-radiative ground state recovery [20–25]. More recent studies have revealed new interesting features, such as the possible involvement of dark ($n\pi^*$ or $\pi\sigma^*$) and/or of higher lying ππ* excited states in the decay mechanism, and the existence of a broad plateau on the excited-state PES, affecting the dynamics [25–34]. The studies performed in the gas phase have thus provided very useful information on the intramolecular mechanisms underlying the very efficient non-radiative excited state decay of nucleobases, providing fundamental insights to interpret the results of the gas phase experiments. On the other hand, it is clear that the behavior in solution, especially in water, is more directly connected to biological processes occurring in vivo and in vitro. Our knowledge of the excited state dynamics of polynucleotides is essentially based on experiments, either steady-state or time-resolved (TR), performed in solution, using the results obtained on the isolated bases (or the corresponding nucleoside/nucleotide) as references [3–9].

It is thus important to obtain a detailed picture of the excited state behavior in condensed phases, trying to assess how solvent affects the nature of the excited states, their relative energy (in the FC region and along the reaction path), their crossings and, eventually, the mechanism of the excited state decay. In parallel, theoretical studies are expected to help the assignment and the interpretation of the optical spectra (both steady state and TR) of nucleobases. It is clear that dealing with such issues, in order to reach at least a qualitative agreement with experiments, requires the use of a suitable solvation model.

On the other hand, until some years ago, the number of studies tackling the excited state dynamics of nucleobases in solution was quite limited. While it is at least 30 years since QM methods were routinely applied to the study of medium size isolated molecules, their extension to the study of condensed phases is more recent [35–38]. Inclusion of environmental effects involves additional difficulties since the system under study now contains an extremely large number of molecules. Furthermore, in solution any problem involving excited states becomes intrinsically dynamic. Solvent reaction fields couple the ground state density with the density correction and the orbital relaxation arising from the electronic transition [35–37].

However, thanks to several methodological advances, the number of theoretical studies of nucleobases in solution has steadily increased in the last few years, and several important steps have been made toward a deeper understanding of their excited state dynamics. For all the nucleobases, especially in water, we now have a fairly accurate picture of the excited state ordering in solution in the FC region of their minima (allowing the assignment of absorption and emission spectra). We have also obtained important insights into the structure of the CoIs among different electronic states, and, therefore, on the mechanism of the non-radiative decay. This chapter is devoted to reviewing the most significant results obtained in the study of isolated nucleobases in solution and trying to highlight the most relevant open issues. We shall focus mainly on the papers that have appeared in the last 10 years, since other reviews are available discussing older contributions [3, 20–22], focusing on the singlet excited states. In general, we do not discuss the results of

microhydration studies, where a model including the solute and a limited number of solvent molecules is studied in the gas phase [39], since they are more directly relevant for interpreting experiments on similar systems in the gas phase than for the condensed phase.

The next section will be devoted to discuss concisely some of the methodological issues most relevant to the study of molecular electronic excited states in condensed phases, reviewing the basic foundations of the methods most commonly applied to the study of nucleobases. In the following paragraphs we shall discuss the studies of the Franck–Condon region, more relevant to the interpretation of the absorption spectra, before focusing on the papers tackling the calculation of the excited state PES and describing the minima and/or the CoIs among the different electronic states. In the last section some general remarks will be reported.

# 2 Methodology

## 2.1 Dynamical Solvation Effects

Before proceeding with our analysis of the main solvation models, let us briefly mention a critical issue that has to be carefully analyzed in any study of the excited state dynamics of nucleobases, as well as of any photoactivated process in solution: the dynamics of solvent effects. Absorption or emission of light and, more generally, any change of the electronic state (e.g., at a CoI) leads to a sudden variation of the solute electron density: full equilibration of solvent degrees of freedom to the excited state density is not instantaneous, but requires a finite time. Analogously, during the motion on the PES of a given excited state, structural changes are mirrored by changes, usually small but never vanishing, of the electron density. These effects affect the optical spectra to different extents, and several studies, including some on nucleobases, show that they can even change the energy ordering of the different excited states in the FC region. It is thus fundamental that the characteristic times of solvent degrees of freedom are properly taken into account [36, 37].

From the physical point of view, the electronic density of the solvent molecules rearranges almost instantaneously to any change of the solute density, and it can always be considered to be in equilibrium with the latter (fast solvent degrees of freedom). At the other extreme, there are the effects due to the reorientation of solvent molecules, as well as those related to the rearrangement of the outer solvation shells. The characteristic times of these processes depend on the solvent, but they are usually on the picosecond time scale (slow solvent degrees of freedom) [40, 41].

When dealing with the absorption process, only the fast solvent degrees of freedom are in equilibrium with the excited state density – the slow ones remaining in equilibrium with that of the ground electronic state. The study of the fluorescence

process and, more generally, that of excited state population transfer, especially at CoI, is rather more complex, since in this case dynamical solvent effects cannot be rigorously decoupled from the intramolecular effects due to the motion of the wave packet (WP) on the excited state surface.

Soon after the electronic transition has occurred, the system starts evolving on the excited state PES toward its energy minimum and/or the crossings with the other electronic states. At the same time, slow solvent degrees of freedom start equilibrating to the excited state electron density. These two processes cannot be rigorously decoupled, especially when they exhibit similar time scales, and thus we cannot expect that a single strategy is suitable for all the possible decay processes, especially in the proximity of CoIs. However, it is useful to define some limit reference models, and intuitive considerations about the properties of the solvent and/or of the excited state PES are often sufficient to define the most suitable model to treat the case under study [38]. For nucleobases, equilibration of intramolecular degrees of freedom can be considered faster than solvent equilibration (though in the presence of a phospho-deoxyribose moiety some large amplitude motions, slower than solvent characteristic times could, in principle, be available). Furthermore, most of the photoexcited population in nucleobases decays on the ~100–200 femtosecond time scale [3, 9], and then only fast solvent degrees of freedom are expected to be in equilibrium with the excited state density.

## 2.2 Solvation Models

Several excellent reviews of the different solvation models are available [35–37, 42–45]. We limit ourselves to a very concise review of the basic features of the methods more frequently used to study nucleobases.

One direct procedure to take environmental effects into account, adopted in several studies on nucleobases (see below), consists in including in the calculations a reduced number of explicit solvent molecules [42, 44, 45]. This approach has several advantages. It has a clear physical meaning, with a direct correspondence to a "real" solution. It allows the inclusion of all the solute–solvent interactions (for example hydrogen bonds or non-bonding interactions) and it is possible to take into account any "direct" participation of solvent molecules in the process of interest. For nucleobases, as an example, we can monitor how the rearrangement of the solvent molecules affects the path of the solute from the FC region to the CoI. These "explicit" models can easily, at least in principle, be extended to dynamical treatments, allowing one, for example, to include solvent fluctuations in the calculation of the spectra or the response of the slow solvent degrees of freedom to the photoexcitation of the solute.

On the other hand, a conventional "supermolecule" approach has to face two serious difficulties: (1) the number of solvent molecules necessary to reproduce the bulk properties of a liquid is very large; (2) a dynamical treatment averaging all the possible configurations of the solvent molecules is, in principle, necessary.

This approach thus has a huge computational cost, especially when used for studying excited states, which need rather expensive QM computational methods. As a consequence, most of the applications to nucleobases rely on the commonly used approximation of treating most, if not all, solvent molecules by using classical force fields within a mixed Quantum Mechanics/Molecular Mechanics (QM/MM) approach. However, standard MM force fields can meet significant difficulties in correctly placing the first solvation shell molecules [46], in treating non-bonding interactions accurately and, especially if polarization is not explicitly taken into account, fast dynamical solvent effects. Many of the commonly used MM force fields assign to each atom a fixed charge, which is usually parameterized in order to reproduce ground state properties. Within this approximation, the solvent molecules do not react to the change of the solute electron density, leading to an underestimation of the solvent reaction field and to inaccuracies in the computation of the excitation energies, especially in the case of electronic transitions involving a large variation of the electron density. In any case, a large number of QM/MM calculations are necessary to reach converged excitation energies for each point of the reaction path, significantly increasing the computational cost of this approach.

In order to avoid this bottleneck, Aguilar et al. proposed an alternative procedure (also used for DNA nucleobases) where MD simulations should provide a realistic description of the structure of the solvent around the solute. The electrostatic potential for all configurations determines the averaged solvent electrostatic potential (ASEP) on grid points enveloping the van der Waals surface of the molecule, which is calculated and represented by fitted partial charges, to be used for determining ground- and excited-state wave functions and energies [47, 48].

Some of the limitations of explicit solvation models can be overcome by using continuum solvation models, which, after having been used successfully for decades in the study of ground state processes [36, 49], have become very effective tools for evaluating solvent effects on excited state properties [35, 37, 38]. In continuum models the solvent is described as a homogeneous dielectric, polarized by the solute, which is placed within a cavity in the solvent medium and experiences the solvent reaction field [36].

Among continuum models, the Polarizable Continuum Model (PCM) is probably the most commonly used and it has been frequently employed to study nucleobases [37, 49]. It relies on a realistic definition of the solute cavity (built as the envelope of spheres centered on the solute atoms), and especially on an accurate solution of the proper electrostatic problem at the cavity surface, by using a boundary element approach [37]. In the following we thus focus mainly on this latter method, but many of its advantages and limitations are shared by other continuum approaches [37, 49].

The first difficulty arises from the high nonlinearity of the solution of the electrostatic problem in the presence of time-dependent (e.g., photoactivated) phenomena. Indeed, one should variationally determine the solvent reaction field together with all the other parameters of the adopted electronic method (molecular orbitals and CI coefficients, etc.), but all those parameters also depend on the solvent reaction field. The most used approaches to deal with this problem can be

grouped into two classes: State-Specific (SS) and Linear Responses (LR) approaches [50–54]. In SS methods (for example, CASSCF/PCM) a different effective Shroedinger equation is solved for each state of interest, achieving a fully variational formulation of solvent effects on the excited state properties. In methods exploiting the LR response formalism (e.g., TD-DFT) the exact excited electron density is not necessary to compute the excitation energies, which are "directly" determined, by plugging in the original (e.g., TD-DFT) equations a PCM contribution [55]. As discussed below, SS and LR methods have, in some cases, provided very different estimates of solvent effects on the excited state properties of nucleobases, confirming the results obtained on several other classes of compounds [38]. In any case, very effective and fast algorithms have been devised both for SS-PCM and LR-PCM calculations [38], allowing a full QM treatment of molecular systems containing dozens of atoms (easily up to ~150) in their excited states. Just to limit ourselves to the study of NAs, we can recall the study of a tetranucleotide of Ade, including the phospho-deoxyribose backbone and the cation [13, 56], of different hydrogen bonded dimers and trimers [12, 57], and of eight guanine bases, modeling a guanine quadruple helix [58].

Studies on nucleobases confirm the traditional advantages of PCM: (1) its limited computational cost, allowing easy coupling to any electronic method; (2) the implicit averaging procedure, allowing a good reproduction of bulk solvent effects; and (3) the conceptual ease and effective inclusion of dynamical solvation effects. Concerning the first aspect, we cite here the very recent developments in PCM/CCSD calculations [59], including polarizable MM charges [60]. Although several approaches have been developed to include dynamical effects within the framework of PCM and of other continuum models [35], a simple and effective treatment (the most commonly used) involves the definition of two limit time-regimes, the equilibrium (EQ) and the non-equilibrium (NEQ) ones. In the former regime all the solvent degrees of freedom are in equilibrium with the electron density of the excited state, and the solvent reaction field depends on the static dielectric constant of the embedding medium. In the latter regime, only solvent electronic polarization (fast degrees of freedom) is in equilibrium with the excited state electron density of the solute, while the slow solvent degrees of freedom remain equilibrated with the ground state electron density. In the NEQ time-regime the "fast" solvent reaction field is ruled by the dielectric constant at optical frequency ($\epsilon_{opt}$, usually related to the square of the solvent refractive index) [37].

Obviously, PCM suffers from some limitations. It is expected to provide a good estimate of the electrostatic contribution to the solute–solvent interaction, whereas less accurate results can be obtained when dealing with non-polar or hydrogen bonding solvents. In the former case, the non-electrostatic contributions (dispersion interactions, electronic repulsion) to the solute–solvent interaction are larger than the electrostatic ones. Interesting attempts to treat non-electrostatic solute–solvent interactions [61] within the framework of PCM/TD-DFT calculations have been made [62], but it cannot be taken for granted that standard calculations are able to reproduce solvent effects in non-polar solution (dielectric constant <4) or when dealing with non-polar solutes.

Another delicate issue concerns the choice of the parameters used in this method (and in any continuum model), such as the radii [63] used to build the solute cavity, which determines the volume of the cavity and, thus, the distance between the atoms and its surface. It is well known that the computed properties depend on the adopted atomic radii, and this is also obviously true for the excited state energies, as shown by a purposely tailored study on uracil [63]. This feature has thus to be considered with particular attention when comparing different kinds of transitions. Furthermore, since the choice of the cavity affects the relative energy of the transition, some critical features (the presence of a crossing, for example) can depend on the cavity choice.

In the PCM framework (and in any continuum model), the solvent loses its molecularity and, especially in hydrogen bonding solvents, the explicit inclusion of solute–solvent interactions is very important for getting accurate results. In hydrogen-bonding solvents, the solute–solvent interactions can be highly directional and have a strongly molecular nature that cannot properly be described by simple electrostatic interactions. This is the case, for example – very important in the study of nucleobases – of the hydrogen bond formed by a water molecule and the lone pairs (LP) of a carbonyl group (see next sections).

An accurate estimate of the effects of the hydrogen bond interactions on the electronic transitions can be obtained only explicitly, including the solvent molecule in the computational model. Although PCM alone can provide useful hints on the solvent shift in hydrogen bonding solvents, many studies, including several on nucleobases, have shown that an accurate determination of the relative energy of the excited states requires the use of mixed discrete/continuum models, where a limited number of solvent molecules (e.g., the first solvation shell) is included in the computational model. Although there is no general rule concerning the number and geometry of the solvent molecules to be considered, combining chemical intuition with experimental results can provide fairly reliable models. Just considering uracil in water an example, NMR experiments indicate that no water molecule is strongly bonded to C5 and C6 carbon atoms, and that O7 and O8 are coordinated by two and one water molecules, respectively [64]. Car–Parrinello dynamics suggest that the first coordination shell of uracil (up to 2.5 Å) is formed by six water molecules, four in the molecular plane (as in Fig. 1) and two more or less perpendicular to it [65]. Although a full description of the first solvation shell in solution requires a proper dynamic treatment, a number of studies have confirmed that the PCM is able to account accurately for the effect of water molecules that are more distant and/or not directionally bound to the carbonyl oxygen lone pairs. The model depicted in Fig. 1 thus appears to be a reasonable guess, although some test calculations on the dependence of the results on the number and the position of the solvent molecules included in the calculations are always very useful. Within mixed methods, interesting advances have also been made for combining QM/MM calculations with PCM [66, 67].

As anticipated above, a review of all the different solvation models falls outside the scope of this chapter. Besides the approaches described above, here we limit
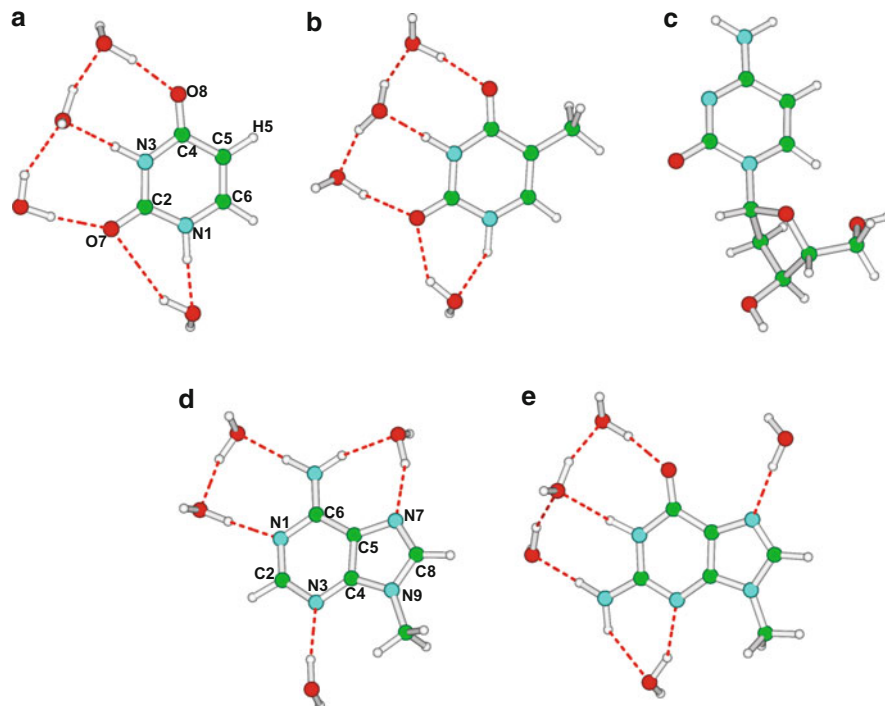
**Fig. 1** Schematic description (and atom labeling) of the five nucleobases. (**a**) Uracil, including four water molecules of the first solvation shell. (**b**) Thymine, including four water molecules of the first solvation shell. (**c**) Cytidine. (**d**) 9-Methyladenine, mimicking adenosine, including five water molecules of the first solvation shell. (**e**) 9-Methylguanine, mimicking guanosine, including five water molecules of the first solvation shell

ourselves to citing two other approaches that have been applied to the study of nucleobases. In the fragment molecular orbitals (FMO) approach, the molecules of interest are divided into different layers (one option is using one layer for the solute and another for the solvent molecules), and then monomer, dimer, and optionally trimer ab initio calculations of fragments are performed and the obtained results combined. It can also be used for studying excited states (fragment molecular orbital multiconfigurational self consistent field – FMO-MCSCF) and partially includes quantum effects in the description of the solute–solvent interactions [68, 69]. Mutually polarizable solute–solvent interactions are also achieved in the effective fragment potential (EFP) explicit solvent method, which includes electrostatic (Coulombic), polarization (induction), and exchange repulsion/charge-transfer solute/solvent interactions [70, 71]. Implementation of the EFP method with CASSCF and multiconfigurational quasidegenerate perturbation theory (MCQDPT) methods allows the calculations of spectra in solution [72].

## 2.3   Coupling Electronic Methods to Solvation Model

Almost all the most important electronic structure calculations have been applied to the study of nucleobases, and a complete and critical review of their performances is obviously outside the scope of the present chapter. Postponing some specific considerations to the sections devoted to each nucleobase, we report here only some examples of the possible problems that can be encountered when coupling a given electronic method with a solvation model.

Regarding PCM/TD-DFT calculations, as anticipated above, the standard implementation is based on the linear response theory. The excitation energies are "directly" determined, without computing the excited state density, by plugging in a PCM contribution in the TD-DFT equations [55]. For this implementation, analytical gradients have been derived, providing excited state geometry optimizations and (by numerical differentiation) harmonic vibrational frequencies [73]. A significant part of solvent effects on the excited state energies is recovered by LR approaches by using ground state electron densities computed in solution (and, thus, including the polarization due to solvent reaction field) [50, 51]. However, since the exact excited state electron density is never computed, all the solvent contributions depending on the variation of the multipole moment upon excitation are missing in LR computations [50, 51]. As a consequence, LR-PCM/TD-DFT significantly underestimates solvent effects on electronic transitions involving large shifts of the electron density (as those with partial CT character), and it cannot treat dynamical solvent effects accurately, limiting the reliability of the computed absorption and, especially, emission energies [54]. Some of these limitations are recovered by using state-specific implementations of PCM/TD-DFT [52–54], where the nonlinear problem of determining the polarization charges corresponding to excited state density is solved by using a self-consistent iterative procedure [53, 54]. Starting from a TD-DFT calculation in vacuo, a first approximation to the state-specific reaction field is computed using the electron density of the state of interest. In the next step, a TD-DFT calculation is performed in the presence of this first set of polarization charges, providing an updated excited state density and, consequently, a new set of polarization charges. This iterative procedure is continued until convergence of the reaction field is achieved. SS-PCM/TD-DFT provides a balanced description of strong and weak electronic transitions (see also the results reported below) together with accurate estimates of dynamical solvent effects on the absorption and emission processes, of solvent reorganization energy, and, thus, of the inhomogeneous broadening. Unfortunately, SS-PCM/TD-DFT excited state analytical gradients are not available. Furthermore, SS-PCM has an iterative implementation, which not only increases the possibility of convergence failures but would also make geometry optimizations rather cumbersome. These considerations show that when analyzing the results of PCM/TD-DFT calculations it is important to verify whether they have been obtained by using LR-PCM or SS-PCM implementations.

Regarding the use of PCM with other methods, it is important to remember that the accuracy of the results depends critically on the quality of the electron density computed for the solute. In this respect, state-averaging procedures, like those usually adopted in CASPT2/PCM and often also CASSCF/PCM calculations [74], are not fully adequate for the study of absorption and emission processes, especially when involving electronic states with strongly different polarities.

Particular attention has to be paid to the basis set adopted in PCM excited state calculations. PCM cavity radii most commonly adopted have been parameterized in order to reproduce solvation energies (i.e., a ground state property) at a specific level of theory (HF/6-31G(d), HF/6-31 + G (d,p) for the anions, PBE0/6-31G(d), etc.) [75]. When using different basis sets, different results can be obtained, especially when thinking that excitation involves virtual molecular orbitals, which are usually more diffuse than the occupied ones, and whose "optimal" radii are likely different with respect to those used for the ground state. PCM results obtained with very large basis sets, such as those used to get accurate excitation energies, especially in wave-function-based method, have to be thus considered with some caution.

Several methodological issues also obviously concern explicit solvation methods. Just to make an example, we can cite, for all the QM/MM approaches, the way the MM charges are included in the QM Hamiltonian [66].

# 3 The FC Region: Vertical Absorption Energies of Isolated Nucleobases

As anticipated above, solvent affects the relative energy of the different excited states with respect to the gas phase and, in some case, changes their relative stability in the Franck–Condon region, i.e., around the ground state minimum. Although the excited state dynamics is modulated by several different chemical-physical effects, the behavior of the system in the FC region is surely relevant, since it can determine which are the vibrational degrees of freedom "triggered" by the electronic excitation and, therefore, the inertia of the reaction. In this section we shall review the computational studies of the Vertical Excitation Energies ($\nu_A$) in solution. At least for bright excited states, computed $\nu_A$ are often compared with the experimental absorption spectra. On the other hand, it is important to remember that experimental spectra have their line-shape, depending on the vibrational features of ground and excited state and on the inhomogeneous broadening, that cannot be reduced to a single number. Although $\nu_A$ is correlated to the maximum of the absorption band, the two quantities are not formally equivalent and deviations of a few tenths of an electronvolt are possible [76–85].
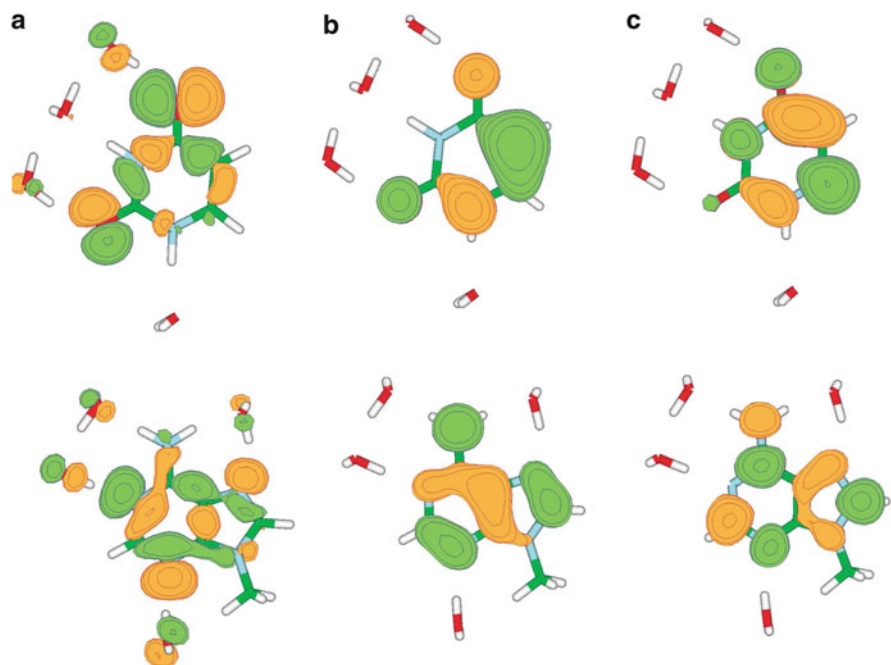
**Fig. 2** Schematic description of the frontier orbitals of uracil (*top*) and 9-methyladenine (*bottom*) nucleobases. (**a**) Non-bonding MO involved in the $S_0 \rightarrow Sn\pi^*$ transition. (**b**) $\pi$ HOMO and (**c**) $\pi^*$ LUMO involved in the $S_0 \rightarrow S\pi\pi^*$ (for Ura) and the $S_0 \rightarrow L_a$ (for Ade) transitions

## 3.1    Uracil and Thymine

Experiments on uracil (Ura) show a strong absorption band at ~4.8–5.0 eV (depending on the solvent), and all the computational methods agree on its assignment to an intense $\pi\pi^*$ transitions (hereafter $S\pi\pi^*$) [86]. $S\pi\pi^*$ can be described as a HOMO $\rightarrow$ LUMO excitation (see Fig. 2), the two frontier orbitals having a clear-cut bonding and antibonding character with respect to the C5–C6 double bond (see Fig. 1 for atom labeling) [87, 88]. The picture obtained for thymine is similar, but for a weak red-shift of the absorption band, which can be rationalized by the inductive effect of the methyl group on C5 atom [3, 87]. Different computational methods also agree in predicting that for both Ura and thymine (Thy) a dark $n\pi^*$ state ($Sn\pi^*$) lies very close to $S\pi\pi^*$ in the FC region. $Sn\pi^*$, that in the gas phase for Ura is the lowest energy excited state [87, 88], mainly arises from the excitation of an electron from the LP (HOMO-1) of the C4–O8 carbonyl group to the $\pi^*$ LUMO (see Fig. 2).

Independently of the specific solvation model adopted, all the computational studies in solution indicate that solvent noticeably affects the energy of the excited states and their relative stability [86, 89–104]. In particular, $Sn\pi^*$ is strongly destabilized in water and, more generally, in hydrogen bonding solvents. This

electronic transition involves the transfer of an electron from the oxygen LP, with can potentially act as hydrogen-bond acceptor, toward the more diffuse $\pi^*$ molecular orbital, leading to a decrease of the solute–solvent hydrogen-bond strength. For this reason, several studies have shown that a proper description of solvent shifts of uracil excited states in aqueous solution requires that both bulk solvent effects and solute–solvent hydrogen bond interactions are taken into account [86, 90–92].

Inclusion of bulk solvent effects by the PCM model decreases by 0.1 eV $\nu_A$ of S$\pi\pi^*$ and increases by 0.35 eV that of S$n\pi^*$. When four water molecules of the first solvation shell are included in the model (see Fig. 1), gas phase calculations display similar trends. When both effects are considered, S$n\pi^*$ is strongly destabilized (by ~0.5 eV), whereas the computed solvent red-shift for S$\pi\pi^*$ (0.2 eV) approaches that predicted by the experiments (~0.25–0.3 eV) [86]. The absorption band maximum of uracil in water is indeed ~0.25 eV red-shifted with respect to the vapor phase [105]. Etinski and Marian have studied uracil in solution at the RI/CC2/aug-cc-pVDZ level by including six water molecules of the first solvation shell and taking into account bulk solvent effects by the COSMO model [106] (that also belongs to the family of polarizable continuum models). In very good agreement with the PCM/TD-DFT estimate, S$n\pi^*$ is blue-shifted by 0.56 eV while S$\pi\pi^*$ is red-shifted by 0.19 eV with respect to the gas phase results [97].

The $\nu_A$s of uracil in aqueous solution have also been studied by using other approaches [98–101]. MRCI/cc-pVDZ/MM calculations (considering 257 water molecules with fixed charges, whose positions are averaged by means of MD simulations) predicts that in water $\nu_A$ is red-shifted by ~0.05–0.1 eV for S$\pi\pi^*$ and blue-shifted by ~0.4 eV S$n\pi^*$ with respect to the gas phase [98]. Another QM/MM study, exploiting molecular dynamical simulations and TD-CAMB3LYP and CC2 QM methods, gives very similar estimates: [101] the solvatochromic shift for S$\pi\pi^*$ is −0.12 eV using CAM-B3LYP/MM and −0.20 eV using CC2/MM, whereas for S$n\pi^*$ it is 0.42 eV (CAMB3LYP/MM) and 0.43 eV (CC2/MM). Monte Carlo simulations on 200 water molecules to generate solvent configurations around uracil, which have then been used for INDO excited state calculations, indicate +0.5 and −0.19 eV solvent shifts for S$n\pi^*$ and S$\pi\pi^*$, respectively [100].

With regard to solvent effects by a fragment molecular orbital multiconfigurational self consistent field (FMO-MCSCF), Matsika et al. obtained solvent shifts close to the experimental estimates and to the results of the hybrid approaches just described: for S$\pi\pi^*$ ~ −0.15/−0.18 eV, for S$n\pi^*$ ~ +0.42/+0.47 eV [98]. Analogously, EFP/CASSCF and MCQDPT calculations predict for S$n\pi^*$ a blue-shift of 0.43 eV and for S$\pi\pi^*$ a red-shift of −0.26 eV. Only EOM-CCSD(T)/MM calculations provide different results with respect to those discussed above: a blue-shift is indeed predicted not only for S$n\pi^*$ (+0.44 eV) but also for S$\pi\pi^*$ (+0.05 eV), and this latter result is in qualitatively disagreement with experiments [98].

On average we can thus estimate that, when going from the gas phase to water, S$n\pi^*$ is destabilized by ~0.7 eV with respect to S$\pi\pi^*$. As a consequence, in the FC region S$n\pi^*$ is less stable than S$\pi\pi^*$ by just ~0.2 eV. Such a difference is fully compatible with the partial S$\pi\pi^*$ → S$n\pi^*$ population transfer evidenced by time-resolved experiments for uracil in water [104, 107].

From the methodological point of view, it seems that a mixed discrete-continuum approach, notwithstanding being by far the computationally less demanding, provides very accurate predictions.

For thymine a similar picture is found. According to Etinski and Marian (six water molecules +COSMO solvent model), in water $Sn\pi^*$ is blue-shifted by 0.51 eV while $S\pi\pi^*$ is red-shifted by 0.18 eV with respect to the gas phase results [97]. The estimates obtained by TD-DFT/PBE0/6-311+G(2d,2p) calculations on a model including four water molecules are +0.41 and −0.09 eV for $Sn\pi^*$ and $S\pi\pi^*$, respectively [86].

This picture does not change significantly when studying thymidine and thymidine monophosphate, including deoxyribose and phospho-deoxyribose groups, that can be more directly related to the experimental results on oligonucleotides [94].

The number of studies devoted to other solvents is more limited, but there are some PCM/TD-DFT studies of uracil derivatives in acetonitrile [91, 92]. The $\nu_A$ computed in acetonitrile falls between that obtained in water and in the gas phase both for $S\pi\pi^*$ and $Sn\pi^*$. Calculations provide solvent shifts in very good agreement with experiment [92–96], and show that the HOMO/LUMO gap decreases with the solvent polarity, accounting for the trend found for $S\pi\pi^*$. $Sn\pi^*$ $\nu_A$ is more sensitive to the presence of solute–solvent hydrogen bonds, although it is also relatively destabilized in acetonitrile with respect to $S\pi\pi^*$ due to its smaller dipole moment [92]. As discussed in more detail below, these results are fully consistent with the experimental studies of solvent effects on the excited state dynamics of uracil derivatives [92–96].

Several non-natural pyrimidine bases have also been studied by using, usually, mixed discrete/continuum models [92, 108, 109], with uracil derivatives with different methyl substituents, 5-fluorouracil, 5-aminouracil, and 6-aminouracil always giving a similar picture. Taking the gas phase results as references, $Sn\pi^*$ is destabilized in water by 0.4/0.5 eV and $S\pi\pi^*$ stabilized by 0.1/0.2 eV. Interestingly, 5-fluorouracil has been studied both in water and in acetonitrile [91, 92], and in a recent study different solvation models have been employed, allowing an interesting comparison between continuum and discrete approaches [102]. Although the different approaches provide similar results, the most accurate determination of water $\rightarrow$ acetonitrile solvent shifts is obtained by a discrete approach, where some solvent molecules close to the solute are explicitly included and the remaining solvent molecules are treated as an electrostatic embedding generated by more than 200 molecules, carrying out the calculations over 100 statistically uncorrelated configurations obtained by Monte Carlo simulations [102].

## 3.2 Cytosine

All the QM methods applied to the study of cytosine (Cyt) in the gas phase predict that the $S_1$ state is a $\pi\pi^*$ excitation that can be described as a HOMO $\rightarrow$ LUMO transition, similar to that found in uracil and thymine. There is more disagreement,

instead, on the energy ordering of $S_2$ and $S_3$, that are dark $n\pi^*$ states, involving the lone pairs on nitrogen ($Sn_N\pi^*$) and oxygen ($Sn_O\pi^*$), together with the $\pi^*$ LUMO [87].

The number of studies of Cyt in the condensed phases is much smaller than for uracil derivatives. The most detailed study is that of Matsika [98], using two methods, i.e., QM/MM calculations with the approach developed by Aguilar and colleagues [47] and FMO-MCSCF calculations [68, 69]. Both approaches provide similar indications, with all the lowest energy transitions blue-shifted with respect to the gas phase: $S_1$ $\nu_A$ by ~0.2 eV, $S_2$ by ~0.6 eV, and $S_3$ by ~0.8 eV. MCSCF/PCM calculations provide much smaller blue-shifts, i.e., 0.03 eV for $S_1$, 0.23 eV for $S_2$, and 0.28 eV for $S_3$. This picture is confirmed by Blancafort and Migani [110] (CASSCF/CPCM calculations), who obtained a blue-shift of +0.2, +0.6, +0.8 eV for $S_1$, $S_2$, and $S_3$ states, respectively. These shifts have been explained by the smaller dipole moments of the three lowest energy excited states with respect to $S_0$ [98], though it is likely that for $S_2$ and $S_3$ $n\pi^*$ transitions the weakening of solute-solvent hydrogen bonds also plays a role in explaining solvent effects. It is not easy to check the accuracy of these estimates: indeed solvent is also expected to shift the conformational equilibrium among the different cytosine tautomers, which have different absorption spectra, making a careful averaging procedure necessary [111].

## 3.3 Adenine

According to QM computations on adenine (Ade) in the gas phase, three singlet excited states lie close in energy in the FC region, one dark with $n\pi^*$ character (HOMO-1 $\rightarrow$ LUMO, hereafter labeled $Sn\pi^*$) and two bright $\pi\pi^*$ excited states ($L_a$ and $L_b$) [26, 87]. The $L_a$ excited state corresponds mainly to a HOMO $\rightarrow$ LUMO excitation and carries most of the oscillator strength (see Fig. 2). The $L_b$ excited state results from the combination of HOMO-2 $\rightarrow$ and HOMO $\rightarrow$ +1 excitations and is consequently characterized by a much smaller oscillator strength. In the gas phase $Sn\pi^*$ should be the lowest energy excited state, whereas the predicted relative stability of $L_a$ and $L_b$ (which are within 0.2 eV) changes with the adopted computational method [112–114].

PCM/TD-PBE0/6-31G(d) calculations on 9-methyladenine including four water molecules of the first solvation shell predict that $L_a$ and $L_b$ $\nu_A$ in water are red-shifted by −0.16 and −0.12 eV, respectively, with respect to the gas phase, whereas $Sn\pi^*$ is strongly blue-shifted (+0.45 eV) [115]. These predictions, especially the relative destabilization of $Sn\pi^*$ with respect $L_a$ and $L_b$, are in good agreement with those reached by other computational studies of 9(H)Ade in solution [116–119].

CASSCF calculations – including solvent effects – by means of a linear response free energy procedure [116] predict for $Sn\pi^*$ a strong blue-shift (+0.22 eV) with respect to the gas phase, while a weak blue-shift is obtained for $L_a$ (−0.10 eV) and $L_b$ (−0.04 eV). A Monte Carlo MM/CASPT2 study [117] indicates that in aqueous

solution $L_a$ and $L_b$ are red-shifted by 0.34 and 0.17 eV, respectively with respect to the gas phase, while S$n\pi^*$ is blue-shifted by 0.58 eV. A multireference perturbed CI approach coupled with PCM predicts that for 9H-adenine in water $L_a$ ($-0.36$ eV) and $L_b$ ($-0.36$ eV) exhibit a substantial red-shift with respect to the gas phase results and S$n\pi^*$ a +0.07 blue-shift [118]. MM/QM calculations by Thiel and colleagues [119], including water molecules at the MM level, treating Ade by the OM2/MRCI semiempirical method, and taking into account the thermal motion of the system, provide similar indications, with S$n\pi^*$ blue-shifted by 0.1/0.3 eV with respect to the gas phase and $L_a$ red-shifted by 0.1 eV. In this latter study, however, significant mixing of the different diabatic states in the FC region is found.

Some of the studies just discussed have also analyzed the behavior of Ade in acetonitrile. CASSCF calculations predict small solvent shifts with respect to the gas phase: for S$n\pi^*$ a small blue-shift (+0.05 eV) and a small red-shift for $L_a$ ($-0.02$ eV) and $L_b$ ($-0.02$ eV). LR-PCM/TD-PBE0 calculations reach similar conclusion: small blue-shift (+0.10 eV) for S$n\pi^*$, small red-shift for $L_a$ ($-0.07$ eV) TD-DFT and $L_b$ ($-0.07$ eV) [115]. Please note, however, that the shifts predicted by SS-PCM/calculations are ~0.1 eV larger [115].

A methyl substituent on N9 leads to a relative stabilization of ~0.1 eV for $L_a$ and $L_b$ with respect to S$n\pi^*$ but does not change our considerations about solvent effect, as well as the presence of a deoxyribose or a phosphodeoxyribose moiety [94].

## 3.4 Guanine

The lowest transition in guanine (Gua) in the gas phase can be described as HOMO → LUMO; the excited state has $\pi\pi^*$ character and the excited state is usually labeled as $L_a$. Another strong band on the blue corresponds to the $\pi\pi^*$ transition (HOMO → LUMO + 1 excitation) labeled $L_b$. Two dark electronic states are relatively close to $L_b$. One corresponds to an $n\pi^*$ excitation with a significant contribution from the LP of the C6–O11 carbonyl group, and another (HOMO → LUMO + 2) with $\pi\sigma^*$ character. In the FC region it corresponds to a Rydberg state [87, 120].

Inclusion of solvent effects by a mixed discrete/continuum model (PCM/TD-PBE0 calculations on a model including five water molecules of the first solvation shell) leads to very good agreement with the experimental absorption spectrum of Gua (at both neutral and acidic pH when N7 is protonated) [121]. For the neutral compound, at the LR-PCM/TD-PBE0 level of theory, a solvent red-shift is predicted for both $L_a$ ($-0.25$ eV) and $L_b$ (~ $-0.1$ eV), while the dark states are destabilized, especially S$n\pi^*$ (~ + 0.5 eV). S$_0$ → S$n\pi^*$ transition promotes an electron from the LP, which can potentially act as a hydrogen bond acceptor, toward a more diffuse $\pi^*$ molecular orbital, leading to weakening of the solute–solvent hydrogen bond. When only bulk solvent effects are considered the computed blue-shift is smaller by ~0.2 eV, confirming that the inclusion of the first solvation shell is important for a correct estimate of the relative stability of different

electronic states. Interestingly, SS-PCM/TD-DFT calculations indicate a larger solvent red-shift (−0.29 eV) for $L_a$ and a much smaller one for $L_b$ (only −0.03 eV), confirming the large blue-shift of S$n\pi^*$ [121].

Thiel and colleagues have also studied guanine in solution using 50–500 MD snapshots of guanine in the gas phase (QM) and in solution (QM/MM) [122]. The excited-state calculations employ TD-DFT and the DFT-based multireference configuration interaction (DFT/MRCI) method in combination with two basis sets. Independently of the QM method used, $L_a$ exhibits a weak red-shift (0.1–0.2 eV) while $L_b$ shows a ~0.2 eV blue-shift. Using structures issuing from MD simulations in the calculation of the spectra allows one to take into account the effect of the deviation of the ground state geometry from equilibrium due to intramolecular vibrations. When the purine ring geometry is not planar, the coupling between the different excited states is larger, and the electronic transitions often exhibit mixed $\pi\pi^*/n\pi^*$ character, making their assignment more cumbersome. On the other hand, the transition with the lowest average oscillator strength in the gas phase (0.078), corresponding to the S$n\pi^*$ diabatic state, is red-shifted by ~0.5 eV in aqueous solution and its oscillator strength falls to 0.018, indicating a smaller coupling with the bright $\pi\pi^*$ states.

According to some studies, when only bulk solvent effects are considered in the calculations, very weak solvent shifts are usually predicted for both $L_a$ and $L_b$. For example, CASPT2/SCRF calculations in water provide shifts of −0.03 eV for $L_a$ and +0.02 eV for $L_b$ [123]. On the other hand, the SS-PCM/TD-PBE0/6-31G (d) estimates are ~ −0.03 eV for $L_b$, but ~ −0.3 eV for $L_a$ [121]. At the other extreme, PCM/CIPSI calculations provide very large solvent shifts for both $L_a$ (~ −0.35 eV) and $L_b$ (~ −0.7 eV) [124].

As we can see, for Gua there is a larger disagreement among the different methods than that found for the other nucleobases. On balance, we can assume that in water S$n\pi^*$ is significantly blue-shifted with respect to the gas phase (~ +0.5 eV), while $L_a$ experiences a noticeable red-shift (between −0.1 and −0.3 eV depending on the methods). For $L_b$ most of the methods predict a weak solvent effect.

Gua excited states have also been studied in apolar solvents, and in this case inclusion of bulk solvent effects by PCM is sufficient to provide fairly accurate spectra [57].

## 4 Excited State Decay Paths and Emission

The number of studies determining the minima of the excited state (which rule fluorescence spectra) and the crossing with the ground electronic state (which rule non-radiative decays) is significantly smaller than that focusing on the FC region. In fact, for most of the accurate QM electronic methods analytic gradient allowing excited state geometry in solution have not yet been implemented, a remarkable exception being LR-PCM/TD-DFT [73].
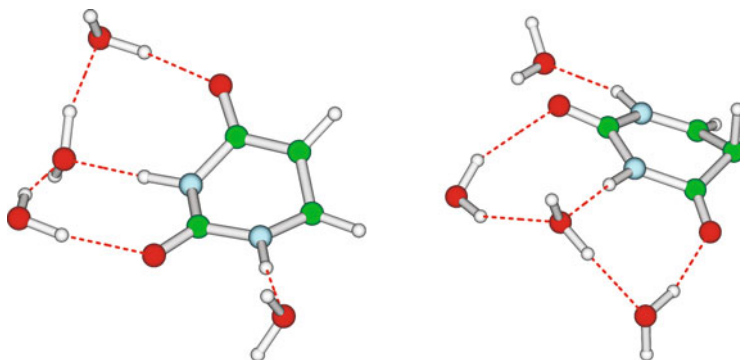
**Fig. 3** Schematic description of the Sππ* minimum and of a structure representative of the Sππ*/ S$_0$ crossing region for Ura·4H$_2$O studied in aqueous solution by PCM/TD-PBE0 calculations [92]

## 4.1 Uracil and Thymine

PCM/TD-PBE0/6-31G(d) geometry optimizations of Sππ* for Thy and Ura in water predict that, after photoexcitation, a steep path leads to a flat region of the PES, where the pyrimidine ring maintains a planar geometry, while the most significant geometry shifts mainly involve the bond lengths and bond angles of the ethylene-carbonyl moiety (O8C4C5C6 atoms) [92, 109]. C4C5 distance decreases by 0.03 Å, C4O8 increases by 0.03 Å, and, especially, the C5C6 bond length increases by 0.1 Å in line with the bonding/antibonding character of HOMO and LUMO with respect to the C5C6 double bond (Sππ*-min*-pla). In Sππ*-min*-pla, the oscillator strength is rather high and the calculation of the emission energy suggests that the region around Sππ*-min*-pla is the main cause of the maximum of the fluorescence spectrum [109]. On the other hand, frequency calculations at Sππ*-min*-pla show the existence of an imaginary frequency and that this structure is a saddle-point in a path leading to the absolute minimum of Sππ* (Sππ*-min), where the pyrimidine ring takes a bent conformation (see Fig. 3), with N3 and C6 out of the plane defined by N1, C2, C4, and C5 that are indeed close to being coplanar. Sππ*-min and Sππ*-min*-pla are almost isoenergetic (their energy difference is <0.05 eV), the bond lengths and bond angles of these two minima also being similar [92]. Several studies show that Sππ*-min is separated by a very small energy barrier (0–100 cm$^{-1}$) from a crossing region with S$_0$ [86, 90–92]. CASSCF(8/8) calculations on Ura·4H$_2$O in the gas phase indeed allow location of the conical intersection with the ground electronic state. One of the key motions to reach this CoI is the pyramidalization at C5, while an out-of-plane motion leads the C5 substituent toward a "pseudo-perpendicular" arrangement with respect to the molecular plane (see Fig. 3). PCM/TD-DFT calculations on Ura·4H$_2$O in water indicate that Sππ and S$_0$ surfaces are extremely close at this CoI, confirming that this crossing region also exists in solution [92]. Although the mechanism of the excited state decay of uracil

and thymine in the gas phase is extremely debatable [29–33], the existence of an almost barrierless path on Sππ* leading to a CoI with a structure similar to that just described is confirmed by several other post-HF methods [30]. Although TD-DFT calculations cannot be expected to provide an accurate description of a system in the proximity of a CoI with $S_0$ [24, 125], it is noteworthy that several studies of nucleobases (see also below) provide a description of the crossing region with $S_0$ qualitatively very similar to that obtained by post-HF methods, confirming the results obtained in other systems [126–129].

PCM/TD-PBE0 geometry optimizations predict, instead, that the minimum of the Snπ* state retains a planar structure. The most relevant geometry shifts with respect to the ground-state structure involve the C4O8 and C5C6 bond lengths that increase by 0.1 and 0.04 Å, respectively. The nπ* transition involves the transfer of an electron from an orbital corresponding mainly to the O8 LP to a π* orbital localized mainly on the C5C6 and C4O8 bonds.

The structures of the Sππ* and Snπ* minima computed in acetonitrile are very similar to those obtained in water. The most significant result of the optimizations in aqueous solution concerns the dependence of the hydrogen-bond distances on the electronic state. Just to take an example, in the optimized Snπ* solvation shell the distance between the water molecule hydrogen-bonded to C4O8 carbonyl is significantly longer (by 0.2 Å) than in the ground electronic state. This electronic transition decreases the electron population of the O8 lone pairs, leading to a weakening of the hydrogen bond involving the C4O8 carbonyl group.

Solvent does not affect the structure of the CoI and the energy barrier on Sππ*. Nonetheless, it can strongly modulate the excited-state lifetime of uracil by modifying the relative energy and the interaction between their bright Sππ* and dark Snπ* states. The latter state indeed provides an extra decay channel for the WP moving on Sππ*, inducing a faster fluorescence decay. For some compounds this crossing is active in some solvents only. On this basis it is possible to explain the strong dependence on the solvent exhibited by some nucleobases according to Fluorescence Upconversion (FU) experiments. These experiments, monitoring the disappearance of bright state fluorescence, indeed show that the excited-state lifetimes of thymine and 5-fluorouracil (5FU) in acetonitrile are significantly shorter than in water [91]. On the other hand, the final outcome also depends on the relative energy of Sππ* and dark Snπ* in the gas phase, related to the substituent on the pyrimidine scaffold. When, for example, Sππ* is the lowest energy state already in the gas phase, solvent is not expected to induce additional crossings with Snπ* and, therefore, to play a relevant role in tuning the excited state lifetime. Alternatively, the Sππ* → Snπ* decay could be operative in all solvents. This is the case of uracil and, in fact, Transient Absorption experiments, which can also be sensitive to the population of dark excited states, show that for uracil a significant part of the bright state population decays to Sππ* in several solvents [107].

Studies on modified bases (the aforementioned 5FU, 6amino-uracil, and 5-aminouracils) support the picture just described and confirm the key role of the five substituents in modulating the excited state decay. Some substituents can

increase the energy barrier associated with the path leading to the $S\pi\pi^*/S_0$ CoI (which indeed involves the five substituent) leading to slower decays [86, 108, 109].

The $S\pi\pi^* \to Sn\pi^*$ population transfer in uracil and in 5FU has also been studied in water and in acetonitrile by means of quantum dynamical calculations [103, 104]. The results obtained agree nicely with experimental evidence. For U, an ultrafast (<50 fs) $S\pi\pi^* \to Sn\pi^*$ decay with 10–25% yields, weakly dependent on the solvent, is predicted, in full agreement with the experimental estimates [107, 130]. At variance, dynamical calculations confirm that this decay channel is open in acetonitrile and closed in water, in agreement with the much faster decay observed experimentally in the first solvent [91].

## 4.2 Cytosine

The mechanism of the excited state decay of Cyt in the gas phase is lively debated, and a detailed analysis is outside the aim of the present chapter [131–133]. Briefly, some studies propose that the main deactivation channel involves $Sn_O\pi^*$ states, others that the two main decay routes involve the $S\pi\pi^*$ state, via an ethylene-like conical intersection with $S_0$, and/or the $Sn_N\pi^*$ state, via a sofa-like CoI with $S_0$ where N3 is displaced from the molecular plane.

Blancafort and Migani have studied these two paths by CASSCF/PCM calculations, also including one water molecule in the model, suggesting that water lowers the energy barrier of the path passing through the ethylenic conical intersection. The path involving $Sn_N\pi^*$ is instead destabilized by hydrogen bonding, but nonetheless it should remain energetically accessible [110]. Kistler and Matsika also focused on $S\pi\pi^*$ and $Sn_N\pi^*$ states and estimate solvent effects by means of single point calculations, exploiting a mean field QM/MM approach combined with MRCI calculations, on the most relevant geometries of these paths (optimized in the gas phase). According to their analysis, solvent slightly increases the energy barrier associated with both paths: for $S\pi\pi^*$ from 0.15 to 0.23 eV and for $Sn_N\pi^*$ from 0.14 to 0.31 eV [134].

## 4.3 Adenine

The decay of adenine excited states has recently been studied by means of PCM/TD-DFT calculations on a model including a 9-methyladenine molecule + four water molecules of the first solvation shell, adopting both PBE0 and M052X functionals [115]. Both functionals predict that, starting from the FC region, a very steep path leads to a planar pseudo-minimum ($L_a$-min*pla) characterized by a significant lengthening of the C2N1 and C2N3 bond lengths, in line with the bonding/antibonding character of the frontier orbitals of 9Me-Ade with respect to
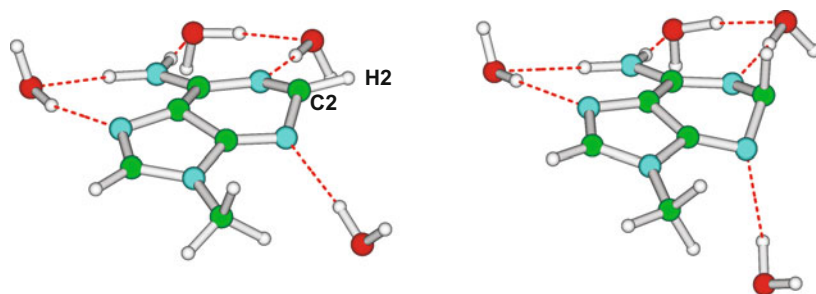
**Fig. 4** Schematic description of the $L_a$-minC2 pseudo-minimum and of a structure representative of the $L_a/S_0$ crossing region for 9Me-Ade·4H$_2$O studied in aqueous solution by PCM/TD-PBE0 calculations [115]

those bonds. Emission from $L_a$-min*pla is fairly intense and is likely responsible for the experimental emission maximum, according to the computed Stokes shift and fluorescence anisotropy [115]. PCM/TD-PBE0 calculations then show that a rather flat path leads from $L_a$-min*pla to a region where the purine ring is no longer planar, and the C2 atom moves out from the molecular plane ($L_a$-minC2; see Fig. 4). Emission from the region surrounding $L_a$-minC2 should be responsible for the red-tail present, especially in water, in the experimental fluorescence spectrum of dA and 9Me-Ade [115]. However, $L_a$-minC2 is separated by a vanishingly small energy barrier (~200 cm$^{-1}$) from a crossing region with S$_0$, reached by out-of-plane motion of the H2 atom. The M052X functional provides a similar picture, but in this case $L_a$-minC2 is no more a minimum of the PES and optimization leads directly to the crossing region with S$_0$ via out-of-plane motion of the C2–H2 bond. The picture obtained in water is very similar to that obtained in the gas phase by many post-HF studies, indicating the presence of an $L_a/S_0$ CoI, involving a large out-of-plane motion of the C2–H2 bond [112–114].

Geometry optimizations of $L_b$ and S$n\pi$* predict instead a decay to $L_a$, and thereafter the system follows the same $L_a$ path as depicted above, showing the observed fluorescence anisotropies [115].

Calculations in acetonitrile (considering only bulk solvent effects by using PCM) provide a similar picture, but in the latter solvent S$n\pi$* is relatively more stable than in water and therefore some involvement of this state in the dynamics is possible in principle. Especially when considering that a large diabatic coupling exists between $L_a$ and S$n\pi$*, which could be further increased by inclusion of thermal motion and solvent fluctuations, a small part of the photoexcited population could be trapped in S$n\pi$*.

In any case, since TD-PBE0 calculations in the gas phase predict instead that a significant part of the excited state population on $L_a$ is trapped in S$n\pi$* [27], in agreement with several other QM studies, solvent dramatically affects the excited state dynamics of adenine. $L_a$ is the only excited state significantly involved in the
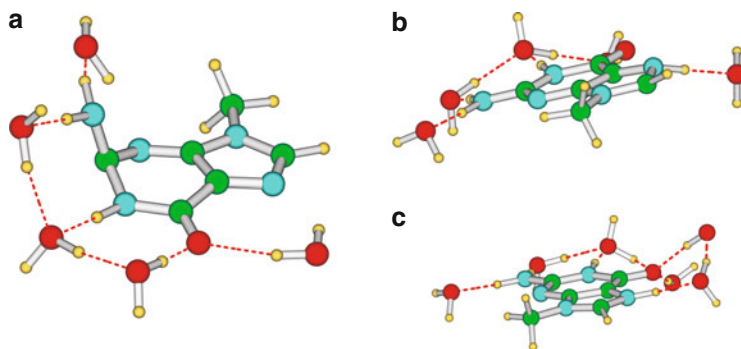
**Fig. 5** Schematic description of a structure representative of the $L_a/S_0$ crossing region in 9Methyl-Gua·5 $H_2O$ (**a**) and of the $L_a$ minima of N7-protonated 9Methyl-Gua in water, computed in water at the PCM/TD-PBE0/6-31G(d) level by using a model including five (**b**) or six (**c**) water molecules

dynamics and all the experimental results can be explained by the shape of the $L_a$ PES.

A QM/MM dynamical study by Thiel [119], using the semi-empirical OM2 model, provides a different picture: the simulations yield ultrafast $S_2 \rightarrow S_1$ decay within 40 fs and that ground state recovery occurs with a time constant of 410 fs, mainly through the $Sn\pi*/S_0$ CoI, reached by out-of-plane motion of the $-NH_2$ moiety, following the same $L_a \rightarrow Sn\pi* \rightarrow S_0$ mechanism predicted by the same method in the gas phase. This conclusion could depend on the underestimation of the energy barrier associated with the $Sn\pi* \rightarrow S_0$ decay and to the fact that for 9H-adenine $Sn\pi*$ is ~0.1 eV closer to $L_a$ than for 9Me-Ade (and adenosine), increasing the possibility of $L_a \rightarrow Sn\pi*$ population transfer.

## 4.4 Guanine

PCM/TD-PBE0 calculations on a model including a 9-methylGua molecule + five water molecules of the first solvation shell provide a picture close to that just described for Ade. In water, after an initial very steep region, the $L_a$ surface exhibits a flat plateau, likely responsible for those emission maxima [121]. A barrierless path connects this region with an $L_a/S_0$ CoI, which is reached by the out-of-plane motion of the amino substituent, while the ring adopts a puckered structure, as in the gas phase (see Fig. 5) [120]. $n\pi*$ and $\pi\sigma*$ states are also not expected to be involved in the excited state dynamics. For guanine the picture provided by PCM/TD-PBE0 geometry optimizations is similar to that obtained by means of QM/MM dynamical simulations, where the QM part (9H-guanine) was treated at the semiempirical OM2/MRCI level, while the MM part (water) was described by the TIP3P force field [135]. The dynamics simulations show ultrafast non-radiative decay for

9H-guanine in water that is even slightly faster than in the gas phase, with time constants of 20 fs and around 0.3 ps for the $S_2 \rightarrow S_1$ and $S_1 \rightarrow S_0$ internal conversions, respectively. They predict a change in the $S_1 \rightarrow S_0$ decay mechanism when going from the gas phase to aqueous solution: the major pathway for 9H-guanine in water involves a conical intersection with an out-of-plane distortion of the carbonyl oxygen atom, which does not play any significant role in the gas phase, where the decay mainly proceeds via two other conical intersections characterized by ring distortions and out-of-plane displacement of the amino group, respectively [135].

PCM/TD-PBE0 calculations can also give an account of the much longer excited state lifetime at acidic pH. In this case, a real and stable minimum is present on the $L_a$ surface, where the N7 and C8 hydrogen atoms are out of the molecular plane (see see Fig. 5) [121]. The results obtained including a different number (five or six) explicit water molecules in the computational model have been compared, and, interestingly, the out-of-plane distortion is larger for the model with five water molecules, since with six water molecules, an additional hydrogen bond between the solvent molecules of the first solvation shell decreases the conformational flexibility of the water molecule hydrogen bonded to the N7–H group (see Fig. 5). Although the general picture is qualitatively the same for both models, the computed fluorescence energies are different (by 0.25 eV), suggesting that the choice of the number and/or the position of the water molecules that are explicitly included in the QM calculations is not anodyne.

## 5    Concluding Remarks

In this chapter we have concisely reviewed the outcome of the theoretical studies tackling the description of nucleobase excited states in solution.

From the methodological point of view, notwithstanding the fact that the study of photoactivated processes in condensed phases involves additional difficulties with respect to that of isolated molecules, thanks to the impressive advances made in the last few years, a range of methods are available for getting a fairly accurate description of solvent effects in the Franck–Condon region, and, thus, a reliable interpretation of absorption spectra. As we have discussed above, each method has its own advantages and limitations, and the choice between them depends on the process/system of interest.

PCM appears as a cheap but reliable model to estimate bulk solvent effects on the different excited states. On the other hand, accurate absorption and emission energies can be obtained only by using state-specific approaches and, when treating hydrogen bonding solvents, by explicitly including the cybotactic region in the calculations. In general, mixed continuum/discrete approaches are effective, and recent advances in mixed PCM/QM/MM approaches very promising.

For what concerns the study of the FC region, for all the bases (with the possible exception of cytosine, for which the number studies in solution is more limited)

several theoretical studies in solution, employing different electronic methods and solvation models, are available. It can be considered a fact that $n\pi^*$ transitions are disfavored both by an increase of solvent polarity and, especially, of the solvent hydrogen bond ability. On the other hand, solvent effects are smaller for $\pi\pi^*$ transitions which are, in general, weakly red-shifted with respect to the gas phase (cytosine should be an exception, likely exhibiting the opposite behavior). From the quantitative point of view, $n\pi^*$ transitions can be relatively destabilized by up to 0.7 eV with respect $\pi\pi^*$ transitions, when going from the isolated molecules to the water solution. For some bases (uracil, thymine, and adenine) solvent can reverse the energy ordering with respect to the gas phase, changing the position and the effectiveness of the crossings among the different excited states. As a consequence, much caution has to be used when employing calculations on isolated molecules to interpret experimental results obtained in condensed phases. Furthermore, since the nature of the crossings depends both on the solvent and on the features of the PES for the isolated molecules, we cannot expect that a given solvent always affects the decay in the same direction. In other words, for some compounds water can increase the population transfer between two excited states, for others it can have the opposite effect (or no effect at all).

Besides the obvious effect on the relative energy of the excited states (and of the different tautomers), solvent can also affect the dynamics in more subtle ways. For example, as suggested in some studies on purines [121], it can modulate the shape of the PES, affecting the motion to the CoI with $S_0$ and the interplay between planar and non-planar regions of the PES. For guanine, the CI is reached in the gas phase by out-of-plane motion of the amino substituent: this process is expected to lead to a significant rearrangement of its solvation shells, affecting the dynamical behavior of guanine and giving account of the slower excited-state decay with respect to the gas phase. In this regard, we can understand why Gua is the only base for which solvent could change the structural rearrangements necessary to reach the CoI with $S_0$ [135]. On the other hand, the studies available for the other bases suggest that solvent does not qualitatively change the motion to the CoIs with $S_0$ with respect to the results obtained on the isolated bases.

In any case, the number of studies tackling the analysis of the excited state minima and/or of the crossings with $S_0$, and therefore of the radiative and non-radiative decay in solution, is much smaller than for the FC region (not mentioning those existing in the gas phase). This is likely one of the most significant challenges for the future. Methodological advances in the calculation of analytic energy gradient in solution for a larger number of electronic methods would be extremely useful. At the same time, in order to get a good estimate of vibrational effects on the emission spectra, the development of procedures able to treat accurately large amplitude structural rearrangements is important.

From a dynamical point of view, solvent has been suggested to affect the diabatic couplings between the nucleobase excited states [104, 119], and a reliable treatment of these effects is very important to obtain an accurate description of the excited state dynamics. Also in this respect, the number of dynamical (fully

quantum or semiclassical) studies of nucleobases in solution is much more limited than in the gas phase.

The large number of degrees of freedom to be considered for studying a molecule in condensed phases is very challenging for quantum dynamical methods, though approaches based on hierarchical representation of the nonadiabatic Hamiltonian in blocks [136] are promising tools for studying large systems, with the possibility of including solvent as a bath [137]. Regarding semiclassical simulations, they often rely on an "ad hoc" parameterization of the electronic semiempirical Hamiltonian [135, 138] and/or include solvent effects by QM/MM methods, and the accuracy of this approach in the study of the dynamics at CoIs always has to be careful checked.

A last issue, often overlooked, concerns vibrational cooling, the process responsible for the dissipation of the energy deposited in a molecule by light absorption. Solvent controls this process [139], which can directly affect the photophysical and photochemical reactivity: until the energy is dissipated, it is available for further reaction. Also in this case, suitable theoretical treatments, likely based on dynamical simulation explicitly including solvent molecules, would be very useful.

In conclusion, computational studies of photoexcited bases in solution have known impressive advances in the last decade. On the other hand, further developments of dynamical approaches are necessary to overcome the last obstacles towards a full and direct comparison between experiments and calculations in this challenging but fascinating field.

# References

1. Cadet J, Vigny P (1990) In: Morrison H (ed) The photochemistry of nucleic acids. New York, Wiley
2. Taylor JS (1994) Acc Chem Res 27:76
3. Crespo-Hernandez CE, Cohen B, Kohler B (2004) Chem Rev 104:1977
4. Middleton CT, de La Harpe K, Su C, Law YK, Crespo-Hernadez CE, Kohler B (2009) Annu Rev Phys Chem 60:13
5. Shukla MK, Leszcynski J (eds) (2008) Radiation induced molecular phenomena in nucleic acids: a comprehensive theoretical and experimental analysis. Springer, Amsterdam
6. Markovitsi D, Gustavsson T, Talbot F (2007) Photochem Photobiol Sci 6:717
7. Markovitsi D, Gustavsson T, Vayá I (2010) J Phys Chem Lett 1:3271
8. Kohler B (2010) J Phys Chem Lett 1:2047
9. Gustavsson T, Improta R, Markovitsi D (2010) J Phys Chem Lett 1:2025
10. de La Harpe K, Kohler B (2011) J Phys Chem Lett 2:133
11. Santoro F, Barone V, Improta R (2009) J Am Chem Soc 131:15232
12. Biemann L, Kovalenko SA, Kleinermanns K, Mahrwald R, Markert M, Improta R (2011) J Am Chem Soc 133:19664
13. Improta R, Barone V (2011) Angew Chem 50:12016

14. Takaya T, Su C, de La Harpe K, Crespo-Hernandez CE, Kohler B (2008) Proc Natl Acad Sci U S A 105:10285
15. Crespo-Hernandez CE, Cohen B, Kohler B (2005) Nature 436:1141
16. Lu Y, Lan Z, Thiel W (2011) Angew Chem Int Ed 50:6864
17. Conti I, Altoé P, Stenta M, Garavelli M, Orlandi G (2010) Phys Chem Chem Phys 12:5016
18. Santoro F, Barone V, Improta R (2007) Proc Natl Acad Sci U S A 104:9931
19. Improta R (2008) Phys Chem Chem Phys 10:2656
20. Serrano-Andrés L, Merchán M (2009) J Photochem Photobiol C 10:21
21. Shukla MK, Leszczynski J (2007) J Biomol Struct Dyn 25:93
22. Matsika S, Krause P (2011) Ann Rev Phys Chem 62:621. Leone SR, Cremer PS, Groves JT, Johnson MA (eds)
23. Kleinermanns K, Nachtigallová D, de Vries MS (2013) Int Rev Phys Chem 32:308
24. Gonzalez L, Escudero D, Serrano-Andrés L (2012) Chemphyschem 13:28
25. Barbatti M, Nachtigallova D, Aquino AJA, Szymczak JJ, Hobza P, Lischka H (2010) Proc Natl Acad Sci U S A 107:21453
26. Barbatti M, Lan Z, Crespo-Otero R, Szymczak JJ, Lischka H, Thiel W (2012) J Chem Phys 137:22A503
27. Picconi D, Ferrer FJA, Improta R, Lami A, Santoro F (2013) Faraday Disc 163:223
28. Hudock HR, Martinez TJ (2008) Chemphyschem 9:2486
29. Hudock HR, Levine BG, Thompson AL, Satzger H, Townsend D, Gador N, Ullrich S, Stolow A, Martinez TJ (2007) J Phys Chem A 111:8500
30. Merchán M, Gonzalez-Luque R, Climent T, Serrano-Andres L, Rodriguez E, Reguero M, Pelez DJ (2006) J Phys Chem B 110:26471
31. Lan ZG, Fabiano E, Thiel W (2009) J Phys Chem B 113:3548
32. Asturiol D, Lasorne B, Worth GA, Robb MA, Blancafort L (2010) Phys Chem Chem Phys 12:4949
33. Picconi D, Barone V, Lami V, Santoro F, Improta R (2011) Chemphyschem 12:1957
34. Richter M, Marquetand P, González-Vázquez J, Solá I, González L (2012) J Phys Chem Lett 3:3090
35. Mennucci B, Cammi R (eds) (2007) Continuum solvation models in chemical physics: from theory to applications. Wiley, New York
36. Tomasi J, Persico M (1994) Chem Rev 94:2027
37. Tomasi J, Mennucci B, Cammi R (2005) Chem Rev 105:2999
38. Improta R (2011) UV-visible absorption and emission energies in condensed phase by PCM-TD-DFT methods. In: Barone V (ed) Computational strategies for spectroscopy: from small molecules to nanosystems. Wiley, Chichester, pp 39–76
39. Shukla MK, Leszczynski J (2010) Electronic-excited-state structures and properties of hydrated DNA bases and base pairs. In: Han K-L, Zhao G-J (eds) Hydrogen bonding and transfer in the excited state, vol 1 and 2. Wiley, Chichester
40. Horbg MO, Gardecki JA, Papazyan A, Maroncelli M (1995) J Phys Chem 99:17311
41. Maroncelli M, Fleming GR (1987) J Chem Phys 86:6221
42. Orozco M, Luque FJ (2000) Chem Rev 100:4187
43. Cramer CJ, Truhlar DG (1999) Chem Rev 99:2161
44. Gao J (1996) Acc Chem Res 29:298
45. Monard G, Merz KM Jr (1999) Acc Chem Res 32:904
46. Pavone M, Crescenzi O, Morelli G, Rega N, Barone V (2006) Theor Chem Acc 116:456
47. Sanchez ML, Aguilar MA, Olivares del Valle FJ (1997) J Comput Chem 18:313
48. Martin ME, Sanchez ME, Olivares Del Valle FJ, Aguilar MA (2000) J Chem Phys 113:6308
49. Miertus S, Scrocco E, Tomasi J (1981) J Chem Phys 55:117
50. Cammi R, Corni S, Mennucci B, Tomasi J (2005) J Chem Phys 122:104513
51. Corni S, Cammi R, Mennucci B, Tomasi J (2005) J Chem Phys 123:134512
52. Caricato M, Mennucci B, Tomasi J, Ingrosso F, Cammi R, Corni S, Scalmani G (2006) J Chem Phys 124:124520

53. Improta R, Barone V, Scalmani G, Frisch MJ (2006) J Chem Phys 125:54103
54. Improta R, Scalmani G, Frisch MJ, Barone V (2007) J Chem Phys 127:74504
55. Cossi M, Barone V (2001) J Chem Phys 115:4708
56. Banyasz A, Gustavsson T, Onidas D, Changenet-Barret P, Markovitsi D, Improta R (2013) Chem Eur J 19:3762
57. Hunger K, Buschhaus L, Biemann L, Braun M, Kovalenko S, Improta R, Kleinermanns K (2013) Chem Eur J 19:5425
58. Improta R (2014) Chem. Eur. J. in press. 10.1002/chem.201400065
59. Caricato M (2013) J Chem Phys 139:044116
60. Caricato M, Lipparini F, Scalmani G, Cappelli C, Barone V (2013) J Chem Theor Comp 9:3035
61. Weijo V, Mennucci B, Frediani L (2010) J Chem Theor Comp 11:3358
62. Cossi M, Barone V (2000) J Chem Phys 112:2427
63. Improta R, Barone V (2009) Theochem 914:87
64. Chahinian M, Seba HB, Ancian B (1998) Chem Phys Lett 285:337
65. Gaigeot MP, Sprik M (2004) J Phys Chem B 108:7458
66. Mennucci B (2013) Phys Chem Chem Phys 18:6583
67. Lipparini F, Cappelli C, Barone V (2012) J Chem Theor Comp 8:4153
68. Fedorov DG, Kitaura K (2005) J Chem Phys 122:054108
69. Fedorov DG, Ishida T, Kitaura K (2005) J Phys Chem A 109:2638
70. Gordon M, Freitag M, Bandyopadhyay P, Jensen J, Kairys V, Stevens W (2001) J Phys Chem A 105:293
71. Gordon MS, Fedorov DG, Pruitt SR, Slipchenko LV (2012) Chem Rev 112:632
72. DeFusco A, Ivanic J, Schmidt MW, Gordon MS (2011) J Phys Chem A 115:4574
73. Scalmani G, Frisch MJ, Mennucci B, Tomasi J, Cammi R, Barone V (2006) J Chem Phys 124:094107
74. Karlstrom G, Lindh R, Malmqvist P-A, Roos BO, Ryde U, Veryazov V, Widmark P-O, Cossi M, Schimmelpfennig B, Neogrady P, Seijo L (2003) Comput Mater Sci 28:222
75. Barone V, Cossi M, Tomasi J (1997) J Chem Phys 107:3210
76. Improta R, Barone V, Santoro F (2007) Angew Chem Int Ed 46:405
77. Improta R, Barone V, Santoro F (2007) J Phys Chem B 111:14080
78. Santoro F, Improta R, Lami A, Bloino J, Barone V (2007) J Chem Phys 126:84509
79. Biczysko M, Bloino J, Santoro F, Barone V (2011) Time-independent approaches to simulate electronic spectra lineshapes: from small molecules to macrosystems. In: Barone V (ed) Computational strategies for spectroscopy: from small molecules to nanosystems. Wiley, Chichester, UK, p 361
80. Barone V, Improta R, Rega N (2008) Acc Chem Res 41:605
81. Ferrer FJA, Improta R, Santoro F, Barone V (2011) Phys Chem Chem Phys 13:17007
82. Baiardi A, Bloino J, Barone V (2013) J Chem Theor Comp 9:4097
83. Lami A, Santoro F (2011) Time-dependent approaches to calculation of steady-state vibronic spectra: from fully quantum to classical approaches. In: Barone V (ed) Computational strategies for spectroscopy: from small molecules to nanosystems. Wiley, Chichester, p 475
84. Barone V, Baiardi A, Biczisko M, Bloino J, Cappelli C, Lipparini F (2012) Phys Chem Chem Phys 14:12404
85. Ferrer FJA, Cerezo J, Stendardo E, Improta R, Santoro F (2013) J Chem Theor Comp 9:2072
86. Gustavsson T, Banyasz A, Lazzarotto E, Markovitsi D, Scalmani G, Frisch MJ, Barone V, Improta R (2006) J Am Chem Soc 128:607
87. Szalay PG, Watson T, Perera A, Lotrich VF, Bartlett RJ (2012) J Phys Chem A 116:6702
88. Epifanovsky E, Kowalski K, Fan P-D, Valiev M, Matsika S, Krylov AI (2008) J Phys Chem A 112:9983
89. Improta R, Barone V (2004) J Am Chem Soc 126:14320
90. Mercier Y, Santoro F, Reguero M, Improta R (2008) J Phys Chem B 112:10769

91. Gustavsson T, Sarkar N, Lazzarotto E, Markovitsi D, Barone V, Improta R (2006) J Phys Chem B 110:12843
92. Santoro F, Barone V, Gustavsson T, Improta R (2006) J Am Chem Soc 128:16312
93. Gustavsson T, Sarkar N, Lazzarotto E, Markovitsi D, Improta R (2006) Chem Phys Lett 429:551
94. Improta R, Barone V (2008) Theor Chem Acc 120:491
95. Gustavsson T, Sarkar N, Banyasz A, Markovitsi D, Improta R (2007) Photochem Photobiol 83:595
96. Gustavsson T, Banyasz A, Sarkar N, Markovitsi D, Improta R (2008) Chem Phys 350:186
97. Etinski M, Marian CM (2010) Phys Chem Chem Phys 12:4915
98. Kistler KA, Matsika S (2009) J Phys Chem A 113:12396
99. Zazza C, Amadei A, Sanna N, Grandi A, Chillemi G, Di Nola A, D'abramo M, Aschi M (2006) Phys Chem Chem Phys 8:1385
100. Ludwig V, Coutinho K, Canuto S (2007) Phys Chem Chem Phys 9:4907
101. Olsen JM, Aidas K, Mikkelsen KV, Kongsted J (2010) J Chem Theor Comp 6:249
102. Bistafa C, Canuto S (2013) Theor Chem Acc 132:1299
103. Santoro F, Improta R, Barone V (2009) Theor Chem Acc 123:273
104. Improta R, Barone V, Lami A, Santoro F (2009) J Phys Chem B 113:14491
105. Clark LB, Tinoco I Jr (1965) J Am Chem Soc 87:11
106. Klamt A, Schüürmann (1993) J Chem Soc Perkin Trans 2 799
107. Hare PM, Crespo-Hernandez C, Kohler B (2007) Proc Natl Acad Sci U S A 104:435
108. Gustavsson T, Improta R, Banyasz A, Vaya I, Markovitsi D (2012) J Photochem Photobiol A 234:37
109. Banyasz A, Karpati S, Mercier Y, Reguero M, Gustavsson T, Markovitsi D, Improta R (2010) J Phys Chem B 114:12708
110. Blancafort L, Migani A (2007) J Photochem Photobiol A 190:283
111. Bazso G, Tarczay G, Fogarasi G, Szalay PG (2011) Phys Chem Chem Phys 13:6799
112. Conti I, Garavelli M, Orlandi G (2009) J Am Chem Soc 131:16108
113. Perun S, Sobolewski AL, Domcke W (2005) J Am Chem Soc 127:6257
114. Serrano-Andres L, Merchán M, Borin AC (2006) Proc Natl Acad Sci U S A 103:8691
115. Gustavsson T, Sarkar N, Vaya I, Jimenez MC, Markovitsi D, Improta R (2013) Photochem Photobiol Sci 12:1375
116. Shohei Y, Kato S (2007) J Am Chem Soc 129:2901
117. Ludwig V, da Costa ZM, do Amaral MS, Borin AC, Canuto S, Serrano-Andres L (2010) Chem Phys Lett 492:164
118. Mennucci B, Toniolo A, Tomasi J (2001) J Phys Chem A 105:4749
119. Lan ZG, Lu Y, Fabiano E, Thiel W (2011) Chemphyschem 12:1989
120. Serrano-Andrés L, Merchán M, Borin AC (2008) J Am Chem Soc 130:2473
121. Karunakaran K, Kleinermanns K, Improta R, Kovalenko SA (2009) J Am Chem Soc 131:5839
122. Parac M, Doerr M, Marian CM, Thiel W (2010) J Comp Chem 3:90
123. Fulscher MP, Serrano-Andres L, Roos BO (1997) J Am Chem Soc 119:6168
124. Mennucci B, Toniolo A, Tomasi J (2001) J Phys Chem A 105:7126
125. Levine BG, Ko C, Quenneville J, Martinez TJ (2006) Mol Phys 104:1039
126. Tapavicza E, Tavernelli I, Rothlisberger U (2007) Phys Rev Lett 98:023001
127. Tapavicza E, Tavernelli I, Rothlisberger U, Filippi C, Casida ME (2008) J Chem Phys 129:124108
128. Improta R (2012) J Phys Chem B 116:14261
129. Banyasz A, Douki T, Improta R, Gustavsson T, Onidas D, Vayá I, Perron M, Markovitsi D (2012) J Am Chem Soc 134:14834
130. Hare PM, Crespo-Hernandez CE, Kohler B (2006) J Phys Chem B 110:18641
131. Kistler KA, Matsika S (2008) J Chem Phys 128:215102

132. Barbatti M, Aquino AJA, Szymczak JJ, Nachtigallova D, Lischka H (2011) Phys Chem Chem Phys 13:6145
133. Blancafort L (2007) Photochem Photobiol 83:603
134. Kistler KA, Matsika S (2010) Phys Chem Chem Phys 12:5024
135. Heggen B, Lan Z, Thiel W (2012) Phys Chem Chem Phys 14:8137
136. Cederbaum LS, Gindensperger E, Burghardt I (2005) Phys Rev Lett 94:113003
137. Balevicius V Jr, Gelzinis A, Abramavicius D, Mancal T, Valkunas L (2012) Chem Phys 404:94
138. Cusati T, Granucci G, Marténez-Núnez E, Martini F, Persico M, Vázquez S (2012) J Phys Chem A 116:98
139. Middleton CT, Cohen B, Kohler B (2007) J Phys Chem A 111:10460

# Index